

## 研究課題名：パラメトリック X線を用いた高圧下における XANES 研究

研究代表者：滝沢 武男 (日本大学文理学部物理学科)

研究従事者：高橋 博樹 (日本大学文理学部物理学科)

共同研究者：松下 裕亮 (東海大学開発工学部情報通信工学科)

### 【研究目的】

磁性体、超伝導体、半導体の物理的性質には、内部の電子状態が大きく反映される。例えば、現在、多くの研究者の興味を引きつけている高温超伝導体は、共通の性質として Cu-O ネットワークを有し、このネットワーク中の Cu の電子状態（価数）は、酸素量や構成元素により影響を受け、ある価数の条件のもとで超伝導を示す。また、金属磁性の本質を見極めるために精力的に研究が進められているヘビーフェルミオンといわれる物質群においては、伝導電子と局在電子との相互作用が磁性の発現の根幹であると考えられ、その電子状態の実験的説明は重要であり、また、大きな期待が寄せられている。半導体も含めこれらの物質の物理的性質を調べるためには、元素置換を行いその電子状態への影響を調べる人が多い。ところが元素置換では置換量が限られ、ランダムネス等の副次的な効果が混入するため本質が見えてこない場合がある。

これに対し、高圧力技術を利用した実験では物質を静水圧的に圧縮することにより連続的に原子間距離等の構造を変化させながら電子状態の変化を調べることができる。高圧下の電気抵抗、帯磁率測定による超伝導転移温度  $T_c$ 、磁気転移温度の圧力効果など非常にたくさんの圧力下の物性が報告されている。しかし、これらを解釈するための電子状態に関する情報がきわめて少ない。特に高温超伝導体では圧力をかけることによって  $\text{HgBa}_2\text{Ca}_2\text{Cu}_3\text{O}_{10}$  が世界最高の  $T_c=164\text{ K}$  を示すことが報告されているが、メカニズムに関する理解は進んでおらず、電子状態に関する実験データもほとんどない。それ故、Cu の圧力下の電子状態に関する実験への期待は大きい。

高圧下で光学的に電子状態を調べるためには、光学的測定のほかに X線吸収実験(XANES)が考えられる。特に X線吸収実験では特性吸収端付近に現れるスペクトルの微細構造が元素の電子構造や対称性を強く反映することから、価数などの電子状態に関する情報が得られる。現在、ダイヤモンドアンビル高圧発生装置を用いることによって 100 万気圧以上の圧力下での実験が可能である。このような流れの中で、本研究グループ（高橋）は、すでに磁性体  $\text{Yb}_4\text{As}_3$  の磁性の起源を調べるために高エネ研 P F で高圧下の XANES 測定を行い、Yb の価数の圧力効果を調べた。この物質は圧力下で様々な電氣的・磁氣的測定が行われており XANES 測定からは物性理解のための基礎データが得られている。

現在、日本大学電子線利用施設では波長可変でエネルギー分解能に優れたパラメトリック X線の施設利用の準備が進められており、本研究ではこの施設に高圧 XANES 測定システムを構築し、共同利用施設として整備すると同時に、磁性体、超伝導体、半導体の電子状態に関する基礎データを蓄積する事を目的とする。

### 【研究概要】

ダイヤモンドアンビルセル(DAC)を用いた高圧下の XANES 測定はすでに海外でも行われ、また国内でも我々のグループによって有用なデータが得られているが高圧技術上の問題、限られたマシンタイムの問題やデータの解釈の問題からさほど進展していないのが現状である。特に高圧実験で

はダイヤモンドが全波長領域にわたって透明ではないので、吸収端を測定できる元素が限られてくる。このような事情から今までのところ高圧下の XANES 測定は特定の希土類元素に限られることが多かった。また高温超伝導体中の Cu の吸収端のエネルギー領域ではダイヤモンドは X 線に対し不透明であるので、X 線をダイヤモンドアンビルの間の Be 製のガスケットを透過させて実験を行うことを計画している。このため DAC を購入し Be をガスケットとして加圧試験を行う。圧力測定には DAC 内にルビーのチップを入れ、その蛍光波長を測定することによって行う。そのための蛍光測定システムを構築する。

次に、日本大学電子線利用施設のパラメトリック X 線ビームラインに XANES 測定用の X 線検出システムを構築する。試料の前後にビームの強度を測定する検出器をおき前後の強度比から吸収係数を求める。大気圧中でいくつかの典型的な物質のスペクトルの測定を行う。さらに低温測定ができるように 4K まで冷却できる冷凍機を購入し、冷却テストを行う。低温での圧力テストも行う。DAC 内にセットした試料について吸収係数の測定を行う。

1. 高温超伝導体中の Cu の XANES を高圧下で測定し超伝導転移温度  $T_c$  と Cu 価数との関連を調べる。特に最高の  $T_c$  を示す Hg 系酸化物超伝導体について高圧下で測定を行う。Cu の XANES を測定するために X 線はダイヤモンドを通さないでガスケットの Be を透過させるようにする。
2. ヘビーフェルミオンと呼ばれる物質群について高圧下での XANES 測定を行う。Yb、Tm の化合物については実績がある。Ce、Eu の化合物など価数変化によって電気的・磁氣的性質が大きく変化し注目を集めている物質の XANES 測定を行う。Ce、Eu も X 線はダイヤモンドを通さないで Be 製のガスケットを透過させるようにする。
3. 圧力下で半導体金属転移を示す物質の金属の価数変化を調べる。半導体金属転移は様々な要因で起こることが知られているが、価数を圧力下で調べた例はなく、転移機構解明に新たな情報を提供できる。

## 【研究業績等】

### ・ 発表論文

- (1) Ho-Ba-Cu-O 系バルク超伝導材料の臨界電流密度と捕捉磁場特性, 田中弘信, 成木紳也, 坂井直道, 村上雅人, 平林泉, 滝沢武男: 日本金属学会誌 第 68 卷 第 9 号 (2004) 693-697
- (2) Flux motion in Y-Ba-Cu-O bulk superconductors during pulse field magnetization, K.Yoshizawa, S.Nariki, N.Sakai, M.Murakami, I.Hirabayashi, and T.Takizawa: Superconductor Science and Technology 17 74-78 (2004)
- (3) Phase diagrams of the pseudo-binary systems of BaS-Ga<sub>2</sub>S<sub>3</sub> and BaS-In<sub>2</sub>S<sub>3</sub>, C. Hidaka, E. Yamagishi and T. Takizawa: In press
- (4) Single Crystal growth of SrIn<sub>2</sub>VI<sub>4</sub> (VI=Se,S) Compounds Solidifying through Supercooling, C. Hidaka, E. Yamagishi and T. Takizawa: Journal of Crystal Growth 275 433-437 (2005)
- (5) Effect of pinning on the flux motion of Gd-Ba-Cu-O bulk superconductors, K. Yoshizawa, S. Nariki, M. Murakami, T. Takizawa: Physica C, 392-396 (2003) 391-395
- (6) Radiative and non-radiative processes of Ce related transitions in CaGa<sub>2</sub>S<sub>4</sub> and SrGa<sub>2</sub>S<sub>4</sub>, A. Kato, M. Yamazaki, H. Najafov, K. Iwai, A. Bayramov, C. Hidaka, T. Takizawa and S. Iida: Journal of Physics and Chemistry of Solids 64 1511-1517 (2003)
- (7) Determination of a pseudo-binary SrSe--Ga<sub>2</sub>Se<sub>3</sub> phase diagram and single crystal growth of SrGa<sub>2</sub>Se<sub>4</sub> compounds, Chiharu Hidaka, Nobuyasu Makabe and Takeo Takizawa: Journal of Physics and Chemistry of Solids 64 1797-1800 (2003)
- (8) ESR study of Ce<sup>3+</sup> ions doped in the CdIn<sub>2</sub>S<sub>4</sub> lattice, Takeo Takizawa, Hiroyuki Ozawa and Chiharu Hidaka: Journal of Physics and Chemistry of Solids 64 1807-1810 (2003)
- (9) Light figure spectroscopy of optically active anisotropic materials Nobuyuki Yamamoto, Nazim Mamedov, Yonggu Shim, Chiharu Hidaka, Takeo Takizawa, Eiji Niwa and Katashi Masumoto Journal of Physics and Chemistry of Solids 64 1959-1962 (2003)
- (10) Schottky properties of CuInSe<sub>2</sub> single crystals grown by the Horizontal Bridgman method with controlling Se vapor pressure Hiroki Matsushita, Yukio Tojo and Takeo Takizawa Journal of Physics and Chemistry of Solids 64 1825-1829 (2003)
- (11) Extended Application of Light Figures to Optically Active Materials with Transversally Isotropic Dielectric Function Nazim Mamedov, Nobuyuki Yamamoto, Yonggu Shim, Yuichiro Ninomiya and Takeo Takizawa Jpn. J. Appl.Phys. 42 5145-5152 (2003)
- (12) IIa-III<sub>2</sub>-VI<sub>4</sub> 系化合物の単結晶作製, 滝沢武男, 日高千晴 応用物理 第 71 卷 第 5 号 (2002) 553-556
- (13) Flux creep properties in Dy-Ba-Cu-O bulk superconductors, H.Enomoto, K.Inoue, S.Nariki, M.Murakami, T.Takizawa: Physica C 378-381 513--516 (2002)
- (14) Cu-based multinary compounds and their crystal growth: synthesis processes, phase diagrams and control of vapor pressures, Hiroaki Matsushita, Akinori Katsui and Takeo Takizawa: Journal of Crystal Growth 237-239 1986-1992 (2002)
- (15) Single-crystal growth and optical properties of undoped and Ce<sup>3+</sup> doped CaGa<sub>2</sub>S<sub>4</sub>, C.Hidaka and T.Takizawa: Journal of Crystal Growth 237-239 2009-2013 (2002)
- (16) Thermal analysis of chemical reaction processes of chalcopyrite compound semiconductors, Hiroaki

Matsushita and Takeo Takizawa: IPAP Book Series 1, Japanese Research Review for Pioneering Ternary and Multinary Compounds in the 21st Century, 11-16 (2002)

- (17) Single crystal growth of  $\text{CaGa}_2\text{S}_4$  and  $\text{SrGa}_2\text{S}_4$ , Chiharu Hidaka and Takeo Takizawa: IPAP Book Series 1, Japanese Research Review for Pioneering Ternary and Multinary Compounds in the 21st Century, 68-72 (2002)
- (18) Phase diagrams and crystal structures of the  $\text{CdS-In}_2\text{S-Ga}_2\text{S}_3$  system, Kimitaka Asaka, Chiharu Hidaka, Takeo Takizawa and Hiroaki Matsushita: IPAP Book Series 1, Japanese Research Review for Pioneering Ternary and Multinary Compounds in the 21st Century, 73-78 (2002)
- (19) Defect physics of  $\text{CuInSe}_2$  and  $\text{CuGaSe}_2$  bulk single crystals grown by the horizontal Bridgman method, Hiroaki Matsushita and Takeo Takizawa: IPAP Book Series 1, Japanese Research Review for Pioneering Ternary and Multinary Compounds in the 21st Century, 190-196 (2002)
- (20) The viscous flux flow and flux creep induced by pulsed magnetic field in YBCO disk, T. Kono, M. Tomita, M. Murakami and T. Takizawa: *Physica C*, 357-360 537-540 (2001)
- (21) AC susceptibility measurement for Nd-Ba-Cu-O superconductor, Y. Akamatsu, K. Waki, K. Inoue, M. Murakami and T. Takizawa: *Physica C* 357-360 541-544 (2001)
- (22) Two-step transition of  $(\text{Nd}_{0.33}\text{Eu}_{0.33}\text{Gd}_{0.33})\text{Ba}_2\text{Cu}_3\text{O}_x$  superconductors in high fields, T. Matano, M. R. Koblishka, M. Muralidar, M. Murakami and T. Takizawa: *Physica C* 357-360 548-551 (2001)
- (23) AC susceptibility of high- $T_c$  superconductor  $\text{REBa}_2\text{Cu}_3\text{O}_y$ , H. Enomoto, K. Inoue, M. Muralidhar, M. Murakami and T. Takizawa: *Physica C* 357-360 545-547 (2001)
- (24) Defect properties of  $\text{CuInS}_2$  single crystals grown by horizontal Bridgman method with controlling S vapor pressure, Hiroaki Matsushita, Tomohiro Mihira and Takeo Takizawa: *Jpn. Journal of Applied Physics* 40 4789-4793 (2001)
- (25) Phase diagram of the  $\text{CaS-Ga}_2\text{S}_3$  system and melt growth of  $\text{CaGa}_2\text{S}_4$  single crystals, C. Hidaka-Komatsu and T. Takizawa: *Journal of Crystal Growth* 222-3 574-578 (2001)
- (26) Growth and Crystallographic Properties of II-III<sub>2</sub>-VI<sub>4</sub> Compounds --- Focusing on the Sulfides---(Invited), T. Takizawa, C. Hidaka, K. Asaka, T. Isomoto and H. Matsushita: *Jpn. Journal of Applied Physics* 39 35-40 (2000) Supp. 39-1 Proc. of 12th ICTMC, R.O.C., 2000
- (27) Probing the Interface and Microstructures in  $\text{CdS/CuInSe}_2$  and  $\text{InGaAsN/GaAs}$  Heterojunctions by Synchrotron Radiation (Invited), Y.L. Soo, S. Huang, Y.H. Kao, S.K. Deb, K. Ramanathan and T. Takizawa: *Jpn. Journal of Applied Physics* 39 29-34 (2000) Supp. 39-1 Proc. of 12th ICTMC, R.O.C., 2000
- (28) Single Crystal Growth of  $\text{SrGa}_2\text{S}_4$  by the Self-Flux Method, C. Hidaka and T. Takizawa: *Jpn. Journal of Applied Physics* 39 67-68 (2000) Supp. 39-1 Proc. of 12th ICTMC, R.O.C., 2000
- (29) Thermal and Crystallographic Analysis of  $\text{Cd}(\text{In}_x\text{Ga}_{1-x})_2\text{S}_4$  Compounds, K. Asaka, C. Hidaka, T. Takizawa and H. Matsushita: *Jpn. Journal of Applied Physics* 39 139-140 (2000) Supp. 39-1 Proc. of 12th ICTMC, R.O.C., 2000
- (30) Flux Motion in melt-processed YBCO in pulsed magnetic fields, T. Kono, M. Tomita, M. Murakami and T. Takizawa: *Physica C: Superconductivity*, 341-348 2437-2438 (2000)
- (31) Confirmation of Ba-rich  $\text{Nd}_{1+x}\text{Ba}_{2-x}\text{Cu}_3\text{O}_{7-\delta}$  solid solutions, G. Osabe, S.I. Yoo, N. Sakai, T. Higuchi, T. Takizawa, K. Yasohama and M. Murakami: *Supercond. Sci. Technol.* 13 637-640 (2000)
- (32) Flux motion in bulk YBCO induced by pulsed magnetic fields: T. Kohno, M. Tomita, M. Murakami and

T.Takizawa: Physica C, 341-348 (2000) 2437-2438

- (33) Ac susceptibility measurements for Nd-Ba-Cu-O superconductor, Y.Akamatsu, K.Waki, K.Inoue, M.Murakami and T.Takizawa: Supercond. Sci. Technol. 13 802-804 (2000)
- (34) Superconducting transitions of YBa<sub>2</sub>Cu<sub>3</sub>O<sub>x</sub> superconductors in high fields, T.Matano, M.R.Koblischka, B.W.Veal, M.Murakami and T.Takizawa: Supercond. Sci. Technol. 13 805-806 (2000)
- (35) V-I characteristics of a melt grown YBCO as revealed by a pulsed field, T.Takizawa, M.Yamazaki and M.Murakami: Physica B: Physics of Condensed Matter 284-288 845-846(2000)
- (36) Phase diagram of the SrS - Ga<sub>2</sub>S<sub>3</sub> system and its application to the single crystal growth of SrGa<sub>2</sub>S<sub>4</sub>, C.Komatsu and T.Takizawa: Journal of Crystal Growth 210 677-682 (2000)
- (37) Thermal analysis and synthesis from the melts of Cu-based quaternary compounds Cu-III-IV-VI<sub>4</sub> and Cu<sub>2</sub>-II-IV-VI<sub>4</sub> (II = Zn, Cd; III = Ga, In; IV = Ge, Sn; VI = Se), Hiroaki Matsushita, Takashi Maeda, Akinori Katsui and Takeo Takizawa: Journal of Crystal Growth 208 416-422 (2000)
- (38) Pressure Effect on the Antiferromagnetic Transition Temperature in CuFeO<sub>2</sub>, H. Takahashi, Y.Motegi, R.Tsuchigane, and M. Hasegawa, J.Magn.Magn.Mat. Vol.272-276 (2004) pp.216-217.
- (39) High pressure studies of anomalous electronic states of Y<sub>1-x</sub>U<sub>x</sub>Pd<sub>3</sub>, G.Oomi, T.Kagayama, Y.Aoki, H.Sato, Y.Onuki, H.Takahashi, N.Mori, J.Phys.:Condens. Matter Vol.16 (2004) pp.3385-3400.
- (40) Pressure effect on a ferromagnetic transition temperature of RuSr<sub>2</sub>GdCu<sub>2</sub>O<sub>8</sub>, J.Shibata, H.Goto, H.Takahashi, A.Matsushita, Y.Yamada, Physica C Vol.388-389 (2003) pp.235-236.
- (41) N.Motoyama, H.Eisaki, S.Uchida, N.Takeshita, N.Mori, T.Nakanishi, H.Takahashi, Electronic phase diagram of a hole-doped two-leg ladder system, Sr<sub>14-x</sub>Ca<sub>x</sub>Cu<sub>24</sub>O<sub>41</sub>, Europhys. Lett. Vol.58 , (2002), pp.758-763.
- (42) Metal to insulator transition of filled skutterudite PrRu<sub>4</sub>P<sub>12</sub> at low temperature and high pressures, I.Shirotni, J.Hayashi, T.Adachi, C.Sekine, T.Kawakami, T.Nakanishi, H.Takahashi, J.Tang, A.Matsushita, T.Matsumoto, Physica B Vol.322 (2002) pp.408-412.
- (43) 圧力装置の現状, 高橋博樹, 高圧力の科学と技術 第12巻第4号 (2002) pp.272-279.
- (44) H.Takahashi, H.Takahashi, T.Nakanishi, T.Arima, M.Noguchi, M.Oyanagi, N.Takashita, N.Môri, High-pressure effect on transport properties of spin-ladder compound Na<sub>1-x</sub>Ca<sub>x</sub>V<sub>2</sub>O<sub>5</sub> and Ca<sub>0.7</sub>Li<sub>0.3</sub>V<sub>2</sub>O<sub>5</sub>, J.Magn.Magn.Mat. Vol.226-230, (2001), pp.246-248.
- (45) H.Kobayashi, N.Takashita, N.Mori, H.Takahashi, T.Kamimura, Pressure-induced semiconductor-metal-semiconductor transitions in FeS, Phys. Rev.B Vol.63, (2001), p.115203.
- (46) T.Nakanishi, N.Motoyama, H.Mitamura, N.Takeshita, H.Takahashi, H.Eisaki, S.Uchida, T.Goto, H.Ishimoto, N.Môri, Pressure and field dependence in the spin-ladder Sr<sub>14-x</sub>Ca<sub>x</sub>Cu<sub>24</sub>O<sub>41</sub>, J.Magn.Magn.Mat. Vol.226-230 , (2001), pp.449-451.
- (47) DAC を用いた低温物性測定, 高橋博樹, 高圧力の科学と技術 第11巻 第3号 (2001) pp.195-202.
- (48) T.Nakanishi, H.Takahashi, N.Takeshita, N.Môri, N.Motoyama, H.Eisaki, S.Uchida, H.Fujino, T.Nagata, J.Akimitsu, Upper critical field of spin-ladder Sr<sub>2</sub>Ca<sub>12</sub>Cu<sub>24</sub>O<sub>41</sub>, Physica Vol.B281&282, (2000) ,pp.957-958.
- (49) I.Shirotni, K.Ohno, C.Sekine, T.Yagi, T.Kawakami, T.Nakanishi, H.Takahashi, J.Tang, A.Matsushita, T.Matsumoto, Electrical conductivity and superconductivity of La<sub>4</sub>As<sub>12</sub> (T=Fe, Ru, and Os) with

skutterudite-type structure., Physica Vol.B281&282, (2000) ,pp.1021-1023.

- (50) H.Hedo, T.Nakama, A.T.Burkov, K.Yagasaki, Y.Uwatoko, H.Takahashi, T.Nakanishi, N.Môri, Pressure-induced structural-phase transition of CeRu<sub>2</sub>, Physica Vol.B281&282 , (2000) ,pp.88-89.
- (51) S.Miyasaka, H.Takagi, Y.Sekine, H.Takahashi, N.Môri, R.J.Cava, Metal-Insulator transition and itinerant antiferromagnetism in NiS<sub>2-x</sub>Sex pyrite, J.Phys. Soc.Jpn Vol.69, (2000) ,pp.3166-3169.
- (52) H.Nozaki, H.Ikuta, Y.Yamada, A.Matsushita, H.Takahashi, I.Hirabayashi, U.Mizutani, Substitution effect on ferromagnetism in La<sub>4</sub>Ba<sub>2</sub>Cu<sub>2</sub>O<sub>10</sub>, Phys. Rev.B Vol.62 , (2000) ,pp.9555-9560.
- (53) T.Nakanishi, N.Motoyama, H.Mitamura, N.Takeshita, H.Takahashi, H.Eisaki, S.Uchida, N.Mori, Critical Field of Superconducting Spin-Ladder Sr<sub>14-x</sub>CaxCu<sub>24</sub>O<sub>41</sub>, Int.J.Mod.Phys. Vol.B14, (2000) , p.3617.

#### ・学会発表

- (1) H. Tanaka<sup>1,2</sup>, S. Nariki<sup>1</sup>, N. Sakai<sup>1</sup>, M. Murakami<sup>1,3</sup>, I. Hirabayashi<sup>1</sup>, T. Takizawa<sup>2</sup> ,  
1Superconductivity Research Laboratory, ISTE, 2Nihon University, 3Shibaura Institute of Technology,  
MICROSTRUCTURE AND SUPERCONDUCTING PROPERTIES OF Dy-Ba-Cu-O BULK  
SUPERCONDUCTORS FABRICATED IN VARIOUS OXGEN PARTIAL PRESSURES, 新潟コンベン  
ションセンター (朱鷺メッセ) , 平成 16 年 11 月
- (2) S. Nariki<sup>1</sup>, A. Mogi<sup>1,2</sup>, H. Tanaka<sup>1,2</sup>, N. Sakai<sup>1</sup>, M. Murakami<sup>1,3</sup>, I. Hirabayashi<sup>1</sup>, T. Takizawa<sup>2</sup>  
1Superconductivity Research Laboratory, ISTE, 2Nihon University, 3Shibaura Institute of  
Technology) EFFECT OF Y-Ba-Cu-O-M (M = Zr, Sn AND Ce) ADDITION ON THE  
SUPERCONDUCTING PROPERTIES OF MELT-TEXTURED Y123 BULK, 新潟コンベンションセ  
ンター (朱鷺メッセ) , 平成 16 年 11 月
- (3) Kato, S. Iida, M. Yamazaki, E. Yamagishi, C. Hidaka , T. Takizawa, Optical Gain due to the Eu  
Transition in the Alloy of Ca<sub>1-x</sub>EuxGa<sub>2</sub>S<sub>4</sub>, The 14th International Conference on Ternary and  
Multinary Compounds, 平成 16 年 10 月
- (4) C. Hidaka, E. Yamagishi, T. Takizawa, Photoluminescence spectra of rare earth doped CaGa<sub>2</sub>S<sub>4</sub> single  
crystals , The 14th International Conference on Ternary and Multinary Compounds, 平成 16 年 10  
月
- (5) S. Nomura, T. Takizawa, S. Endo, Electronic States of Lanthanide in the Ternary Thiogallate CaGa<sub>2</sub>S<sub>4</sub>,  
The 14th International Conference on Ternary and Multinary Compounds, 平成 16 年 10 月
- (6) E. Yamagishi, C. Hidaka, T. Takizawa, Preparation of Ca<sub>1-x</sub>EuxGa<sub>2</sub>S<sub>4</sub> crystals and their  
photoluminescence, absorption and excitation spectra, The 14th International Conference on Ternary  
and Multinary Compounds 平成 16 年 10 月
- (7) 田中弘信, 成木紳也, 坂井直道, 村上雅人, 平林泉, 滝沢武男, 種々の酸素分圧下で作製した  
Dy-Ba-Cu-O 系バルク材料の超伝導特性, 第 65 回応用物理学会学術講演会, 東北学院大学, 平  
成 16 年 9 月
- (8) 加藤有行, 飯田誠之, 山崎誠, 山岸恵利, 日高千晴, 滝沢武男, Ca<sub>1-x</sub>EuxGa<sub>2</sub>S<sub>4</sub> 混晶の Eu 遷  
移による光学利得, 第 65 回応用物理学会学術講演会, 東北学院大学, 平成 16 年 9 月
- (9) 野村重孝, 滝沢武男, 遠藤三郎, 三元チオガレート化合物 CaGa<sub>2</sub>S<sub>4</sub> 中のランタノイド元素の  
電子状態, 第 65 回応用物理学会学術講演会, 東北学院大学, 平成 16 年 9 月

- (10) Hiroaki Matsushita, Koji Mitake, Takeo Takizawa, Single crystal growth of Cu(Ga,In)Se<sub>2</sub> solid solutions by horizontal Bridgman method with controlling Se vapor pressure and their defect properties, The 14th International Conference on Crystal Growth, フランス, 平成 16 年 8 月
- (11) C. Hidaka, M. Goto, M. Kubo, T. Takizawa, Phase diagrams of the pseudo-binary systems of BaS-In<sub>2</sub>S<sub>3</sub> and BaS-Ga<sub>2</sub>S<sub>3</sub>, The 14th International Conference on Crystal Growth, フランス 平成 16 年 8 月
- (12) 久保雅和, 日高千晴, 滝沢武男, BaIn<sub>2</sub>S<sub>4</sub> の単結晶作製, 第 65 回応用物理学関連連合講演会, 東京工科大学, 平成 16 年 3 月
- (13) 山岸恵利, 日高千晴, 滝沢武男, Ca<sub>1-x</sub>EuxGa<sub>2</sub>S<sub>4</sub> 化合物の発光・光吸収・励起スペクトル, 第 65 回応用物理学関連連合講演会, 東京工科大学, 平成 16 年 3 月
- (14) 吉沢克規, 深井尋史, 成木紳也, 坂井直道, 村上雅人, 平林泉, 滝沢武男, パルス着磁過程における高温超電導体バルク体中の磁束挙動と発熱の評価, 秋季低温工学・超電導学会, 平成 15 年 12 月
- (15) 山岸恵利, 日高千晴, 滝沢武男, Ca(1-x)EuxGa<sub>2</sub>S<sub>4</sub> 化合物混晶の作製とその光吸収及び発光特性, 多元系機能材料研究会年末講演会, 平成 15 年 11 月
- (16) 久保雅和, 日高千晴, 滝沢武男, SrIn<sub>2</sub>S<sub>4</sub> 化合物の単結晶作製, 多元系機能材料研究会年末講演会, 平成 15 年 11 月
- (17) Hironobu TANAKA, Shinya NARIKI, Naomichi SAKAI, Masato MURAKAMI, Izumi HIRABAYASHI, Takeo TAKIZAWA, Field Trapping Properties of Melt-Textured Ho-Ba-Cu-O Bulk Superconductors with Fine Ho-211 Inclusions The 16th International Symposium on Superconductivity, 平成 15 年 10 月 27 日~29 日
- (18) 田中弘信, 成木紳也, 坂井直道, 村上雅人, 平林泉, 滝沢武男, Ho-Ba-Cu-O 系 バルク超伝導体の作製及びその超伝導特性, 第 64 回 秋季応用物理学会学術講演会, 平成 15 年 8 月 31p-N-5
- (19) 吉沢克規, 深井尋史, 成木紳也, 坂井直道, 村上雅人, 平林泉, 滝沢武男, パルス磁場励磁下における超伝導バルク体中の磁束挙動と発熱の評価, 応用物理学会, 平成 15 年 8 月 31p-N-8
- (20) 山岸恵利, 日高千晴, 滝沢武男, Ca(1-x)EuxGa<sub>2</sub>S<sub>4</sub> 化合物の発光特性, 第 64 回 秋季応用物理学会学術講演会, 平成 15 年 9 月 1p-ZE-2
- (21) 久保雅和, 日高千晴, 滝沢武男, SrIn<sub>2</sub>VI<sub>4</sub>(VI=S,Se)の単結晶作製, 第 64 回 秋季応用物理学会学術講演会, 平成 15 年 9 月 1p-ZE-3
- (22) 吉沢克則, 深井尋史, 成木紳也, 坂井直道, 村上雅人, 平林泉, 滝沢武男, Flux motion and its temperature dependence in the YBCO bulk superconductors during pulse field magnetization, 11th International workshop on critical currents in superconductors, Tokyo, June 31, 2003
- (23) 田中弘信, 坂井直道, 村上雅人, 平林泉, 滝沢武男, Fabrication and superconducting properties of Ho-Ba-Cu-O bulk superconductors, 11th International workshop on critical currents in superconductors, Tokyo, 2003/6/30
- (24) A. Kato, M. Yamazaki, H. Najafov, K. Iwai, A. Bayramov, C. Hidaka, T. Takizawa, S. Iida, Radiative and non-radiative processes of Ce related transitions in CaGa<sub>2</sub>S<sub>4</sub> and SrGa<sub>2</sub>S<sub>4</sub>, The 13th International Conference on Ternary and Multinary Compounds, フランス パリ, 平成 14 年 10 月
- (25) T. Takizawa, H. Ozawa, C. Hidaka, ESR study of Ce<sup>3+</sup> ions doped in the CdIn<sub>2</sub>S<sub>4</sub> lattice, The 13th International Conference on Ternary and Multinary Compounds, フランス パリ, 平成 14 年 10 月
- (26) C. Hidaka, N. Makabe, T. Takizawa, Determination of a pseudo-binary SrSe-Ga<sub>2</sub>Se<sub>3</sub> phase diagram and

single crystal growth of SrGa<sub>2</sub>Se<sub>4</sub> compounds, The 13th International Conference on Ternary and Multinary Compounds フランス パリ, 平成 14 年 10 月

- (27) 真壁伸寧, 日高千晴, 滝沢武男, SrGa<sub>2</sub>Se<sub>4</sub> 単結晶の良質化, 第 63 回応用物理学会学術講演会, 新潟大学, 平成 14 年 9 月
- (28) 小沢広之, 宮田有祐, 日高千晴, 滝沢武男, Ce<sup>3+</sup> をドーブした CdIn<sub>2</sub>S<sub>4</sub> 単結晶の ESR 測定, 第 49 回応用物理学関連連合講演会, 東海大学, 平成 14 年 3 月
- (29) 真壁伸寧, 日高千晴, 滝沢武男, SrGa<sub>2</sub>Se<sub>4</sub> 単結晶の作製, 第 49 回応用物理学関連連合講演会, 東海大学, 平成 14 年 3 月
- (30) 二宮祐一郎, 日高千晴, 沈用球, ナジム・マメドフ, 山本信行, 滝沢武男, 旋光性をもつ一軸性結晶 TeO<sub>2</sub> の Light Figure, 第 49 回応用物理学関連連合講演会, 東海大学, 平成 14 年 3 月
- (31) 小沢広之, 宮田有祐, 日高千晴, 滝沢武男, CdIn<sub>2</sub>S<sub>4</sub>:Ce<sup>3+</sup> の ESR 測定, 三元多元機能性材料研究会, 平成 13 年 11 月
- (32) 日高千晴, 滝沢武男, SrGa<sub>2</sub>S<sub>4</sub>:Ce<sup>3+</sup> 単結晶の光吸収スペクトル, 三元多元機能性材料研究会, 平成 13 年 11 月
- (33) 磯本徳之, 日高千晴, 滝沢武男, SrS-Ga<sub>2</sub>S<sub>3</sub> 系状態図と Sr<sub>2</sub>Ga<sub>2</sub>S<sub>5</sub> 単結晶作製の試み, 三元多元機能性材料研究会, 平成 13 年 11 月
- (34) 真壁伸寧, 日高千晴, 滝沢武男, SrGa<sub>2</sub>Se<sub>4</sub> の状態図作成と単結晶成長, 三元多元機能性材料研究会, 平成 13 年 11 月
- (35) 真壁伸寧, 日高千晴, 滝沢武男, (Ca,Sr)-(Ga,In)<sub>2</sub>-(S,Se)<sub>4</sub> 系化合物単結晶作製のための熱分析, 第 62 回応用物理学会学術講演会, 愛知工業大学, 平成 13 年 9 月
- (36) 磯本徳之, 日高千晴, 滝沢武男, Sr<sub>2</sub>Ga<sub>2</sub>S<sub>5</sub> の単結晶作製, 第 62 回応用物理学会学術講演会, 愛知工業大学, 平成 13 年 9 月
- (37) 日高千晴, 滝沢武男, CaGa<sub>2</sub>S<sub>4</sub> 単結晶の良質化, 第 62 回応用物理学会学術講演会, 愛知工業大学, 平成 13 年 9 月
- (38) 日高千晴, 滝沢武男, CaGa<sub>2</sub>S<sub>4</sub>:Ce<sup>3+</sup>単結晶作製と光学的特性, 第 48 回応用物理学関連連合講演会, 明治大学, 平成 13 年 3 月
- (39) 小沢広之, 日高千晴, 滝沢武男, 希土類元素をドーブした CdIn<sub>2</sub>S<sub>4</sub> 単結晶の ESR 測定, 第 48 回応用物理学関連連合講演会, 明治大学, 平成 13 年 3 月
- (40) 磯本徳之, 日高千晴, 滝沢武男, 松下裕亮, II<sub>a,b</sub>-III<sub>2</sub>-VI<sub>4</sub> 系化合物の構造変化, 第 48 回応用物理学関連連合講演会, 明治大学, 平成 13 年 3 月
- (41) 浅香王隆, 日高千晴, 滝沢武男, 松下裕亮, CdS-In<sub>2</sub>S<sub>3</sub>-Ga<sub>2</sub>S<sub>3</sub> 系における層状化合物, 第 48 回応用物理学関連連合講演会, 明治大学, 平成 13 年 3 月
- (42) 山崎, 岩井, ナジャホフ, 加藤, 日高千晴, 滝沢武男, 飯田, CaGa<sub>2</sub>S<sub>4</sub> 結晶中の Ce 不純物中心の発光・非発光過程, 第 48 回応用物理学関連連合講演会, 明治大学, 平成 13 年 3 月
- (43) 山崎, 岩井, K.Nadjafov, 加藤, 日高千晴, 滝沢武男, 飯田, CaGa<sub>2</sub>S<sub>4</sub> 結晶中の Ce 不純物中心の光学特性 II -- 吸収・励起 --, 三元多元機能性材料研究会, 平成 12 年 11 月
- (44) 岩井, K.Nadjafov, 加藤, 山崎, 日高千晴, 滝沢武男, 飯田, CaGa<sub>2</sub>S<sub>4</sub> 結晶中の Ce 不純物中心の光学特性 I -- 発光 --, 三元多元機能性材料研究会, 平成 12 年 11 月
- (45) 日高千晴, 滝沢武男, CaGa<sub>2</sub>S<sub>4</sub>:Ce<sup>3+</sup> 単結晶作製とその光吸収スペクトル, 三元多元機能性材料研究会, 平成 12 年 11 月

- (46) 浅香王隆, 日高千晴, 滝沢武男, 松下裕亮, CdS-In<sub>2</sub>S<sub>3</sub>-Ga<sub>2</sub>S<sub>3</sub> 系における層状化合物の結晶構造と光物性, 三元多元機能性材料研究会, 平成 12 年 11 月
- (47) H.Enomoto, K.Inoue, M.Muralidhar, M.Murakami, T.Takizawa, AC susceptibility of high-Tc superconductor REBa<sub>2</sub>Cu<sub>3</sub>O<sub>y</sub>, International Symposium on Superconductivity, 平成 12 年 10 月
- (48) Y.Akamatsu, K.Waki, K.Inoue, M.Murakami, T.Takizawa, AC susceptibility measurements for Nd-Ba-Cu-O superconductor, International Symposium on Superconductivity, 平成 12 年 10 月
- (49) T.Matano, M.R.Koblishka, M.Muralidhar, M.Murakami, T.Takizawa, Superconducting transitions of REBa<sub>2</sub>Cu<sub>3</sub>O<sub>x</sub> superconductors in high fields, International Symposium on Superconductivity, 平成 12 年 10 月
- (50) T.Kono, M.Tomita, M.Murakami, T.Takizawa, The viscous flux flow and flux creep induced by pulsed magnetic fields in YBCO disk, International Symposium on Superconductivity, 平成 12 年 10 月
- (51) 赤松優一, 脇耕一郎, 村上雅人, 滝沢武男, Nd-Ba-Cu-O 超伝導体における交流帯磁率測定, 第 61 回応用物理学会学術講演会, 北海道大学, 平成 12 年 9 月
- (52) 亦野智宏, Michael R.Koblishka, 村上雅人, 滝沢武男, 高磁場下における高温超伝導体の超伝導転移, 第 61 回応用物理学会学術講演会, 北海道大学, 平成 12 年 9 月
- (53) 河野猛, 富田優, 村上雅人, 滝沢武男, パルス磁場により誘起された MTG-YBCO 中の粘性磁束フロー, 第 61 回応用物理学会学術講演会, 北海道大学, 平成 12 年 9 月
- (54) 滝沢武男, 多元化合物研究: 新しい機能材料への期待, シンポジウム 緒言, 第 61 回応用物理学会学術講演会, 北海道大学, 平成 12 年 9 月
- (55) 浅香王隆, 日高(小松)千晴, 滝沢武男, 松下裕亮, CdS-Ga<sub>2</sub>S<sub>3</sub>-In<sub>2</sub>S<sub>3</sub> 系における層状化合物の構造多形, 第 61 回応用物理学会学術講演会, 北海道大学, 平成 12 年 9 月
- (56) 日高(小松)千晴, 滝沢武男, CaGa<sub>2</sub>S<sub>4</sub>:Ce<sup>3+</sup>単結晶の発光特性と Ce<sup>3+</sup>濃度依存性, 第 61 回応用物理学会学術講演会, 北海道大学, 平成 12 年 9 月
- (57) 柳川郁雄, 高橋博樹, 山本繁, 石川文洋, 山田裕, 辺土正人, 上床美也, 酸化物超伝導体 Pr<sub>2</sub>Ba<sub>4</sub>Cu<sub>7</sub>O<sub>15-d</sub> の圧力効果, 第 4 5 回高圧討論会, 草津市, 平成 16 年 10 月
- (58) 柳川郁雄, 高橋博樹, 増田雄一郎, 山本繁, 山田裕, 辺土正人, 上床美也, 新しい超伝導体 Pr<sub>2</sub>Ba<sub>4</sub>Cu<sub>7</sub>O<sub>15-d</sub> の磁氣的性質の圧力効果 II, 日本物理学会 2004 秋季大会, 青森市, 平成 16 年 9 月
- (59) 柳川郁雄, 高橋博樹, 土金利佳, 増田雄一郎, 山本繁, 山田裕, 新しい超伝導体 Pr<sub>2</sub>Ba<sub>4</sub>Cu<sub>7</sub>O<sub>15-d</sub> の磁氣的性質の圧力効果, 日本物理学会第 5 9 回年次大会, 福岡市, 平成 16 年 3 月
- (60) 高橋博樹, 茂木祐介, 長谷川正, 高圧下におけるデラフォサイト型遷移金属酸化 CuFeO<sub>2</sub> の磁氣的性質, 日本物理学会第 5 9 回年次大会, 福岡市, 平成 16 年 3 月
- (61) I.Yanagawa, T.Shimoda, and H. Takahashi, Pressure and Substitution Effect on Superconducting and Magnetic Transition Temperature in Oxide Superconductors Bi<sub>2</sub>201 and La<sub>2</sub>14, 第 1 9 回高圧力の科学と技術に関する国際会議(AIRAPT-19), フランス国ボルドー, 平成 1 5 年 7 月
- (62) Y.Motegi, N.Kamata, H. Takahashi, R.Tsuchigane, and M. Hasegawa, Pressure effect on the magnetic transition in the delafossite-type oxides, 第 1 9 回高圧力の科学と技術に関する国際会議(AIRAPT-19), フランス国ボルドー, 平成 1 5 年 7 月
- (63) H. Takahashi, Y.Motegi, R.Tsuchigane, and M. Hasegawa, Pressure Effect on the Antiferromagnetic Transition Temperature in CuFeO<sub>2</sub>, International Conference on Magnetism (ICM2003), イタリア国

ローマ, 平成15年7月

- (64) 柳川郁雄, 下田尚幸, 高橋博樹, 酸化物超伝導体 Bi2201 と La214 における超伝導と磁性転移温度の圧力効果, 置換効果, 日本物理学会 2003 秋季大会, 平成15年9月
- (65) 増田雄一郎, 山田裕, 山本繁, 高橋博樹, 松川倫明, 松下明行, Pr<sub>2</sub>Ba<sub>4</sub>Cu<sub>7</sub>O<sub>15-d</sub> 酸化物の熱処理に伴う圧力効果, 日本物理学会 2003 秋季大会, 平成15年9月
- (66) 谷口芳隆, 小坂昌史, 毛利信男, 高橋博樹, SQUID 磁束計で測定可能なダイヤモンドアンビルセルの開発, 第43回高圧討論会, 平成14年11月
- (67) 茂木佑介, 高橋博樹, Co 酸化物(La, Sr)<sub>2</sub>CoO<sub>4</sub> の電気抵抗の圧力効果, 日本物理学会 2002 秋季大会, 平成14年9月
- (68) 下田尚幸, 高橋博樹, 辺土正人, 上床美也, TC の圧力効果から見た銅酸化物超伝導体の Cu サイト置換効果, 日本物理学会 2002 秋季大会, 平成14年9月
- (69) 柴田淳, 高橋博樹, 山田裕, 松下明行, 名嘉節, RuSr<sub>2</sub>RECu<sub>2</sub>O<sub>8</sub> (RE=Gd, Eu)の強磁性状態の磁場・圧力効果, 日本物理学会 2002 秋季大会, 平成14年9月
- (70) 山田裕, 柴田智広, 濱田洋昭, 松下明行, 名嘉節, 高橋博樹, 柴田淳, 大石泰生, 久保衆伍, RuSr<sub>2</sub>GdCu<sub>2</sub>O<sub>8</sub> 酸化物超伝導体の高圧下での物性と結晶構造, 日本物理学会 2002 秋季大会, 平成14年9月
- (71) 加賀山朋子, 白石人士, 泉田学, 黒田規敬, 増田雄一郎, 山田裕, 葉金花, 松下明行, 高橋博樹, 大石泰生, セリウム系光触媒酸化物の高圧下光吸収 II, 日本物理学会 2002 秋季大会, 平成14年9月
- (72) 柴田淳, 後藤宏紹, 高橋博樹, 山田裕, RuSr<sub>2</sub>GdCu<sub>2</sub>O<sub>8</sub> の強磁性転移温度の圧力効果, 日本物理学会第57回年次大会, 平成14年3月
- (73) 下田尚幸, 柴田淳, 瓜生健哉, 高橋博樹, Ni をドーブした銅酸化物超伝導体の圧力効果, 日本物理学会第57回年次大会, 平成14年3月
- (74) 後藤宏紹, 柴田淳, 下田尚幸, 高橋博樹, DAC による酸化物超伝導体の圧力効果, 第42回高圧討論会, 神戸市, 平成13年11月
- (75) 瓜生健哉, 下田尚幸, 高橋博樹, Sr ドープした La<sub>2</sub>NiO<sub>4</sub> の高ドーブ領域における圧力効果, 第42回高圧討論会, 神戸市, 平成13年11月
- (76) 高橋博樹, 竹下直, 毛利信男, キュービックアンビル装置での低温物性測定, 第41回高圧討論会, 柏市, 平成12年11月
- (77) 高橋秀隆, 中西剛司, 高橋博樹, 小林達生, 清水克哉, 毛利信男, DAC による酸化物超伝導体の圧力効果第41回高圧討論会, 柏市, 平成12年11月
- (78) 中西剛司, 本山直樹, 三田村裕幸, 竹下直, 高橋博樹, 永崎洋, 内田慎一, 毛利信男, スピンドラダー系圧力誘起超伝導物質 Sr<sub>14-x</sub>CaxCu<sub>24</sub>O<sub>41</sub> の上部臨界磁場, 第41回高圧討論会, 柏市, 平成12年11月
- (79) T.Nakanishi, H.Takahashi, N.Takeshita, N.Mori, N.Motoyama, H.Eisaki, S.Uchida, H.Fujino, T.Nagata, J.Akimitsu, Resistive Upper Critical Field of Superconduction Spin-Ladder Sr<sub>14-x</sub>CaxCu<sub>24</sub>O<sub>41</sub>, STRIPE 2000, Rome, Italy,平成12年9月
- (80) H.Takahashi, H.Takahashi, T.Nakanishi, T.Arima, M.Noguchi, M.Oyanagi, N.Takeshita, N.Mori, High-pressure effect on transport properties of spin-ladder compounds Na<sub>1-x</sub>CaxV<sub>2</sub>O<sub>5</sub> and Ca<sub>0.7</sub>Li<sub>0.3</sub>V<sub>2</sub>O<sub>5</sub>, International Conference on Magnetism 2000, Recife, Brazil, 平成12年8月

(81) T.Nakanishi, N.Motoyama, H.Mitamura, N.Takeshita, H.Takahashi, H.Eisaki, S.Uchida, T.Goto, H.Ishimoto, N.M?ri, Pressure and field dependence of superconductivity in the spin-ladder  $\text{Sr}_{14-x}\text{Ca}_x\text{Cu}_{24}\text{O}_{41}$ , International Conference on Magnetism 2000, Recife, Brazil, 平成 12 年 8 月

# Ho-Ba-Cu-O 系バルク超伝導材料の臨界電流密度と 捕捉磁場特性

田中 弘信<sup>1,2,\*</sup> 成木 紳也<sup>2</sup> 坂井 直道<sup>2</sup> 村上 雅人<sup>2,3</sup>  
平林 泉<sup>2</sup> 滝沢 武男<sup>1</sup>

<sup>1</sup>日本大学文理学部

<sup>2</sup>財団法人国際超伝導産業技術研究センター超伝導工学研究所

<sup>3</sup>芝浦工業大学工学部

J. Japan Inst. Metals, Vol. 68, No. 9 (2004), pp. 693-697  
Special Issue on Superconducting Materials Science and Technology  
© 2004 The Japan Institute of Metals

## Critical Current Density and Trapped Field Properties of Ho-Ba-Cu-O Bulk Superconductors

Hironobu Tanaka<sup>1,2,\*</sup>, Shinya Nariki<sup>2</sup>, Naomichi Sakai<sup>2</sup>, Masato Murakami<sup>2,3</sup>,  
Izumi Hirabayashi<sup>2</sup> and Takeo Takizawa<sup>1</sup>

<sup>1</sup>Department of Physics, College of Humanities and Sciences, Nihon University, Tokyo 156-8550

<sup>2</sup>Superconductivity Research Laboratory, International Superconductivity Technology Center, Tokyo 105-0023

<sup>3</sup>Shibaura Institute of Technology, Tokyo 108-8548

We have fabricated melt-textured Ho-Ba-Cu-O bulk superconductors with a composition of  $\text{HoBa}_2\text{Cu}_3\text{O}_7(\text{Ho123}) + 0.4\text{Ho}_2\text{BaCuO}_5(\text{Ho211})$  in air. Several kinds of precursor compounds having Ho211 starting powders with different sizes are prepared by calcining  $\text{Ho}_2\text{O}_3$ ,  $\text{BaO}_2$  and  $\text{CuO}$  at 1173~1273 K. The diameter of Ho211 secondary particles dispersed in the Ho123 phase is reduced with decreasing the particle size of the Ho211 starting powder, resulting in the improvement in  $J_c$  properties. The maximum  $J_c$  value is  $7.2 \times 10^8 \text{ A/m}^2$  at 77 K in self-field. The Ag added large single-domain bulk of 32 mm in diameter is also fabricated. The trapped-field of 1.2 T has been achieved at 77 K for this bulk sample.

(Received March 19, 2004, Accepted May 19, 2004)

**Keywords:** bulk superconductor, melt-texturing,  $\text{HoBa}_2\text{Cu}_3\text{O}_7$ ,  $\text{Ho}_2\text{BaCuO}_5$ , critical current density, trapped magnetic field

## 1. 緒 言

溶融法により作製した  $\text{REBa}_2\text{Cu}_3\text{O}_7$  (RE123; RE は Y および希土類元素)系バルク超伝導材料は、結晶配向した RE123 超伝導相中に、 $\text{RE}_2\text{BaCuO}_5$  (RE211)常伝導相粒子を分散させた複合材料である。超伝導バルク材料は、永久磁石との組み合わせで安定浮上を可能にすることから、電力貯蔵用フライホイールや搬送装置などへの応用が注目されている。また、棒状に加工することにより、電流リード等への応用がなされている。一方、バルク超伝導材料に磁場を印加後、冷却して外部磁場を取り去ると、磁束がピンニングセンターに捕捉され、強力な永久磁石として使用することができ、これを利用した磁気分離装置、着磁装置、超伝導モータ、スパッタリング装置などへの応用が進展している。

バルク体の捕捉磁場を向上させるには、臨界電流密度( $J_c$ )の向上とバルクの大型化が必要である。 $J_c$ を高くするためには磁束のピンニングセンターとして添加した RE211 粒子を

微細化することが有効である。これまでバルク超伝導材料の研究の多くは Y123 系を中心に行われてきたが、捕捉磁場の大きさは液体窒素温度(77 K)で 1 T 程度であり、従来の永久磁石が発生する磁場をやや超える程度の値にとどまっていた<sup>1)</sup>。しかしながら、低酸素分圧下で作製した LRE123 (LRE は Nd, Sm, Gd などの軽希土類元素)系材料が Y123 系よりも高い臨界温度( $T_c$ )を有していることが報告されて以来<sup>2)</sup>、軽希土類元素を含む材料の開発が盛んに行われるようになり、Sm123 系や Gd211 系材料はすでに市販されるに至っている。これらの材料では微小な LRE/Ba 置換領域が存在し、これが磁場誘起型ピンニングセンターとして作用するため、 $J_c$ - $B$  特性においてピーク効果が発現する<sup>3)</sup>。Sm123 系や Nd123 系超伝導材料では Ag を添加して機械的強度を改善することにより、配向制御された大型バルク体の作製が可能となり、高い捕捉磁場が達成されている<sup>4,7)</sup>。著者らは低酸素分圧下で作製した Gd123 系超伝導材料に関して、前駆体原料として微細な RE211 粉末を用いることにより、試料中の Gd211 相を微細化し、 $J_c$  を大きく向上できることを報告<sup>5)</sup>した。今回、この微細化をさらに進め、粒径を 20~50 nm に小型化することにより 1.5~3 T (77 K) の非常に高い捕捉磁場を

\* 日本大学大学院生 (Graduate Student, Nihon University)

達成している<sup>10-14)</sup>。

これに対し、Ho や Er 等の重希土類元素を含むバルク材料は軽希土類元素を含む材料系に比べて  $T_c$  が低いため、これまであまり注目されておらず、研究例は少なかった。しかしながら、これらの材料は Y123 系同様、大気中で作製しても特性が低下しないことや、 $T_c$  が最適となる酸素アニール温度が比較的高く、アニールが短時間で済むなどの特徴があり、大型バルク体の特性を調べることは、応用面から重要であると考えられる。著者らは最近、大気中で作製した Ho123 系および Er123 系バルク体の超伝導特性に及ぼす 211 添加量および酸素アニール温度の影響について検討し、211 量が少ない試料では  $J_c$ - $B$  曲線において顕著なピーク効果が見られるという興味深い性質があることを報告した<sup>15,16)</sup>。また、Ho211 量が多い Ho123 系材料では、良好な  $J_c$ - $B$  特性が得られることが明らかとなった。本研究では、種々の粒径を有する Ho211 粉末を添加原料として Ho123 バルク体を作製し、 $J_c$ - $B$  特性に及ぼす Ho211 粒子の大きさの影響を検討した。さらに、大型のバルク体の作製を試み、捕捉磁場特性の検討を行った。

## 2. 実験方法

### 2.1 種々の Ho211 粒径を有するバルク体の作製

最初に、 $J_c$ - $B$  特性を検討するための試料として、直径約 16 mm の比較的小型のバルク体を作製した。まず、 $\text{Ho}_2\text{O}_3$ 、 $\text{BaO}_2$ 、 $\text{CuO}$  の各粉末を所定の割合で混合し、仮焼することにより、Ho123 および Ho211 仮焼粉をそれぞれ作製した。ここで、Ho211 については Table 1 に示すように、仮焼条件が異なる 3 種類の仮焼粉を作製した。Ho123 と Ho211 をモル比で 100 : 40 となるよう混合した。この際、Ho211 相の粒成長を抑制する目的から、Pt を 0.5 mass% 添加した。混合粉 0.02 kg を内径 20 mm の金型に詰め、一軸加圧成形を行い、前駆体とした。前駆体上面に大きさ約 2 mm の Nd123(001)バルク種結晶を付着させた後、1293 K に加熱し、Ho123 相を分解熔融させた。温度を 1273 K に下げた後、 $-0.33$  K/h の速度で 1233 K まで徐冷することにより結晶成長を行い、バルク試料を作製した。結晶成長後のバルク体の  $c$  軸に平行な面を切断・研磨後、走査型電子顕微鏡(SEM)を用いて微細組織の観察を行った。

超伝導特性を測定するため、各々のバルク試料の中心部分から大きさ約 1 mm × 1 mm × 1 mm の試料片を切り出し、酸素雰囲気中、673 K で 100 h アニール処理を行った。超伝導量子干渉型磁束計(SQUID)を用いて磁化率の温度依存性と液体窒素温度(77 K)における磁化曲線を測定し、試料の  $T_c$  および  $J_c$  を評価した。

Table 1 Composition of calcinations for Ho211 starting powders.

Ho211 powder	Condition of calcination
Ho211-A	1173 K, 4 h
Ho211-B	1173 K, 4 h + 1273 K, 4 h
Ho211-C	1173 K, 4 h + 1273 K, 4 h + 1323 K, 4 h

### 2.2 大型バルク体の作製

バルク体の捕捉磁場特性を検討するため、2.1 で作製した試料よりも大型のバルク体の作製を試みた。まず、1173 K で仮焼した Ho211 を原料として、2.1 と同組成の直径 30 mm の前駆体を作製し、1343 K まで加熱して前駆体を半溶融状態にした。その後、1293 K に温度を下げ、Nd123 結晶を種付けした。1263 K から 1238 K までの温度範囲を  $-0.25$  K/h の速度で徐冷することにより、結晶を育成した。徐冷の際、試料の底面の温度が上面よりも高くなるように 0.2 K/mm の温度勾配をつけた。

さらに、機械強度の向上のため、 $\text{Ag}_2\text{O}$  を 10 mass% 添加した直径 40 mm の前駆体を用いてバルク体の作製を行った。Ag を添加した場合、Ho123 相の分解熔融温度が Ag 無添加の試料に比べて低下するため、温度パターンを無添加のものよりも約 20 K 低くして結晶成長を行った。

各々のバルク体を酸素気流中で、673 K で 200 h アニールを行った。捕捉磁場評価のため、3 T の定常磁場下でバルク体を液体窒素中に浸漬して磁場中冷却し、外部磁場を除去した後、バルク体の上面をホール素子で二次元的に走査することにより 77 K における捕捉磁場分布を測定した。この際、ホール素子とバルク体上面との距離は 1.0 mm とした。

## 3. 結果および考察

### 3.1 微細組織、超伝導特性に及ぼす Ho211 原料粉粒径の影響

Fig. 1 に Ho211 仮焼粉の SEM 写真を示す。Ho211 粉末の焼結の進行に伴い、最終仮焼温度が高い粉末ほど粒径が大きくなっていることが分かる。Fig. 2 に得られたバルク体の写真を示す。種結晶を起点として結晶成長が進み、結晶配向した単一粒からなるバルク体を得られた。次に、各試料断面の SEM 写真を Fig. 3 に示す。写真中の白い粒子は Ho211 相を、その周りの黒色領域は、Ho123 超伝導相を示している。粒径が小さい Ho211 仮焼粉を原料とした試料ほど、結晶成長後の Ho211 粒子が微細になっていることが分かる。これは Gd123 系や Y123 系材料等に関して既に報告したように<sup>8,9,17,18)</sup>、以下の理由に基づくものである。すなわち、RE123 相が高温で分解熔融する際に生成する RE211 相は、最初に RE211 が過剰に添加されている場合、それらを核として生成することが知られている<sup>19)</sup>。微細な RE211 原料を添加することは、RE123 相の分解熔融時に生成する RE211 相の核の数が多くなることに相当するため、微細な RE211 が生成しやすくなる。したがって、包晶反応後も微細な RE211 粒子が残存すると考えられる。ただし、この RE211 粒子の成長は、試料の部分熔融時には Pt の添加によって大きく抑制されるものの、促進されてしまう。その成長速度は RE 元素の液相中溶解度に大きく影響され、イオン半径の大きな RE 元素は液相中溶解度が大きくなる傾向があり<sup>20)</sup>、211 粒子の成長が速くなる。著者らの実験によれば、Sm123 系材料<sup>21)</sup>、Y123 系材料<sup>22)</sup>、Gd123 系材料<sup>23)</sup>、RE211 原料を用いた場合でも、211 相の微細化効果が小さくなった。本研究の

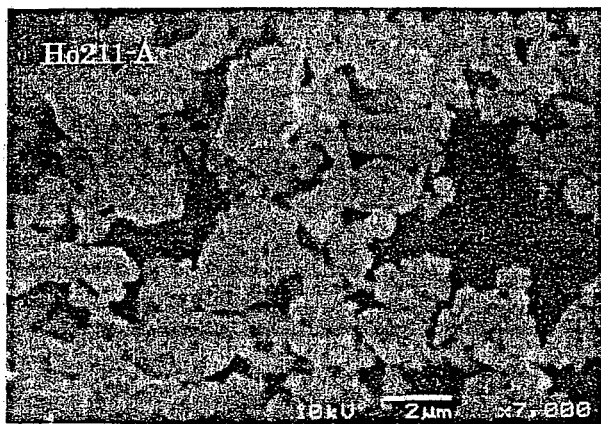


Fig. 1 SEM photographs of calcined Ho211 powder: Ho211-A and Ho211-C listed in Table 1.

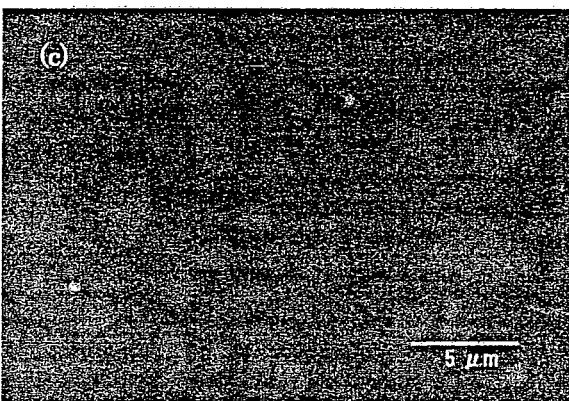
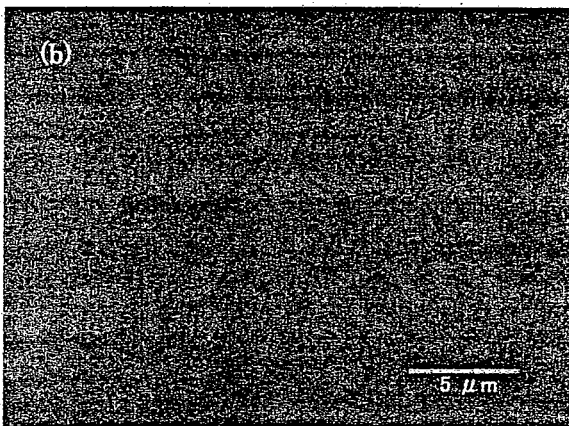
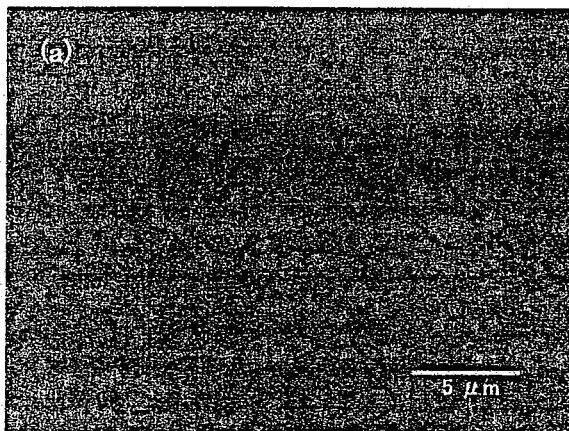


Fig. 3 SEM photographs for the polished surfaces of (100) cross section of Ho123 bulk samples. The samples were fabricated using different Ho211 starting powders; (a) Ho211-A, (b) Ho211-B, (c) Ho211-C in Table 1.

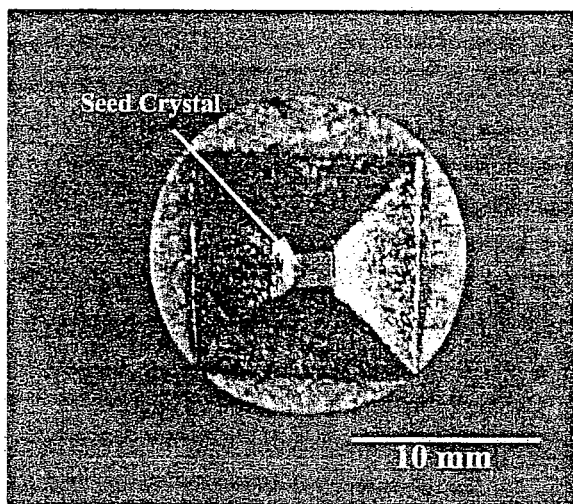


Fig. 2 Photograph of the top view of Ho123 bulk sample fabricated from the employment of Ho211-A starting powder.

Ho123系材料の場合、 $\text{Ho}^{3+}$  イオンのイオン半径(0.1015 nm)は  $\text{Y}^{3+}$  イオン(0.1019 nm)と同様、イオン半径が小さく、液相中溶解度が小さいと考えられることから、部分熔融時のHo211粒子の成長が遅く、微細なHo211を得るのに適した材料であると考えられる。

Fig. 4にハルク体から切り出した試料片の磁化率の温度依存性を示す。試料の厚さ1.0mm、測定磁場10 Oeを示し、onset- $T_c$ は約92 Kであった。Fig. 5にヒステリシス

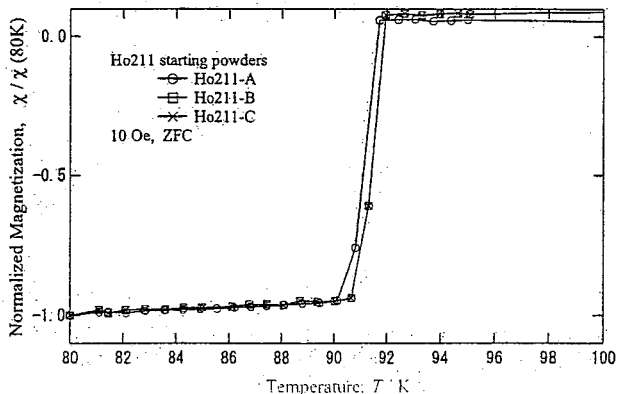


Fig. 4 Temperature dependence of dc susceptibility for Ho123 specimens (1 mm × 1 mm × 1 mm) cut from bulk samples.

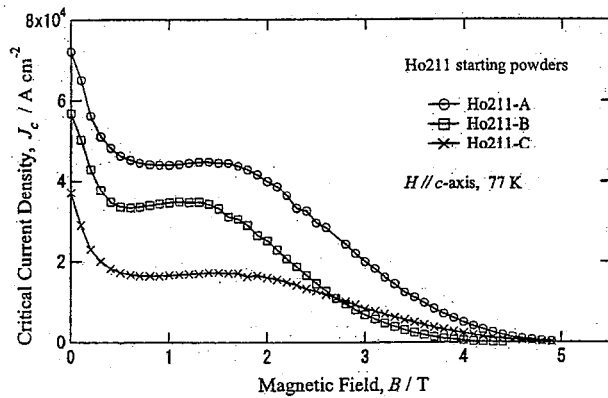


Fig. 5  $J_c$ - $B$  curves at 77 K for the Ho123 bulk samples.

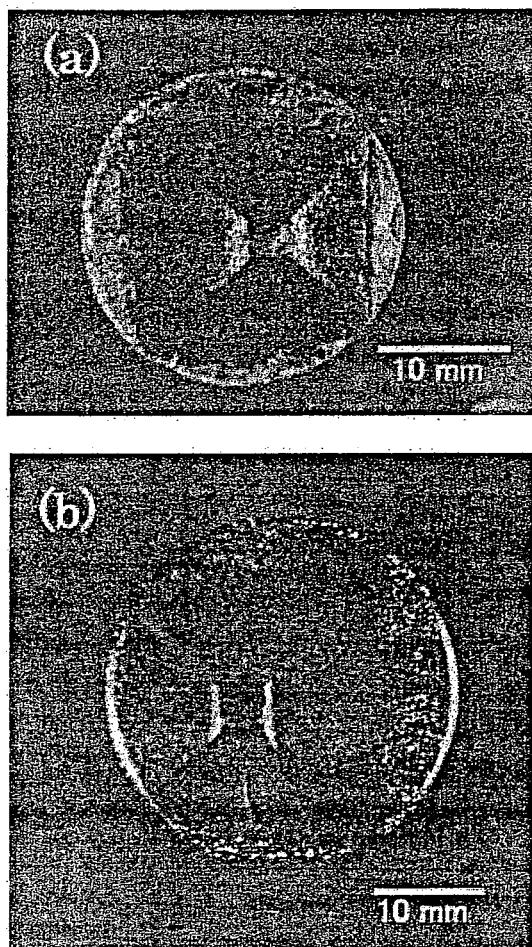


Fig. 6 Top view of large single grain Ho123 bulk samples; (a) 25 mm in diameter, and (b) 32 mm in diameter with Ag addition.

曲線から拡張 Bean モデル<sup>21)</sup>を用いて算出した 77 K における  $J_c$ - $B$  特性を示す。微細な Ho211 粒子が分散している試料ほど低磁場領域における  $J_c$  は向上しており、1173 K で仮焼した Ho211 を原料とした試料では、自己磁場において  $7.2 \times 10^8$  A/m<sup>2</sup> の  $J_c$  が得られた。また、いずれの試料においても中磁場領域において、緩やかなピーク効果が観測され、大型バルク体試料の場合、高い捕捉磁場を得ることに好ましい  $J_c$ - $B$  特性を有していることが分かった。Ho 系においては

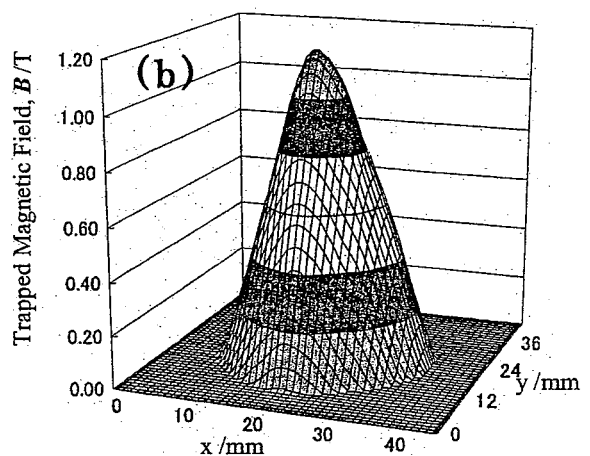
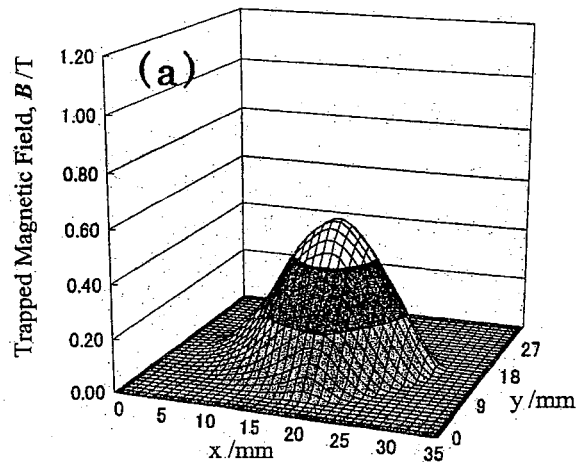


Fig. 7 Trapped field distributions of large grain bulk samples at 77 K. The maximum values of trapped field were (a) 0.54 T, and (b) 1.2 T, respectively.

Ho/Ba 置換が起こらないため、ピーク効果は酸素欠損の不均一性に起因するものと考えられる<sup>15,16,22)</sup>。

### 3.2 大型バルク体の捕捉磁場特性

最も高い  $J_c$  が得られた Ho211-A を原料として、直径 30 mm および直径 40 mm の前駆体から作製した大型バルク体の写真を Fig. 6 に示す。得られたバルク体の直径は各々 (a) 25 mm, (b) 32 mm であり、(a) はほぼ単一相からなるバルク体が、(b) は全体が単一粒からなるバルク体を得ることができた。Fig. 7 に各々のバルク体の 77 K における捕捉磁場分布を示す。ともに捕捉磁場分布は単一ピークの分布を示しており、クラックやサブグレイン等の弱結合が無い良好な試料であることが分かる。特に直径 32 mm の試料の捕捉磁場の最大値は約 1.2 T の高い値を示しており、これは低酸素分圧下で作製した同程度の大きさの Sm123 系や Nd123 系バルク体とはほぼ同じ捕捉磁場である<sup>5-7)</sup>。この場合、 $J_c$  の向上、試料の大型化以外に Ag 添加による微小クラックの除去が捕捉磁場の向上に寄与しているものと考えられる。

## 4. ま と め

3種類の異なる粒径を有する Ho211 原料粉を添加して Ho123 系バルク超伝導体を熔融法で作製し、材料の微細組織と超伝導特性を検討した。バルク体中に分散する Ho211 粒子は粒径が細かい Ho211 原料粉を用いる程、小さくなった。Ho211 の粒径の微細化に伴い、試料の、 $J_c$  は向上した。直径 32 mm の Ag を添加した大型単一粒バルク体の作製も行い、77 K で 1.2 T の高い捕捉磁場が得られた。

## 文 献

- 1) S. Nariki, N. Sakai and M. Murakami: J. Cryogenic Soc. Jpn. **37**(2002) 589-600.
- 2) S. I. Yoo, N. Sakai, H. Takaichi, T. Higuchi and M. Murakami: Appl. Phys. Lett. **65**(1994) 633-635.
- 3) M. Murakami, N. Sakai, T. Higuchi and S. I. Yoo: Supercond. Sci. Technol. **9**(1996) 1015-1032.
- 4) H. Ikuta, A. Mase, Y. Yanagi, M. Yoahikawa, Y. Itoh, T. Oka and U. Mizutani: Supercond. Sci. Technol. **11**(1998) 1345-1347.
- 5) H. Ikuta, S. Ikeda, A. Mase, M. Yoahikawa, Y. Yanagi, Y. Itoh, T. Oka and U. Mizutani: Appl. Supercond. **6**(1998) 107-109.
- 6) H. Ikuta, T. Hosokawa, M. Yoahikawa and U. Mizutani: Supercond. Sci. Technol. **13**(2000) 1559-1568.
- 7) M. Matsui, T. Miyamoto, S. Nariki, N. Sakai and M. Murakami: Physica C **357-360**(2001) 694-696.
- 8) S. Nariki, S. J. Seo, N. Sakai and M. Murakami: Supercond. Sci. Technol. **13**(2000) 778-784.
- 9) S. Nariki, N. Sakai and M. Murakami: Physica C **357-360**(2001) 811-813.
- 10) S. Nariki, N. Sakai and M. Murakami: Physica C **341-348**(2000) 2409-2412.
- 11) S. Nariki, N. Sakai and M. Murakami: Physica C **357-360**(2001) 629-634.
- 12) S. Nariki, N. Sakai and M. Murakami: Supercond. Sci. Technol. **15**(2002) 648-652.
- 13) S. Nariki, N. Sakai and M. Murakami: Physica C **378-381**(2002) 631-635.
- 14) S. Nariki, N. Sakai and M. Murakami: Supercond. Sci. Technol. in press.
- 15) S. Nariki, N. Sakai and M. Murakami: J. Cryogenic Soc. Jpn. **37**(2002) 652-658.
- 16) S. Nariki, N. Sakai and M. Murakami: Physica C **392-396**(2003) 516-520.
- 17) S. Nariki, M. Matsui, N. Sakai and M. Murakami: Supercond. Sci. Technol. **15**(2002) 679-682.
- 18) S. Nariki, N. Sakai, M. Murakami and I. Hirabayashi: Supercond. Sci. Technol. **17**(2004) S30-S35.
- 19) D. K. Balkin and P. J. McGinn: Supercond. Sci. Technol. **7**(1994) 72-79.
- 20) M. Kambara, T. Umeda and Y. Shiohara: Bull. Ceram. Soc. Jpn. **32**(1997) 196-200.
- 21) E. M. Gyorgy, R. B. van Dover, K. A. Jackson, L. F. Schneemeyer and J. V. Waszczak: Appl. Phys. Lett. **55**(1989) 283-285.
- 22) S. Nariki and M. Murakami: Supercond. Sci. Technol. **15**(2002) 786-790.

# Flux motion in Y–Ba–Cu–O bulk superconductors during pulse field magnetization

K Yoshizawa<sup>1,2</sup>, S Nariki<sup>2</sup>, N Sakai<sup>2</sup>, M Murakami<sup>2,3</sup>, I Hirabayasi<sup>2</sup>  
and T Takizawa<sup>1</sup>

<sup>1</sup> Department of Physics, College of Humanities and Sciences, Nihon University,  
3-25-40 Sakura-Josui, Setagaya-ku, Tokyo 156-8550, Japan

<sup>2</sup> Division of Material Science and Physics, Bulk Superconductor Laboratory,  
1-16-25 Shibaura, Minato-ku, Tokyo 105-0023, Japan

<sup>3</sup> Department of Materials Science and Engineering, Shibaura Institute of Technology,  
3-9-14 Shibaura, Minato-ku, Tokyo 105-0023, Japan

E-mail: yoshizawa@istec.or.jp

Received 6 October 2003, in final form 15 December 2003

Published 12 January 2004

Online at stacks.iop.org/SUST/17/S74 (DOI: 10.1088/0953-2048/17/2/066)

## Abstract

We have studied the relationship between the magnetization and temperature change in Y–Ba–Cu–O bulk superconductor during pulse field magnetization (PFM). The flux motion was monitored using both Hall sensors and pick-up coils that are placed on a surface of a Y–Ba–Cu–O disc having dimensions of 15 mm in diameter and 0.95 mm in thickness. The peak value of the field was varied from 0.2 to 0.8 T. The effect of the static bias field was also studied in the range of 0–3 T. The temperature of the sample surface was measured using a resistance temperature sensor. The temperature increased with the magnitude of the applied pulsed magnetic field, and the amount of temperature rise decreased with increasing static bias field.

(Some figures in this article are in colour only in the electronic version)

## 1. Introduction

Recent advancement in the processing technology for bulk Y–Ba–Cu–O superconductors has made it possible to trap an extremely high field of 17 T at 29 K [1]. For the magnetization of bulk Y–Ba–Cu–O superconductors, a superconducting magnet is commonly used, since it can generate a very high magnetic field. However such an activation method requires big apparatus and is not suitable for activating a Y–Ba–Cu–O magnet installed in industrial machines. On the other hand, high magnetic field can also be generated by using pulse field magnetization (PFM) in a relatively small and simple device [2]. However, when a pulse magnetic field is imposed on a bulk superconductor, the heat caused by flux motion poses a new problem.

Ikuta *et al* [3] measured the *in situ* local magnetic flux density of Y–Ba–Cu–O and Sm–Ba–Cu–O in liquid nitrogen immediately after a PFM pulse, and determined the time and

positional dependence of the temperature rise ( $\Delta T$ ) at the bulk surface [3]. They showed that the temperature of the bulk sample rises faster in the outer side, and  $\Delta T$  increases with increasing pulse field strength. However, these measurements were made without the bias static field. It is now common to repeat PFM pulses in order to enhance the fields trapped by bulk superconductors like in the IMRA method [4]. In such a case, a pulse field is applied in the presence of trapped field. The flux motion will be strongly affected by the presence of the static field. Hence, we studied magnetization behaviour of bulk superconductors during PFM with emphasis on the relationship between the flux motion and the temperature variation.

## 2. Experimental details

The samples used in this study have a cylindrical shape with dimensions of 15.03 mm in diameter and 0.95 mm in

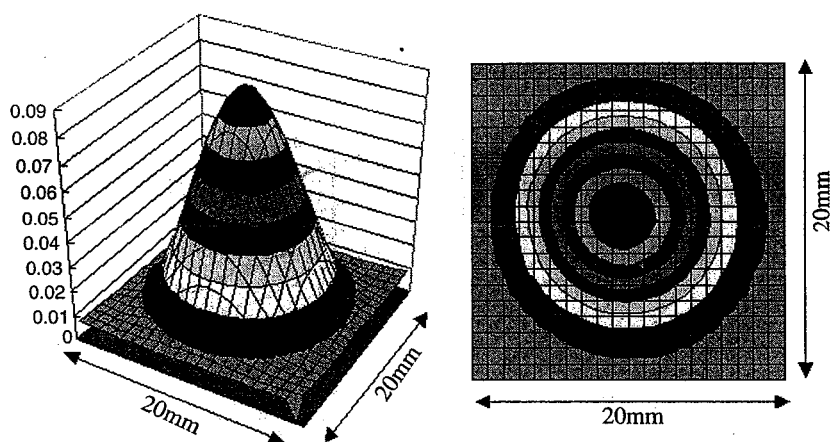


**Figure 1.** Trapped field distributions for (a) Y-Ba-Cu-O and (b) Gd-Ba-Cu-O samples about 15 mm in diameter measured by scanning a Hall sensor at 1 mm above the sample surface.

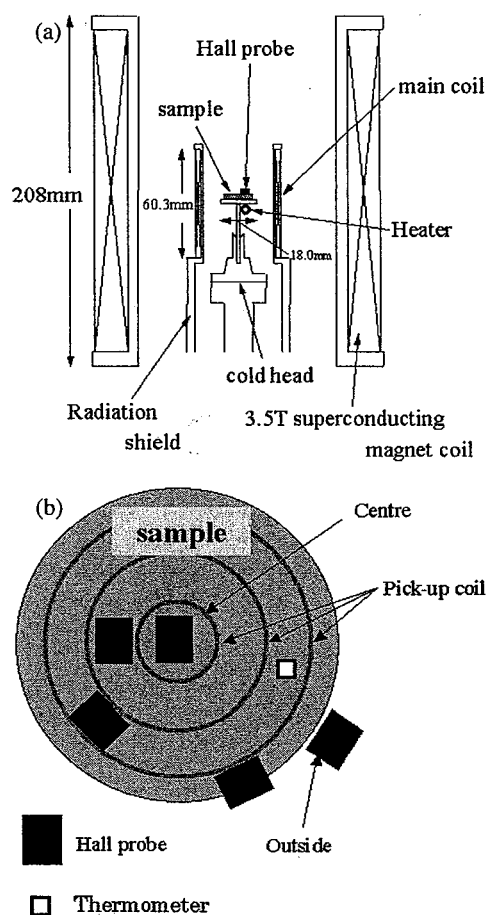
thickness. The samples were cut out from a massive Y-Ba-Cu-O bulk superconductor produced by a top-seeded melt-growth method [5]. Figure 1 shows the distribution of the  $z$  component of the trapped flux density  $B_z$  at 77 K for a Y-Ba-Cu-O disc sample. The sample was cooled in the presence of a static magnetic field (1 T) [6]. Trapped flux distribution has a single peak with good symmetry, showing that the sample is made of single grains of good quality.

Figure 2 shows a schematic illustration of the PFM method and the arrangement of magnetic sensors [7]. As shown in figure 2(a), a sample is placed at the centre of a copper solenoid coil and a superconducting coil such that a magnetic field is applied parallel to the  $c$  axis of a sample. The pulse magnetic fields of 0.2–0.8 T were imposed on a sample using the copper solenoid coil at 77 K. The time from the onset to the peak pulse field was set to be a constant value of 16 ms. Static bias magnetic fields of 0–3 T were also superposed on a sample using a superconducting magnet during PFM. Five Hall probe sensors used for field measurements were arranged as shown in figure 2(b). The distance from the centre to each Hall element was set to 0.00 m, 2.93 mm, 5.64 mm, 7.14 mm, and 8.68 mm. Three pick-up coils were also arranged concentrically with their centre positioned at the sample centre. The diameter of each pick-up coil was 3.84 mm (coil 1), 8.21 mm (coil 2), and 12.84 mm (coil 3). In order to measure the change in the sample temperature, a Cernox resistance thermometer (Lake Shore Cryotronics Inc.) was used.

### 3. Results and discussion

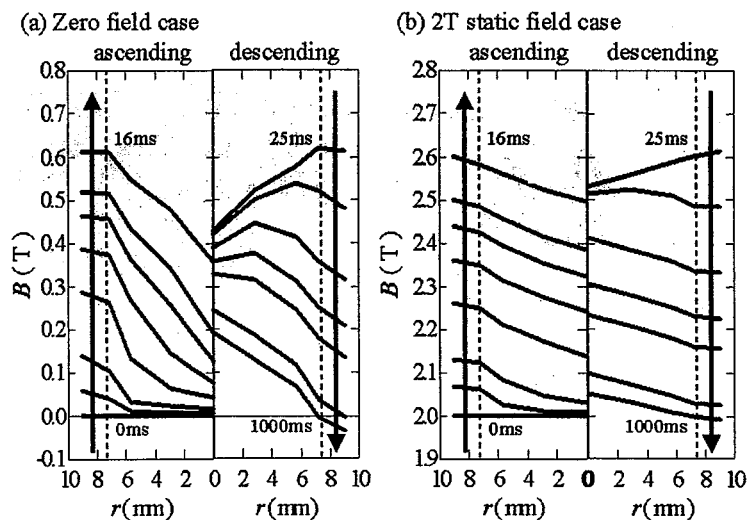
#### 3.1. $E$ - $J$ characteristics

Figure 3 shows the time change in the flux density  $B$  on the surface of the sample during PFM when a single pulse of 0.6 T was applied at 77 K in the presence of the static magnetic field of 0–2 T. The magnetic flux penetrated from the edge and its density decreased toward the centre. With increasing external magnetic field, the slope of the flux density at the periphery decreases, although there is a region with a steep field gradient inside the sample, showing that the flux could not move freely due to viscosity. One can also see that the flux is moving toward the centre, even when the external field was decreasing. This is evidenced by the presence of a transient field peak of the



**Figure 2.** (a) A schematic illustration of an experimental set-up. A pulsed magnetic field is generated by the main coil, and the static field is generated by the superconducting magnet coil. A sample was set at the centre of the main coil. (b) The magnetic field of a sample surface was measured with five Hall sensors and three pick-up coils placed on the sample surface.

sample (see the right-hand side of figure 3(a)). This is probably due to the inertia of flux moving toward the centre or normal conducting electrons in the flux. With further decreasing external field, the field gradient was gradually reversed, and the field became the highest at the centre, and finally the field was trapped in the sample forming a central peak. When a



**Figure 3.** Flux density distribution during pulse field magnetization in Y-Ba-Cu-O samples at 77 K. The origin is at the centre of the sample. The data on the left-hand side are for the increasing field process and those on the right-hand side for the decreasing field process.

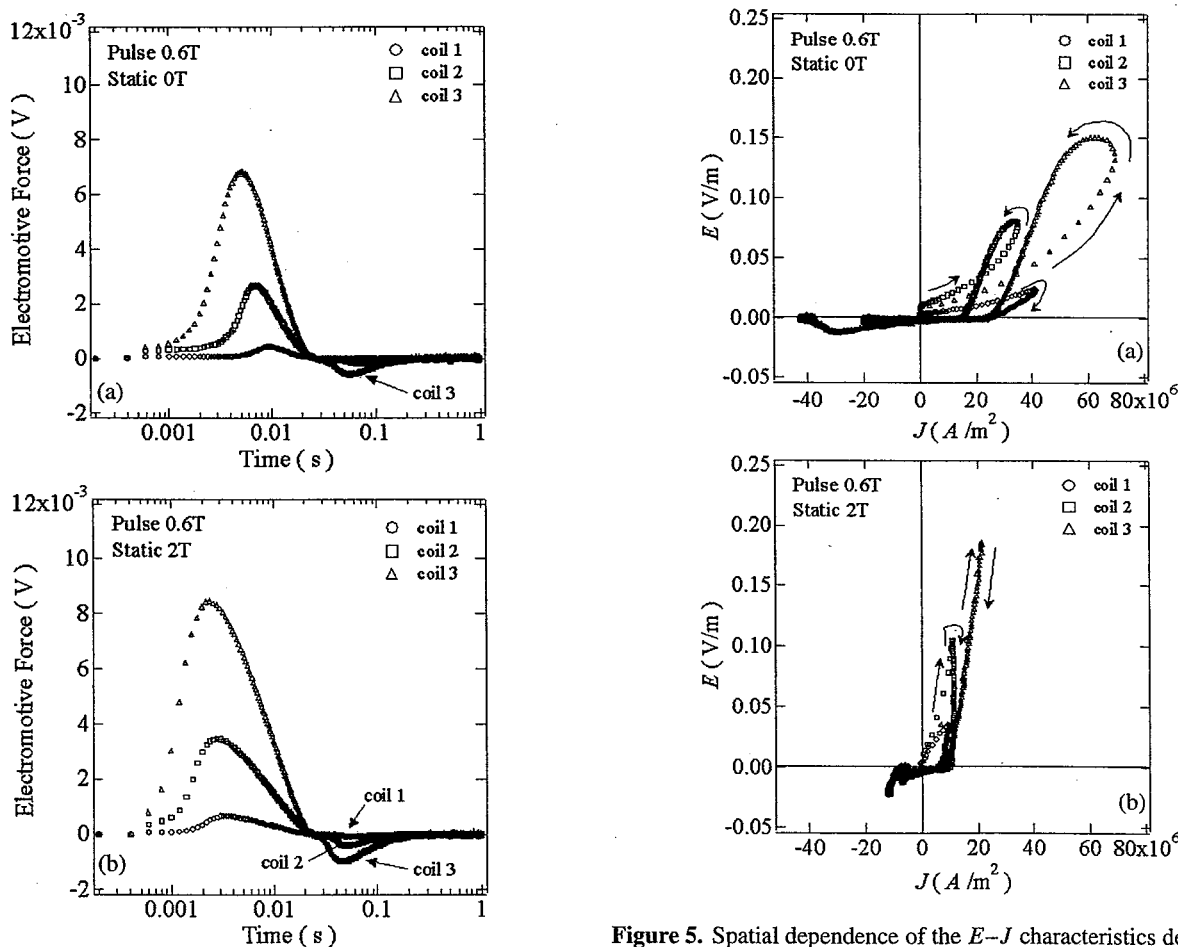


**Figure 4.** Time change in the signal obtained from each pick-up coil under the (a) non-static field and (b) the 2 T static magnetic field. The superposition of the static magnetic field enlarges the signal, and shortens the time for the signal to reach the peak.

static magnetic field of 2 T was applied, the gradient of the flux density was almost constant in the sample both in the field increasing and decreasing processes. In addition, a general trends of flux in and out were almost the same in the two cases.

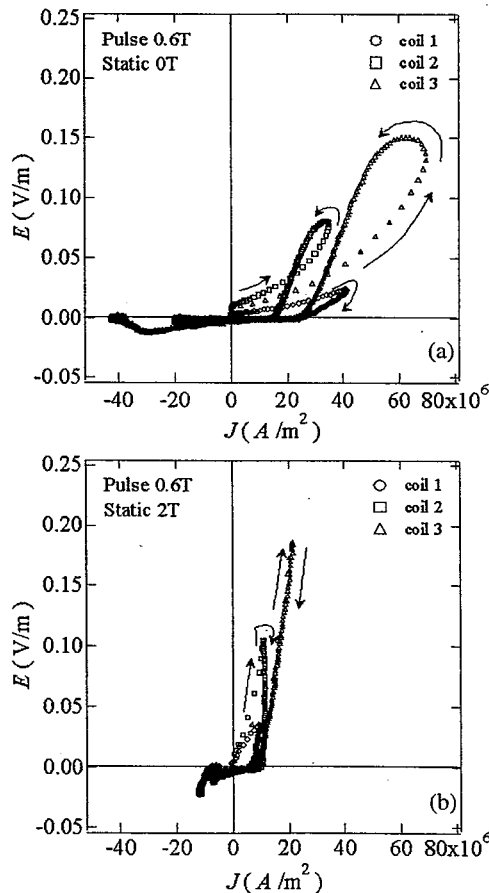


**Figure 5.** Spatial dependence of the  $E$ - $J$  characteristics deduced from the PFM experiments: (a) in a non-static magnetic field; (b) in a 2 T static magnetic field. The superposition of static magnetic field enlarges the electric field, and the slope of  $E$ - $J$  curve shifted toward a lower  $J$  region.

Figure 4 shows the time dependence of the signal obtained from the pick-up coils at the pulsed magnetic field of 0.6 T with and without the bias field. This signal corresponds to the total amount of flux crossing the pick-up coil per unit time. The positive and negative signals show the entrance and the escape

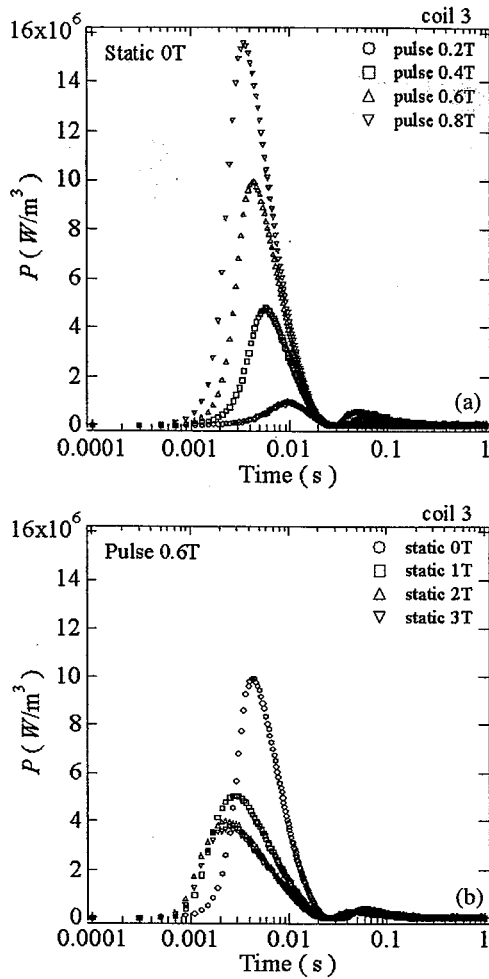


**Figure 6.** The time dependence of the loss power density at coil 3. (a) The loss power density increases with increasing pulse magnetic field. (b) The superposition of the static magnetic field decreases the signal and shortens the time for the signal to reach a peak.

of the flux, respectively. The signal of the outer coil (coil 3) was the largest, and the time to reach a peak sequentially increased from the outer coil to the inner coil. When a static field of 2 T was applied, the pick-up coil signal was larger than the signal without a static field as shown in figure 4(b). This suggests that more flux is moving in the sample due to a smaller flux pinning in the presence of the static field.

We deduced the  $E$ - $J$  characteristics from PFM measurements. Here the current density  $J$  was determined from the field gradient, and the electric field  $E$  was determined from the signal of the pick-up coil. The  $E$ - $J$  characteristics thus determined are presented in figure 5. As shown in figure 5(a), both  $E$  and  $J$  increase with increasing pulse magnetic field. However,  $E$  and  $J$  start to decrease rapidly at a certain point where the flux flow state takes place [7]. When figures 5(a) and (b) are compared, one can see that the superposition of the static magnetic field decreases the field gradient or  $J_c$  value, while it raises the  $E$  values presumably due to the easier flux motion.

### 3.2. Loss of energy and temperature change

It is seen from figure 5 that high voltage and current are generated inside the sample in the field increasing process.

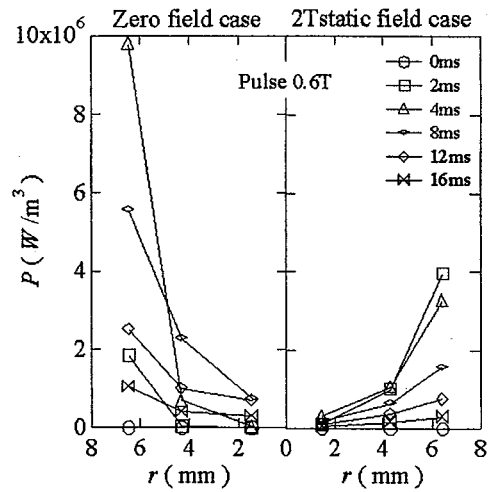


**Figure 7.** Loss power distribution during the PFM process. The left-hand side shows the results under a non-static magnetic field, and the right-hand side shows the results under a 2 T static magnetic field superposition.

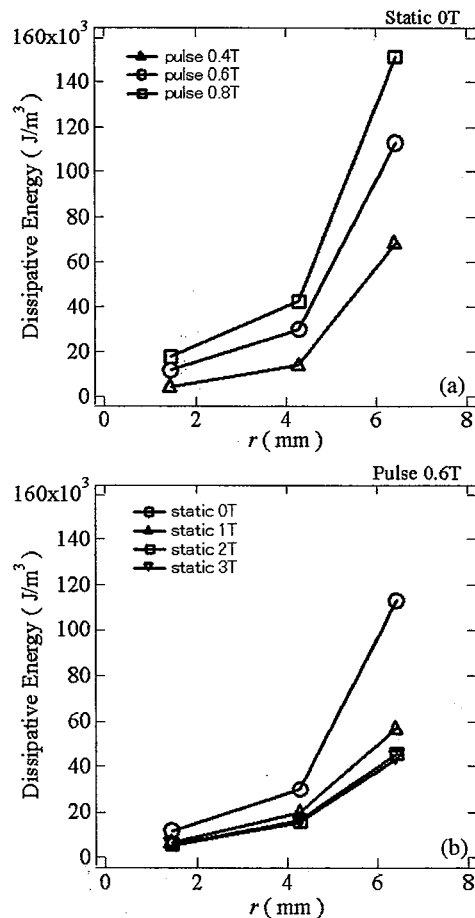


**Figure 8.** The distribution of dissipative energy. (a) Dissipative energy increases with increasing pulse magnetic field. (b) The superposition of the static magnetic field decreased the dissipation energy.

The loss in the power density  $P$  is given by the following formula:

$$P = EJ \text{ (W m}^{-3}\text{)}.$$

Figure 6(a) shows the pulse field dependence of the loss in zero magnetic field in the position at coil 3. The value of

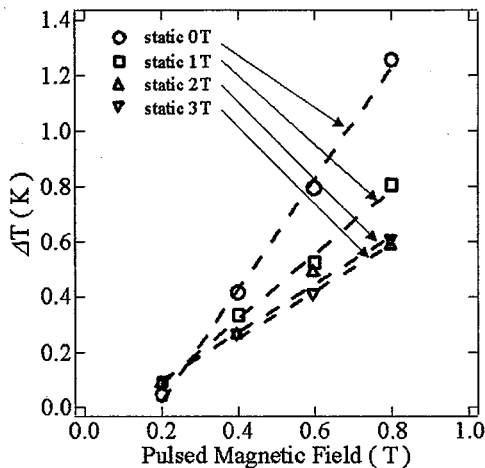


**Figure 9.** Temperature change dependence on the pulsed magnetic field.

the loss power density increases with increasing peak value of the imposed pulse magnetic field. It was found that the loss increased from the start of flux intrusion until the beginning of flux flow, and thereafter the loss started to decrease. Figure 6(b) shows the dependence of the power loss on the magnitude of the static magnetic field at the pulse magnetic field of 0.6 T. The figure shows that the loss decreases sharply on increasing the static magnetic field. It is thus probable that the viscosity decreases with superposition of static magnetic fields [8]. The peak in the loss decrease moves towards shorter times as the static field increases, because flux moves easily when the static magnetic field is superposed. In addition, the peak value of the amount of the flux that enters the sample moves towards shorter times.

Figure 7 shows the spatial variation of the loss power density. The value of loss power density rises from the sample edge. The value of the loss power density is very small at 16 ms when an external magnetic field reaches a peak. The value of the loss power density at the sample edge changes significantly, while it hardly changes near the centre. In zero magnetic field, the loss power density at coil 3 reached a peak of about  $10^7 \text{ W m}^{-2}$  in 4 ms. On the other hand, under a static magnetic field of 2 T, the loss reached a peak value of  $5 \times 10^6 \text{ W m}^{-2}$  in 2 ms, which was about a half that in zero magnetic field.

Figure 8 shows the spatial variation of the dissipative energy which is lost in one second. As shown in figure 8(a), the loss energy increases with increasing pulse magnetic field in zero bias magnetic field. The value of the loss energy at the sample edge is much higher than that at the centre due to a greater flux motion at the edge compared to the centre. The

increase of pulse magnetic field causes the increase of the loss energy. Figure 8(b) shows the positional dependence of the loss energy when static magnetic fields are imposed. The peak value of the applied pulse magnetic field is 0.6 T. It is clear that the superposition of static magnetic fields suppresses the loss of energy. When the static field exceeded 1 T, the loss energy value stayed almost constant.

The dissipative energy causes heat generation. Figure 9 shows the temperature change in the sample surface 1000 ms after applying a pulse field. And the temperature of the sample increases with increasing pulse magnetic field. When static magnetic fields were superposed, the generation of heat was reduced. These results were in good agreement with the calculation results on the loss energy.

#### 4. Summary

We studied the temperature change and the flux motion in melt-processed Y-Ba-Cu-O during pulse field magnetization using pick-up coils and Hall probe sensors. It turns out that the loss energy inside the superconductor increases rapidly immediately after the application of a pulse field, and decreases in the flux flow state. We found that  $\Delta T$  increased with increasing magnitude of the peak field, and was suppressed by the superposition of a static magnetic field.

#### Acknowledgment

This work was supported by the New Energy and Industrial Technology Development Organization (NEDO) as Collaborative Research and Development of Fundamental Technologies for Superconductivity Applications.

#### References

- [1] Tomita M and Murakami M 2003 *Nature* **421** 517
- [2] Mizutani U, Ikuta H, Hosokawa T, Ishihara H, Tazoe K, Oka T, Itoh Y, Yanagi Y and Yoshikawa M 2000 *Supercond. Sci. Technol.* **13** 836
- [3] Ikuta H, Ishihara H, Hosokawa T, Yanagi Y, Itoh Y, Yoshikawa M, Oka T and Mizutani U 2000 *Supercond. Sci. Technol.* **13** 836
- [4] Mizutani U, Oka T, Yanagi Y, Yoshikawa M and Ikuta H 1998 *Appl. Supercond.* **6** 235
- [5] Hari Babu N, Kambara M, Smith P J, Cardwell D A and Shi Y 2000 *J. Mater. Res.* **15** 1235
- [6] Nagashima K, Higuchi T, Sok J, Yoo S I, Fujimoto H and Murakami M 1997 *Cryogenics* **37** 577
- [7] Kono T, Tomita M, Murakami M and Takizawa T 2000 *Supercond. Sci. Technol.* **13** 794
- [8] Kono T, Tomita M, Murakami M and Takizawa T 2000 *Physica C* **341-348** 2437



# Single crystal growth of $\text{SrIn}_2\text{VI}_4$ (VI = S,Se) compounds solidifying through supercooling

T. Takizawa\*, M. Kubo, C. Hidaka

*Department of Physics, College of Humanities and Sciences, Nihon University, Sakura-josui 3-25-40, Setagaya-ku, Tokyo 156-8550, Japan*

Available online 8 December 2004

## Abstract

The  $\text{IIa-III}_2\text{-VI}_4$  (IIa = Ca,Sr, III = Ga,In, VI = S,Se) compounds generally have high melting points more than  $1100^\circ\text{C}$ , and some of them, e.g.,  $\text{SrIn}_2\text{VI}_4$  (VI = S,Se) prefer freezing with supercooling, which makes their crystal growth very difficult. Here, we have adopted a carbon crucible sealed in a quartz ampoule to escape from both the supercooling and the reactivity near the melting point. We have devised the shape of a crucible by preparing a small capillary followed by a bigger hollow pipe for obtaining a large single crystal. A compound is filled in the hole of a crucible by setting the thin part down. It is first heated above the melting point to melt and then cooled down below the supercooling point, where it is solidified. It is again heated to melt but this time keeping the temperature of the small bottom part of a capillary a little below the melting point. Then the melt is slowly cooled down. The nucleation is started from the polycrystalline remainder near the bottom, resulting in a seed crystal in the rest of the thin part as temperature lowers. With the help of the seed, a single crystal continues to grow in a bigger hollow-pipe part of a crucible. Single crystals of  $\text{SrIn}_2\text{S}_4$  and  $\text{SrIn}_2\text{Se}_4$  are grown by this method, and their optical absorption is measured. © 2004 Elsevier B.V. All rights reserved.

PACS: 81.10.-h

Keywords: A1. Supercooling; A2. Horizontal Bridgman method; B1.  $\text{SrIn}_2\text{S}_4$ ; B1.  $\text{SrIn}_2\text{Se}_4$

## 1. Introduction

Recently rare earth element doped  $\text{IIa-III}_2\text{-VI}_4$  (IIa = Ca,Sr, III = Ga,In, VI = S,Se) compounds attract much attention as host materials for visible-light emitting devices. In general, the

constituent elements of these compounds are chemically very reactive with each other, so that explosion of the sealed container sometimes happens during their synthesis. In addition, the resultant compounds have high melting points more than  $1100^\circ\text{C}$ , making their synthesis rather difficult. Further, some of them, e.g.,  $\text{SrIn}_2\text{VI}_4$  (VI = S,Se) prefer freezing with supercooling, also making crystal growth difficult.  $\text{SrIn}_2\text{VI}_4$

\*Corresponding author. Tel./fax: +81 3 5317 9772.

E-mail address: [takiz@chs.nihon-u.ac.jp](mailto:takiz@chs.nihon-u.ac.jp) (T. Takizawa).

(VI = S,Se) compounds were first studied by Klee [1] in 1979, followed by Kipp [2], Donohue [3] and Eisenmann [4]. However, the single crystals having enough size for optical assessment were not obtained up to now mainly due to the reason stated above.

Here, we have adopted a carbon crucible sealed in a quartz ampoule to escape from both the supercooling and the sticking between a melt and its container near the melting point, and succeeded in growing their single crystals for the first time. The key point was how to make a seed for the initial crystal growth and actually it was the shape of the carbon crucible in our case. Single crystals of  $\text{SrIn}_2\text{S}_4$  and  $\text{SrIn}_2\text{Se}_4$  are grown by this method, and the results of their optical absorption are presented.

## 2. Thermal properties

To begin with, the thermal properties of the compounds composing  $\text{SrIn}_2\text{S}_4$  and  $\text{SrIn}_2\text{Se}_4$  were examined by means of differential thermal analysis (DTA) [5]. In Fig. 1(a) and (b), exothermic and endothermic chemical reactions were seen as DTA signals with peaks and dips, respectively. Sr reacted with S and Se around 250 and 450 °C

accompanying abrupt emission of heat, respectively. This reaction sometimes gave strong thermal shock to cause quartz ampoules break. The chemical reaction between In and (S and Se) also occurred with abrupt heat emission around 650 and 250 °C, respectively, producing compounds of  $\text{In}_2\text{S}_3$  and  $\text{In}_2\text{Se}_3$ . The former often causes explosion of a quartz ampoule due to the high vapor pressure of S, while the latter scatters  $\text{In}_2\text{Se}_3$  droplets inside the whole ampoule due to the violent chemical reaction. To escape from those phenomena, compounds of  $\text{In}_2\text{S}_3$  and  $\text{In}_2\text{Se}_3$  prepared in advance were used instead of raw elements (see the third and fourth DTA curves from the top in Fig. 1). Finally, it should be noted that a big supercooling occurred around 900 and 800 °C, respectively, far below each melting point on cooling (see the dotted curves in Fig. 1).

Next, pseudo-phase diagrams of the  $\text{SrS-In}_2\text{S}_3$  and  $\text{-In}_2\text{Se}_3$  systems were constructed using DTA and powder X-ray diffraction, as shown Fig. 2(a) and (b). Experimental details are described elsewhere [5–7]. As seen in Fig. 2, eutectic reactions appear in both diagrams. In the case of  $\text{SrIn}_2\text{S}_4$ , it forms a congruent melt, while  $\text{SrIn}_2\text{Se}_4$  is an incongruent one having peritectic reaction. Thus for the former compound, both melt and flux (using  $\text{In}_2\text{S}_3$  as a self flux) growth methods can be

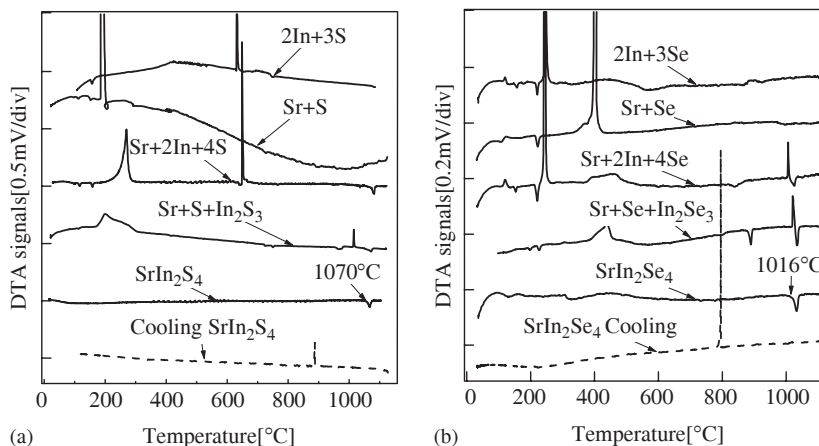


Fig. 1. DTA signals of the composing compounds for (a)  $\text{SrIn}_2\text{S}_4$  and (b)  $\text{SrIn}_2\text{Se}_4$ . The positive one shows the exothermic reaction, while the negative one the endothermic one. The solid line expresses the heating process, and the dashed line the cooling process. The numerals show the melting points of each compound.

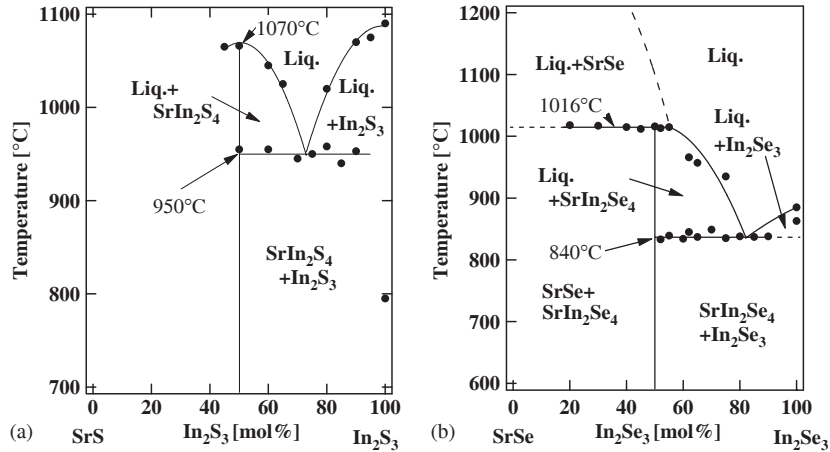


Fig. 2. The pseudo-binary phase diagrams of (a) SrS–In<sub>2</sub>S<sub>3</sub> and (b) SrS–In<sub>2</sub>Se<sub>3</sub>. SrIn<sub>2</sub>S<sub>4</sub> forms a congruent melt, while SrIn<sub>2</sub>Se<sub>4</sub> does a peritectic one.

applied for preparing single crystals, while for the latter one, the flux growth (using In<sub>2</sub>Se<sub>3</sub> as a self flux in this case) is preferred.

In conclusion of this section, we have to avoid the supercooling when growing single crystals of SrIn<sub>2</sub>S<sub>4</sub> and SrIn<sub>2</sub>Se<sub>4</sub> and also the peritectic reaction in the case of SrIn<sub>2</sub>Se<sub>4</sub>. Based on these results, we have decided to grow single crystals using seeds. If seeds exist, single crystals are expected to grow without occurrence of supercooling even at the peritectic point [8].

### 3. Crystal growth

#### 3.1. Preparation of precursors

The precursors of SrIn<sub>2</sub>S<sub>4</sub> and SrIn<sub>2</sub>Se<sub>4</sub> were prepared by combining Sr, S, and Se elements with In<sub>2</sub>S<sub>3</sub> and In<sub>2</sub>Se<sub>3</sub> compounds, respectively. The metal and indium compounds were set in one end of a long quartz ampoule, while S and Se elements were set in the other end. The metal part was heated and hold at 700 °C and the chalcogen part at 400 °C. After 1 day, all chalcogen was absorbed by the metal. Then the metal part was heated up to about 5 °C below the melting point, while keeping the chalcogen part at 600 °C. Thus the precursors were finally prepared by the solid-state reaction, which was important to prevent the products from

sticking to the ampoule wall. These products were supplied for the crystal growth described below.

#### 3.2. A specially devised crucible and the crystal growth

How to make a seed just before the single crystal growth starts is the key problem to be solved for the successful crystal growing [8]. For this purpose, the form of a crucible was specially devised. Carbon was adopted as a constructing material. A small (3 mm in diameter) hole was drilled in a carbon rod of 12 mm<sup>φ</sup> × 100 mm for 40 mm in depth, and a bigger hollow cylinder of 8 mm in diameter and 60 mm in length was made coaxially following it. A photo of the crucible is shown in Fig. 3(a). For easily taking out a grown crystal, a crucible was cut into two parts along the central axis, and two caps were prepared for both ends for preventing the melt from flowing out. A compound is filled in the hole of a crucible by setting the thin part down, that is, in the left-hand side in Fig. 3. The crucible was then set in a horizontal Bridgman furnace and heated above the melting point and then cooled down below the supercooling point, where the compound is solidified. It is again heated to melt but this time keeping the bottom part of the crucible a little below the melting point, that is, a temperature gradient was intentionally made for it. Then it is slowly cooled

down. The nucleation is started from the remaining polycrystals near the bottom, resulting in a seed crystal in the rest part of the thin hole as temperature lowers. With the help of the seed, a

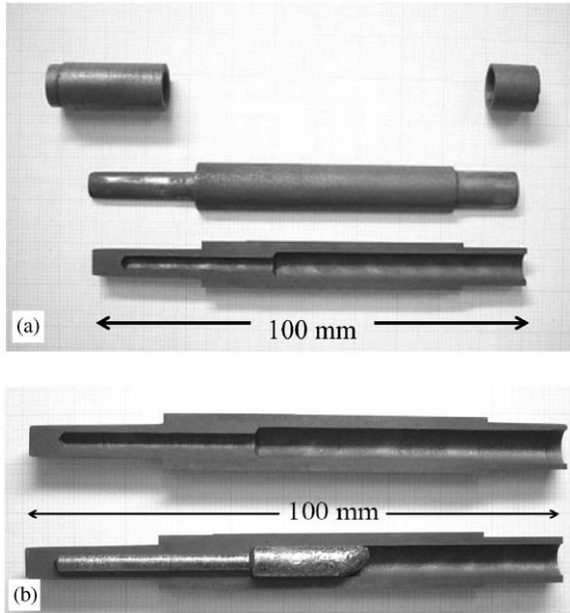


Fig. 3. (a) A set of a specially devised crucible. Two type holes are coaxially drilled in a carbon rod, which is then split into two parts along the cylinder axis to remove a grown crystal easily from the crucible. (b) A grown crystal in a crucible. A single-crystal part was observed from after 10 mm from the left of the crystalline rod.

single crystal continues to grow in a bigger hollow part of a crucible as shown in Fig. 3(b). Cleaved surfaces were clearly observed at both thin and thick parts of a grown  $\text{SrIn}_2\text{S}_4$  crystal. A single crystal was grown from about 10 mm after the beginning of the thin part. Two kinds of single crystals of  $\text{SrIn}_2\text{S}_4$  and  $\text{SrIn}_2\text{Se}_4$  were grown by this method.

#### 4. Optical absorption measurements

Absorption measurements were carried out using single crystal plates with thickness of  $20\ \mu\text{m}$  in the temperature range from 10 to 300 K as shown in Fig. 4(a) and (b). The insets are photographs of each sample plate used.  $\text{SrIn}_2\text{S}_4$  is transparent and colorless, while  $\text{SrIn}_2\text{Se}_4$  is transparent but dark-orange colored. The absorption edge energies,  $E_g$  of  $\text{SrIn}_2\text{S}_4$  and  $\text{SrIn}_2\text{Se}_4$  were estimated as 3.6 and 2.8 eV at 0 K, respectively, and their temperature variations were expressed as follows:

$$E_g(T) = E_g(0) - \frac{\alpha T^2}{T + \beta},$$

where  $\alpha$  are given as  $8.8 \times 10^{-4}$  and  $7.8 \times 10^{-4}$  eV/K, and  $\beta$  are 106 and 197 K, respectively. These values are comparable with those of  $\text{CaGa}_2\text{S}_4$  ( $\alpha = 1.2 \times 10^{-3}$  eV/K and  $\beta = 235$  K) and  $\text{SrGa}_2\text{S}_4$

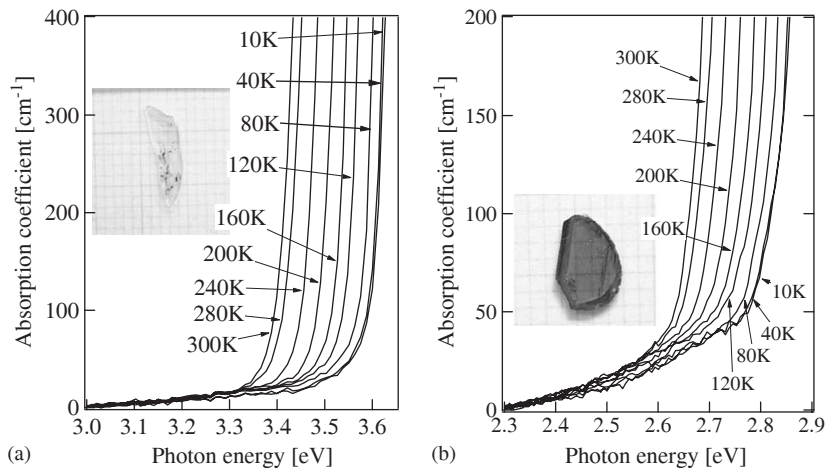


Fig. 4. Optical absorption spectra of (a)  $\text{SrIn}_2\text{S}_4$  and (b)  $\text{SrIn}_2\text{Se}_4$ . The insets are photos of each crystal plate (the thickness is  $20\ \mu\text{m}$ ).

( $\alpha = 1.7 \times 10^{-3}$  eV/K and  $\beta = 459$  K) [7]. The smaller values of  $\beta$  may indicate the weaker bond strength in SrIn<sub>2</sub>S<sub>4</sub> and SrIn<sub>2</sub>Se<sub>4</sub> in comparison to Ca and Sr thiogallates.

## 5. Summary

Single crystals of SrIn<sub>2</sub>S<sub>4</sub> and SrIn<sub>2</sub>Se<sub>4</sub> were successfully grown using a specially devised carbon crucible for escaping from the supercooling. It was also found that the carbon crucible was effective for preventing the high-temperature melt from sticking to the wall inside quartz ampoules. Absorption measurements were carried out to determine the energy gaps of both materials.

## Acknowledgements

This work is partly supported by the grant for the High-Technology Research Center Project

for private universities from Ministry Of Education, Sports, Science, Culture and Technology, Japan.

## References

- [1] W. Klee, H. Schaefer, Rev. Chim. Miner. 16 (1979) 465.
- [2] D.O. Kipp, C.K. Lowe-Ma, T.A. Vanderah, Chem. Mater. 2 (1990) 506.
- [3] P.C. Donohue, J.E. Hanlon, J. Electrochem. Soc. 121 (1974) 137.
- [4] B. Eisenmann, A. Hofmann, Z. Kristallogr. 197 (1991) 167.
- [5] H. Matsushita, T. Takizawa, Jpn. J. Appl. Phys. 34 (1995) 4699.
- [6] C. Komatsu, T. Takizawa, J. Crystal Growth 210 (2000) 677.
- [7] C. Hidaka, T. Takizawa, J. Crystal Growth 237 (2002) 2009.
- [8] E. Niwa, K. Masumoto, Ternary and Multinary Compounds in the 21st Century IPAP Books, vol. 1, 2001, p. 39.



ELSEVIER

Available online at [www.sciencedirect.com](http://www.sciencedirect.com)

SCIENCE @ DIRECT®

Physica C 392–396 (2003) 391–395

PHYSICA C

[www.elsevier.com/locate/physc](http://www.elsevier.com/locate/physc)

# Effect of pinning on the flux motion of Gd–Ba–Cu–O bulk superconductors

K. Yoshizawa<sup>a,b,\*</sup>, S. Nariki<sup>b</sup>, M. Murakami<sup>b</sup>, T. Takizawa<sup>a</sup>

<sup>a</sup> *Department of Physics, College of Humanities and Sciences, Nihon University, 3-25-40 Sakura-Josui, Setagaya-ku, Tokyo 156-8550, Japan*

<sup>b</sup> *Superconductivity Research Laboratory, International Superconductivity Technology Center, 1-16-25 Shibaura, Minato-ku, Tokyo 105-0023, Japan*

Received 13 November 2002; accepted 17 February 2003

## Abstract

We have observed the flux motion using Hall probe sensors that are placed on the surface of high quality Y–Ba–Cu–O and Gd–Ba–Cu–O disks 15 mm in diameter with 0.95 mm thickness with applying pulsed magnetic field. The peak value of the field was varied from 0.1 to 0.8 T. The effects of static bias fields was also studied in the field range of 0–3 T at 77 K. Gd–Ba–Cu–O shows the clear secondary peak effect on the  $J_c$ – $B$  curve so that the pinning property was different from Y–Ba–Cu–O for which  $J_c$  monotonically decreases with field. The flux motion was enhanced in Y–Ba–Cu–O with increasing static bias field, while that was suppressed in Gd–Ba–Cu–O, reflecting the secondary peak effect.

© 2003 Elsevier B.V. All rights reserved.

PACS: 74.72.–h; 74.60.Ge

Keywords: Pulsed-magnetic magnetization; Peak effect; GdBa<sub>2</sub>Cu<sub>3</sub>O<sub>y</sub>; YBa<sub>2</sub>Cu<sub>3</sub>O<sub>y</sub>

## 1. Introduction

Bulk Y–Ba–Cu–O exhibits the critical current density ( $J_c$ ) exceeding  $1 \times 10^4$  A/cm<sup>2</sup> at 77 K and has potential for various engineering applications. Recently, LRE–Ba–Cu–O (LRE: Nd, Sm, Eu and Gd) superconductors have been found to exhibit

higher  $J_c$  values of  $5\text{--}10 \times 10^4$  A/cm<sup>2</sup> at 77 K accompanied by the secondary peak effect on the  $J_c$ – $B$  curve [1]. Hence LRE–Ba–Cu–O bulk superconductors are promising candidates for high field applications such as high trapped-field magnets. The secondary peak effect of LRE–Ba–Cu–O has been intensively studied in a static magnetic field [2–4]. It will be interesting to study how the peak effect affects the dynamical motion of flux lines.

In this work, we therefore studied the response of Y–Ba–Cu–O and Gd–Ba–Cu–O disk samples to pulse magnetic fields with an emphasis placed on the effect of secondary peak on flux pinning properties.

\* Corresponding author. Address: Superconductivity Research Laboratory, International Superconductivity Technology Center, 1-16-25 Shibaura, Minato-ku, Tokyo 105-0023, Japan. Tel.: +81-3-3454-9284; fax: +81-3-3454-9287.

E-mail address: [yoshizawa@istec.or.jp](mailto:yoshizawa@istec.or.jp) (K. Yoshizawa).

## 2. Experimental

Bulk Y–Ba–Cu–O ( $\text{YBa}_2\text{Cu}_3\text{O}_y$ ;  $\text{Y}_2\text{BaCuO}_5 = 10:4$ ) and Gd–Ba–Cu–O ( $\text{GdBa}_2\text{Cu}_3\text{O}_y$ ;  $\text{Gd}_2\text{BaCuO}_5 = 10:4$ ) were prepared with the top-seeded melt-growth (TSMG) process in air [5,6]. The disk samples with dimensions of 15.03 mm in diameter and thickness of 0.95 mm were cut from TSMG processed blocks with the  $c$ -axis perpendicular to the wide surface.

Fig. 1 shows the distribution of the axial component of the trapped flux density  $B_z$  at 77 K for Y–Ba–Cu–O and Gd–Ba–Cu–O disk samples. A single-peak profile indicates that the both samples are single-grain without weak-links. Fig. 2 shows the  $J_c$ – $B$  curves for Y–Ba–Cu–O and Gd–Ba–Cu–O specimens. The  $J_c$  values were estimated based on the extended Bean model [7]. The Gd–Ba–Cu–O specimen exhibited the secondary peak effect at about 2 T. Fig. 3 illustrates the geomet-

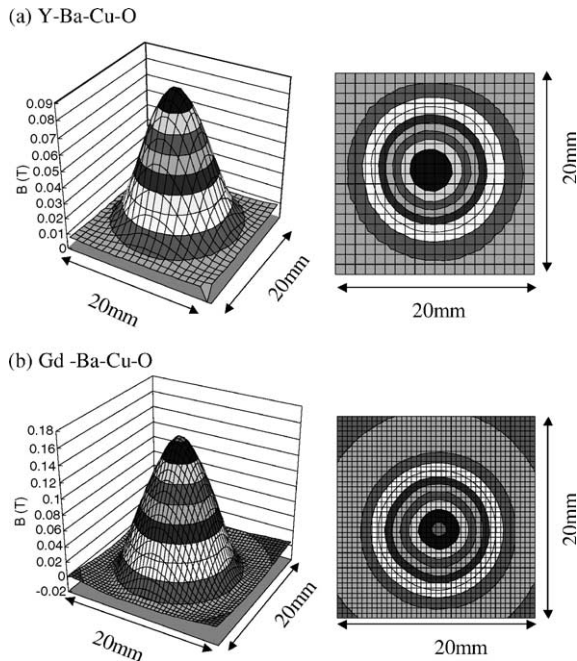


Fig. 1. Trapped field distribution for (a) Y–Ba–Cu–O and (b) Gd–Ba–Cu–O samples about 15 mm in diameter measured by scanning a Hall sensor at 1 mm above the sample surface.

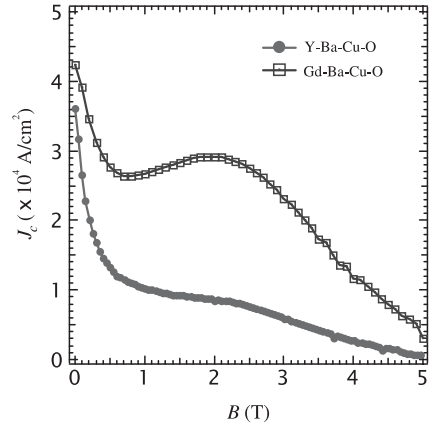


Fig. 2. Field dependence of the critical current density ( $J_c$ ) for the Y–Ba–Cu–O and Gd–Ba–Cu–O samples. It should be noted that Gd–Ba–Cu–O exhibits clear secondary peak effect on the  $J_c$ – $B$  curve.

rical configuration of the main part of our experimental apparatus [8]. The sample was set at the center of the inner normal conducting coil set in a superconducting magnet. The peak value of the applying pulsed field was varied from 0.1 to 0.8 T with static bias fields in the range of 0–3 T at 77 K. Magnetic flux distribution on the sample surface was measured with five Hall probe sensors placed along radial direction as shown in Fig. 3(b).

## 3. Results and discussion

### 3.1. Magnetic flux density distribution

Fig. 4 shows the time-dependence of the field distribution on the surface of Gd–Ba–Cu–O and Y–Ba–Cu–O samples when a single pulse of 0.6 T was applied at 77 K in the presence of the static magnetic field of 0–2 T. The magnetic flux penetrated from the edge of the sample, and its density decreased from the edge toward the center. In the case of Y–Ba–Cu–O, the amount of penetrated field was always greater in the presence of static bias field than that in the absence of the static field. In contrast, the resistance against flux penetration in case of Gd–Ba–Cu–O was enhanced with

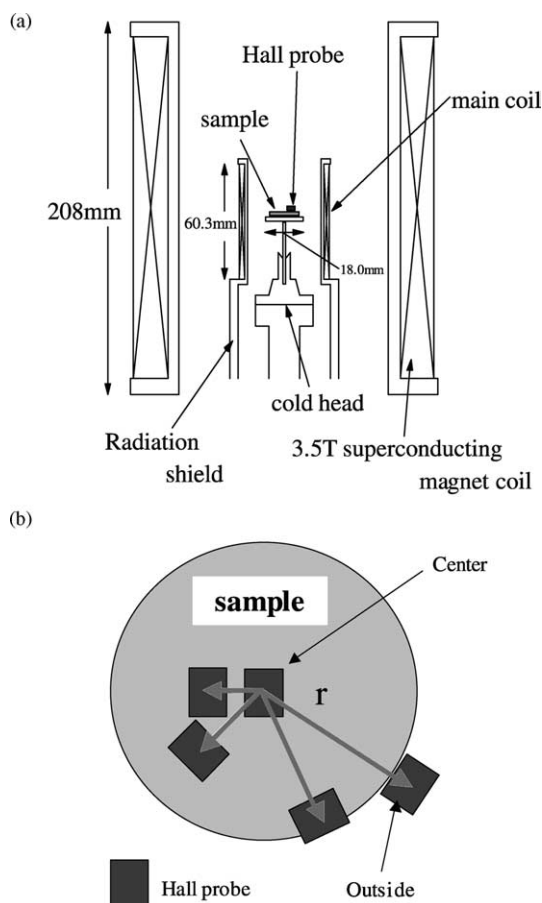


Fig. 3. (a) Schematic diagram of an experimental setup. A pulsed magnetic field is generated by the main coil, and the static field is generated by the superconducting magnet coil. The sample was set at the center of the main coil. (b) The magnetic field of a sample surface was measured with five Hall sensors placed on the sample surface.

increasing static bias field, which reflects the secondary peak effect.

### 3.2. Voltage–current characteristics

It is seen from Fig. 4 that the flux gradient is steeper near the edge in the field increasing process. The radial field gradient ( $\partial B/\partial r$ ) and the time derivative ( $\partial B/\partial t$ ) of magnetic field correspond to the current and voltage, respectively [8]. Based on this, the static field dependence of voltage–current

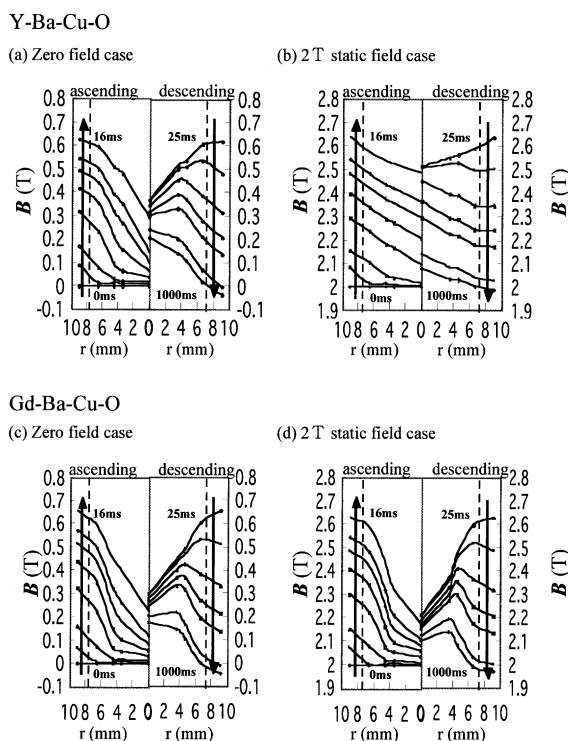


Fig. 4. Flux density distribution during the pulse field magnetization process in Y–Ba–Cu–O and Gd–Ba–Cu–O samples at 77 K. The center of a sample is the origin. The data on the left hand side is for the increasing field process and those on the right hand side for the decreasing field process.

( $V$ – $I$ ) characteristics was deduced from Fig. 4, and the results are shown in Fig. 5. In the case of Y–Ba–Cu–O, the slope of  $V$ – $I$  curve became steeper and shifted toward the lower  $I$  region as the static field increased. In the case of Gd–Ba–Cu–O, however, at first the inclination of  $V$ – $I$  curve became steeper, and it became gradual by piecemeal when the static field topped 2 T. In addition, as the superimposed static magnetic field increased, the value of  $I$  at  $V = 0$  ( $J_c$ ) was larger than the value without static bias field.

### 3.3. Flow resistivity

As is clearly seen from Fig. 5,  $V$ – $I$  curves have gradient like a normal conducting state, showing that some resistance is created by flux motion,

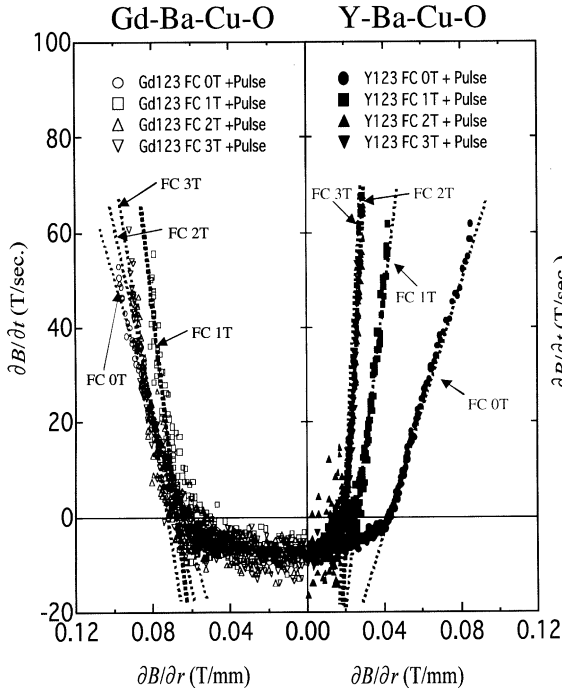


Fig. 5. Static field dependence of the voltage–current ( $V$ – $I$ ) characteristics deduced from the pulse field magnetization experiments. The time derivative ( $\partial B/\partial t$ ) and the radial field gradient ( $\partial B/\partial r$ ) of the magnetic field correspond to  $V$  and  $I$ , respectively. The left hand side shows the characteristic of Gd–Ba–Cu–O and the right side for Y–Ba–Cu–O.

which is called the flow resistivity. Here the flux flow resistivity  $\rho_f$  is given by the following relation:

$$\rho_f = \frac{E}{J}, \quad (1)$$

where  $E$  is the electric field and  $J$  the current density.

The motion of quantized fluxoids are governed by the balance of the pinning force  $F_p$  the Lorentz force  $F_L$  and the viscosity force  $F_v$ . These forces are expressed by the following equation:

$$F_p = J_c \times B, \quad (2)$$

$$F_L = J \times B, \quad (3)$$

$$F_v = -\eta \left( \frac{|B|}{\Phi_0} \right), \quad (4)$$

where  $J$ ,  $J_c$ ,  $\Phi_0$  and  $\eta$  is the current density, the critical current density, the flux quantum and

the viscous coefficient, respectively. For  $J > J_c$ , the electric field is  $E = \rho_f(J - J_c)$ . Consequently,  $\eta$  is obtained from the following relation:

$$\eta = \frac{\Phi_0 B}{\rho_f}. \quad (5)$$

Fig. 6 shows the viscosity coefficients  $\eta$  evaluated. The effect of the static magnetic field on the viscosity coefficient is much greater than that of

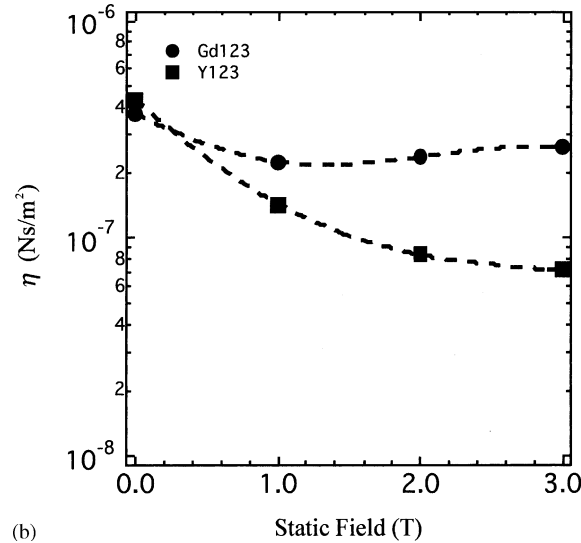
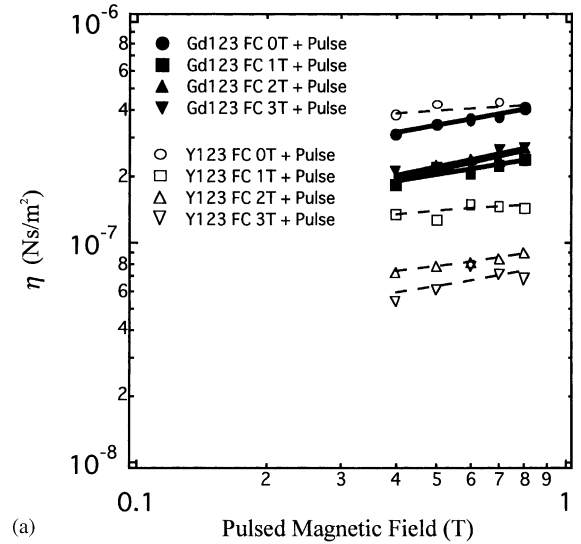


Fig. 6. Plots of the viscosity coefficients  $\eta$  (a) as a function of pulsed magnetic field and (b) as a function of static magnetic field when the peak value of the pulsed magnet field is fixed at 0.6 T.

the pulsed magnetic field. And the value of viscosity coefficient  $\eta$  of Y–Ba–Cu–O decreased with increasing the static bias field. In sharp contrast, the static field did not decrease the viscosity coefficient  $\eta$  of Gd–Ba–Cu–O. It is also notable that the value of viscosity coefficient  $\eta$  of Gd–Ba–Cu–O reached minimum at 1 T, which also reflects the secondary peak effect.

#### 4. Summary

In this work, we have measured the flux motion induced by pulsed magnetic field in Y–Ba–Cu–O and Gd–Ba–Cu–O disks. The effect of static bias field on the flux motion was also studied in the range of 0–3 T at 77 K. In the presence of the static bias field, the flux motion of Gd–Ba–Cu–O was different from that of Y–Ba–Cu–O, reflecting the secondary peak effect. The flux motion was enhanced with increasing static bias field in Y–Ba–Cu–O, while the flux motion in Gd–Ba–Cu–O was suppressed and the viscosity was enhanced with increasing static field.

#### Acknowledgements

This work was supported by the New Energy and Industrial Technology Development Organization (NEDO) as Collaborative Research and Development of Fundamental Technologies for Superconductivity Applications.

#### References

- [1] M. Muralidhar, M.R. Koblischka, M. Murakami, *Adv. Supercond.* 12 (2000) 494.
- [2] M.R. Koblischka, T.H. Johansen, M. Murakami, *Supercond. Sci. Technol.* 13 (2000) 745.
- [3] T. Mochida, N. Chikumoto, M. Murakami, *Phys. Rev. B* 64 (2001) 64518.
- [4] T. Matsushita, E.S. Otabe, *Physica C* 335 (2000) 153.
- [5] A. Endo, H.S. Chauhan, T. Egi, Y. Shiohara, *J. Mater. Res.* 11 (1996) 795.
- [6] H. Hinai, S. Nariki, S.-J. Seo, N. Sakai, M. Murakami, M. Otsuka, *Supercond. Sci. Technol.* 13 (2000) 676.
- [7] E.M. Gyorgy, R.B. van Dover, K.A. Jackson, L.F. Schneemeyer, J.V. Waszczak, *Appl. Phys. Lett.* 55 (1989) 283.
- [8] T. Kono, M. Tomita, M. Murakami, T. Takizawa, *Supercond. Sci. Technol.* 13 (2000) 794.



ELSEVIER

Journal of Physics and Chemistry of Solids 64 (2003) 1511–1517

JOURNAL OF  
PHYSICS AND CHEMISTRY  
OF SOLIDS

[www.elsevier.com/locate/jpcs](http://www.elsevier.com/locate/jpcs)

## Radiative and non-radiative processes of Ce related transitions in $\text{CaGa}_2\text{S}_4$ and $\text{SrGa}_2\text{S}_4$

A. Kato<sup>a,\*</sup>, M. Yamazaki<sup>b</sup>, H. Najafov<sup>a</sup>, K. Iwai<sup>a</sup>, A. Bayramov<sup>a</sup>, C. Hidaka<sup>c</sup>,  
T. Takizawa<sup>c</sup>, S. Iida<sup>a</sup>

<sup>a</sup>Nagaoka University of Technology, Nagaoka 940-2188, Japan

<sup>b</sup>Nagaoka National College of Technology, Nagaoka 940-8532, Japan

<sup>c</sup>College of Humanities and Sciences, Nihon University, Tokyo 156-8550, Japan

### Abstract

The Ce emission appearing in the blue–green region was investigated for  $\text{CaGa}_2\text{S}_4$  and  $\text{SrGa}_2\text{S}_4$ . The room temperature quantum efficiency as high as 73% was observed for a 0.4 wt% Ce-doped  $\text{CaGa}_2\text{S}_4$  single crystal grown by the melt method. The quantum efficiency decreased for a 0.8 wt% Ce-doped  $\text{CaGa}_2\text{S}_4$  crystal and clear photoacoustic signal was detected in this sample, indicating an increase of non-radiative transition. For each of these compounds, ultraviolet (UV) excitation produced a hitherto unreported new UV emission which is thought to originate from  $5d(E_g)$  level of the Ce ion. Temperature dependent intensity changes observed in this UV emission and in the blue–green emission suggest temperature dependent population transfer from the upper level of  $E_g$  to the lower level of  $T_{2g}$  in the excited state of 5d electrons.

© 2003 Elsevier Ltd. All rights reserved.

### 1. Introduction

Ce-doped alkaline earth thiogallates are regarded as promising host materials for blue–green light emitting devices including lasers [1,2]. Photoluminescence spectra of  $\text{CaGa}_2\text{S}_4:\text{Ce}$  and  $\text{SrGa}_2\text{S}_4:\text{Ce}$  are known to exhibit the characteristic blue–green double bands [1]. In order to realize light emitting device applications, it is necessary to fully understand radiative and non-radiative processes of this Ce impurity center. This study is concerned with photoluminescence (PL) and photoluminescence excitation (PLE) spectra, absorption and photoacoustic (PA) spectra, photoluminescence quantum efficiencies, and relations among them, mainly with  $\text{CaGa}_2\text{S}_4$  crystals of different Ce concentrations.

In the ultraviolet region of the spectrum of each compound, a new emission which was not reported before has been found in this study. Temperature dependent intensity changes of the UV and blue–green emissions are

discussed in terms of a configuration coordinate model for the Ce ion.

### 2. Experimental

Polycrystalline  $\text{CaGa}_2\text{S}_4:\text{Ce}$  and  $\text{SrGa}_2\text{S}_4:\text{Ce}$  samples were synthesized from  $\text{CaS}/\text{SrS}$  and  $\text{Ga}_2\text{S}_3$  powders mixed in stoichiometric composition and annealed at 900 °C under a stream of  $\text{H}_2\text{S}(10\%) + \text{Ar}$  for 15 h. The initially obtained polycrystalline samples were re-ground and then re-annealed in the same atmosphere for 24 h. The dopant was added into the source powder in the form of  $\text{Ce}_2\text{S}_3$ . General emission characteristics are compared for polycrystalline  $\text{CaGa}_2\text{S}_4:\text{Ce}$  and  $\text{SrGa}_2\text{S}_4:\text{Ce}$ . In order to know detailed characteristics of the blue–green emission, single crystals of  $\text{CaGa}_2\text{S}_4:\text{Ce}$  were grown by the melt method at an ampoule cooling speed of 0.5 cm/h from 1150 to 1100 °C [3]. The sizes of crystals were about  $2 \times 2 \times 1 \text{ mm}^3$ . For absorption measurements, the crystals were polished to be about 0.1 mm thickness.

For PL measurements, the sample was excited by monochromatic light obtained by combining a 150 W Xe

\* Corresponding author. Fax: +81-258-47-9500.

E-mail address: [arikato@vos.nagaokaut.ac.jp](mailto:arikato@vos.nagaokaut.ac.jp) (A. Kato).

lamp (Hamamatsu, L2175) and a double monochromator (Ritsu, MC-30NW) or by the 3250 Å line of a He–Cd laser (Omnichrome, 3056-M-A01). Photoluminescence from the sample was dispersed through a monochromator (Nalumi, RM-23) and detected by a photomultiplier (Hamamatsu, R943-02) coupled to a photon counter (Hamamatsu, C767). For PLE measurements, the sample was excited by monochromatic light obtained by combining the 150 W Xe lamp and the double monochromator. The sample was mounted on the cold finger of an optical cryostat coupled to a closed cycle He-refrigerator (Iwatani, CryoMini D105) for measurements of temperature dependence. For time decay measurements, a dye laser (Lambda Physics, FL 3002E, dye:stilbene 420) pumped by a Xe–Cl laser (Lambda Physics, LEXTRA 200) or the Xe–Cl laser was used as the excitation source. Emission from sample was dispersed through a monochromator (Instruments SA, HR-320) and temporal variation of the emission was monitored on a digital oscilloscope (Sony Tektronix, TDS380P) coupled with a photomultiplier (Toshiba, PM55).

For absorption measurements, monochromatic light obtained by combining the 150 W Xe lamp and the double monochromator was transmitted through the sample. The transmitted light was detected by the photomultiplier (Toshiba, PM55). The absorption coefficient was derived from the measured transmittance taking into account of multiple internal reflections. PA spectrum measurements were done by gas-microphone method. The sample was excited by monochromatic light obtained by combining a 500 W Xe lamp and a monochromator (Jobin Yvon, HR-320). PA signal was detected by a microphone coupled to a lock-in amplifier (Stanford Research, SR-530).

Quantum efficiency measurements were performed at room temperature with an integration glass semi-sphere having a small hole at the top to introduce laser light for exciting photoluminescence of the sample inside. The diameter of this semi-sphere is 60 mm and the bottom of the semi-sphere is covered by a glass plate. The inner surfaces of the semi-sphere and the glass plate were frosted to diffuse light and the outer surface was coated by thick Al evaporation to reflect and confine light inside. The light inside thus constructed semi-sphere is believed to be completely diffused. The glass plate has a small non-Al-coated portion through which light inside the semi-sphere can be detected by a photomultiplier. Construction details were given in Ref. [4]. A He–Cd laser (Omnichrome, 4056-M-A01) emitting the 4416 Å line was used as a light source. The absorbed amount of excitation light and the emitted amount of photoluminescence were determined by measuring photomultiplier outputs with the help of a band pass filter (Hoya, B390) or a cut-off filter (Toshiba, Y46) by placing the sample inside in comparison with the output for a small piece of non-absorbing opaque quartz. In calculating the quantum efficiency values these outputs were corrected by taking into account of measured transmittances of the filters and the spectral sensitivity

of the photomultiplier given by the manufacturer (Hamamatsu). For these obtained quantum efficiency values, the error corresponding to the experimental accuracy was checked to be less than 5% by measuring the output corresponding to incident laser light whose power was known.

### 3. Results

#### 3.1. Blue–green emission

Fig. 1 shows PL and PLE spectra of 2 wt% Ce-doped polycrystalline  $\text{CaGa}_2\text{S}_4:\text{Ce}$  (a) and  $\text{SrGa}_2\text{S}_4:\text{Ce}$  (b) at room temperature. The PL and PLE spectra of both compounds are quite similar. The PL spectra consist of two overlapping bands in the blue–green region. The PLE spectra consist of a main blue band and an UV band. The mirror image relation looks to hold between the higher energy band of the PL spectra and the main band of the PLE spectra for both compounds, showing the phonon terminated transition character. The difference of these emissions between  $\text{CaGa}_2\text{S}_4:\text{Ce}$  and  $\text{SrGa}_2\text{S}_4:\text{Ce}$  is only the peak position. For PL spectrum of  $\text{CaGa}_2\text{S}_4:\text{Ce}$ , the peaks are at 2.65 eV (4680 Å) and at 2.40 eV (5170 Å). The main band of the PLE spectrum of  $\text{CaGa}_2\text{S}_4:\text{Ce}$  is seen at 2.8 eV. An almost parallel shift to higher energy by about 0.1 eV is seen for all corresponding peaks in the case of  $\text{SrGa}_2\text{S}_4:\text{Ce}$ .

Fig. 2 shows PL and PLE spectra of  $\text{CaGa}_2\text{S}_4:\text{Ce}$  single crystals for various Ce concentrations at room temperature. The excitation photon energy of the PL spectra was 2.89 eV and the monitoring photon energy of the PLE spectra was 2.65 eV. The width of the main PLE band becomes broader and the peak position shifts towards lower energy with increasing Ce concentration. The shape of the band shows some changes at higher energy side. On the other hand,

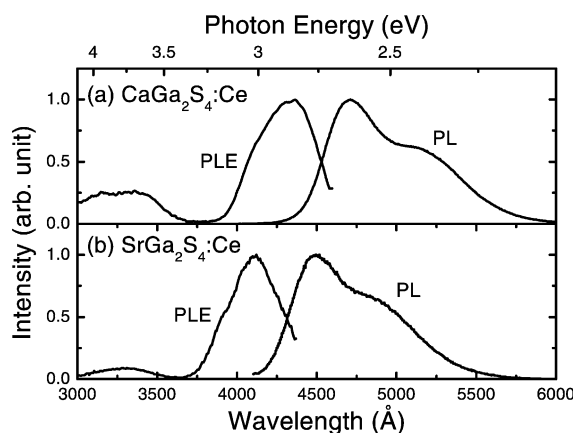


Fig. 1. PL and PLE spectra of (a)  $\text{CaGa}_2\text{S}_4:\text{Ce}$  (2 at%) and (b)  $\text{SrGa}_2\text{S}_4:\text{Ce}$  (2 at%).

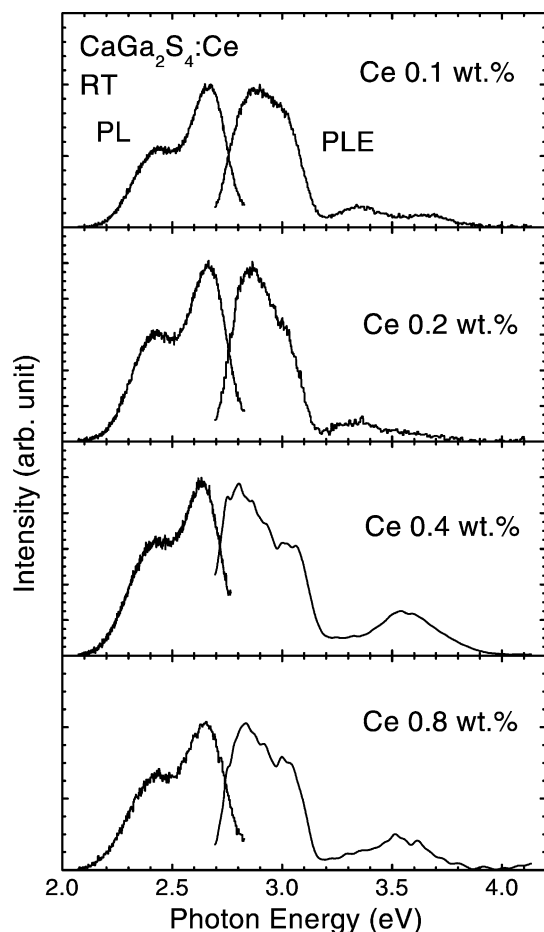


Fig. 2. PL spectra excited by 2.89 eV and PLE spectra monitored at 2.65 eV for different Ce concentrations of  $\text{CaGa}_2\text{S}_4:\text{Ce}$  single crystals (0.1–0.8 wt%).

the PL spectra do not show changes corresponding to the PLE spectra except a slight peak shift to lower energy with increasing Ce concentration. For the PLE spectrum of polycrystalline  $\text{CaGa}_2\text{S}_4:\text{Ce}$  (2 wt%) shown in Fig. 1(a), the peak energy of the main PLE band is close to that of the single crystal  $\text{CaGa}_2\text{S}_4:\text{Ce}$  (0.8 wt%). However, the peak energy of the PL spectrum is slightly lower than that of the single crystal.

The quantum efficiency as high as 73% was observed for the 0.4 wt% Ce-doped single crystal, however the lower value of 32% was observed for the 0.8 wt% Ce-doped single crystal.

Fig. 3(a) shows absorption spectrum of the 0.8 wt% Ce-doped  $\text{CaGa}_2\text{S}_4:\text{Ce}$  single crystal at room temperature. The peak of the Ce absorption band is seen at 2.92 eV and the half width is about 180 meV. The shape of this observed band does not change with Ce concentration. Fig. 3(b) shows peak absorption coefficient as a function of Ce concentration.

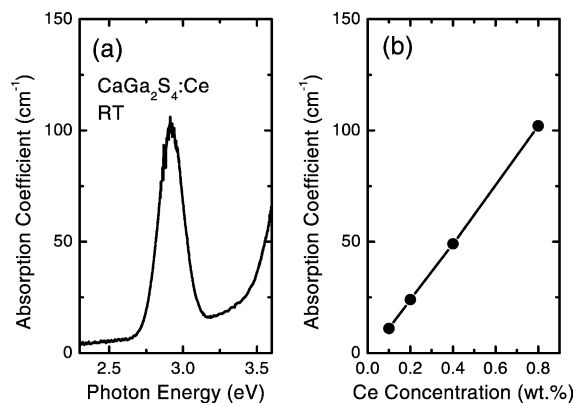


Fig. 3. (a) Absorption spectrum of the  $\text{CaGa}_2\text{S}_4:\text{Ce}$  single crystal (0.8 wt%), (b) peak absorption coefficient as a function of Ce concentration.

Fig. 4(a) shows the PA spectrum of the 0.8 wt% Ce-doped single crystal. For comparison, the absorption spectrum is shown again in Fig. 4(b), and the PL and PLE spectra in Fig. 4(c). From samples where the Ce concentrations are 0.1, 0.2 and 0.4 wt%, detectable PA signal was not observed. The peak of the PA band corresponds to that of the absorption band. The half width of the PA band is about 220 meV, being broader than that of the absorption band of 180 meV. The PA band broadens to higher energy region compared to the absorption band.

### 3.2. UV emission

The solid line of Fig. 5 shows the PL spectrum of 0.1 wt% Ce-doped polycrystalline  $\text{CaGa}_2\text{S}_4$  at 10 K excited by the 3250 Å line of the He–Cd laser. UV excitation was found to produce an emission in the region of 3500–4250 Å in addition to the blue–green emission. To the best of our knowledge, there is no report on this UV emission of  $\text{CaGa}_2\text{S}_4:\text{Ce}$ . The spectral shape of the UV emission is not similar to that of the blue–green emission which consists of two overlapping bands. The PL spectrum of this UV emission can be well reproduced by superposition of three Gaussian components (the first component peaked at 3.39 eV (3650 Å), the second at 3.30 eV (3750 Å), the third at 3.10 eV (3995 Å)) as shown in the inset of Fig. 5. The energy difference of the peaks between the first and the third components is 0.29 eV. The difference between the second and the third components is 0.20 eV. The intensity of the UV emission decreased with increasing Ce concentrations. The UV emission was not observed in undoped samples, indicating a relation with Ce doping. The dotted line of Fig. 5 shows the PLE spectrum of the UV emission monitored at 3995 Å. The PLE spectrum consists of a single band peaked at 3285 Å (3.77 eV). The shape and the peak position of this band were found to be independent of the monitoring wavelength. For  $\text{SrGa}_2\text{S}_4:\text{Ce}$ , the situation was similar. Under UV excitation, the UV emission of

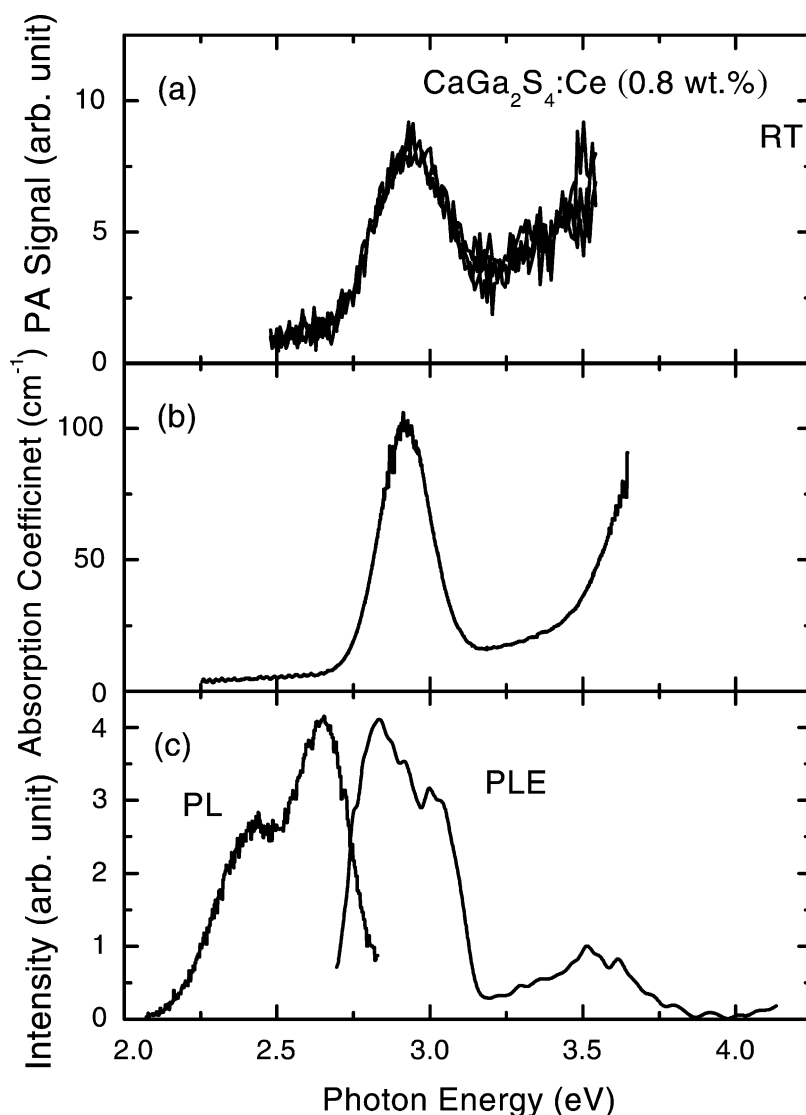


Fig. 4. Comparison among PA, absorption, PL and PLE spectra of the 0.8 wt% Ce-doped single crystal. (a) PA spectrum, (b) absorption spectrum, (c) PL and PLE spectra.

$\text{SrGa}_2\text{S}_4:\text{Ce}$  which was not reported before, similarly as in  $\text{CaGa}_2\text{S}_4:\text{Ce}$ , was found to appear in the region of 3300–4000 Å.

The intensity of the UV emission of  $\text{CaGa}_2\text{S}_4:\text{Ce}$  gradually decreases with increasing temperature. The emission disappears totally at temperatures higher than 220 K. In exchange of this quenching, an increase of the blue–green emission intensity is seen with increasing temperature under UV excitation. Fig. 6(a) shows PLE spectra of the UV emission at various temperatures monitored at 3995 Å. The intensity gradually decreases with increasing temperature and the peak position shifts towards longer wavelengths. The activation energy of this decrease is obtained to be 0.08 eV. Fig. 6(b) shows the UV

part of the PLE spectra of the blue–green emission monitored at 4620 Å at various temperatures. The PLE spectrum at 25 K consists of a band peaked at 3080 Å and a shoulder at 3320 Å. The shoulder at 3320 Å gradually grows with increasing temperature and becomes a well-resolved band at temperatures higher than 77 K. The peak of the band appearing above 77 K shifts towards longer wavelengths with increasing temperature. A comparison between Figs. 6(a) and (b) shows that the peak position of the PLE band of the blue–green emission appearing above 77 K coincides with that of the UV emission at each temperature. The corrected shape of the PLE band of the UV emission by removing the contribution of the lower energy band tail, and that of the blue–green emission by removing

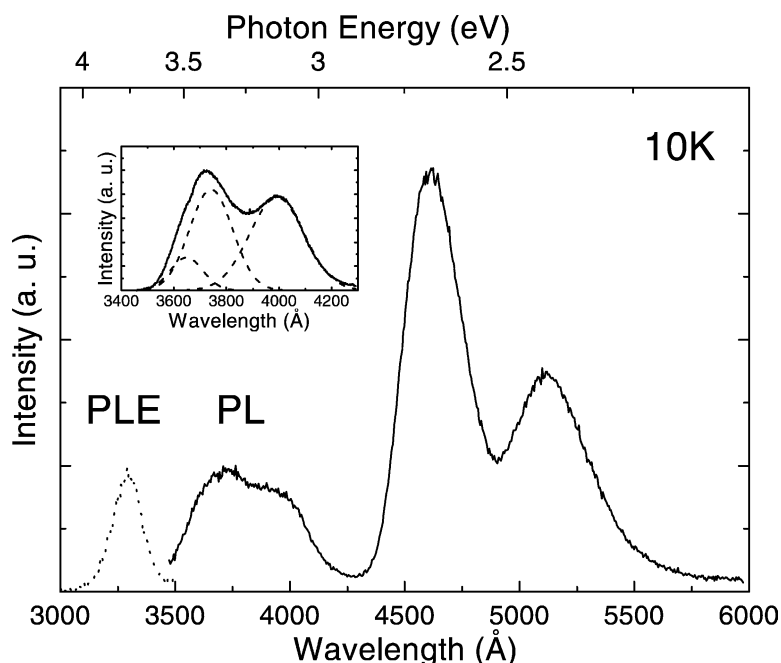


Fig. 5. PL spectrum excited by 3250 Å (solid line) and PLE spectrum monitored at 3995 Å (dotted line) of CaGa<sub>2</sub>S<sub>4</sub>:Ce (0.1 wt%). The inset shows three Gaussian curves (dotted lines) reproducing the ultraviolet part of the PL spectrum (solid line).

the contribution of the higher energy band tail are quite similar for each corresponding temperature above 77 K. The decay time constant of the UV emission was found to be about 15 ns, independent of the monitoring wavelength. This value is smaller than the reported value of the blue–green emission of 24 ns [5].

#### 4. Discussion

The PL and PLE spectra of the blue–green emission of CaGa<sub>2</sub>S<sub>4</sub>:Ce and SrGa<sub>2</sub>S<sub>4</sub>:Ce are similar. For the UV emission, the PL spectra of both compounds are also similar. Discussions are given mainly using the results of CaGa<sub>2</sub>S<sub>4</sub>:Ce.

##### 4.1. Radiative and non-radiative processes related with the blue–green emission

The two overlapping bands seen in the PL spectra (Fig. 1) of CaGa<sub>2</sub>S<sub>4</sub>:Ce and SrGa<sub>2</sub>S<sub>4</sub>:Ce are known to originate from radiative transition from the 5d(T<sub>2g</sub>) level of the excited state to levels of 4f(<sup>2</sup>F<sub>7/2</sub>) and 4f(<sup>2</sup>F<sub>5/2</sub>) of the ground state of the Ce ion split by spin–orbit interaction [6].

The shape difference between the absorption and PLE spectra may be related with the difference of the thickness among the samples, since the PLE spectra were obtained from thicker samples. Since the depths where the Ce ions are

excited in the PLE measurements are much larger than in the absorption measurements, the shape of the PLE spectrum is apt to be affected by inhomogeneous broadening. In this system of trivalent Ce ions substituting divalent Ca sites, inhomogeneous broadening is expected to increase with increasing Ce concentration. Data suggesting the presence of the inhomogeneous broadening are given in Ref. [7]. The slight shift of the PL band may be related with an effect associated with the selective excitation at 2.89 eV in the inhomogeneous PLE band.

The appearance of PA signal and the reduction of the quantum efficiency under 4416 Å excitation which cannot excite the UV emission in the 0.8 wt% Ce-doped sample indicate an increase of non-radiative transition from the excited state of the blue–green emission. The PA band broadens to higher energy region compared to the absorption band as shown in Fig. 4. This indicates that the quantum efficiency has excitation photon energy dependence. These quantum efficiency changes with Ce concentration and excitation photon energy may also have some relation with the inhomogeneous broadening. To clarify the details, PLE measurements using samples having the same thickness and quantum efficiency measurements under different excitation photon energies are necessary.

##### 4.2. UV emission and its relation with the blue–green emission

The UV and the blue–green parts of the PL spectra exhibit opposite temperature dependences. As the intensity

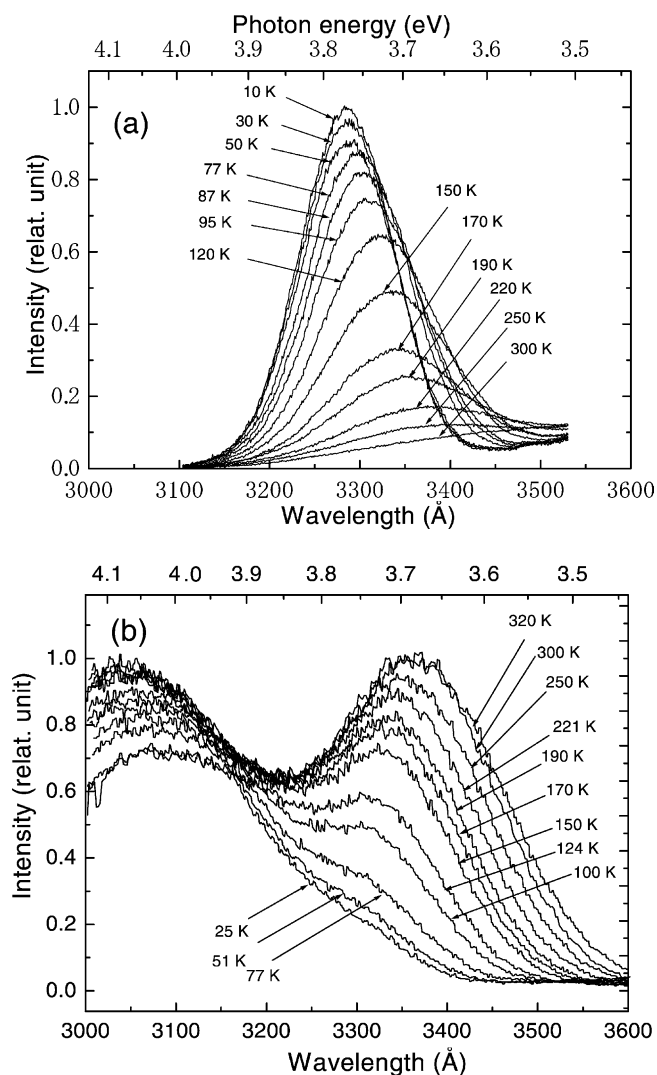


Fig. 6. (a) PLE spectra of the UV emission at various temperatures monitored at 3995 Å. (b) PLE spectra of the blue Ce emission at various temperatures (UV region) monitored at 4620 Å for  $\text{CaGa}_2\text{S}_4:\text{Ce}$  (0.1 wt%).

of the UV emission decreases with increasing temperature, the intensity of the blue–green emission increases. Fig. 6(b) shows the saturation of this new band intensity at 300–320 K. The difference between the observed intensity at each temperature and the saturated intensity was plotted as a function of temperature. An activation energy value for the blue–green emission was calculated from this plot to be 0.09 eV. This value is practically the same as that of the temperature quenching of the UV emission (0.08 eV). The coincidence of the two activation energies strongly suggests the occurrence of temperature-dependent population transfer between the excited states of these transitions. This view is supported by the fact that the peak positions and shapes of both PLE spectra are practically the same as explained in Section 3.2.

The excited state  $5d$  of the Ce ion in cubic crystal symmetry is known to split into two levels  $E_g$  and  $T_{2g}$  [6]. Fig. 7(a) shows the energy level diagram of the Ce ion with cubic symmetry and spin–orbit splitting ( $^2F_{7/2}$  and  $^2F_{5/2}$ ) of the  $4f$  ground state. As the first approximation, this diagram is applicable to the Ce ion in  $\text{CaGa}_2\text{S}_4$  having symmetry close to cubic. Two bands of the blue–green emission peaked at 2.68 and 2.41 eV in Fig. 5 are known to be originated from radiative transitions from  $5d(T_{2g})$  to  $4f(^2F_{5/2})$  and from  $5d(T_{2g})$  to  $4f(^2F_{7/2})$ , respectively, as mentioned in Section 4.1. The energy difference (0.27 eV) between the peak positions of the two bands is close to that between the first and the third components peaked at 3.39 and 3.10 eV in the UV emission spectrum (0.29 eV). This suggests that the terminal states are the same both for

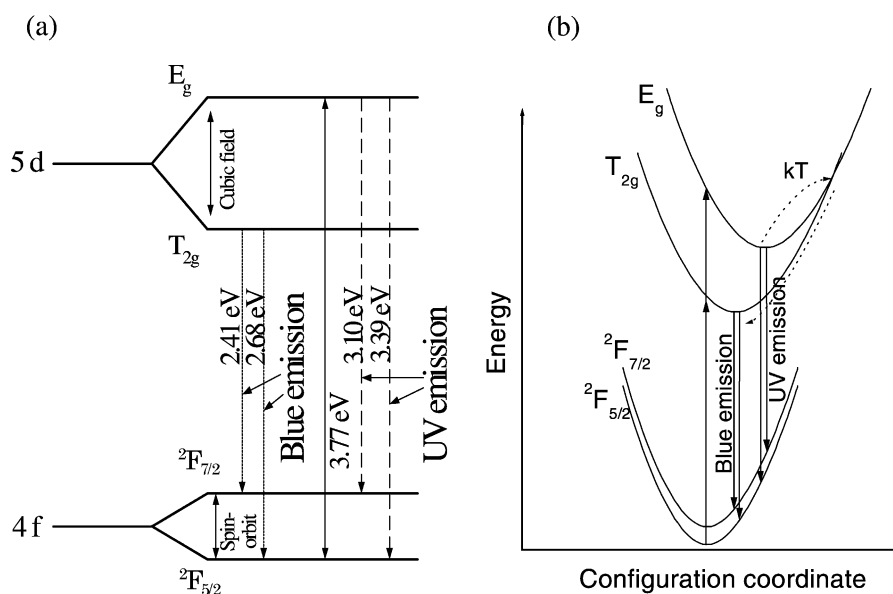


Fig. 7. (a) Energy level diagram of 4f5d configuration of the Ce ion in  $\text{CaGa}_2\text{S}_4$ . (b) Qualitative configuration coordinate description of the Ce ion.

this UV emission pair and the blue–green bands. On the other hand, the different decay time constants of the UV and the blue–green emission (15 and 24 ns [5], respectively) suggest that these two emissions originate from different excited states. For the case of Ce-doped  $\text{SrGa}_2\text{S}_4$ , the separation between levels  $4f(^2F_{5/2})$  and  $5d(E_g)$  was reported to be about 3.71 eV [8]. The peak energy of the PLE spectrum of the UV emission (3.77 eV) is close to the above reported value. The similarity of PL and PLE spectra between  $\text{CaGa}_2\text{S}_4$  and  $\text{SrGa}_2\text{S}_4$  mentioned in Sections 3.1 and 3.2 suggest that the reported value approximately holds true also for the present case of  $\text{CaGa}_2\text{S}_4$ . Taking this situation into account, the excited state of the UV emission is assigned to the level  $5d(E_g)$ . Therefore, the first and the third components peaked at 3.39 and 3.10 eV are considered to originate from the transitions from  $5d(E_g)$  to  $4f(^2F_{5/2})$  and from  $5d(E_g)$  to  $4f(^2F_{7/2})$ , respectively. To the best of our knowledge, the observation of this UV emission from the  $5d(E_g)$  level is the first one in thiogallate compounds. The UV emission observed from Ce-doped elpasolite compounds  $\text{Cs}_2\text{LiLaCl}_6$  was interpreted as to be due to core-valence processes [9], but not to the transition from the  $5d(E_g)$  level.

Fig. 7(b) shows the configuration coordinate description of the Ce ion based on the energy level diagram discussed above. The temperature-dependent population transfer discussed above is thought to occur through the cross-point between the parabolas  $5d(E_g)$  and  $5d(T_{2g})$  located at 0.08 eV above the minimum of the parabola  $5d(E_g)$ . The origin of the second component peaked at 3.30 eV is still

uncertain. The origin may be related to the symmetry of the Ce ion in this thiogallate, which is lower than the cubic symmetry.

For the case of  $\text{SrGa}_2\text{S}_4:\text{Ce}$ , the UV emission as well as the blue–green emission are seen and the PLE spectrum of the latter is similar to that of  $\text{CaGa}_2\text{S}_4:\text{Ce}$ . These facts suggest that the processes in  $\text{SrGa}_2\text{S}_4:\text{Ce}$  are also explainable by the same scheme, since the energy level diagrams of the Ce ion in these compounds are the same.

## References

- [1] A.N. Georgobiani, B.G. Tagiev, O.B. Tagiev, B.M. Izzatov, R.B. Jabbarov, *Cryst. Res. Technol.* 31 (S-2) (1996) 849.
- [2] S. Iida, T. Matsumoto-Aoki, T. Morita, N. Mamedov, B.G. Tagiev, F.M. Gashimzade, K. Sato, *Jpn. J. Appl. Phys.* 39 (Suppl. 39-1) (2000) 429.
- [3] C. Komatsu, T. Takizawa, *J. Cryst. Growth* 222 (2001) 574.
- [4] K. Maeda, *Oyo Butsuri* 40 (1971) 289 (in Japanese).
- [5] H. Najafov, A. Kato, H. Toyota, K. Iwai, A. Bayramov, S. Iida, *Jpn. J. Appl. Phys.* 41 (2002) 1424.
- [6] T.E. Peters, J.A. Baglio, *J. Electrochem. Soc.* 119 (1972) 230.
- [7] K. Iwai, Kh. Nadjafov, A. Kato, M. Yamazaki, C. Hidaka, T. Takizawa, S. Iida, *Ann. Rep. Professional Group Ternary Multinary Compound* (2001) 62 (in Japanese).
- [8] L. Eichenauer, B. Jarofke, H.-C. Mertins, J. Dreyhsig, W. Busse, H.-E. Gumlich, P. Bénalloul, C. Barthou, J. Benoit, C. Fouassier, A. Garcia, *Phys. Status Sol. (a)* 153 (1996) 515.
- [9] P.A. Rodyni, V.B. Mikhailik, G.B. Stryganyuk, A.S. Voloshinovskii, C.W.E. van Eijk, G.F. Zimmerer, *J. Lumin.* 86 (2000) 161.



ELSEVIER

Journal of Physics and Chemistry of Solids 64 (2003) 1797–1800

JOURNAL OF  
PHYSICS AND CHEMISTRY  
OF SOLIDS

[www.elsevier.com/locate/jpcs](http://www.elsevier.com/locate/jpcs)

# Determination of a pseudo-binary SrSe–Ga<sub>2</sub>Se<sub>3</sub> phase diagram and single crystal growth of SrGa<sub>2</sub>Se<sub>4</sub> compounds

Chiharu Hidaka\*, Nobuyasu Makabe, Takeo Takizawa

*Department of Physics, College of Humanities and Sciences, Nihon University,  
3-25-40 Sakurajosui, Setagaya-ku, Tokyo 156-8550, Japan*

## Abstract

We have investigated chemical reaction processes and thermal characteristics of IIa–III<sub>2</sub>–VI<sub>4</sub> compounds in order to grow their single bulk crystals. Up to now, single crystals of Ca and Sr thiogallates have been successfully grown by the melt growth method based on their pseudo-binary phase diagrams. Here, a similar diagram of the SrSe–Ga<sub>2</sub>Se<sub>3</sub> system has been constructed for the first time, where a eutectic reaction is found in the range of excess Ga<sub>2</sub>Se<sub>3</sub> concentration, and it is shown that the SrGa<sub>2</sub>Se<sub>4</sub> compound has a congruent melting point (1110 °C) suitable for the melt growth. A single crystal is grown from the melt by the horizontal Bridgman method. A trial is also made to grow a high-quality single crystal of CaGa<sub>2</sub>S<sub>4</sub> already known as being grown easily.

© 2003 Elsevier Ltd. All rights reserved.

## 1. Introduction

The compounds of alkaline earth thio- and selenogallates (Ca,Sr,Ba)(Ga,In)<sub>2</sub>(S,Se)<sub>4</sub> doped with rare earth elements such as Ce<sup>3+</sup> are expected as blue-light emitting materials for full color displays [1]. Many studies concerning the brightness and efficiency of the devices have been reported [2–5], since they were regarded as promising for EL devices [1].

On the other hand, few basic properties of these compounds have been reported. These properties have ever been studied by using single crystals prepared exclusively by the solid state reaction [6,7] and vaporization reaction [8], where a single crystalline domain is inevitably limited to a smaller size than that by the melt growth method. To obtain more detailed information on these materials, larger single crystals of good quality are indispensable.

We have already constructed the pseudo-binary phase diagrams of the CaS–Ga<sub>2</sub>S<sub>3</sub> and SrS–Ga<sub>2</sub>S<sub>3</sub> systems, and grown crystals of CaGa<sub>2</sub>S<sub>4</sub> and SrGa<sub>2</sub>S<sub>4</sub> with a single domain as large as 7 mm × 5 mm by the melt method [9,10].

The purpose of the present study is to investigate the suitability of the other compounds in the same group for the melt growth of single crystals. A trial to grow a high-quality single crystal of CaGa<sub>2</sub>S<sub>4</sub> is also made. The latter compound is already known to be grown easily but the crystals still contain cracks and voids.

## 2. Differential thermal analysis of the IIa–III<sub>2</sub>–VI<sub>4</sub> compounds

Differential thermal analysis (DTA) was carried out using mixtures of three elements (IIa = Ca or Sr, III = Ga or In, VI = S or Se). The elements (three nine or better purity) were weighted to about 0.3 g in total in a stoichiometric composition and sealed in a quartz ampoule of 7 mmϕ (inner dia.) × 40 mm under vacuum. DTA measurements [11] were run twice at a speed of 2 °/min. The chemical reaction process was investigated in the first run, and the melting and transition point were determined in the second one.

Figs. 1 and 2 show DTA signals of a series of IIa–III<sub>2</sub>–VI<sub>4</sub> compounds (IIa = Ca, Sr, III = Ga, In, VI = S, Se) in the second run. Four compounds (CaIn<sub>2</sub>Se<sub>4</sub>, CaGa<sub>2</sub>S<sub>4</sub>, SrGa<sub>2</sub>Se<sub>4</sub> and SrGa<sub>2</sub>S<sub>4</sub>) were found to melt congruently,

\* Corresponding author.

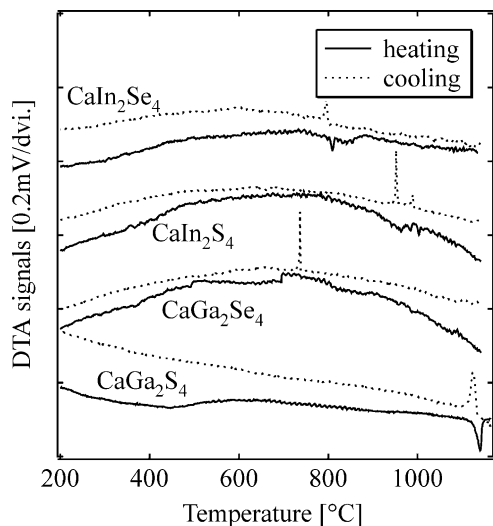


Fig. 1. DTA signals of Ca-III<sub>2</sub>-VI<sub>4</sub> compounds in the cooling process (2 °/min).

i.e. the melting and solidifying temperatures were exactly the same.

After DTA measurements, powder X-ray diffraction patterns (Cu K $\alpha$ , 40 keV, 30 mA, step of 0.02°) of the products were measured to check if they were of a single phase or not. Three compounds (CaGa<sub>2</sub>S<sub>4</sub>, SrGa<sub>2</sub>S<sub>4</sub> and SrGa<sub>2</sub>Se<sub>4</sub>) were confirmed comparing to JCPDS's data as a single phase within an experimental error of 2 mol%. Since CaGa<sub>2</sub>S<sub>4</sub> and SrGa<sub>2</sub>S<sub>4</sub> were already known to be grown [9,10], only the procedure of single crystal growth of SrGa<sub>2</sub>Se<sub>4</sub> will be presented later in Section 5.

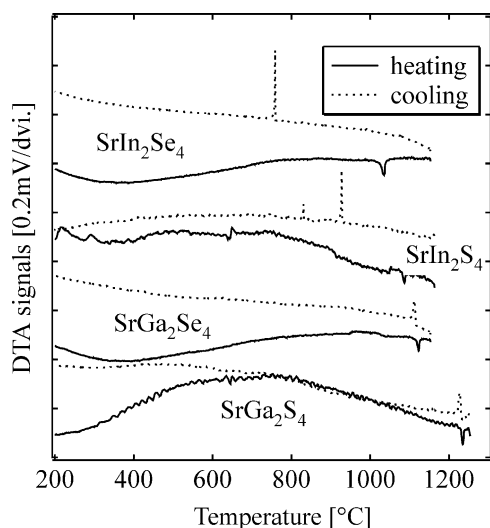


Fig. 2. DTA signals of Sr-III<sub>2</sub>-VI<sub>4</sub> compounds in the cooling process (2 °/min).

### 3. Pseudo-binary phase diagram of the SrSe–Ga<sub>2</sub>Se<sub>3</sub> system

Pseudo-binary phase diagram of the SrSe–Ga<sub>2</sub>Se<sub>3</sub> system was constructed by DTA and XRD following the procedure shown in Refs. [9,10]. Fig. 3 shows a part of the diagram. The SrGa<sub>2</sub>Se<sub>4</sub> compound is formed just at the concentration of 50 mol% Ga<sub>2</sub>Se<sub>3</sub>. The two-phase region of SrGa<sub>2</sub>Se<sub>4</sub> and Ga<sub>2</sub>Se<sub>3</sub> was identified by XRD patterns in the concentration range from 50 to 100 mol% Ga<sub>2</sub>Se<sub>3</sub>.

The melting point of SrGa<sub>2</sub>Se<sub>4</sub> was determined as 1110 ± 2 °C. A eutectic reaction was found in the excess Ga<sub>2</sub>Se<sub>3</sub> concentration in this figure. Fig. 3 is very similar to those of the CaS–Ga<sub>2</sub>S<sub>3</sub> and SrS–Ga<sub>2</sub>S<sub>3</sub> systems [9,10], and shows that single crystal growth is also possible for SrGa<sub>2</sub>Se<sub>4</sub> compound by the melt method at 50 mol% Ga<sub>2</sub>Se<sub>3</sub> and by the self flux method using Ga<sub>2</sub>Se<sub>3</sub> as a flux in the 50–75 mol% Ga<sub>2</sub>Se<sub>3</sub> range. It should be mentioned that quartz can be used as an ampoule material for the crystal growth.

### 4. The chemical reaction processes of the SrGa<sub>2</sub>Se<sub>4</sub> compound

Before growing single crystals, the chemical reaction processes between elements should be investigated. The first scan of DTA measurements for binary (Ga–Se, Sr–Se) and ternary (Sr–Ga–Se) mixtures gave us the information. The results in the heating process are shown in Fig. 4, where the exothermic reaction appeared as positive peaks and the endothermic one as negative dips. It is seen in Fig. 4 that Sr compounds were synthesized between 270 and 400 °C, where exothermic chemical reaction occurred. This is very similar to the formation of SrS compounds [9]. Then Ga<sub>2</sub>Se<sub>3</sub> compounds were synthesized around 800 °C, where exothermic reaction also occurred. This sometimes broke ampoules. Escaping this explosive reaction, we used Ga<sub>2</sub>Se<sub>3</sub>

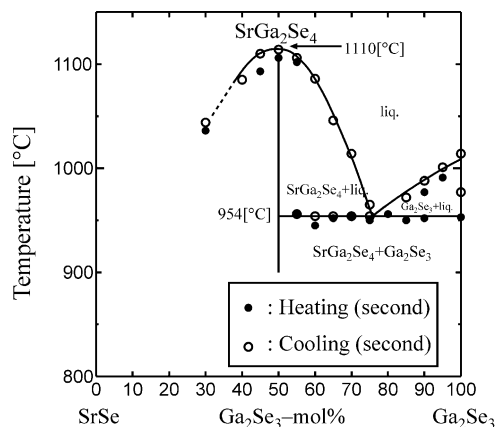


Fig. 3. Pseudo-binary phase diagram of the SrSe–Ga<sub>2</sub>Se<sub>3</sub> system.

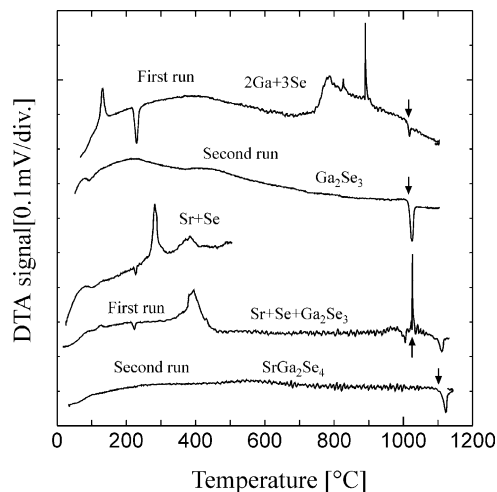


Fig. 4. DTA spectra of Sr–Se, Ga–Se and Sr + Ga + Ga<sub>2</sub>Se<sub>3</sub> in the heating process. The down-arrows show the melting points.

compounds together with Sr and Se elements as starting materials (see the bottom of Fig. 4). It is seen that SrGa<sub>2</sub>Se<sub>4</sub> compounds were synthesized at the melting point (1014 °C, shown by the up-arrow in Fig. 4) of Ga<sub>2</sub>Se<sub>3</sub>. It should be noted that the exothermic reaction due to III<sub>2</sub>VI<sub>3</sub> compounds disappeared. This was also very similar to the cases of CaGa<sub>2</sub>S<sub>4</sub> and SrGa<sub>2</sub>S<sub>4</sub> [9,10].

### 5. Crystal growth of the SrGa<sub>2</sub>Se<sub>4</sub> compound

Following the procedure as used in the single crystal growth of Ca and Sr thiogallates [9,10], a single crystal of SrGa<sub>2</sub>Se<sub>4</sub> was prepared. The only difference is the selenization of the Sr element. Since the Sr element easily sublimates above 700 °C, and the boiling point of Se is 685 °C very close to the sublimation temperature of Sr, a special care should be taken for the selenization of Sr. We set both the Sr element and Ga<sub>2</sub>Se<sub>3</sub> compound into a carbon-coated quartz ampoule (7 mmϕ (inner dia.) × 100 mm) with a hole for gas to flow in and out. The ampoule was sealed in another larger ampoule (13 mmϕ (inner dia.) × 150 mm) under vacuum together with the Se element of the stoichiometric amount separately set outside the inner ampoule. For the selenization of Sr, the whole ampoule was kept at 650 °C for 24 h, where Se evaporated and reacted with solid Sr. Then the temperature was elevated to a value 60 °C above the melting point (1014 °C) of Ga<sub>2</sub>Se<sub>3</sub>. This temperature should be kept lower than the melting point (1110 °C) of SrGa<sub>2</sub>Se<sub>4</sub> to prevent the reaction between the melt and the wall of the quartz ampoule. That is, the precursor is prepared by the so-called solid state reaction. At this stage, the precursor of SrGa<sub>2</sub>Se<sub>4</sub> was prepared. The single phase was assured by XRD. The precursor was taken out to be powdered and put in a carbon boat (8 mmϕ (inner dia.) × 100 mm) which was again sealed

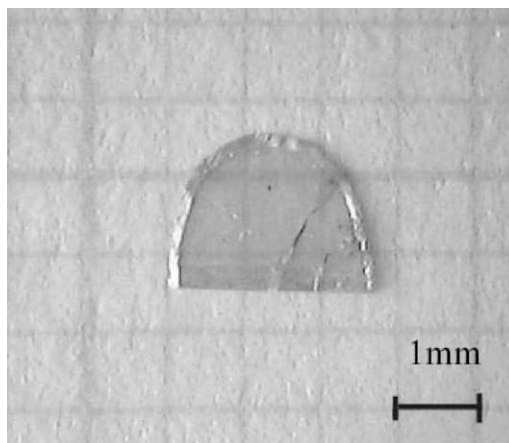


Fig. 5. A photograph of a SrGa<sub>2</sub>Se<sub>4</sub> single crystal grown by the melt method. A sliced and polished surface is shown.

in a larger quartz ampoule as mentioned above. A single crystal was grown from melt by the horizontal Bridgman method by moving a temperature profile (temperature gradient ~8 °C/cm, speed of growth 0.25 cm/h, without seed) [11]. Fig. 5 shows a photograph of a grown SrGa<sub>2</sub>Se<sub>4</sub> single crystal with a grain as large as 2 mm × 2 mm × 0.1 mm (a sliced and polished surface).

### 6. Crystal growth of CaGa<sub>2</sub>S<sub>4</sub> of high quality

The single crystals of the thiogallates, CaGa<sub>2</sub>S<sub>4</sub> and SrGa<sub>2</sub>S<sub>4</sub> were already successfully grown [9,10]. Especially CaGa<sub>2</sub>S<sub>4</sub> can be stably grown. However, many cracks and voids were still found in these crystals. The crystallinity prepared from the melts could not be controlled even under

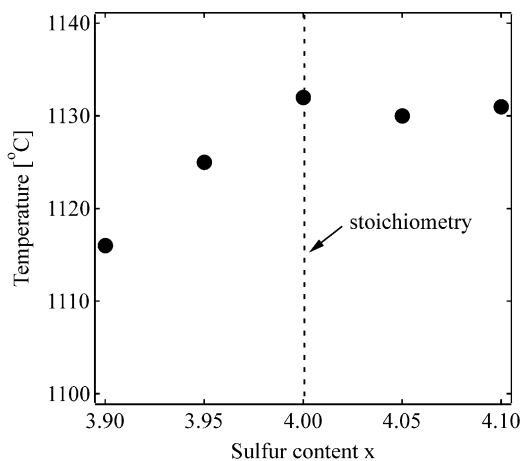


Fig. 6. The variation of the melting point against the sulfur content  $x$  of the starting composition of CaGa<sub>2</sub>S <sub>$x$</sub> .

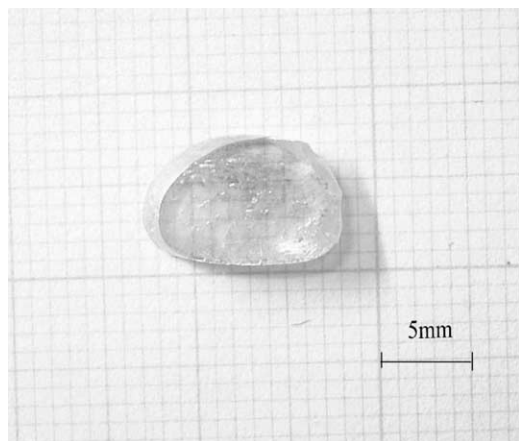


Fig. 7. A photograph of a  $\text{CaGa}_2\text{S}_4$  single crystal grown under excess sulfur. A cleaved surface is shown.

the same growth condition. It was thought that the sulfur was deficient in a grown crystal because of the repeated pulverization followed by vacuum seals in quartz ampoules. We have investigated the variation of the melting temperature of  $\text{CaGa}_2\text{S}_x$  with sulfur content by means of DTA used in Section 2. As shown in Fig. 6, the melting point decreased with decreasing sulfur content from the stoichiometry, while no phase other than  $\text{CaGa}_2\text{S}_4$  was detected by XRD in this sulfur range. As increases sulfur content, the melting point seems to reach a constant value. Similarly the lattice constants slightly increased with sulfur content and kept the maximum value above the stoichiometric composition. In addition, when the sulfur content increased above  $x = 4.05$ , excess sulfur was clearly deposited on the wall of DTA ampoules. Thus, it is considered that the compounds were stable above the stoichiometric composition and no excess sulfur could be introduced in the compound if sulfur content was increased more than the stoichiometric amount. Preliminary measurements for the  $\text{SrGa}_2\text{Se}_4$  compound showed that the same behavior was also observed in the selenide. It is thought that the decrease of sulfur or selenium in the compounds worsened the quality of the crystals, mainly due to the change in the melting temperature caused by the slight loss of the volatile VI elements. Then the crystal growth was performed under the condition with excess VI group element. Fig. 7 shows a photograph of a grown  $\text{CaGa}_2\text{S}_4$  crystal at an excess sulfur content ( $x = 4.05$ ). The crystallinity of the compounds was much improved in this case.

## 7. Summary

DTA measurements of various IIa–III<sub>2</sub>–VI<sub>4</sub> compounds were executed. Apart from  $\text{CaGa}_2\text{S}_4$  and  $\text{SrGa}_2\text{S}_4$  already grown as single crystals,  $\text{SrGa}_2\text{Se}_4$  was found suitable for the melt growth. Then, a pseudo-binary phase diagram of the SrSe– $\text{Ga}_2\text{Se}_3$  system was constructed, and the  $\text{SrGa}_2\text{Se}_4$  single crystal was successfully melt-grown on the bases of the diagram.

It was also found that to keep the vapor pressure of the VI element to an appropriate value during the crystal growth was very important to get a high quality single crystal.

## Acknowledgements

This work was partly supported by the Research Grant from Nihon University.

## References

- [1] W.A. Barrow, R.C. Coover, E. Dickey, C.N. King, C. Laakso, S.S. Sun, R.T. Tuenge, R. Wetross, J. Kane, *SID Int. Symp. Dig.* (1993) 761.
- [2] S.S. Sun, R.T. Tuenge, J. Kane, M. Ling, *J. Electrochem. Soc.* 141 (1994) 2877.
- [3] K. Tanaka, Y. Inoue, S. Okamoto, K. Kobayashi, *J. Cryst. Growth* 150 (1995) 1211.
- [4] T. Yang, K. Wagner, M. Chaichimansour, W. Park, Z.L. Wang, C.J. Summers, *J. Vac. Sci. Technol. B* 14 (1996) 2263.
- [5] K. Tanaka, Y. Inoue, S. Okamoto, K. Kobayashi, K. Takizawa, *Jpn. J. Appl. Phys.* 36 (1997) 3517.
- [6] T.E. Peter, J.A. Baglio, *J. Electrochem. Soc.* 119 (2) (1972) 230.
- [7] B. Eisenmann, M. Jakowski, W. Klee, H. Schäfer, *Rev. Chim. Miner.* 20 (1983) 225.
- [8] K. Tanaka, T. Ohgoh, K. Kimura, H. Yamamoto, K. Shinagawa, K. Sato, *Jpn. J. Appl. Phys.* 34 (1995) L1651.
- [9] C. Komatsu, T. Takizawa, *J. Cryst. Growth* 210 (2000) 677–682.
- [10] C. Komatsu-Hidaka, T. Takizawa, *J. Cryst. Growth* 222 (2001) 574–578.
- [11] H. Matsushita, T. Takizawa, *J. Cryst. Growth* 160 (1996) 71–77.



ELSEVIER

Journal of Physics and Chemistry of Solids 64 (2003) 1807–1810

JOURNAL OF  
PHYSICS AND CHEMISTRY  
OF SOLIDS

[www.elsevier.com/locate/jpcs](http://www.elsevier.com/locate/jpcs)

# ESR study of $\text{Ce}^{3+}$ ions doped in the $\text{CdIn}_2\text{S}_4$ lattice

Takeo Takizawa\*, Hiroyuki Ozawa, Chiharu Hidaka

*Department of Physics, College of Humanities and Sciences, Nihon University, 3-25-40 Sakurajosui, Setagaya-ku, Tokyo 156-8550, Japan*

## Abstract

Rare earth elements doped IIa–III<sub>2</sub>–VI<sub>4</sub> compounds are expected as host materials for fluorescent devices. In particular, since blue emission was observed in alkaline earth thiogallates doped with  $\text{Ce}^{3+}$  ions, much attention has been paid to develop full color displays made of thin films of the compounds above. Especially  $\text{Ce}^{3+}$  ions are thought as promising candidates for dopants realizing blue light emission. Normally doped  $\text{Ce}^{3+}$  ions are considered to substitute the sites which are occupied with divalent elements such as Ca or Cd. However, the substituting mechanism is not fully understood, since in view of the number of valence, it is natural for a Ce atom to substitute a trivalent one.

In this report, we have grown single crystals of  $\text{CdIn}_2\text{S}_4$  as host materials for Ce doping and investigated the site substitution of the Ce atom in this crystal lattice by means of ESR. Two types of ESR centers are found. One consists of a  $\text{Ce}^{3+}$  ion substituting a Cd site and a sulfur vacancy, and the other consists of a similar  $\text{Ce}^{3+}$  ion with 4 tetrahedrally surrounding sulfur atoms.

© 2003 Elsevier Ltd. All rights reserved.

## 1. Introduction

Rare earth elements doped (Ca,Sr,Ba)–(Al,Ga,In)<sub>2</sub>–(S,Se)<sub>4</sub> compounds emit light with various color when excited by UV light, high electric field or high energy electron beam [1,2]. In particular, since blue emission is observed in alkaline earth thiogallates doped with  $\text{Ce}^{3+}$  ions, practical researches are energetically developed to apply them to AC thin-film electroluminescent (ACTFEL) full-color displays [2,3].

In the emission above,  $\text{Ce}^{3+}$  ions play an important role, since the inner core states of the isolated  $\text{Ce}^{3+}$  ion, i.e. 4f–5d electronic transitions mainly cause the blue light emission. These electronic states are strongly affected by host crystals, and the color of the emission changes according to the surrounding atomic configuration. The changes in the electronic states can be studied by luminescence measurements which include the complex variation in both ground and excited states. On the other hand, ESR studies can reveal exclusively the ground states of the doped ions which may serve to

the full understanding of the ion substitution and the host affection to it.

Normally the doped  $\text{Ce}^{3+}$  ion is considered to substitute the site which is occupied with a divalent element such as Ca or Cd. However its mechanism is not fully understood, since in view of the number of valence, it is natural for a Ce atom to substitute a trivalent one.

In this report, we have adopted single crystals of  $\text{CdIn}_2\text{S}_4$  as host materials for Ce doping and investigated the site substitution of the Ce atom in this crystal lattice using ESR measurement. The above crystal is chosen because it is easily grown and in addition, has a rather simple lattice structure with both di- and tri-valent cation sites.

## 2. Experimental procedure

Single crystals of  $\text{CdIn}_2\text{S}_4$  were grown from a melt using the three constituent elements. The details of this procedure were described elsewhere [4,5] Ce doping was carried out by mixing appropriate amount (0.1–0.5 wt%) of  $\text{Ce}_2\text{S}_3$  powder into a ground  $\text{CdIn}_2\text{S}_4$  having been grown beforehand. No codoping was tried. The mixture was again melted, and a Ce doped crystal was grown by the Horizontal

\* Corresponding author. Tel.: +81-3-5317-9772; fax: +81-3-5317-9772.

E-mail address: [takiz@chs.nihon-u.ac.jp](mailto:takiz@chs.nihon-u.ac.jp) (T. Takizawa).

Bridgman method (hereafter abbreviated as an ‘as-grown sample’). The grown crystal was cut into blocks of  $2 \times 2 \times 5 \text{ mm}^3$  in size, the longest edge of which were determined so as to be the [110] direction by the reflection Laue method.

Alternative Ce doping was also made by annealing  $\text{CdIn}_2\text{S}_4$  single crystals in  $\text{Ce}_2\text{S}_3$  powder at  $950^\circ\text{C}$  for several hours (hereafter abbreviated as ‘annealed samples’). These crystals were oriented to the [110] direction in advance. The difference in the ESR results of both samples with different dopings will be described later.

ESR spectra were measured using an X band microwave and a  $\text{TE}_{110}$  cavity by applying the magnetic field perpendicular to the [110] direction, the axis of rotation of samples.

### 3. Results and discussions

The observed ESR spectra of as-grown samples at 77 K are summarized and shown in Fig. 1, where every curve was normalized to each sample weight and the integrated ESR line of DPPH used as a standard. Two types ESR signals are seen in the figure. One is designated as S1, S2, S3 and S4 (hereafter called as Type 1), and the other as S5 and S6 (hereafter called as Type 2). ESR curves are arranged in Fig. 1 according to the integrated strength of the S4 signal, which is thought to indicate the true concentration of  $\text{Ce}^{3+}$  ions. The order is not proportional to the as-doped values of  $\text{Ce}^{3+}$ , showing that the true  $\text{Ce}^{3+}$  concentration is determined by the growing process and not by the starting amount of  $\text{Ce}^{3+}$ . The temperature variation of the intensities of each line was measured by varying temperature down to 4.2 K. The results showed that every ESR line obeyed the so-called Curie law.

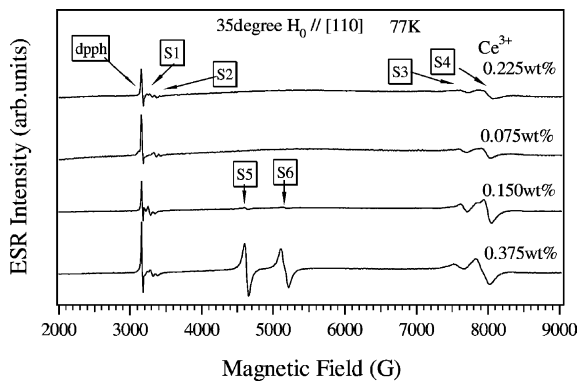


Fig. 1. ESR curves of  $\text{CdIn}_2\text{S}_4$  with different  $\text{Ce}^{3+}$  concentration. S1 to S4 signals are classified as the ESR centers of Type 1, and S5 and S6 as those of Type 2. Curves are arranged according to the integrated intensities of the S4 signal, which indicate the true concentration of  $\text{Ce}^{3+}$  doped. Type 2 signals appear only above a certain value of  $\text{Ce}^{3+}$  concentration.

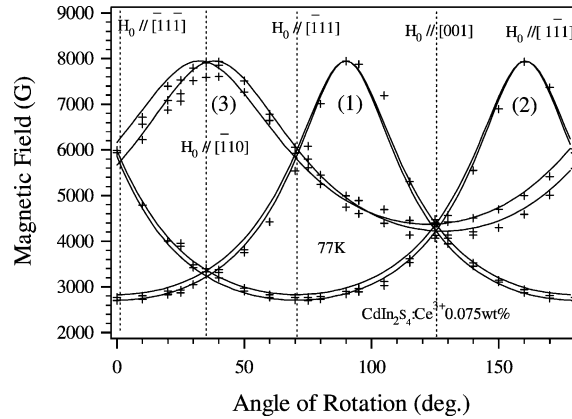


Fig. 2. Resonant magnetic field vs. angle of rotation of ESR signals (at 77 K) of a  $\text{Ce}^{3+}$  0.075 wt% sample. These ESR signals are classified as Type 1. Curves (a), (b) and (c) correspond to the Eqs. (2)–(4) in the text, respectively. The splitting of each line is due to the misalignment of the [110] direction from the axis of rotation (estimated as about  $2^\circ$ ). The (a) and (b) lines split into two, and the (c) line into 4, though only two of them are shown for simplicity.

The resonant magnetic field vs. the angle of rotation for the ESR curve of the 0.075 wt% sample is shown in Fig. 2, where only the signals of Type 1 are seen. The curves of Fig. 2 is describable if we assume a simple spin-Hamiltonian

$$H_S = \beta \mathbf{H} \cdot \mathbf{g} \cdot \mathbf{S} \quad (1)$$

where  $\beta$  is the Bohr magneton,  $\mathbf{H}$  the magnetic field,  $\mathbf{g}$  the so-called  $g$ -tensor and  $\mathbf{S}$  the effective spin. Here we have checked possibilities of several symmetry sites such as tetragonal, tetrahedral and octahedral ones. However, no good results were obtained except for the tetrahedral site, i.e.  $\text{Ce}^{3+}$  substituting  $\text{Cd}^{2+}$  in a tetrahedron. More precisely, we should take tetrahedral sites occupied by  $\text{Ce}^{3+}$  ions in the  $\text{CdIn}_2\text{S}_4$  lattice with  $S = 1/2$  to reproduce the observed angle dependence of ESR curves.

There are eight equivalent directions from the center of a tetrahedron to its tetrahedral corners in the spinel lattice. If the translational symmetry is taken into account, these are classified into three independent ones ( $[\bar{1}\bar{1}\bar{1}]$ ,  $[\bar{1}11]$ ,  $[111]$ ), where the [110] direction is taken as the rotation axis. The magnetic field is applied perpendicular to this axis. Diagonalization of the spin-Hamiltonian leads to the following resonant magnetic fields for the respective direction [6]

$$H_1 = \frac{h\nu}{\beta \sqrt{g_\perp^2 \sin^2 \theta + g_\parallel^2 \cos^2 \theta}} \text{ for } [\bar{1}\bar{1}\bar{1}] \text{ manifolds} \quad (2)$$

$$H_2 = \frac{h\nu}{\beta \sqrt{g_\perp^2 \sin^2(70.53 - \theta) + g_\parallel^2 \cos^2(70.53 - \theta)}} \text{ for } [\bar{1}11] \text{ manifolds} \quad (3)$$

$$H_3 = \frac{hv}{\beta \sqrt{g_{\perp}^2 \left(1 - \frac{1}{3} \cos^2 \theta\right) + \frac{1}{3} g_{\parallel}^2 \cos^2 \theta}} \text{ for } [111]$$

manifolds. (4)

If we used the values,  $g_{\parallel} = 2.3$  and  $g_{\perp} = 0.8$ , the best fitting was obtained as shown in Fig. 2 by the solid lines, where the misalignment of the [110] direction from the axis of rotation was taken into account. The misalignment caused the splitting of each curve so that curves (1) and (2) in Fig. 2 split into two, and curve (3) into 4, that is, the eight manifolds separately appeared as ESR signals. In the fitting, the misalignment was set to  $2^{\circ}$ . These splittings were more clearly observed at 4.2 K.

Fig. 3 shows ESR curves of a  $\text{CdIn}_2\text{S}_4$  sample doped with 0.375 wt%  $\text{Ce}^{3+}$  ions. As mentioned previously, two types of ESR signals were observed. Type 1 was specified by the  $g$ -values of  $g_{\parallel} = 2.3$  and  $g_{\perp} = 0.8$ , the same values as obtained in Fig. 2. It is interesting to note that Type 2 could be also reproduced by the same model used for Type 1 but using the  $g$ -values of  $g_{\parallel} = 1.13$  and  $g_{\perp} = 1.37$ . Thus the  $g$ -value's anisotropy of Type 2 is very small compared with that of Type 1. The eight manifolds due to the misalignment of the rotation axis were also clearly observed at 4.2 K (though difficult at 77 K) in this case. This strongly indicates that Type 2 is also ascribed to an ESR center at the tetrahedral site. However, the order of the magnitude of  $g_{\parallel}$  and  $g_{\perp}$  were reversed in Type 1 and 2. This finding and the small anisotropy suggest that the wave-function of the unpaired electron around the ESR center of Type 2 spread out by escaping the bonding direction to the surrounding sulfur atoms, while that of Type 1 is confined mainly to the direction toward a sulfur vacancy. That is, Type 1 consists of a substituted  $\text{Ce}^{3+}$  ion and a sulfur vacancy, and Type 2

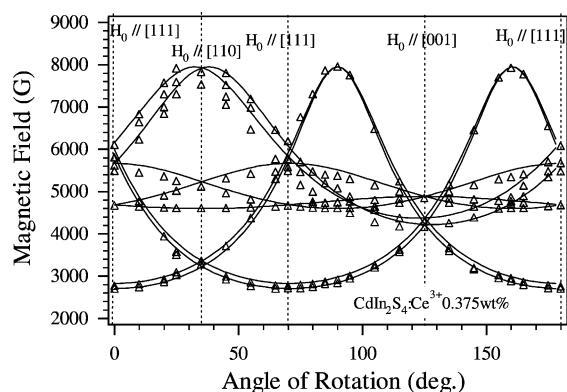


Fig. 3. Resonant magnetic field vs. angle of rotation of ESR signals (at 77 K) of a  $\text{Ce}^{3+}$  0.375 wt% doped sample. Both Type 1 and 2 signals appeared. In the fitting,  $g_{\parallel} = 2.3$  and  $g_{\perp} = 0.8$  for Type 1, and  $g_{\parallel} = 1.13$  and  $g_{\perp} = 1.37$  for Type 2 were used in the Eqs. (2)–(4) in the text.

consists of a similar  $\text{Ce}^{3+}$  ion centered at tetrahedrally arranged four sulfur atoms.

From Fig. 1, it is seen that Type 2 emerges according to the doped amount of  $\text{Ce}^{3+}$  ions. To clarify the origin of both the ESR centers, the  $\text{Ce}^{3+}$  doping was carried out by annealing undoped samples in  $\text{Ce}_2\text{S}_3$  powder at high temperature below the melting point of  $\text{CdIn}_2\text{S}_4$ . The annealing temperature was determined so as to get most effective doping after several trials by varying the temperature systematically. Fig. 4 shows ESR resonance curves using a sample annealed at  $950^{\circ}\text{C}$  for 2 h. Here only ESR signals of Type 2 were observed. The annealing time was extended to 50 h at the same temperature. Then small signals due to Type 1 centers emerged in addition to Type 2 signals. These were so small as to be detected only at 4.2 K.

Annealing was also conducted for the 0.225 wt%  $\text{Ce}^{3+}$  doped sample, having been shown at the top in Fig. 1. In this case, Type 1 signals were decreased as annealing time was elongated, and Type 2 signal emerged in the same way stated above.

From the results of annealing, it can be said that the formation energy of Type 1 ESR centers is greater than that of Type 2, since the ESR center of Type 1 was created exclusively at high temperature as a pair of a  $\text{Ce}^{3+}$  center and a sulfur vacancy. In the melt grown process, the ESR center of Type 2 was formed only after the concentration was increased up to a certain appropriate value. This center is considered to consist of a  $\text{Ce}^{3+}$  ion placed in the center of a sulfur tetrahedron, where a sulfur vacancy may exist somewhere apart from the center to keep the charge neutrality.

The center of Type 1 is difficult to be formed by annealing in  $\text{Ce}_2\text{S}_3$  powder below the melting temperature of  $\text{CdIn}_2\text{S}_4$ , where Type 2 centers are easily formed. However, it seems that there is finite probability to create Type 1 centers when the annealing time is kept longer than

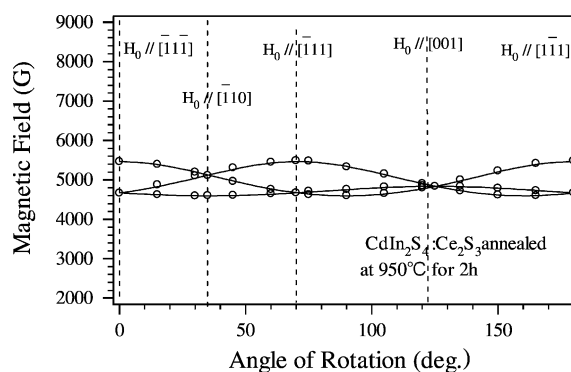


Fig. 4. Resonant magnetic field vs. angle of rotation of ESR signals at 77 K of an undoped sample which was annealed in  $\text{Ce}_2\text{S}_3$  powder at  $950^{\circ}\text{C}$  for 2 h. Here the fitting was made using  $g_{\parallel} = 1.13$  and  $g_{\perp} = 1.37$  in the Eqs. (2)–(4) in the text.

50 h. Thus it is considered that Type 1 needs a larger creation energy than Type 2.

#### 4. Conclusion

To investigate the substitution mechanism of RE atoms doped in a crystal lattice of the IIa–III<sub>2</sub>–IV<sub>4</sub> system, dopings of Ce<sup>3+</sup> into CdIn<sub>2</sub>S<sub>4</sub> by melt and by annealing were carried out. ESR measurement revealed two types of centers. One (Type 1) consists of a Ce<sup>3+</sup> ion accompanied by a sulfur vacancy at its nearest neighbor site. The ion substitutes a divalent Cd site and not a trivalent In one. The other (Type 2) consists of a similar Ce<sup>3+</sup> ion placed in a sulfur tetrahedron, where a charge compensating sulfur vacancy is expected to exist at an appropriate sulfur site apart from the Ce<sup>3+</sup> ion. The formation energy of a Type 1 center is considered to be larger than that of Type 2.

#### Acknowledgements

This work was partly supported by the Research Grant from Nihon University.

#### References

- [1] T.E. Peter, J.A. Baglio, J. Electrochem. Soc. 119 (230) (1972) 1720.
- [2] W.A. Barrow, R.C. Covert, E. Dickey, C.N. King, C. Laakso, S.S. Sun, R.T. Tuenge, R. Wetross, J. Kane, SID Int. Symp. Dig. (1993) 761.
- [3] K. Tanaka, S. Okamoto, Y. Izumi, Y. Inoue, K. Kobayashi, Jpn J. Appl. Phys. 38 (1999) L1419.
- [4] T. Takizawa, E. Christoffel, A. Goltzené, C. Schwab, Jpn J. Appl. Phys. 33 (1994) 1951.
- [5] T. Takizawa, C. Komatsu, H. Matsushita, A. Goltzené, C. Schwab, Cryst. Res. Technol. 31 (1996) 173.
- [6] A. Yariv, in: W. Low (Ed.), Proceedings of first International Conference on Paramagnetic Resonance, Jerusalem, July, 1962, p. 189.



ELSEVIER

Journal of Physics and Chemistry of Solids 64 (2003) 1959–1962

JOURNAL OF  
PHYSICS AND CHEMISTRY  
OF SOLIDS

[www.elsevier.com/locate/jpcs](http://www.elsevier.com/locate/jpcs)

# Light figure spectroscopy of optically active anisotropic materials

Nobuyuki Yamamoto<sup>a,\*</sup>, Nazim Mamedov<sup>a</sup>, Yonggu Shim<sup>a</sup>, Chiharu Hidaka<sup>b</sup>,  
Takeo Takizawa<sup>b</sup>, Eiji Niwa<sup>c</sup>, Katashi Masumoto<sup>c</sup>

<sup>a</sup>*Department of Physics and Electronics, Graduate School of Engineering, Osaka Prefecture University,  
Gakuen-cho 1-1, Sakai, Osaka 599-8531, Japan*

<sup>b</sup>*Department of Physics, College of Humanities and Sciences, Nihon University, 3-25-40 Sakurajosui,  
Setagaya-ku, Tokyo 156-8550, Japan*

<sup>c</sup>*Research Institute for Electric and Magnetic Materials, 2-1-1 Yagiyama-minami, Taihoku-ku, Sendai 982-0807, Japan*

## Abstract

Low order interference curves in optic-axis light figures of the optically active AgGaS<sub>2</sub> and TeO<sub>2</sub> are investigated in the visible spectral range at room temperature. Light figure patterns of AgGaS<sub>2</sub> are found not to be affected by optical activity within the incidence angles of 10° for which, according to our symmetry considerations, the normal component of gyration tensor is small and evolution of light figures with wavelength is overwhelmingly determined by optical anisotropy. The absolute value of this anisotropy is falling down to null when passing through the isotropic point, with the result of a remarkable change of the parameters of light figure patterns. Unlike the case of AgGaS<sub>2</sub> and consistently with our symmetry considerations, light figures of TeO<sub>2</sub> are influenced by optical activity especially strongly in low orders of interference. The obtained results are compared with similar results for optically inactive CaCO<sub>3</sub> and discussed in the frameworks of our recent analyses.

© 2003 Elsevier Ltd. All rights reserved.

**Keywords:** A. Inorganic compounds; A. Optical materials; D. Crystal structure; D. Dielectric properties; D. Optical properties

## 1. Introduction

Light figure spectroscopy is a very informative and valuable tool for optical characterization of the anisotropic materials and phase transitions [1–2]. Using a newly designed experimental set-up for determination of light figure parameters with high accuracy [1], and a new method for determination of the relative dispersion of the refractive indices [3], we have already managed to extend the application of light figure method beyond the usual standards. An excellent agreement has then been achieved between experimental and numerical results for the optically inactive uniaxial material, CaCO<sub>3</sub> (point group of crystal symmetry-*D*<sub>3d</sub>) [4].

In this work we extend the application of light-figure method further by addressing optically active uniaxial

materials, AgGaS<sub>2</sub> (*D*<sub>2d</sub>) [5] and TeO<sub>2</sub> (*D*<sub>4</sub>) [6], with especially large optical rotatory power.

## 2. Light figures of CaCO<sub>3</sub>, AgGaS<sub>2</sub> and TeO<sub>2</sub>

The samples of CaCO<sub>3</sub>, AgGaS<sub>2</sub> and TeO<sub>2</sub> used in this work were all (001)-cut plane-parallel plates with a thickness of 1.225, 8.20, and 1.42 mm, respectively. The details of the experimental setup for light figure acquisition were already reported earlier [1].

Like all uniaxial materials, above crystals are characterized by a single birefringence. As seen from Fig. 1, the birefringence in these crystals assumes negative, positive-to-negative, and positive values depending on material. In principle, isochromatic curves in optic-axis light figures of these materials are supposed to be circles with radius

$$R_m \approx M \frac{m\lambda}{2\Delta n} \sqrt{1 + \sqrt{1 + \left(\frac{2d\Delta n}{m\lambda}\right)^2}}, \quad (1)$$

\* Corresponding author. Fax: +81-722-54-9908.

E-mail address: [yamamoto@pe.osakafu-u.ac.jp](mailto:yamamoto@pe.osakafu-u.ac.jp) (N. Yamamoto).

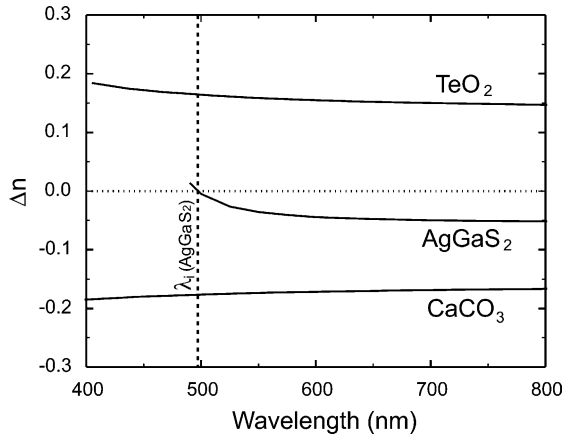


Fig. 1. Wavelength dependences of optical anisotropy of TeO<sub>2</sub>, AgGaS<sub>2</sub> and CaCO<sub>3</sub>. The cross-point of vertical and horizontal dashed lines is the isotropic point ( $\lambda_i$ ) of AgGaS<sub>2</sub>.

where  $M$  is the magnification factor for the employed optical system,  $\Delta n$ -birefringence,  $d$ -sample thickness, and  $m$ -the order of interference curve [1].

2.1. Optically inactive case

Fig. 2 displays most important features of the change of light figure patterns of CaCO<sub>3</sub> [4] and AgGaS<sub>2</sub> with wavelength.

As for CaCO<sub>3</sub>, we can see more than four isochromate circles whose radiuses increase monotonically with increasing wavelength in the visible spectral range. For AgGaS<sub>2</sub> the radiuses of the observed isochromates first increase with increasing wavelength from 476 to 484 nm, then decrease with further increasing wavelength beginning from 510 nm. In the range between 488 and 504 nm, including the accidental isotropic point (497.3 nm) with null value of birefringence [5], birefringence-dependent contrast function determining visibility of interference pattern dramatically

falls down and observation of the well-defined light figure patterns becomes practically impossible.

As estimations show, for a 1.225 mm-thick plate of CaCO<sub>3</sub> condition  $2d\Delta n/m\lambda \gg 1$  is fulfilled up to 100th order of interference in all the accessed spectral range and relation (1), as well as expression for ratio  $R_{m+1}/R_m$ , can be simplified down to

$$R_m \approx M \sqrt{\frac{md\lambda}{2\Delta n}} \tag{2}$$

and

$$\frac{R_{m+1}}{R_m} \approx \sqrt{\frac{m+1}{m}}, \tag{3}$$

respectively. For 8.20 mm-thick plate of AgGaS<sub>2</sub> relations (2) and (3) should be fully justified at least for interference curves with  $m = 1$  and  $m = 2$ , and for all wavelengths longer than 540 nm. Experimental  $R_2/R_1$  ratios obtained for the plane-parallel plates of all investigated materials, including TeO<sub>2</sub>, are given in Fig. 3.

Indeed, for CaCO<sub>3</sub> this ratio is everywhere the same as the ‘thick-sample’ limit given by Eq. (3) as  $\sqrt{2}$ . For AgGaS<sub>2</sub>, this ratio is 2 for all wavelengths above 540 nm. For smaller wavelengths, such as 476 and 450 nm that are below isotropic point, this ratio is respectively 1.47 and 1.50 in full agreement with relation (1). The relations (1)–(3) are written for the optically inactive case and the fact that experimental data for AgGaS<sub>2</sub> follow this case means that no influence of optical activity is observed for low order interference curves, which is consistent with results of our recent symmetry analysis [7].

For the measured thick TeO<sub>2</sub> plate, the ratio  $R_2/R_1$  only approaches 2 with wavelength increase, remaining larger than 2 and significantly exceeding this value in the neighborhood of some short-wavelength limit, denoted as  $\lambda_1$  in Fig. 2. Such behavior of  $R_2/R_1$  can be explained only with allowance for optical activity of TeO<sub>2</sub>.

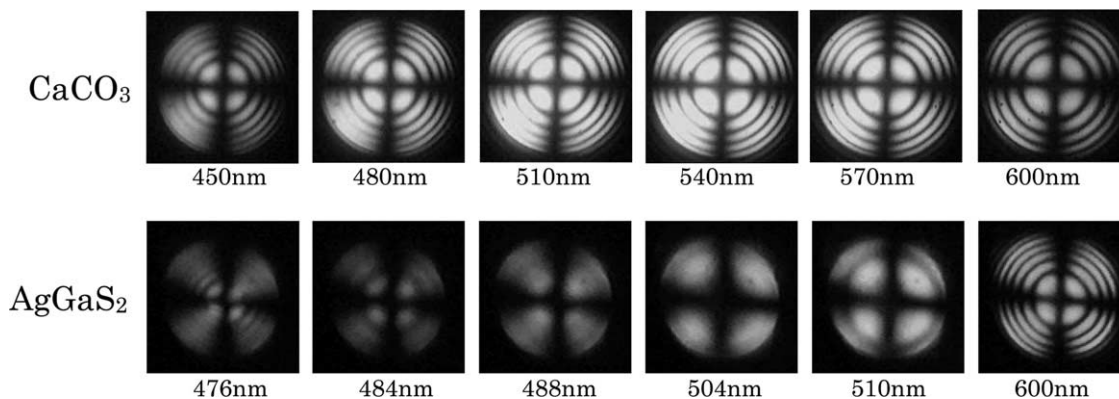


Fig. 2. Light figure patterns of CaCO<sub>3</sub> and AgGaS<sub>2</sub> for different wavelengths.

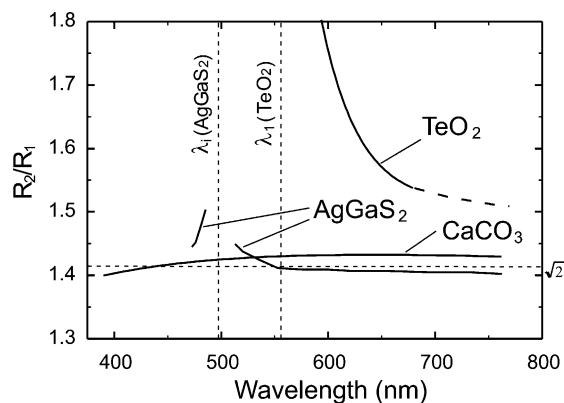


Fig. 3. Wavelength dependences of the ratio of the radii of the second and first isochromatic curves of TeO<sub>2</sub>, AgGaS<sub>2</sub> and CaCO<sub>3</sub>. Horizontal dashed line shows the ‘thick-sample’ limit equal to  $\sqrt{2}$ . Vertical dashed lines outline isotropic point ( $\lambda_i$ ) of AgGaS<sub>2</sub> and short-wavelength limit ( $\lambda_1$ ) for observation of the first-order ( $m = 1$ ) isochromatic curve of TeO<sub>2</sub>. Dashed curve (TeO<sub>2</sub>) is drawn speculatively to show that experimental curve approaches ‘thick-sample’ limit with increasing wavelength.

### 2.2. Optically active case

In the presence of optical activity the radius of an  $m$ th order isochromatic curve differs from that in the absence of optical activity and the difference  $\Delta R_m$  is given approximately as [7]

$$|\Delta R_m| \approx M \sqrt{\frac{m\lambda d}{2\Delta n}} n^3 \rho G, \quad (4)$$

where refractive index,  $n$ , of the ordinary ray and optical anisotropy  $\Delta n$  are taken with their optically inactive values. As follows from Eq. (4), the change  $\Delta R_m$  brought in by optical activity is greatly dependent on the always positive product  $\rho G$ , where  $\rho$  is ellipticity and  $G$  is normal component of gyration tensor, and  $\rho$  and  $G$ , both are incident angle dependent functions. This product strongly depends upon incident angle,  $\theta_m$ , at which  $m$ th order isochromate is observed.

For TeO<sub>2</sub> the value of  $\rho G$  strongly decreases with increasing  $\theta_m$  [7] and higher interference orders are less influenced by optical activity than lower ones. Accordingly, for a thick TeO<sub>2</sub> plate the ratio  $R_2/R_1$  will be larger than 2 and deviation from this value will increase with decreasing interference angle or when approaching short-wavelength limit  $\lambda_1$  in the neighborhood of which  $R_1 \rightarrow 0$  much faster than  $R_2$ .

Total picture with wavelength dependencies of interference curves up to fifth interference order is given in Fig. 4 including light figure patterns (inset) that reflect key elements of evolution of light figures of TeO<sub>2</sub> with wavelength. Every  $m$ th order isochromatic curve has its own wavelength limit and tends to shrink into zero-size isochromate when approaching this limit given by

$$\lambda_m = \frac{1}{m} n^3 (\lambda_m) G_{\parallel}(\lambda_m) d, \quad (5)$$

where  $G_{\parallel}$  is the absolute value of  $G_{33}$  component of gyration tensor of TeO<sub>2</sub> [7]. Condition (5) corresponds to multiples of  $\pi/d$  for rotatory power [7] and each  $\lambda_m$  in Fig. 4 is given together with the corresponding  $\pi/d$  value in the brackets.

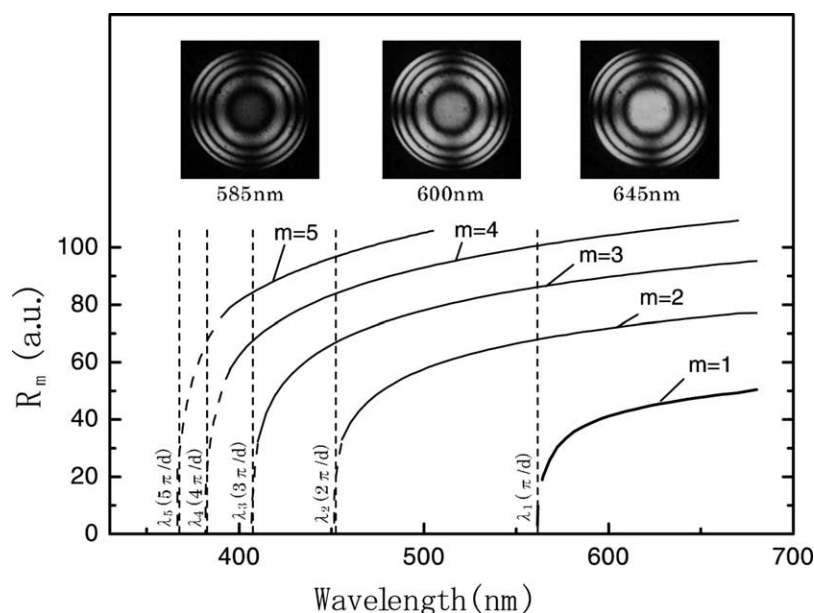


Fig. 4. Wavelength dependences of the radii of isochromatic curves with different interference orders ( $m$ ) for TeO<sub>2</sub>. Vertical dashed lines indicate the short-wavelength limits for each interference order. Inset: light figure patterns, for  $m = 1$ , of TeO<sub>2</sub>.

For AgGaS<sub>2</sub> only two major components,  $G_{11}$  and  $G_{22}$  ( $G_{11} = -G_{22}$ ), of gyration tensor are different from null. Component  $G_{33}$  is null and the situation is just the opposite of that for TeO<sub>2</sub>. The value of  $\rho G$  strongly decreases with decreasing interference angle and most favorable conditions for observation of the optical activity effect are realized at interference angles close to 90°. The use of large numerical apertures of  $\sim 60^\circ$  may provide necessary conditions for observation of this effect, as well as determination of gyration parameter in the visible spectral range. Presently this parameter is known only for one wavelength from the data on rotatory power for isotropic point [5]. It is also interesting to investigate whether the shape of interference curves does really deviate from circular, as predicted by our recent analysis [7].

### 3. Conclusion

By this work we have shown that light figure spectroscopy is a valuable tool for visualization of optical activity effect on optical constants of anisotropic materials.

### References

- [1] N. Yamamoto, N. Mamedov, T. Shinohara, T. Kunie, Visualization of light dispersion and structural phase transitions with light figures, *J. Cryst. Growth* 237–239 (2002) 2023–2027.
- [2] N. Mamedov, Y. Shim, N. Yamamoto, Polarized transmission intensity studies of off-zone-center incommensurate semiconductors-ferroelectrics TIMeX<sub>2</sub>, *Jpn. J. Appl. Phys.* 41 (2002) 7254–7259.
- [3] N. Mamedov, N. Yamamoto, T. Kunie, Light figures and group-to-phase velocity ratio in anisotropic media, *Jpn. J. Appl. Phys.* 40 (2001) 4938–4942.
- [4] Y. Shim, N. Mamedov, N. Yamamoto, Numerical and experimental approbation of extended application of light figures, *J. Appl. Phys.* 91 (2002) 4110–4113.
- [5] M. Susaki, N. Yamamoto, H. Horinaka, W.Z. Huang, Y. Cho, Performance of AgGaS<sub>2</sub> crystal filter for Raman spectroscopy, *Jpn. J. Appl. Phys.* 33 (1994) 1561–1565.
- [6] T. Takizawa, Optical absorption and reflection spectra of paratellurite, TeO<sub>2</sub>, *J. Phys. Soc. Jpn* 48 (1980) 505–510.
- [7] N. Mamedov, N. Yamamoto, Y. Shim, Y. Ninomiya, T. Takizawa, Extended application of light figures to optically active materials with transversally isotropic dielectric function, *Jpn. J. Appl. Phys.* (2003) in press.



ELSEVIER

Journal of Physics and Chemistry of Solids 64 (2003) 1825–1829

JOURNAL OF  
PHYSICS AND CHEMISTRY  
OF SOLIDS

[www.elsevier.com/locate/jpcs](http://www.elsevier.com/locate/jpcs)

# Schottky properties of $\text{CuInSe}_2$ single crystals grown by the horizontal Bridgman method with controlling Se vapor pressure

Hiroaki Matsushita<sup>a,\*</sup>, Yukio Tojo<sup>b</sup>, Takeo Takizawa<sup>b</sup>

<sup>a</sup>*Department of Material Science and Technology, School of High-Technology for Human Welfare, Tokai University, 317 Nishino, Numazu-city, Shizuoka 410-0395, Japan*

<sup>b</sup>*Department of Physics, College of Humanities and Sciences, Nihon University, 3-25-40 Sakurajosui, Setagaya-ku, Tokyo 156-8550, Japan*

## Abstract

The electrical properties of the Schottky barriers fabricated by using good quality single crystals of  $\text{CuInSe}_2$  grown by the horizontal Bridgman method with controlling Se vapor pressure have been investigated, since the Schottky effect gives us useful information concerning defect physics. The electrical resistivities, Hall coefficients and mobilities are measured as a function of temperature down to 20 K, and the activation energy  $E_A$  and the density  $N_A$  of acceptors are estimated. Schottky junctions are prepared by vacuum evaporation of Al or In on chemically etched surfaces of the samples. From the current-voltage characteristics of these junctions, the ideality factor and barrier height are estimated as 3.6–4.8 and 0.60–0.61 eV for junctions using Al, and as 1.9–3.0 and about 0.54–0.59 eV for those using In. The capacitance-voltage characteristics are also measured. Based on these results, it is expected that the prepared junctions do not follow the Schottky model, but rather obey the MIS one.

© 2003 Elsevier Ltd. All rights reserved.

## 1. Introduction

Many trials fabricating photovoltaic cells using  $\text{CuInSe}_2$  solid solutions, e.g. n-CdS/p-Cu(Ga,In)Se<sub>2</sub> heterojunctions have been carried out, and recently some of them are practically utilized. On the other hands, rather few studies of the Schottky junctions using p-CuInSe<sub>2</sub> crystals were reported [1–3], though the Schottky effect gives us useful information concerning defect physics as well as electric transport through metal-semiconductor junctions. In addition, the electrical properties of  $\text{CuInSe}_2$  bulk crystals have scarcely been taken into account in the analysis of the Schottky junctions. This is because the high-quality single crystals such that electrical properties could be measured down to liq. N<sub>2</sub> temperature were not available before.

In this study, we report the results on the electrical properties of the Schottky barriers fabricated by using good quality single crystals of  $\text{CuInSe}_2$  grown by the horizontal Bridgman method with controlling Se vapor pressure [4,5].

## 2. Experimental procedure

$\text{CuInSe}_2$  bulk single crystals were grown under controlling Se vapor pressure from 5 to 25 Torr [4,5]. Here, the profile of temperature gradient of 3 K/cm was electrically moved at a speed of about 1 cm/h after selenizing the CuIn alloy. Grown crystals were cut into three parts along the growth direction, i.e. 'Top (T)', 'Middle (M)' and 'End (E)'. 'T' denotes the initial part of solidifying. The prefixed number such as '10T' denotes Se vapor pressure in Torr during the crystal growth. The composition was determined using an electron probe microanalyzer (EPMA). The Hall coefficient and mobility

\* Corresponding author. Tel.: +81-559-68-1211-4407; fax: +81-559-68-1155.

E-mail address: [matusita@wing.ncc.u-tokai.ac.jp](mailto:matusita@wing.ncc.u-tokai.ac.jp) (H. Matsushita).

Table 1  
Composition and electrical properties of CuInSe<sub>2</sub> bulk crystals at room temperature

Sample	Cu/ In	Se/ metal	Res. (ohm-cm)	mob. (cm <sup>2</sup> /Vs)	$E_A$ (meV)	$N_A$ (cm <sup>-3</sup> )
10E	0.95	1.05	0.5	30	10	$2 \times 10^{18}$
20M	1.00	1.03	11.6	38	60	$3 \times 10^{17}$
25T	0.93	1.06	0.7	20	5	$2 \times 10^{18}$

were measured using the six-electrode method as a function of temperature down to about 20 K, and the activation energy  $E_A$  and the density  $N_A$  of acceptors were estimated from the change in Hall coefficients with respect to temperature.

CuInSe<sub>2</sub> plates were mechanically polished by using Al<sub>2</sub>O<sub>3</sub> powder, and then rinsed by supersonic syringe in acetone, and after it in distilled water. Generally, K<sub>2</sub>Cr<sub>2</sub>O<sub>7</sub> saturation water solution (i.e. K<sub>2</sub>Cr<sub>2</sub>O<sub>7</sub> aq.) + H<sub>2</sub>SO<sub>4</sub> [1,2,6] and Br<sub>2</sub>+CH<sub>3</sub>OH solution [2,3,7,8] were used as an etchant for those metal-semiconductor junctions. In this study, sample plates were etched in K<sub>2</sub>Cr<sub>2</sub>O<sub>7</sub> aq. + H<sub>2</sub>SO<sub>4</sub> for one minute, followed by the same procedure in Br<sub>2</sub>+CH<sub>3</sub>OH for one minute. Schottky junction was formed by vacuum evaporation of Al or In on one chemically etched (112) surface, while the other surface was DC sputtered by Au to make ohmic contact.

Both of the forward and reverse current-voltage (I–V) characteristics were measured for these junctions in the dark at room temperature. From the results of the I–V characteristics, the ideality factor  $n$  and barrier height  $V_B$

were estimated, whereby the electron effective mass in p-CuInSe<sub>2</sub>,  $m_n^* = 0.73m_0$ , [9] was used, where  $m_0$  is the rest mass of an electron. The capacitance-voltage (C–V) characteristics were also measured in the dark at 10–100 kHz frequencies, using ANDO AG-4311 LCR meter. The carrier concentrations were estimated from the slope of C<sup>-2</sup>-V plots, where the specific dielectric constant of 8.5 was adopted.

### 3. Results and discussion

#### 3.1. Hall effects

Table 1 shows the atomic compositions and electrical properties of several p-type CuInSe<sub>2</sub> samples. Fig. 1 shows the temperature dependence of electrical resistivity, Hall coefficient and Hall mobility of these samples. Among the samples, the 20 M has a higher Hall mobility of p-type conduction within the Se pressure range of crystal growth. On the other hands, the other samples are like degenerate semiconductors.

There were varieties in the Hall coefficient vs. temperature curves of p-type samples, and the Hall coefficient overshoots, which are typical in two carrier conduction of binary and ternary compensated semiconductors, were often observed [4,5]. All of samples as shown in Fig. 1 do not show the Hall coefficient overshoots, and thus these samples have lower donor density as compared with the acceptor density. We have classified the p-type samples into the deep (D), shallow (S) or a combination of both (B) types, on the basis of

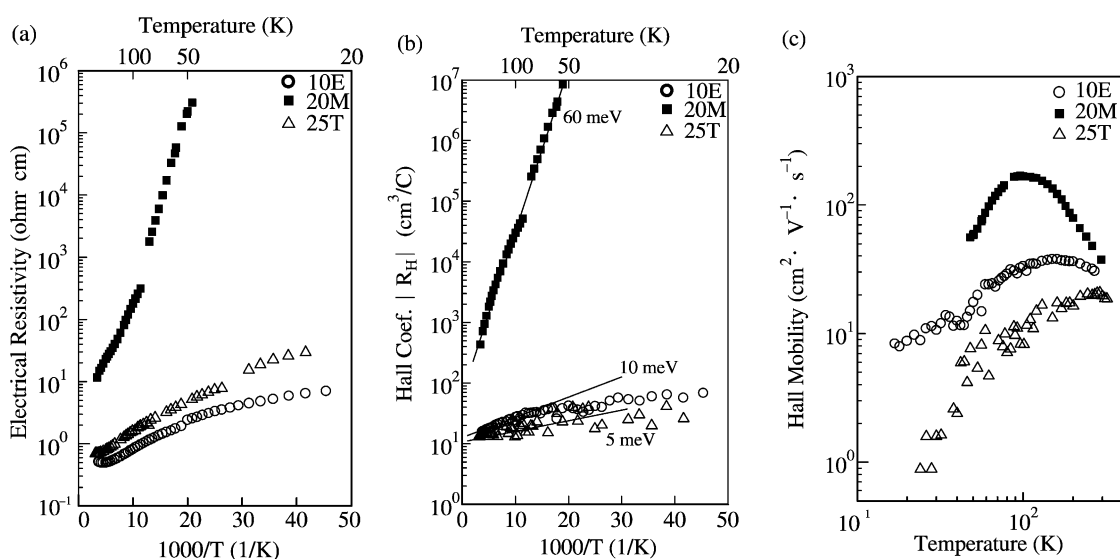


Fig. 1. Temperature dependence of (a) electrical resistivity, (b) Hall coefficient and (c) Hall mobility of p-type samples grown by the horizontal Bridgman method with controlling Se vapor pressure.

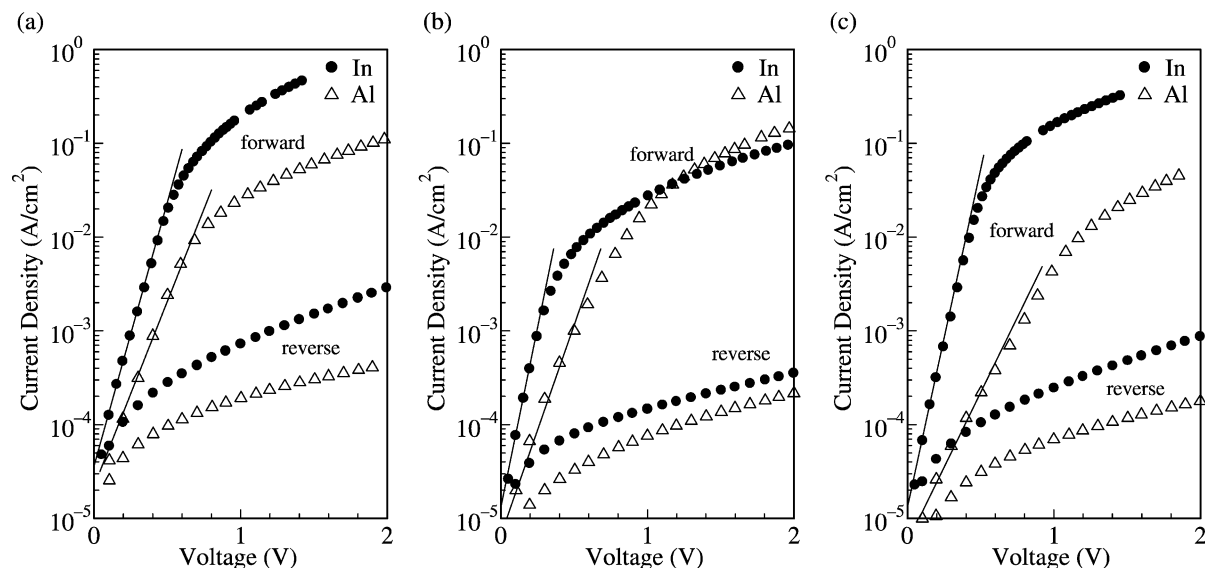


Fig. 2. I–V characteristics of Schottky junctions of Al/p-CuInSe<sub>2</sub> and In/p-CuInSe<sub>2</sub> in the dark at room temperature; (a) 10 E, (b) 20 M and (c) 25 T.

the density ratio between the shallow and deep acceptors [4,10]. Two kinds of acceptors are revealed, one with an activation energy of about 10 meV such as 10E and 25T and the other with an activation energy of about 60 meV such as 20 M. The shallow acceptors exist in the S-type samples with Cu-poor composition, where the origin of the acceptors was ascribed to Cu vacancies. On the other hand, the origin of the deep acceptors in the D- and B-type samples (Cu/In = 1 and Cu/In > 1, respectively) was ascribed to In vacancies.

### 3.2. Etching effects

In order to understand the effect of etching on CuInSe<sub>2</sub> crystals, the surface SEM images and the composition variations before and after chemical etching were investigated. As the result of the SEM observation by varying the concentration of K<sub>2</sub>Cr<sub>2</sub>O<sub>7</sub> aq. from 0 to 15%, the K<sub>2</sub>Cr<sub>2</sub>O<sub>7</sub> aq. (5%) + H<sub>2</sub>SO<sub>4</sub>, where the effect of etching seemed remarkable, was adopted as the first etchant. However, during the measurement of I–V characteristic, the current values in the voltage elevating process did not coincide with that in the voltage lowering one. In addition, the electrical condition was not stable on the measurement. Then, Br<sub>2</sub>+CH<sub>3</sub>OH solution was adopted to test as the second etchant. In this case, the problems above were improved remarkably. From the SEM observation of the sample surface treated in the Br<sub>2</sub>+CH<sub>3</sub>OH solution with Br<sub>2</sub> concentration of 0.5, 1, 3 and 5%, it was found the crystallization surface etched by the Br<sub>2</sub> + CH<sub>3</sub>OH solution (3%) was uniformly shaved.

The Cu/In ratio increased a little after etching with K<sub>2</sub>Cr<sub>2</sub>O<sub>7</sub> aq. + H<sub>2</sub>SO<sub>4</sub> solution, and the Se content seemed to decrease by etching with Br<sub>2</sub> + CH<sub>3</sub>OH solution.

### 3.3. Schottky barriers

Fig. 2 shows I–V characteristics of Al/p-CuInSe<sub>2</sub> and In/p-CuInSe<sub>2</sub> Schottky junctions. It is seen that the rectification ratio of all samples is more than two orders of magnitude at the bias of about 1 V. The ideality factor  $n$  and barrier height  $V_B$  estimated from the I–V characteristics are shown in Table 2. Here, the ideality factor was determined from the exponential curves of the current density vs. forward voltages at a voltage less than 1 V as shown in Fig. 2. In the case of the forward bias, the cut-in voltages of Al/p-CuInSe<sub>2</sub> junctions are somewhat larger than those of In/p-CuInSe<sub>2</sub>, and thus it is expected that the diffusion potentials of Al/p-CuInSe<sub>2</sub>

Table 2  
Schottky properties of junctions using p-CuInSe<sub>2</sub> bulk crystals

Sample	Metal	$n$	$V_B$ (eV)	Carrier concentration from C–V characteristic (cm <sup>-3</sup> )	Carrier concentration from Hall effect (cm <sup>-3</sup> )
10E	Al	3.6	0.60	$5.9 \times 10^{15}$	$4.2 \times 10^{17}$
	In	3.0	0.54	$4.2 \times 10^{16}$	
20M	Al	3.5	0.61	–	$1.4 \times 10^{16}$
	In	1.9	0.59	$1.7 \times 10^{15}$	
25T	Al	4.8	0.62	$2.2 \times 10^{15}$	$4.6 \times 10^{17}$
	In	2.2	0.57	$5.9 \times 10^{16}$	

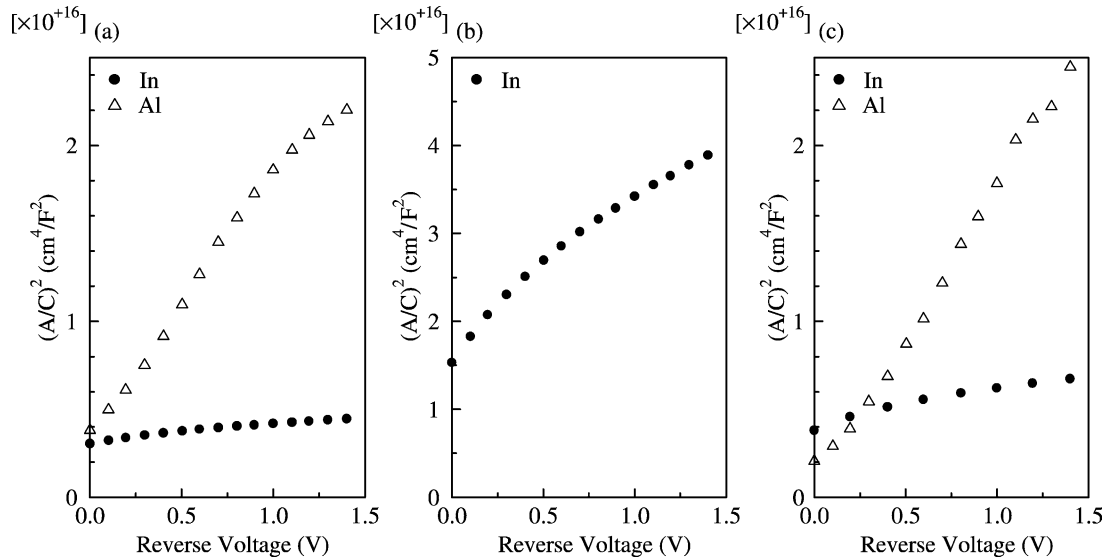


Fig. 3.  $C$ - $V$  characteristics of Schottky junctions of Al/p-CuInSe<sub>2</sub> and In/p-CuInSe<sub>2</sub> at 50 kHz frequency in the dark at room temperature; (a) 10 E, (b) 20 M and (c) 25 T.

junctions become larger. In addition, it is found that the ideality factors of In/p-CuInSe<sub>2</sub> junctions are closer to 1 than that of Al/p-CuInSe<sub>2</sub>. In the case of the reverse bias, the leak current was very low in the Al/p-CuInSe<sub>2</sub> junctions, and no breakdown current was observed in the voltage range down to  $-10$  V. Judging from the finding that the ideality factors was far from unity, it is suggested that insulation layers (for instance, oxidation layers) and/or carrier trap levels for surface states were formed between metals and semiconductors.

Fig. 3 shows the plots of  $C^{-2}$ - $V$  characteristics at 50 kHz frequency of Al/p-CuInSe<sub>2</sub> and In/p-CuInSe<sub>2</sub> Schottky junctions. In the case of Al/p-CuInSe<sub>2</sub> junctions, the frequency dependence of  $C^{-2}$ - $V$  characteristics was observed. This may be due to the existence of insulation layers in the junction interface. The junction capacitance decreased as the frequency increased from 10 to 100 kHz. In the case of In/p-CuInSe<sub>2</sub> junctions, the capacitance was almost independent of frequency. The measured capacitances of In/p-CuInSe<sub>2</sub> junctions are seen to be generally larger than those of Al/p-CuInSe<sub>2</sub> junctions. Furthermore, two straight-line regions of  $C^{-2}$ - $V$  plots exist in the low and high bias regions, respectively. It was reported by Fonash that the slope of  $C^{-2}$ - $V$  plots at a low bias in the MIS type metal-semiconductor junctions is sometimes different from that in the perfect metal-semiconductor junctions [11]. The carrier concentrations determined from the slope of  $C^{-2}$ - $V$  plots at a high bias were shown in Table 2, where the carrier concentrations obtained by Hall effect were also shown for comparison. It is shown that the carrier concentrations of all samples estimated from  $C^{-2}$ - $V$

characteristics are one to two orders of magnitude lower than those from Hall effect. It is because Se vacancies increased in the depletion layer, which were formed at the surface of CuInSe<sub>2</sub> crystals by the decrease of Se contents after etching with Br<sub>2</sub> + CH<sub>3</sub>OH solution. In other words, the carriers in the depletion layer are compensated by donors for Se vacancies. Thus, the  $C^{-2}$ - $V$  characteristics may not reflect the bulk properties, since the composition of bulk crystal is different from that of the crystal surface. In addition, the influence of insulation layers to the capacitance seem to lower the carrier concentrations estimated from  $C^{-2}$ - $V$  characteristics.

#### 4. Summary

Schottky barriers were fabricated by using good quality single crystals of CuInSe<sub>2</sub> grown by the horizontal Bridgman method with controlling Se vapor pressure. The defect physics of the metal/p-CuInSe<sub>2</sub> junctions was investigated for samples having shallow or deep acceptors.

Judging from the results of the investigations by SEM and EPMA before and after etching, the etching condition was determined to use Br<sub>2</sub>+CH<sub>3</sub>OH (3%) for one minute after etching in K<sub>2</sub>Cr<sub>2</sub>O<sub>7</sub> aq. (5%) + H<sub>2</sub>SO<sub>4</sub> for 1 min. From the I- $V$  characteristics of the metal/p-CuInSe<sub>2</sub> junctions, the ideality factor and barrier height are estimated as 3.6–4.8 and 0.60–0.61 eV for Al/p-CuInSe<sub>2</sub>, and as 1.9–3.0 and about 0.54–0.59 eV for In/p-CuInSe<sub>2</sub>. The  $C$ - $V$  characteristics are also measured and analyzed in the 10–100 kHz frequency range, and it is expected

that the prepared junctions do not follow the Schottky model, but rather obey the MIS one.

## References

- [1] C.L. Chan, I. Shih, *J. Appl. Phys.* 68 (1990) 156.
- [2] B. Koscielniak-Mucha, A. Opanowicz, *Phys. Stat. Sol. A* 141 (1994) K67.
- [3] M.A. Magomedov, V.D. Prochukhan, Yu. V. Rud, *Sov. Phys. Semicond.* 26 (1992) 1123.
- [4] H. Matsushita, T. Takizawa, *J. Cryst. Growth* 160 (1996) 71.
- [5] H. Matsushita, A. Iwabuchi, T. Takizawa, S. Endo, *Cryst. Res. and Technol.* 31 (1996) 77.
- [6] A.L. Li, I. Shih, *J. Elec. Mater.* 22 (1993) 195.
- [7] F.A. Abou-Elfotouh, L.L. Kazmerski, R.J. Matson, D.J. Dunlavy, T.J. Coutts, *J. Vac. Sci. Technol. A* 8 (1990) 3251.
- [8] E. Moon, *J. Elec. Mater.* 22 (1993) 275.
- [9] S. Endo, T. Irie, *Solar Cells* 16 (1986) 1.
- [10] H. Matsushita, T. Takizawa, *Jpn. J. Appl. Phys.* 37 (1998) 4258.
- [11] S.J. Fonash, *J. Appl. Phys.* 54 (1983) 1966.

## Extended Application of Light Figures to Optically Active Materials with Transversally Isotropic Dielectric Function

Nazim MAMEDOV, Nobuyuki YAMAMOTO, Yonggu SHIM, Yuichiro NINOMIYA and Takeo TAKIZAWA<sup>1</sup>

*Department of Physics and Electronics, Osaka Prefecture University, Gakuen-cho 1-1, Sakai, Osaka 599-8531, Japan*

<sup>1</sup>*Department of Physics, Nihon University, 3-25-40 Sakura-josui, Setagaya-ku, 156-8550 Tokyo, Japan*

(Received August 23, 2002; accepted for publication April 2, 2003)

An analytical approach to optic-axis light figures of optically active transparent materials with transversally isotropic linear dielectric function is developed. The ratio of the gyration constant to the parameter of anisotropy of this function is shown to be essential for the scale of the gyration effect on light figures. An algorithm for determination of all material-related optical parameters is proposed in the form covering both symmetries possible for optical activity in uniaxial materials, such as AgGaS<sub>2</sub> and TeO<sub>2</sub>. For AgGaS<sub>2</sub>, a deviation of the shape of the interference curves from circular is expected at enough large angles of interference. In full agreement with the performed theoretical analysis, the shrinking of interference curves into zero-size isochromates is observed at multiples of  $\pi$  for rotation angle of a thick 1420  $\mu\text{m}$ -plate of TeO<sub>2</sub>. Transversal component of gyration pseudo-tensor of TeO<sub>2</sub> is determined for the first time. The recently proposed relative light-figure method is reformulated and briefly discussed with allowance for optical activity. [DOI: 10.1143/JJAP.42.5145]

KEYWORDS: light figures, optical activity, gyration pseudo-tensor, rotatory power, isogyros, isochromus

### 1. Introduction

Recent developments<sup>1–4</sup> in light figure (LF) spectroscopy, which is used for optical characterization of anisotropic materials since long time ago,<sup>5,6</sup> give a hope that application of LF can be extended to investigation of optical effects in substances with nanosize structures. Most promising for this purpose is thought to be relative LF method<sup>1</sup> that has already received comprehensive experimental approval.<sup>2</sup> At the same time absolute LF method may also be useful. This method was sensitive to the formation of an incommensurate superstructure with correlation length of the order of  $\sim 10\text{ nm}$  and spatial dispersion of the order parameter was then found to give a significant optical anisotropy of the order of  $\sim 10^{-3}$  with the background value of  $\sim 10^{-4}$  for basic lattice.<sup>3,4</sup> For comparison, spatial dispersion in optically non-active materials with usual interatomic distances can give only a very small correction of the order of  $10^{-6}$  to the refraction index.<sup>7</sup>

Optical activity is a first order spatial dispersion effect that usually influences refraction index in the order of  $\sim 10^{-4}$  or less. Conventional methods face difficulties in measuring such small variations of refraction indices and full characterization of many anisotropic optically-active substances has not been done yet.<sup>8</sup> LF, which, in our opinion, is basically free of the deficiencies inherent to the other methods, can assist in solving the problem. However a relevant analytical approach is currently in lack.<sup>5,6</sup>

Here we are considering optic-axis LFs of optically active materials with transversally isotropic linear dielectric function in trial to find analytical approximations qualifying for practical use in the frames of both absolute and relative LF methods. Basing on the obtained results, we accomplish numerical and experimental application to the TeO<sub>2</sub> having one of the two symmetries possible for optical activity in uniaxial materials, and give general analysis to a representative of the other symmetry, AgGaS<sub>2</sub>. As far as gyration-induced variations of refraction indices are concerned, we demonstrate that LFs are able to expose such variations down to at least  $\sim 10^{-5}$ , which is still above the level of variations ( $\sim 10^{-6}$ ) caused by thermal fluctuations ( $\sim 0.1\text{ K}$ ).

### 2. Influence of Optical Activity on Refraction Indices

Maxwell equations for transparent materials with gyration permit solution in the form of the two elliptically polarized waves.<sup>7</sup> If we select a coordinate system with Z-axis parallel to the optic axis, we can write refraction indices of these waves in the form

$$n_{oG} = \sqrt{\left(\frac{1}{\varepsilon_{\perp}} \mp \rho_o G_o\right)^{-1}} \quad (1)$$

and

$$n_{eG} = \sqrt{\left(\frac{\varepsilon_{\parallel} \cos^2 \theta_e + \varepsilon_{\perp} \sin^2 \theta_e}{\varepsilon_{\parallel} \varepsilon_{\perp}} \pm \rho_e G_e\right)^{-1}} \quad (2)$$

Here subscripts o and e are related to the ordinary and extraordinary waves, respectively. Parameter  $\rho$ , or ellipticity, is determined as

$$\rho_{o,e} = \frac{1}{2G_{o,e}} \left( \sqrt{\gamma^2 \sin^4 \theta_e + 4G_{o,e}^2} - \gamma \sin^2 \theta_{o,e} \right) \quad (3)$$

It has always the same sign as  $G_{o,e}$ . Parameter  $\gamma$ , or parameter of anisotropy of dielectric function, introduced into eq. (3) equals

$$\gamma = \left| \frac{\varepsilon_{\perp} - \varepsilon_{\parallel}}{\varepsilon_{\perp} \varepsilon_{\parallel}} \right| \quad (4)$$

Angle  $\theta_{o,e}$  is the angle between  $k_{o,e}$  and optic axis,  $\varepsilon_{\perp}$  and  $\varepsilon_{\parallel}$  are transversal and parallel components of the dielectric function tensor  $\varepsilon$ , respectively. The upper and lower signs in (1) and (2), as well as all the other expressions given hereafter are taken for  $\varepsilon_{\perp} > \varepsilon_{\parallel}$  and  $\varepsilon_{\perp} < \varepsilon_{\parallel}$  cases, respectively. Analytical form of the parameter  $G_{o,e}$  that is nothing else but a normal component of gyration pseudo-tensor  $G$  in  $k$  direction can be found as

$$G_{o,e} = k_{o,e} \mathbf{G} k_{o,e} \quad (5)$$

This form depends on the class of symmetry of optical activity. In materials under consideration tensor  $\mathbf{G}$  has either  $\infty 2$  or  $42m$  symmetry. Note that this symmetry is not necessarily the same as crystal point symmetry.

For  $\alpha 2$  symmetry ( $\alpha$ -axis parallels  $Z$ ), tensor  $G$  has eigen value  $G_{\parallel}$  for eigen vector that parallels  $Z$  and  $G_{\perp}$  for all eigen vectors in  $XY$  plane. Therefore this tensor is transversally isotropic and normal component can be written as

$$G_{o,e} = G_{\parallel} + (G_{\perp} - G_{\parallel}) \sin^2 \theta_{o,e} \quad (6)$$

For  $\bar{4}2m$ -symmetry ( $\bar{4}$ -axis parallels  $Z$ , 2-axes coincide with  $X$  and  $Y$ ) tensor  $G$  is not transversally isotropic because it has three different principal components  $G_{11} = G_o$ ,  $G_{22} = -G_o$  and  $G_{33} = 0$ . At the same time, only one of these components is unknown and normal component can be written as

$$G_{o,e} = G_0 \cos 2\varphi \sin^2 \theta_{o,e} \quad (7)$$

where  $\varphi$  is an angle counted from  $X$  or  $Y$ . Note that for some crystal symmetries with above symmetry of optical activity  $X$  and  $Y$  axes do not coincide with crystal axes  $a$  and  $b$ . But this has no influence on LFs for which only the symmetry of optical activity is essential.

### 3. Influence of Optical Activity on Optic-Axis Light Figures

The general condition of interference<sup>5)</sup> for a uniaxial optically non-active plate with thickness  $d$  can be re-written to the form

$$\left| \sqrt{n_e^2 - \sin^2 \theta_m} - \sqrt{n_o^2 - \sin^2 \theta_m} \right| = \alpha_m \quad (8)$$

where

$$\alpha_m = \frac{m\lambda}{d} \quad (9)$$

For optically active materials the general condition of interference remains valid in the form eq. (8) after making transformation

$$n_o \rightarrow n_{oG} = \sqrt{\frac{\varepsilon}{1 \mp \varepsilon \rho_o G_o}} \quad (10)$$

$$n_e \rightarrow n_{eG} = \sqrt{\frac{\varepsilon(1 \mp \gamma \sin^2 \theta_{mG})}{1 \pm \varepsilon \rho_e G_e}} \quad (11)$$

Here,  $\varepsilon$  is transversal component  $\varepsilon_{\perp}$ ,  $\theta_m$  and  $\theta_{mG}$  are the incident angles at which the  $m$ -th order isochromatic curve is observed in optically non-active and active cases, respectively. Parameter  $\sin \theta_m$  or  $\sin \theta_{mG}$  can be determined experimentally and separately for each interference curve by using an objective (or condensing) lens with variable numerical aperture.

The effect of optical activity on LF will obviously depend on how much the interference condition (8) written for optically non-active case will be affected after allowance for gyration. Examination of eqs. (10) and (11) immediately shows that influence of optical activity on LF will be determined by the  $\varepsilon \rho G$ -terms related to ordinary and extraordinary waves, respectively.

In contrast with the optically non-active case, now the interference effect is possible even at  $\theta_{mG} = 0$  for which condition (8) transforms into

$$\left| \sqrt{\frac{\varepsilon}{1 \pm \varepsilon \rho_o G_o}} - \sqrt{\frac{\varepsilon}{1 \mp \varepsilon \rho_o G_o}} \right| = \alpha_m \quad (12)$$

It is clear that optical activity will modify not only the interference angles ( $\theta_m \rightarrow \theta_{mG}$ ) but also the radiuses ( $r_m \rightarrow r_{mG}$ ) of interference curves.

The effect of optical activity on light figures can be observed if difference  $|r_{mG} - r_m|$  is larger than diffraction limited resolving power of the objective lens with numerical aperture  $\sin \theta$ , or

$$|r_{mG} - r_m| > 0.61\lambda / \sin \theta \quad (13)$$

According to condition (13), the use of variable numerical aperture with  $\sin \theta = \sin \theta_{mG}$  is justified only for enough large interference angles. For small interference angles variable numerical aperture is less useful and information we can obtain is restricted to the values of the radiuses of the isochromatic curves.

It can be shown that the effect of optical activity on the radius of an  $m$ -th order interference curve can be roughly evaluated as

$$|r_{mG} - r_m| \sim \sqrt{\frac{m\lambda d}{2\Delta n}} n^3 \rho_m G_m \quad (14)$$

where optical anisotropy  $\Delta n$  is the difference between refraction indices of extraordinary and ordinary rays,  $n$ -refraction index of ordinary ray. Here  $\rho_m G_m$  is taken for the direction of mean path ray having refraction index  $n_m$  (see Appendix).

### 4. Optical Activity and Optic-Axis Light Figures of Silver Thiogallate and Paratellurite

#### 4.1 State of art

Silver thiogallate,  $\text{AgGaS}_2$ , and paratellurite,  $\text{TeO}_2$ , are representatives of two different symmetries ( $\bar{4}2m$  and  $\alpha 2$ , respectively) possible for optical activity in non-center-symmetrical materials with transversally isotropic tensor of linear dielectric function. To the best of our knowledge, there are no reports on LFs of the above materials.

$\text{AgGaS}_2$  with  $\bar{4}2m$  ( $D_{2d}$ )-point group of crystal symmetry has only one independent component ( $G_o$ ) of gyration pseudo-tensor. This component is known only for the isotropic point ( $\lambda = 497.3 \text{ nm}$ ),<sup>9)</sup> and finding  $G_o$  in a wide spectral range is yet to be done, in particular, by using optic-axis (or perpendicular-to-optic-axis) LFs.

As follows from (3) and (7), for  $\text{AgGaS}_2$  a  $\varepsilon \rho_m G_m$ -term can be written as

$$\varepsilon \rho_m G_m = \frac{\gamma \varepsilon \sin^2 \theta_{mG}}{2n_m^2} \left( \sqrt{1 + 4 \left( \frac{G_o}{\gamma} \right)^2 \cos^2 2\varphi} - 1 \right) \quad (15)$$

For most cases the second term under the square root is much smaller than the first one. Therefore, expression (15) can be evaluated by

$$\varepsilon \rho_m G_m \approx \frac{G_o^2}{\gamma} \cos^2 2\varphi \sin^2 \theta_{mG} \quad (16)$$

where we have taken  $n_m = \sqrt{\varepsilon}$  for simplicity.

As follows from (15) and (16), LF patterns will not be influenced by optical activity at  $\theta_{mG} = 0$  and  $\varphi = \pi/4 \pm l\pi$ , where  $l$  is an integer. In all the other cases this influence depends upon values of  $\theta_{mG}$  and  $\varphi$ , being largest when  $\varphi = l\pi$  and  $\theta_{mG} = \pi/2$ . Strictly speaking,  $\cos 2\varphi$ -modulation in

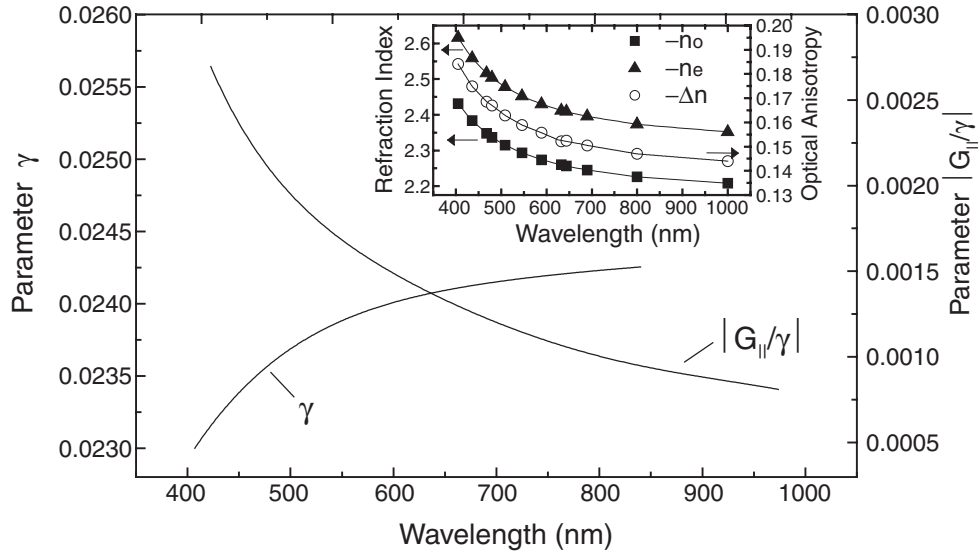


Fig. 1. Parameter  $\gamma$  and parameter  $|G_{\parallel}/\gamma|$  for  $\text{TeO}_2$ , as restored from the previous data.<sup>11,12)</sup> Inset: optical constants and optical anisotropy of  $\text{TeO}_2$  according to the work.<sup>11)</sup>

eq. (15) or (16) will lead to the similar modulation of interference angles and radiuses of interference curves so that one can expect deviation of the shape of interference curves from circular at least at enough large angles of interference. More details related to this deviation, as well as numerical estimates and experimental data for  $\text{AgGaS}_2$  will be given in another work.<sup>10)</sup>

Here we focus on the representative of the other symmetry of optical activity, paratellurite (crystal symmetry 422 ( $D_4$ )), which is optically well studied.<sup>11,12)</sup> As follows from eqs. (3) and (6), a  $\varepsilon\rho_m G_m$ -term of paratellurite can be written as

$$\varepsilon\rho_m G_m = \frac{\gamma\varepsilon \sin^2 \theta_{mG}}{2n_m^2} \times \left\{ \left[ 1 + 4 \left( n_m^2 \frac{|G_{\parallel}|}{\gamma \sin^2 \theta_{mG}} + \frac{\pm |G_{\perp} - G_{\parallel}|}{\gamma} \right)^2 \right]^{\frac{1}{2}} - 1 \right\} \quad (17)$$

Here the superscript  $\pm$  indicates that  $|G_{\perp} - G_{\parallel}|$  should be taken with sign  $+$  if gyration constants have the same sign, and with sign  $-$  if they have opposite signs. The estimations based on the available data<sup>11,12)</sup> show that the second term under the square root of (17) is much larger than the first one for all incident angles less than  $7^\circ$ , which is slightly larger than our experimental angular aperture ( $\sim 6^\circ$ ). Therefore, for  $\theta_{mG} < 7^\circ$  we have

$$\varepsilon\rho_m G_m \approx \varepsilon |G_{\parallel}| + \left( \frac{\pm |G_{\perp} - G_{\parallel}|}{\gamma} - \frac{1}{4} \right) \gamma \sin^2 \theta_{mG} \quad (18)$$

Unlike the case of  $\text{AgGaS}_2$ , now we can expect strong influence of optical activity on LF at small angles of interference, too. For sufficiently large interference angles, such as  $\theta_{mG} > 7^\circ$  in the case of  $\text{TeO}_2$ , the second term under the square root of relation (17) becomes smaller than 1 and we have

$$\varepsilon\rho_m G_m \approx \frac{|G_{\parallel}|}{\gamma} \left( \frac{\varepsilon^2 |G_{\parallel}|}{\sin^2 \theta_{mG}} + 2\varepsilon^{\pm} |G_{\perp} - G_{\parallel}| \right)$$

$$+ \frac{|G_{\perp} - G_{\parallel}|^2}{|G_{\parallel}|} \sin^2 \theta_{mG} \quad (19)$$

Wavelength dependence of parameter  $\gamma$ , as well as the ratio  $|G_{\parallel}|/\gamma$  essential for both the scale of the gyration effect on LF of  $\text{TeO}_2$  and the best conditions for observation of the effect from transversal component of gyration (see Appendix) is shown in Fig. 1. We used the reported values<sup>11)</sup> of optical constants (inset) to obtain data on Fig. 1. Component  $G_{\parallel}$  was calculated using the well-known expression for rotatory power,  $\chi$ ,

$$G_{\parallel} = \frac{\chi\lambda}{\pi n^3} \quad (20)$$

where  $n = \sqrt{\varepsilon}$ , and values of  $n$  and  $\chi$  from the works.<sup>11,12)</sup> Note that optical anisotropy of  $\text{TeO}_2$  (inset) and  $\gamma$  depend upon wavelength just in an opposite way. In the next section we will give an extended analysis of our experimental results on  $\text{TeO}_2$  for which transversal component ( $G_{\perp}$ ) of pseudotensor of gyration is unknown and will be determined in this work for the first time.

#### 4.2 Experimental results and analyses for paratellurite

Experimental results were obtained in the range 400–700 nm at room temperature for a 1420  $\mu\text{m}$ -thick  $\text{TeO}_2$ -plate cut perpendicular to the optic axes. The details concerning with experimental set-up and digital processing of the data were described earlier.<sup>2,3)</sup>

A typical transformation of LFs with wavelength is shown in Fig. 2 including radial distribution of light intensity in LF patterns (inset) obtained at wavelengths of 510 nm, 480 nm and 450 nm. The radius  $R_s$  of the smallest interference ring is decreasing with decreasing wavelength and the ring, itself, becomes unobservable around a wavelength of 450 nm for which full extinction in the central part of LF pattern is observed.

The key elements of the above transformation are preserved over all visible spectral range and can be understood from Fig. 3.

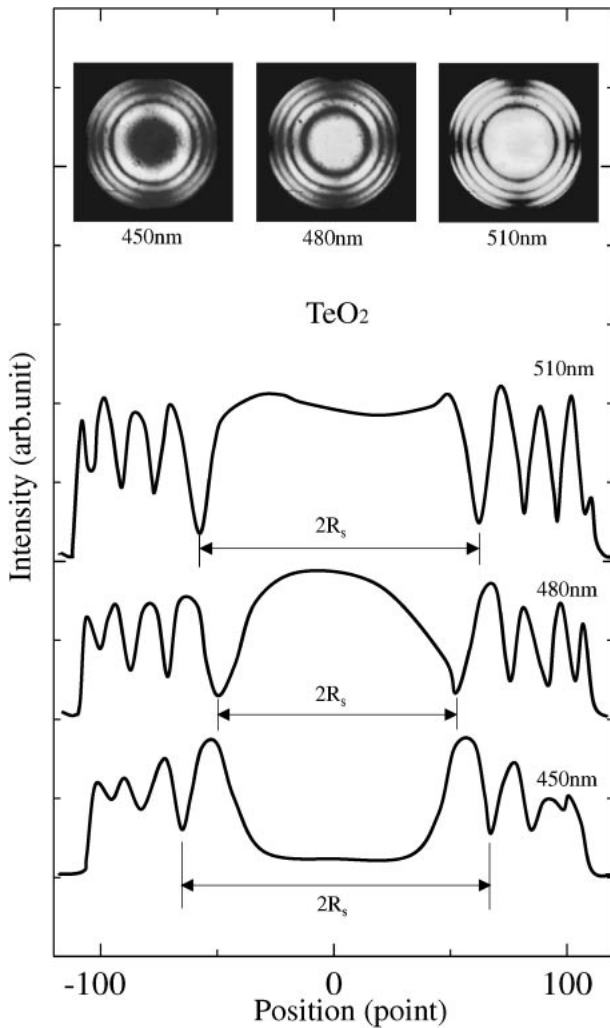


Fig. 2. Experimental radial distribution of light intensity in light figure patterns (upper part) of a thick plate of TeO<sub>2</sub> at different wavelengths.

Every interference curve with the lowest interference order tends to shrink into zero-size isochromate at multiples of  $\pi/d$  for rotatory power. After shrinking, the interference curve disappears from the LF pattern in full agreement with the fact that interference order  $m$  in optically active material can not exist below a wavelength,  $\lambda_m$ , given, according to condition (12), by

$$n^3(\lambda_m)G_{\parallel}(\lambda_m)d \approx m\lambda_m \quad (21)$$

Condition (21) immediately leads to the corresponding condition for rotatory power

$$\chi(\lambda_m) \approx m \frac{\pi}{d} \quad (22)$$

Numbering of interference orders  $m$  in Fig. 3 is therefore done according to the last relationship that can be reformulated as a condition of multiples of  $\pi$  for rotation angle ( $\varphi = \chi d$ ).

In Fig. 4 we show the results of comparison of the experimental modified-by-gyration ratio  $R_{m+1}/R_m$  for neighboring interference orders  $m$  and  $m + 1$  with that calculated for optically non-active case according to the approximate expression

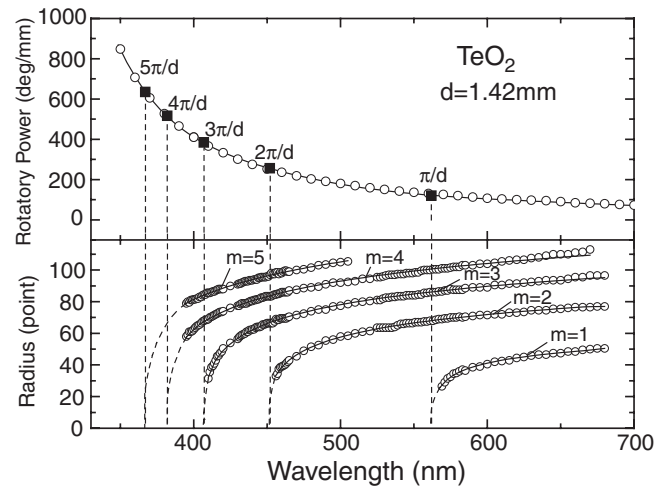


Fig. 3. Rotatory power of TeO<sub>2</sub> from the works<sup>11,12)</sup> and experimental radiuses of interference curves of a thick plate of TeO<sub>2</sub> as functions of wavelength. Open circles-experimental data; solid curves-results of polynomial fitting; dashed continuations of the solid curves-speculative behavior.

$$\frac{R_{m+1}}{R_m} \approx \frac{m+1}{m} \left( 1 + \sqrt{1 + \left( \frac{2\Delta nd}{(m+1)\lambda} \right)^2} \right)^{\frac{1}{2}} \times \left( 1 + \sqrt{1 + \left( \frac{2\Delta nd}{m\lambda} \right)^2} \right)^{-\frac{1}{2}} \quad (23)$$

that can be easily derived from our previous results.<sup>1,3)</sup> Here, we use large  $R$  instead of small  $r$  for radius of interference curve since experimental radius  $R$  is enlarged in comparison with real (small) radius  $r$ .

Note that ratio (23) is always within the following limits

$$\sqrt{\frac{m+1}{m}} \leq \frac{R_{m+1}}{R_m} \leq \frac{m+1}{m} \quad (24)$$

For thick samples, such as in our case, when condition

$$d \gg \frac{m\lambda}{2\Delta n} \quad (25)$$

is fulfilled, this ratio is supposed to be close to the values given by the left-hand limit of relation (24). On the right scale of Fig. 4 these values are given as  $\sqrt{2}$ ,  $\sqrt{3}/2$ ,  $\sqrt{4}/3$  and  $\sqrt{5}/4$ . The calculated ratios are practically independent of wavelength since interference angles for the involved interference orders are very small. Experimental ratios, however, behave very differently from and approach the calculated values only in the long-wavelength regions where rotatory power is decreased. As seen from Fig. 4, every  $R_{m+1}/R_m$  ratio has its own long-wavelength limit given by numbers  $\sqrt{2}$ ,  $\sqrt{3}/2$ ,  $\sqrt{4}/3$  and  $\sqrt{5}/4$ . Therefore one can determine the interference orders of any two neighboring interference curves.

Above we have described two independent methods for correct determination of the interference order  $m$  in the case of optically active material. Note that this case is different from the case of optically non-active material for which the smallest interference ring always has  $m = 1$  and numbering of interference orders presents no difficulty.

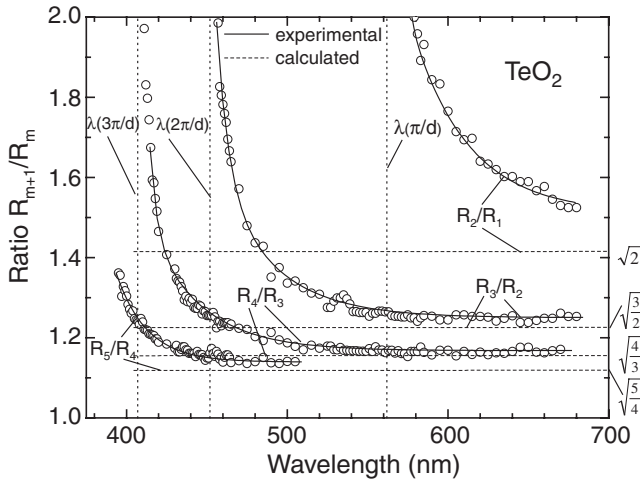


Fig. 4. Experimental (open circles—experimental data; solid curves—results of polynomial fitting) and calculated (horizontal dashed curves) ratios of the radiuses of the two neighboring interference curves as functions of wavelength for a thick plate of TeO<sub>2</sub>.

At least to an observable extent given by Fig. 4 we can see that the lower  $m$  is the stronger the experimental values of  $R_{m+1}/R_m$  deviate from their long-wavelength limits for any chosen wavelength. This can be understood if normal component of gyration pseudo-tensor is decreasing with increasing interference angle. The traces of black isogyros curve in the distant from central parts of LF patterns (Fig. 2, inset) are also witnessing that higher interference orders are less influenced by optical activity than lower interference orders.

Since we used a thick plate and low interference orders, and did not determine interference angles, we employed our experimental data together with available data on optical constants<sup>11)</sup> to obtain transversal component  $G_{\perp}$  of the gyration pseudo-tensor of TeO<sub>2</sub>. The sign of this component turned out to be opposite with that of  $G_{\parallel}$ .

Both components are shown in Fig. 5. As far as  $G_{\parallel}$  is negative (left-hand rotation),<sup>11,12)</sup> positive sign (right-hand rotation) is appropriate for  $G_{\perp}$ . A relative mistake of 70% should be assigned to the obtained values of  $G_{\perp}$  because of

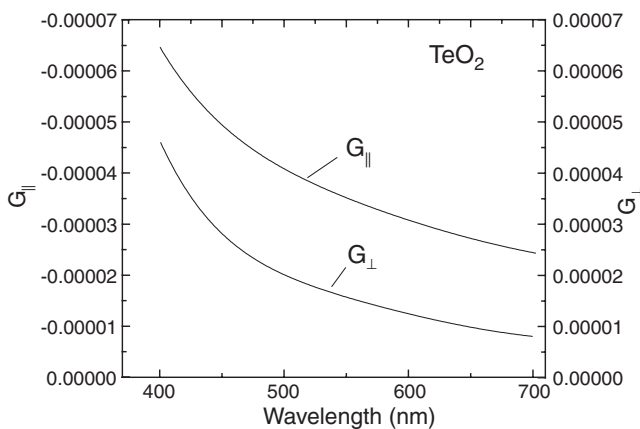


Fig. 5. Parallel component ( $G_{\parallel}$ ) of gyration pseudo-tensor, as restored from the previous data,<sup>11,12)</sup> and transversal component ( $G_{\perp}$ ) of this tensor, as firstly obtained in this work by using optic-axis light figures and the data on  $\gamma$  and  $\varepsilon$  restored from the work.<sup>11)</sup>

the insufficient accuracy of the experimental values<sup>11)</sup> of the optical anisotropy that influenced parameter  $\gamma$  and the final solution obtained according to the proposed algorithm (see Appendix).

### 5. Optical Activity and Relative Light-Figure Method

The relative optic-axis LF method is based on the following relation justified for small angles of interference<sup>1)</sup>

$$\frac{\lambda}{n} \frac{dn}{d\lambda} = -\frac{\lambda}{R_m} \frac{dR_m}{d\lambda} + \lambda \cot \theta_m(\lambda) \frac{d\theta_m(\lambda)}{d\lambda} \quad (26)$$

Note that in regions with normal dispersion (or below energy gap) the relative dispersion of the refraction index always assumes negative values. The first term in the right-hand part of eq. (26) can be negative or positive depending on whether optical anisotropy ( $\Delta n$ ) decreases or increases with increasing wavelength. The sign of the second term in the right-hand part of eq. (26) is always opposite with that of the first term.

In the presence of optical activity eq. (26) transforms into

$$\begin{aligned} \frac{\lambda}{n} \frac{dn}{d\lambda} \pm \frac{n^2 \rho G}{1 \mp n^2 \rho G} \left( \frac{\lambda}{n} \frac{dn}{d\lambda} + \frac{1}{2} \frac{\lambda}{\rho G} \frac{d\rho G}{d\lambda} \right) \\ = -\frac{\lambda}{R_{mG}} \frac{dR_{mG}}{d\lambda} + \lambda \cot \theta_{mG}(\lambda) \frac{d\theta_{mG}(\lambda)}{d\lambda} \end{aligned} \quad (27)$$

For TeO<sub>2</sub>, the lower sign must be selected. The first term in the right-hand part of relation (27) behaves as shown in Fig. 6. It assumes quite large negative values ( $\sim -2$ ) even at wavelengths distant from  $\lambda_m$  [see relation (21)] for which gyration-related correction to the refraction index  $n$  is maximal ( $\sim 10^{-4}$ ) and this term is already of the order of  $\sim -10$ . For comparison, thick plates [see condition (25)] of optically non-active materials typically display smaller values of this term, such as hardly above  $\sim -1$ .<sup>1,2)</sup> As seen from Fig. 6, this term is nearly constant in the regions far from  $\lambda_m$ . For these regions the gyration-related correction is already of the order of  $\sim 10^{-6}$ , as indicated by  $\varepsilon \rho_m G_m$  increasing downward on the right-hand scale of Fig. 6. Since  $\varepsilon \rho_m G_m = |G_{\parallel}|$  at  $\theta_{mG} = 0^\circ$ , we can figure out that we

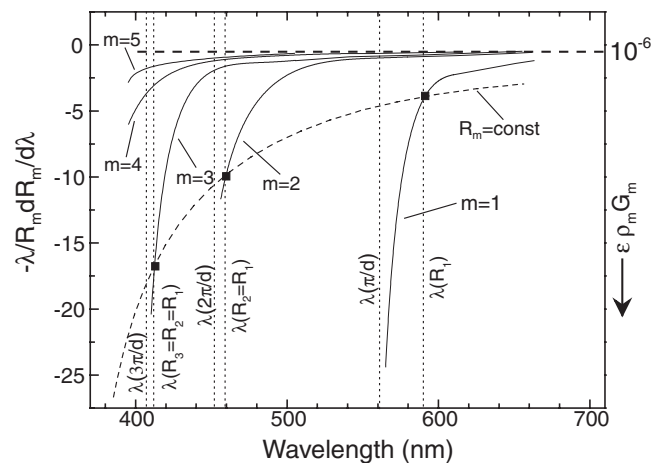


Fig. 6. Relative wavelength dispersion of the radiuses of interference curves of a thick plate of TeO<sub>2</sub>. Gyration-induced correction to the refraction index is shown on the right-hand scale. Dashed curve connects the points with equal radiuses on different interference curves.

reliably detect every gyration-induced variation from  $2 \times 10^{-5}$  down to  $\sim 10^{-6}$ . According to Fig. 6, and as expected, influence of optical activity on LFs increases with decreasing wavelength, as shown by dashed curve connecting the points with equal radiuses on different interference curves.

Simple estimations show that the absolute value of the relative dispersion of the refraction index of  $\text{TeO}_2$ , as well as most materials, is less than  $\sim 0.1$ . On the other hand, we have giant values of the relative dispersion of the radiuses of interference curves (Fig. 6). As calculations show, for  $\text{TeO}_2$  the second term in the right-hand part of eq. (27) behaves nearly in the same manner and has nearly the same (but positive) amplitude as the first term. Both terms together give very small total dispersion that equals the value given by the left-hand part of eq. (27). Separately, however, each term reflects very strong dependence of interference angles in eq. (8) upon gyration. This is in the heart of high sensitivity of both absolute and relative light-figure methods to the optical activity.

## 6. Conclusions

An analytical approach to LF of optically active materials with transversely isotropic linear dielectric function was developed and an algorithm for finding all material-related optical parameters from experiment was proposed. The recently introduced relative LF method was re-formulated with allowance for optical activity. The developed approach was successfully applied to  $\text{TeO}_2$ . The transversal component of gyration pseudo-tensor of  $\text{TeO}_2$  was determined for the first time. For  $\text{AgGaS}_2$ , a deviation of the shape of interference curves from circular might be expected at enough large angles of interference.

## Acknowledgement

One of the authors (N. M.) would like to cordially thank Prof. H. Horinaka and Professor Y. Kayanuma for the fruitful comments after reading the manuscript. Also, the same author is very grateful to Professor H. Naito, Professor Y. Nakayama, Professor K. Wakita, Professor K. Wada, and Professor T. Ishida for the constant interest and support. Thanks are also due to the reviewer for the suggestions that led to the improvement of the manuscript. The authors are thankful to Mr. N. Uneme for preparation of LaTeX version of the paper.

## Appendix: Determination of All Optical Parameters of a Uniaxial Optically-Active Material from Optic-Axis Light Figures

If interference angles or radiuses of interference curves are known for three interference orders, we can in principle determine three unknown parameters ( $\gamma, \varepsilon$  and  $G_\perp$  or  $G_0$ ;  $|G_\parallel|$  is not an additional unknown parameter since, using eq. (20), it can be expressed, through  $\varepsilon$  and  $\chi$  that can always be restored from the data for central part of LF) by solving numerically a set of eq. (8) for optically active case. However, in practice it is preferable to reduce the number of the used interference orders for the accuracy-related problems (see below). Here we are considering an additional equation that relates the radius of interference curve and the mean path ray refraction index. This equation can be used to reduce the number of the necessary interference orders down

to 2 provided that interference angle and radius of interference curve, both are known for any chosen wavelength.

Let us leave equation for radius of interference curve in the previous form<sup>2)</sup>

$$r_{mG} = \frac{d \sin \theta_{mG}}{\sqrt{n_{omG}^2 - \sin^2 \theta_{mG}}} + \frac{d \sin^3 \theta_{mG}}{2} \times \left| \frac{1}{\sqrt{n_{omG}^2 - \sin^2 \theta_{mG}}} - \frac{1}{\sqrt{n_{emG}^2 - \sin^2 \theta_{mG}}} \right| \quad (\text{A}\cdot 1)$$

and re-write auxiliary equations for mean path ray refraction index,  $n_{mG}$ , and mean path length,  $d_m$ , as one equation

$$n_{mG} = \frac{A_m}{2B_m} \quad (\text{A}\cdot 2)$$

$$A_m = \frac{n_{omG}^2}{\sqrt{n_{omG}^2 - \sin^2 \theta_{mG}}} + \frac{n_{emG}^2}{\sqrt{n_{emG}^2 - \sin^2 \theta_{mG}}} \quad (\text{A}\cdot 3)$$

$$B_m = \left\{ 1 + \frac{\sin^2 \theta_{mG}}{4} \left( \frac{1}{\sqrt{n_{omG}^2 - \sin^2 \theta_{mG}}} + \frac{1}{\sqrt{n_{emG}^2 - \sin^2 \theta_{mG}}} \right)^2 \right\} \quad (\text{A}\cdot 4)$$

For all  $\theta_{mG}$  less than  $\pi/4$ , the ratio between the second and first terms of relation (A·1) is very small

$$\sim \frac{0.25 \sin^4 \theta_{mG} (\sqrt{\varepsilon} - 0.5 \sin^2 \theta_{mG}) (2 + \gamma)}{\varepsilon - 0.5 \sqrt{\varepsilon} (2 + \gamma) \sin^2 \theta_{mG} + 0.25 (1 + \gamma) \sin^4 \theta_{mG}} \leq 10^{-3} \quad (\text{A}\cdot 5)$$

Therefore, for all practical purposes one can take only the first term into account.

If we use variable numerical aperture, the following parameters of LF will be known

$$a_m = \frac{r_{mG}}{Md}, \quad \sin \theta_{mG} = \beta_m, \quad n_{mG} = \frac{\beta_m}{\alpha_m} \sqrt{1 - a_m^2}, \quad \text{and} \quad \frac{m\lambda_m}{d} = \alpha_m \quad (\text{A}\cdot 6)$$

where  $M$  is a calibration constant determined according to the reported procedure.<sup>2)</sup>

After making transformations (10) and (11) in interference condition (8), and by combining (A·2) and (A·6), we have two independent equations for any interference order  $m$  to determine  $n_{omG}$  and  $n_{emG}$

$$\left| \sqrt{n_{emG}^2 - \beta_m^2} - \sqrt{n_{omG}^2 - \beta_m^2} \right| = \alpha_m \quad (\text{A}\cdot 7)$$

and

$$\frac{\beta_m}{\alpha_m} \sqrt{1 - a_m^2} = \frac{A_m}{2B_m} = f_m(n_{omG}, n_{emG}, \beta_m) \quad (\text{A}\cdot 8)$$

On the other hand, we can obtain expressions for  $G_\perp$  or  $G_0$  in analytical form by using eqs. (3), (6) and (7) and

remembering that according to eqs. (1) and (2)

$$\varepsilon \rho_{om} G_{om} = \mp \frac{\varepsilon - n_{omG}^2}{n_{omG}^2} \quad (\text{A}\cdot 9)$$

and

$$\varepsilon \rho_{em} G_{em} = \pm \frac{\varepsilon(1 - \gamma \beta_m^2) - n_{emG}^2}{n_{emG}^2} \quad (\text{A}\cdot 10)$$

After exclusion of  $G_{\perp}$  or  $G_0$ , we can finally get an equation that relates only two unknown parameters,  $\gamma$  and  $\varepsilon$ , for any order of interference. Note that the just-described algorithm requires data only for two interference orders to obtain  $\gamma$  and  $\varepsilon$ . After  $\gamma$  and  $\varepsilon$  are obtained  $G_{\perp}$  or  $G_0$  are found from eq. (3). In some cases this algorithm can be simplified by replacing both  $\rho_{om} G_{om}$  and  $\rho_{em} G_{em}$  with  $\rho_m G_m$ , which is taken for the direction of the mean path ray with refraction index,  $n_{mG}$ .

To understand the consequences of such replacement, let us analyze the relationship between  $n_{omG}$  and  $n_{emG}$  before and after replacement is done. Respectively, we have

$$\frac{n_{omG}^2}{n_{emG}^2} = \frac{1}{1 \mp \gamma \sin^2 \theta_{mG}} \frac{1 \pm \varepsilon \rho_{em} G_{em}}{1 \mp \varepsilon \rho_{om} G_{om}} \quad (\text{A}\cdot 11)$$

and

$$\frac{n_{omG}^2}{n_{emG}^2} = \frac{1}{n_m^2 \mp \gamma \sin^2 \theta_{mG}} \times \frac{n_m^2 \pm \varepsilon \rho_m G_m (n_m^2 \mp \sin^2 \theta_{mG})}{1 \mp \varepsilon \rho_m G_m} \quad (\text{A}\cdot 12)$$

Both (A-11) and (A-12) follow from eqs. (1) and (2). In particular, (A-12) was obtained by considering that refraction indices of the waves propagating along the same direction  $m$  (direction of the mean path ray) in an optically active material should obey the following relationships

$$n_{omG}^{-2} = n_{om}^{-2} \mp \rho_m G_m \quad n_{emG}^{-2} = n_{em}^{-2} \pm \rho_m G_m \quad (\text{A}\cdot 13)$$

The difference between (A-11) and (A-12) approximately equals  $\sim \gamma \sin^2 \theta_{mG}$  which should be less than desirable accuracy (or  $\varepsilon \rho_m G_m$ ) in order to apply this approach. As estimations show, the last condition is fulfilled for TeO<sub>2</sub> only at  $\theta_{mG} < 1^\circ$  and application of this approximation is not justified for most incident angles at which experimental data were obtained.

Obviously enough, the above described procedure could be also applied to optically non-active case and only one interference order would be necessary to determine  $\gamma$  and  $\varepsilon$ .

If interference angles are unknown like in our case, the information we obtain from LFs is restricted to the radiuses ( $a_m$ ) of the interference curves. In such case, determination of all optical parameters requires, in principle, three interference orders. But, as we found after the examination of our experimental data (see Fig. 3), the accuracy of determination of  $G_{\perp}$  may become insufficient in this case. At least for TeO<sub>2</sub> and rather small interference angles ( $\theta_{mG} < 7^\circ$ ) we could not get a reliable value of  $G_{\perp}$  by using simultaneously three interference orders for the same wavelength. Therefore we could not determine transversal component unless we used the data for  $\gamma$  and  $\varepsilon$ . In our case  $\gamma$  and  $\varepsilon$  were restored from the data on optical constants in the work.<sup>11)</sup> Generally, however, we could obtain  $\gamma$  and  $\varepsilon$  from LF of optically active material by solving the problem

for optically non-active case and optimizing the obtained values afterwards. Indeed, as follows from eqs. (16) and (18), the influence of optical activity will be negligible for some angles of interference. In optically non-active case, we need, in principal, to know only the radiuses of interference curves (or interference angles) for two orders of interference to obtain  $\gamma$  and  $\varepsilon$ . After getting  $\gamma$  and  $\varepsilon$  we can determine gyration constants, using the interference condition (A-7) in the form

$$\alpha_m = \left| \sqrt{\frac{\varepsilon(1 \mp \gamma \sin^2 \theta_{mG})}{1 \pm \varepsilon \rho_{em} G_{em}} - \sin^2 \theta_{mG}} - \sqrt{\frac{\varepsilon}{1 \mp \varepsilon \rho_{om} G_{om}} - \sin^2 \theta_{mG}} \right| \quad (\text{A}\cdot 14)$$

where

$$\varepsilon \rho_{om} G_{om} = \frac{1}{2} \left\{ \left[ \gamma^2 \sin^4 \theta_{mG} + 4(\varepsilon |G_{\parallel}| \pm |G_{\perp} - G_{\parallel}| \sin^2 \theta_{mG})^2 \right]^{\frac{1}{2}} - \gamma \sin^2 \theta_{mG} \right\} \quad (\text{A}\cdot 15)$$

and

$$\varepsilon \rho_{em} G_{em} = \frac{1}{2(1 \mp \gamma \sin^2 \theta_{mG})} \left( \left\{ \gamma^2 \sin^4 \theta_{mG} + 4[\varepsilon |G_{\parallel}| + (\gamma - \pm |G_{\perp} - G_{\parallel}|) \sin^2 \theta_{mG}]^2 \right\}^{\frac{1}{2}} - \gamma \sin^2 \theta_{mG} \right) \quad (\text{A}\cdot 16)$$

On the other hand, it follows from (A-1) and (A-6) that

$$n_m = \sqrt{\frac{1 + a_m^2}{a_m^2}} \sin \theta_{mG} \quad (\text{A}\cdot 17)$$

Equation (A-2) with left-hand part given by (A-17) and right-hand part given by (A-3), and (A-4) with refraction indices

$$n_{omG} = \sqrt{\frac{\varepsilon}{1 \pm \varepsilon \rho_{om} G_{om}}}, \quad n_{emG} = \sqrt{\frac{\varepsilon(1 \mp \gamma \sin^2 \theta_{mG})}{1 \pm \varepsilon \rho_{em} G_{em}}} \quad (\text{A}\cdot 18)$$

where  $\varepsilon \rho_{om} G_{om}$  and  $\varepsilon \rho_{em} G_{em}$  are given respectively by eqs. (A-15) and (A-16), and eq. (A-14) are two equations from which interference angle and transversal component of gyration are determined by using only one interference order. In practice, however, we have to analyze a number of interference orders to find the one(s) that provides best conditions for determination of the transversal component.

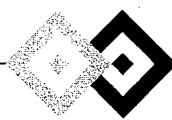
Following the just-described procedure, we performed calculations for all interference curves in Fig. 3. We first determined the angle of interference by living in eqs. (A-15) and (A-16) only the known parallel component of gyration and then included both components ( $|G_{\parallel}|$  and  $|G_{\perp} - G_{\parallel}|$ ) to see how much was the difference between the interference angles. This difference was maximal ( $\sim 0.3^\circ$ ) only at some angles from  $2^\circ$  to  $5^\circ$  depending on the wavelength. And, these angles were found to be very close to the angles for which

$$\sin \theta_{mG} \sim \sqrt{2 \frac{|G_{\parallel}|}{\gamma}} \quad (\text{A}\cdot 19)$$

The  $G_{\perp}$  was determined exactly within a range of these angles of interference. Below and above this range determination of  $G_{\perp}$  was exceedingly difficult because the influence of  $|G_{\perp} - G_{\parallel}|$  was down to a negligible value of  $\sim 0.01^{\circ}$ . For this reason, we used only some section of any interference curve in Fig. 3 to obtain  $G_{\perp}$ . Therefore,  $G_{\perp}$ -curve in Fig. 5 is a resultant curve composed from experimental results for different interference orders.

- 1) N. Mamedov, N. Yamamoto and A. Kunie: Jpn. J. Appl. Phys. **40** (2001) 4938.
- 2) Y. Shim, N. Mamedov and N. Yamamoto: J. Appl. Phys. **91** (2002) 4110.

- 3) N. Yamamoto, N. Mamedov, T. Shinohara and A. Kunie: J. Cryst. Growth **237–239** (2002) 2023.
- 4) N. Mamedov, Y. Shim and N. Yamamoto: Jpn. J. Appl. Phys. **41** (2002) 7254.
- 5) M. Born and E. Wolf: *Principles of Optics* (Pergamon, London, 1970).
- 6) E. E. Wahlstrom: *Optical Crystallography* (Wiley, New York, 1979).
- 7) V. M. Agranovich and V. L. Ginzburg: *Crystal Optics with Spatial Dispersion and Excitons* (Springer, Tokyo, 1984).
- 8) H. Horinaka, K. Tomii, H. Sonomura and T. Miyachi: Jpn. J. Appl. Phys. **24** (1985) 755.
- 9) M. Susaki, N. Yamamoto, H. Horinaka, W. Z. Huang and Y. Cho: Jpn. J. Appl. Phys. **33** (1994) 1561.
- 10) N. Yamamoto, N. Mamedov, Y. Shim, C. Hidaka, T. Takizawa, E. Niwa and K. Masumoto: submitted to Proc. of 13th International Conference on Ternary and Multinary Compounds, Paris, 2002.
- 11) N. Uchida: Phys. Rev. B **4** (1971) 3736.
- 12) T. Takizawa: J. Phys. Soc. Jpn. **50** (1981) 3054.

IIa-III<sub>2</sub>-VI<sub>4</sub>系化合物の単結晶成長

滝沢 武男・日高 千晴

青色発光用蛍光体として有望なIIa-III<sub>2</sub>-VI<sub>4</sub>系化合物の熔融法によるバルク単結晶作製について、アルカリ土類チオガレートを中心として紹介する。この系の化合物は、融点が高いとともに化学反応性が大きく、従来、熔融法による単結晶作製が困難とされていた。筆者らは、示差熱分析と粉末X線解析により、IIa-VIとIII<sub>2</sub>-VI<sub>3</sub>系化合物との擬二元相図を作成し、これをもとに単結晶作製を試みた。さらに、紫外光励起発光特性を測定するために、これらの化合物にCeをドーブした単結晶の作製も行ったのであわせて報告する。

Keywords : single crystal growth, melt growth, thiogallates, CaGa<sub>2</sub>S<sub>4</sub>, SrGa<sub>2</sub>S<sub>4</sub>, SrGa<sub>2</sub>Se<sub>4</sub>

## 1. ま え が き

ダイヤモンド型構造から派生した結晶構造をもつ化合物は、原子周期率表のIV族の両側に位置する元素の組み合わせで合成でき、二元(III-Vあるいは、II-VI)系では、せん垂鉛鉱型構造、三元(II-IV-V<sub>2</sub>あるいは、I-III-VI<sub>2</sub>)系では、カルコパイライト型構造をもつものがよく知られている。これらの化合物は、電気・光学的にIV族半導体と異なる多様な特性を示し、応用的にもまた結晶学的にも興味ある対象として、古くから研究されてきた<sup>1)</sup>。

3種の異なる元素から成る化合物は、上述以外にも元素の組み合わせにより、多数存在する。この中で、IIb-III<sub>2</sub>-VI<sub>4</sub>系の化合物は、ダイヤモンド型構造をとると必然的に欠陥サイトを生ずる。この欠陥サイトは、結晶に構造的不安定性を与え、この結果、これらの化合物の結晶構造は、元素の置換により構造相転移を起こすとか、多形を生ずるなどの多様性を有する<sup>2,3)</sup>。

これに対し、上述の化合物の構成元素であるIIb族元素をIIa族元素に置換すると結晶構造のまったく異なる物質が出現する。IIa族元素は、IIb族元素に比してイオン性が強いので、この化合物はもはやダイヤモンド型構造をとらず、複雑な斜方晶となる<sup>4-6)</sup>。これに伴い電子帯構造の禁制帯幅(バンドギャップ)も増加し(4~5 eV)、これらの化合物は絶縁体(誘電体)に近い性質を示すようになる。

このIIa-III<sub>2</sub>-VI<sub>4</sub>系化合物は古くから知られており、特にアルカリ土類チオガレート(アルカリ土類硫化ガリウム化合物)は、希土類元素をドーブするとその種類に応じて赤色から青色までの蛍光を発するため、多くの研究者の興味を引いてきた<sup>4,6)</sup>。しかし、これらの化合物は構成元素間の化学活性が大きく、また高融点であるため、合成ならび

に結晶成長が困難であった。したがって、従来は専ら固相反応により作製された多結晶を用いて、地道な研究が行われてきた。表1にこれまでに求められている(Ca, Sr, Ba)(Ga, In)<sub>2</sub>(S, Se)<sub>4</sub>化合物の結晶構造などのデータを示す。

最近になって、多源蒸着法やMBE(Molecular Beam Epitaxy)法などで、これらの物質の高品質薄膜を比較的低温度で作製する技術が開発された<sup>7-10)</sup>。同時に、表示素子(テレビ、コンピューター端末、携帯電話など)や光伝送機器(レーザー装置、光ケーブルなど)への需要が増加した。そして特に、純粋色を得るのが困難であった青色発光材料への期待が高まり、IIa-III<sub>2</sub>-VI<sub>4</sub>系の化合物が青色電場発光母体材料として注目を浴びるようになった<sup>7-11)</sup>。ちなみに、現在使用されている半導体系の電場発光材料を表2に示す。

この表から青色電場発光に関して、IIa-III<sub>2</sub>-VI<sub>4</sub>系化合物

表1 IIa-III<sub>2</sub>-VI<sub>4</sub>系化合物の結晶構造と融点<sup>4-6)</sup>

CaGa <sub>2</sub> S <sub>4</sub>	斜方晶	20.11	20.08	12.13	1132*	黄色
CaGa <sub>2</sub> Se <sub>4</sub>	斜方晶	21.06	20.10	12.66		
CaIn <sub>2</sub> S <sub>4</sub>	斜方晶	—	—	—	(986)*	
CaIn <sub>2</sub> Se <sub>4</sub>	斜方晶	—	—	—		
SrGa <sub>2</sub> S <sub>4</sub>	斜方晶	20.84	20.50	12.21	1230*	無色透明
SrGa <sub>2</sub> Se <sub>4</sub>	斜方晶	21.73	21.42	12.77	1117*	無色透明
SrIn <sub>2</sub> S <sub>4</sub>	斜方晶	20.90	21.13	13.02	1070*	
SrIn <sub>2</sub> Se <sub>4</sub>	斜方晶	21.86	21.95	13.49	(1016)*	
BaGa <sub>2</sub> S <sub>4</sub>	立方晶	12.61	—	—	—	
BaIn <sub>2</sub> S <sub>4</sub>	斜方晶	21.68	21.77	13.11	(1066)*	
BaAl <sub>2</sub> S <sub>4</sub>	立方晶	12.59	—	—	>1250*	

\* 融点は、筆者らが求めた値である。なお、( )は推定値である。

物が、II-VI系化合物に比して、かなり優位な位置を占めていることがわかる。

表示素子への応用においては、薄膜材料が有望視されているが、バルク材料もレーザー母体材料などとして期待されている<sup>12)</sup>。特に単結晶は、応用面のみでなく、これらの物質の基礎物性を研究するうえで欠くことのできない物でもある。

上記化合物のバルク結晶は固相反応法によるほか<sup>4)</sup>、化学気相成長法 (Chemical Vapor Deposition, 以下, CVD と称す) により作製されてきた<sup>13)</sup>。しかし、熔融法による結晶作製はこれらの物質が高融点、高化学反応性をもつゆえに困難であり、筆者らが知る限り、この方法による単結晶作製の報告は存在しない。

本稿では、筆者らが行ってきたIIa-III<sub>2</sub>-VI<sub>4</sub>系化合物の単結晶作製について、チオガレート系の化合物を中心として紹介する<sup>14,15)</sup>。

## 2. IIa-III<sub>2</sub>-VI<sub>4</sub>系化合物の化学反応と相図

一般に硫化物は、石英管などに真空封入して合成すると硫黄の高い蒸気圧のため、しばしば封入管の爆発を引き起こす。これを防ぐためには、あらかじめ化合物を構成する元素間の化学反応を調べておかねばならない。筆者らは、この調査を示差熱分析 (Differential Thermal Analysis, 以下, DTA と称す) により行った。

図1はCa, Sr, Ga, InとSおよびSe間の化学反応のDTA信号である。DTA信号は昇温と降温の両過程で現れる。図1には、わかりやすくするため昇温過程の信号のみ載せてある。この図において正負のピークは、それぞれ発熱および吸熱反応に対応する。

通常、昇温時における発熱反応は元素間の化学反応を示し、吸熱反応は合成物の一次相転移点を示す。元素間の化学反応の起こる温度は元素の形状、混合状態などにより変化し一定しないが、およそ100°C程度の温度幅をもって予想できる。これに対し相転移点の温度は、混合した元素の成分比が一定ならば、約1°C以内の精度で決定される。

図1より、Ca, SrとS, Seとの化学反応が約350°C, GaとSとのそれが約950°C, また、InとSとでは約650°C, InとSeとでは約250°Cで起こっていることがわかる。同図をみ

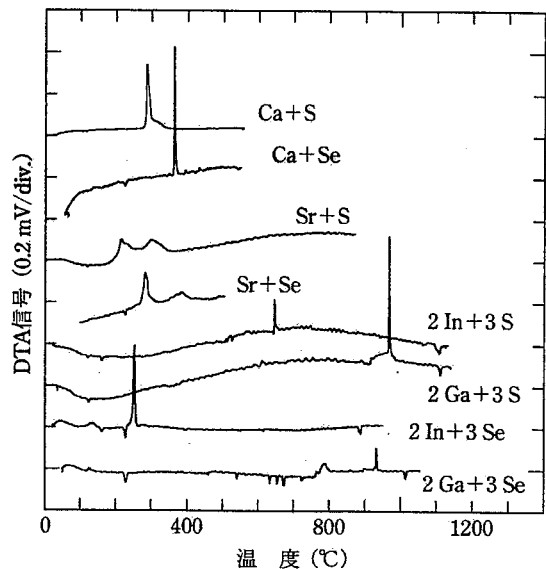


図1 (Ca, Sr, Ga, In)と(S, Se)との化学反応の示差熱信号。(Ca, Sr)は、300~400°Cで激しい化学反応を伴い硫化、あるいはセレン化される。Gaの硫化は約950°C, セレン化は800°C付近で起こる。Inの硫化は約650°C, セレン化は約250°Cで起こる。

ると、これらの反応はいずれも短時間内に起こり、急激な発熱を伴っている。

実際、これらの反応により封入石英管が破裂することが多い。400°C以下での封入石英管の破損は、元素の蒸気圧によるものではなく、急激な発熱による大きな熱こう配のためである。したがって、化合物の合成の際には、これらの化学反応を制御し、ゆっくり進行させなければならない。この具体的な方法は後述する。

DTAは、このような化学反応を調べるほか、相図の作成に有用である。IIa-III<sub>2</sub>-VI<sub>4</sub>系化合物の単結晶を熔融法で作製する際に必要なもう一つの情報は、IIa-VIとIII<sub>2</sub>-VI<sub>3</sub>系化合物との擬二元系相図から得られる。この相図は、IIa-VIとIII<sub>2</sub>-VI<sub>3</sub>系化合物をそれぞれ一つの元素と見なし、両者を適当な比で混合した混合物のDTAを測定し、相転移点の温度を混合比の関数としてプロットすることにより得られる。この際、DTAは2回測定する。1回目は化合物の合成過程における発熱反応を観測し、2回目で合成物の相転移点を観測する。また、DTA後の合成物の粉末X線解析により、合成物の組成を決定する。このようにして得たSrGa<sub>2</sub>S<sub>4</sub>の擬二元相図を図2に示す。

ここで、図の横軸はIII<sub>2</sub>-VI<sub>3</sub>系化合物の含有量である。この量が50%のところでは融解曲線が上に凸になっており、この点でこの化合物が調和融解することを示している。表1にあげた研究対象物質の中で、現在までに相図の得られた物質は、CaGa<sub>2</sub>S<sub>4</sub>, SrGa<sub>2</sub>S<sub>4</sub>, SrGa<sub>2</sub>Se<sub>4</sub>の3物質である。いずれの相図も図2とほぼ類似の形状である。そのほかの化合物については測定中であるが、現時点でのデータから判断すると、調和融解するものはいずれも図2と類似の傾向を示している。

ここで、IIa-III<sub>2</sub>-VI<sub>4</sub>系化合物を添え字の数字で124系

表2 半導体系電場発光素子の発光特性。

化合物	ドープ元素	発光特性			色
		波長 (nm)	量子効率 (%)	寿命 (ns)	
ZnS <sup>9)</sup>	Tb	2100	0.32	0.60	緑
SrS <sup>9)</sup>	Ce	220	0.10	0.26	青緑
CaGa <sub>2</sub> S <sub>4</sub> <sup>7)</sup>	Ce	10*	0.14	0.19	青
SrGa <sub>2</sub> S <sub>4</sub> <sup>16)</sup>	Ce	85	0.14	0.12	青
BaAl <sub>2</sub> S <sub>4</sub> <sup>11)</sup>	Eu	800*	0.12	0.11	青

\* 文献値として公表されていないが、現在はさらに大きな値になっている。

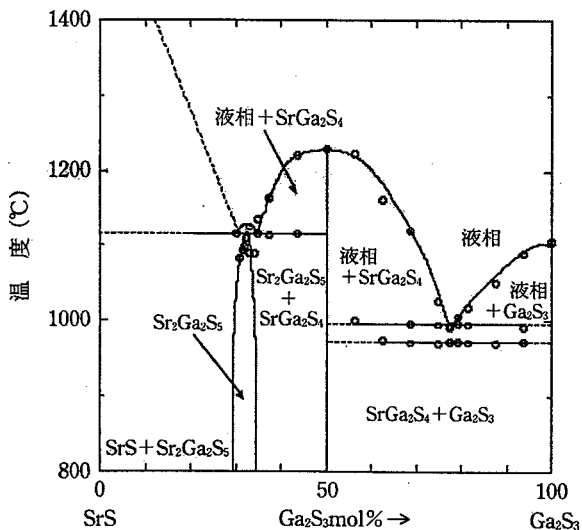


図2 SrSとGa<sub>2</sub>S<sub>3</sub>との擬二元相図。横軸にとつたGa<sub>2</sub>S<sub>3</sub>の濃度が50%の位置が、SrGa<sub>2</sub>S<sub>4</sub>化合物。同33.3%の位置がSr<sub>2</sub>Ga<sub>2</sub>S<sub>5</sub>化合物。SrGa<sub>2</sub>S<sub>4</sub>化合物が調和融解するのに対し、Sr<sub>2</sub>Ga<sub>2</sub>S<sub>5</sub>化合物は包晶型である。

と短縮して呼ぶことにする。相図より、調和融解する124系化合物は、いずれも溶融法で単結晶作製が行えると判断できる。残る問題は、封入容器の材質の選択と爆発的化学反应の回避である。

### 3. 単結晶作製

前章で述べたように、124系化合物の単結晶作製ではIIa-VIとIII-VI元素間の化学反応をゆっくり行わせ、まず、124系多結晶化合物を合成するのがよい。筆者らは、この合成物を前駆体と呼んでいる。

図3にCaGa<sub>2</sub>S<sub>4</sub>を例にとり、この前駆体を作製する手順を示す。まず、室温、大気中で安定なGa<sub>2</sub>S<sub>3</sub>を作製する。図3上部に示すように、Ga<sub>2</sub>S<sub>3</sub>の化学量論比に秤量したGaとSを石英管中に離して置き真空封入する。2温度帯をもつ電気炉中でGa側を980°C、S側を400°Cにして約1日保持すると、SはほとんどGaに吸収されGa<sub>2</sub>S<sub>3</sub>が作製される。この方法により950°C付近で生ずるGa<sub>2</sub>S<sub>3</sub>の爆発的反應を回避できる。ただし、この方法が有効なのは生成物（この場合、Ga<sub>2</sub>S<sub>3</sub>）の蒸気圧が低いときのみである。

次に、124系化合物の化学量論比に秤量したGa<sub>2</sub>S<sub>3</sub>とCaを石英のポートに入れ、このポートを長めの石英管の一端に、残りのSを他端において真空封入する。そして、石英ポート側を450°C、S側を300°Cにして約1日保持するとCaとSの激しい反応を避けてCaSが合成される。

引き続き、S側（このときSは、ほとんど存在しない）をSの沸点よりやや高い500°Cに保ったまま石英ポート側をGa<sub>2</sub>S<sub>3</sub>の融点より高く、124系化合物の融点よりやや低い温度（この場合、1120°C）まで上昇させ、約1時間保持した後、冷却（炉冷）すると白色の前駆体が合成される。最高温度を124系化合物の融点以上にする化合物と石英ポートとの融着が起り、良質の前駆体が得られない。単

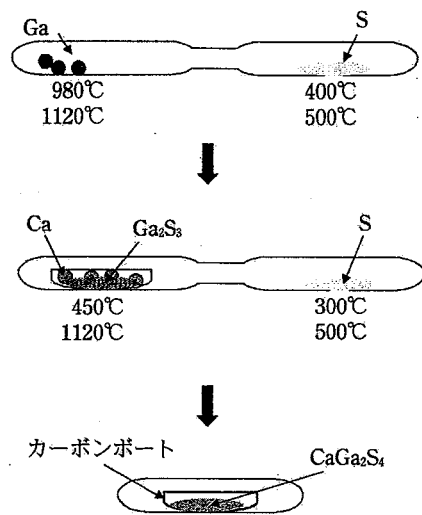


図3 上段はGa<sub>2</sub>S<sub>3</sub>の作製法。まずGa側を980°Cに、S側を400°Cに保持し、SをGaに吸収させる。Sがすべて吸収されてからGa側をGa<sub>2</sub>S<sub>3</sub>の融点以上に上げ、Ga<sub>2</sub>S<sub>3</sub>を合成する。次に（中段）、CaとGa<sub>2</sub>S<sub>3</sub>を混ぜ石英ポートに入れ450°Cに、S側を300°Cに保ち、CaSをゆっくり合成する。Sがすべてポート側に吸収されたら、ポート側をGa<sub>2</sub>S<sub>3</sub>の融点以上に上げ、CaGa<sub>2</sub>S<sub>4</sub>を合成する。最後に（下段）、これをカーボンポートに入れ、温度こう配を移動させて単結晶を成長させる。

結晶育成のためには、合成された前駆体が、少なくともX線の異相を含まない124系化合物になっている必要がある。IIa-VI系化合物には、融点の高いものが多い、この組成の化合物が残留すると単相の結晶が得られないことが多いからである。すなわち、溶融法による単結晶作製で最も重要なのがこの前駆体作製である。

ただし、上述の方法が124系化合物全般に有効であるわけではない。有効な場合は、チオガレートに限られるようである。実際、セレン化物ではSeの蒸気圧がSのそれに比して低いため、Srのセレン化はSeの温度を650°C程度まで上げて行わねばならない。ところが、Srが融点（769°C）以下で蒸発（昇華）するため、Sr側の温度を600°C程度に抑えねばならない。したがって、この場合は両元素を分離して置かず、Srをポート型の内管に入れ、Seをこのポートを隔てて外側に置き、双方を600°C程度に保持（24~48時間）してセレン化する。

また、インジウム化合物の場合は、DTA測定で融点が測定できないものが多い、表1に示すように、筆者らの研究で融点が決められた化合物は、SrIn<sub>2</sub>S<sub>4</sub>のみである。現在、これらの化合物の相図を作成中であるが、融点の出にくい化合物は、包晶などの非調和融解型化合物である可能性が高い。単結晶作製には、各化合物ごとに独自の工夫が必要である。

単結晶作製は、この前駆体をカーボン製のポートに入れ、これを石英管に真空封入し、横型の電気炉で0.25~0.5 cm/hで温度こう配を移動させて行った。得られた単結晶の写真を図4(a)~(d)に示す。それぞれ、CaGa<sub>2</sub>S<sub>4</sub>、SrGa<sub>2</sub>S<sub>4</sub>、SrGa<sub>2</sub>Se<sub>4</sub>、Sr<sub>2</sub>Ga<sub>2</sub>S<sub>5</sub>である。

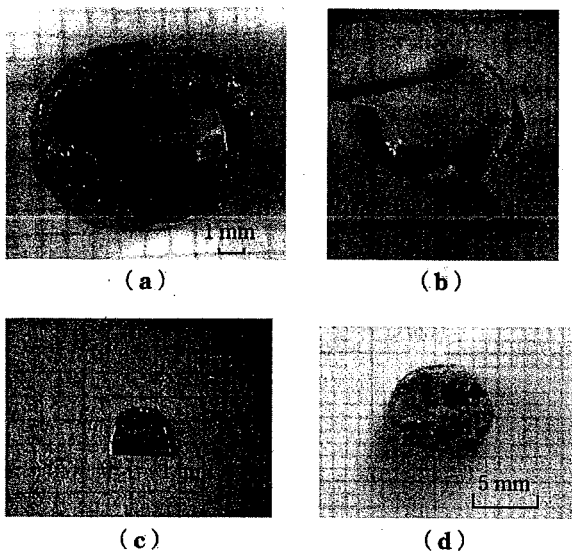


図4 作製した単結晶の写真。(a)CaGa<sub>2</sub>S<sub>4</sub>, (b)SrGa<sub>2</sub>S<sub>4</sub>, (c)CaGa<sub>2</sub>Se<sub>4</sub>, (d)Sr<sub>2</sub>Ga<sub>2</sub>S<sub>5</sub>. (a)~(c)は単結晶, (d)は多結晶。(a), (b)の面は自然へき開面, (c), (d)の面は切断後研磨した面。

図4の(a)~(c)には, まだボイドやクラックが存在するが, 光学測定可能なサイズを有する透明な単結晶が得られている。同図(d)は, 図2の擬二元相図のGa<sub>2</sub>S<sub>3</sub>の濃度が33.3%の位置に相当する化合物である。薄膜EL素子材として有用とのことで結晶作製を試みた。この化合物は包晶型であるので, 包晶点を通る際の降温速度を2°C/hと遅くして成長させた。しかし写真でわかるとおり, 小さい単結晶の集合体にしかならなかった。

#### 4. 希土類ドーブ

青色電場発光(EL)特性の評価のために, CaおよびSrチオガレートに希土類元素のCeを添加した結果を記す。Ceは, いずれの場合もCe<sub>2</sub>S<sub>3</sub>化合物を前駆体に所定量混合し添加した。添加量は, 薄膜の場合, 文献によると10%以上可能とのことであるが, バルク結晶の場合約1.5%が限度であり, これ以上添加すると結晶が黒化しEL素子に使用できない。また, 紫外光励起発光(PL)は, Ce濃度0.8%まで濃度に比例して増大するが, これ以上では飽和し, 減少に転ずる<sup>15)</sup>。

薄膜に比して添加量の限界が極端に低い理由は, 結晶の成長過程が薄膜とバルクの場合で大きく異なることにあると思われる。すなわち薄膜の場合, バルクに比して低温成長であり異分子を排除するエネルギーに乏しいため, 多くの不純物を内部に取り込むことが可能なのであろう。

#### 5. む す び

最近の青色発光のブームに乗って, 非常に地味なバルク単結晶成長に関する研究を本誌に取り上げていただけたこととなった。バルク結晶は, 薄膜に比べると研究効率が悪く, また, 経済効果の点においても劣る研究対象であるが,

大きな単結晶のもつ魅力と未知の物質を合成する喜びに支えられて研究を続けている。元素の数は有限とはいえ, 3以上の元素から成る化合物は非常に多く存在し, まだ研究がし尽くされたとはいえない。今後, 多くの若い研究者が物質探査・合成の研究にも参加されることを期待する。最後に, 本報告を作製するにあたって協力してくれた院生, 学生に謝意を表す。

#### 文 献

- 1) Landolt-Börnstein Numerical Data and Functional Relationship in Science and Technology, New Series, ed. W. Martienssen, Group III/17, Semiconductors Subvolume h: Physics of Ternary Compounds (Springer-Verlag, Germany, 1996).
- 2) H. Haeuseler and S. K. Srivastava: Z. Kristallogr. **215**, 205 (2000).
- 3) K. Asaka, C. Komatsu-Hidaka, T. Takizawa and H. Matsu-shita: Jpn. J. Appl. Phys. **39**, 139 (2000).
- 4) T. E. Peter and J. A. Baglio: J. Electrochem. Soc. **119**, 230 (1972).
- 5) B. Eisenmann, M. Jakowski, W. Klee and H. Schäfer: Rev. Chim. Miner. **20**, 225 (1983).
- 6) P. C. Donohue and J. E. Hanlon: J. Electrochem. Soc. **121**, 137 (1974).
- 7) W. A. Barrow, R. C. Coovert, E. Dickey, C. N. King, C. Laakso, S. S. Sun, R. T. Tuenge, R. Wetross and J. Kane: *SID Int. Symp. Dig., Seattle, 1993*, p. 761.
- 8) S. S. Sun, R. T. Tuenge, J. Kane and M. Ling: J. Electrochem. Soc. **141**, 2877 (1994).
- 9) Y. Inoue, K. Kobayashi, K. Tanaka, S. Okamoto, Y. Tsuchiya and K. Takizawa: IEEE Trans. Broadcast. **42**, 259 (1996).
- 10) Y. Nakanishi, N. Uekura, F. Nakano and Y. Hatanaka: J. Lumin. **72**, 373 (1997).
- 11) N. Miura, M. Kawanishi, H. Matsumoto and R. Nakano: Jpn. J. Appl. Phys. **38**, L1291 (1999).
- 12) S. Iida, T. Matsumoto, N. T. Mamedov, Y. Maruyama, A. I. Bairamov, B. G. Tagiev, O. B. Tagiev and R. B. Dzhabbarov: Jpn. J. Appl. Phys. **36**, 857 (1997).
- 13) K. Tanaka, T. Ohgoh, K. Kimura, H. Yamamoto, K. Shinagawa and K. Sato: Jpn. J. Appl. Phys. **34**, L1651 (1995).
- 14) C. Komatsu-Hidaka and T. Takizawa: J. Cryst. Growth **222**, 574 (2001).
- 15) C. Hidaka and T. Takizawa: J. Cryst. Growth 印刷中.
- 16) K. Tanaka, S. Okamoto, Y. Inoue and K. Kobayashi: Jpn. J. Appl. Phys. **38**, L1419 (1999).

(2002年1月7日 受理)



たきざわ たけお  
滝沢 武男

1972年東京大学大学院博士課程(物理学)修了。日本大学講師, 助教授を経て現教授。物性物理学(実験)。化合物半導体の光物性, 酸化物超伝導体中の量子磁束の動力学。



ひだか ちはる  
日高 千晴

1997年日本大学大学院修士課程(量子理工学)修了。2002年1月工学博士を大阪府立大学より取得。日本大学副手を経て研究員。物性物理学(実験)。II-III<sub>2</sub>-VI<sub>4</sub>系半導体の作製と光物性。



ELSEVIER

Physica C 378–381 (2002) 513–516

PHYSICA C

www.elsevier.com/locate/physc

# Flux creep properties in Dy–Ba–Cu–O bulk superconductors

H. Enomoto<sup>a,b,\*</sup>, K. Inoue<sup>b</sup>, S. Nariki<sup>b</sup>, M. Murakami<sup>b</sup>, T. Takizawa<sup>a</sup><sup>a</sup> Graduate School of Integrated Basic Science, Nihon University, 3-25-40 Sakura-Josui, Setagaya-ku, Tokyo 156-8550, Japan<sup>b</sup> Superconductivity Research Laboratory, ISTEC, 1-16-25 Shibaura, Minato-ku, Tokyo 105-0023, Japan

Received 27 September 2001; accepted 7 January 2002

## Abstract

We have investigated how the oxygen-annealing temperature and RE211 addition influence the flux creep at 77 K in melt-processed DyBa<sub>2</sub>Cu<sub>3</sub>O<sub>7-δ</sub> (Dy123). By making conventional flux creep experiments, we found that Dy211 contents suppress the flux creep. It was also found that the flux creep is more suppressed by the annealing treatment in the lower temperature. A suppression in the flux creep was observed for samples with the secondary peak effect.

© 2002 Published by Elsevier Science B.V.

PACS: 74.60.Ge; 74.60.Jg

Keywords: Magnetic relaxation; Secondary peak; Flux creep; DyBa<sub>2</sub>Cu<sub>3</sub>O<sub>7-δ</sub>

## 1. Introduction

In the field of power applications it is necessary to fabricate superconducting materials with high critical current densities  $J_c$ . An enhancement of  $J_c$  value is in general achieved by increasing the number of effective pinning centers in superconductors. The melt-processed REBa<sub>2</sub>Cu<sub>3</sub>O<sub>y</sub> (RE: Nd, Sm, Eu and Gd) exhibits the secondary peak effect on the magnetization hysteresis curve, which is ascribed to RE rich RE123 clusters with depressed  $T_c$  in the matrix [1].  $J_c$  values are largely enhanced by the secondary peak effect. Recently, Nariki and Murakami [2] has reported that the

superconducting properties of the DyBa<sub>2</sub>Cu<sub>3</sub>O<sub>7-δ</sub> (Dy123) bulk samples were strongly affected by the Dy211 contents and the oxygen-annealing temperature. Although there is no Dy–Ba solid solution and thus no Dy rich clusters, Dy123 exhibits relatively large secondary peak effect, which is ascribed to the presence of oxygen deficient clusters. It is well known that the amount of oxygen vacancies in RE123 phase increases with increasing oxygenation temperature. A large variation in the superconducting properties of the present Dy123 with the oxygen-annealing temperature is thus caused by the variation in the size and distribution of oxygen deficient regions. Oxygen deficient clusters with depressed  $T_c$  act as the field-induced pinning centers, which is the source of the peak effect [3]. In the Dy123/Dy211 composite system containing the low- $T_c$  phase and Dy211 phase, the flux creep behavior is expected to be different from that of a single phase system.

\* Corresponding author. Address: Superconductivity Research Laboratory, ISTEC, 1-16-25 Shibaura, Minato-ku, Tokyo 105-0023, Japan. Tel.: +81-3-3454-9284; fax: +81-3-3454-9287.

E-mail address: [h-enomoto@istec.or.jp](mailto:h-enomoto@istec.or.jp) (H. Enomoto).

In the present work, we investigated the effect of Dy211 addition and oxygen-annealing temperature on the flux creep properties of Dy123/Dy211 composite bulk superconductors by measuring the magnetic hysteresis and magnetic relaxation.

## 2. Experimental

The Dy123/Dy211 composite samples used in the present study were fabricated by the top-seeded melt-growth process, the details of which were described elsewhere [2]. For the measurements of the superconducting properties, rectangular pieces with dimensions of about  $2 \times 2 \times 1$  mm<sup>3</sup> were cut from as-grown bulk samples. To investigate the effect of oxygen-annealing temperature on the flux creep properties, we used Dy123 containing 5 mol% Dy211, which was annealed in flowing oxygen gas at 400, 450, 500, and 550 °C for 100 h. The effects of Dy211 addition on the flux creep properties were also studied with Dy123 containing 5, 10, 20, and 40 mol% Dy211, which were annealed in flowing oxygen gas at 450 °C for 100 h. The hysteresis loop and magnetic relaxation measurements were performed using a commercial SQUID magnetometer (Quantum Design, MPMS) with magnetic field applied parallel to the *c*-axis.

We confirmed that the samples with various Dy211 contents exhibited almost the same  $T_c$  value of 91.5 K. We also confirmed that no appreciable difference in  $T_c$  values was observed for the samples with different annealing temperatures and the  $T_c$  was also around 91.5 K except the sample annealed at 550 °C, which showed a  $T_c$  value of 89 K and a broad transition.

For the magnetic relaxation measurements, it is essential for the external field penetrating to the center of the sample. To establish this condition, the magnetic field of  $-7$  T was first applied to the sample and then swept to the desired value. The time decay of magnetization  $M(t)$  was measured for 4200 s at various fields ranging from 0.25 to 3 T at 77 K. The starting time of decay measurements was defined to be  $t_{\text{init}} = 70$  s. This value of  $t_{\text{init}}$  was certified to be sufficiently long with the two different determination methods of  $\mu$  [4].

## 3. Results and discussion

Fig. 1(a) and (b) shows the magnetic field dependence of  $J_c$  at 77 K, which were calculated from the hysteresis loop using the extended Bean model [5]. As shown in Fig. 1(a) the  $J_c$  in a low field region increases with increasing Dy211 contents. In contrast the secondary peak height decreases with increasing Dy211 contents. Due to the largest peak effect, Dy123 containing 5 mol% Dy211 exhibits

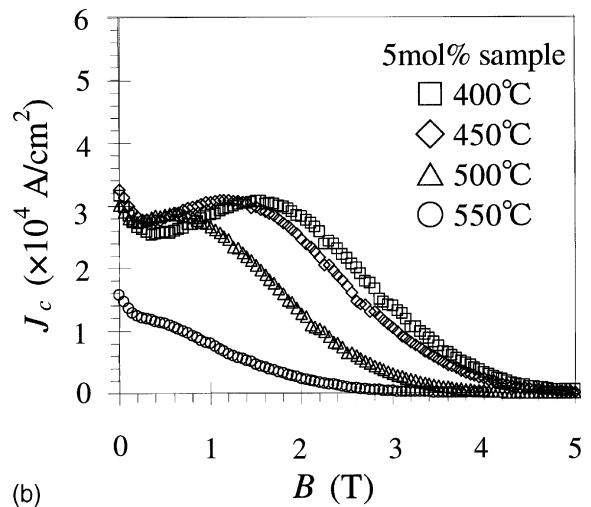
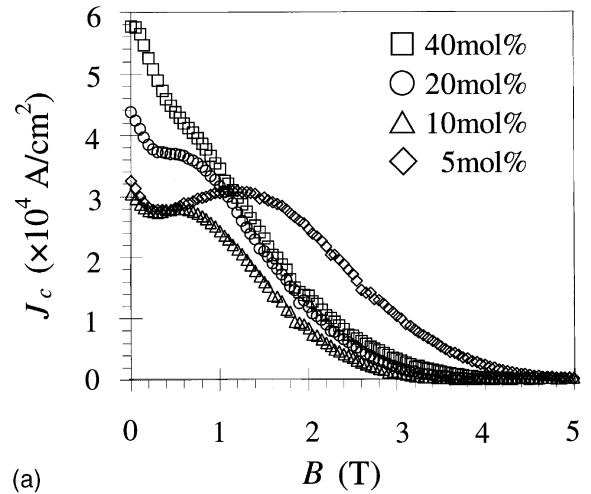


Fig. 1.  $J_c$ - $B$  curves for the bulk Dy123/Dy211 composite samples with (a) the different Dy211 contents annealed in O<sub>2</sub> at 450 °C and (b) 5 mol% Dy211 annealed in O<sub>2</sub> at temperatures of 400–550 °C.

the highest  $J_c$  values even at the higher fields above the secondary peak. Furthermore, in Fig. 1(b) one can see that the secondary peak position gradually shifts to lower fields with increasing oxygen-annealing temperature. The  $J_c$  value was drastically depressed over a wide field range in the sample annealed at 550 °C primarily due to low  $T_c$ . Although no appreciable difference was observed in  $T_c$ , one can see a systematic increase in  $J_c$  and the peak field with lowering annealing temperature. In general the number of oxygen vacancy is increased at lower temperatures. However, for the enhancement of the secondary effect, one needs to have a well annealed matrix wherein the small oxygen deficient clusters are uniformly distributed. We believe that such microstructure is produced by low temperature annealing.

Fig. 2(a) and (b) shows the magnetic field dependence of normalized relaxation rate  $S$  at 77 K, which was obtained from the slope of  $\ln M$  versus  $\ln t$  using the least-square method. For the samples containing 10, 20, 40 mol% Dy211,  $S$  was lowered with increasing the Dy211 contents accompanied by an increase in the  $J_c$  values (see Fig. 1(a)). For the sample containing 5 mol% Dy211, which exhibits the large secondary peak, shows the lowest normalized relaxation rate. These results suggest that both the Dy123/Dy211 interfacial pinning and the field-induced pinning caused by the oxygen deficient clusters are effective in reducing the flux creep. Mochida et al. [6] reported that such a combined effect of two different pinning mechanisms led to the suppression in  $S$  for the Nd123 system, which is consistent with the present Dy123 system. In Fig. 2(b) one can also see that normalized relaxation rate  $S$  is lowered with decreasing oxygen-annealing temperature. This result is also consistent with  $J_c$ - $B$  data for the sample with different oxygen annealing temperatures.

Next, we analyzed the present relaxation data based on the collective pinning theory [7,8]. According to this theory, the exponent  $\mu$  in the plot of  $M^{-\mu}$  versus  $\ln(t)$  is an important parameter to characterize both the relaxation and vortex dynamics. Phenomenologically,  $\mu = -1$  gives a straight line, while  $\mu < -1$  and  $\mu > -1$  gives respective convex and concave curves. In the collective-pinning theory, three different pinning re-

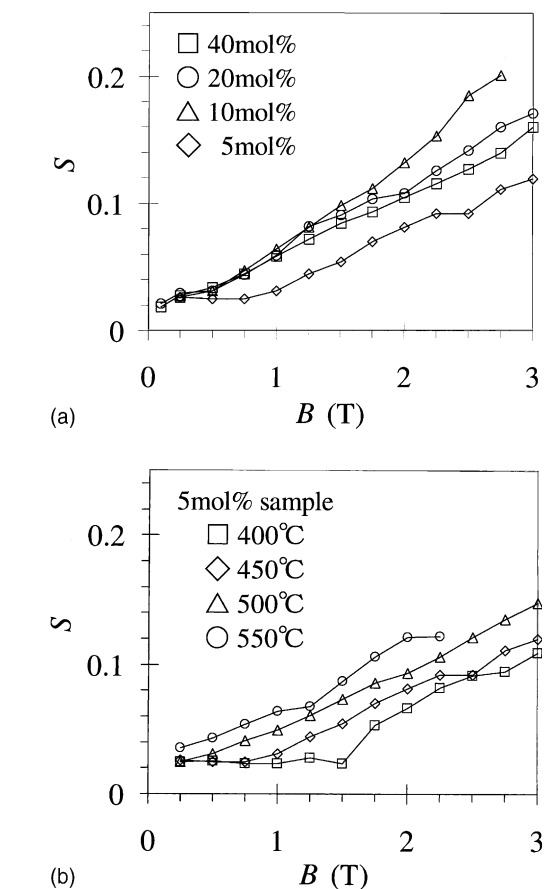


Fig. 2. Field dependence of  $S$  at 77 K for the Dy123/Dy211 bulk samples with (a) the different Dy211 contents annealed in  $O_2$  at 450 °C and (b) 5 mol% Dy211 annealed in  $O_2$  at temperatures of 400–550 °C.

gimes of single-vortex pinning, small and large-flux bundles are characterized by  $\mu = 1/7$ ,  $3/2$ , and  $7/9$ , respectively. Fig. 3(a) and (b) shows the magnetic field dependence of the  $\mu$  at 77 K for the samples with various Dy211 contents and annealing temperatures. The  $\mu$  are estimated by selecting a trial value of  $\mu$  and plotting  $M^{-\mu}$  versus  $\ln(t)$ . For the determination of the  $\mu$  value, a linear regression was repeated until the quantity  $(1 - R^2)$  reached the minimum value, where  $R^2$  is a statistical correlation constant and ideally unity for a perfect fitting. The  $\mu$  exhibits the peak for the sample with 5 mol% Dy211 which has the remarkable secondary peak. The samples with

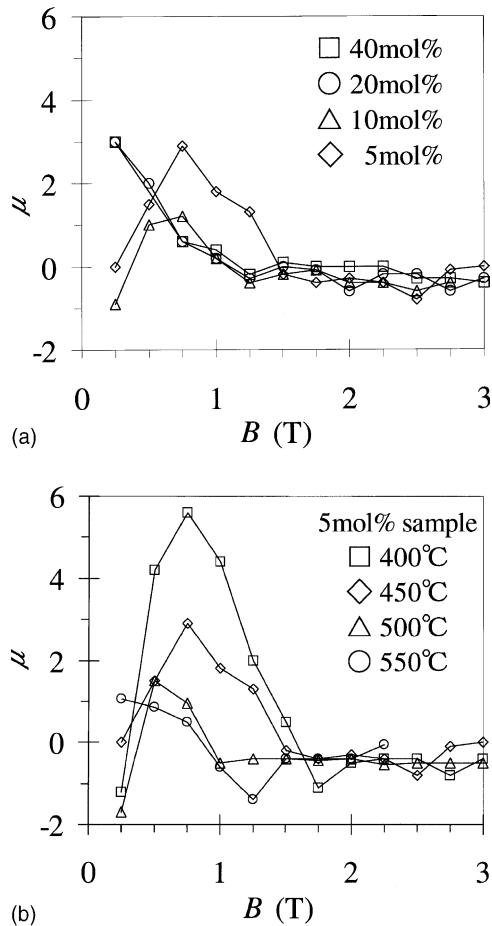


Fig. 3. Field dependence of  $\mu$  at 77 K for the Dy123/Dy211 bulk samples with (a) the different Dy211 contents annealed in  $O_2$  at 450 °C and (b) 5 mol% Dy211 annealed in  $O_2$  at temperatures of 400–550 °C.

higher  $J_c$  which includes 10 and 20 mol% Dy211, have the higher  $\mu$  in the low field. In Fig. 3(b) one can see that the maximum position of  $\mu$  shift to lower field with increasing oxygen-annealing temperature for samples with the clear secondary peak which were annealed at 400, 450 and 500 °C. The positive peak value of  $\mu$  increases with decreasing oxygen-annealing temperature, that shows the  $\mu$  value is the higher for the sample with the larger secondary peak (see Fig. 1(b)). Hence the  $\mu$  value

seems to be strongly correlated with field-induced pinning.

#### 4. Summary

We measured the magnetic relaxation in Dy123/Dy211 composite bulk superconductors. An increase in the Dy211 contents was effective in suppressing the flux creep. The oxygen-annealing at lower temperature could enhance the secondary peak effect and was also effective in reducing the relaxation. A reduction in  $S$  was observed for the sample with the large secondary peak. The positive peak value of  $\mu$  is the higher for the sample with the larger secondary peak. This implies that the  $\mu$  is correlated with the field induced pinning.

#### Acknowledgements

This work was supported by the New Energy and Industrial Technology Development Organization (NEDO) as Collaborative Research and Development of Fundamental Technologies for Superconductivity Applications.

#### References

- [1] M. Murakami, S.I. Yoo, T. Higuchi, N. Sakai, J. Weltz, N. Koshizuka, S. Tanaka, *Jpn. J. Appl. Phys.* 33 (1994) L715.
- [2] S. Nariki, M. Murakami, *Supercond. Sci. Technol.* 15 (2002) 786.
- [3] M. Daeumling, J.M. Seuntjens, D.C. Larbalestier, *Nature* 346 (1990) 332.
- [4] L. Civale, L. Krusin-Elbaum, J.R. Thompson, F. Holtzberg, *Phys. Rev. B* 50 (1994) 7188.
- [5] E.M. Gyorgy, R.B. van Dover, K.A. Jackson, L.F. Schneemeyer, J.V. Waszczak, *Appl. Phys. Lett.* 55 (1989) 283.
- [6] T. Mochida, N. Chikumoto, M. Murakami, *Phys. Rev. B* 64 (2001) 64518.
- [7] M.V. Feigel'man, V.B. Geshkenbein, A.I. Larkin, V.M. Vinokur, *Phys. Rev. Lett.* 63. (1989) 2303.
- [8] M.V. Feigel'man, V.M. Vinokur, *Phys. Rev. B* 41 (1990) 8986.



ELSEVIER

Journal of Crystal Growth 237–239 (2002) 1986–1992

JOURNAL OF  
**CRYSTAL  
GROWTH**

www.elsevier.com/locate/jcrysgr

# Cu-based multinary compounds and their crystal growth: synthesis processes, phase diagrams and control of vapor pressures

Hiroaki Matsushita<sup>a,\*</sup>, Akinori Katsui<sup>a</sup>, Takeo Takizawa<sup>b</sup>

<sup>a</sup> *Department of Material Science and Technology, School of High-Technology for Human Welfare, Tokai University, 317 Nishino, Numazu, Shizuoka 410-0395, Japan*

<sup>b</sup> *Department of Physics, College of Humanities and Sciences, Nihon University, 3-25-40 Sakurajosui, Setagaya-ku, Tokyo 156-8550, Japan*

## Abstract

In order to overcome the difficulties in getting bulk single crystals of Cu-based multinary compounds of high quality, we have investigated the chemical reaction involving single phase formation, the phase diagrams for bypassing the peritectic reaction, and the solid-state phase transition and the effect of VI vapor pressure on the crystal growth. The selenization or sulfurization method of a CuIn alloy is devised to grow single crystals of CuInSe<sub>2</sub> or CuInS<sub>2</sub>. To bypass the peritectic reaction of CuGaSe<sub>2</sub>, solution growth has been performed by using a self-flux, and it is shown that large single crystals can be grown better from a CuSe solvent than from a Cu<sub>2</sub>Se solvent. In addition, a solvent of Sb<sub>2</sub>Se<sub>3</sub> is used to grow CuInSe<sub>2</sub> single crystals at temperatures below the solid-state phase transition. Furthermore, the melt growth under controlled VI vapor pressure is adopted to grow high-quality crystals of CuInSe<sub>2</sub> and CuInS<sub>2</sub>. © 2002 Elsevier Science B.V. All rights reserved.

*PACS:* 81.30.Dz; 81.10.–h

*Keywords:* A1. Phase diagrams; A2. Single crystal growth; B2. Semiconducting ternary compounds

## 1. Introduction

There are few practical opto-electronic devices composed of multinary compounds with tetrahedral coordinations, in spite of their enormous potential for various applications. One of the difficulties is caused by the uncontrollability of the physical properties of these compounds, arising

from the fact that they essentially consist of more than three elements. Actually, each compositional atom has the possibility of occupying various lattice sites and even generating a vacancy and/or an interstitial during growth, inevitably leading to difficulties in getting a bulk single crystal of high quality. In addition, there are always several paths to obtain precursors of multinary compounds. In other words, they can be synthesized through different chemical reaction processes.

In order to overcome the difficulties above-mentioned, we have investigated (1) all the chemical reactions until a single phase is formed,

\*Corresponding author. Tel.: +81-559-68-1211-4407; fax: +81-559-68-1155.

*E-mail address:* matusita@wing.ncc.u-tokai.ac.jp (H. Matsushita).

while at the same time, the intermediate binary products synthesized during the formation process, (2) the pseudo-binary phase diagrams which are necessary for the strategy to grow a single crystal bypassing the peritectic reaction and the solid-state phase transition if they exist, and (3) the effect of vapor pressure of VI group elements on the growth of single crystals.

## 2. Chemical reactions synthesizing a single phase

Prior to the growth of single crystals of better quality, we should know the formation mechanisms, i.e., the chemical reaction process forming a single phase. We present here the results of  $\text{CuInSe}_2$ ,  $\text{CuInS}_2$  and  $\text{CuGaSe}_2$  [1–3]. Differential thermal analysis (DTA) and X-ray diffraction (XRD) are used throughout this report. Figs. 1(a) and (b) show DTA curves of  $\text{Cu} + \text{In} + 2\text{Se}$ ,  $\text{CuIn} + 2\text{Se}$  mixtures and  $\text{Cu} + \text{Ga} + 2\text{Se}$ ,  $\text{CuGa} + 2\text{Se}$  mixtures in the heating process, respectively, where DTA curves of elements and compounds are also shown for comparison.

For  $\text{Cu} + \text{In} + 2\text{Se}$  mixture, the chemical reactions and phase transitions are summarized as follows.

- (1)  $\text{In}, \text{Se} \rightarrow \text{In}_2\text{Se}_3, \text{In}_6\text{Se}_7$  at  $250^\circ\text{C}$ .
- (2)  $\text{Cu}, \text{Se} \rightarrow \text{Cu}_3\text{Se}_2, \text{Cu}_7\text{Se}_4$  at  $280\text{--}420^\circ\text{C}$ .
- (3)  $\text{In}_2\text{Se}_3$ : solid  $\rightarrow$  liquid at  $\sim 500^\circ\text{C}$ .

- (4)  $\text{InSe}, \text{In}_6\text{Se}_7$ : solid  $\rightarrow$  liquid at  $\sim 600^\circ\text{C}$ .
- (5)  $\text{In}_2\text{Se}_3$ : solid  $\rightarrow$  liquid at about  $900^\circ\text{C}$ .
- (6)  $\text{Cu}_7\text{Se}_4, \text{InSe}, \text{In}_2\text{Se}_3 \rightarrow \text{CuInSe}_2$  above  $950^\circ\text{C}$ .
- (7)  $\text{CuInSe}_2$  (sphalerite): solid  $\rightarrow$  liquid at  $996^\circ\text{C}$ .

It was found that a few exothermic reactions just below the melting point of  $\text{CuInSe}_2$  did not necessarily occur, and the solid phases of  $\text{Cu}_{2-x}\text{Se}$  and/or copper sometimes remained even at  $1040^\circ\text{C}$  in the liquid of the mixture [1].

For  $\text{CuIn} + 2\text{Se}$  mixture, the chemical reactions and phase transitions are summarized as follows.

- (1)  $\text{Cu}_{1-x}\text{In}_x$  ( $x > 0.5$ ),  $\text{Se} \rightarrow \text{CuInSe}_2, \text{InSe}$  at  $520^\circ\text{C}$ .
- (2)  $\text{Cu}_{1-x}\text{In}_x$  ( $x < 0.5$ ),  $\text{Se}, \text{InSe} \rightarrow \text{CuInSe}_2$  at  $575^\circ\text{C}$ .
- (3)  $\text{InSe}$ : solid  $\rightarrow$  liquid at about  $650^\circ\text{C}$ .
- (4)  $\text{CuInSe}_2$ : chalcopyrite  $\rightarrow$  sphalerite at about  $810^\circ\text{C}$ .
- (5)  $\text{CuSe}, \text{InSe} \rightarrow \text{CuInSe}_2$  above  $950^\circ\text{C}$ .
- (6)  $\text{CuInSe}_2$  (sphalerite): solid  $\rightarrow$  liquid at  $996^\circ\text{C}$ .

According to the phase diagram of the  $\text{Cu}\text{--}\text{In}$  system [4], it is known that  $\text{CuIn}$  alloy decomposes into  $\text{Cu}$ -rich  $\text{Cu}\text{--}\text{In}$  phase and  $\text{In}$ -rich  $\text{Cu}\text{--}\text{In}$  phase with increasing temperature.

In the selenization reaction of  $\text{In}$ -rich  $\text{Cu}\text{--}\text{In}$  phase at  $520^\circ\text{C}$ ,  $\text{CuInSe}_2$  and  $\text{InSe}$  compounds were formed, and then most of the  $\text{CuInSe}_2$  compound was produced at  $575^\circ\text{C}$ .

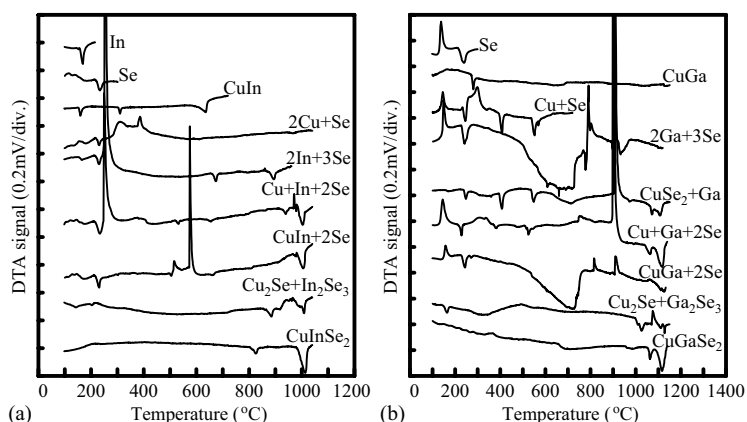


Fig. 1. (a) DTA curves of  $\text{Cu} + \text{In} + 2\text{Se}$ ,  $\text{CuIn} + 2\text{Se}$  mixtures, and (b)  $\text{Cu} + \text{Ga} + 2\text{Se}$ ,  $\text{CuGa} + 2\text{Se}$  mixtures in the heating process, where DTA curves of elements and compounds are also shown for comparison.

Similar to  $\text{CuInSe}_2$ , most of the  $\text{CuInS}_2$  compound was also formed from a  $\text{Cu} + \text{In} + 2\text{S}$  mixture below the melting point of  $\text{CuInS}_2$  through the chemical reaction between  $\text{Cu}_{2-x}\text{S}$  and  $\text{In}_2\text{S}_{3-x}$  [3]. Considerable amounts of heterogeneous phases, for instance, Cu sulfides having melting points higher than that of  $\text{CuInS}_2$ , are considered to coexist with the  $\text{CuInS}_2$  phase at about  $1100^\circ\text{C}$ . On the other hand, the explosive exothermic reactions from a  $\text{CuIn} + 2\text{S}$  mixture at  $480^\circ\text{C}$  and  $700^\circ\text{C}$  were ascribed to the sulfurization of the Cu–In phase, where most of the  $\text{CuInS}_2$  compound is formed [3]. In conclusion, the selenization or sulfurization method of a CuIn alloy at temperatures other than  $575$  or  $700^\circ\text{C}$  is one of the best methods to grow single crystals of  $\text{CuInSe}_2$  or  $\text{CuInS}_2$ .

In contrast to the cases mentioned above, the chemical reactions and phase transitions of  $\text{Cu-Ga} + 2\text{Se}$  are summarized as follows.

- (1)  $\text{CuSe}$ : solid  $\rightarrow$  liquid at  $\sim 550^\circ\text{C}$ .
- (2)  $\text{Cu-Ga}$  alloy,  $\text{Se} \rightarrow \text{GaSe}$ ,  $\text{Ga}_2\text{Se}_3$ ,  $\text{CuSe}$  at  $550\text{--}750^\circ\text{C}$ .
- (3)  $\text{Ga}$  and  $\text{Cu}$  selenides: decomposition and/or selenization at  $\sim 800^\circ\text{C}$  and  $\sim 900^\circ\text{C}$ .
- (4)  $\text{CuGaSe}_2$  (chalcopyrite)  $\rightarrow$   $\text{CuGaSe}_2$  (sphalerite) + liquid at  $1060^\circ\text{C}$ .
- (5)  $\text{Cu}_7\text{Se}_4$ ,  $\text{GaSe}$ ,  $\text{Ga}_2\text{Se}_3 \rightarrow \text{CuGaSe}_2$  (sphalerite) above  $1080^\circ\text{C}$ .
- (6)  $\text{CuGaSe}_2$  (sphalerite): solid  $\rightarrow$  liquid at  $1105^\circ\text{C}$ .

The  $\text{CuGa}$  alloy decomposes into Cu-rich Cu–Ga phase and Ga-rich Cu–Ga phase with increasing temperature, in accordance with the phase diagram of the Cu–Ga system [5]. The  $\text{CuGaSe}_2$  phase has already been derived below  $950^\circ\text{C}$  through the liquid phase reaction between the Cu–Ga phase, mentioned above, and selenium [2]. About a half of the  $\text{CuGaSe}_2$  phase was confirmed to be formed, judging from the following two results.

- (1) XRD intensities of the  $\text{CuGaSe}_2$  phase reduced to about half after heating up to  $950^\circ\text{C}$  in comparison to those up to  $1150^\circ\text{C}$  [2].
- (2) The heat of transition from the chalcopyrite phase to the (sphalerite + liquid) phase at

$1060^\circ\text{C}$  of  $\text{CuGa} + 2\text{Se}$  was smaller than that of  $\text{CuGaSe}_2$  as shown in Fig. 1(b).

In addition,  $\text{CuGaSe}_2$  compound was not perfectly formed at about  $1100^\circ\text{C}$  since the heat of fusion at about  $1100^\circ\text{C}$  of  $\text{CuGa} + 2\text{Se}$  was lesser than that of  $\text{CuGaSe}_2$  as seen in Fig. 1(b). Thus, the selenization of the  $\text{CuGa}$  alloy is not necessarily needed for the  $\text{CuGaSe}_2$  single phase in contrast to the cases of  $\text{CuInSe}_2$  and  $\text{CuInS}_2$ .

To find another preparation method except for the selenization of the  $\text{CuGa}$  alloy, we investigated the chemical reaction process of  $\text{Cu} + \text{Ga} + 2\text{Se}$  mixture as follows.

- (1)  $\text{Cu}$ ,  $\text{Se} \rightarrow \text{CuSe}_2$ ,  $\text{CuSe}$ ,  $\text{Cu}_3\text{Se}_2$  at  $280\text{--}380^\circ\text{C}$ .
- (2)  $\text{CuSe}_2$ ,  $\text{CuSe}$ : solid-phase transition at about  $380^\circ\text{C}$ .
- (3)  $\text{CuSe}_2$ ,  $\text{CuSe}$ : solid  $\rightarrow$  liquid at about  $530^\circ\text{C}$ .
- (4)  $\text{Ga}$ ,  $\text{Se} \rightarrow \text{GaSe}$  at  $700\text{--}800^\circ\text{C}$ .
- (5)  $\text{Ga}$ ,  $\text{CuSe}_2$ ,  $\text{CuSe}$ ,  $\text{GaSe} \rightarrow \text{CuGaSe}_2$  at about  $900^\circ\text{C}$ .
- (6)  $\text{CuGaSe}_2$  (chalcopyrite)  $\rightarrow$   $\text{CuGaSe}_2$  (sphalerite) + liquid at  $1060^\circ\text{C}$ .
- (7)  $\text{CuGaSe}_2$  (sphalerite): solid  $\rightarrow$  liquid at  $1105^\circ\text{C}$ .

The heat of transition at  $1060^\circ\text{C}$  of  $\text{Cu} + \text{Ga} + 2\text{Se}$  is in good agreement with that of  $\text{CuGaSe}_2$  as seen in Fig. 1(b). Hence, the  $\text{CuGaSe}_2$  phase is formed by the exothermic reaction at about  $900^\circ\text{C}$ . Thus, it is considered that the  $\text{CuGaSe}_2$  phase is completely formed from a  $\text{Cu} + \text{Ga} + 2\text{Se}$  mixture below  $1060^\circ\text{C}$ . In addition, the heats of transition and fusion at about  $1060^\circ\text{C}$  and  $1100^\circ\text{C}$  of a  $\text{CuSe}_2 + \text{Ga}$  mixture are also in agreement with those of  $\text{CuGaSe}_2$ . Therefore, it is expected that the chemical reaction between Cu selenides and gallium is one of the best preparation methods for  $\text{CuGaSe}_2$ .

### 3. Phase diagrams and solution growth

On the basis of the pseudo-binary phase diagram of  $\text{Cu}_2\text{Se-Ga}_2\text{Se}_3$  system, it is shown that the  $\text{CuGaSe}_2$  chalcopyrite phase is formed through a peritectic reaction from the (sphalerite + liquid) phase to the chalcopyrite phase [6,7]. Therefore, a

large single crystal is difficult to be grown from the stoichiometric melt, and hence the solution method using a self-flux is recommended to obtain a single crystal of higher quality. Actually, the crystal growth of  $\text{CuGaSe}_2$  has been performed by the self-flux method, using  $\text{Cu}_2\text{Se}$  and  $\text{CuSe}$  solvents [8,9].

The  $\text{Cu}_2\text{Se}$ – $\text{CuGaSe}_2$  phase diagram shows that the transition line from sphalerite to chalcopyrite phase exists at  $1054^\circ\text{C}$  in 55–100 mol%  $\text{CuGaSe}_2$ . In addition, a eutectic line was deduced at  $996^\circ\text{C}$  in 25–100 mol%  $\text{CuGaSe}_2$ , and the eutectic point exists at  $996^\circ\text{C}$  for 34 mol%. In this case, single crystals of  $\text{CuGaSe}_2$  could be grown using the liquidus line in the composition ranging from 35 to 50 mol%  $\text{CuGaSe}_2$ , resulting in a short (20 mm at most) single crystal [8].

In contrast to the  $\text{Cu}_2\text{Se}$  solvent, the phase diagram of the  $\text{CuSe}$ – $\text{CuGaSe}_2$  system was deduced as shown in Fig. 2(a). The transition line from sphalerite to chalcopyrite phase is considered to be between 58 and 100 mol%  $\text{CuGaSe}_2$ . The

(chalcopyrite + liquid) phase exists under the liquidus line in the composition ranging from 0 to 58 mol%  $\text{CuGaSe}_2$ , which can be used to grow the  $\text{CuGaSe}_2$  crystals. Here, the crystal growth was achieved using the 10–55 mol%  $\text{CuGaSe}_2$  range. As the liquidus line for the chalcopyrite phase to be precipitated is wide in comparison to the  $\text{Cu}_2\text{Se}$  case, a long single crystal of 50 mm in length was obtained as shown in Fig. 2(b). The XRD patterns of the grown ingot are shown in Fig. 2(c). The top 50 mm of it (“15 mm” and “45 mm” in this figure) had the single chalcopyrite phase of  $\text{CuGaSe}_2$ . The XRD intensity of the  $\text{CuSe}$  phase shown by open circles increases as it moves from “65 mm” to the end of the ingot. It was found that the composition of the top (“15 mm” and “45 mm”) was nearly stoichiometric ( $\text{Cu} = 26\%$ ,  $\text{Ga} = 24\%$ ,  $\text{Se} = 50\%$ ). It was also shown that larger single crystals were grown from a  $\text{CuSe}$  solvent than a  $\text{Cu}_2\text{Se}$  solvent.

On the other hand, we have attempted to grow  $\text{CuInSe}_2$  single crystals at temperatures below the solid-state phase transition using  $\text{Sb}_2\text{Se}_3$

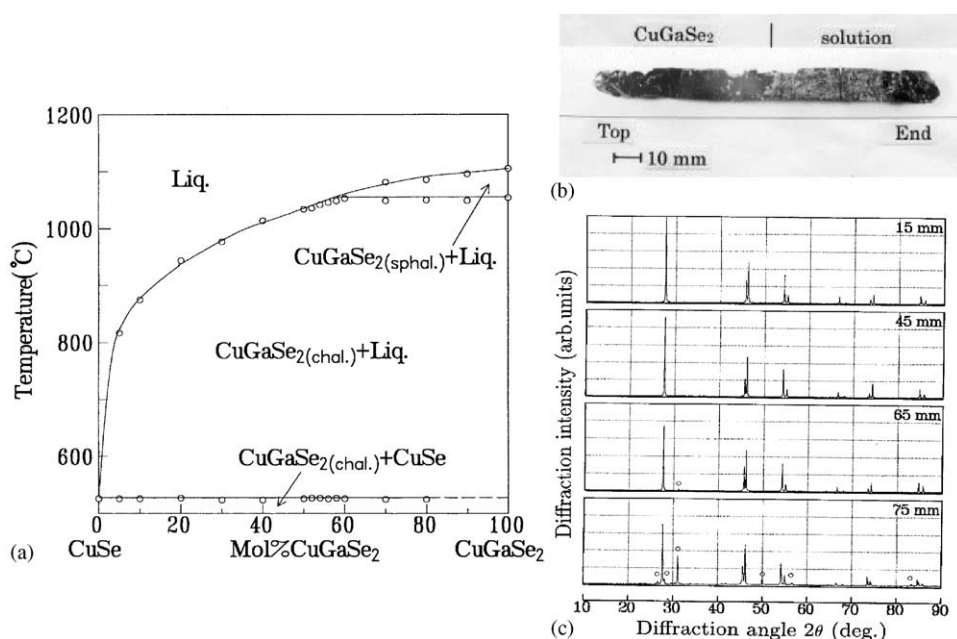


Fig. 2. (a) Pseudo-binary phase diagram of the  $\text{CuSe}$ – $\text{CuGaSe}_2$  system, (b) a photograph of an as-grown ingot and (c) XRD patterns of ingots grown using a  $\text{CuSe}$  solvent. The  $\text{CuSe}$  phase is indicated by open circles. Each spectrum is normalized to the (1 1 2) line of “15 mm”.

as a solvent [10]. It is expected that  $\text{Sb}_2\text{Se}_3$  is not incorporated in  $\text{CuInSe}_2$  crystals, which is considered from the results of the liquid phase epitaxial growth of  $\text{AgGaS}_2$  using an  $\text{Sb}_2\text{S}_3$  solvent [11]. The phase diagram of the  $\text{Sb}_2\text{Se}_3$ – $\text{CuInSe}_2$  system determined from the XRD and DTA results is shown in Fig. 3(a). The eutectic temperature is deduced as  $520^\circ\text{C}$  between 5 and 90 mol%  $\text{CuInSe}_2$ . The eutectic composition is evaluated to be 10 mol%  $\text{CuInSe}_2$ . The transition point from sphalerite to chalcopyrite phase exists at about  $800^\circ\text{C}$  in 50–100 mol%  $\text{CuInSe}_2$ . Hence, it is expected that a  $\text{CuInSe}_2$  chalcopyrite phase rises much lower than the transition point in 10–50 mol%  $\text{CuInSe}_2$  at  $520$ – $800^\circ\text{C}$ .

Based on the phase diagram of Fig. 3(a), the bulk single crystals were grown from a solution of 50 mol%  $\text{CuInSe}_2$ . A photograph of a typical grown boule is shown in Fig. 3(b). A single crystal of about 11 mm in length was grown from the bottom of the boule along the growth direction. From XRD patterns of three parts labeled “a”,

“b” and “c” of the boule, only the “a” part showed the pure  $\text{CuInSe}_2$  chalcopyrite phase. In the “b” and “c” parts, the  $\text{Sb}_2\text{Se}_3$  phase was included. Fig. 3(c) shows the composition variation along the growth direction of the boule measured by EPMA. The Cu:In:Se ratio is shown to be about 1:1:2 and is uniform throughout the region “a” of the single crystal, while antimony is detected in the boule above 12 mm. The impurity analysis of the “a” part was performed by means of inductively coupled plasma (ICP) spectrometry. The result indicated that the region “a” contained antimony at a level  $<0.1$  mol%.

#### 4. Crystal growth under controlling VI vapor pressure

It is sometimes effective to grow bulk single crystals of multinary selenides and sulfides by applying vapor pressure of VI group element, because the VI vapor pressure is normally very

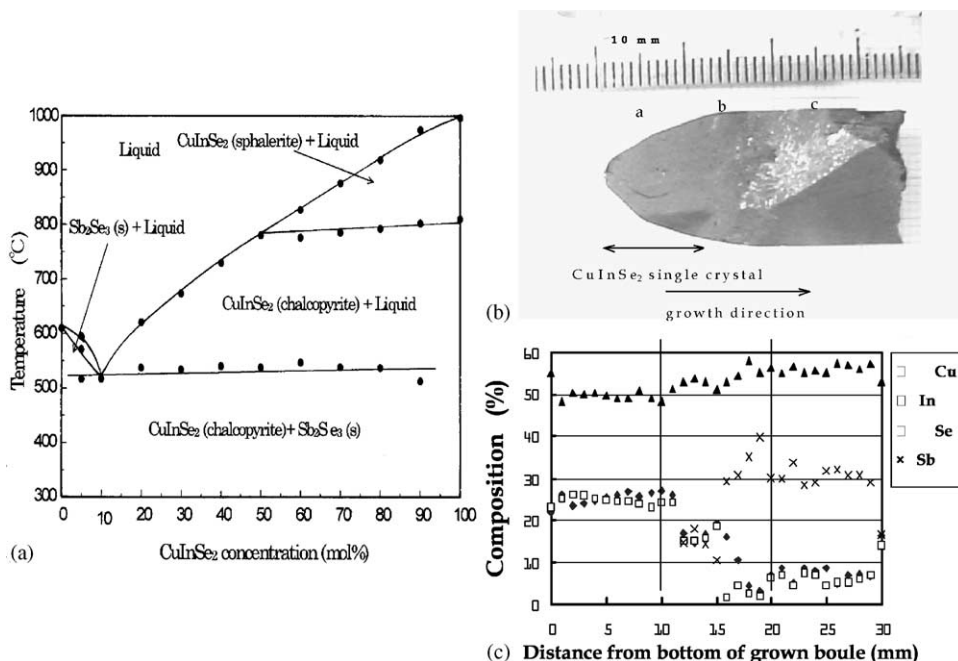


Fig. 3. (a) Pseudo-binary phase diagram of the  $\text{Sb}_2\text{Se}_3$ – $\text{CuInSe}_2$  system, (b) a photograph of a grown boule, region “a” corresponds to the  $\text{CuInSe}_2$  single crystal in the bottom, and (c) variations of Cu, In, Se and Sb compositions of a grown boule along the growth direction.

high in comparison to that of the other compositional elements so that the VI elements are easily evaporated from the products even after final compounds are synthesized. In addition, the solidifying points were found to be sensitive to the vapor pressure of VI group elements as well as the compositional deviation from stoichiometry [12]. Fig. 4(a) shows the VI vapor pressure dependence of the solidifying points of  $\text{CuInSe}_2$ ,  $\text{CuGaSe}_2$ ,  $\text{AgGaSe}_2$ ,  $\text{AgInSe}_2$  and  $\text{CuInS}_2$  compounds. For example, the solidifying point of  $\text{CuInSe}_2$  decreased by about  $130^\circ\text{C}$  with increasing Se vapor pressure up to 760 Torr. The phase transition point from chalcopyrite to sphalerite structure decreased down to about  $800^\circ\text{C}$  as Se composition increased at the (CuIn)–2Se system [13], while the transition point was found to be almost fixed at  $\sim 820^\circ\text{C}$  with varying Se vapor pressure [14]. It is expected that the heterogeneous

phases in the  $\text{CuInSe}_2$  phase are not produced in the region under 760 Torr of Se vapor pressure. The solidifying point without applying Se vapor pressure was  $996^\circ\text{C}$  in good agreement with that of 5 Torr. It is suggested that  $\text{CuInSe}_2$  crystals grown under the applied Se vapor pressure of  $>5$  Torr have Se-rich compositions, while the crystals grown under  $<5$  Torr have the (CuIn)-rich compositions. This can be explained by the facts that the Se-poor crystals grown under lower Se vapor pressures (2–7 Torr) showed the n-type conduction, and the others (Se-rich crystals) showed the p-type conduction [15,16].

Fig. 4(b) shows a photograph of the as-grown crystal by horizontal Bridgman method controlling Se vapor pressure. The part of a Cu+In mixture was first heated to  $700^\circ\text{C}$  and then solidified to make a CuIn alloy. Next, the CuIn alloy in the high-temperature zone was heated up to  $1020^\circ\text{C}$ , while the low-temperature zone was heated to a temperature corresponding to the desired Se vapor pressure. At the high-temperature zone, the CuIn phase was selenized to form the  $\text{CuInSe}_2$  phase. Then, the temperature gradient of  $3^\circ\text{C}/\text{cm}$  was moved electrically at a speed of about 1 cm/h. All portions of bulk crystal grown from “T” to “E” in Fig. 4(b) had a single phase of the chalcopyrite structure and no extra XRD lines were observed. It is seen that the single crystals of p-type conduction with large Hall coefficients and mobilities were prepared at Se vapor pressures from 10 to 25 Torr [16]. Here, it was shown in view of the phase diagram of CuIn–2Se system [13] that single crystals of high quality could be grown by controlling the Se vapor pressure. The crystals contained no cracks and twins so that the Hall effect could be successfully measured down to about 20 K [16,17].

In addition, we attempted the growth of  $\text{CuInS}_2$  bulk single crystals by the same preparation method as that of  $\text{CuInSe}_2$  [3]. On visual inspection, the crystallinity of the bulk crystals became better with decreasing S vapor pressure down to 200 Torr. In other words, the samples prepared under higher S vapor pressures contained many voids and cracks, and single crystals of better crystalline quality were grown under S vapor pressure around 200 Torr.

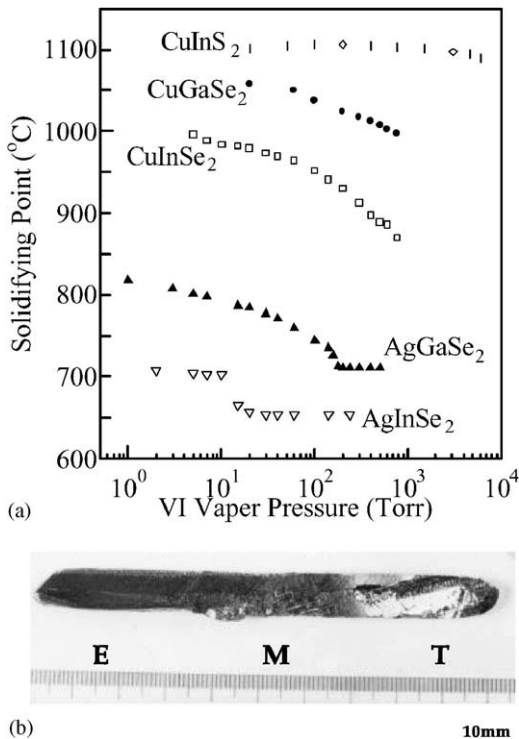


Fig. 4. (a) VI vapor pressure dependence on solidifying points of several ternary compounds and (b) a photograph of the as-grown crystal by horizontal Bridgman method controlling Se vapor pressure.

## 5. Summary

- (1) Prior to the growth of better quality single crystals of multinary compounds, we have investigated the formation mechanisms, i.e., the chemical reaction process forming the single phase. For the most suitable preparation method, the selenization or sulfurization method of a CuIn alloy was devised to grow single crystals of CuInSe<sub>2</sub> or CuInS<sub>2</sub>, respectively, but at the same time it was shown that this was not the case for CuGaSe<sub>2</sub>.
- (2) To obtain a CuGaSe<sub>2</sub> single crystal of higher quality, where the chalcopyrite phase is formed through a peritectic reaction from the (sphalerite + liquid) phase to the chalcopyrite phase, the solution growth of CuGaSe<sub>2</sub> has been performed based on the phase diagrams of the Cu<sub>2</sub>Se–CuGaSe<sub>2</sub> and CuSe–CuGaSe<sub>2</sub> systems. The results showed that large single crystals could be grown better from a CuSe solvent than from a Cu<sub>2</sub>Se solvent. On the other hand, we attempted to grow CuInSe<sub>2</sub> single crystals using Sb<sub>2</sub>Se<sub>3</sub> as a solvent at temperatures below the solid-state phase transition. The phase diagram of the Sb<sub>2</sub>Se<sub>3</sub>–CuInSe<sub>2</sub> system showed that an Sb<sub>2</sub>Se<sub>3</sub> solvent was suitable for the growth of CuInSe<sub>2</sub> crystals, which was also proved to be correct for the actual crystal growth.
- (3) It is sometimes effective to grow bulk single crystals of multinary selenides and sulfides by applying VI vapor pressure, since the solidifying points are found to be sensitive to the VI vapor pressure. For example, in the case of CuInSe<sub>2</sub>, it was shown that the single crystals of high quality without cracks and twins could be grown by controlling Se vapor pressure. In addition, the crystal growth of CuInS<sub>2</sub> was performed by the same preparation method as that of CuInSe<sub>2</sub>.

Finally, we also described the synthesis solute diffusion method by controlling the growth rate for the single crystal growth of CuInSe<sub>2</sub> [18]. The CuInSe<sub>2</sub> phase precipitated from CuIn and Se solutions at temperatures below the melting point

of CuInSe<sub>2</sub> as was predicted by the phase diagrams of the CuIn–2Se system.

Recently, we have been applying the investigations mentioned above to grow bulk single crystals of Cu-based chalcopyrite-like quaternary compounds [19,20].

## References

- [1] H. Matsushita, T. Takizawa, *Jpn. J. Appl. Phys.* 34 (1995) 4699.
- [2] H. Matsushita, H. Jitsukawa, T. Takizawa, *Jpn. J. Appl. Phys.* 35 (1996) 3830.
- [3] H. Matsushita, T. Mihira, T. Takizawa, *J. Crystal Growth* 197 (1999) 169.
- [4] F.A. Shunk, *Second Supplement to the Constitution of Binary Alloys*, McGraw-Hill, New York, 1969.
- [5] M. Hansen, *Constitution of Binary Alloys*, McGraw-Hill, New York, 1958.
- [6] J.C. Mikkelsen Jr., *J. Electron. Mater.* 10 (1981) 541.
- [7] L.S. Palatnik, E.K. Belova, *Izu. Acad. Nauk. SSSR., Neorgan. Mater.* 3 (1967) 2194.
- [8] H. Jitsukawa, H. Matsushita, T. Takizawa, *J. Crystal Growth* 186 (1998) 587.
- [9] H. Matsushita, H. Jitsukawa, H. Sugano, T. Takizawa, S. Endo, *Institutional Physics Conference Series No 152: Proceedings of the 11th International Conference on Ternary and Multinary Compounds*, Salford, 1997, p. 535.
- [10] S. Ai, H. Matsushita, A. Katsui, *J. Mater. Sci.* 35 (2000) 2553.
- [11] S.R. Sashital, A.L. Gentile, *J. Crystal Growth* 69 (1984) 379.
- [12] M.L. Fearheiley, *Sol. Cell* 16 (1986) 91.
- [13] H. Matsushita, T. Takizawa, *J. Crystal Growth* 179 (1997) 503.
- [14] H. Matsushita, H. Jitsukawa, T. Takizawa, *Transac. Mater. Res. Soc. Japan* 20 (1996) 715.
- [15] H. Matsushita, T. Suzuki, S. Endo, T. Irie, *Jpn. J. Appl. Phys.* 34 (1995) 3774.
- [16] H. Matsushita, T. Takizawa, *J. Crystal Growth* 160 (1996) 71.
- [17] H. Matsushita, T. Takizawa, *Jpn. J. Appl. Phys.* 37 (1998) 4258.
- [18] H. Matsushita, S. Ai, A. Katsui, *J. Crystal Growth* 224 (2001) 95.
- [19] H. Matsushita, T. Maeda, A. Katsui, T. Takizawa, *J. Crystal Growth* 208 (2000) 416.
- [20] H. Matsushita, T. Maeda, A. Katsui, T. Takizawa, *Jpn. J. Appl. Phys.* 39; *Proceedings of the 12th International Conference on Ternary and Multinary Compounds*, Hsinchu, 2000, p. 62.



ELSEVIER

Journal of Crystal Growth 237–239 (2002) 2009–2013

JOURNAL OF  
**CRYSTAL  
GROWTH**

www.elsevier.com/locate/jcrysgr

# Single-crystal growth and optical properties of undoped and $\text{Ce}^{3+}$ doped $\text{CaGa}_2\text{S}_4$

C. Hidaka, T. Takizawa\*

*Department of Physics, College of Humanities and Sciences, Nihon University, 3-25-40 Sakurajosui, Setagaya-ku, Tokyo 156-8550, Japan*

## Abstract

To improve the crystallinity of  $\text{CaGa}_2\text{S}_4$  single crystals, we have grown the crystals under various conditions by the horizontal Bridgman method using a travelling temperature gradient. If we lower the growth speed to  $<0.5$  cm/h while keeping the growth temperature close to but a little higher than the melting point, cracks and voids in the crystals are substantially reduced. A carbon boat is adopted in order to avoid the reaction of an ampoule with the material solution, which is found effective to improve the quality of a grown crystal. However, an absorption band with a peak at 3.2 eV newly emerges to turn a grown crystal yellowish.

Absorption spectra of  $\text{Ce}^{3+}$ -doped crystals are also measured. As a result, the energy separation between the 5d sublevels of  $\text{Ce}^{3+}$  ion, i.e.,  $T_{2g}$  and  $E_g$  is first estimated as 0.8 eV. © 2002 Elsevier Science B.V. All rights reserved.

*PACS:* 81.10.-h

*Keywords:* A1. Doping; A2. Bridgman technique; A2. Growth from melt; A2. Single crystal growth; B1. Calcium compounds; B1. Sulfides

## 1. Introduction

$\text{Ce}^{3+}$ -doped alkaline earth thiogallates ( $\text{MGa}_2\text{S}_4$ ,  $\text{M} = \text{Ca, Sr, Ba}$ ) have been regarded as host materials for blue electro-luminescent devices. So far, thin films of these thiogallates have been exclusively investigated, because they were the candidates closest to practical applications, since the first EL device using  $\text{CaGa}_2\text{S}_4:\text{Ce}^{3+}$  thin films was fabricated by Barrow et al. in 1993 [1].

Another interesting property found in these materials is a laser oscillation which has been first recognized in a  $\text{Eu}^{2+}$ -doped  $\text{CaGa}_2\text{S}_4$  single crystal [2]. In the case of  $\text{Ce}^{3+}$  doping, a similar phenomenon is also expected in the same or similar thiogallates. However, to check the usefulness of the material for laser devices, a large host single crystal which is free from strain, voids and cracks is needed. It should also be homogeneous with respect to the distribution of the rare earth element doped. Thus, growing high-quality single crystals is highly desired from both practical and basic research points of view.

Driven by the motivations above, we have constructed the pseudo-binary phase diagrams of

\*Corresponding author. Tel.: +81-3-5317-9733; fax: +81-3-5317-9432.

*E-mail address:* takiz@chs.nihon-u.ac.jp (T. Takizawa).

the CaS–Ga<sub>2</sub>S<sub>3</sub> and SrS–Ga<sub>2</sub>S<sub>3</sub> systems using the differential thermal analysis (DTA) and powder X-ray diffraction [3,4]. It is found that both materials have congruent melting points with eutectic reactions between SrGa<sub>2</sub>S<sub>4</sub> or CaGa<sub>2</sub>S<sub>4</sub> (50 mol% Ga<sub>2</sub>S<sub>3</sub>) and Ga<sub>2</sub>S<sub>3</sub> (100 mol% Ga<sub>2</sub>S<sub>3</sub>). It has already been reported that alkaline earth thiogallates have high melting points of > 1150°C which is too high to utilize quartz ampoules for the crystal growth. One of the methods to overcome this difficulty is the single-crystal growth using a self-flux, whereby single crystals can be grown at temperatures lower than a melting point.

In the processes of constructing the phase diagrams, the melting points of CaGa<sub>2</sub>S<sub>4</sub> and SrGa<sub>2</sub>S<sub>4</sub> have been exactly determined as 1132°C and 1230°C, respectively. The former value is low enough to use a quartz ampoule for the crystal growth. Thus, we try to grow single crystals of CaGa<sub>2</sub>S<sub>4</sub> by the melt method using a vacuum-sealed quartz ampoule. However, in the case of SrGa<sub>2</sub>S<sub>4</sub>, the melting point is too high to use quartz, and the flux method (Ga<sub>2</sub>S<sub>3</sub> is used as a flux) should be adopted instead. In this case, even if a conventional furnace with an appropriate temperature gradient is used, compositional deviation may take place along the growing direction, and special care should be taken to keep the homogeneity of the Ce<sup>3+</sup> concentration in the growing process. Here, for simplicity, we confine ourselves only to CaGa<sub>2</sub>S<sub>4</sub> and describe its crystal growth in detail together with its optical absorption and photoluminescence (PL).

A single, transparent and colorless crystal of CaGa<sub>2</sub>S<sub>4</sub> has been successfully grown, and Ce<sup>3+</sup> doping has also been carried out [4]. However, the resultant crystals contained many voids and cracks. In addition, as the amount of Ce<sup>3+</sup> content was increased, the crystallinity became worse and if the content was increased more than 1.0 wt%, crystals were colored too blackish to be used for optical measurement.

In order to improve the crystallinity of undoped CaGa<sub>2</sub>S<sub>4</sub>, we searched for the proper temperature and the growth speed for single-crystal growth of CaGa<sub>2</sub>S<sub>4</sub>. In what follows, we report the results ever obtained and also the relation between doping

content and crystallinity as well as the optical absorption and PL of the resultant crystals.

## 2. Crystal growth of CaGa<sub>2</sub>S<sub>4</sub> in a horizontal furnace

Two elements of Ca, S and a compound of Ga<sub>2</sub>S<sub>3</sub> were weighed approximately to 7 g. The mixtures of Ca + Ga<sub>2</sub>S<sub>3</sub> and sulfur element were separately set in both sides of a quartz ampoule of 13 mm  $\phi$   $\times$  300 mm. The Ca + Ga<sub>2</sub>S<sub>3</sub> side was controlled at 400°C and the sulfur side at 300°C for 24 h. After this treatment, the precursor was synthesized by heating the whole ampoule up to 1120°C. The details were described in a previous paper [4]. The precursor thus prepared was divided into two or three parts. Each part was poured into a respective carbon boat and sealed in another ampoule and was grown under various conditions described below. A carbon boat was used for preventing reaction between an ampoule and the precursor at high temperature. Growth speeds were chosen at 0.5 cm/h and 0.25 cm/h. Three solidifying temperatures, 1130°C, 1132°C (melting point) and 1135°C were adopted to grow single crystals. The melts were kept for 1 h at these temperatures, respectively, and cooled down at each speed in a horizontal Bridgman furnace. Thus six different types of samples were grown. The solidifying temperature 1135°C, a little higher than the melting point (1132°C) together with the slower growth speed gave the best result of all. Temperature much higher than the melting point resulted in many cracks in the grown crystals. Fig. 1(a) shows a photograph of a product grown at a speed of 0.25 cm/h at 1132°C. It was approximately 2 cm in length and yellow in color. As shown in this figure, it was like a sintered polycrystal composed of small grains. Fig. 1(b) shows a photograph of a crystal prepared at 0.25 cm/h at 1135°C. In this case, the crystal was transparent for the whole length. The grain size of the resultant crystals was plotted against solidifying temperatures at two growing speeds (Fig. 2). It was estimated by measuring the maximum diameter of single grains in a crystal under an optical microscope. As the maximum temperature of the

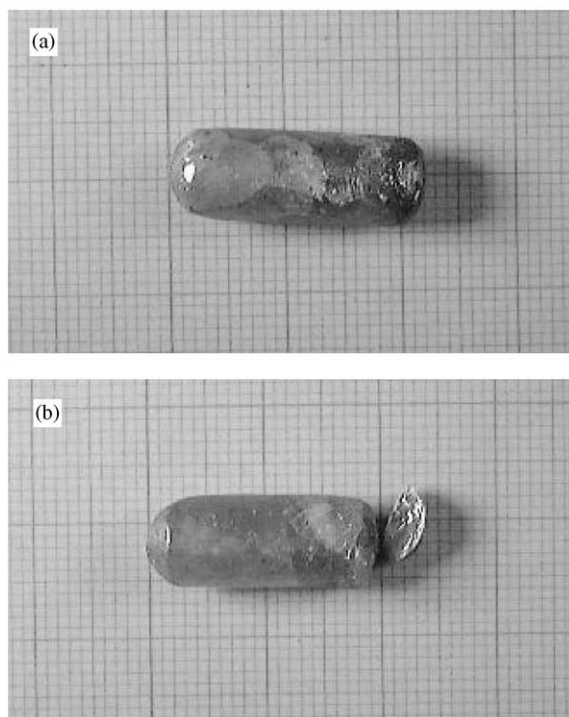


Fig. 1. Photographs of single crystals grown at a speed of 0.25 cm/h from: (a) 1132°C and (b) 1135°C.

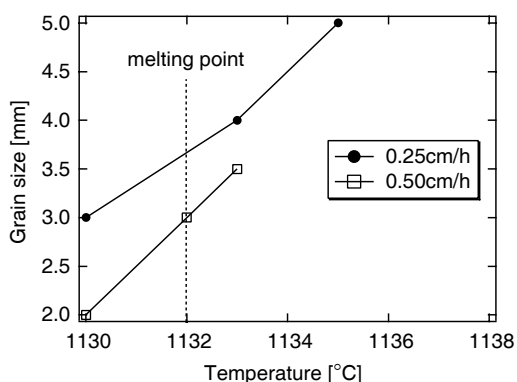


Fig. 2. Maximum grain sizes in crystals grown from different temperature vs. the maximum temperature of each melt.

melt was increased and the growth speed was slowed, a grain with larger size was obtained. Fig. 3 shows the relationship between the lengths of single-crystal domains along the growth direction and solidifying temperatures. At a speed of

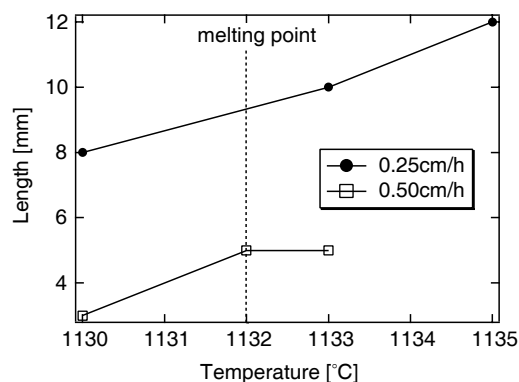


Fig. 3. Variation of the length of a single domain in a grown crystal along the growth direction vs. the maximum temperature of each melt.

0.25 cm/h, the size of a single domain became larger with increasing temperature. On the other hand, those of the single crystals grown at 0.50 cm/h did not show remarkable variations with solidifying temperature. In conclusion, the size of a single domain in a grown crystal along the growth direction was determined mainly by the growth speed. The crystals prepared by this method were a little opaque and yellowish, while the crystals grown without a carbon boat was transparent and colorless as reported in a previous paper [4]. To investigate the origin of the yellowish color of the crystals grown in a carbon boat, optical absorption spectra were measured and the results are discussed in the next section.

### 3. Absorption spectra of a crystal grown in a carbon or a quartz boat

Absorption spectra were measured using a deuterium lamp as a light source. Light from a monochromator (NALUMI RM-23-I) was transmitted through a sample attached to a cold head of a cryostat and detected by a photomultiplier (HAMAMATSU R562). Temperature was varied between 10 and 300 K. Fig. 4 shows light absorption spectra of two respective single crystals at a speed of 0.50 cm/h at 1135°C. One is grown in a carbon boat and the other in a quartz boat coated

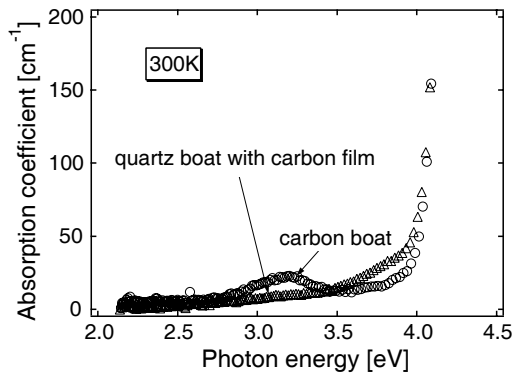


Fig. 4. Absorption spectra of crystals grown in a carbon boat and a quartz boat coated with carbon film.

with carbon film. The crystal grown in a quartz boat shows only the fundamental absorption. In contrast, an absorption band with a peak at 3.2 eV was observed in the crystal grown in a carbon boat. By measuring temperature variation of the absorption at 3.2 eV, it was found that the peak position, shape of the absorption spectrum showed almost no change with temperature. The origin of this absorption was not made clear at this stage, but was considered to be related with the impurities incorporated from a carbon boat.

Fig. 5 shows temperature variation of the band edge of an undoped crystal with temperature. The band edge was estimated by extrapolating the slope of the square of absorption coefficient against photon energy to zero absorption. From the temperature gradient  $> 100$  K, the temperature coefficient of the absorption band edge was estimated as  $1.2 \times 10^{-3}$  eV/K. The coefficient is almost the same as that of the ionic crystals such as AgCl, suggesting that the  $\text{CaGa}_2\text{S}_4$  crystal has a strong ionic character.

#### 4. Absorption spectra of $\text{Ce}^{3+}$ -doped crystals

In crystals doped with  $\text{Ce}^{3+}$ , absorption spectra were also observed. The crystals used in this measurement were grown in quartz boats. The concentration of  $\text{Ce}^{3+}$  was varied from 0.1 to 1.5 wt%. Absorption spectra of the crystals with

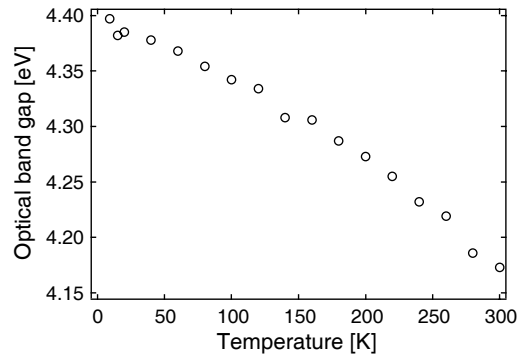


Fig. 5. Temperature variation of the band edge of an undoped crystal.

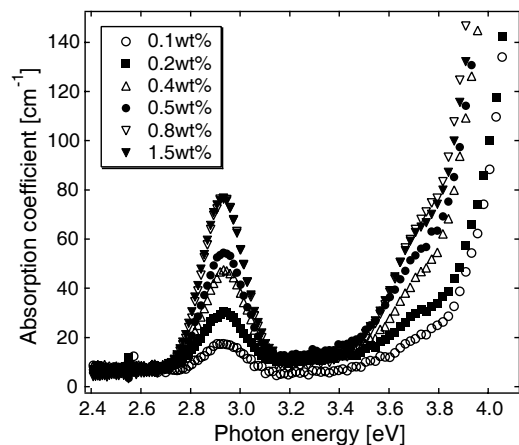


Fig. 6. Absorption spectra of crystals with various  $\text{Ce}^{3+}$  concentrations.

various  $\text{Ce}^{3+}$  concentration at room temperature are shown in Fig. 6. Two absorption bands were observed. One has a peak at 2.9 eV and the other appears as a shoulder near the band edge. The intensities of the absorption of the two bands increased with increasing  $\text{Ce}^{3+}$  concentration. The absorption band around 2.9 eV was already known to arise from  $\text{Ce}^{3+}$  and was attributed to the optical transition between 4f and 5d states. The 4f states of  $\text{Ce}^{3+}$  ions split into the spin-orbit pair consisting of  $^2F_{7/2}$  and  $^2F_{5/2}$ , while the upper 5d states split into an upper  $E_g$  and a lower  $T_{2g}$  due to the crystal field. The absorption around 2.9 eV is assigned to the transition from  $^2F_{7/2}$  to  $T_{2g}$ . The

absorption band appearing as a shoulder near the fundamental absorption edge was observed for the first time, thanks to the high quality of the crystal used in this experiment. The new band is considered to be the transition from  ${}^2F_{7/2}$  to  $E_g$ . Now, the difference between  $E_g$  and  $T_{2g}$  can be estimated as 0.8 eV.

## 5. Conclusion

We have grown single crystals of  $\text{CaGa}_2\text{S}_4$  under various conditions. A slower growth speed and higher temperature of the melt were found to be effective in growing a large single crystal. The growth speed was also a key factor to make a large single domain along the growth direction. Although a carbon boat was used to avoid reaction of a quartz ampoule with the crystal, the resultant crystal became a little opaque and yellowish, giving rise to a new absorption band around 3.2 eV. The origin of the absorption is believed to be due to the contaminations from a carbon boat.

Absorption spectra were measured for  $\text{Ce}^{3+}$ -doped crystals grown in quartz boats and two absorptions were found at 2.9 eV and near the band edge. As a result, the energy separation between  $T_{2g}$  and  $E_g$  of the 5d multiplets of  $\text{Ce}^{3+}$  was estimated as 0.8 eV for the first time.

## Acknowledgements

This work was partially supported by the Research Grant from Nihon University.

## References

- [1] W.A. Barrow, R.C. Coover, E. Dickey, C.N. King, C. Laakso, S.S. Sun, R.T. Tuenge, R. Wetross, J. Kane, SID Int. Symp. Dig. (1993) 761.
- [2] S. Iida, T. Matsumoto, N.T. Mamedov, Y. Maruyama, A.I. Bairamov, B.G. Tagiev, O.B. Tagiev, R.B. Dzhabbarov, Jpn. J. Appl. Phys. 36 (1997) L857.
- [3] C. Komatsu, T. Takizawa, J. Crystal Growth 210 (2000) 677.
- [4] C. Komatsu-Hidaka, T. Takizawa, J. Crystal Growth 222–223 (2001) 574.

## Thermal Analysis of Chemical Reaction Processes of Chalcopyrite Compound Semiconductors

Hiroaki MATSUSHITA and Takeo TAKIZAWA<sup>1</sup>

*Department of Material Science and Technology, School of High-Technology for Human Welfare, Tokai University,  
317 Nishino, Numazu-city, Shizuoka 410-0395, Japan*

<sup>1</sup>*Department of Physics, College of Humanities and Sciences, Nihon University,  
3-25-40 Sakurajosui, Setagaya-ku, Tokyo 156-0045, Japan*

In order to overcome the difficulties in growing CuInSe<sub>2</sub>, CuGaSe<sub>2</sub> and CuInS<sub>2</sub> bulk single crystals of high quality, we have investigated the chemical reaction until a single phase is formed, using the differential thermal analysis and X-ray diffraction, and also the variation of the solidifying points by varying vapor pressures of VI group element. From the results, it is shown that the formation of lattice defects and heterogeneous products will be greatly suppressed if the selenization or sulfurization method of a CuIn phase is adopted at temperatures higher than 600 or 700°C to grow single crystals of CuInSe<sub>2</sub> or CuInS<sub>2</sub>, respectively. On the other hand, the selenization of the CuGa phase is not necessarily required for the CuGaSe<sub>2</sub> single phase. A chemical reaction between Cu selenides and Ga at higher temperature than 900°C is effective in this case. In addition, the solidifying points are found to be sensitive to the VI vapor pressure. The single crystals of high quality can be grown by optimizing the temperature profiles under the respective Se vapor pressures.

**KEYWORDS:** chalcopyrite single phase, chemical reaction process, intermediate product, DTA, XRD, VI vapor pressure

### 1. Introduction

CuInSe<sub>2</sub>, CuGaSe<sub>2</sub> and CuInS<sub>2</sub>, the promising materials for solar cells have been investigated by many researchers. However, the fundamental properties of lattice defects and impurities in the bulk crystals, which are important to understand the electrical and optical properties of these thin films, have not been fully investigated. One of the obstacles is caused by the uncontrollability of the physical properties, arising from the fact that they essentially consist of three elements. Actually, each compositional atom has possibility of occupying various lattice sites and even generating a vacancy and/or an interstitial in the case of growing those crystals, which inevitably lead to difficulties in growing a bulk single crystal of high quality. In addition, there are always several paths to obtain precursors of ternary compounds.

In order to overcome the difficulties above mentioned, we have investigated the chemical reaction until a single phase is formed, using the differential thermal analysis (DTA) and X-ray diffraction (XRD), and also the variation of the solidifying points under various vapor pressures of VI group element. Finally, we design the most suitable preparation method for those compounds on the basis of these thermal analyses.

### 2. Analysis Method of Chemical Reaction Processes

DTA was employed to observe the phase transition and chemical reaction as shown in a previous work.<sup>1)</sup> The temperature difference between a sample and a reference material, i.e., DTA signal, is directly measured by thermocouples (CA). The temperatures of phase transition and chemical reaction were determined from the extrapolated onset of DTA peaks in the heating and cooling process. DTA curves of elements, binary compounds, mixtures of elements and compounds were also measured and analyzed. The rate of heating and cooling was held constant at 2°C/min. DTA signals were corrected by the known melting points of Sn, Zn, Al, Ag and Cu metals, and the systematic error of the observed temperature was confirmed to be 2°C at the most.

The products synthesized after DTA were identified based on powder X-ray diffraction (XRD) at room temperature using the Cu-K $\alpha$  characteristic line (1.5405Å). The reference materials used for comparison of XRD patterns were naturally prepared during DTA. XRD patterns were also compared with the JCPDS files.

An example of analysis in the case of Cu+In+2Se mixture is shown as follows. From powder XRD patterns of the products synthesized in a Cu+In+2Se mixture at temperatures up to 300, 600, 700 and 1040°C,<sup>1)</sup> it was found that the following products are formed at the respective temperatures.

- (1) In<sub>2</sub>Se, Cu<sub>3</sub>Se<sub>2</sub>, In<sub>6</sub>Se<sub>7</sub>, Cu<sub>7</sub>Se<sub>4</sub> and Se at 300°C.
- (2) Cu<sub>7</sub>Se<sub>4</sub>, InSe, Cu<sub>3</sub>Se<sub>2</sub>, In<sub>2</sub>Se<sub>3</sub>, CuInSe<sub>2</sub>, In<sub>6</sub>Se<sub>7</sub> and Se at 600°C.
- (3) Cu<sub>7</sub>Se<sub>4</sub>, InSe, Cu<sub>3</sub>Se<sub>2</sub>, CuInSe<sub>2</sub>, In<sub>6</sub>Se<sub>7</sub>, In<sub>2</sub>Se<sub>3</sub> and Se at 700°C.
- (4) CuInSe<sub>2</sub> at 1040°C.

Figures 1(a) and (b) show DTA curves of a Cu+In+2Se mixture in the heating process, where DTA curves of elements and compounds are also shown for comparison. Here, DTA peaks cannot be observed in the following cases of reaction.

- (1) Selenium atoms enter slowly into a mother crystal with increasing temperature.
- (2) A solid dissolves slowly in a liquid with increasing temperature.
- (3) A solid-phase reaction occurs over a long time scale.

From the comparison of the DTA curve of a Cu+In+2Se mixture with that of by-products, the origins of DTA peaks are identified as follows. A few DTA peaks from 100 to 250°C are ascribed to the melting points of indium and selenium and the metal-semiconductor phase transition of selenium.

- (1) An explosive exothermic reaction at 250°C is ascribed to the selenization reaction of indium forming In<sub>2</sub>Se and In<sub>6</sub>Se<sub>7</sub> compounds.
- (2) The broad DTA peak with an exothermic reaction at 280 to 420°C is ascribed to the selenization reaction of copper forming Cu<sub>3</sub>Se<sub>2</sub> and Cu<sub>7</sub>Se<sub>4</sub> compounds.
- (3) A weak endothermic reaction at ~500°C is ascribed to the

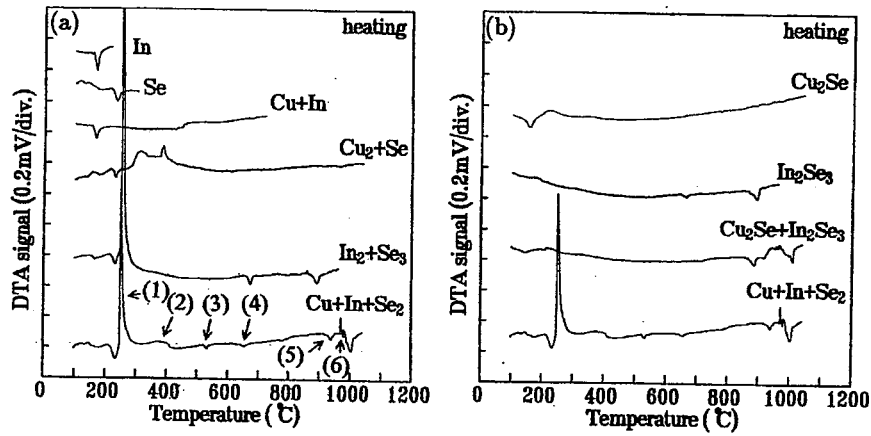


Fig. 1. (a) DTA curves of In, Se, Cu+In, 2Cu+Se, 2In+3Se and Cu+In+2Se mixtures obtained during the heating process, and (b) DTA curves of Cu<sub>2</sub>Se, In<sub>2</sub>Se<sub>3</sub> compounds, Cu<sub>2</sub>Se+In<sub>2</sub>Se<sub>3</sub> and Cu+In+2Se mixtures in the heating process.<sup>1)</sup>

solid-liquid phase transition of In<sub>2</sub>Se compound.<sup>2)</sup> (4) A weak endothermic reaction at ~650°C is similar to those of the In<sub>2</sub>Se<sub>3</sub> compound and the 2In+3Se mixture. The In<sub>2</sub>Se<sub>3</sub> compound has a transition point at ~650°C, and InSe and In<sub>6</sub>Se<sub>7</sub> compounds also have melting points at ~650°C.<sup>2)</sup> Therefore, this reaction is due to the phase transition or decomposition of In<sub>2</sub>Se<sub>3</sub> compound and/or the melting of InSe and In<sub>6</sub>Se<sub>7</sub> compounds. (5) An endothermic reaction near 900°C is related to the melting point of In<sub>2</sub>Se<sub>3</sub> compound. (6) A few DTA peaks with exothermic reaction just below the melting point of CuInSe<sub>2</sub> are ascribed to the chemical reactions between Cu<sub>2-x</sub>Se and In<sub>2</sub>Se<sub>3-x</sub> compounds, whereby a CuInSe<sub>2</sub> phase is formed.

We also identify the origins of DTA signals of CuIn+2Se, Cu+Ga+2Se, CuGa+2Se, Cu+In+2S and CuIn+2S mixtures by the method above-mentioned by comparison of the DTA curves with XRD data.<sup>1,3,4)</sup>

### 3. Results and Discussion

#### 3.1 Chemical reaction process forming CuInSe<sub>2</sub> phase

On the basis of DTA and XRD data,<sup>1)</sup> it was confirmed that CuInSe<sub>2</sub> compound has a phase transition point from

chalcopyrite to sphalerite structure<sup>5,6)</sup> at 815°C and a melting point at 996°C, and we constructed schematic diagrams of the chemical reaction process for a Cu+In+2Se and CuIn+2Se mixtures as shown in Fig. 2.

The origins of DTA peaks are explained in the case of Cu+In+2Se. We do not go into detail for phase transitions from 100 to 250°C, because these are already described. The resultant chemical reactions and phase transitions are summarized as follows.

- (1) In, Se → In<sub>2</sub>Se, In<sub>6</sub>Se<sub>7</sub> at 250 °C.
- (2) Cu, Se → Cu<sub>3</sub>Se<sub>2</sub>, Cu<sub>7</sub>Se<sub>4</sub> at 280 to 420°C.
- (3) In<sub>2</sub>Se: solid → liquid at ~500°C.
- (4) InSe, In<sub>6</sub>Se<sub>7</sub>: solid → liquid at ~600°C.
- (5) In<sub>2</sub>Se<sub>3</sub>: solid → liquid at about 900°C.
- (6) Cu<sub>7</sub>Se<sub>4</sub>, InSe, In<sub>2</sub>Se<sub>3</sub> → CuInSe<sub>2</sub> above 950°C.
- (7) CuInSe<sub>2</sub>(sphalerite): solid → liquid at 996°C.

It was found that the amounts of the In<sub>2</sub>Se<sub>3-x</sub> compounds with Se-rich contents increased gradually with increasing temperature.<sup>1)</sup> As the quantities of Cu<sub>3</sub>Se<sub>2</sub> and In<sub>6</sub>Se<sub>7</sub> compounds decrease somewhat with increasing temperature, CuInSe<sub>2</sub> compound is already formed below 950°C through the following solid-phase reaction

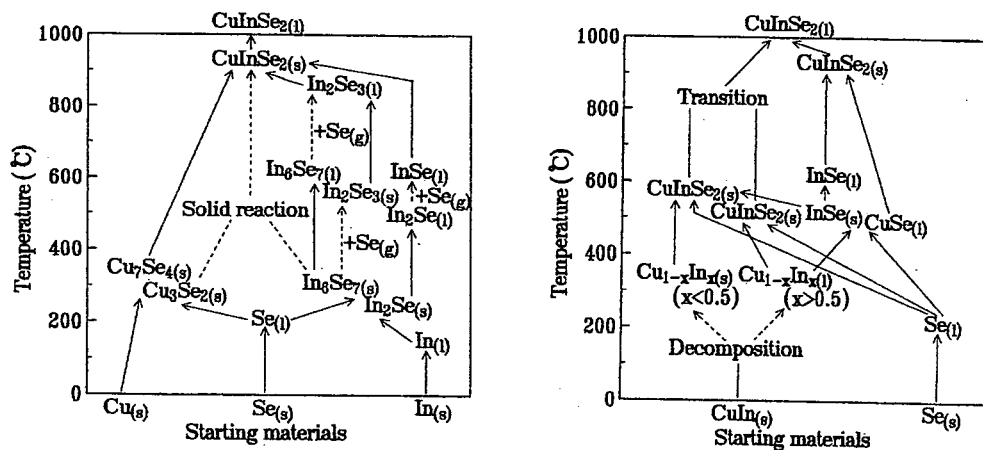
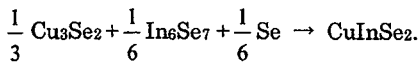
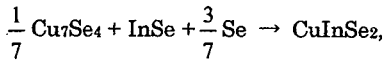
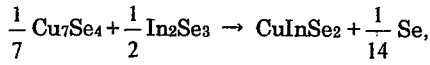


Fig. 2. Schematic diagram of chemical reaction process from Cu+In+2Se and CuIn+2Se mixtures. The suffix symbol of (s), (l) or (g) denotes the solid, liquid or gas condition, respectively. The solid line denotes a chemical reaction and the dashed line denotes a reaction in a long time scale.<sup>1)</sup>



However, only a little  $\text{CuInSe}_2$  compound was formed by this reaction, since DTA peaks could hardly be detected at  $815^\circ\text{C}$ .<sup>1)</sup> Furthermore, most of the  $\text{CuInSe}_2$  compound was formed above  $950^\circ\text{C}$  by the following reactions

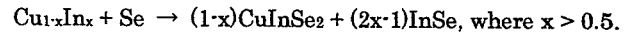


which suggests why the quantities of  $\text{Cu}_7\text{Se}_4$ ,  $\text{In}_2\text{Se}_3$  and  $\text{InSe}$  compounds did not decrease with increasing temperature. Here, it is known that a few exothermic reactions just below the melting point of  $\text{CuInSe}_2$  did not necessarily occur.<sup>1)</sup> In other words, the solid phases of  $\text{Cu}_{2-x}\text{Se}$  and copper sometimes remain at  $1040^\circ\text{C}$ , and the  $\text{CuInSe}_2$  phase was precipitated from an In-rich liquid phase in the cooling process.

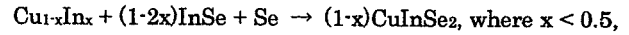
In the case of  $\text{CuIn}+2\text{Se}$  mixture, a few phase transitions from 100 to  $500^\circ\text{C}$  are ascribed to the transition or decomposition of  $\text{CuIn}$  alloy and the melting and metal to semiconductor phase transition of selenium. On the base of the phase diagram of the  $\text{Cu-In}$  system,<sup>7)</sup> it should be remembered that  $\text{CuIn}$  alloy decomposes into Cu-rich  $\text{Cu-In}$  solid and In-rich  $\text{Cu-In}$  liquid with increasing temperature. The resultant chemical reactions and phase transitions are summarized as follows.

- (1)  $\text{Cu}_{1-x}\text{In}_x$  ( $x > 0.5$ ),  $\text{Se} \rightarrow \text{CuInSe}_2$ ,  $\text{InSe}$  at  $520^\circ\text{C}$ .
- (2)  $\text{Cu}_{1-x}\text{In}_x$  ( $x < 0.5$ ),  $\text{Se}$ ,  $\text{InSe} \rightarrow \text{CuInSe}_2$  at  $575^\circ\text{C}$ .
- (3)  $\text{InSe}$ : solid  $\rightarrow$  liquid at about  $650^\circ\text{C}$ .
- (4)  $\text{CuInSe}_2$ : chalcopyrite  $\rightarrow$  sphalerite at about  $810^\circ\text{C}$ .
- (5)  $\text{CuSe}$ ,  $\text{InSe} \rightarrow \text{CuInSe}_2$  above  $950^\circ\text{C}$ .
- (6)  $\text{CuInSe}_2$ (sphalerite): solid  $\rightarrow$  liquid at  $996^\circ\text{C}$ .

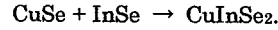
By the selenization reaction of some In-rich  $\text{Cu-In}$  liquid at  $520^\circ\text{C}$ , some  $\text{CuInSe}_2$  and  $\text{InSe}$  compounds are formed by the following reaction



In addition, the formation of  $\text{CuInSe}_2$  compound according to the following reaction



has already been almost completed by  $600^\circ\text{C}$ , since the quantity of  $\text{CuInSe}_2$  compound increases and that of  $\text{InSe}$  compound decreases with increasing temperature from  $550$  to  $650^\circ\text{C}$ . Furthermore, some  $\text{CuInSe}_2$  compound is formed above  $\sim 950^\circ\text{C}$  by the following reaction



Therefore, it is concluded that if the selenization of  $\text{CuIn}$  phase is adopted at temperatures higher than  $600^\circ\text{C}$ , the formation of  $\text{CuSe}$  and  $\text{InSe}$  compounds will be greatly suppressed.

### 3.2 Chemical reaction process forming $\text{CuGaSe}_2$ phase

We have attempted the growth of  $\text{CuGaSe}_2$  bulk single crystals by the same selenization method as  $\text{CuInSe}_2$ . However, we have not still succeeded in growing the crystals good enough to measure the Hall effect without noisy signals. To investigate the reason why high-quality  $\text{CuGaSe}_2$  single crystals cannot be grown by the selenization method, we first analyzed the chemical reaction process of a  $\text{CuGa}+2\text{Se}$  mixture. On the basis of DTA and XRD data,<sup>3)</sup> the melting point and phase transition were observed at  $1105^\circ\text{C}$  and about  $1060^\circ\text{C}$ , respectively, and we constructed schematic diagrams of the chemical reaction process from a  $\text{Cu}+\text{Ga}+2\text{Se}$  and  $\text{CuGa}+2\text{Se}$  mixtures as shown in Fig. 3.

In the case of  $\text{CuGa}+2\text{Se}$  mixture, the phase transition and melting points of selenium were observed at about  $130$  and  $220^\circ\text{C}$ , respectively, and the transition or decomposition of the  $\text{CuGa}$  alloy was observed at about  $250^\circ\text{C}$ . It should be remembered on the base of the phase diagram of the  $\text{Cu-Ga}$  system<sup>7)</sup> that the  $\text{CuGa}$  alloy decomposes into Cu-rich  $\text{Cu-Ga}$  solid and Ga-rich  $\text{Cu-Ga}$  liquid with increasing temperature. The resultant chemical reactions and phase transitions are

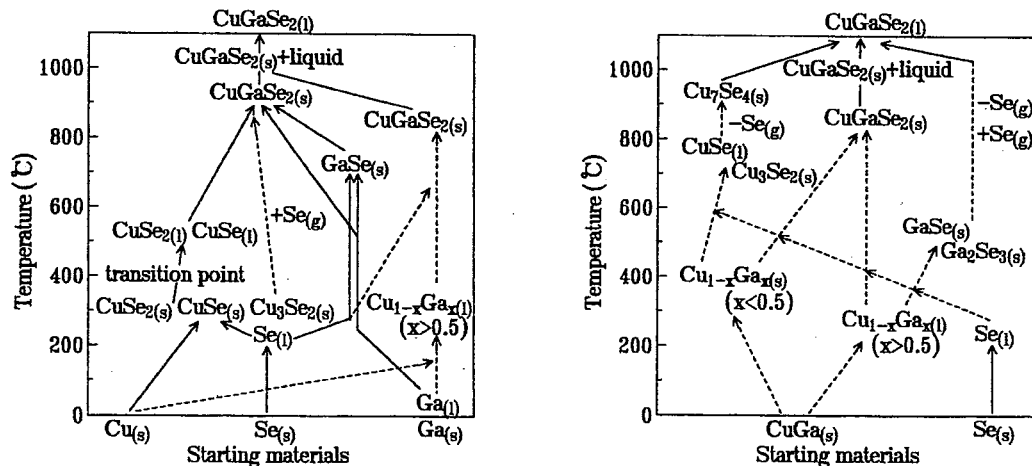
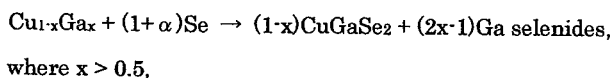


Fig. 3. Schematic diagram of chemical reaction process from  $\text{Cu}+\text{Ga}+2\text{Se}$  and  $\text{CuGa}+2\text{Se}$  mixtures. The suffix symbol of (s), (l) or (g) denotes the solid, liquid or gas condition, respectively. The solid line denotes a chemical reaction and the dashed line denotes a reaction in a long time scale.<sup>3)</sup>

summarized as follows.

- (1) CuSe: solid  $\rightarrow$  liquid at  $\sim 550$  °C.
- (2) Cu-Ga alloy, Se  $\rightarrow$  GaSe, Ga<sub>2</sub>Se<sub>3</sub>, CuSe at 550 to 750°C.
- (3) Ga and Cu selenides: decomposition and/or selenization at  $\sim 800$  and  $\sim 900$ °C.
- (4) CuGaSe<sub>2</sub>(chalcopyrite)  $\rightarrow$  CuGaSe<sub>2</sub>(sphalerite)+liquid at 1060°C.
- (5) Cu<sub>7</sub>Se<sub>4</sub>, GaSe, Ga<sub>2</sub>Se<sub>3</sub>  $\rightarrow$  CuGaSe<sub>2</sub>(sphalerite) above 1080°C.
- (6) CuGaSe<sub>2</sub>(sphalerite): solid  $\rightarrow$  liquid at 1105°C.

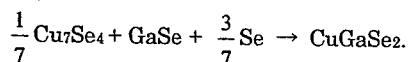
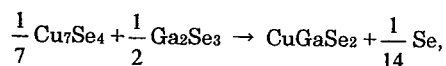
The CuGaSe<sub>2</sub> phase may have already been made below 950°C through the following liquid phase reactions between the Cu-Ga and Se phases, where the CuGa alloy decomposes into two phases with increasing temperature,



Here, about a half of the CuGaSe<sub>2</sub> phase was formed by these reactions being indicated from the following two results.

- (1) XRD intensities of the CuGaSe<sub>2</sub> phase became about a half after heating up to 950°C in comparison to those up to 1150°C.
- (2) The heat of transition of a CuGa+2Se mixture at 1060°C was smaller than that of a grown CuGaSe<sub>2</sub>.

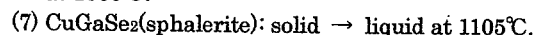
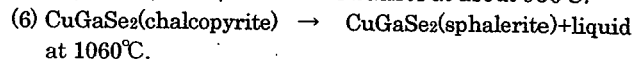
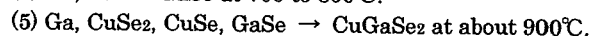
The CuSe and GaSe phases decreases, and the Cu<sub>7</sub>Se<sub>4</sub> and Ga<sub>2</sub>Se<sub>3</sub> phases increases gradually with increasing temperature in the 800 to 900°C range. Thus, Se atoms are removed from CuSe and absorbed into to GaSe in this temperature range. The remaining of the CuGaSe<sub>2</sub> phase was formed at above 1080°C by the following two reactions,



This explains why the Cu<sub>7</sub>Se<sub>4</sub>, Ga<sub>2</sub>Se<sub>3</sub> and GaSe phases exist at 950°C but the Cu<sub>3</sub>Se<sub>2</sub> phase does little.<sup>3)</sup> The heat of fusion at about 1100°C of a CuGa+2Se mixture is smaller than that of a grown CuGaSe<sub>2</sub>.<sup>3)</sup> Therefore, some heterogeneous phases, for instance, Cu selenides having melting points higher than that of CuGaSe<sub>2</sub>, may be included in the mother crystal in the case of a CuGa+2Se mixture. In other words, CuGaSe<sub>2</sub> are not perfectly formed at about 1100°C.

From the results of CuGaSe<sub>2</sub> formed from a CuGa+2Se mixture, the selenization of the CuGa alloy is not necessarily needed for the CuGaSe<sub>2</sub> single phase in contrast to the case of CuInSe<sub>2</sub>. To search for another preparation method except for the selenization of the CuGa alloy, we analyzed the chemical reaction process of Cu+Ga+2Se mixture. It is well known that CuSe<sub>2</sub> and CuSe compounds have a transition point at about 380°C and a melting point at about 530°C.<sup>8)</sup> The chemical reactions and phase transitions are summarized as follows.

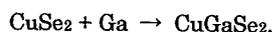
- (1) Cu, Se  $\rightarrow$  CuSe<sub>2</sub>, CuSe, Cu<sub>3</sub>Se<sub>2</sub> at 280 to 380°C.
- (2) CuSe<sub>2</sub>, CuSe: solid phase transition at about 380°C.
- (3) CuSe<sub>2</sub>, CuSe: solid  $\rightarrow$  liquid at about 530°C.



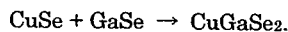
The CuSe<sub>2</sub> (including CuSe) phase increases and the Cu<sub>3</sub>Se<sub>2</sub> phase decreases, i.e., Se atoms are absorbed in the Cu<sub>3</sub>Se<sub>2</sub> phase, with increasing temperature in the 600 to 850°C range. Judging from XRD intensities of the CuGaSe<sub>2</sub> phase after heating up to 850°C,<sup>3)</sup> a small amount of CuGaSe<sub>2</sub> phase (less than 10%) have already been formed below 900°C through the liquid phase reaction described as follows,



The heat of transition at 1060°C in a Cu+Ga+2Se mixture is in good agreement with that of the transition point from the chalcopyrite to (sphalerite+liquid) phase<sup>5,6)</sup> in the CuGaSe<sub>2</sub> compound. Hence, the CuGaSe<sub>2</sub> phase is completely formed by the exothermic reaction at about 900°C as follows,



The melting point of GaSe was confirmed to be  $\sim 950$ °C by DTA, but it was not observed in the DTA curve of a Cu+Ga+2Se mixture.<sup>3)</sup> Thus, we believe that the remnant GaSe phase was consumed gradually by the following reaction,

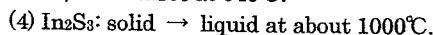
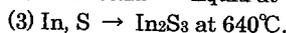
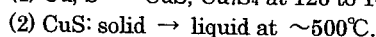
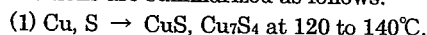


This may not be clearly distinguished because of the explosive reaction between CuSe<sub>2</sub> and Ga. In contrast to CuInSe<sub>2</sub>, it is considered that the CuGaSe<sub>2</sub> single phase is not formed by the selenization of the CuGa alloy, but the chemical reaction of three compositional elements (Cu+Ga+2Se mixture). The CuGaSe<sub>2</sub> phase is completely formed below 1060°C, since the heats of transition and fusion at about 1060 and 1100°C of a CuSe<sub>2</sub>+Ga mixture are in agreement with these of a grown CuGaSe<sub>2</sub>. It is expected that the chemical reaction between Cu selenides and Ga is one of the best preparation method for CuGaSe<sub>2</sub>.

### 3.3 Chemical reaction process forming CuInS<sub>2</sub> phase

Based on the thermal analysis of the CuInSe<sub>2</sub> single phase, we investigated whether high-quality CuInS<sub>2</sub> crystals are prepared by the sulfurization method or not. On the basis of DTA and XRD data,<sup>4)</sup> The melting point of CuInS<sub>2</sub> was observed at 1090°C, and the other two phase transitions, i.e., the sphalerite-chalcopyrite and hexagonal-sphalerite transitions<sup>5,6)</sup> were observed at 1050 and 980°C, respectively. We constructed schematic diagrams of the chemical reaction process from a Cu+In+2S and CuIn+2S mixtures as shown in Fig. 4, which resemble those in the case of CuInSe<sub>2</sub>.

In the case of Cu+In+2S mixture, the melting point of sulfur and indium are observed at about 120 and 150°C, respectively. The resultant chemical reactions and phase transitions are summarized as follows.



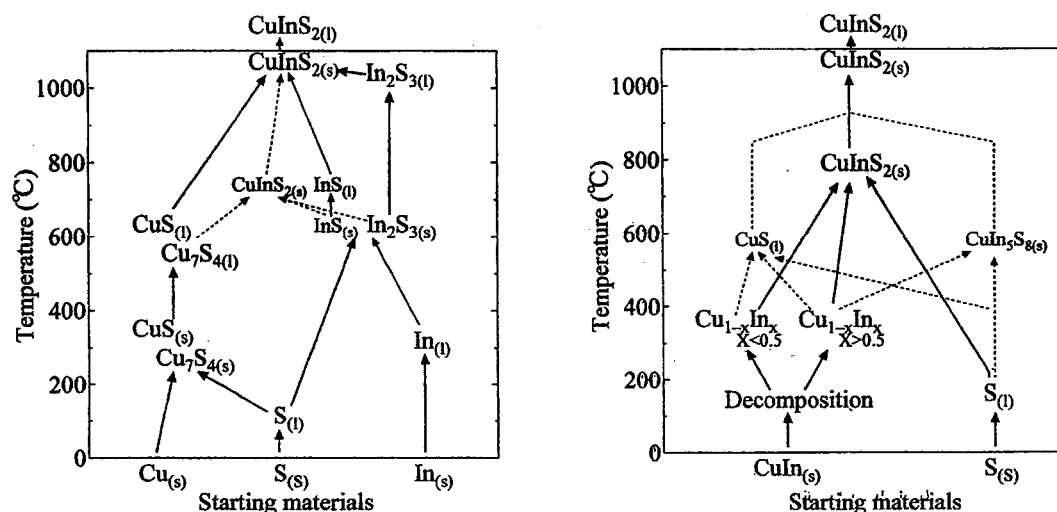


Fig. 4. Schematic diagram of chemical reaction process from Cu+In+2S and CuIn+2S mixtures. The suffix symbol of (s), (l) or (g) denotes the solid, liquid or gas condition, respectively. The solid line denotes a chemical reaction and the dashed line denotes a reaction in a long time scale.

(5)  $\text{Cu}_7\text{S}_4$ ,  $\text{CuS}$ ,  $\text{In}_2\text{S}_3 \rightarrow \text{CuInS}_2$  above  $1050^\circ\text{C}$ .

(6)  $\text{CuInSe}_2(\text{hexagonal})$ : solid  $\rightarrow$  liquid at  $1090^\circ\text{C}$ .

Most of the  $\text{CuInS}_2$  compound was formed below the melting point of  $\text{CuInS}_2$  by the reactions between  $\text{Cu}_{2-x}\text{S}$  and  $\text{In}_2\text{S}_{3-x}$  compounds though a part of  $\text{CuInS}_2$  compound may be already formed below  $750^\circ\text{C}$  through the solid phase reaction and/or by the sulfurization of indium at the same time. Considerable amount of heterogeneous phases, for instance, Cu sulfides having melting points higher than that of  $\text{CuInS}_2$ , may still exist together with the  $\text{CuInS}_2$  phase at about  $1100^\circ\text{C}$ .

In contrast to the above case, the XRD pattern of the products synthesized from a  $\text{CuIn}+2\text{S}$  mixture at  $750^\circ\text{C}$  showed that the  $\text{CuInS}_2$  compound is mainly formed below  $750^\circ\text{C}$  with a small inclusion of  $\text{CuS}$  and  $\text{CuIn}_5\text{S}_8$  phases.<sup>4)</sup> The melting of sulfur and the phase transition and/or decomposition of a  $\text{CuIn}$  alloy were observed at 100 to  $350^\circ\text{C}$ . It should be remembered that a  $\text{CuIn}$  alloy decomposes into a Cu-rich Cu-In solid and an In-rich Cu-In liquid with increasing temperature.<sup>7)</sup> The resultant chemical reactions and phase transitions are summarized as follows.

(1)  $\text{Cu}_{1-x}\text{In}_x$  ( $x > 0.5$ ),  $\text{S} \rightarrow \text{CuInS}_2$ ,  $\text{CuIn}_5\text{S}_8$ ,  $\text{CuS}$  at  $480^\circ\text{C}$ .

(2)  $\text{Cu}_{1-x}\text{In}_x$  ( $x < 0.5$ ),  $\text{S} \rightarrow \text{CuInS}_2$ ,  $\text{CuS}$  at  $700^\circ\text{C}$ .

(3)  $\text{CuInS}_2$ : chalcopyrite  $\rightarrow$  sphalerite at about  $980^\circ\text{C}$ .

(4)  $\text{CuInS}_2$ : sphalerite  $\rightarrow$  hexagonal at about  $1050^\circ\text{C}$ .

(5)  $\text{CuInS}_2(\text{hexagonal})$ : solid  $\rightarrow$  liquid at  $1090^\circ\text{C}$ .

The explosive exothermic reaction at 480 and  $700^\circ\text{C}$  is ascribed to the sulfurization of the Cu-In phase, where the  $\text{CuInS}_2$  compound is formed. These also lead to the formation of some  $\text{CuIn}_5\text{S}_8$  as well as a little amount of  $\text{CuS}$  may be formed at the same time. It is concluded that the formation of  $\text{CuS}$  and  $\text{CuIn}_5\text{S}_8$  compounds will be greatly suppressed, if the sulfurization of  $\text{CuIn}$  phase is achieved at temperatures higher than  $700^\circ\text{C}$ .

### 3.4 Effect on the solidifying points of vapor pressure of VI group element

The Se vapor pressure could to some extent control the Se content in  $\text{CuInSe}_2$  crystals,<sup>9-11)</sup> and it is known that the

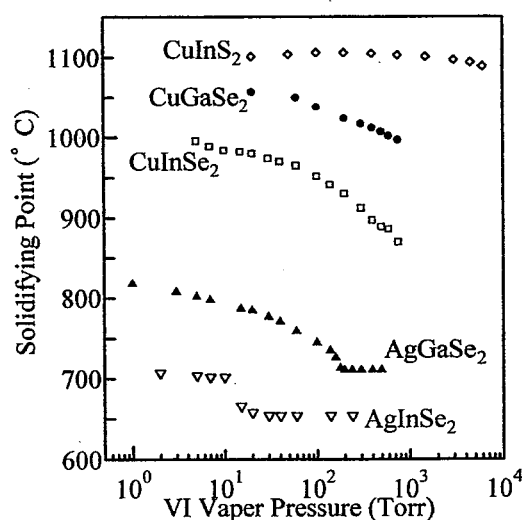


Fig. 5. The solidifying points of  $\text{CuGaSe}_2$ ,  $\text{CuInSe}_2$ ,  $\text{AgGaSe}_2$ ,  $\text{AgInSe}_2$  and  $\text{CuInS}_2$  as a function of VI vapor pressure.<sup>4,13,14)</sup>

compositional deviation of Se from stoichiometry is effective to the solidifying point of  $\text{CuInSe}_2$ .<sup>12)</sup> To grow high-quality single crystals under controlling Se vapor pressure, it becomes essential to investigate the Se vapor pressure dependence of the solidifying points. The DTA under controlling vapor pressure of VI element was used as described in previous papers.<sup>13,14)</sup> Figure 5 shows the VI vapor pressure dependence of the solidifying points of  $\text{CuInSe}_2$ ,  $\text{CuGaSe}_2$ ,  $\text{AgGaSe}_2$ ,  $\text{AgInSe}_2$  and  $\text{CuInS}_2$  compounds.

The solidifying point of  $\text{CuInSe}_2$  decreases by about  $130^\circ\text{C}$  with increasing the Se vapor pressure up to 760 Torr. The phase transition point from chalcopyrite to sphalerite structure is known to decrease down to about  $800^\circ\text{C}$  from the pseudo-binary phase diagram of  $(\text{CuIn})\text{-}2\text{Se}$  system.<sup>14)</sup> The transition point was found to be almost fixed at  $\sim 820^\circ\text{C}$  with varying the Se vapor pressure.<sup>13)</sup> Thus, the compositional deviation from stoichiometry is not so great as to produce the heterogeneous phases in the  $\text{CuInSe}_2$  phase under 760 Torr of Se vapor pressure. That is, the variation of the solidifying

point is mostly due to the Se vapor pressure. The solidifying point without applying Se vapor pressure is 996°C in good agreement with that of 5 Torr. Thus, CuInSe<sub>2</sub> crystals grown under applying the Se vapor pressure more than 5 Torr have Se-rich compositions, resulting in the p-type conduction. On the other hand, the crystals grown under less than 5 Torr may have the (CuIn)-rich compositions. This can be explained by the facts that the Se-poor crystals grown under low Se vapor pressures (2~7 Torr) showed the n-type conduction and contained heterogeneous phases.<sup>10,11</sup> The Hall effect at low temperature of the crystals grown under applying more than 50 Torr could not be measured owing to noisy signals.<sup>10</sup> The reason is that the temperature width of the temperature gradient zones of our growing furnace<sup>10</sup> deviated the solidifying point when the Se vapor pressure more than 50 Torr was applied, so that a good crystal could not be obtained. Thus, we should optimize the temperature width of the temperature gradient zones under the respective Se vapor pressures.

The melting and transition points of CuGaSe<sub>2</sub> were observed at 1105 °C and 1055 °C, which are ascribed to CuGaSe<sub>2</sub> (sphalerite): solid → liquid and CuGaSe<sub>2</sub> (chalcopyrite) → CuGaSe<sub>2</sub> (sphalerite) + liquid, respectively. The solidifying point decreases by about 100 °C with increasing the Se vapor pressure up to 760 Torr. The transition point was found to disappear above 300 Torr. Consequently, it might be possible to precipitate the CuGaSe<sub>2</sub> chalcopyrite single phase under the higher Se vapor pressure. On the basis the phase diagram of the CuGa<sub>1-x</sub>In<sub>x</sub>Se<sub>2</sub> system without applying Se vapor and under applying typical Se vapor pressures,<sup>15</sup> the solidus and liquidus points of the whole system were found to decrease more than 100°C with increasing Se vapor pressure up to 760 Torr, and the temperature zone of the sphalerite + liquid phase narrowed in the region of same pressure. The reason is that the transition point of CuInSe<sub>2</sub> compound is almost independent of the Se vapor pressure, while the transition point of CuGaSe<sub>2</sub> compound is found to depend on the Se vapor pressure.

The AgGaSe<sub>2</sub> compound has the solidifying point at 850°C but no phase transition point was observed. The solidifying point of AgGaSe<sub>2</sub> decreases by about 140°C with increasing the Se vapor pressure up to 200 Torr but keeps a constant value of about 710°C above 200 Torr. Based on the phase diagram of the Ag<sub>2</sub>Se-Ga<sub>2</sub>Se<sub>3</sub> system,<sup>16</sup> it is expected that the phase transition of about 710°C is due to the precipitation of the Ag<sub>2</sub>Se phase from liquid phase. Therefore, it is necessary to apply a Se vapor pressure less than 200 Torr to form the AgGaSe<sub>2</sub> single phase.

The solidifying point of AgInSe<sub>2</sub> decreases with increasing the Se vapor pressure less than 20 Torr but keeps a constant value of about 655°C above 20 Torr. In contrast to CuInSe<sub>2</sub>, CuGaSe<sub>2</sub> and AgGaSe<sub>2</sub>, the difference in the DTA curves for the heating and cooling process above 10 Torr might be due to the decomposition of the liquid phase.<sup>13</sup> It may be recommended to apply a Se vapor pressure less than 10 Torr to form the AgInSe<sub>2</sub> single phase.

Finally, the melting point of CuInS<sub>2</sub> decreases by 17°C as S vapor pressure increases from 200 Torr to 8 atm. It shows a

maximum at 1106°C under a pressure between 100 and 200 Torr. The variation in the S vapor pressure from 20 Torr to 8 atm. does not cause such a great change in the melting points of AgGaSe<sub>2</sub> and AgInSe<sub>2</sub>. Two kinds of phase transition points were found at the almost fixed temperatures of 980 and 1050°C independent of S vapor pressure

#### 4. Conclusion

We should know the formation mechanisms, i.e., the chemical reaction process forming the single phase to grow single crystals of high quality. We investigated that of CuInSe<sub>2</sub>, CuGaSe<sub>2</sub> and CuInS<sub>2</sub> using differential thermal analysis and X-ray diffraction. The results give hints for the most suitable preparation method. If the selenization or sulfurization method of a CuIn phase is adopted at temperatures higher than 600 or 700 °C to grow single crystals of CuInSe<sub>2</sub> or CuInS<sub>2</sub>, respectively, the formation of lattice defects and heterogeneous products will be greatly suppressed. On the other hand, the selenization of the CuGa phase is not necessarily required for the CuGaSe<sub>2</sub> single phase. A chemical reaction between Cu selenides and Ga at higher temperature than 900°C is found to be effective in removing the heterogeneous phases in the growth of CuGaSe<sub>2</sub> single phase.

It is sometimes effective to grow bulk single crystals of selenides and sulfides by applying vapor pressure of VI group element. The solidifying points of CuInSe<sub>2</sub>, CuGaSe<sub>2</sub>, AgGaSe<sub>2</sub>, AgInSe<sub>2</sub> and CuInS<sub>2</sub> compounds were found to be sensitive to the VI vapor pressure. In the case of CuInSe<sub>2</sub> as an example, it was shown on the base of the phase diagram of CuIn<sub>2</sub>Se system that the single crystals of high quality can be grown by optimizing the temperature profiles under the respective Se vapor pressures.

#### References

- 1) H. Matsushita and T. Takizawa: Jpn. J. Appl. Phys. 34 (1995) 4699.
- 2) F. A. Shunk: *Second Supplement to the Constitution of Binary Alloys*, (McGraw-Hill, New York, 1969).
- 3) H. Matsushita, H. Jitsukawa and T. Takizawa: Jpn. J. Appl. Phys. 35 (1996) 3830.
- 4) H. Matsushita, T. Mihira and T. Takizawa: J. Cryst. Growth 197 (1999) 169.
- 5) H. Matsushita, S. Endo and T. Irie: Jpn. J. Appl. Phys. 30 (1991) 1181.
- 6) A. Zunger: Appl. Phys. Lett. 50 (1987) 164.
- 7) M. Hansen: *Constitution of Binary Alloys*, (McGraw-Hill, New York, 1958).
- 8) H. Rau and A. Rabenau: J. Solid State Chem. 1 (1970) 515.
- 9) H. Matsushita, S. Endo, T. Irie and H. Nakanishi: J. Cryst. Growth 128 (1993) 655.
- 10) H. Matsushita, T. Suzuki S. Endo and T. Irie: Jpn. J. Appl. Phys. 34 (1995) 3774.
- 11) H. Matsushita and T. Takizawa: J. Cryst. Growth 160 (1996) 71.
- 12) M. L. Fearheiley, Sol. Cell, 16 (1986) 91.
- 13) H. Matsushita, H. Jitsukawa and T. Takizawa: *Transactions of the Materials Research Society of Japan vol. 20* (1996) 715.
- 14) H. Matsushita and T. Takizawa: J. Cryst. Growth 179 (1997) 503.
- 15) H. Matsushita and T. Takizawa: J. Cryst. Growth 191 (1998) 455.
- 16) L. S. Palatnik and E. I. Rogacheva: Sov. Phys. Doklady 12 (1967) 503.

## Single Crystal Growth of $\text{CaGa}_2\text{S}_4$ and $\text{SrGa}_2\text{S}_4$

Chiharu HIDAKA\* and Takeo TAKIZAWA

Department of Physics, College of Humanities and Sciences, Nihon University, 3-25-40 Sakurajosui, Setagaya-ku, Tokyo 156-8550, Japan

We have constructed the pseudo-binary phase diagrams of the  $\text{CaS-Ga}_2\text{S}_3$  and  $\text{SrS-Ga}_2\text{S}_3$  systems by the differential thermal analysis and powder X-ray diffraction. A eutectic reaction is found between 50 and 100 mol% $\text{Ga}_2\text{S}_3$  in both systems. The compounds are shown to melt congruently and be crystallized by cooling down the melt passing through the melting point. Based on the phase diagrams, single crystals of  $\text{CaGa}_2\text{S}_4$  and  $\text{SrGa}_2\text{S}_4$ , both undoped and  $\text{Ce}^{3+}$  doped ones, are grown by the melt method and self-flux method, respectively. The crystals consist of several domains. They are transparent, and colorless for the undoped ones and slightly yellowish for the Ce doped ones. In the case of  $\text{CaGa}_2\text{S}_4:\text{Ce}^{3+}$ , a crystal having a typical size of 7mm $\phi$  in diameter and 5mm in length is obtained. It well cleaves along the [100] crystal direction. Photoluminescence (PL) spectra of  $\text{CaGa}_2\text{S}_4:\text{Ce}^{3+}$  and  $\text{SrGa}_2\text{S}_4:\text{Ce}^{3+}$  crystals are also measured. The relation of PL with  $\text{Ce}^{3+}$  ion concentration is discussed.

KEYWORDS:  $\text{CaGa}_2\text{S}_4$ ,  $\text{SrGa}_2\text{S}_4$ , phase diagram, horizontal Bridgman method, self-flux method, PL spectra

### 1. Introduction

$\text{Ce}^{3+}$  doped alkaline earth thiogallates ( $\text{M}\text{Ga}_2\text{S}_4$ ;  $\text{M} = \text{Ca}, \text{Sr}, \text{Ba}$ ) are now regarded as promising host materials for blue light devices, since Barrow et.al fabricated EL devices using  $\text{CaGa}_2\text{S}_4:\text{Ce}^{3+}$  thin films.<sup>1)</sup> Though the brightness was about one tenth of that of a commercially available EL element at present, its purity of color is nearly of an ideal blue with respect to the C.I.E. color coordinate. It is also expected that the emission intensity of the blue light can be strengthened by one order of magnitude, if the special cares are taken on the fabrication of EL elements, such as to keep the stoichiometry of the films as well as to ensure their overall crystallinity.

Moreover, a laser oscillation was observed in  $\text{Eu}^{2+}$  doped  $\text{CaGa}_2\text{S}_4$  single crystals in the red region.<sup>2)</sup> The similar lasing operation is also expected for the blue emission from  $\text{Ce}^{3+}$  doped  $\text{CaGa}_2\text{S}_4$  single crystals, leading us to hope that an optically pumped blue light laser may be realized using  $\text{Ce}^{3+}$  doped thiogallate crystals.

To use the single crystals in the optical devices, they should have no cracks and no voids throughout the whole region used. Needless to say, their refractive index should be homogeneous. Thus, to grow single crystals of good quality is the first step to realize the practical laser devices using the RE doped thiogallates.

Many trials have been achieved to grow single crystals of these materials.<sup>3,4)</sup> However, as far as our knowledge is concerned, most of the crystals were made by the solid state reaction or CVD, and a success in growing a single crystal by the melt method has never been reported. This is probably because of the high melting temperature and high chemical reactivity of the compounds.

In this report, we first present the pseudo-binary phase diagrams of the  $\text{CaS-Ga}_2\text{S}_3$  and the  $\text{SrS-Ga}_2\text{S}_3$  systems,<sup>5,6)</sup> indispensable for the single crystal growth by the melt method. Then, we describe in detail the growth method of  $\text{CaGa}_2\text{S}_4$  and  $\text{SrGa}_2\text{S}_4$  based on these phase diagrams. Photoluminescence spectra of  $\text{Ce}^{3+}$  doped (0.1 to 1.5 wt%) crystals are also presented.

### 2. Phase Diagrams of the (Ca,Sr)- $\text{Ga}_2\text{S}_3$ System

The phase diagrams were constructed by means of DTA and powder X-ray diffraction. The DTA furnace used here was the same one as in a previous paper.<sup>7)</sup> The scanning speed of heating and cooling processes was set at a constant value of 2 °C/min and the scan was repeated twice. In the first scan, we can see the chemical reaction processes between elements, and in the second one, we can determine the melting point and structural phase transition of the compounds. The samples after DTA measurements was identified by powder X-ray diffraction using  $\text{Cu-K}\alpha$  line at room temperature.

In DTA measurements, the elements of  $\text{Ca}(3\text{N})$  or  $\text{Sr}(3\text{N})$ ,  $\text{S}(6\text{N})$  and the compound of  $\text{Ga}_2\text{S}_3$  were used as starting materials and weighed to about 0.2g in total under argon gas. The mixtures was sealed in a quartz ampoule of 7 mm $\phi$   $\times$  40 mm under a vacuum of  $10^{-3}$  Torr. The inside wall of a quartz ampoule was coated with carbon film by firing acetone in air. The compound of  $\text{Ga}_2\text{S}_3$  used here was synthesized following the procedure being described in the next section.

Figure 1(a) shows the DTA signals of the cooling processes between 50 and 75 mol% $\text{Ga}_2\text{S}_3$  of the  $\text{CaS-Ga}_2\text{S}_3$  system. The melting point of the compounds lowers with increasing the concentration of  $\text{Ga}_2\text{S}_3$ . The signals at 975°C was found in the DTA curves at  $\text{Ga}_2\text{S}_3$  concentration above 50 mol%. On the contrary, in the concentration range between 75 and 100 mol% $\text{Ga}_2\text{S}_3$ , the melting point rises as  $\text{Ga}_2\text{S}_3$  concentration increases. The peak at 975 °C was also found in every DTA curve except one at 100 mol% $\text{Ga}_2\text{S}_3$ , which will be later ascribed to a eutectic line.

Figure 1(b) shows the powder X-ray diffraction patterns of the samples between 50 and 75 mol% $\text{Ga}_2\text{S}_3$  after DTA measurements. The diffraction intensity was normalized to each main peak. The diffraction lines due to  $\text{Ga}_2\text{S}_3$  compounds are shown by the dots in the figure. Their intensities decreased as the  $\text{Ga}_2\text{S}_3$  concentration decreased and only the lines due to  $\text{CaGa}_2\text{S}_4$  were observed in the compounds at 50 mol% $\text{Ga}_2\text{S}_3$ . The lattice parameters of  $\text{CaGa}_2\text{S}_4$  did not change by varying the

\*E-mail address: komaz@phys.chs.nihon-u.ac.jp

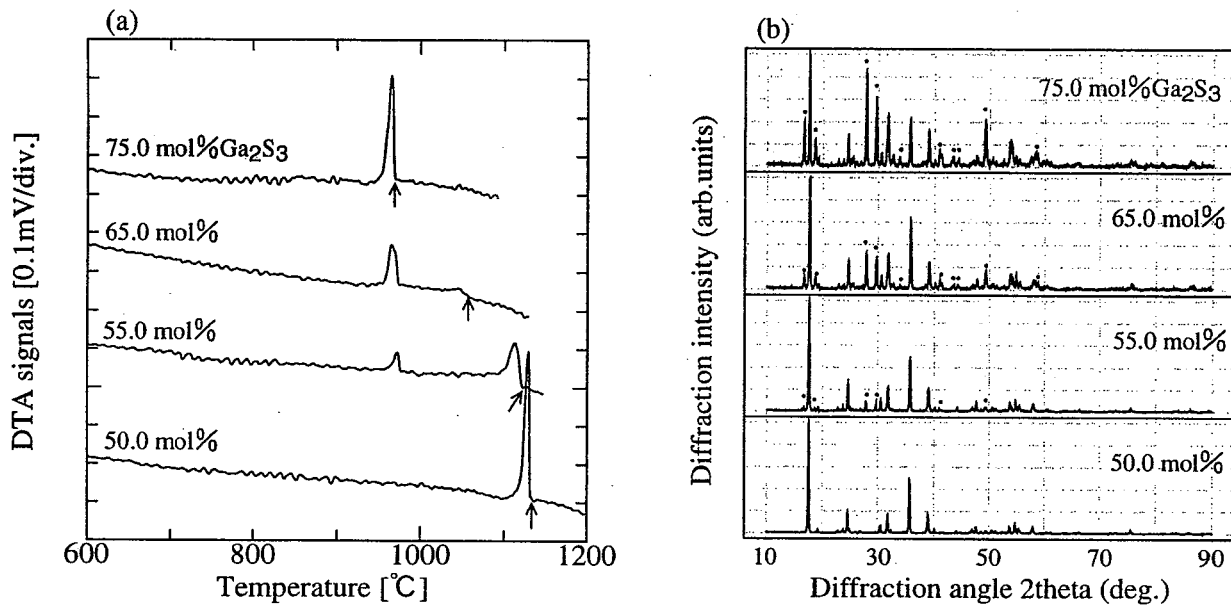


Fig. 1. (a) DTA curves of 50-75 mol%Ga<sub>2</sub>S<sub>3</sub> in the cooling processes in the CaS-Ga<sub>2</sub>S<sub>3</sub> system. (b) X-ray diffraction patterns of 50-75 mol%Ga<sub>2</sub>S<sub>3</sub> in the CaS-Ga<sub>2</sub>S<sub>3</sub> system after DTA measurements.<sup>6)</sup>

concentration of Ga<sub>2</sub>S<sub>3</sub>.

The DTA signals of the cooling processes of the SrS-Ga<sub>2</sub>S<sub>3</sub> system between 50 and 75 mol%Ga<sub>2</sub>S<sub>3</sub> were shown in Fig.2(a). The melting point of the mixed compounds lowers as the Ga<sub>2</sub>S<sub>3</sub> concentration increases. Two peaks at 975 and 995 °C were found in the Ga<sub>2</sub>S<sub>3</sub> concentration range except for 50 mol%Ga<sub>2</sub>S<sub>3</sub>.

Similarly to the CaS-Ga<sub>2</sub>S<sub>3</sub> system, the melting point of the compounds rises with increasing the Ga<sub>2</sub>S<sub>3</sub> concentration above 75 mol%Ga<sub>2</sub>S<sub>3</sub>. The product after DTA measurement was identified by powder X-ray diffraction at room temperature as shown in Fig.2(b).

In the concentration between 77.5 and 100 mol%Ga<sub>2</sub>S<sub>3</sub>, the mixed diffraction patterns of two compounds, SrGa<sub>2</sub>S<sub>4</sub> and Ga<sub>2</sub>S<sub>3</sub> were observed. The change in lattice parameters of the compounds was not found in the range of 50-100 mol%Ga<sub>2</sub>S<sub>3</sub>.

From these results, the phase diagrams of the CaS-Ga<sub>2</sub>S<sub>3</sub> and SrS-Ga<sub>2</sub>S<sub>3</sub> systems were deduced as shown in Figs. 3 and 4, respectively. Both the phase diagrams show eutectic reactions between CaGa<sub>2</sub>S<sub>4</sub> or SrGa<sub>2</sub>S<sub>4</sub> and Ga<sub>2</sub>S<sub>3</sub>. It is seen from the phase diagrams that the melt method as well as the self-flux one is suitable for the single crystal growth for both materials.

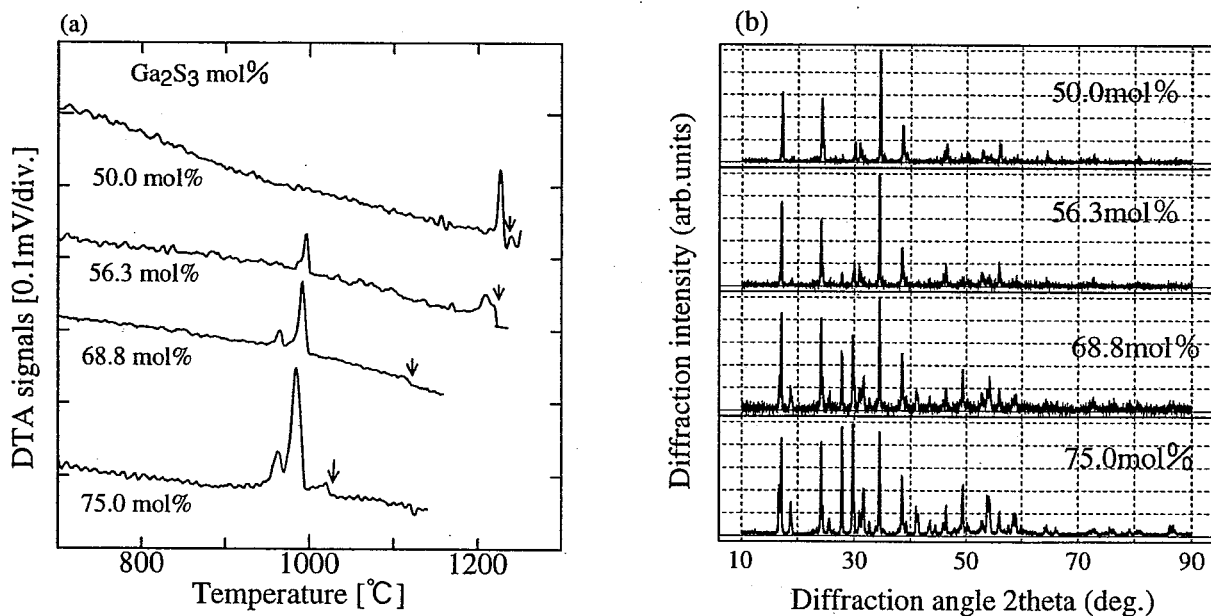
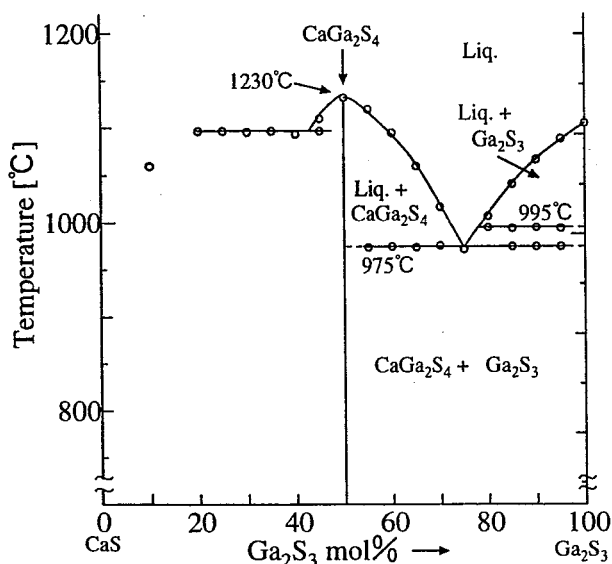
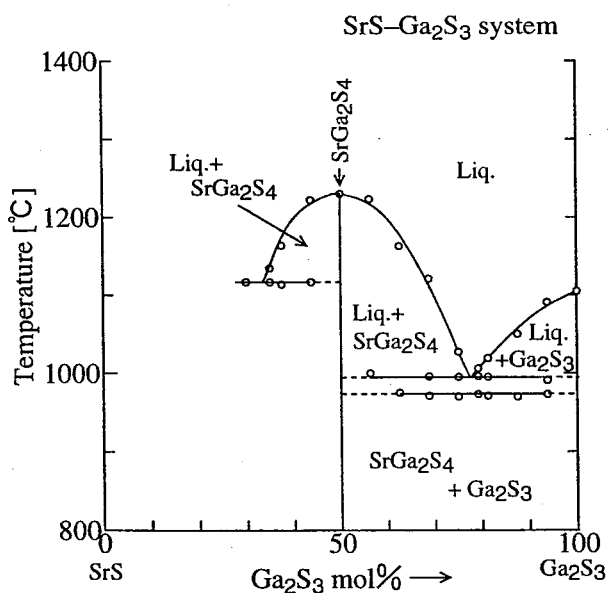


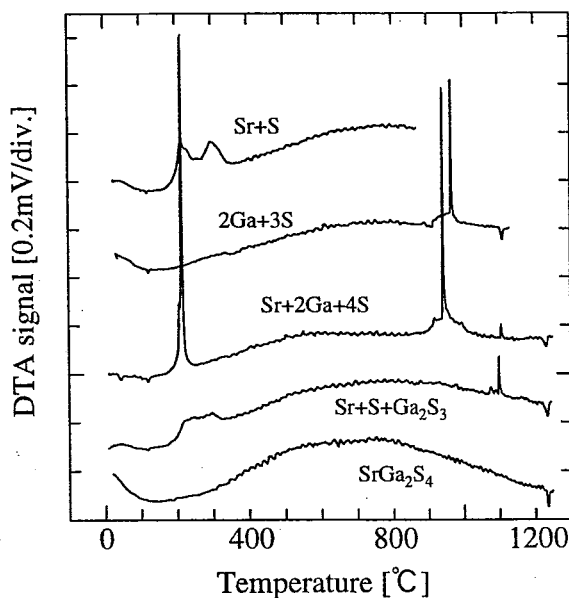
Fig. 2. (a) DTA curves of 50-75 mol%Ga<sub>2</sub>S<sub>3</sub> in the SrS-Ga<sub>2</sub>S<sub>3</sub> system in the cooling process (b)X-ray diffraction patterns of 50-75 mol%Ga<sub>2</sub>S<sub>3</sub> after DTA measurements.<sup>5)</sup>

Fig. 3. Pseudo-binary phase diagram of the CaS-Ga<sub>2</sub>S<sub>3</sub> system.<sup>6)</sup>Fig. 4. Pseudo-binary phase diagram of the SrS-Ga<sub>2</sub>S<sub>3</sub> system.<sup>5)</sup>

### 3. Preparation of Precursors

To achieve the crystal growth by means of the melt method using quartz ampoules, we first investigated the chemical reaction processes of the constituent elements and binary compounds in a quartz ampoule using DTA data shown in Fig. 5 which was already observed in the previous section. Here, it should be noted that a peak of DTA signals shows an exothermic reaction and a dip an endothermic one. If Sr and S were mixed in the ratio of 1:1, they reacted around 200-400°C as shown in the top of Fig. 5. As seen in the second curve from the top of Fig. 5, the reaction of 2Ga+3S occurred strongly around 950°C whereby Ga<sub>2</sub>S<sub>3</sub> compounds were produced. The

temperature of the reactions was not definite but varied in several tens of degrees, probably because they occurred under an inequilibrium condition depending on the size and shape of elements. When three elements of Sr, Ga and S were mixed and heated, three peaks were detected around 400, 950 and 1100°C in the third curve from the top of Fig. 5. The reaction around 950°C due to the formation of Ga<sub>2</sub>S<sub>3</sub> sometimes caused a break of an ampoule of the mixture. To avoid the explosive reaction, Ga<sub>2</sub>S<sub>3</sub> compounds were used with Sr and S elements in the formation of SrGa<sub>2</sub>S<sub>4</sub>. In DTA curve of Sr+S+Ga<sub>2</sub>S<sub>3</sub> in Fig. 5, there is no more strong reaction around 950°C but two small exothermic reactions around 250°C and 1105°C. One is due to the formation SrS and the other corresponds to the melting point of Ga<sub>2</sub>S<sub>3</sub>, whereby SrGa<sub>2</sub>S<sub>4</sub> is produced. The compound of SrGa<sub>2</sub>S<sub>4</sub> was completely synthesized after the exothermic reactions at 1105°C and melted congruently at 1230°C. In the case of CaGa<sub>2</sub>S<sub>4</sub>, the chemical reaction processes were similar to that of SrGa<sub>2</sub>S<sub>4</sub>. The CaS compounds were produced by the exothermic reaction of Ca+S around 400°C, and the CaGa<sub>2</sub>S<sub>4</sub> compounds were formed at the melting point of Ga<sub>2</sub>S<sub>3</sub>. It is also shown that the CaGa<sub>2</sub>S<sub>4</sub> compounds have a congruent melting point at 1132°C. Based on the results of the chemical reaction processes, we decided to use the melt growth method for CaGa<sub>2</sub>S<sub>4</sub>. This is because the melting point is low enough to carry out the crystal growth using quartz ampoules. However, for the crystal growth of SrGa<sub>2</sub>S<sub>4</sub>, we adopted the flux method, because the melting temperature was too high to use quartz ampoules. The alkaline earth metal (Ca or Sr), S and Ga<sub>2</sub>S<sub>3</sub> were weighed to about 7g in total under argon gas in the stoichiometric ratio for a Ca thiogallate, and in the ratio of SrS:Ga<sub>2</sub>S<sub>3</sub>=35:65 for a Sr thiogallate. The alkaline earth metal and Ga<sub>2</sub>S<sub>3</sub> were poured into a

Fig. 5. DTA signals of chemical reaction processes of the constituent elements in the heating process.<sup>5)</sup>

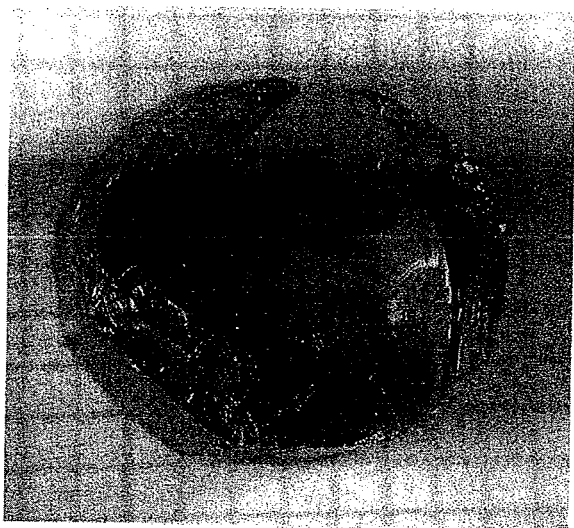


Fig. 6. A photograph of 0.8 wt% doped  $\text{CaGa}_2\text{S}_4$  single crystal by the melt method.<sup>6)</sup> The interval of lines in this photo is 1 mm.

quartz boat coated with carbon film which was set at one end of a quartz ampoule of  $13\text{mm}\phi \times 300\text{mm}$  and set separately from sulfur element at the other end of the ampoule for controlling the sulfur vapor pressure. The ampoule was put in a furnace having two temperature zones, the temperature of which could be controlled separately. The part of Ca and  $\text{Ga}_2\text{S}_3$  mixture was kept at  $400^\circ\text{C}$  for 24 hours, while the sulfur part was kept at  $300^\circ\text{C}$ . Then, the temperature of the whole ampoule was elevated to  $1120^\circ\text{C}$  slightly above the melting point of  $\text{Ga}_2\text{S}_3$  ( $1105^\circ\text{C}$ ). It was held for one hour at the temperature for ensuring the homogenized melt. It was cooled down to room temperature at a speed of  $120^\circ\text{C}/\text{h}$ , and the product was taken out. This was done because the quartz boat inside was sometimes broken due to the thermal stress during the reaction; a small amount of the melt flowed out from gaps or cracks of the inner boat, giving damages in the final stage of the crystal growth. The precursor thus produced was ground and again poured into another quartz boat coated by carbon and sealed in a  $13\text{mm}\phi \times 150\text{mm}$  quartz ampoule. In the case of  $\text{Ce}^{3+}$  doping, powdered  $\text{Ce}_2\text{S}_3$  compounds were mixed in the precursor. Crystals doped with  $\text{Ce}^{3+}$  in the concentration between 0.1 and 1.5 wt% were grown. The furnace used here was of the horizontal Bridgman having three temperature zones, which could be separately controlled.

#### 4. Crystal Growth of $\text{CaGa}_2\text{S}_4$ by Melt Method

A crystal of  $\text{CaGa}_2\text{S}_4$  was grown at a speed of  $0.5\text{cm}/\text{h}$  by cooling the temperature of an ampoule from  $1150^\circ\text{C}$  to  $1100^\circ\text{C}$ , whereby the molten compound passed through  $1132^\circ\text{C}$ , the solidifying temperature of  $\text{CaGa}_2\text{S}_4$ . The  $\text{Ce}^{3+}$  doped crystals were also grown by the same method. The grown crystals were transparent and doped ones were yellowish. However, in the  $\text{Ce}^{3+}$  concentration above 1.5 wt%, the resultant crystals became colored black and were tightly stuck to the wall of a quartz boat. Figure 6 shows a photograph of the

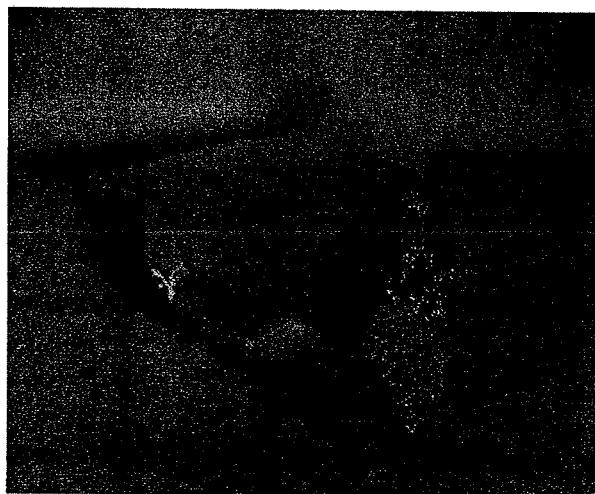


Fig. 7. A photograph of undoped single crystal of  $\text{SrGa}_2\text{S}_4$  grown in  $\text{Ga}_2\text{S}_3$  flux.<sup>6)</sup> The interval of lines in this photo is 1 mm.

crystal doped with 0.8 wt%  $\text{Ce}^{3+}$ . The size of the crystal was about  $7\text{mm}\phi \times 5\text{mm}$  and it had still many cracks and black precipitates especially at the edge of the ingot. The normal direction of the cleaved surface as shown in Fig. 6 was  $[100]$  which was parallel to the growth direction.

#### 5. Crystal Growth of $\text{SrGa}_2\text{S}_4$ by Flux Method

Crystals of  $\text{SrGa}_2\text{S}_4$  were grown at speeds of  $4^\circ\text{C}/\text{h}$  and  $2^\circ\text{C}/\text{h}$  using  $\text{Ga}_2\text{S}_3$  as a flux. The melting point of the mixture of  $\text{SrGa}_2\text{S}_4$  and  $\text{Ga}_2\text{S}_3$  was estimated to be  $1150^\circ\text{C}$  from the phase diagram of the  $\text{SrS}-\text{Ga}_2\text{S}_3$  system. (Fig. 4) A crystal was grown from the temperature  $20^\circ\text{C}$  above the melting point. The melt was kept at the maximum temperature for 12 hours to assure the homogenization of the liquid of the mixture. The effect of the growth speeds on the crystallinity is hardly seen, because the size of the resultant crystals was still too small to be compared at the two growing speeds tried. One of the problems is that the chemical reaction between the wall of a quartz ampoule and the liquid mixture progressed, if the growth speed slowed down. Crystals of 2-3mm in size were obtained as shown in Fig. 7. Crystals having concentrations of 0.1~1.5 wt%  $\text{Ce}^{3+}$  were also grown. However, the crystal above 1.5 wt%  $\text{Ce}^{3+}$  concentration was colored black with many cracks inside and was easily broken into pieces. Several pieces of the crystals above 1.5 wt%  $\text{Ce}^{3+}$  which had transparent single domains were selected for photoluminescence measurements.

#### 6. Photoluminescence Spectra

We measured the photoluminescence spectra of  $\text{CaGa}_2\text{S}_4:\text{Ce}^{3+}$  and  $\text{SrGa}_2\text{S}_4:\text{Ce}^{3+}$ . Samples were excited by a He-Cd laser (Omnichrome 3056-15M) of 325 nm with an output power of 23 mV at room temperature. Luminescence spectra were detected with a photomultiplier (HAMAMATSU R562) using a monochromator (NALUMI RM-23-1).

As the light emission from a crystalline sample

strongly depends on the size and shape of the sample, every single crystal was powdered using an agate mortar, so as to reduce the size effect. The powdered sample was tightly filled in a quartz capillary and mounted on a sample holder.

In the case of  $\text{CaGa}_2\text{S}_4:\text{Ce}^{3+}$ , the emission spectra strikingly changed as the  $\text{Ce}^{3+}$  concentration varied as shown in Fig.8. The intensity of the emission varies almost linearly with the  $\text{Ce}^{3+}$  concentration between 0.1 and 0.5 wt%. The emission intensity seems to be saturated in the  $\text{Ce}^{3+}$  concentration above 0.5 wt%. We also measured the dependence of the excitation intensity on photoluminescence. The luminescence spectra were measured as a function of the intensity of excitation light, by reducing it by ND filters. The linear relation was observed between the emission spectra and the excitation intensity. This tendency is seen in all samples with the concentration between 0.1 to 1.5 wt%  $\text{Ga}_2\text{S}_3$ .

The dependence of the emission on the growth direction was also observed. Sample crystals were cut out from 1, 3 and 6cm away from the growth start position along the growth direction. The intensity of the emission was almost shown constant against the growth direction. This means that the  $\text{Ce}^{3+}$  ions were distributed homogeneously along the growth direction.

In the case of  $\text{SrGa}_2\text{S}_4:\text{Ce}^{3+}$ , sample crystals were taken away from an ingot by separating the flux of  $\text{Ga}_2\text{S}_3$ . From the flux itself, no emission was detected when it was irradiated with a 325 nm He-Cd laser. The photoluminescence spectra of  $\text{SrGa}_2\text{S}_4:\text{Ce}^{3+}$  with various  $\text{Ce}^{3+}$  concentrations were shown Fig. 9. The emission intensity increases as  $\text{Ce}^{3+}$  concentration increases from 0.1 to 1.5 wt%. This is different from the results of  $\text{CaGa}_2\text{S}_4:\text{Ce}^{3+}$ .

## 7. Summary

The pseudo-phase diagrams of the  $\text{CaS-Ga}_2\text{S}_3$  and  $\text{SrS-Ga}_2\text{S}_3$  systems were constructed by means of DTA measurements and powder X-ray diffraction.

Based on the diagrams, we have grown single crystals of  $\text{CaGa}_2\text{S}_4$  by the melt method and those of  $\text{SrGa}_2\text{S}_4$  by the self-flux method. The  $\text{Ce}^{3+}$  doped single crystals were also grown by the same methods. A larger single crystal was obtained in the case of  $\text{CaGa}_2\text{S}_4:\text{Ce}^{3+}$  compared to the  $\text{SrGa}_2\text{S}_4:\text{Ce}^{3+}$  case. The crystals had a tendency to be cleaved at the surface normal to the growth direction.

From the dependence of the emission on the growth direction,  $\text{Ce}^{3+}$  was thought to be distributed homogeneously along the growth direction of the  $\text{CaGa}_2\text{S}_4$  crystal. The emission intensity was almost proportional to the intensity of the excitation light in the whole  $\text{Ce}^{3+}$  concentration range.

In the case of  $\text{SrGa}_2\text{S}_4:\text{Ce}^{3+}$ ,  $\text{Ce}^{3+}$  could be doped linearly up to 1.5 wt%.

## Acknowledgements

This work was partly supported by the Research Grant from Nihon University.

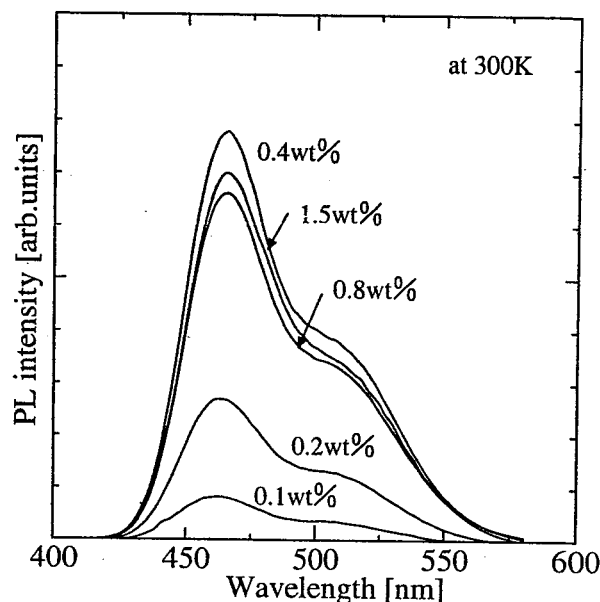


Fig. 8. Photoluminescence spectra of  $\text{CaGa}_2\text{S}_4:\text{Ce}^{3+}$ .<sup>6)</sup>

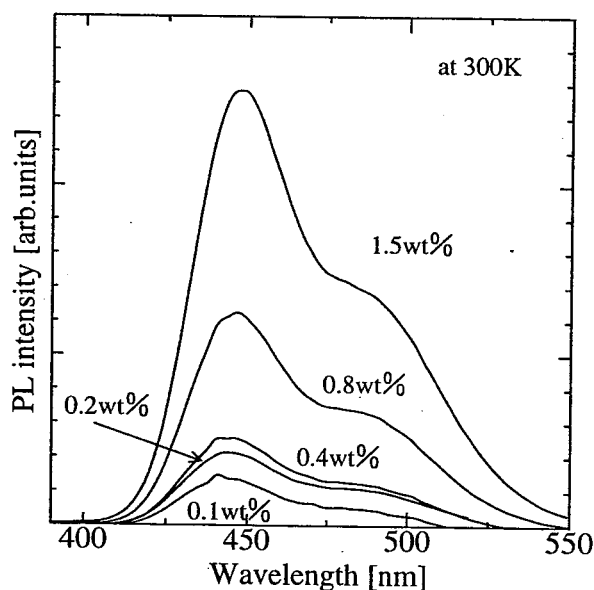


Fig. 9. Photoluminescence spectra of  $\text{SrGa}_2\text{S}_4:\text{Ce}^{3+}$ .

## References

- 1) W. A. Barrow, R. C. Covert, E. Dickey, C. N. King, C. Laakso, S. S. Sun, R. T. Tuenge, R. Wetross and J. Kane: 1993 SID Int.Symp.Dig. (1993) p.761.
- 2) S. Iida, T. Matsumoto, N.T. Mamedov, Y. Maruyama, A.I. Bairamov, B.G. Tagiev, O.B. Tagiev and R.B. Dzhabbarov: Jpn. J. Appl. Phys. **36** (1997) Lett.857.
- 3) R.Eholie, O.Gorochev, M.Guittard, A.Mazurier, and J.Flahaut: Bulletin de la société chimique de France, No. 3, (1971)p. 747.
- 4) T. E. Peter and J. A. Baglio: J. Electrochem. Soc., **119**, (1072) 230.
- 5) C. Komatsu and T.Takizawa : J. Cryst. Growth. **210** (2000) 677.
- 6) C. Hidaka and T.Takizawa : J. Cryst. Growth. **222** (2001) 574.
- 7) H. Matsushita and T. Takizawa: Jpn. J. Appl. Phys. **34** (1995) 4699.

## Phase Diagram and Crystal Structures of the CdS – In<sub>2</sub>S<sub>3</sub> – Ga<sub>2</sub>S<sub>3</sub> System

Kimitaka ASAKA, Chiharu HIDAKA, Takeo TAKIZAWA\*, and Hiroaki MATSUSHITA<sup>1</sup>

*Department of Physics, College of Humanities and Sciences, Nihon University,  
 3-25-40 Sakurajosui, Setagaya-ku, Tokyo 156-8550, Japan.*

<sup>1</sup>*Department of Material Science and Technology, School of High-Technology for Human Welfare, Tokai University,  
 317 Nishino, Numazu-city, Shizuoka 410-03, Japan.*

We have investigated the phase equilibrium and crystal structures of the CdS – In<sub>2</sub>S<sub>3</sub> – Ga<sub>2</sub>S<sub>3</sub> system ((i) CdGa<sub>2</sub>S<sub>4</sub> – CdIn<sub>2</sub>S<sub>4</sub> (ii) CdGa<sub>2</sub>S<sub>4</sub> – 2GaInS<sub>3</sub> (iii) CdS – GaInS<sub>3</sub> systems). We have constructed the phase diagram of the (i) system and found a new layer compound in the (ii) and (iii) systems. The newly found layer compound crystallizes in the trigonal space group P $\bar{3}$ m1-164 (hexagonal cell;  $a = 3.80$ ,  $c = 18.3$  Å). We have also determined the optical band gaps of both the new layer and already known ZnIn<sub>2</sub>S<sub>4</sub>(III) phase compounds.

**KEYWORDS:** CdS – In<sub>2</sub>S<sub>3</sub> – Ga<sub>2</sub>S<sub>3</sub> system, layer structure, phase diagram, lattice parameter, DTA, X-ray diffraction, optical absorption

### 1. Introduction

Several different kinds of crystal structures have been found in the CdS – In<sub>2</sub>S<sub>3</sub> – Ga<sub>2</sub>S<sub>3</sub> system, such as tetrahedral, layer and spinel structures. The compounds found in this system are shown in Fig. 1,<sup>1–10</sup> where layer compounds have a structure analogous to those of the  $m$ ZnS–In<sub>2</sub>S<sub>3</sub> ( $m = 1, 2, 3$ ) system. The layer phase in this system was first found by Shand.<sup>1</sup> It crystallized in the ZnIn<sub>2</sub>S<sub>4</sub>(III) type. Later, Haeuseler reported that the Zn<sub>2</sub>In<sub>2</sub>S<sub>5</sub>(IIb) type structure was found in the Ga<sub>2</sub>S<sub>3</sub> – CdIn<sub>2</sub>S<sub>4</sub> system.<sup>2</sup> Recently, we have investigated the phase diagram of the CdGa<sub>2</sub>S<sub>4</sub> – CdIn<sub>2</sub>S<sub>4</sub> to study the structural phase change due to the exchange of the cation ions<sup>11,12</sup> but no new layer phase was observed except for the ZnIn<sub>2</sub>S<sub>4</sub>(III) type.

Many layer phases have been observed in the pseudoternary AX – B<sub>2</sub>X<sub>3</sub> – B'<sub>2</sub>X<sub>3</sub> (A=Mg, Mn, Fe, Co, Ni, Zn, Cd, Hg; B, B'=Al, Ga, In, Sc, V, Cr; X=S, Se) systems and the number of new layer compounds in these systems is still growing.<sup>3</sup> The layer compounds have attracted much attention because of the polytypic form, superstructure, and anisotropic physical properties. However, the phase equilibrium, crystal structures and physical properties of these compounds in the CdS – In<sub>2</sub>S<sub>3</sub> – Ga<sub>2</sub>S<sub>3</sub> system have not been fully clarified. Our present purpose is to investigate phase diagrams, complex crystal structures and optical properties of the compounds in this ternary system.

In this paper, we have studied the following three systems.

- (i)  $(1 - x)\text{CdGa}_2\text{S}_4 - x\text{CdIn}_2\text{S}_4$  ( $x = 0 \sim 1$ )
- (ii)  $(1 - x)\text{CdGa}_2\text{S}_4 - 2x\text{GaInS}_3$  ( $x = 0 \sim 1$ )
- (iii)  $(1 - x)\text{CdS} - x\text{GaInS}_3$  ( $x = 0 \sim 1$ )

In the (i) system, the crystal structure changes from the defect chalcopyrite through the ZnIn<sub>2</sub>S<sub>4</sub> (III) type finally to spinel one, as the value of  $x$  varies. Haeuseler et al. proposed a “structure field map” of sulfides having a formula AB<sub>2</sub>X<sub>4</sub><sup>13</sup> to predict possible compositions as well as to find new quaternary layer compounds. The map was constructed by using the mean values of the Zunger coordinates  $R_\sigma$  and  $R_\pi$ , where  $R_\sigma$  is a measure of the

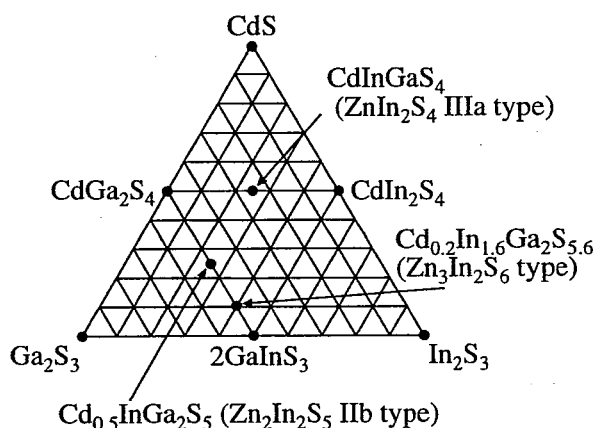


Fig. 1. Compounds in the CdS – In<sub>2</sub>S<sub>3</sub> – Ga<sub>2</sub>S<sub>3</sub> system.<sup>1–10</sup> CdInGaS<sub>4</sub>,<sup>1</sup> Cd<sub>0.5</sub>InGa<sub>2</sub>S<sub>5</sub>,<sup>2</sup> Cd<sub>0.2</sub>In<sub>1.6</sub>Ga<sub>2</sub>S<sub>5.6</sub> (this paper).

difference between the total effective core radii of cation and anion atoms, and  $R_\pi$  measures the sum of the orbital nonlocality of the  $s$  and  $p$  electrons on each atom.<sup>14</sup> They succeeded in getting the relation between the defect chalcopyrite, layer and spinel in the AB<sub>2</sub>X<sub>4</sub> compounds. However, the mechanism of the phase transformation caused by the atomic exchange has not been fully clarified. Here, we have investigated the phase diagram of the (i) system to investigate the structural transformation due to the exchange of the cation atoms.

We have also studied the stacking periodicity of the layer phase in the CdS – In<sub>2</sub>S<sub>3</sub> – Ga<sub>2</sub>S<sub>3</sub> system. The stacking period in the  $m$ ZnS–In<sub>2</sub>S<sub>3</sub> ( $m = 1, 2, 3$ ) system changes with  $m$ . In the (i) system, we could not find any layer phase but the ZnIn<sub>2</sub>S<sub>4</sub>(III) one. Thus, we have studied whether a new layer compound exists or not in the two regions (ii) and (iii) of the CdS – In<sub>2</sub>S<sub>3</sub> – Ga<sub>2</sub>S<sub>3</sub> system (see Fig. 1), where a layer compound was reported at the intermediate point of the lines, respectively.

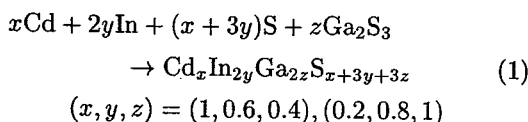
### 2. Experimental

DTA (Differential Thermal Analysis) measurements<sup>15</sup> were employed to observe the melting point, phase transition and chemical reaction. Samples, weighing the elements (Cd, Ga, In, S) to about 0.2 g in total were sealed in quartz tubes having dimensions of 7mm $\phi$   $\times$  40mm un-

\*E-mail address: takiz@chs.nihon-u.ac.jp

der vacuum. The rate of heating and cooling was held at a constant value of 2 deg./min. The products synthesized after DTA measurements were identified by powder X-ray diffraction (Rigaku RINT) using the Cu-K $\alpha$  line at room temperature. The RIETAN-94 (the program for the Rietveld analysis<sup>16,17</sup>) was used for structural analysis. Based on the data above, we have constructed the phase diagram of the pseudo-binary system and investigated the structural phase transformation by the atomic exchange.

Single crystals for the optical measurement were grown by a furnace having a uniform temperature gradient. The precursor for the crystal growth was synthesized by using the following chemical reaction in an evacuated ampoule.



We used Ga<sub>2</sub>S<sub>3</sub> compounds (synthesized by the same procedure as mentioned in a reference<sup>18</sup>) in the starting mixtures to suppress the sulfur vapor pressure which may cause the explosion of the quartz ampoules mainly triggered by an abrupt exothermic reaction between Ga and S atoms. The crystal structure was analyzed by powder X-ray diffraction.

Optical absorption spectra for the CdIn<sub>1.2</sub>Ga<sub>0.8</sub>S<sub>4</sub> and Cd<sub>0.2</sub>In<sub>1.6</sub>Ga<sub>2</sub>S<sub>5.6</sub> single crystals were measured at room temperature. Samples were cleaved perpendicular to the c axis and transmission spectra were measured in the wavelength region of 4000~7000 Å. The sample thickness  $d$  was measured by a digital micrometer. The absorption coefficient  $\alpha$  was calculated using the following relation.

$$T = \frac{(1 - R)^2 \exp(-\alpha d)}{1 - R^2 \exp(-2\alpha d)} \quad (2)$$

where  $T$  and  $R$  are transmittance and reflectance, respectively. We obtained reflectivity  $R$  needed for the calculation using the refractive index deduced by the following relation,<sup>19,20</sup>

$$n = \frac{1}{2d(1/\lambda_1 - 1/\lambda_2)} \quad (3)$$

where  $\lambda_1$ ,  $\lambda_2$  are the wavelengths at which two adjacent maxima appear in the transmission spectrum and the refractive index  $n$  is a mean value between  $\lambda_1$  and  $\lambda_2$ .

### 3. Experimental Results and Discussion

#### 3.1 The phase diagram of the CdGa<sub>2</sub>S<sub>4</sub>-CdIn<sub>2</sub>S<sub>4</sub> system

Fig. 2 shows the phase diagram of the CdGa<sub>2</sub>S<sub>4</sub> - CdIn<sub>2</sub>S<sub>4</sub> system.<sup>12</sup> In this system, three phases, defect chalcopyrite, layer and spinel were observed. The defect chalcopyrite phase appeared between  $x = 0$  and 0.56, and the spinel one between  $x = 0.7$  and 1. The layer phase was observed in the entire region except for the compositions at  $x = 0$  and  $x = 1$ .

Fig. 3 shows the powder X-ray diffraction patterns of the CdGa<sub>2</sub>S<sub>4</sub> - CdIn<sub>2</sub>S<sub>4</sub> system. It is apparent that

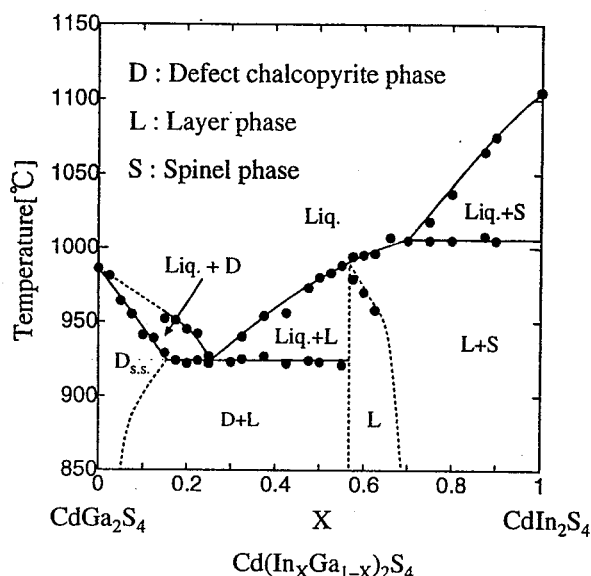


Fig. 2. The phase diagram of the CdGa<sub>2</sub>S<sub>4</sub>-CdIn<sub>2</sub>S<sub>4</sub> pseudo-binary system.<sup>12)</sup>

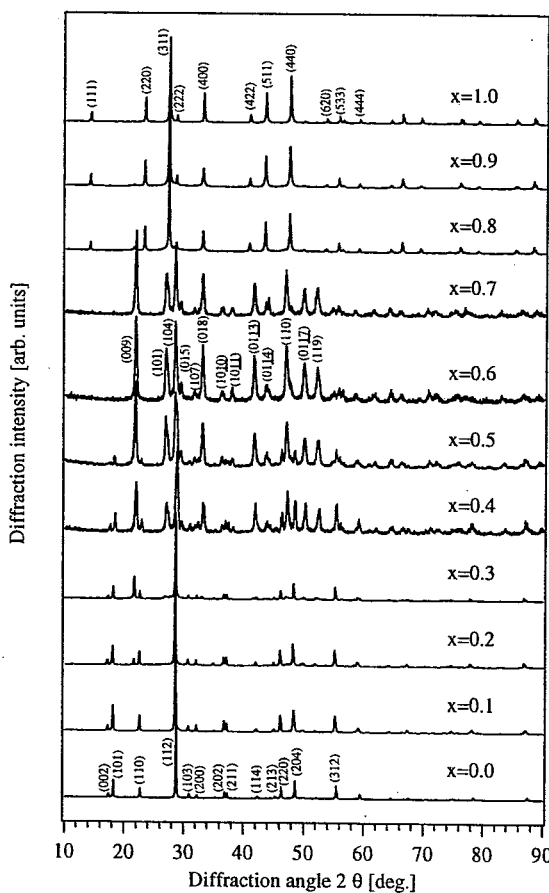


Fig. 3. Powder X-ray diffraction patterns in the  $(1-x)\text{CdGa}_2\text{S}_4-x\text{CdIn}_2\text{S}_4$  ( $x = 0 \sim 1$ ) system.<sup>12)</sup>

the XRD pattern at  $x = 0.5$  is the same as that of the mixture of the defect chalcopyrite phase and the layer one. The single layer phase was found to be realized only in between  $x = 0.58$  and 0.68. This result is different from the earlier one that the single phase of layer was formed only at  $x = 0.5$ .<sup>1)</sup> The X-ray diffraction peaks of

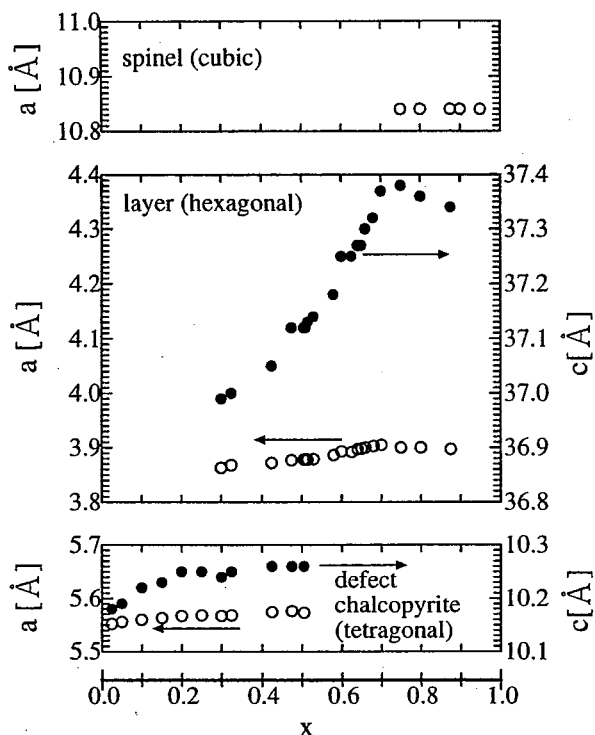


Fig. 4. Lattice parameters as a function of  $x$  in the  $\text{Cd}(\text{In}_x\text{Ga}_{1-x})_2\text{S}_4$  ( $x = 0 \sim 1$ ) system.<sup>11)</sup>

the layer phase shift to the lower angle side as  $x$  increases from  $x = 0.3$  to  $0.7$ , indicating the elongation of the layer lattice along the  $c$ -axis with  $x$ .

The lattice parameters of each phase determined by means of RIETAN-94 are shown in Fig. 4 as a function of  $x$ . The lattice parameters of pure three phases are  $\text{CdGa}_2\text{S}_4$  (tetragonal;  $a = 5.55$ ,  $c = 10.17$  Å),  $\text{CdIn}_{1.2}\text{Ga}_{0.8}\text{S}_4$  (hexagonal;  $a = 3.89$ ,  $c = 37.25$  Å) and  $\text{CdIn}_2\text{S}_4$  (cubic;  $a = 10.84$  Å). The defect chalcopyrite lattice expands with  $x$  in the  $x = 0$  to  $0.2$  region, while the layer one expands with  $x$  in the  $x = 0.3$  to  $0.7$ . The lattice parameters of both layer and spinel lattice seem irrespective of  $x$  for  $x \geq 0.7$ . The lattice expansion of the defect chalcopyrite phase and the layer one is mainly explained by the solid solution, where Ga atoms are gradually replaced by In atoms. However, in the layer phase between  $x = 0.3$  and  $x = 0.56$ , this explanation fails because the lattice parameters of the two phases must be unchanged in the eutectic region. One reason for this may be that the layer lattice is unstable and the stacking is affected by the tetragonal phase mixed.

The region between  $x = 0$  and  $0.56$  is the eutectic type phase diagram, though the unusual change of the layer lattice parameter in the region between  $x = 0.3$  and  $0.56$  is observed. In the pure layer phase between  $x = 0.56$  and  $0.7$ , a part of Ga atoms are gradually replaced by In atoms, leading to the expansion of the layer lattice. At  $x \geq 0.7$ , the rigid spinel lattices may be formed, resulting in no change in the lattice constant.

### 3.2 The Layer compounds in the $\text{CdS-In}_2\text{S}_3\text{-Ga}_2\text{S}_3$ system

The layer compounds in the pseudo-ternary  $\text{AX-B}_2\text{X}_3 - \text{B}'_2\text{X}_3$  ( $\text{A}=\text{Mg, Mn, Fe, Co, Ni, Zn, Cd, Hg}$ ;  $\text{B, B}'=\text{Al, Ga, In, Sc, V, Cr}$ ;  $\text{X}=\text{S, Se}$ ) systems have the following characteristics.<sup>2,3,21-25)</sup> (1) Anion atoms form the hcp (hexagonal close packing) type sublattice or the mixture of the hcp and ccp (cubic close packing) type stacking. (2) The stacking forms slabs, one of which consists of four to six anion layers. The slabs are combined with each other by the Van der Waals force between the sulfur layers. (3) Cations are coordinated tetrahedrally or octahedrally. The octahedrally coordinated cations are located near the center of a slab. (4) The octahedral site is exclusively occupied by In atoms.

We searched for a new layer compounds and polytypic form in the  $\text{CdS-In}_2\text{S}_3\text{-Ga}_2\text{S}_3$  system. Fig. 5 shows the X-ray diffraction patterns of the  $\text{CdGa}_2\text{S}_4 - 2\text{GaInS}_3$  system. Two types of the layer phases were observed in this system. One was the  $\text{Zn}_2\text{In}_2\text{S}_5$  (IIb) type structure at  $x = 0.5$  (hexagonal;  $a = 3.83$ ,  $c = 30.6$  Å) already reported by Haeuseler et.al.<sup>2)</sup> However, it is seen in Fig. 5 that this phase appears only as a mixing partner with  $\text{Ga}_2\text{S}_3$  phase (hexagonal;  $a = 6.46$ ,  $c = 17.9$  Å). This layer phase was observed in the region from  $x = 0.25$  to  $0.75$  but we could not find its pure single phase and polytype in the (ii) system.

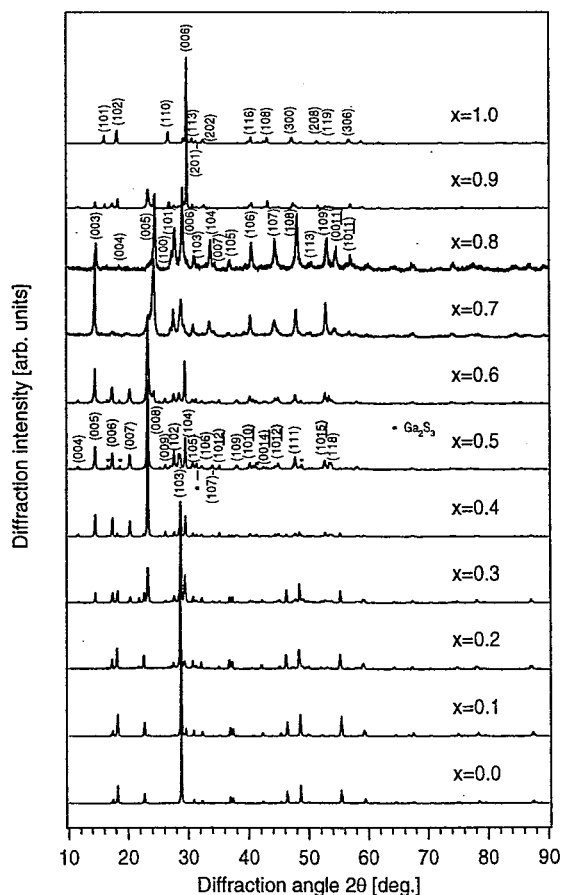


Fig. 5. Powder X-ray diffraction patterns in the  $(1-x)\text{CdGa}_2\text{S}_4 - 2x\text{GaInS}_3$  ( $x = 0 \sim 1$ ) system

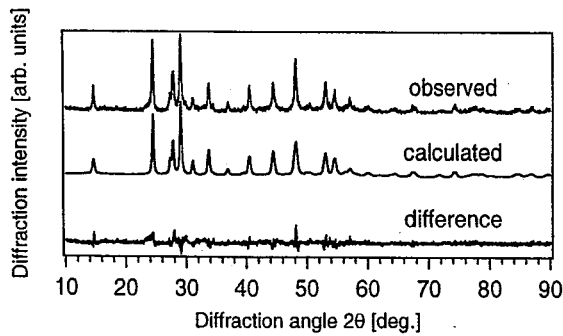


Fig. 6. Fitting of the observed datum to a calculated one in terms of the Rietveld analysis for  $\text{Cd}_{0.2}\text{In}_{1.6}\text{Ga}_2\text{S}_{5.6}$ .

A new layer phase of  $\text{Cd}_{0.2}\text{In}_{1.6}\text{Ga}_2\text{S}_{5.6}$  was found in the  $\text{CdS-In}_2\text{S}_3-\text{Ga}_2\text{S}_3$  system. Figure 6 and Table I show the results of the Rietveld analysis by means of the RIETAN-94, where the  $\text{Zn}_3\text{In}_2\text{S}_6$  (I) type ( $\text{P}\bar{3}\text{m}1;164$ ) structure<sup>21)</sup> was assumed. In addition, we assumed that the octahedral 1(b) and tetrahedral 2(d) cation sites were occupied by the In atoms and the remaining other cation atoms, respectively. All anion atoms were located in 2(d) sites like those in the  $\text{Zn}_3\text{In}_2\text{S}_6$  (I) compound. The goodness of fit indicator “*s*”<sup>16,17)</sup> is 1.31 (If the indicator “*s*” equals to one, the fitting is perfect). From this fitting, we determined the crystal structure of  $\text{Cd}_{0.2}\text{In}_{1.6}\text{Ga}_2\text{S}_{5.6}$  as the trigonal space group  $\text{P}\bar{3}\text{m}1$  (hexagonal;  $a = 3.80$ ,  $c = 18.3$  Å). The positions of the atoms are shown in Table I. This phase was observed in the region  $x = 0.8$  to 0.9 and the lattice parameters stayed constant in this region. Fig. 7 shows the X-ray diffraction patterns of the (iii) system ( $x = 0.5 \sim 1$ ). A half of this system, i.e., the  $\text{CdS-CdInGaS}_4$  region is already studied by Irie et.al.<sup>27,28)</sup> Their results, the mixing of the CdS and  $\text{ZnIn}_2\text{S}_4$  (III) type phases just corresponded to this region. On the contrary, three types of the layer phases

Table I.  $\text{Cd}_{0.2}\text{In}_{1.6}\text{Ga}_2\text{S}_{5.6}$ : space group;  $\text{P}\bar{3}\text{m}1$   
Hexagonal cell;  $a = 3.80$ ,  $c = 18.3$  Å.

Atom	Position	x	y	z	*s.o.f.
Cd/Ga	2(d)	1/3	2/3	0.301±0.01	0.1/0.6
Ga/In	2(d)	1/3	2/3	0.877±0.01	0.5/0.4
In	1(b)	0	0	0.500	1.0
S1	2(d)	1/3	2/3	0.425±0.02	1.0
S2	2(d)	1/3	2/3	0.748±0.02	1.0
S3	2(d)	1/3	2/3	0.085±0.02	1.0

Interatomic distance:

(Cd/Ga) - S; 2.32Å, (Ga/In) - 2.33Å, In - S; 2.59Å

\*s.o.f.= site occupation factor.

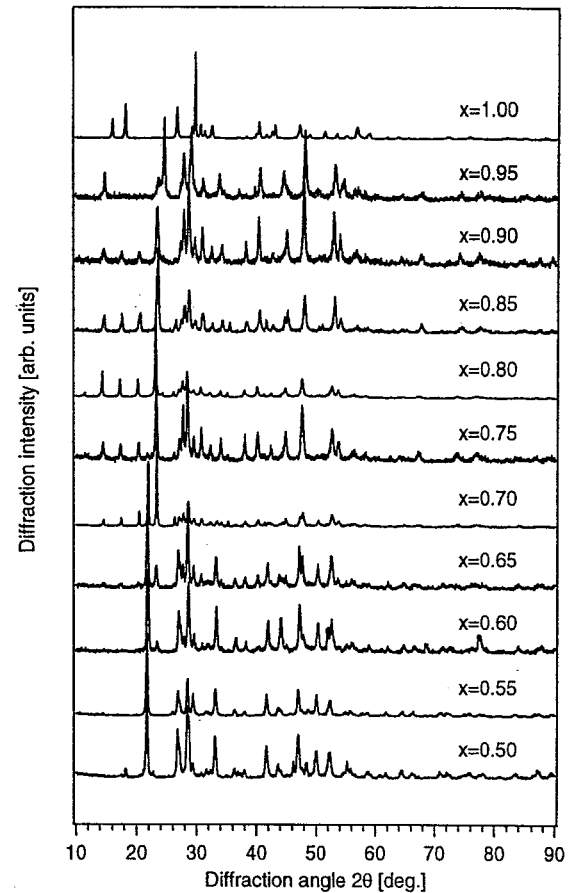
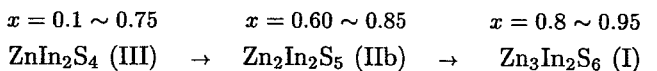


Fig. 7. Powder X-ray diffraction patterns in the  $(1-x)\text{CdS}-x\text{GaInS}_3$  ( $x = 0 \sim 1$ ) system.

were observed in the other half of this system ( $x = 0.5 \sim 1$ ). However, no new layer phase except for the  $\text{Zn}_3\text{In}_2\text{S}_6$  (I) type mentioned above was found. The layer structures in the  $(1-x)\text{CdS}-x\text{GaInS}_3$  system changes with  $x$  as the following.



The number of anion stacking which forms a slab increases from four to six with  $x$ . All the layer compounds found in the  $\text{CdS-In}_2\text{S}_3-\text{Ga}_2\text{S}_3$  system are shown in Table II.

### 3.3 Optical absorption measurement

Fig. 8 shows absorption spectra of the  $\text{CdIn}_{1.2}\text{Ga}_{0.8}\text{S}_4$  and  $\text{Cd}_{0.2}\text{In}_{1.6}\text{Ga}_2\text{S}_{5.6}$  single crystals. The optical absorption edge of the  $\text{Cd}_{0.2}\text{In}_{1.6}\text{Ga}_2\text{S}_{5.6}$  is greater in energy than that of the  $\text{CdIn}_{1.2}\text{Ga}_{0.8}\text{S}_4$ . In the optical

Table II. Layered compounds in the  $\text{CdS-In}_2\text{S}_3-\text{Ga}_2\text{S}_3$  system.

compound	Structure	S.G.	Lattice parameter(hex.)	Anion staking	Cation *C.N. Tetra:Octa
$\text{CdIn}_{1.2}\text{Ga}_{0.8}\text{S}_4$	$\text{ZnIn}_2\text{S}_4$ (III)type	R3m(160)	$a = 3.89$ , $c = 37.25$ Å	ABCA CABCB CAB	2:1
$\text{Cd}_{0.5}\text{InGa}_2\text{S}_5$	$\text{Zn}_2\text{In}_2\text{S}_5$ (IIb)type	$\text{P}\bar{3}\text{m}1(164)$	$a = 3.82$ , $c = 30.6$ Å	ABABA BABAB	3:1
$\text{Cd}_{0.2}\text{In}_{1.6}\text{Ga}_2\text{S}_{5.6}$	$\text{Zn}_3\text{In}_2\text{S}_6$ (I)type	$\text{P}\bar{3}\text{m}1(164)$	$a = 3.80$ , $c = 18.3$ Å	ABABAB	4:1

\*C.N.= Coordination Number.

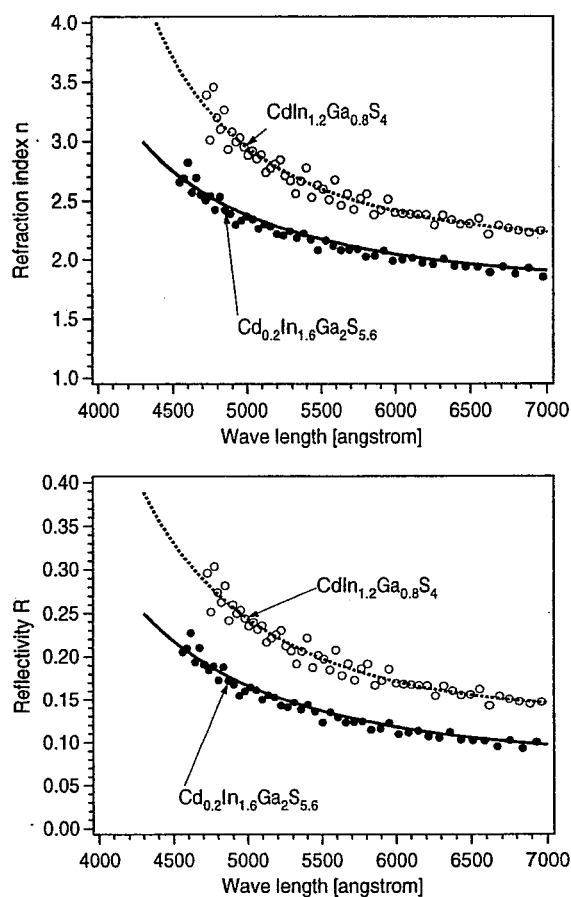
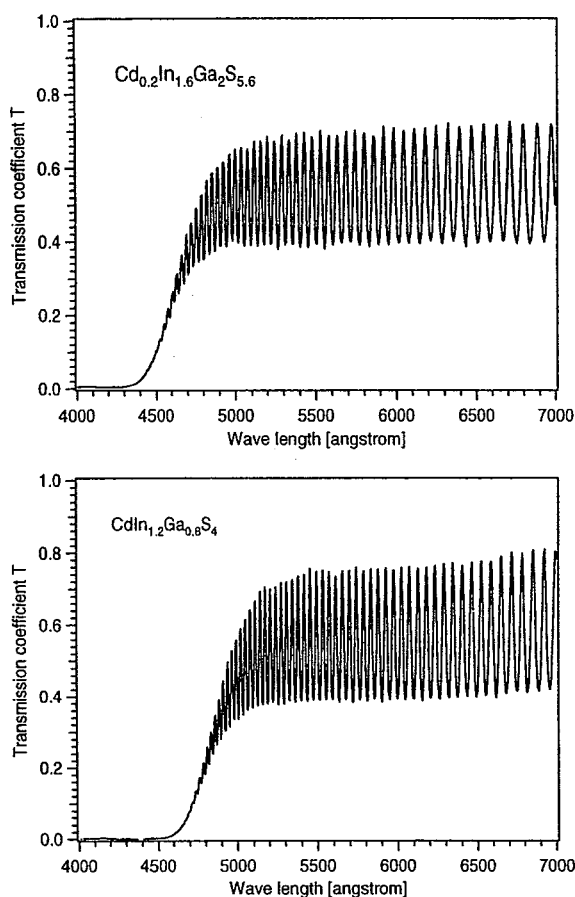


Fig. 8. The transmission coefficient for  $\text{Cd}_{0.2}\text{In}_{1.6}\text{Ga}_2\text{S}_{5.6}$  ( $d = 15 \mu\text{m}$ ) and  $\text{CdIn}_{1.2}\text{Ga}_{0.8}\text{S}_4$  ( $d = 14 \mu\text{m}$ ).

Fig. 9. The refraction index and reflectivity for  $\text{Cd}_{0.2}\text{In}_{1.6}\text{Ga}_2\text{S}_{5.6}$  ( $d = 15 \mu\text{m}$ ) and  $\text{CdIn}_{1.2}\text{Ga}_{0.8}\text{S}_4$  ( $d = 14 \mu\text{m}$ ).

transparent region, the interference effect was clearly observed. We calculated mean refractive index  $n$  and reflectivity  $R$  by using equation (3). Fig. 9 shows the dependence of the refractive index and reflectivity on wavelength. Based on the results and equation (2), we calculated the band gap by using  $(\alpha h\nu)^l$  v.s.  $h\nu$  ( $l = 1/2, 2$ ) plot. The band gaps are  $E_g = 2.58$  eV (indirect), 2.76 eV (direct) for  $\text{Cd}_{0.2}\text{In}_{1.6}\text{Ga}_2\text{S}_{5.6}$  and  $E_g = 2.49$  eV (indirect), 2.65 eV (direct) for  $\text{CdIn}_{1.2}\text{Ga}_{0.8}\text{S}_4$ . The difference in the energy gap between two phases is understood by the interatomic distance; the energy gap is inversely proportional to the mean interatomic distance. Actually, the mean atoms distance between cation and anion of the  $\text{Cd}_{0.2}\text{In}_{1.6}\text{Ga}_2\text{S}_{5.6}$  and  $\text{CdIn}_{1.2}\text{Ga}_{0.8}\text{S}_4$  are 2.41 and 2.53 Å, respectively.

Table III shows the interatomic distances and energy gaps in the  $\text{CdS} - \text{In}_2\text{S}_3 - \text{Ga}_2\text{S}_3$  system. Interatomic distance of cation and anion atoms depends on both the surrounding atoms and coordination numbers. For example, the distance between Cd and S in the  $\text{CdIn}_2\text{S}_4$  lattice is shorter than that of other compounds such as  $\text{CdS}$ ,  $\text{CdGa}_2\text{S}_4$  and  $\text{CdIn}_{1.2}\text{Ga}_{0.8}\text{S}_4$ , which have Cd atoms in the formula. In this ternary system, the mean interatomic distance increases by the following order: tetrahedral < layer < spinel. This is because the interatomic distance of the tetrahedral cation is larger than that of the octahedral one in the  $\text{CdS} - \text{In}_2\text{S}_3 - \text{Ga}_2\text{S}_3$  system. Consequently, as the number of the octahedral atoms increases, the mean interatomic distance increases and energy gap decreases.

Table III. Interatomic distances and energy gap.

Compound	Structure	Cd-S [Å]	Ga-S [Å]	In <sub>tet.</sub> -S [Å]	In <sub>oct.</sub> -S [Å]	mean value	E <sub>g</sub> [eV]
CdS	wurtzite	2.51	-	-	-	2.51	2.42
Ga <sub>2</sub> S <sub>3</sub>	defect wurtzite	-	2.26	-	-	2.26	3.44
In <sub>2</sub> S <sub>3</sub>	defect spinel	-	-	2.33	2.69	2.57	2.03
CdGa <sub>2</sub> S <sub>4</sub>	defect chalcopyrite	2.56	2.27	-	-	2.36	3.58
CdIn <sub>2</sub> S <sub>4</sub>	spinel	2.20	-	-	2.80	2.60	2.44
GaInS <sub>3</sub>	P6 <sub>1</sub>	-	2.34	-	2.57	2.46	-
CdIn <sub>1.2</sub> Ga <sub>0.8</sub> S <sub>4</sub>	layer	2.4	2.5	-	2.7	2.53	2.49

#### 4. Summary

We have constructed the phase diagram of the  $\text{CdGa}_2\text{S}_4 - \text{CdIn}_2\text{S}_4$  system. The single layer phase was found between  $x = 0.58 \sim 0.68$ . We have also found a new layer phase  $\text{Cd}_{0.2}\text{In}_{1.6}\text{Ga}_2\text{S}_{5.6}$  in the  $\text{CdGa}_2\text{S}_4 - 2\text{GaInS}_3$  system. The phase crystallizes in the trigonal space group  $\text{P}\bar{3}\text{m}1$  (164) having hexagonal lattice parameters,  $a = 3.80$ ,  $c = 18.3$  Å. The atomic positions were determined by the Rietveld analysis. The optical band gap of the newly found layer compound was larger than that of  $\text{CdIn}_{1.2}\text{Ga}_{0.8}\text{S}_4$  at room temperature. This is explained by the difference in the interatomic distance of both compounds.

#### Acknowledgements

This work was partly supported by the Research Grant from Nihon University.

#### References

- 1) W. A. Shand; *Phys. Stat. Sol. (a)* **3** (1970) K77.
- 2) H. Haeuseler, A. Cansiz, M. Himmrich and M. Jung; *J. Solid State Chemistry* **74** (1988) 171.
- 3) H. Haeuseler and S. K. Srivastava; *Z. Kristallogr.* **215** (2000) 205.
- 4) C. Razzetti, P. P. Lottici, L. Tarricone and L. Zanotti; *Prog. Cryst. Growth and Charact.* **10** (1984) 353.
- 5) V. P. Mushinsky, V. P. Ambross; *Kristall und Technik* **5** (1970) K5.
- 6) M. P. Pardo, J. Flahaut and L. Gastaldi; *Mat. Res. Bull.* **19** (1984) 735.
- 7) H. Nakanishi, S. Endo and T. Irie; *Jpn. J. Appl. Phys.* **19** (1980) 261.
- 8) G. A. Steigmann, H. H. Sutherland and J. Goodyear; *Acta Cryst.* **19** (1965) 967.
- 9) Wyckoff; *Crystal Structures*, Vol. 2 p22-24, Interscience Publishers.
- 10) G. G. Guseinov, I. R. Amiraslanov, A. S. Kuliev and Kh. S. Mamedov; *Inorg. Materials* **23** (1987) 766.
- 11) T. Takizawa, C. Hidaka, K. Asaka, T. Isomoto and H. Matsushita; *Jpn. Appl. Phys.* **39** (2000) 35.
- 12) K. Asaka, C. K. Hidaka, T. Takizawa and H. Matsushita; *Jpn. J. Appl. Phys.* **39** (2000) 139.
- 13) H. Haeuseler; *J. Solid state Chemistry*; **86** (1990) 275.
- 14) A. Zunger; *Physical Review B* **22** (1980) 5839.
- 15) H. Matsushita and T. Takizawa; *Jpn. J. Appl. Phys.* **34** (1995) 4699.
- 16) R. A. Young; *The Rietveld Method*, Oxford (1993)
- 17) Y. I. Kim and F. Izumi; *J. Ceram. Soc. Jpn.* **102** (1994) 401.
- 18) C. Komatsu and T. Takizawa; *J. Crystal Growth* **210** (2000) 677.
- 19) H. Nakanishi; *Jpn. J. Appl. Phys.* **19** (1980) 103.
- 20) J. I. Pankove; *Optical Processes in Semiconductors*, Prentice Hall (1973)
- 21) F. G. Donika, G. A. Kiosse, S. I. Radautsan, S. A. Semiletov and V. F. Zhitar; *Sov. Phys. Cryst.* **12** (1971) 745.
- 22) F. Lappe, A. Niggli, R. Nitshe and J. G. White; *Z. Kristallogr.* **117** (1962) 146.
- 23) F. G. Donika, S. I. Radautsan, G. A. Kiosse, S. A. Semiletov, T. V. Donika and I. G. Mustya; *Sov. Phys. Cryst.* **15** (1971) 698.
- 24) S. I. Radautsan, F. G. Donika and I. G. Moustia; *J. Crystal Growth* **13/14** (1972) 385.
- 25) F. G. Donika, S. I. Radautsan, S. A. Semiletov, T. V. Donika and I. G. Mustya; *Sov. Phys. Cryst.* **17** (1972) 578.
- 26) F. Huliger; *Structural Chemistry of Layer-type Phases*, Reidel, Dordrecht (1976)
- 27) H. Matsushita, S. Nomura, S. Ando, S. Endo and T. Irie; *Jpn. J. Appl. Phys.* **29** (1990) L872.
- 28) T. Irie, S. Ando, Y. Noda and S. Endo; *Jpn. J. Appl. Phys.* **31** (1992) 2508.

## Defect Physics of CuInSe<sub>2</sub> and CuGaSe<sub>2</sub> Bulk Single Crystals Grown by the Horizontal Bridgman Method

Hiroaki MATSUSHITA and Takeo TAKIZAWA<sup>1</sup>

*Department of Material Science and Technology, School of High-Technology for Human Welfare, Tokai University, 317 Nishino, Numazu-city, Shizuoka 410-0395, Japan*

<sup>1</sup>*Department of Physics, College of Humanities and Sciences, Nihon University, 3-25-40 Sakurajosui, Setagaya-ku, Tokyo 156-0045, Japan*

The defect physics of CuInSe<sub>2</sub> and CuGaSe<sub>2</sub>, especially on the origins and values of the activation energies in these bulk crystals have been analyzed by means of the Hall effect, electron spin resonance, optical absorption, photoluminescence measurements and electron probe microanalysis. The activation energies of donors in the n-type CuInSe<sub>2</sub> are estimated to be ~30meV and 5-10meV, while those of acceptor in the p-type CuInSe<sub>2</sub> are estimated to be 50-60meV and 10-20meV, on the basis of the Hall effect. From the results of the electron spin resonance and the annealing effect in Se atmosphere, the deep and shallow acceptors can be ascribed to the In vacancies and the Cu vacancies or Cu in the In site, respectively. The deep and shallow donors can be ascribed to In in the Cu site and the Se vacancies, respectively. On the other hand, the acceptor levels of CuGaSe<sub>2</sub> are about 20meV for Cu-vacancies and/or Cu in the Ga site and about 80meV for Ga-vacancies, and the donor level is about 60meV for Se-vacancies from the annealing results in vacuum and Se atmosphere.

**KEYWORDS:** CuInSe<sub>2</sub>, CuGaSe<sub>2</sub>, intrinsic defect, Hall effect, ESR, optical band gap, PL, acceptor level, donor level

### 1. Introduction

There are still many controversial problems in interpreting the defect physics of CuInSe<sub>2</sub> and CuGaSe<sub>2</sub>, especially on the origins and values of the activation energies of acceptors and donors. These are mainly due to the difficulties in reducing and controlling lattice defects in ternary semiconductors as compared to those of binary ones. The important problems to be solved are as follows:

- (1) To reduce microcracks and extrinsic defects in the growing process.
- (2) To grow bulk single crystals with sufficiently well-controlled compositions to identify intrinsic defects clearly.
- (3) To stabilize electrical and optical properties, very sensitive to compositional deviation from stoichiometry.

To settle these problems, we have grown the bulk single crystals of CuInSe<sub>2</sub> and CuGaSe<sub>2</sub> by the horizontal Bridgman method with controlling Se vapor pressure as well as the flux method using self-flux as a solvent. The electronic energy levels and densities of intrinsic defects in these crystals have been analyzed in terms of the Hall effect, electron spin resonance (ESR), optical absorption, photoluminescence measurements and electron probe microanalysis (EPMA), and their origins are discussed in comparison to the annealing effect in vacuum and/or Se atmosphere.

### 2. Growth of Bulk Single Crystals

#### 2.1 CuInSe<sub>2</sub> crystals grown by selenization method

CuInSe<sub>2</sub> bulk single crystals were grown using the selenization horizontal Bridgman method with controlling Se vapor pressure from 5 to 25 Torr.<sup>1,2)</sup> A CuIn alloy was first produced by reacting the two elements at 700°C. Then it was heated to 1020°C, while the Se element sealed at the other end of the quartz tube was heated to a temperature corresponding to the desired Se vapor pressure. After selenizing the CuIn alloy, the profile of temperature gradient which was set to 3°C/cm was electrically moved at a speed of about 1cm/h under the Se vapor pressure. Crystals thus

grown were cut into three parts along the growth direction, i.e., "Top (T)", "Middle (M)" and "End (E)". "T" denotes the portion initially solidified. The prefixed number such as "10T" denotes Se vapor pressure in Torr during the crystal growth.

In previous papers,<sup>1,3)</sup> we reported that CuInSe<sub>2</sub> crystals showed n-type conduction, when they were prepared under low Se vapor pressures (less than 5-7 Torr), but they sometimes contained heterogeneous phases which were inhomogeneously distributed inside. The Hall mobilities of these n-type samples were lower than those grown by the normal freezing method, indicating their degraded characteristics.<sup>1)</sup> In order to obtain n-type single crystals of good quality, we have used the horizontal Bridgman method without applying Se vapor pressure. These crystals were prepared using mixtures of Cu, (1+x)In and (2+x)Se as a starting material by fixing the compositions to Se/metal=1 and Cu/In ≤ 1, where x was varied from 0 to 0.01.

#### 2.2 CuGaSe<sub>2</sub> crystals grown by solution method

To avoid the peritectic reaction at the interface between the (sphalerite + liquid) phase and the chalcopyrite phase,<sup>4)</sup> CuGaSe<sub>2</sub> crystals have been already grown by the solution method using In, CuI, Pb and Bi solvents.<sup>5-8)</sup> However, it has a problem of contamination by the solvents used. To overcome the problem, the growth of bulk crystals using the self-flux may be effective. For this purpose, we have constructed the phase diagram of the CuSe-CuGaSe<sub>2</sub> system.<sup>9)</sup> On the base of this phase diagram, bulk single crystals were grown by the horizontal Bridgman method using the liquidus line of 10 to 55mol%CuGaSe<sub>2</sub> solute.<sup>9)</sup> The solute was held at 1060°C for 24h, and the crystal was grown at a speed of 2°C/h.

### 3. Defect Physics of Bulk Single Crystals

#### 3.1 Hall effects

The Hall coefficient and mobility of CuInSe<sub>2</sub> and CuGaSe<sub>2</sub> bulk single crystals were measured in the temperature range from 20 to 300K under a constant magnetic field of about 1 T using the six-electrode method. The electrodes for n- and

p-CuInSe<sub>2</sub> were made by electrodeposition of Ni onto the samples. On the other hand, Ni and Pt electrodes were adopted for p-type CuGaSe<sub>2</sub> crystals with low and high resistivities, respectively.

Most of the p-type CuInSe<sub>2</sub> crystals grown in our work show overshoots in the Hall coefficient vs temperature curves. These overshoots are typical for the two carrier conduction and frequently observed in the case of compensated III-V semiconductors such as InSb.<sup>10</sup> The Hall coefficient  $R_H$  with overshoot is expressed as follows,

$$R_H = \frac{\gamma(p - nb^2)}{e(p + nb)^2}, \text{ where } b \equiv \frac{\mu_n}{\mu_p} \quad (1)$$

where  $\gamma$  is the Hall factor,  $e$  the elementary charge and  $\mu_n/\mu_p$  the Hall mobility ratio. Here, the electron and the hole concentrations,  $n$  and  $p$  are expressed as a function of temperature as follows, except for the degenerate region where the conductivity becomes independent of temperature,

$$n = \frac{N_D}{1 + 2 \exp(E_D/kT)}, \text{ for } N_D > N_A \gg n, \quad (2)$$

$$p = \frac{N_A}{1 + 2 \exp(E_A/kT)}, \text{ for } N_A > N_D \gg p, \quad (3)$$

where  $N_D$  and  $N_A$  are the donor and acceptor densities, and  $E_D$  and  $E_A$  are the donor and acceptor levels, respectively.

The behavior of the Hall coefficient vs temperature curves of n-type CuInSe<sub>2</sub> samples is classified into two types<sup>11</sup> as shown in Fig. 1. The conduction characteristics for n-type samples was well described by assuming the one-carrier model, and the activation energies of donors were estimated to be ~30meV ( $E_{D(\text{deep})}$ ) and 5-10meV ( $E_{D(\text{shallow})}$ ). Since the formation energies of the antisite In<sub>Cu</sub> (1.4-1.6eV) or Se vacancy V<sub>Se</sub> (2.2-2.8eV) are much lower than those for the interstitial impurities Cu<sub>i</sub> (4.4eV) and In<sub>i</sub> (9.1eV) and the cation and anion antisites In<sub>Se</sub> (5.0eV) and Se<sub>Cu</sub> (6.0-7.5eV),<sup>12-14</sup> the intrinsic defects constituting these donors can be ascribed to In<sub>Cu</sub> or V<sub>Se</sub>. From the results of EPMA, the

samples with  $E_{D(\text{deep})}$  have In-rich compositions, i.e., Cu/In < 1, while the samples with  $E_{D(\text{shallow})}$  have Cu/In ~ 1 and Se-poor compositions. The samples with  $E_{D(\text{deep})}$  were also prepared using the selenization horizontal Bridgman method under a low Se vapor pressure.<sup>1</sup> Hence, the donors with  $E_{D(\text{deep})}$  and  $E_{D(\text{shallow})}$  can probably be ascribed to In<sub>Cu</sub> and V<sub>Se</sub>, respectively.

The effect of the electron concentration on the Hall coefficient of p-type CuInSe<sub>2</sub> samples may be negligible compared to that of the hole concentration at high temperature. Hence, the activation energies of acceptors were estimated using the curves at high temperature where the logarithm of Hall coefficients increases nearly linearly with decreasing temperature. Two acceptor levels were derived as 10-20 meV ( $E_{A(\text{shallow})}$ ) and 50-60 meV ( $E_{A(\text{deep})}$ ). On the other hand, in the region of the Hall coefficient overshoots, the Hall mobility ratio on the equation (1) are assumed as

$$b \propto T^{-\eta}, \quad (4)$$

indicating the difference in the temperature dependence of the electron and hole mobilities.<sup>1,15</sup> We classified the  $R_H$  behaviors of p-type samples into three types, i.e., deep (D), shallow (S) and double (W) by using the density ratio between shallow and deep acceptors.<sup>1</sup> The results of the Hall effect of D-, S- and W-type samples are shown in Figs. 2, 3 and 4, respectively. The densities of shallow and deep acceptors are designated as  $N_{A(\text{shallow})}$  and  $N_{A(\text{deep})}$ , respectively.  $N_{A(\text{shallow})}$  is much larger than  $N_{A(\text{deep})}$  in the S-type samples, while  $N_{A(\text{shallow})}$  is much less than  $N_{A(\text{deep})}$  in the D-type samples, and the conductivity type sometimes changes from p to n at low temperature. The W-type samples have two kinds of the overshoot peaks, indicating that  $N_{A(\text{shallow})}$  is almost comparable with  $N_{A(\text{deep})}$ .

On the other hand, the electrical properties with only the p-type conduction were obtained for the CuGaSe<sub>2</sub> crystals prepared using CuSe solvent as shown in Fig. 5. This was in contrast to those prepared with In solvent,<sup>6</sup> where only a highly resistive sample was available because of the compensation. The activation energies of acceptors were

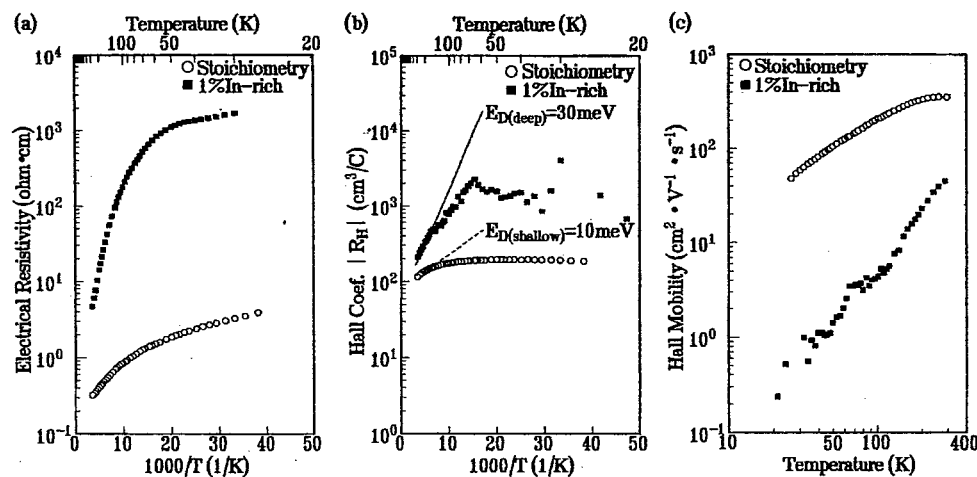


Fig. 1. Temperature dependence of (a) the electrical resistivity, (b) the Hall coefficient and (c) the Hall mobility of n-type CuInSe<sub>2</sub>.<sup>11</sup>

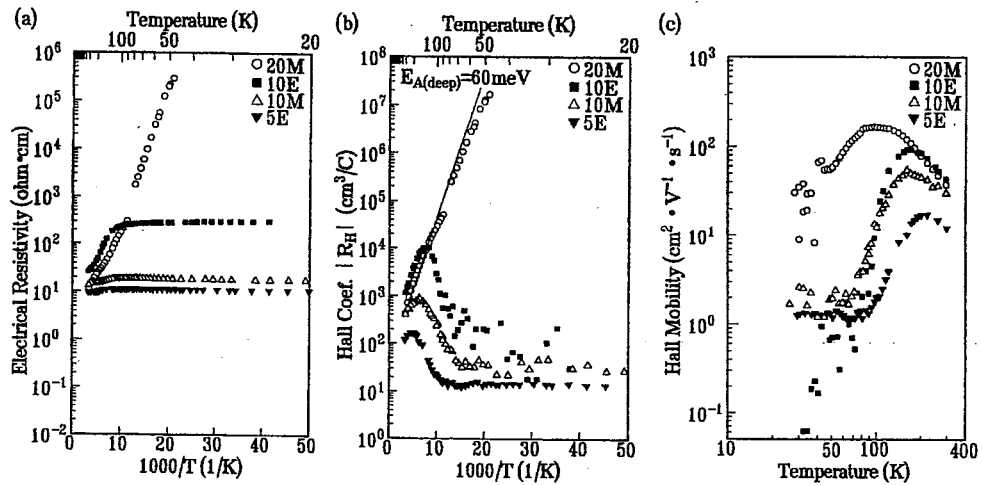


Fig. 2. Temperature dependence of (a) the electrical resistivity, (b) the Hall coefficient and (c) the Hall mobility of the D-type samples.

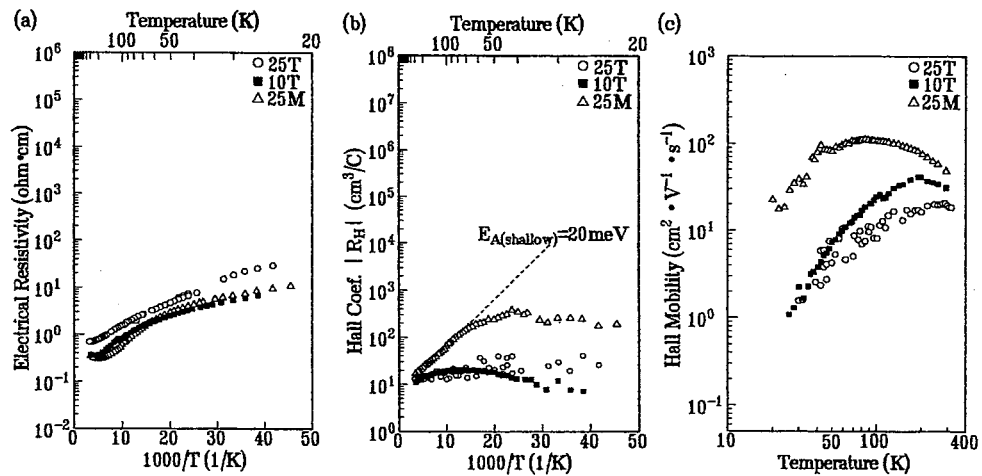


Fig. 3. Temperature dependence of (a) the electrical resistivity, (b) the Hall coefficient and (c) the Hall mobility of the S-type samples.

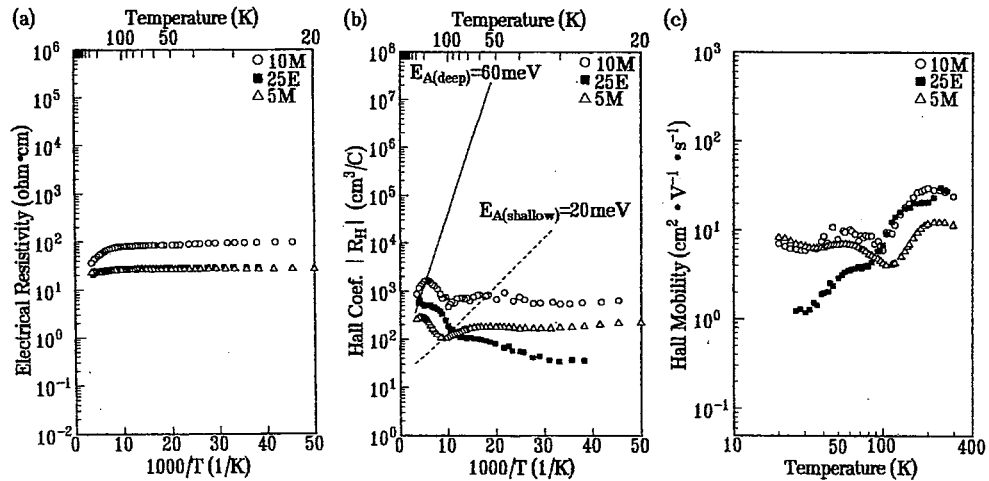


Fig. 4. Temperature dependence of (a) the electrical resistivity, (b) the Hall coefficient and (c) the Hall mobility of the W-type samples.

estimated using the temperature variation of Hall coefficient curves. Two acceptor levels were deduced as about 20 and 80 meV. According to the temperature variation of the resistivity curves, we classified the samples into two types, i.e., H-type such as samples A and B, and L-type such as samples C, D

and E.<sup>16</sup> The resistivity and mobility of the H-type changed drastically as temperature varies, while those of the L-type changed little.

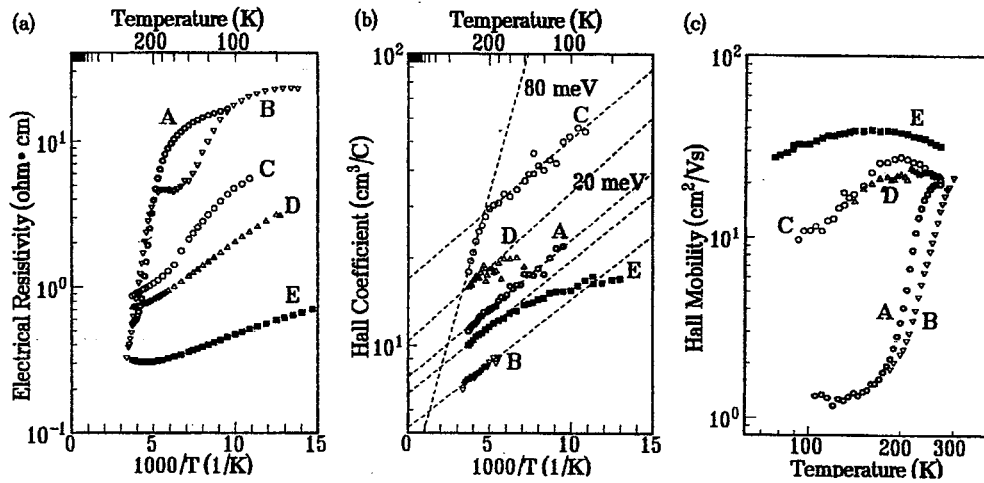


Fig. 5. Temperature dependence of (a) the electrical resistivity, (b) the Hall coefficient and (c) the Hall mobility of as-grown  $\text{CuGaSe}_2$ .<sup>16)</sup>

### 3.2 Electron spin resonance

Most of  $\text{CuInSe}_2$  single crystals grown from melts or solvents are inevitably contaminated by iron ions. ESR was carried out by utilizing the iron contamination, and ESR signals related to  $\text{Fe}^{3+}$  and  $\text{Fe}^{2+}$  were observed.<sup>17,18)</sup> ESR was performed with 9.35 GHz at liquid He temperature (4.2K), using a  $\text{TE}_{102}$  cavity.<sup>19)</sup> We have also studied the effect of lattice defects on ESR using the same p-type  $\text{CuInSe}_2$  samples in §3.1 whose ternary compositional diagram determined by EPMA is shown in Fig. 6. Figure 7 shows the ESR spectra of the D-, S- and W-type samples. Here, ESR intensities were normalized to the respective weights of the samples. Therefore, the ESR intensities directly yield the paramagnetic ion concentrations. The  $\text{Fe}^{3+}$  related signals, i.e., "II", "III" and "IV" are observed strongly in the D-type samples having stoichiometric compositions, and also observed weakly in the W-type samples having Cu-rich and Se-poor compositions. On the contrary, the  $\text{Fe}^{2+}$  related signal "I" are observed only in the S-type samples. In addition, the

isotropic line at  $g \sim 2$ , which is the strongest for the S-type samples, was ascribed previously to Cu vacancies.<sup>18)</sup> Here, 25M in the S-type samples show ESR signals as containing partly the D-type samples. This may relate to the donor density in 25M which is less than that of 10T and 25T at low temperature (see Fig. 3).

These results may give us hints on the origins of the intrinsic defects, in particular, acceptors, since all samples show p-type conduction. Those defects may be expected arising mainly from cation vacancies which are substituted by iron atoms. As the ESR intensities for  $\text{Fe}^{2+}$  or  $\text{Fe}^{3+}$  are irrespective of acceptor densities of  $\sim 20$  or  $\sim 60 \text{ meV}$ , we rule out these defects because they have no relation with iron. The formation energies of the antisite  $\text{Cu}_{\text{In}}$  (1.5-1.9eV), Cu vacancy  $\text{V}_{\text{Cu}}$  (2.6-3.2eV) or In vacancy  $\text{V}_{\text{In}}$  (2.4-2.8eV) are much lower than those for the interstitial impurities  $\text{Se}_{\text{i}}$  (22.4eV), the cation and anion antisites  $\text{Cu}_{\text{Se}}$  (5.4-7.5eV) and  $\text{Se}_{\text{In}}$ , (5.2-5.5eV).<sup>12-14)</sup> Thus, both acceptor levels  $E_{\text{A}}(\text{shallow})$  and  $E_{\text{A}}(\text{deep})$  may be tentatively ascribed to  $\text{V}_{\text{Cu}}$ ,  $\text{V}_{\text{In}}$  and/or  $\text{Cu}_{\text{In}}$ .

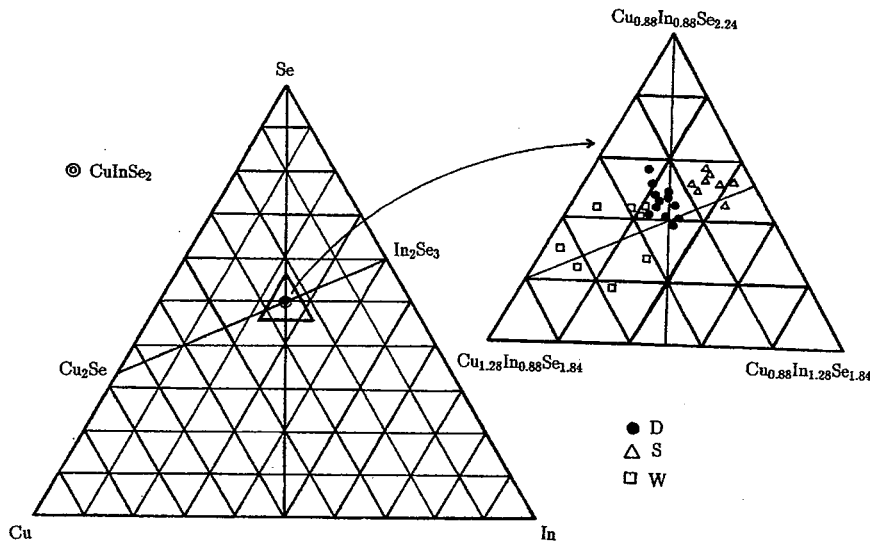


Fig. 6. Relative atomic ratios of the D-, S- and W-type samples in the ternary composition diagram.<sup>11)</sup>

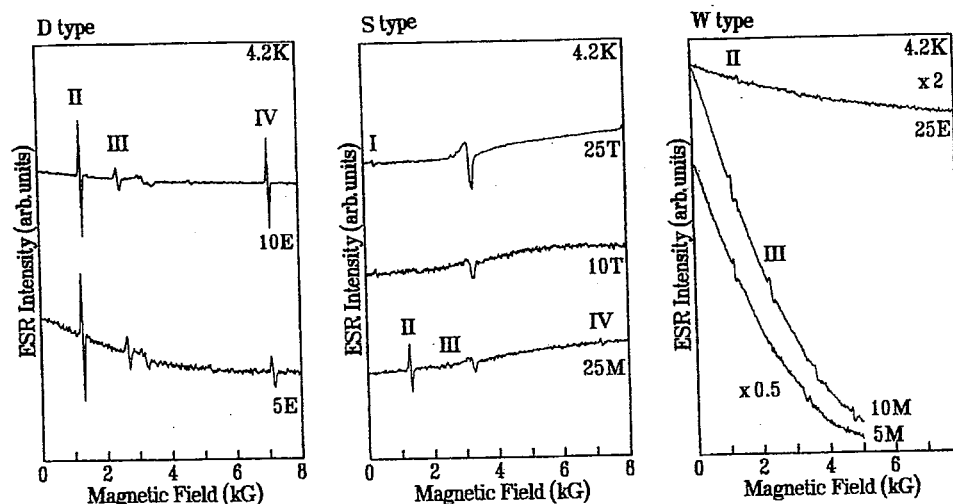
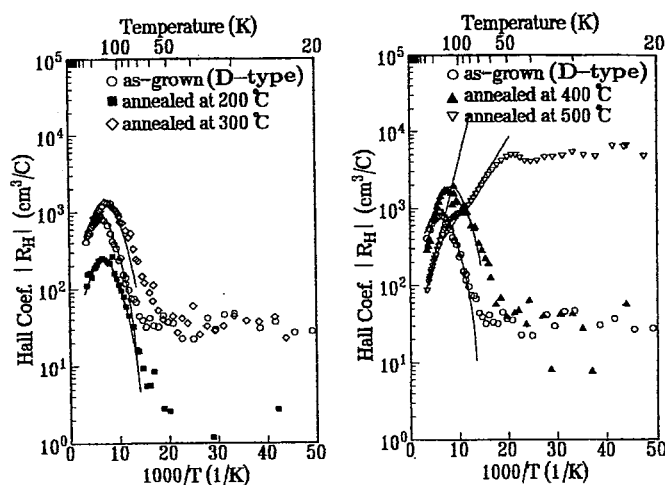


Fig. 7. ESR spectra at 4.2K of the D-, S- and W-type samples.

The acceptor with  $E_{A(\text{shallow})}$  in S-type samples is ascribed to  $V_{\text{Cu}}$  for  $\text{Cu}/\text{In} < 1$ , and Fe atoms substituting Cu sites give rise to the ESR signals for  $\text{Fe}^{2+}$ . The acceptor with  $E_{A(\text{shallow})}$  in the W-type samples may be due to  $\text{Cu}_{\text{In}}$  for  $\text{Cu}/\text{In} > 1$ . The acceptor with  $E_{A(\text{deep})}$  in the D- and W-type samples is expected to be due to  $V_{\text{In}}$  which is the best candidate remaining. If the donor density decreases in p-type samples with  $\text{Cu}/\text{In} < 1$ , the density of  $V_{\text{Cu}}$  does not only increase but the density of  $V_{\text{In}}$  also increases a little. ESR signals for  $\text{Fe}^{3+}$  with  $\text{Cu}/\text{In} < 1$  indicates that iron atoms preferably occupy  $V_{\text{In}}$  to  $V_{\text{Cu}}$ .

### 3.3 Annealing effect

To identify the origin of the donors in p-type  $\text{CuInSe}_2$ , a D-type sample with a higher donor density ( $\text{Cu}/\text{In} \sim 1$ ) was annealed in Se atmosphere which is controlled in the range of 200 to 500°C.<sup>11)</sup> The Hall coefficient vs temperature curves were obtained after each of four kinds of annealing under different Se vapor pressures, and shown in Fig. 8. Following the same procedure as in previous papers,<sup>1,15)</sup> we deduced the densities of acceptors and donors,  $N_{A(\text{deep})}$ ,  $N_{A(\text{shallow})}$  and  $N_{D(\text{shallow})}$ , using the estimated activation energies of  $E_{A(\text{deep})} = 50\text{meV}$ ,  $E_{A(\text{shallow})} = 20\text{meV}$  and  $E_{D(\text{shallow})} = 10\text{meV}$ .<sup>11)</sup> The results are summarized in Table I. The donor density was found to decrease with increasing Se vapor pressure.<sup>1,2,15)</sup> In the case of annealing under a low Se vapor pressure of  $5.0 \times 10^{-3}$  Torr (at 200°C), the donor density becomes higher than that for an as-grown sample. As Se vapor pressure in annealing increases to more than  $2.8 \times 10^{-1}$  Torr (at 300°C), the peak of the Hall overshoot shifts to the lower temperature side, finding that the donor densities annealed at 300 and 400°C become lower than that for an as-grown sample. After annealing under 43 Torr (at 500°C), the Hall overshoot disappears, and shallow acceptors ascribed to  $V_{\text{Cu}}$  are observed newly, i.e., the corresponding donor density decreases drastically. Therefore, the donor level  $E_{D(\text{shallow})}$ , the density of which was affected by annealing, is confirmed to be due to  $V_{\text{Se}}$ , as expected in §3.1. The W- and S-type samples were also annealed, where the temperature at the Se side was controlled in the range of 200 to 300°C. The change in the

Fig. 8. Temperature variation of the Hall coefficient of the D-type sample ( $\text{Cu}/\text{In} \sim 1$ ) by annealing in Se atmosphere.<sup>11)</sup>

Hall coefficient vs temperature curves of the W-type samples by annealing was similar to that of the D-type samples, while the Hall coefficient vs temperature curve of the S-type samples changed little by annealing.

To determine these defect levels and origins in p-type  $\text{CuInSe}_2$  samples, the results of optical absorption and photoluminescence<sup>11)</sup> are also summarized as follows. The samples with  $\text{Cu}/\text{In} \geq 1$  have an optical band gap of 1.04eV, while the p-type samples with  $\text{Cu}/\text{In} < 1$  have an optical band gap of  $\sim 1.00\text{eV}$ . The optical band gap of the p-type compensated samples with  $\text{Cu}/\text{In} < 1$  is  $\sim 40\text{meV}$  shallower than that of any other sample. The band tail spreads towards the lower energy side as Cu and/or Se vacancies increase. For the D- and W-type samples with  $\text{Cu}/\text{In} \geq 1$ , an emission peak was observed at 0.97-0.98eV, and often other emissions at  $\sim 1.00$  and 1.04eV, while for the S-type samples with  $\text{Cu}/\text{In} < 1$ , emission peaks were observed at 0.93 and/or 0.95-0.96eV. We could identify the emission peaks of the D- and W-type samples to the D-A pair recombination of  $V_{\text{Se}} \cdot V_{\text{In}}$  and  $V_{\text{Se}} \cdot \text{Cu}_{\text{In}}$ .

Table I. Effect of Annealing on the D-type sample (Cu/In~1) in Se atmosphere.<sup>11)</sup>

annealing temperature (°C)	Se vapor pressure (Torr)	$N_{A(\text{deep})}$ (50 meV)*	$N_{A(\text{shallow})}$ (20 meV)*	$N_{D(\text{shallow})}$ (10 meV)*
(as-grown)	—	$2 \times 10^{17}$	—	$2 \times 10^{18}$
200	$5.0 \times 10^{-3}$	$8 \times 10^{17}$	—	$5 \times 10^{18}$
300	$2.8 \times 10^{-1}$	$2 \times 10^{17}$	—	$9 \times 10^{17}$
400	$5.0 \times 10^0$	$2 \times 10^{17}$	—	$6 \times 10^{17}$
500	$4.3 \times 10^1$	$8 \times 10^{17}$	$2 \times 10^{17}$	—

\* activation energies

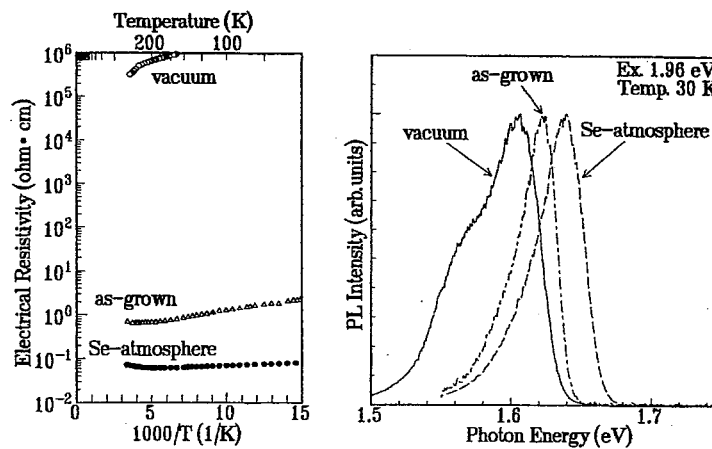
Table II. Origins and levels of defects related with emissions of the D- (Cu/In~1), B- (Cu/In>1) and S-type samples (Cu/In<1).<sup>11)</sup>

type	$E_T$ (eV)	emission peak (eV)	donor source	activation energy of donor (meV)	acceptor source	activation energy of acceptor (meV)
D, B	~1.04	1.04 ~1.00 0.97~0.98	— $V_{Se}$ $V_{Se}$	— 5~10 5~10	— $Cu_{In}$ $V_{In}$	— ~20 50~60
S	~1.00	(0.98)* 0.95~0.96 0.93	$V_{Se}$ $In_{Cu}$ unknown ( $V_{Se}$ ?)	5~10 ~30 ~60	$V_{Cu}$ $V_{Cu}$ $V_{Cu}$	10~20 10~20 10~20

The results are shown in Table II. On the other hand, the emission peaks of the S-type samples are ascribed to the D-A pair recombination of  $In_{Cu}-V_{Cu}$  and (unknown defect)- $V_{Cu}$  as shown in Table II. The impurity level corresponding to the emission peak at 0.93eV, i.e.,  $E_{D(\text{unknown})}$ , cannot be identified by the Hall effect in our work. However, the S-type sample is expected to have donors with an activation energy of ~60 meV, probably relating to  $V_{Se}$ . The emission peak at ~0.98eV (marked as "\*" in Table II) is sometimes known to be observed in In-rich samples as the D-A pair emission of  $V_{Se}-V_{Cu}$ . However, this peak was not observed in our work.

In the case of photoluminescence spectra of  $CuGaSe_2$ , we have classified the emission peaks as H- and L-types, according to  $Cu/Ga < 1$  and  $Cu/Ga > 1$ , respectively.<sup>16)</sup> The peak appearing at about 1.6eV is classified in the H-type, while that at 1.62-1.65eV in the L-type. The optical band gap of the H-type was estimated to be 1.685eV at 30K from transmission and reflectivity measurements, being 30-50 meV smaller than that of L-type and that of thin films

prepared by MBE.<sup>20)</sup> We have investigated the temperature variation of resistivity and photoluminescence spectra by annealing  $CuGaSe_2$  crystals in vacuum and Se atmosphere.<sup>16)</sup> Samples were heated to 500°C in vacuum, and held for 24h. After electrical and optical measurements, the samples were again heated to 500°C under Se vapor pressure of 5 Torr, and held for 24h. Figure 9 shows the annealing effect for sample D of the L-type. After the sample was annealed in vacuum, its resistivity increased five orders, and the emission peak shifted to lower energy side by ~0.2 eV. Fitting the relation of the peak energy of emission against the intensity of excitation light to the well known equation of D-A pair recombination,<sup>21,22)</sup> the levels of acceptor and donor in the vacuum annealed sample D were deduced as  $E_A \sim 80\text{meV}$  and  $E_D \sim 60\text{meV}$ , respectively. In addition, the Se contents of sample D decreased from  $Se/metal = 0.97$  to 0.92 by annealing in vacuum. The conduction type can be changed from degenerate to semi-insulating through an appropriate annealing as shown in Fig. 9. Therefore, the compensation

Fig. 9. Annealing effects for the resistivity and the emission of sample D (L-type).<sup>16)</sup>

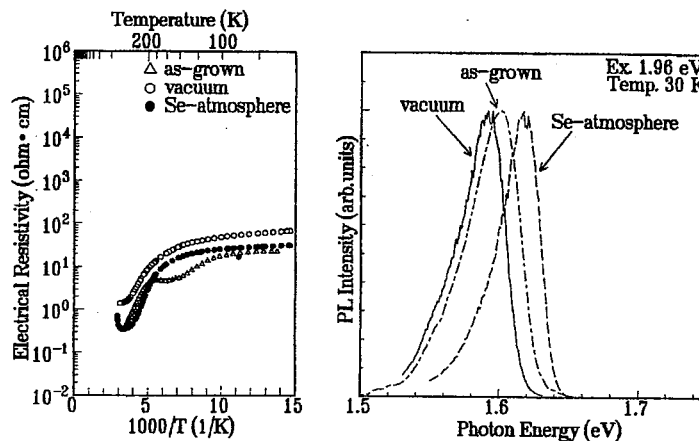


Fig. 10 Annealing effects for the resistivity and the emission of sample B (H-type).<sup>16)</sup>

donor is ascribed to  $V_{Se}$  with the activation energy of about 60meV. On the contrary, the annealing both in vacuum and in Se atmosphere affected little the resistivity of sample B of the H-type as shown in Fig. 10. The Se content was also constant of Se/metal $\sim$ 1 despite of annealing. In addition, the shift of the emission peak was smaller than that of sample D, and the peak energy did not shift with varying the intensity of excitation light. Hence, the emission may be due to the free-to-band recombination. From those results, the conduction band tail of the H-type is expected to spread toward the levels of about 60meV, indicating that the optical band gap is 30-50 meV smaller than that of the L-type. The intrinsic defects constituting acceptors can be ascribed to  $Cu_{Ga}$ ,  $V_{Cu}$  and  $V_{Ga}$ , but  $V_{Cu}$  was reported to be easily formed among them.<sup>6,23,24)</sup> Thus, the acceptor of about 20meV can be due to  $V_{Cu}$ , but is also possible to be  $Cu_{Ga}$  in the case of samples with Cu-rich composition. The remaining acceptor of about 80meV may be due to  $V_{Ga}$ , because it was only observed in Ga-poor samples of  $Cu/Ga > 1.05$ .

#### 4. Conclusion

We have analyzed the intrinsic defects of  $CuInSe_2$  and  $CuGaSe_2$  bulk single crystals by the Hall effect, electron spin resonance, optical absorption, photoluminescence and EPMA.

The activation energies of donors in the n-type  $CuInSe_2$  samples were estimated to be  $\sim$ 30 and 5-10meV, while those of acceptor in the p-type  $CuInSe_2$  samples were estimated to be 50-60 and 10-20meV, on the basis of Hall effect. From the results of electron spin resonance as well as the analysis of the effect of annealing of the p-type samples in Se atmosphere, the deep and shallow acceptors, and the deep and shallow donors can be ascribed as follows.

- acceptors: 50-60meV for  $V_{In}$ , 10-20meV for  $V_{Cu}$  or  $Cu_{In}$ .
- donors: 30meV for  $In_{Cu}$ , 5-10meV (and also 60meV) for  $V_{Se}$ .

On the other hand, the acceptor levels of  $CuGaSe_2$  are about 80 and 20meV, on the basis of Hall effect. The donor level is about 60meV from the annealing results in vacuum and Se atmosphere, and those origins were identified as follows.

- acceptors: 80meV for  $V_{Ga}$ , 20meV for  $V_{Cu}$  (or  $Cu_{Ga}$ ).
- donors: 60meV for  $V_{Se}$ .

#### References

- 1) H. Matsushita and T. Takizawa: *J. Cryst. Growth* **160** (1996) 71.
- 2) H. Matsushita, A. Iwabuchi, T. Takizawa and S. Endo: *Cryst. Res. & Technol.* **31** (1996) Special Issue, 77.
- 3) H. Matsushita, T. Suzuki, S. Endo and T. Irie: *Jpn. J. Appl. Phys.* **34** (1995) 3474.
- 4) J. C. Mikkelsen, Jr.: *J. Electron. Mater.* **10** (1981) 541.
- 5) K. Sugiyama, A. Sawada, K. Ito, S. Iwasaki and T. Endo: *J. Cryst. Growth* **84** (1987) 673.
- 6) H. Miyake, M. Hata and K. Sugiyama: *J. Cryst. Growth* **130** (1993) 383.
- 7) K. Sugiyama and A. Sawada: *J. Cryst. Growth* **91** (1988) 527.
- 8) H. Asai and K. Sugiyama: *Jpn. J. Appl. Phys.* **20** (1981) 1401.
- 9) H. Jitsukawa, H. Matsushita and T. Takizawa: *J. Cryst. Growth* **186** (1998) 587.
- 10) K. Seeger: *Semiconductor Physics* (Springer-Verlag Heidelberg, 1989).
- 11) H. Matsushita and T. Takizawa: *Jpn. J. Appl. Phys.* **37** (1998) 4258.
- 12) S. W. Wasim: *Spl. Cell* **16** (1986) 289.
- 13) C. Ricon, C. Ballabamka, J. Gonzalez and G. Sanchez Perez: *Sol. Cell* **16** (1986) 335.
- 14) H. J. Möller: *Sol. Cell* **31** (1991) 77.
- 15) S. Nomura, J. Itoh and T. Takizawa: *Proc. 9th Int. Conf. Ternary and Multinary Compounds, Yokohama, 1993*, *Jpn. J. Appl. Phys.* **32** Suppl. 32-3 (1993) 97.
- 16) H. Matsushita, H. Jitsukawa, H. Sugano, T. Takizawa and S. Endo: *Inst. Phys. Conf. Ser. No 152: Proc. 11th Int. Conf. Ternary and Multinary Compounds*, p. 535, (Salford, 1997)
- 17) S. Nomura, T. Takizawa, A. Goltzene and C. Schwab: *Proc. 9th Int. Conf. Ternary and Multinary Compounds, Yokohama, 1993*, *Jpn. J. Appl. Phys.* **32** Suppl. 32-3 (1993) 196.
- 18) J. M. Tchapkui-Niat, A. Goltzene and C. Schwab: *J. Phys. C* **15** (1982) 4671.
- 19) H. Matsushita, T. Takizawa, S. Nomura, A. Goltzene and C. Schwab: *Cryst. Res. & Technol.* **31** (1996) Special Issue, 903.
- 20) A. Yamada, Y. Makita, S. Niki, A. Obara, P. Fons, H. Shibata, M. Kawai, S. Chichibu and H. Nakanishi: *J. Appl. Phys.* **79** (1996) 4318.
- 21) E. Zack and A. Halperin: *Phys. Rev. B* **6** (1972) 3072.
- 22) S. Shirakata, S. Chichibu, S. Matsumoto and S. Isomura: *Jpn. J. Appl. Phys.* **33** (1994) L345.
- 23) J. Stankiewicz, W. Giritat, J. Ramos and M. P. Vecchi: *Solar Energy Mater.* **1** (1979) 369.
- 24) B. Tell, J. L. Shay and H. M. Kasper: *J. Appl. Phys.* **43** (1972) 2469.



ELSEVIER

Physica C 357–360 (2001) 537–540

PHYSICA C

www.elsevier.com/locate/physc

# The viscous flux flow and flux creep induced by pulsed magnetic field in YBCO disk

T. Kono <sup>a,b,\*</sup>, M. Tomita <sup>b</sup>, M. Murakami <sup>b</sup>, T. Takizawa <sup>a</sup>

<sup>a</sup> Graduate School of Integrated Basic Science, Nihon University, 3-25-40 Sakura-Josui, Setagaya-ku, Tokyo 156-8550, Japan

<sup>b</sup> Superconductivity Research Laboratory, ISTEC, 1-16-25 Shibaura, Minato-ku, Tokyo 105-0023, Japan

Received 16 October 2000; accepted 23 December 2000

## Abstract

We have investigated the magnetic flux motion in a high quality YBCO disk induced by a pulsed magnetic field. The effect of static bias fields was also studied in the temperature range of 30–95 K. The flux flow resistivity  $\rho_f$  increased with increasing the pulsed magnetic field approximately according to the Bardeen–Stephen model, that is  $\rho_f/\rho_n \approx B/B_{c2}$ . The viscosity coefficient  $\eta$  decreased with increasing temperature and static bias field. © 2001 Published by Elsevier Science B.V.

PACS: 74.72.Bk; 74.60.Ge

Keywords: Viscous flux flow; Flux creep; Pulsed magnetic field; YBCO; Flow resistivity; Viscosity coefficient

## 1. Introduction

The observation of dynamic flux motion in superconductors has attracted renewed interest with advent of high-temperature superconductors and is very informative for the understanding of flux pinning behavior. In particular, the viscosity coefficient  $\eta$  gives us information of pinning properties. The experimental determination of this parameter was revealed by means of some experimental techniques such as high frequency methods, resonator, pulsed d.c. current and high d.c. current [1]. The aim of this work is to derive the viscosity coefficient  $\eta$  in melt-processed  $\text{YBa}_2\text{Cu}_3\text{O}_{7-\sigma}$  (YBCO) induced by pulsed magnetic field

having lower frequency in the level of 50–60 Hz. In this case, flux motion is driven by steep magnetic field gradient (Lorentz force).

In previous paper, we reported the temperature dependence of flux motion during the increasing and decreasing processes of pulsed magnetic field [2,3]. In this paper, we will report the experimental results of temperature dependence of the viscosity coefficient  $\eta$  induced by pulsed magnetic fields in a melt-processed YBCO. The relationship between flux flow and creep are also discussed.

## 2. Experimental

The disk sample with dimensions of 15.03 mm  $\phi \times 0.95$  mm  $t$  was cut from a melt-processed massive YBCO block with its  $c$ -axis perpendicular to the disk surface. The trapped field measurements

\* Corresponding author. Fax: +81-3-3454-9287.

E-mail address: murakami@istec.or.jp (M. Murakami).

showed that the sample is a single grain without weak links.

For flux motion measurements, static bias fields were first applied at 95 K in the normal conducting state, and cooled to desired temperature, which is the field-cooling process. The magnetic flux distribution was observed with applying pulsed magnetic fields using several Hall probe sensors placed along the radial direction of the sample surface. The experimental setup is described elsewhere [2].

### 3. Results and discussion

During the field-increasing process of 5–16 ms which is rising time of pulsed field, we proposed a new method to derive  $V$ - $I$  curve [4] and estimated the flux flow resistivity  $\rho_f$  from the gradient of the  $V$ - $I$  curve. Fig. 1 shows plots of the applied pulse field versus the flux flow resistivity  $\rho_f$ . The flux flow resistivity  $\rho_f$  increased with increasing applied pulsed field. Assuming that the viscosity coefficient  $\eta$  is independent of magnetic field, the results were well approximated with the Bardeen–Stephen model [5].

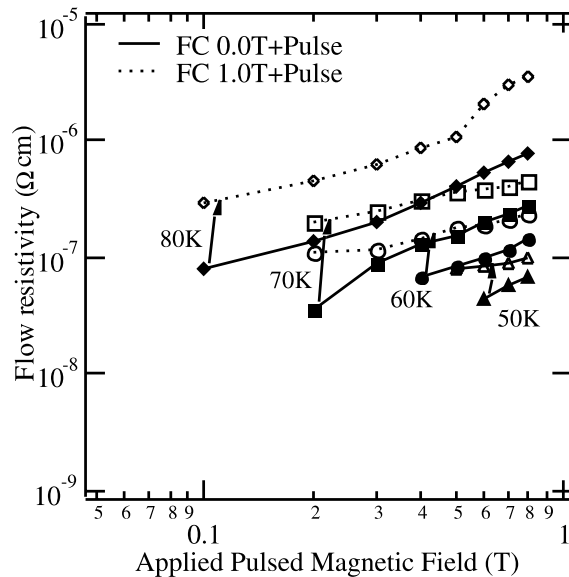


Fig. 1. The applied pulse field versus the flux flow resistivity  $\rho_f$ . One can see that the flux flow resistivity  $\rho_f$  is almost proportional to the applied pulse field.

The viscosity coefficient  $\eta$  was also estimated from the following expression [5,6]:

$$\eta = \frac{\phi_0 B}{\rho_f} \tag{1}$$

Fig. 2 shows temperature dependence of the viscosity coefficient  $\eta$  thus determined. The  $\eta$  decreased with increasing temperature and static bias field. Such a decrease in  $\eta$  with the static bias field is explained in terms of a decrease in the pinning potential energy with magnetic field.

We found that fluxes start to escape from the sample in the field-decreasing portion of 50–100 ms when the flux flow resistivity  $\rho_f$  appears inside the sample in the field-increasing process [3]. The flow rate  $R_f$  was defined and evaluated using the following expression

$$R_f = -\frac{1}{M_0} \frac{dM(t)}{dt} \tag{2}$$

where  $M(t)$  was calculated from the difference between the magnetic field at the sample periphery and external field. Fluxes begin to flow at a certain temperature as shown in Fig. 3 and are pinned at only strong pinning centers and followed by logarithmic time decay.

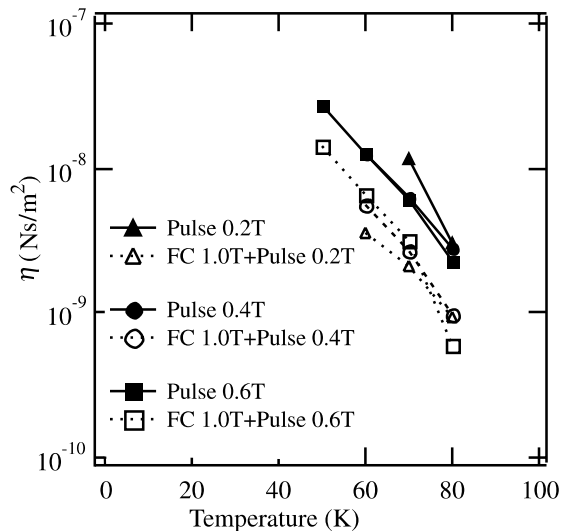


Fig. 2. The viscosity coefficient  $\eta$  as a function of the temperature for different pulse peak fields with and without the bias field.

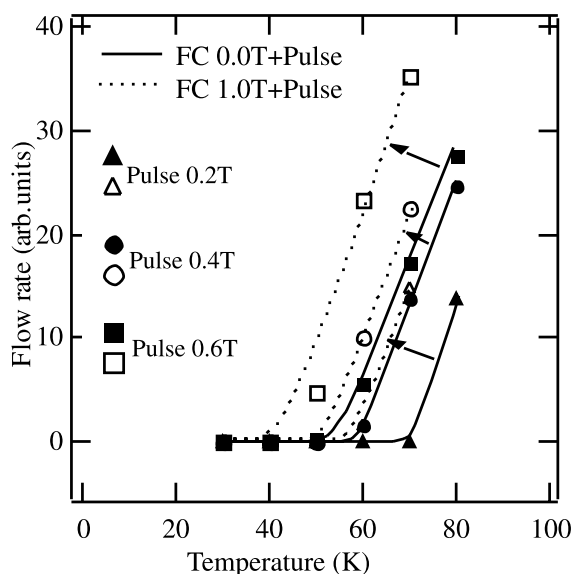


Fig. 3. The relationship between the flow rate  $R_f$  and temperature for different pulse peak fields with and without the bias field. The flow rate increased linearly with temperature once the flux starts to flow.

Fig. 4 shows plots of the creep rate versus temperature, in which the effects of bias field and pulse fields are presented. The flux creep depends strongly on both temperature and magnetic field. The creep rate  $R_c$  was deduced in the time range of 1–2400 s at different temperature using the following equation

$$R_c = -\frac{1}{M_0} \frac{dM(t)}{d \ln t} \quad (3)$$

The creep rate increased with increasing temperature and reached its peak at a certain temperature, which shifted to the lower temperature as the applied pulse field increased. It is interesting to note that the temperature at which the flow rate appears is almost equal to that flux creep appears. Since the flux moves from the pinning center to the direction of the Lorentz force, the creep rate should depend on the current density and the trapped field. Hence we should consider flux creep rate per the Lorentz force when we derive the pinning potential energy. Although the flux flow (the field-increasing and decreasing process) and creep regime occur at different time, both might be closely related.

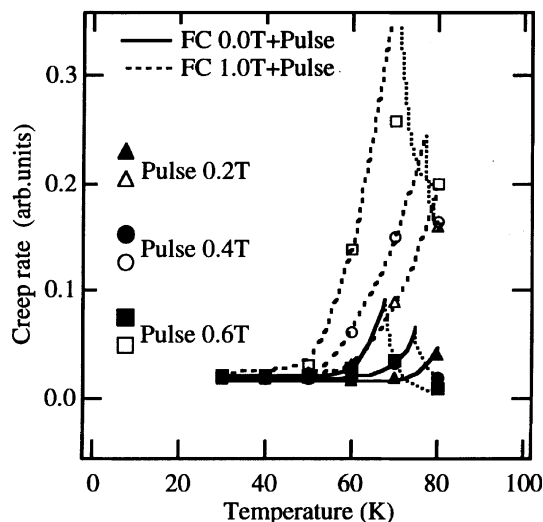


Fig. 4. The creep rate versus temperature for different pulse peak fields with and without the bias field. The creep rate increased with increasing temperature and reached the peak at a certain temperature, which shifted to the lower temperature as the applied pulse field was increased.

#### 4. Conclusion

We have investigated the viscous flux flow and creep induced by pulsed magnetic field in YBCO disk. It was found that the flux flow resistivity  $\rho_f$  increased with increasing applied pulsed field approximately according to the Bardeen–Stephen model and that viscosity coefficient  $\eta$  decreased with increasing temperature and static bias field. The flux flow rate and creep rate increased with increasing temperature and static bias field. It is interesting to note that the temperature at which the flow rate appears is almost equal to that flux creep appears.

#### Acknowledgements

This work was supported by the New Energy and Industrial Technology Development Organization (NEDO) as collaborative Research and Development of Fundamental Technologies for Superconductivity Applications under the New Sunshine Program administered by the Agency of Industrial Science and Technology (AIST) of the

Ministry of International Trade and Industry (MITI) of Japan.

### References

- [1] M. Golosovsky, M. Tsindlekht, D. Davidov, *Supercond. Sci. Technol.* 9 (1996) 1–15.
- [2] T. Kono, M. Tomita, M. Murakami, T. Takizawa, *Supercond. Sci. Technol.* 13 (2000) 794–797.
- [3] T. Kono, M. Tomita, M. Murakami, T. Takizawa, *Proceedings of the Sixth International Conference on Superconductivity and High Temperature Superconductors, Physica C* 341–348 (2000) 2437–2438.
- [4] T. Takizawa, M. Yamazaki, M. Murakami, *Physica B* 284–288 (2000) 845–846.
- [5] J. Bardeen, M.J. Stephen, *Phys. Rev.* 140 (1965) A1197.
- [6] M. Thinkham, *Introduction to Superconductivity*, Krieger, New York, 1980.



ELSEVIER

Physica C 357–360 (2001) 541–544

PHYSICA C

www.elsevier.com/locate/physc

# AC susceptibility measurement for Nd–Ba–Cu–O superconductor

Y. Akamatsu <sup>a</sup>, K. Waki <sup>b,c</sup>, K. Inoue <sup>b</sup>, M. Murakami <sup>b,\*</sup>, T. Takizawa <sup>a</sup>

<sup>a</sup> Graduate School of Integrated Basic Sciences, Nihon University, 3-25-40 Sakura-Jousui, Setagaya-ku, Tokyo 156-0045, Japan

<sup>b</sup> Superconductivity Research Laboratory, 1-16-25 Shibaura, Minato-ku, Tokyo 105-0023, Japan

<sup>c</sup> Railway Technical Research Institute, Hikari-cho, Kokubunji, Tokyo 185-8540, Japan

Received 16 October 2000; accepted 23 December 2000

## Abstract

Nd–Ba–Cu–O sample fabricated by the oxygen-controlled-melt-growth method exhibits large  $J_c$  values in a high field region and also shows a secondary peak effect. In the present study, the Nd–Ba–Cu–O sample was characterized by using the flux profile technique, in which the  $\chi'$  signal is plotted against the amplitude of AC field.  $J_c$  values determined with the flux profile technique also showed a clear secondary peak effect. In addition, such  $J_c$  values were higher than those measured with DC susceptibility, presumably due to a difference in the electric field to determine  $J_c$ . © 2001 Published by Elsevier Science B.V.

PACS: 74.60.Ge; 74.60.Jg

Keywords: AC susceptibility; Flux profile; Peak effect

## 1. Introduction

It is well known that RE–Ba–Cu–O (RE: Nd, Eu, Sm, Gd) superconductors fabricated by the oxygen-controlled-melt-growth (OCMG) method [1] exhibit large critical current density ( $J_c$ ) values, in particular in a high temperature and high magnetic field region [2]. Thus, it is interesting to study the pinning mechanism in RE–Ba–Cu–O superconductors. AC susceptibility measurements are known to be useful method for understanding flux pinning properties in irreversible type II superconductors, in that the flux profile can be determined by plotting the  $\chi'$  signal against the

amplitude of AC field. Flux profile directly provides the flux gradient within the superconductor and thereby the critical current density is determined. We thus measured AC susceptibility and determined the flux profile in Nd–Ba–Cu–O superconductors. The critical current density ( $J_c^{AC}$ ) determined by the flux profile technique was compared with the critical current density ( $J_c^{DC}$ ) measured by DC magnetization measurements.

## 2. Experimental detail

The sample used in the present study is a NdBa<sub>2</sub>Cu<sub>3</sub>O<sub>y</sub> containing 20 mol% Nd<sub>4</sub>Ba<sub>2</sub>Cu<sub>2</sub>O<sub>10</sub> fabricated by the OCMG method, the details of which are described elsewhere [1]. The sample with

\* Corresponding author. Fax: +81-3-3454-9287.

E-mail address: murakami@istec.or.jp (M. Murakami).

dimensions of  $2.18 \times 1.98 \times 1.06 \text{ mm}^3$  was cut from a melt-grown block. The critical temperature,  $T_c$ , is 94.5 K with a sharp transition  $<1 \text{ K}$  as magnetically measured using a commercial SQUID magnetometer. The magnetic flux profiles were measured using the AC inductive method, which was first proposed by Campbell [3]. The applied DC field was increased up to 8.5 T at various temperatures. We fixed AC frequency at 125 Hz with varying its amplitude up to 28.3 Oe. For comparative study the DC magnetization measurement and the relaxation of magnetization were also performed with a SQUID magnetometer (Quantum Design).

**3. Result and discussion**

Fig. 1 shows the results of the temperature dependence of AC susceptibility with AC field amplitude of 14.1 Oe in the presence of various static DC fields for Nd–Ba–Cu–O superconductor. The observed results are typical response of in-phase ( $\chi'$ ) and out-of-phase ( $\chi''$ ) components. A similar response was observed when we changed AC field amplitude from 0 to 28.3 Oe. In zero fields, however, the observed response was somewhat different.

Fig. 2 shows the field dependence of the peak temperature ( $T_{\text{peak}}$ ), the onset temperature ( $T_{\text{onset}}$ )

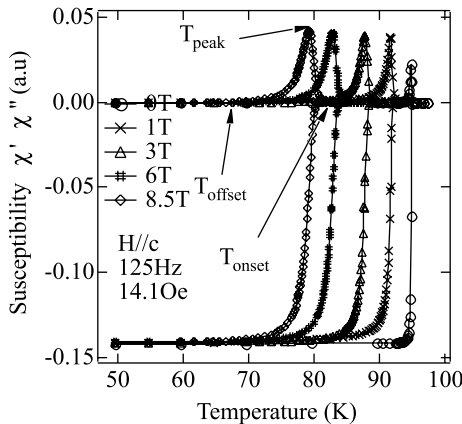


Fig. 1. The temperature dependence of AC susceptibility for OCMG-processed Nd–Ba–Cu–O sample in the presence of several external magnetic fields.

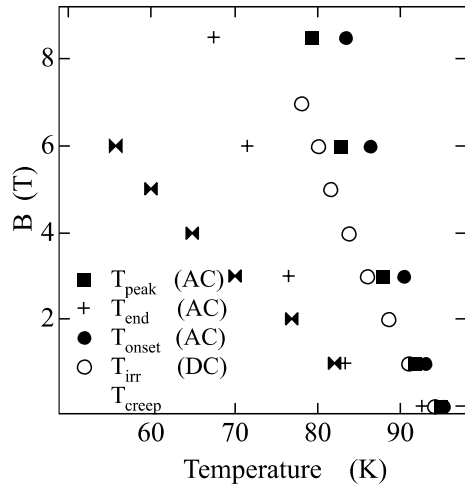


Fig. 2. The magnetic field dependence of  $T_{\text{onset}}$ ,  $T_{\text{peak}}$  and  $T_{\text{end}}$  determined by the imaginary part ( $\chi''$ ) of AC susceptibility and  $T_{\text{irr}}$  determined by  $J_c$  criterion.

and the end temperature ( $T_{\text{end}}$ ) of imaginary part and irreversible temperature ( $T_{\text{irr}}$ ) determined by  $J_c$  criterion. Their relative locations are in the order:  $T_{\text{onset}} > T_{\text{peak}} > T_{\text{irr}} > T_{\text{end}}$ . Here one can suppose that AC susceptibility measurement is the most sensitive to detect the magnetic field, at which the flux pinning starts to function. In the case of DC measurements the relaxation will easily take place during the time scale of measurements, and consequently the irreversible field is lower than that for AC susceptibility.

When AC field is applied to the superconductor, the field penetrates into the superconductor. AC penetration depth can be obtained from the differentiation of the amount of penetrated AC field,  $H_{\text{AC}}$  and it can be determined by plotting the  $\chi'$  signal against the amplitude of AC field. AC penetration depth is thus expressed by

$$\lambda = \frac{\omega + t}{4} \left\{ 1 - \left( 1 - \frac{4}{\mu_0(\omega + t)^2} \frac{d\phi}{dH_{\text{AC}}} \right)^{1/2} \right\}$$

where  $\mu_0$ ,  $\phi$ ,  $\omega$  and  $t$  are the permeability of vacuum, the magnetic flux quantum and the width and thickness of the sample, respectively [4].

Fig. 3 shows the flux profile at 77 K in various fields. With increasing AC field amplitude, AC

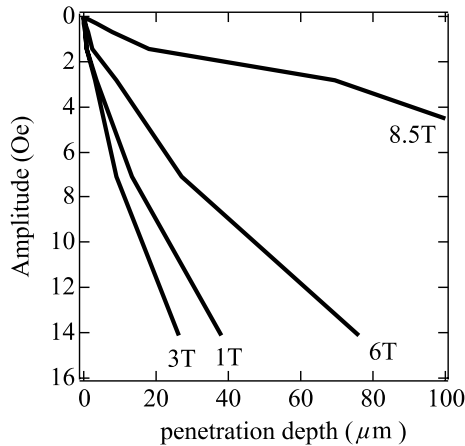


Fig. 3. Flux profiles as a function of the AC field at several fields.

magnetic flux gradually penetrates into the sample. The rate of increment of AC penetration depth becomes larger with increasing AC field amplitude. However, in the small AC field region, AC magnetic flux cannot penetrate into the sample, presumably because the flux motion is reversible near the pinning potential. In this region, AC penetration depth deviates from the prediction of the critical state model. In large AC field region, the variation of the field in the sample reflects the critical state model and then the critical current density is determined with the slope of the penetration depth. Fig. 4 shows the field dependence of  $J_c$  determined by magnetization curve and flux profiles at 77 K. Both curves show a secondary peak effect around 3 T. Comparing  $J_c^{\text{DC}}$  with  $J_c^{\text{AC}}$ ,  $J_c^{\text{AC}}$  has a higher value than  $J_c^{\text{DC}}$  value.  $J_c$  determined by flux profiles shows the secondary peak effect up to 84 K, while  $J_c$  value determined from magnetization curve does not show a peak effect around 84 K. Fig. 5 shows temperature dependence of  $J_c$  at several fields. It has been shown that  $J_c$  is expressed by  $J_c \propto \{1 - (T/T_c)\}^{m'}$ . The value of  $m'$  is known to decrease with increasing pinning force, and melt-processed Y–Ba–Cu–O sample has a typical  $m'$  value of 1.9 [5]. In the present study, the value of  $m'$  was 1.7, supporting the fact Nd–Ba–Cu–O superconductor fabricated by the OCMG method has a strong pinning force. We also observed a strong pinning force from flux

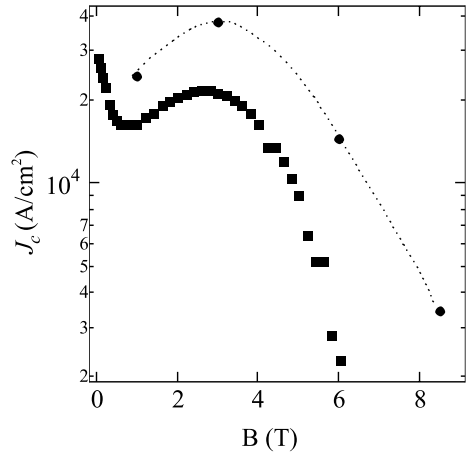


Fig. 4. The field dependence of the critical current density determined by the magnetization curve and the flux profiles at 77 K.

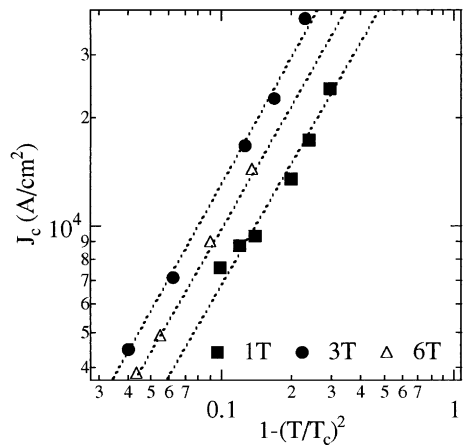


Fig. 5. The temperature dependence of the critical current density at various fields. The temperature is transferred to  $1 - (T/T_c)$ . The obtained  $m'$  value was almost 1.7 in each case.

profile. From the temperature dependence of  $J_c$  at several fields, the irreversible field was determined with a criterion of 100 A/cm<sup>2</sup>. The obtained values at external fields of 1, 3 and 6 T were 91.6, 86.6 and 82.5 K, respectively. These values were very close to  $T_{\text{onset}}$ . From these results, we think that the electric field to determine the critical current density in AC measurements is higher than that of DC measurements. Consequently, the  $J_c^{\text{AC}}$  value is higher than the  $J_c^{\text{DC}}$  value and the irreversible field shifted to higher temperature region.

#### 4. Conclusion

We measured the temperature dependence of AC susceptibility for OCMG-processed Nd–Ba–Cu–O sample and compared the irreversible field determined by DC susceptibility.  $T_{\text{irr}}$  values obtained with DC measurements were strongly affected by flux creep and smaller than the values obtained with AC susceptibility. We also determined  $J_c^{\text{AC}}$  using flux profile techniques. The obtained  $J_c^{\text{AC}}$  values showed a clear secondary peak effect even at 84 K. In addition, the  $J_c^{\text{AC}}$  values were higher than the  $J_c^{\text{DC}}$  values. We believe that this is ascribed to a difference in the electric field to determine the critical current density.

#### Acknowledgements

This work was supported by the New Energy and Industrial Technology Development Organi-

zation (NEDO) as collaborative Research and Development of Fundamental Technologies for Superconductivity Applications under the New Sunshine Program administered by the Agency of Industrial Science and Technology (AIST) of the Ministry of International Trade and Industry (MITI) of Japan.

#### References

- [1] S.I. Yoo, N. Sakai, H. Takaichi, M. Murakami, *Appl. Phys. Lett.* 65 (1994) 633.
- [2] M. Murakami, S.I. Yoo, T. Higuchi, N. Sakai, J. Weltz, N. Koshizuka, S. Tanaka, *Jpn. J. Appl. Phys.* 33 (1994) 715.
- [3] A.M. Campbell, *J. Phys. C2* (1969) 1492.
- [4] H. Kawamura, T. Fujiyoshi, K. Miyahara, *Supercond. Sci. Technol.* 8 (1995) 806.
- [5] T. Matsushita, E. Otabe, B. Ni, K. Kimura, M. Morita, *Jpn. J. Appl. Phys.* 30 (1991) L342.



ELSEVIER

Physica C 357–360 (2001) 548–551

---

---

**PHYSICA** C

---

---

www.elsevier.com/locate/physc

# Two-step transition of $(\text{Nd}_{0.33}\text{Eu}_{0.33}\text{Gd}_{0.33})\text{Ba}_2\text{Cu}_3\text{O}_x$ superconductors in high fields

T. Matano <sup>a,\*</sup>, M.R. Koblishka <sup>b</sup>, M. Muralidar <sup>c</sup>, M. Murakami <sup>c</sup>, T. Takizawa <sup>a</sup><sup>a</sup> Graduate School of Integrated Basic Sciences, Nihon University, 3-25-40 Sakura-Josui, Setagaya-ku, Tokyo 156, Japan<sup>b</sup> Nordic Superconductor Technologies AIS, Priorparken 685, DK-2605 Brøndby, Denmark<sup>c</sup> Superconductivity Research Laboratory, International Superconductivity Technology Center, 1-16-25, Shibaura, Minato-ku, Tokyo 105, Japan

Received 16 October 2000; accepted 13 January 2001

---

## Abstract

Superconducting transitions were measured in field-cooled cooling and field-cooled warming modes in external magnetic fields ranging between 0.1 and 7 T on  $\text{REBa}_2\text{Cu}_3\text{O}_x$  superconductors (RE: rare earth elements) with fishtail effect. All the samples exhibited a two-step transition when being cooled in high fields. These results show that a two-step transition in magnetization is related to the secondary peak effect. © 2001 Published by Elsevier Science B.V.

PACS: 74.25.q; 74.25.Ha; 74.62.Dh

Keywords: Two step transition;  $\text{REBa}_2\text{Cu}_3\text{O}_x$  superconductor; Peak effect

---

## 1. Introduction

The critical current density ( $J_c$ ) of superconductors usually decreases with the applied magnetic field ( $B$ ). However, there are several reports on anomalous increase in magnetization hysteresis ( $\Delta M$ ) at intermediate fields, which is called “peak effect” or “fishtail” [1,2]. The peak effect is observed in various high temperature superconductors and its origin is still controversial.

Recently,  $\text{NdBa}_2\text{Cu}_3\text{O}_x$  (Nd–Ba–Cu–O) has been found to show double transition in magne-

tization-temperature ( $m(T)$ ) curves in the presence of high fields [1,3], which is ascribed to the peak effect. Therefore, we measured  $m(T)$  curves in Y–Ba–Cu–O samples with and without the peak effect [4,5]. There were two interesting features in the  $m(T)$  curves. First the sample with the peak effect showed a two-step transition, while the sample without the peak showed only a single-step transition. Second a dramatic increase in the magnetization was observed in the sample with the peak effect. Such an increase is ascribed to the Cu ion spins caused by oxygen deficiency, which suggests that oxygen defects are responsible for the secondary peak effect in Y–Ba–Cu–O [6].

In this paper, we measured  $m(T)$  curves for various RE–Ba–Cu–O with the strongly developed secondary peak effect, in which RE site is compounded with Nd, Eu, and Gd.

---

\* Corresponding author. Fax: +81-3-3453-9287.

E-mail address: matano@istec.or.jp (T. Matano).

## 2. Experimental procedure

We used NEG123 samples grown by the oxygen-controlled melt growth (OCMG) method [7]. NEG123 samples were prepared in two groups as presented in Table 1. One type include Eu211 (10–40 mol%) and Pt (0.5 mol%), the other includes 10 mol% of NEG211, in which the ratio of Nd, Eu, Gd is varied.

Superconducting transitions of these crystals were measured both in the field-cooled cooling (FCC) and field-cooled warming (FCW) modes in the presence of external magnetic fields using a commercial SQUID magnetometer (Quantum Design, model XL). This magnetometer enables us to measure magnetic moment in a continuous temperature sweep mode with a controlled temperature sweep rate  $dT/dt = 35 \text{ mK min}^{-1}$  in the transition region; the data points are recorded in steps of 50 mK. Note that the temperature sweep is not stopped for the measurement unlike an ordinary SQUID magnetometer, so that a fast measurement is essential. No averaging of the signal was performed, and the scan length was set to 1 cm.

## 3. Results and discussion

Fig. 1 shows  $J_c$ – $B$  curves for the group of NEG123 + Eu211 samples. One can see that clear secondary peak effect is observed in all the samples. The peak-field  $J_c$  was reduced in the samples with 10, 30 and 50 mol% of Eu211 as the Eu211 content is increased, while the peak position was not shifted. The peaks of 20 and 40 mol% samples moved to lower fields as the Eu211 content increased. Moreover, as the 211 phase increased self-field  $J_c$  is increased accompanied by smearing in the peak effect except for 20 mol% of Eu211. Since

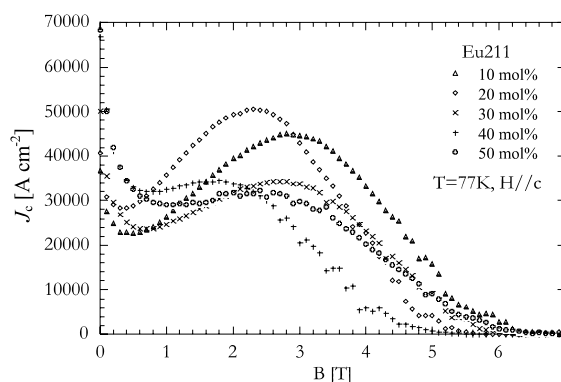


Fig. 1. Field dependence of the critical current density  $J_c$  of the NEG123 + Eu211 + Pt samples obtained from magnetic hysteresis loops at 77 K.

the peak effect originates from the chemical fluctuation in the matrix [8], an increase in the volume fraction of the second phase inclusions led to a depression in the peak effect. In particular, the sample with 50 mol% Eu211, self-field  $J_c$  value was higher than the peak-field  $J_c$  value.

Fig. 2 shows temperature dependence of magnetic moment for NEG123/Eu211 composites in 7 T. One can notice the tendency that the magnitude of magnetic moment is gradually depressed with increasing Eu211 content. This is understandable by considering the fact that Eu has the smallest magnetic moment among these RE elements. Furthermore, a drastic increase in magnetization was not observed at low temperatures in these NEG123 samples, which could be observed in oxygen-deficient Y123 with the secondary peak effect [6]. An  $m(T)$  upturn in Y123 is ascribed to  $\text{Cu}^{2+}$  ion spins associated with oxygen deficiency, and thus the peak effect in Y123 is ascribable to field-induced pinning by oxygen defects as proposed by Daumling et al. [9]. The absence of such upturn in  $m(T)$  curves of NEG123 suggests that oxygen defects are not responsible for the secondary peak effect in

Table 1  
NEG samples grown by OCMG method

Sample	211 phase (mol%)	Pt (mol%)	(Nd, Eu, Gd) ratio in 211
NEG123 + Eu211 + Pt	10–50	0.5	–
NEG123 + NEG211 + Pt	10	0.5	2:2:6, 4:4:2

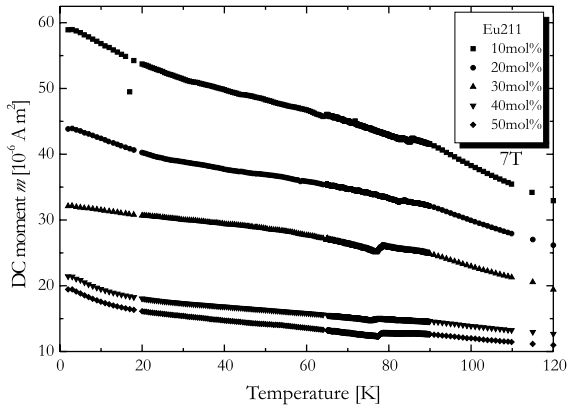


Fig. 2. Temperature scans of the magnetic moment  $m(T)$  on NEG123 + Eu211(10–50 mol%) + Pt samples at 7 T applied field. All data shown were recorded during FCC runs; the FCW data are omitted for clarity since only small differences were observed.

NEG system. These results support the idea that RE-rich clusters are responsible for the peak effect in RE123 with RE–Ba solid solution [10].

One can also notice that a two-step transition in  $m(T)$  is observed in all the samples, although double transition is smaller in the sample with 50 mol% Eu211. Our observation also supports the idea that double transition is associated with the secondary peak effect.

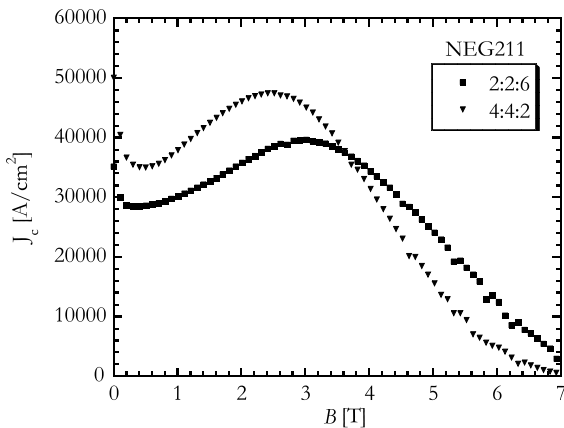


Fig. 3.  $J_c$ – $B$  curves of the NEG123 + 10 mol% of NEG211 + Pt samples obtained from magnetic hysteresis loops at 77 K.

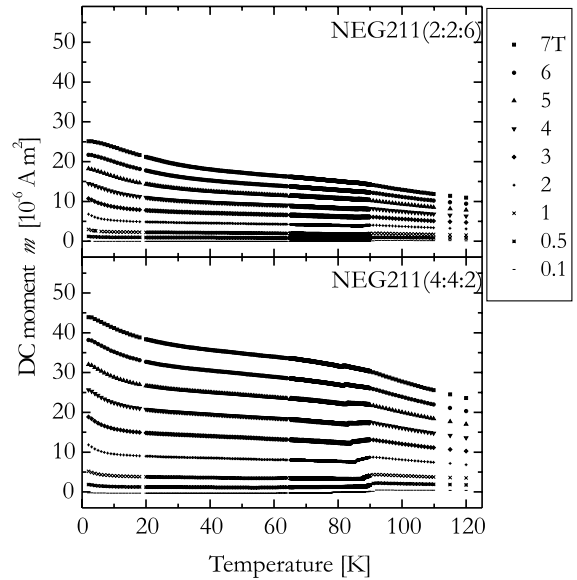


Fig. 4. Temperature scans of the magnetic moment  $m(T)$  on NEG123 + 10 mol% of NEG211 + Pt samples for various applied field (FCC).

Fig. 3 shows  $J_c$ – $B$  curves for the group of NEG123 + 10 mol% NEG211. Here the chemical ratios in the RE site of NEG211 were Nd:Eu:Gd = 2:2:6 and 4:4:2. In both cases one can see clear secondary peak effect. As shown in Fig. 4, in both samples double transition is observed in  $m(T)$  curves. Based on the former observation in Y123, in that a two-step transition is not observed in the sample without the secondary peak effect [6], the double transition is caused by the secondary peak effect or the presence of lower  $T_c$  phase in the sample, as first proposed by Koblichka et al. [1].

However, Inoue et al. [11] also reported that transition behavior in the field-cooled mode is dependent on the experimental conditions. Thus more detailed study is necessary to draw a definite conclusion.

#### 4. Conclusions

We measured temperature dependence of magnetization in the presence of DC bias field for various NEG123 samples with the secondary peak effect. They always showed double step transition,

in that clear double transition is observed in those with clear peak effect. For example, an addition of large amount of the second phase particles smeared the peak effect and thereby double transition. Even in that case, the double transition is observable, and thus the secondary peak effect is responsible for the double transition in  $m(T)$  curves.

### Acknowledgements

This work was supported by the New Energy and Industrial Technology Development Organization (NEDO) as Collaborative Research and Development of Fundamental Technologies for Superconductivity Applications under the New Sunshine Program administered by the Agency of Industrial Science and Technology (AIST) of Ministry of International Trade and Industry (MITI) of Japan.

### References

- [1] M.R. Koblischka, M. Muralidhar, T. Higuchi, K. Waki, N. Chikumoto, M. Murakami, *Supercond. Sci. Technol.* 12 (1999) 288.
- [2] L. Klein, E.R. Yacoby, Y. Yeshurun, A. Erb, G. Müller-Vogt, V. Breit, H. Wühl, *Phys. Rev. B* 49 (1994) 4403.
- [3] T. Wolf, A.-C. Bornarel, H. Küpfer, R. Meier-Hirmer, B. Obst, *Phys. Rev. B* 56 (1997) 6308.
- [4] M. Murakami, N. Akai, T. Higuchi, S.I. Yoo, *Supercond. Sci. Technol.* 9 (1996) 1015.
- [5] X.S. Ling, J.I. Budnick, B.W. Veal, *Physica C* 282–287 (1997) 2191.
- [6] T. Matano, M.R. Koblischka, B.W. Veal, M. Murakami, T. Takizawa, *Supercond. Sci. Technol.* 13 (2000) 805.
- [7] M. Muralidhar, M.R. Koblischka, T. Saitoh, M. Murakami, *Supercond. Sci. Technol.* 11 (1998) 1349.
- [8] T. Higuchi, S.I. Yoo, K. Sawada, N. Sakai, M. Murakami, *Physica C* 263 (1996) 396.
- [9] M. Daeumling, J.M. Seuntjens, D.C. Larbalestier, *Nature* 346 (1990) 332.
- [10] M. Murakami, N. Sakai, N. Chikumoto, H. Kojo, T. Higuchi, S.I. Yoo, *Physica C* 282/287 (1997) 371.
- [11] K. Inoue, M. Muralidhar, K. Waki, M. Murakami, *Supercond. Sci. Technol.* 13 (2000) 766.



ELSEVIER

Physica C 357–360 (2001) 545–547

PHYSICA C

www.elsevier.com/locate/physc

# AC susceptibility of high- $T_c$ superconductor REBa<sub>2</sub>Cu<sub>3</sub>O<sub>y</sub>

H. Enomoto<sup>a,\*</sup>, K. Inoue<sup>b</sup>, M. Muralidhar<sup>b</sup>, M. Murakami<sup>b</sup>, T. Takizawa<sup>a</sup><sup>a</sup> Graduate School of Integrated Basic Science, Nihon University, 3-25-40 Sakura-Josui, Setagaya-ku, Tokyo 156-8550, Japan<sup>b</sup> Superconductivity Research Laboratory, ISTEC, 1-16-25 Shibaura, Minato-ku, Tokyo 105-0023, Japan

Received 16 October 2000; accepted 13 January 2001

## Abstract

The AC susceptibility has been investigated for the three different melt-processed samples: (Nd<sub>0.33</sub>Eu<sub>0.33</sub>Gd<sub>0.33</sub>)-Ba<sub>2</sub>Cu<sub>3</sub>O<sub>7-δ</sub> with the large secondary peak, NdBa<sub>2</sub>Cu<sub>3</sub>O<sub>7-δ</sub> with the moderate secondary peak and YBa<sub>2</sub>Cu<sub>3</sub>O<sub>7-δ</sub> with no secondary peak. We found that the imaginary part ( $\chi''$ ) value is higher for the sample which has the larger secondary peak. This suggests that the effect of the flux creep is more remarkable for the sample with the larger secondary peak. © 2001 Elsevier Science B.V. All rights reserved.

PACS: 74.60.Ge; 74.60.Jg

Keywords: AC susceptibility; Secondary peak; Flux creep; REBa<sub>2</sub>Cu<sub>3</sub>O<sub>y</sub>

## 1. Introduction

The melt processed REBa<sub>2</sub>Cu<sub>3</sub>O<sub>y</sub> (RE: Nd, Sm, Eu and Gd) exhibits the secondary peak effect on the magnetization hysteresis curve [1]. It is known that REBa<sub>2</sub>Cu<sub>3</sub>O<sub>y</sub> has a RE<sub>1+x</sub>Ba<sub>2-x</sub>Cu<sub>3</sub>O<sub>y</sub> (RE123ss) type solid solution. When RE–Ba–Cu–O is melt processed in a reduced oxygen atmosphere, RE-rich RE123ss phase with depressed  $T_c$  is dispersed in the REBa<sub>2</sub>Cu<sub>3</sub>O<sub>y</sub> matrix with high  $T_c$  and such low  $T_c$  phase acts as the field-induced pinning centers, which is the source of the secondary peak effect [1]. In the composite system containing the low- $T_c$  phase, the flux creep behavior is expected to be different from that of the homogeneous system. The AC susceptibility has

been extensively measured in the study of vortex dynamics [2]. It is known that the imaginary part ( $\chi''$ ) value of the AC susceptibility is increased as the effect of the flux creep is enhanced [3].

In the present study, we measured the AC susceptibility of the several melt-processed samples with and without low- $T_c$  phase clusters and investigated the correlation between the secondary peak and the height of  $\chi''$ .

## 2. Experimental

The samples were oxygen-controlled-melt-growth-processed (Nd<sub>0.33</sub>Eu<sub>0.33</sub>Gd<sub>0.33</sub>)Ba<sub>2</sub>Cu<sub>3</sub>O<sub>7-δ</sub> (NEG123) with 10 mol% NEG211 with  $T_c = 92.6$  K, NdBa<sub>2</sub>Cu<sub>3</sub>O<sub>7-δ</sub> (Nd123) with 20 mol% Nd422 with  $T_c = 95.1$  K, and YBa<sub>2</sub>Cu<sub>3</sub>O<sub>7-δ</sub> (Y123) with 40 mol% Y211 with  $T_c = 91.9$  K. The sample dimensions were  $1.8 \times 1.6 \times 0.5$  mm<sup>3</sup>,  $2.2 \times 2.0 \times 1.0$  mm<sup>3</sup>, and  $2.0 \times 1.6 \times 0.3$  mm<sup>3</sup>, respectively.

\* Corresponding author. Tel.: +81-3-3454-9284; fax: +81-3-3454-9287.

E-mail address: h-enomoto@istec.or.jp (H. Enomoto).

The critical current density ( $J_c$ ) was determined from the hysteresis loop with Quantum Design MPMS SQUID magnetometer. AC susceptibility measurements were performed with a Lakeshore 7229 AC susceptometer. The AC field amplitude was 1 mT and the frequency was 125 Hz. The DC field was changed up to 8.5 T. The magnetic field was applied perpendicular to the *ab*-plane and the temperature is kept constant during each measurement.

### 3. Results and discussion

Fig. 1 shows the magnetic field dependence of  $J_c$  at 80 K, which is calculated from the hysteresis loop using the extended Bean model [4]. One can see that NEG123 exhibits the large secondary peak, Nd123 exhibits the moderate secondary peak and Y123 no secondary peak.

Fig. 2 shows the plot of the imaginary part ( $\chi''$ ) versus the real part ( $\chi'$ ) of the AC susceptibility at 80 K for three samples. Since demagnetizing correction would cause  $\chi' = -1$  for low temperature without DC field, we normalized the experimental data with the  $|\chi'|$  value at 50 K. The solid curve is the theoretical curve calculated for a cylinder using the Bean critical state model [2]. The experimen-

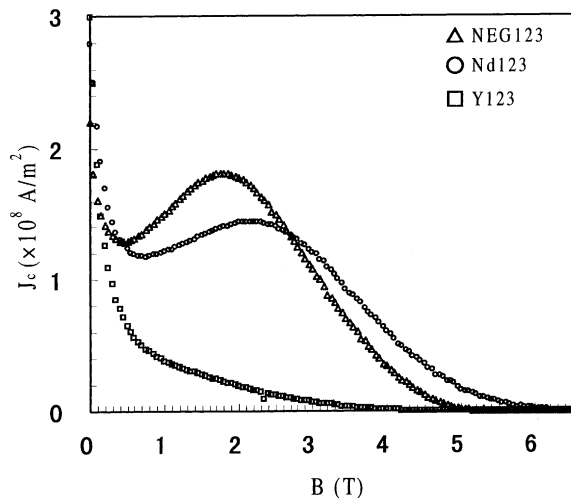


Fig. 1. Magnetic field dependence of  $J_c$  at 80 K for three samples.

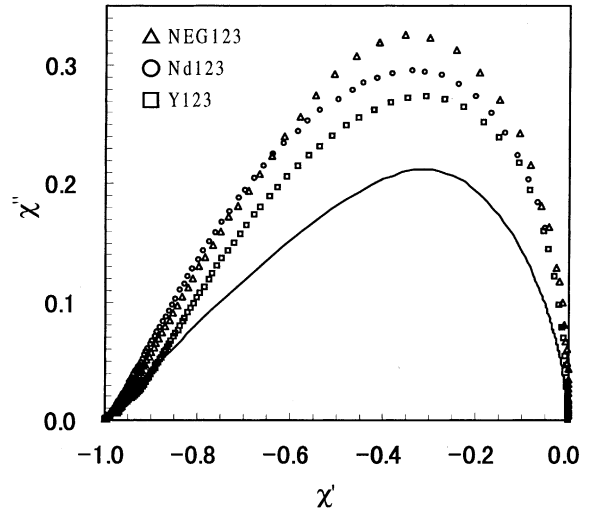


Fig. 2. Plot of  $\chi''$  versus  $\chi'$  at 80 K for three samples. The solid curve is the theoretical curve calculated using the Bean model.

tal curves are higher than the theoretical line. NEG123 with the large secondary peak exhibits the highest curve, while Y123 with no secondary peak exhibits the lowest curve among three samples.

Fig. 3(a) shows the temperature dependence of the maximum value ( $\chi''_{\max}$ ) of  $\chi''$  for three samples. We also plot the normalized temperature ( $T/T_c$ ) dependence of  $\chi''_{\max}$  for three samples, as shown in Fig. 3(b). The thick solid line is the theoretical line calculated using the Bean model. One can see that the  $\chi''_{\max}$  values of NEG123 are the highest at measured temperatures among three samples. It is predicted that when the effect of the loss due to the flux creep is large, the  $\chi''$  value would be high as compared to the case for only the hysteretic loss [3]. Therefore, the present result suggests that the sample with the larger secondary peak is more strongly affected by the flux creep.

Klein et al. [5] explained that the secondary peak is related to the percolating network of reversible regions for Y123 crystals. That is, the low- $T_c$  phase such as the oxygen deficient regions has the lower irreversibility field than the matrix. The oxygen deficient regions become the field-induced pinning centers, which yields an increase in the  $J_c$  with increasing field. When the field exceeds the threshold value, where the percolating network of

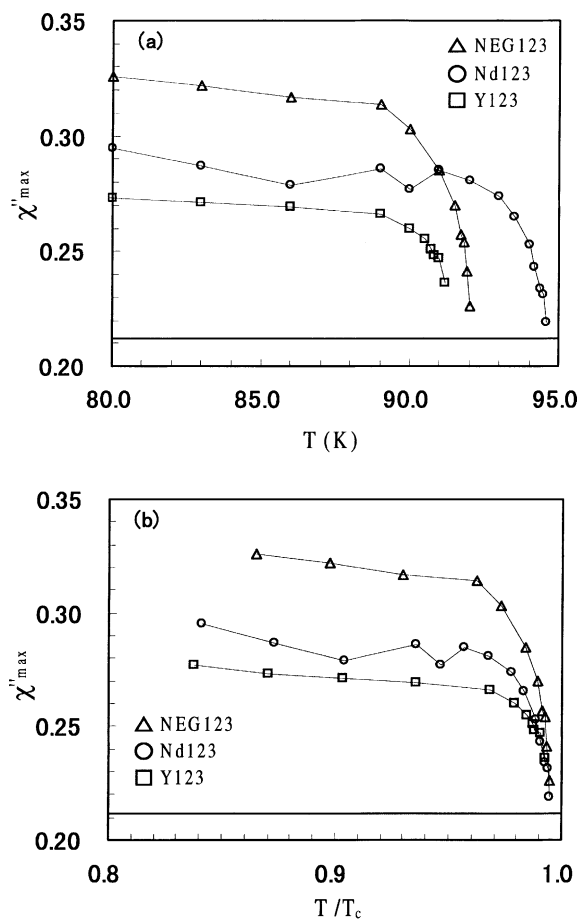


Fig. 3. a) Temperature dependence and (b) normalized temperature ( $T/T_c$ ) dependence of  $\chi''_{\max}$  for three samples. The thick solid line is the theoretical line calculated using the Bean model.

reversible regions is formed, the sample becomes granular and thereby  $J_c$  decreases. In the present system, the field-induced pinning is effective due to the low- $T_c$  phase such as the RE-rich RE123ss phase. The sample with the larger secondary peak is expected to include the larger amount of low- $T_c$  phase clusters, and thus the percolating network of reversible regions is more easily formed above the

peak field. This suggests that the flux creep becomes more remarkable and the  $\chi''$  value is higher for the sample with the larger secondary peak.

#### 4. Summary

We measured the AC susceptibility for the melt-processed NEG123 with the large secondary peak, Nd123 with the moderate secondary peak and Y123 with no secondary peak. It was found that the  $\chi''$  value is higher for the sample which has the larger secondary peak. This suggests that the flux creep is more remarkable above the peak field for the sample with the larger secondary peak.

#### Acknowledgements

We thank Dr. N. Sakai for providing the Y123 sample. This work was supported by the New Energy and Industrial Technology Development Organization (NEDO) as Collaborative Research and Development of Fundamental Technologies for Superconductivity Applications under the New Sunshine Program administered by the Agency of Industrial Science and Technology (AIST) of the Ministry of International Trade and Industry (MITI) of Japan.

#### References

- [1] M. Murakami, S.I. Yoo, T. Higuchi, N. Sakai, J. Weltz, N. Koshizuka, S. Tanaka, *Jpn. J. Appl. Phys.* 33 (1994) L715.
- [2] F. Gömöry, *Supercond. Sci. Technol.* 10 (1997) 523.
- [3] E.H. Brandt, *Phys. Rev. B* 58 (1998) 6523.
- [4] E.M. Gyorgy, R.B. van Dover, K.A. Jackson, L.F. Schneemeyer, J.V. Waszczak, *Appl. Phys. Lett.* 55 (1989) 283.
- [5] L. Klein, E.R. Yacoby, Y. Yeshurun, A. Erb, G. Müller-Vogt, V. Breit, H. Wühl, *Phys. Rev. B* 49 (1994) 4403.

## Defect Properties of CuInS<sub>2</sub> Single Crystals Grown by Horizontal Bridgman Method with Controlling S Vapor Pressure

Hiroaki MATSUSHITA, Tomohiro MIHIRA<sup>1</sup> and Takeo TAKIZAWA<sup>1</sup>

Department of Material Science and Technology, School of High-Technology for Human Welfare, Tokai University,  
317 Nishino, Numazu, Shizuoka 410-0395, Japan

<sup>1</sup>Department of Physics, College of Humanities and Sciences, Nihon University, 3-25-40 Sakurajosui, Setagaya-ku, Tokyo 156-0045, Japan

(Received December 18, 2000; accepted for publication May 8, 2001)

We have analyzed the lattice defects of CuInS<sub>2</sub> bulk single crystals prepared by the horizontal Bridgman method with controlling S vapor pressure. The grown crystals have p-type conduction and electrical resistivities of more than 10<sup>3</sup> Ω·cm at room temperature. From measurements of the Hall effect, photoluminescence, optical absorption and photoconductivity, the activation energies of acceptors in CuInS<sub>2</sub> crystals are shown to be of 85 meV, 115 meV and 360 meV, which are respectively ascribed to Cu-vacancies, In-vacancies and extrinsic impurities; whereas donors of 35 meV activation energy are ascribed to S-vacancies.

KEYWORDS: CuInS<sub>2</sub> single crystal, sulfurization, horizontal Bridgman method, intrinsic defect, Hall effect, optical band gap, PL, PC

### 1. Introduction

The chalcopyrite semiconductor CuInS<sub>2</sub> is known to have a band gap of about 1.5 eV suitable for the optimum conversion efficiency of solar cells, which is calculated to be about 26%.<sup>1)</sup> Thus, many trials fabricating solar cells using CuInS<sub>2</sub> thin films as absorber materials have been reported.<sup>2–7)</sup> However, a conversion efficiency of only 12%, which is much lower than that of CuInSe<sub>2</sub>, has been achieved until now.<sup>5,6)</sup> In addition, there are still controversial problems in interpreting the intrinsic defects in CuInS<sub>2</sub>, mainly because of the difficulties in reducing and controlling lattice defects as compared with those of CuInSe<sub>2</sub>. The insufficiency of fundamental knowledge of the defect properties may have been the obstacle in achieving a higher conversion efficiency.

CuInS<sub>2</sub> bulk single crystals have already been grown using the traveling heater, iodine transport and gradient freeze methods, and the characteristics of the crystals have been analyzed mainly by optical measurements, in particular, by photoluminescence.<sup>8–14)</sup> To obtain CuInS<sub>2</sub> single crystals of better quality that are sufficient for investigating the physical properties of intrinsic defects, we have grown crystals using the horizontal Bridgman method with controlling S vapor pressure.<sup>15)</sup> In this study, the results of the Hall effect, photoluminescence (PL), optical absorption and photoconductivity (PC) measurements of these crystals are reported. The electronic levels and the origins of lattice defects are also discussed in relation to the compositional deviation.

### 2. Experimental Procedure

CuInS<sub>2</sub> single crystals were grown using a horizontal furnace with an electrically moving temperature profile as described in a previous work.<sup>15)</sup> First, a CuIn alloy was heated to a temperature 25°C higher than the melting point of CuInS<sub>2</sub>. Then, the S element was heated to a temperature corresponding to an appropriate S vapor pressure ranging from 30 Torr to 6 atm. The temperature gradient profile of the furnace was electrically moved at a speed of 1 cm/h. On visual inspection, the crystallinity of the bulk crystals appeared better with decreasing S vapor pressure to about 200 Torr. High-quality single crystals without voids or cracks were grown under S vapor

pressure ranging from 30 to 200 Torr. Typically, 5 × 3 × 2 mm<sup>3</sup> single crystal blocks could be cut out and were used for carrying out the Hall effect, PL and PC measurements.

For the Hall effect and PC measurements, each electronic contact should be ohmic over all temperature regions concerned. A previous work showed that a Ni electrode could form an ohmic contact with CuInSe<sub>2</sub> and CuGaSe<sub>2</sub>.<sup>16,17)</sup> This electrode was also assured to be ohmic in the case of CuInS<sub>2</sub> by the current–voltage measurement.

The Hall effect was measured in the temperature range of 200 to 300 K under a magnetic field of about 1 T using the six-electrode method. PC spectra were observed in the temperature range of 50 to 300 K by illuminating samples with chopped (25 Hz) monochromatic light passing through a monochromator (Jasco CT-25GD). PC signals were lock-in detected as a change in voltage across samples, where a steady current was applied.

PL spectra were detected by a photomultiplier (Hamamatsu, R636) under excitation of a He–Ne laser (NEC GLG5740, 632.8 nm, 35 mW) at about 50 K. All the samples were shown to have direct band gaps, and the optical absorption edge was shown to obey the following relationship,  $\alpha h\nu = A(h\nu - E_g)^{1/2}$ , where  $\alpha$  is the absorption coefficient,  $h\nu$  is the photon energy,  $A$  is a constant and  $E_g$  is the band gap. Optical transmission was detected by a PbS cell (Hamamatsu P2682) using monochromatic light in the temperature range of 50 to 300 K.

### 3. Results

#### 3.1 Hall effect

Single crystals of p-type conduction having various compositional deviations from the stoichiometry were obtained by growing them under S vapor pressure ranging from 30 to 200 Torr. The characteristics are summarized in Table I. The temperature dependence of the Hall effect was measured using the four samples in Table I, and the results are shown in Fig. 1. The electrical resistivities of the grown samples were deduced to be more than 10<sup>3</sup> Ω·cm at room temperature, which were three orders of magnitude greater than that reported by Tell *et al.*<sup>18)</sup> The activation energies of acceptors

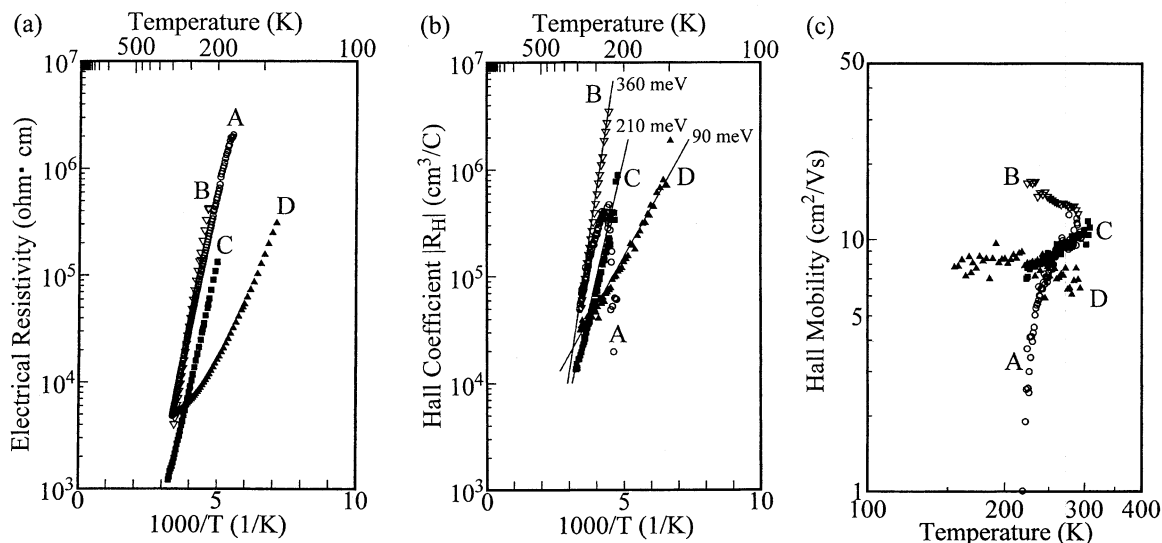


Fig. 1. Temperature dependence of (a) electrical resistivity, (b) Hall coefficient and (c) Hall mobility of the p-type samples grown under S vapor pressures below 200 Torr.

Table I. Cu/In and S/metal ratios and acceptor levels of four samples prepared under respective S vapor pressure.

Sample name	S vapor pressure (Torr)	Cu/In	S/metal	$E_A$ (meV)
A	200	0.990	0.976	(overshoot)
B	200	0.983	0.993	360
C	100	0.990	1.010	210
D	30	0.967	0.989	90

in samples A, B, C and D were estimated using the temperature variation of Hall coefficient curves as shown in Fig. 1(b). These values were different with each other, and scattered in the range of 90 to 360 meV. Only sample A shows the so-called Hall coefficient overshoot which can be understood in terms of the two carriers conduction.<sup>16,19,20</sup> The abrupt decrease in Hall coefficient of sample A at low temperature [see Fig. 1(b)] is one of the characteristics of the overshoot. The Hall mobilities of all samples are about  $10 \text{ cm}^2/\text{Vs}$  at room temperature which is in agreement with the result reported by Tell *et al.*<sup>18</sup>) It is clear that the activation energy of an acceptor or donor has a close relationship to the compositional deviation. However, no definite relationship could be found between the activation energy and Cu/In or S/metal ratio as shown in Table I. Nevertheless, there appears to be a trend that the activation energy decreases as Cu/In ratio decreases and/or S/Metal ratio approaches unity.

### 3.2 Photoluminescence (PL)

Figure 2 shows the PL spectra of samples A, B, C and D at about 50 K. The emission peak at 1.45 eV was observed in all samples, while the small shoulder at 1.41 eV was observed in samples A, B and C. The peak and shoulder shifted to a lower energy as the power of excitation light decreased (see Fig. 3, where only the case of sample B is shown as an example). Following the results reported by Ueng and Hwang<sup>12</sup>) and Wakita *et al.*,<sup>14</sup>) we ascribed the emissions to the D–A pair recombination. The energy levels of donors or acceptors giving rise to the peak i in sample B were deduced to

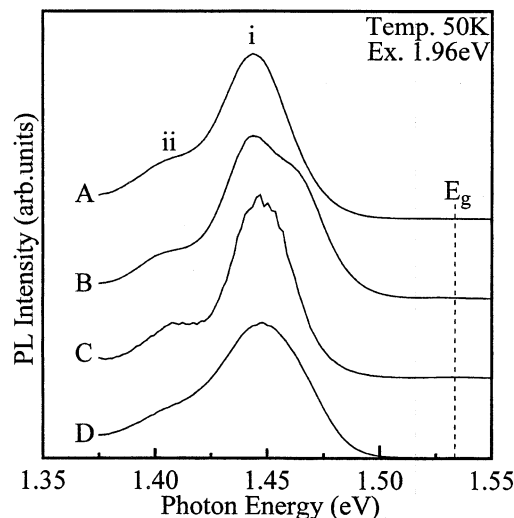


Fig. 2. Photoluminescence spectra at about 50 K for samples A, B, C and D.

be  $\sim 35$  and  $85$  meV, obtained by fitting the relationship of the peak energy of emission against the intensity of excitation light to the well-known equation of D–A pair recombination.<sup>21,22</sup>) The fitting results are shown in Fig. 4. The energies thus obtained are nearly equal to those of samples A and D ( $35$ – $45$  and  $75$ – $85$  meV, respectively). The emission of sample C against the intensity of excitation light could not be measured because it was very weak. The activation energy of acceptors in sample D was also obtained from Hall coefficient of Fig. 1(b) as  $90$  meV which is in agreement with the impurity level of  $\sim 85$  meV. On the other hand, the energy levels of donors or acceptors giving rise to the peak ii were deduced to be  $\sim 35$  and  $115$  meV.

In summary, the energy levels of acceptors and donors were determined as  $E_A \sim 85$  and  $115$  meV, and  $E_D \sim 35$  meV, respectively. It should be noted that the density of the level of  $E_A \sim 115$  meV may be lower than that of the other levels in view of the fact that the emission of peak ii was very weak.

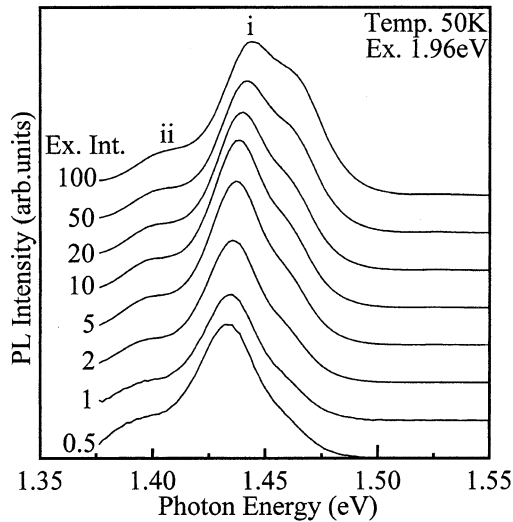


Fig. 3. Photoluminescence spectra against the intensity of excitation light for sample B.

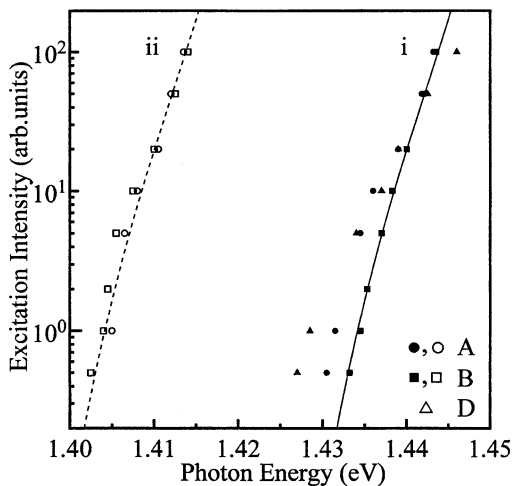


Fig. 4. Peak energy of emissions of peaks i and ii against the intensity of excitation light for samples A, B and D.

### 3.3 Photoconductivity (PC)

Figures 5(a) and 5(b) show the PC spectra of samples A and D, respectively. In sample A, a PC peak (peak I) was observed at 1.54 eV below  $\sim 120$  K, and a PC peak (peak II) was observed at 1.50 eV above  $\sim 90$  K. In addition, a broad peak (peak IV) appeared at about 1.2 eV at higher temperatures. The temperature dependence of the PC spectra of sample C was very similar to that of sample A. In sample D, a PC peak (peak I) was observed at 1.54 eV below  $\sim 250$  K, as well as a PC peak (peak III) at 1.45 eV above 120 K. The PC spectra of sample B could not be measured in this study. Following discussions determined by Susaki *et al.* on PC peaks of p-type  $\text{CuGaS}_2$ ,<sup>23,24</sup> we assigned the origins of PC peaks of  $\text{CuInS}_2$  as follows.

Figure 6 shows the temperature dependence of peaks I, II and III for samples A, C and D together with the optical band gaps estimated from optical absorption data. The peak energy of peak I coincides with the optical band gap, indicating that the peak occurs due to fundamental absorption. At low tem-

peratures, almost all donor and acceptor levels are filled with each carrier (electron and hole), so that the optical excitation of electrons should occur directly from the valence band to the conduction band. Thus, the increase in photocurrent at peak I can be ascribed to the excess carriers in both bands due to the band gap excitation.

The DC peak II appears only above 90 K, and at a photon energy of 35–40 meV lower than that of peak I. This energy difference just corresponds to the activation energy of the donor, i.e.,  $E_D \sim 35$  meV determined by the PL measurement. Thus, peak II is considered to occur due to carriers generated by photo-excited electrons from the valence band via the donor level to the conduction band, since electrons are thermally released from the donor level above 90 K.

On the other hand, the difference between the band gap and peak energy of peak III is estimated to be 85–90 meV which is in good agreement with the activation energy of the acceptor, i.e.,  $E_A \sim 85$  meV, determined by the PL measurement. As shown in Fig. 6, peak III emerges at higher temperatures than peak II. This peak can be ascribed to the increase in carriers through the acceptor level,  $E_A$ .

Finally, the difference between the band gap and peak energy of peak IV is estimated to be about 350 meV which is close to the activation energy of 360 meV obtained by the Hall effect. This broad peak may be due to carriers generated by the excited electrons from the acceptor level of  $\sim 360$  meV to the conduction band due to the reason stated above.

### 4. Discussion

The results of the Hall effect, PL, optical absorption and PC measurements are summarized in the energy diagram in Fig. 7. Three acceptor levels of 85 meV (hereafter designated as  $E_{A1}$ ), 115 meV ( $E_{A2}$ ) and 360 meV ( $E_{A3}$ ) and a donor level of 35 meV ( $E_D$ ) are observed in samples A, B and C. On the other hand, sample D has an acceptor level of  $E_{A1}$  and a donor level of  $E_D$ , but no acceptor levels of  $E_{A2}$  and  $E_{A3}$ .

The densities of acceptors of  $E_{A1}$ ,  $E_{A2}$  and  $E_{A3}$  and that of donor of  $E_D$  are expressed as  $N_{A1}$ ,  $N_{A2}$ ,  $N_{A3}$  and  $N_D$ , respectively. Here, the activation energy related to  $E_{A2}$  was not obtained from the Hall effect or PC measurements. A PC signal related to  $E_{A1}$  was not observed in samples A and C, and a PC signal related to  $E_D$  was not observed in sample D. To explain these features, it is essential to determine the densities of the defects.

The conduction characteristics of p-type samples are well described by assuming the one-carrier model. Based on this model, the temperature variation of the carrier concentration is expressed by the following equation,

$$p + N_D = \frac{N_A}{1 + 2 \frac{p}{N_V} \exp\left(\frac{E_A}{kT}\right)}, \quad (1)$$

where  $p$  is the hole concentration and  $N_V$  is the effective density of the valence state. We extract  $N_{A1}$ ,  $N_{A3}$  and  $N_D$  by fitting the above equation to the observed curves for samples B, C and D as shown in Fig. 8. The results are summarized in Table II, where the deviations from molecularly and valence stoichiometry,  $\Delta x$  and  $\Delta y$ ,<sup>25</sup> determined by EPMA are also shown. Sample A shows the Hall coefficient overshoot in the Hall coefficient vs temperature curves. In this case, it is

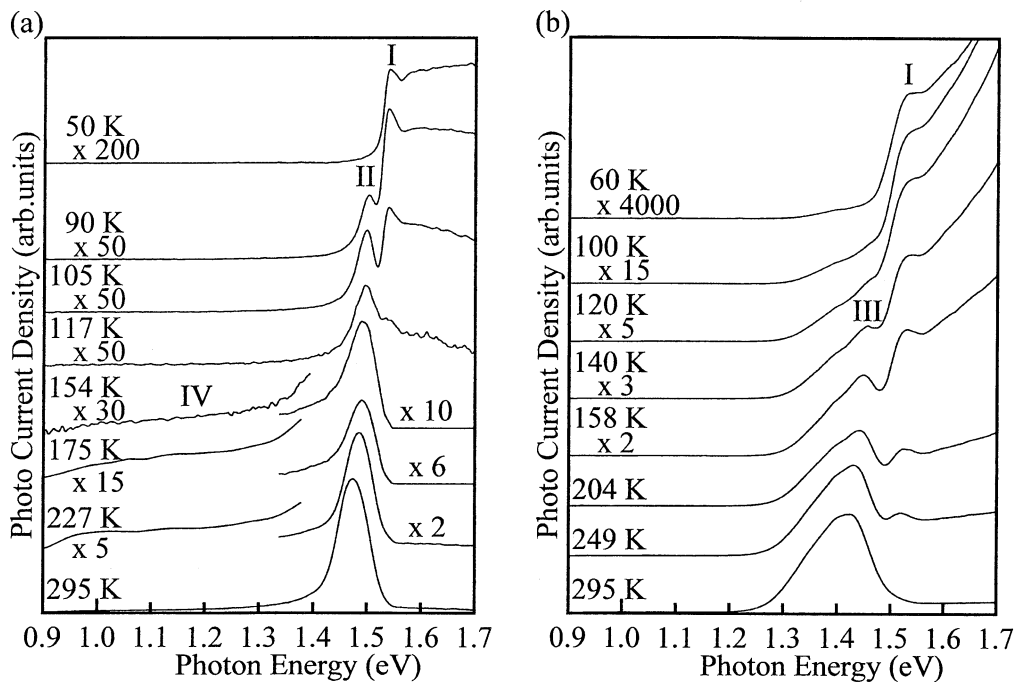


Fig. 5. Photoconductivity spectra at various temperatures for (a) sample A and (b) D.

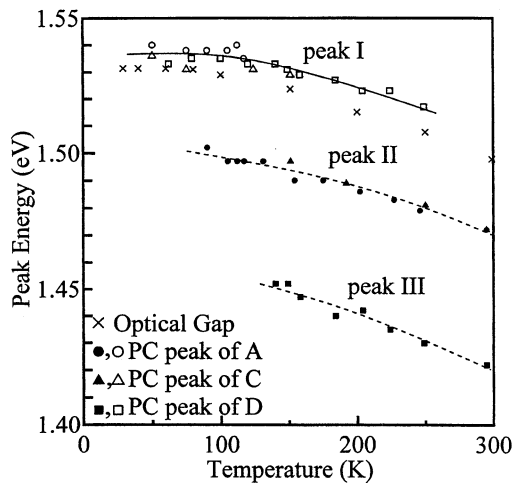


Fig. 6. Temperature dependence of peaks I, II and III for samples A, C and D, as compared with optical band gaps.

difficult to fit the temperature variation of the Hall coefficient curves because of too many fitting parameters.<sup>16,19)</sup> However, as seen in Figs. 1(a) and 1(b), the temperature characteristics of sample A are similar to those of sample B, especially at temperatures above 250 K, so that we can assume that sample A has the same defect levels as sample B.

It is seen from Table II that the densities of the acceptor  $E_{A1}$  in samples B and C (presumably also in sample A) are much less than those of  $E_{A3}$ , and thus the electrical properties are mainly governed by  $E_{A3}$ . This is the reason why the PC peak (peak III in Fig. 5) related to  $E_{A1}$  could not be observed in samples A and C. This also explains why a broad peak (peak IV) appeared at about 1.2 eV at high temperatures only in the above-mentioned samples under the influence of  $E_{A3}$ . On the contrary, in sample D, the densities of  $E_{A1}$  and  $E_D$  are high in

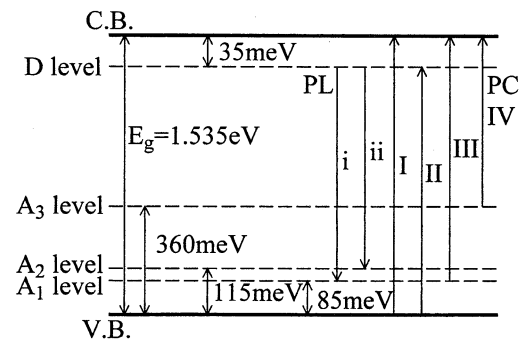


Fig. 7. Band diagram of samples A, B, C and D. Sample D has no acceptor levels of 115 and 360 meV.

comparison to those of the other samples, and the density of  $E_{A3}$  is much less than that of  $E_{A1}$ . The high density of  $E_{A1}$  necessarily broadens the level width, leading to the spread of the corresponding PC peak III (see Fig. 5). The PC peak related to  $E_D$  (peak II) may be immersed in the same signal.

In view of the impurity densities with elemental compositions listed in Table II, two main relationships are shown as follows:

- (1) The density of  $E_{A1}$ , i.e.,  $N_{A1}$ , increases as Cu/In ratio decreases.
- (2) The density of  $E_D$ , i.e.,  $N_D$ , increases as S/metal ratio decreases.

Based on the relationship (1), the acceptor level  $E_{A1}$  is thought to be produced by Cu-poor compositions in  $\text{CuInS}_2$  crystals. In other words, the origin of the acceptor is ascribed to Cu vacancies ( $V_{\text{Cu}}$ ), as reported for I–III–VI<sub>2</sub> compounds.<sup>26)</sup> In addition, the activation energy of the acceptor arising from  $V_{\text{Cu}}$  was reported to be 100 meV<sup>9)</sup> which is in agreement with  $E_{A1}$ . On the other hand, the origin of the acceptor of  $E_{A2}$  may be ascribed to In vacancies ( $V_{\text{In}}$ ), since the

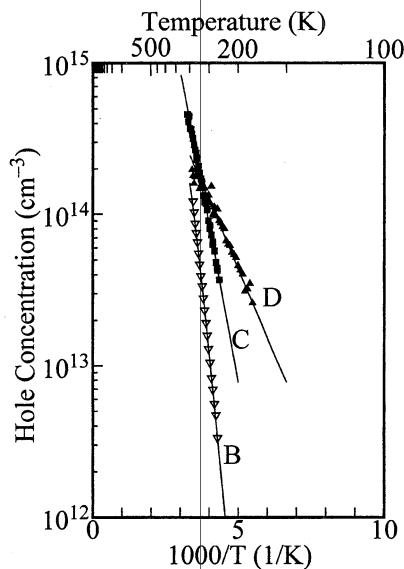


Fig. 8. Temperature dependence of carrier concentration, fitting by the parameters shown in Table II.

Table II. Acceptor and donor densities as well as deviation from molecularity and valence stoichiometry,  $\Delta x$  and  $\Delta y$ , for samples B, C and D.

Sample name	$N_{A1}$ ( $\text{cm}^{-3}$ )	$N_{A3}$ ( $\text{cm}^{-3}$ )	$N_D$ ( $\text{cm}^{-3}$ )	$\Delta x$	$\Delta y$
B	$\ll N_{A3}$	$8 \times 10^{15}$	$3 \times 10^{14}$	-0.017	-0.011
C	$\ll N_{A3}$	$1 \times 10^{16}$	$3 \times 10^{12}$	-0.010	+0.007
D	$2 \times 10^{16}$	$\ll N_{A1}$	$\sim 10^{16}$	-0.033	-0.019

PL peak related to  $E_{A2}$  is not observed in sample D which has the most In-rich composition. Based on the relationship (2), the donor level  $E_D$  is considered to be produced by S-poor compositions in  $\text{CuInS}_2$  crystals, and hence the origin of donor is ascribed to S vacancies ( $V_S$ ).<sup>26)</sup> Here, the activation energy of donor arising from  $V_S$  was also reported to be 35 meV,<sup>9)</sup> which is in good agreement with the value of  $E_D$ . The density of  $E_{A3}$ , i.e.,  $N_{A3}$ , is independent of compositional deviation in  $\text{CuInS}_2$  crystals. The lattice defects in  $\text{CuInS}_2$  have been frequently represented as deviations from the molecularity and valence stoichiometry,  $\Delta x$  and  $\Delta y$ .<sup>25)</sup> Applying this assumption to the case of  $\text{CuInS}_2$ , the acceptor is considered to be due only to  $V_{Cu}$ , because of  $\Delta x < 0$  and  $\Delta y < 0$  for samples B, C and D. However,  $V_{Cu}$  is also a candidate for the acceptor level  $E_{A1}$ . It is expected that the origin of the acceptor level  $E_{A3}$  is not ascribed to the intrinsic defect, but probably to the extrinsic defect.

### 5. Conclusion

We have analyzed the lattice defects of  $\text{CuInS}_2$  bulk single crystals grown by the horizontal Bridgman method with con-

trolling S vapor pressure in terms of the Hall effect, photoluminescence, optical absorption and photoconductivity measurements, along with the results of EPMA. On the basis of these measurements, the activation energies of acceptors in  $\text{CuInS}_2$  crystals were estimated to be 85 meV, 115 meV and 360 meV which were ascribed to Cu-vacancies, In-vacancies and the extrinsic impurity, respectively and the activation energy of donor was estimated to be 35 meV ascribed to S-vacancies. The grown crystals had electrical resistivities of more than  $10^3 \Omega\cdot\text{cm}$  at room temperature, and the densities of lattice defects were three orders of magnitude lower than those of crystals prepared by the traveling heater method.<sup>12)</sup> It was found that the electrical properties can be well controlled without the influence of intrinsic defects.

- 1) H. W. Schock: *Sol. Energy Mater. & Sol. Cells* **34** (1994) 19.
- 2) B. Tell and F. A. Thiel: *J. Appl. Phys.* **50** (1979) 5045.
- 3) H. J. Lewerenz, H. Goslowky and K. D. Husemann: *Nature* **321** (1986) 687.
- 4) Y. Ogawa, A. J. Waldau, Y. Hashimoto and K. Ito: *Jpn. J. Appl. Phys.* **33** (1994) L1775.
- 5) J. Klaer, J. Bruns, R. Henninger, K. Siemer, R. Klenk, K. Ellmer and D. Bräunig: *Semicond. Sci. Technol.* **13** (1998) 1456.
- 6) T. Walter, R. Menner and H. W. Schock: *Proc. 12th EC Photovoltaic Solar Energy Conf.*, Amsterdam, 1994, p. 1775.
- 7) T. Nakabayashi, T. Miyazawa, Y. Hashimoto and K. Ito: *Sol. Energy Mater. & Sol. Cells* **49** (1997) 375.
- 8) G. Masse, N. Lahlou and C. Butti: *J. Phys. Chem. Solids* **42** (1981) 449.
- 9) J. J. Binsma, L. J. Giling and J. Bloem: *J. Lumin.* **27** (1982) 35.
- 10) S. D. Mittleman and R. Singh: *Solid State Commun.* **22** (1977) 659.
- 11) M. P. Vecchi and J. Ramos: *J. Appl. Phys.* **52** (1981) 2958.
- 12) H. Y. Ueng and H. L. Hwang: *J. Phys. Chem. Solids* **50** (1989) 1297.
- 13) M. L. Fearheiley, M. Kanis and S. Fiechter: *J. Electrochem. Soc.* **140** (1993) 1396.
- 14) K. Wakita, H. Hirooka, S. Yasuda, F. Fujita and N. Yamamoto: *J. Appl. Phys.* **83** (1998) 443.
- 15) H. Matsushita, T. Mihira and T. Takizawa: *J. Cryst. Growth* **197** (1999) 169.
- 16) H. Matsushita and T. Takizawa: *J. Cryst. Growth* **160** (1996) 71.
- 17) H. Matsushita, H. Jitsukawa, H. Sugano, T. Takizawa and S. Endo: *Proc. 11th Int. Conf. Ternary and Multinary Compounds, Salford, 1997* (IOP Publishing, Bristol, 1997) *Inst. Phys. Conf. Ser. No. 152*, p. 535.
- 18) B. Tell, J. L. Shay and H. M. Kasper: *J. Appl. Phys.* **43** (1972) 2469.
- 19) S. Nomura, J. Itoh and T. Takizawa: *Proc. 9th Int. Conf. Ternary and Multinary Compounds, Yokohama, 1993*, *Jpn. J. Appl. Phys.* **32** (1993) Suppl. 32-3, p. 97.
- 20) H. Matsushita, A. Iwabuchi, T. Takizawa and S. Endo: *Cryst. Res. & Technol.* **31** (1996) Special Issue, 77.
- 21) E. Zack and A. Halperin: *Phys. Rev. B* **6** (1972) 3072.
- 22) S. Shirakata, S. Chichibu, S. Matsumoto and S. Isomura: *Jpn. J. Appl. Phys.* **33** (1994) L345.
- 23) M. Susaki, H. Horinaka and N. Yamamoto: *Jpn. J. Appl. Phys.* **30** (1991) 2797.
- 24) M. Susaki, H. Horinaka and N. Yamamoto: *Jpn. J. Appl. Phys.* **31** (1992) 301.
- 25) S. W. Wasim: *Sol. Cell* **16** (1986) 289.
- 26) H. Neumann: *Cryst. Res. Technol.* **18** (1983) 483.



ELSEVIER

Journal of Crystal Growth 222 (2001) 574–578

JOURNAL OF  
**CRYSTAL  
GROWTH**

www.elsevier.nl/locate/jcrysgr

# Phase diagram of the CaS–Ga<sub>2</sub>S<sub>3</sub> system and melt growth of CaGa<sub>2</sub>S<sub>4</sub> single crystals

C. Komatsu-Hidaka, T. Takizawa\*

*Department of Physics, College of Humanities and Sciences, Nihon University, 3-25-40 Sakurajosui, Setagaya-ku, Tokyo 156-8550, Japan*

Received 6 June 2000; accepted 2 November 2000

Communicated by T. Hibiya

## Abstract

We have constructed the pseudo-binary phase diagram of the CaS–Ga<sub>2</sub>S<sub>3</sub> system in order to prepare single crystals of CaGa<sub>2</sub>S<sub>4</sub>. Based on the diagram, single crystals doped with 0.1, 0.2, 0.4, 0.8 and 1.5 wt% Ce<sup>3+</sup> are grown from melt by the horizontal Bridgman method. Photoluminescence spectra of these crystals are measured at room temperature. The overall features are in good agreement with the reported data of thin films. However, the emission intensity does not show a linear relation ship with doped Ce<sup>3+</sup> concentration at more than 0.4 wt%, presumably because of the precipitates arising from the overdoping. © 2001 Elsevier Science B.V. All rights reserved.

*PACS:* 81.10.–h

*Keywords:* CaS; Ga<sub>2</sub>S<sub>3</sub>; CaGa<sub>2</sub>S<sub>4</sub>; Phase diagram; Melt growth; Horizontal Bridgman method

## 1. Introduction

Following a previous work on the crystal growth of SrGa<sub>2</sub>S<sub>4</sub> [1], we present here a similar result for CaGa<sub>2</sub>S<sub>4</sub>. As is well known, cerium element doped CaGa<sub>2</sub>S<sub>4</sub> shows blue emission under illumination of ultraviolet light, and is regarded as a promising candidate for a blue element of the full color display [2].

Another point of interest is the laser oscillation that was observed in CaGa<sub>2</sub>S<sub>4</sub>:Eu<sup>2+</sup> single crystals prepared by the iodine transport method [3]. An optically pumped laser using RE-doped

CaGa<sub>2</sub>S<sub>4</sub> is also suggested by Iida et al. [4], which has a good advantage of a wavelength tunable laser in between green and near ultraviolet region. Here, it should be stressed that this possibility will be realized only if a single crystal of high quality is grown.

However, as in the case of SrGa<sub>2</sub>S<sub>4</sub>, single crystals of high quality have not been grown yet, and thus little is known about the basic optical properties of CaGa<sub>2</sub>S<sub>4</sub>. Now, a precise phase diagram of the pseudo-binary system of CaS–Ga<sub>2</sub>S<sub>3</sub> is strongly required for the melt growth of the crystal.

In this report, first, we present the phase diagram of the CaS–Ga<sub>2</sub>S<sub>3</sub> system constructed through DTA curves and powder X-ray diffraction patterns followed by a result of the crystal growth

\*Corresponding author. Tel.: +81-3-3329-1151; fax: +81-3-5317-9432.

*E-mail address:* takiz@chs.nihon-u.ac.jp (T. Takizawa).

of  $\text{CaGa}_2\text{S}_4:\text{Ce}^{3+}$  by the horizontal Bridgman method. Discussion is also made on the room temperature photoluminescence of the single crystals doped with  $\text{Ce}^{3+}$  of a concentration ranging from 0.1 to 1.5 wt%.

## 2. Phase diagram of the $\text{CaS-Ga}_2\text{S}_3$ system

The DTA instrument is the same as in a previous paper [5]. The scan speed of the DTA measurement was fixed to  $2^\circ\text{C}/\text{min}$ . Two elements of calcium and sulfur and a compound of  $\text{Ga}_2\text{S}_3$  were weighed to be in a scheduled compositional ratio in a globebox filled with argon gas and sealed in a quartz ampoule of  $7\text{ mm}\varnothing \times 40\text{ mm}$  under vacuum of  $10^{-3}\text{ Torr}$ . The method of preparation of  $\text{Ga}_2\text{S}_3$  was the same as reported in a previous paper [1]. The inner surface of a quartz ampoule was coated with carbon film by firing acetone in air. This treatment could prevent the melt of the mixture from sticking to the wall inside an ampoule. The products after DTA measurements were analyzed by powder X-ray diffraction at room temperature using the  $\text{Cu-K}_\alpha$  line.

Fig. 1(a) shows DTA curves in the cooling process between 50 and 75 mol%  $\text{Ga}_2\text{S}_3$ . The melting point of the compounds lowers with

increasing  $\text{Ga}_2\text{S}_3$  concentration. The peak at  $975^\circ\text{C}$  was found in every DTA curve of the compounds above 50 mol%  $\text{Ga}_2\text{S}_3$ . Fig. 1(b) shows powder X-ray diffraction patterns of the products after DTA measurements, where the diffraction intensity was normalized to each maximum. The diffraction lines from a sample with 50 mol%  $\text{Ga}_2\text{S}_3$  was in agreement with the reported X-ray pattern of  $\text{CaGa}_2\text{S}_4$  [6]. For clarity, the lines of  $\text{Ga}_2\text{S}_3$  were marked with dots in Fig. 1(b). It is seen that the diffraction patterns of the compounds in the concentration above 50 mol%  $\text{Ga}_2\text{S}_3$  were mixed ones of  $\text{CaGa}_2\text{S}_4$  and  $\text{Ga}_2\text{S}_3$ .

Fig. 2(a) shows DTA curves for the compounds between 75 and 100 mol%  $\text{Ga}_2\text{S}_3$ . Except for 100 mol%  $\text{Ga}_2\text{S}_3$ , there appeared three signals at  $975$ ,  $995^\circ\text{C}$  and at the melting point. Contrary to Fig. 1(a), the melting point rises with increasing  $\text{Ga}_2\text{S}_3$  concentration, as indicated by the arrows in Fig. 2(a). Fig. 2(b) shows powder X-ray diffraction patterns of the products after DTA measurements. The diffraction lines of  $\text{CaGa}_2\text{S}_4$  were indicated by the triangles. It is clearly seen that the compounds consist of the mixtures of  $\text{Ga}_2\text{S}_3$  and  $\text{CaGa}_2\text{S}_4$ .

Based on these results, the pseudo-binary phase diagram of the  $\text{CaS-Ga}_2\text{S}_3$  system was deduced as shown in Fig. 3 very similar to that of  $\text{SrGa}_2\text{S}_4$ .

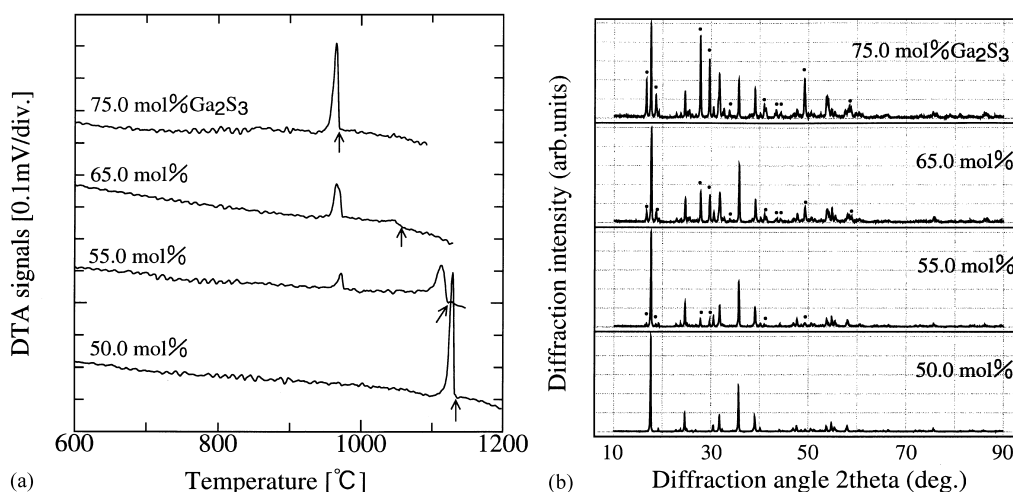


Fig. 1. (a) DTA curves of 50–75 mol%  $\text{Ga}_2\text{S}_3$  in the cooling process in the  $\text{CaS-Ga}_2\text{S}_3$  system. The heating and cooling rates are fixed to  $2^\circ\text{C}/\text{min}$ . (b) the corresponding X-ray powder diffraction patterns normalized to the respective highest line. The dots indicate the  $\text{Ga}_2\text{S}_3$  phase.

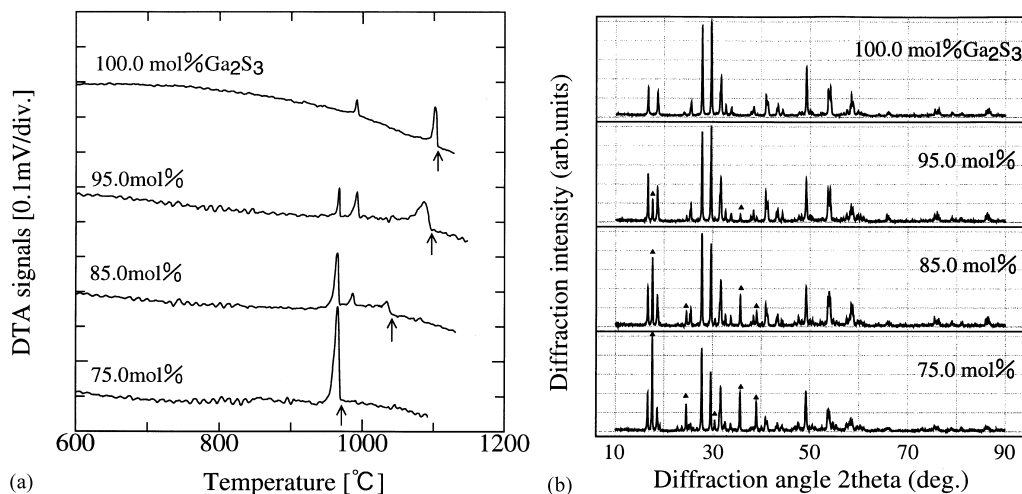


Fig. 2. (a) DTA curves of 75.0–100 mol% Ga<sub>2</sub>S<sub>3</sub> in the cooling process in the CaS–Ga<sub>2</sub>S<sub>3</sub> system. The heating and cooling rates are fixed to 2°C/min and (b) the corresponding X-ray powder diffraction patterns normalized to the respective highest line. The solid triangles indicate the CaGa<sub>2</sub>S<sub>4</sub> phase.

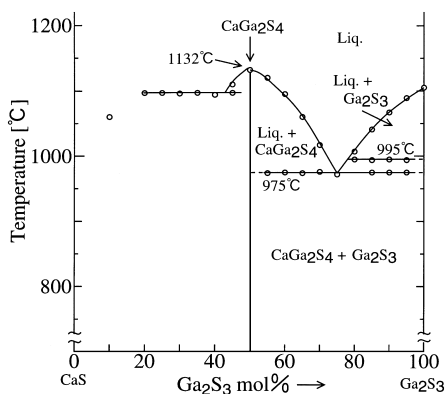


Fig. 3. Pseudo-binary phase diagram of the CaS–Ga<sub>2</sub>S<sub>3</sub> system.

A eutectic reaction was found in the region from 50 to 100 mol% Ga<sub>2</sub>S<sub>3</sub> with the eutectic point at 975°C at 75.0 mol% Ga<sub>2</sub>S<sub>3</sub>. Similar to the case of SrGa<sub>2</sub>S<sub>4</sub>, the self-flux method by using Ga<sub>2</sub>S<sub>3</sub> as a flux will also be recommended for the single-crystal growth of CaGa<sub>2</sub>S<sub>4</sub>. However, the melting point of CaGa<sub>2</sub>S<sub>4</sub> (1132°C) is about 100°C lower than that of SrGa<sub>2</sub>S<sub>4</sub> (1230°C), and is also suitable for the melt growth using a quartz ampoule. In addition, if RE ion doping is required, the melt growth will be better to achieve the homogeneous

doping, because the deviation of composition due to temperature variation can be easily suppressed in the melt growth in comparison to the solution (flux) growth method. Based on this consideration, the crystal growth was performed by the melt method in the present case, and the details are described in the next section.

### 3. Crystal growth of CaGa<sub>2</sub>S<sub>4</sub>

As in the case of SrGa<sub>2</sub>S<sub>4</sub>, IIa element Ca strongly reacts around 300°C with the S element, sometimes causing the destruction of quartz crucibles by the heat of the exothermic reaction. By taking a special care to this reaction, we prepared the precursor of CaGa<sub>2</sub>S<sub>4</sub> in the following procedure. First, two elements of Ca(3N), S(6N) and a pre-reacted compound of Ga<sub>2</sub>S<sub>3</sub> were weighed in the stoichiometric composition to about 7 g in total in argon gas atmosphere. Then the Ca + Ga<sub>2</sub>S<sub>3</sub> mixture was poured into a quartz boat (8 mm $\varnothing$  × 100 mm) coated with carbon film inside. This boat was set in at one end of another quartz ampoule (13 mm $\varnothing$  × 300 mm). The S powder was separately put at the other end of the

ampoule which was finally sealed under vacuum of  $10^{-6}$  Torr.

The evacuated ampoule was set in a two-zone furnace, and the  $\text{Ca} + \text{Ga}_2\text{S}_3$  part was heated to  $400^\circ\text{C}$ , while the sulfur part was kept at  $300^\circ\text{C}$  for 24 h. This led to a complete reaction between Ca and S, i.e., S was completely absorbed in the  $\text{Ca} + \text{Ga}_2\text{S}_3$  mixture in the quartz boat. Then, the whole ampoule was heated up to  $1120^\circ\text{C}$  just above the melting point of  $\text{Ga}_2\text{S}_3$  and kept for 1 h. Thus a white precursor of  $\text{CaGa}_2\text{S}_4$  was synthesized. The precursor was taken out from the ampoule and ground, and refilled in another carbon coated quartz boat. This boat was again doubly sealed in another quartz ampoule ( $13\text{ mm}\varnothing \times 120\text{ mm}$ ) in the same manner as described previously. The crystal growth was performed by elevating the temperature of the ampoule to  $1150^\circ\text{C}$  and by making a temperature gradient of  $7^\circ\text{C}/\text{cm}$  and moving the temperature profile electronically [5]. The growth speed was about  $0.5\text{ cm}/\text{h}$ .

$\text{Ce}^{3+}$  doping was made by mixing powdered  $\text{Ce}_2\text{S}_3$  of an appropriate quantity with the precursor. Thus, dopings of 0.1, 0.2, 0.4, 0.8 and 1.5 wt%  $\text{Ce}^{3+}$  were performed. Crystals doped with less than 0.5 wt%  $\text{Ce}^{3+}$  were colorless, a little yellowish and transparent, but those above 0.5 wt% became colored black though partly transparent. The crystallinity became worse as the concentration of Ce increased. In the present case, if the Ce content was made greater than 1.5 wt%, the resultant crystals became black and no more transparent. In addition, they had many cracks and voids insides.

In Fig. 4 is shown a photograph of a 0.8 wt%  $\text{Ce}^{3+}$  doped crystal. The crystal is about 7 mm in diameter and 5 mm in length. It is easily cleaved along the growth direction, i.e., the  $[100]$  direction, as seen by a transparent cleavage surface in Fig. 4.

#### 4. Emission spectra of $\text{CaGa}_2\text{S}_4:\text{Ce}^{3+}$

The emission spectra of  $\text{CaGa}_2\text{S}_4:\text{Ce}^{3+}$  were measured at room temperature. Samples were excited by a 325 nm He–Cd laser (Omnichrome 3056-

15M) with an output power of 23 mW, the intensity of which was reduced by 1/10 using a neutral filter. The emission was dispersed by a monochromator (NALUMI RM-23-I) and detected by a photomultiplier (HAMAMATSU R562).

Fig. 5 shows emission spectra of single crystals of  $\text{CaGa}_2\text{S}_4$  with various Ce concentrations.

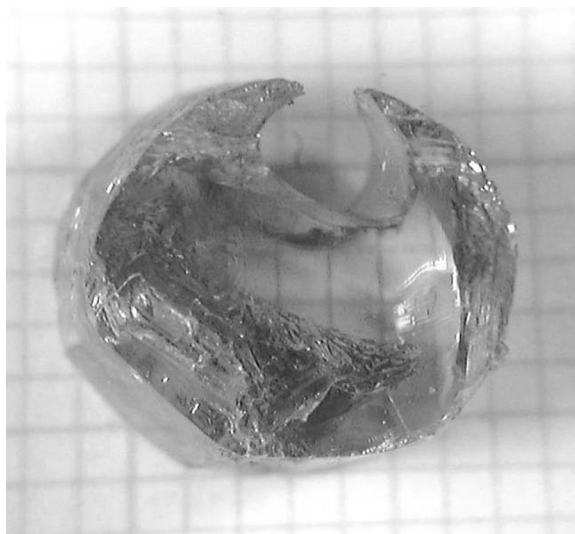


Fig. 4. Photograph of a part of a  $\text{CaGa}_2\text{S}_4$  ingot doped with 0.8 wt%  $\text{Ce}^{3+}$  grown from melt by the horizontal Bridgman method. The mesh size in the figure is  $1\text{ mm} \times 1\text{ mm}$ . The thickness is about 5 mm. The transparent and flat surface is made by cleaving the crystal along the growth direction.

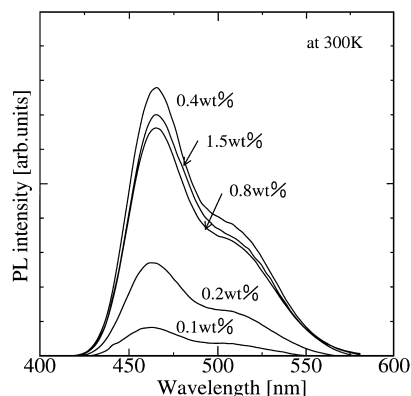


Fig. 5. Emission spectra of  $\text{CaGa}_2\text{S}_4$  doped with various  $\text{Ce}^{3+}$  concentration.

Emission intensity was measured by using powdered samples filled in capillaries having a same size. This method was devised to homogenize the emission from the oriented surfaces of single crystals and to eliminate the effect of the sample size of each crystal.

It is seen from Fig. 5 that the emission intensity increases as the concentration of Ce increases, and that it saturates above 0.4 wt%  $\text{Ce}^{3+}$ . Its overall feature is in good agreement with the reported data of thin films [7]. On the contrary, however, the photo emission from thin films linearly increases up to 6.0 wt% of  $\text{Ce}^{3+}$  and then saturates above it [7].

In the present growth method, it is impossible to keep crystals transparent with doping  $\text{Ce}^{3+}$  more than 1.5 wt% as already mentioned in the previous section. Thus the doping mechanism is thought to be very different between the melt growth and the thin film preparation. In view of the surface morphology, it can be said that the black part in a highly doped crystal consists of precipitates scattered over a region considered. Since the charge compensation is not established if a  $\text{Ce}^{3+}$  ion substitutes the  $\text{Ca}^{2+}$  site of  $\text{CaGa}_2\text{S}_4$ , a vacancy or the like should be introduced in a site near the Ce one to keep the charge neutrality. However, if the concentration of Ce is too high to be compensated by such vacancies, the extra Ce must be precipitated in a crystal, giving dark spots in a grown crystal or if they become large, they may form cracks or voids inside the crystal. The solution limit of Ce in a crystal may also be different in both cases. It is because the thermal equilibrium in the melt growth is established at temperature much higher than that in the thin film. At low temperatures, thermal vibrations between atoms forming a crystal lattice are not so violent as at high temperatures. Therefore the Ce concentration available in a thin film, is considered to be made very high in comparison to that in a melt grown crystal.

For more rigorous discussions of the effect of  $\text{Ce}^{3+}$  doping on photoemission, the precise knowledge on the doping content should be required.

However, optical absorption and ESR measurements as well as the experiments searching for the possibility of laser oscillation are now under way, so that the detailed discussions are postponed until the next paper concerning the optical characteristics of this material is completed.

## 5. Conclusion

We have constructed the pseudo-binary phase diagram of the  $\text{CaS-Ga}_2\text{S}_3$  system. A eutectic reaction was found in the compositional range from 50–100 mol%  $\text{Ga}_2\text{S}_3$ . The  $\text{CaGa}_2\text{S}_4$  compound was found to be congruent with the melting point of 1132°C. We have grown  $\text{Ce}^{3+}$ -doped  $\text{CaGa}_2\text{S}_4$  single crystals from melt by the horizontal Bridgman method. Transparent and yellowish single crystals were obtained. From the saturation of photoemission intensity at the Ce concentration above 0.4 wt%, it is concluded that the solution limit of Ce to the crystal is rather low in comparison to the thin film case.

## Acknowledgements

This work was partly supported by the Research Grant from Nihon University.

## References

- [1] C. Komatsu, T. Takizawa, *J. Crystal Growth* 210 (2000) 677.
- [2] W.A. Barrow, R.C. Coovert, E. Dickey, C.N. King, C. Laakso, S.S. Sun, R.T. Tuenge, R. Wetross, J. Kane, 1993 SID International Symposium Digest, 1993, p. 761.
- [3] S. Iida, T. Matsumoto, N.T. Mamedov, Y. Maruyama, A.I. Bairamov, B.G. Tagiev, O.B. Tagiev, R.B. Dzhabbarov, *Jpn. J. Appl. Phys.* 36 (1997) L857.
- [4] S. Iida: private communication.
- [5] H. Matsushita, T. Takizawa, *Jpn. J. Appl. Phys.* 34 (1995) 4699.
- [6] T.E. Peter, J.A. Baglio, *J. Electrochem. Soc.* 119 (1972) 230.
- [7] S.S. Sun, R.T. Tuenge, J. Kane, M. Ling, *J. Electrochem. Soc.* 141 (1994) 2877.

# Pressure effect on the antiferromagnetic transition temperature in $\text{CuFeO}_2$

H. Takahashi<sup>a,\*</sup>, Y. Motegi<sup>a</sup>, R. Tsuchigane<sup>a</sup>, M. Hasegawa<sup>b</sup>

<sup>a</sup> College of Humanities and Sciences, Nihon University, Sakurajousui, Setagaya-ku, Tokyo 156-8550, Japan

<sup>b</sup> Institute for Material Research, Tohoku University, Katahira, Aoba-ku, Sendai 980-8577, Japan

## Abstract

Effect of pressure on the magnetic transition temperature of  $\text{CuFeO}_2$  with a delafossite-type structure has been investigated using a piston-cylinder-type high-pressure apparatus designed for SQUID magnetometer.  $\text{CuFeO}_2$  having triangular layer of magnetic  $\text{Fe}^{3+}$  shows the successive antiferromagnetic transition at 13 K ( $T_{N1}$ ) and at 9 K ( $T_{N2}$ ). It is found that both transition temperatures decrease with applying pressure up to 0.7 GPa at a rate of  $-1$  K/GPa.

© 2003 Elsevier B.V. All rights reserved.

PACS: 74.62.Fj; 75.30.Kz; 75.50.Ee

Keywords: Delafossite;  $\text{CuFeO}_2$ ; High pressure; Spin frustration

Since the high- $T_C$  superconductor was discovered, great attention has been paid to low-dimensional transition metal oxides, from the view of strongly correlated electron systems.  $\text{CuFeO}_2$  with a delafossite-type structure has been attractive because of its low-dimensional triangular structure. The delafossite structure with space group  $R\bar{3}m$  consists of respective hexagonal layers.  $\text{CuFeO}_2$  has magnetic  $\text{Fe}^{3+}$  layers, which form a layered triangular lattice frustrated antiferromagnet, separated by nonmagnetic  $\text{Cu}^+$  and  $\text{O}^{2-}$  layers. In a frustrated system, the magnetic phase transitions take place under a subtle balance of magnetic interactions.  $\text{CuFeO}_2$  exhibits two successive antiferromagnetic transitions at 13 K ( $T_{N1}$ ) and 9 K ( $T_{N2}$ ) [1]. Mitsuda et al. [2] determined the magnetic structure of  $\text{CuFeO}_2$  by neutron diffraction studies. They reported that the magnetic ground state has a four-sublattice antiferromagnetic structure in which spins are collinear and parallel to the  $c$ -axis, and the high-temperature antiferromagnetic phase is partially distorted. Moreover, they indicated that the Ising character of  $\text{Fe}^{3+}$  in the antiferromagnetic phases is unusual. Thus the origin

of the magnetic orderings is considered to be very complicated.

Ajiro et al. [3] and Kasahara et al. [4] studied impurity effect on the stability of the ground-state spin configuration in  $\text{CuFeO}_2$ . They substituted magnetic  $\text{Cr}^{3+}$  and nonmagnetic  $\text{Al}^{3+}$  to Fe, and reported that a small impurity affects the magnetic states strongly. Hasegawa et al. [5] reported that the oxygen nonstoichiometry largely affects the antiferromagnetism of  $\text{CuFeO}_2$  single crystals. Oxygen nonstoichiometry accompanies changes of cation valences and lattice parameters. In this way, the slight disturbance of the triangular spin lattice strongly affects the magnetic interactions.

The pressure effect is also expected to affect the magnetic state. Zhao et al. [6] carried out X-ray diffraction study of  $\text{CuFeO}_2$  under high pressure up to 10 GPa. From the X-ray experiments, they reported no structural transition and indicated that the  $a$ -axis is about 3.9 times more compressible than  $c$ -axis. However, this situation seems strange if this anisotropic compression is compared to cuprate superconductors, in which  $c$ -axis is usually more compressible than  $a$ -axis, except for  $(\text{La}, \text{Sr})_2\text{CuO}_4$  which accompanies a tilting of  $\text{CuO}_6$  octahedron with applying pressure [7].

In this study, we report the effect of pressure on the antiferromagnetic transition temperature of  $\text{CuFeO}_2$ .

\*Corresponding author. Tel.: +81-3-3329-1151; fax: +81-3-5317-9432.

E-mail address: [hiroki@chs.nihon-u.ac.jp](mailto:hiroki@chs.nihon-u.ac.jp) (H. Takahashi).

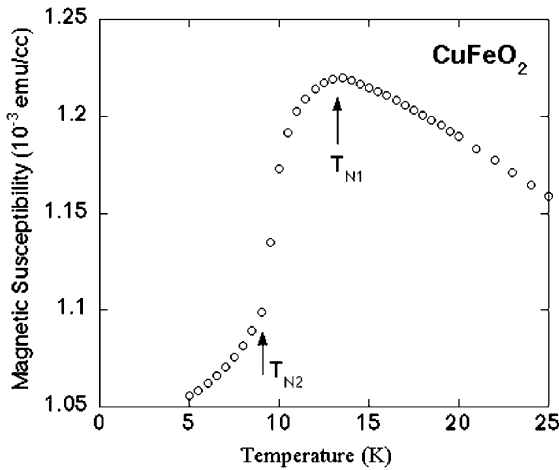


Fig. 1. DC susceptibility of  $\text{CuFeO}_2$ .  $T_{N1}$  and  $T_{N2}$  are indicated by arrows.

Single crystal of  $\text{CuFeO}_2$  was grown by the floating-zone method described elsewhere [8]. Magnetic susceptibility was measured with a SQUID magnetometer (Quantum Design MPMS-XL). A piston-cylinder-type high-pressure apparatus made by Cu–Be alloy designed for SQUID magnetometer was used.

Fig. 1 shows the magnetic susceptibility of  $\text{CuFeO}_2$ , in which  $T_{N1}$  and  $T_{N2}$  are observed. The  $T_{N1}$  and  $T_{N2}$  decrease with pressure up to 0.7 GPa at a rate of  $-1 \text{ K/GPa}$ , as shown in Figs. 1 and 2. During the high-pressure measurements, the shape of anomalies accompanied with transitions in  $\chi(T)$  curve does not change.

Suppression of  $T_{N1}$  and  $T_{N2}$  was also observed when excess oxygen is introduced to  $\text{CuFeO}_2$  [5]. Since  $c/a$  decreases with introduction of excess oxygen while  $c/a$  increases with pressure, the present results cannot be explained by a single source about crystal structure. However, large change of intra-layer magnetic interactions is suggested from the high-pressure X-ray results, in which the  $a$ -axis is about 3.9 times more compressible than  $c$ -axis. If the  $T_{N1}$  and  $T_{N2}$  decrease linearly at a rate of  $-1 \text{ K/GPa}$ , it disappears at 10 GPa. Then it is very interesting to perform high-pressure studies at more than 10 GPa, since a new magnetic phase can be expected at the pressure where the magnetic ordering state disappears, as observed in  $\text{UGe}_2$  [9]. From the

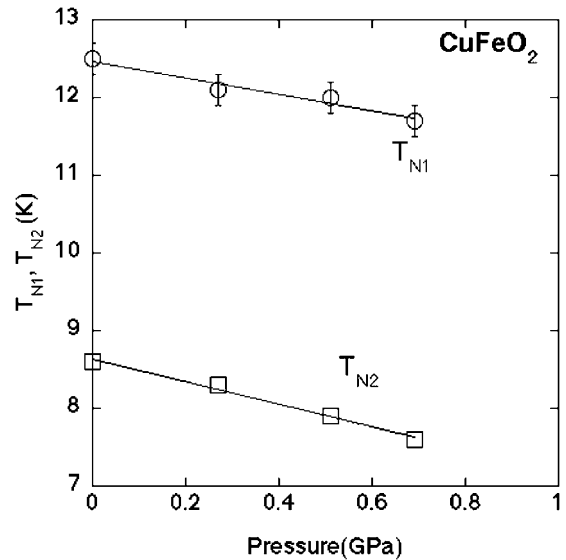


Fig. 2. Pressure dependence of  $T_{N1}$  and  $T_{N2}$ .

preliminary electrical resistivity measurements under high pressure, the resistivity decreases to 0.1 times value at 10 GPa. The susceptibility and electrical resistivity measurements are in progress at higher pressures.

## References

- [1] M. Mekata, N. Yaguchi, T. Takagi, S. Mitsuda, H. Yoshizawa, *J. Magn. Magn. Mater.* 104–107 (1992) 823.
- [2] S. Mitsuda, H. Yoshizaki, N. Yaguchi, M. Mekata, *J. Phys. Soc. Japan* 60 (1991) 1885.
- [3] Y. Ajiro, K. Hanasaki, T. Asano, T. Takagi, M. Mekata, H. Aruga-Katori, *J. Phys. Soc. Japan* 64 (1995) 3643.
- [4] N. Kasahara, Y. Matsumoto, K. Tanaka, S. Mitsuda, H. Yoshizawa, M. Mekata, unpublished.
- [5] M. Hasegawa, M.I. Batrashevich, T.R. Zhao, H. Takei, T. Goto, *Phys. Rev. B* 63 (2001) 184437.
- [6] T.R. Zhao, M. Hasegawa, T. Kondo, T. Yagi, H. Takei, *Mater. Res. Bull.* 32 (1997) 151.
- [7] H. Takahashi, N. Mori, in: A.V. Narlikar (Eds.), *Studies of High Temperature Superconductors*, Vol. 16, Nova Science Publishers, Inc., New York, 1996.
- [8] T.R. Zhou, M. Hasegawa, H. Takei, *J. Crystal Growth* 154 (1995) 322.
- [9] S.S. Saxena, et al., *Nature* 406 (2000) 587.

# High pressure studies of anomalous electronic states of $Y_{1-x}U_xPd_3$

Gendo Oomi<sup>1</sup>, Tomoko Kagayama<sup>2</sup>, Yuji Aoki<sup>3</sup>, Hideyuki Sato<sup>3</sup>,  
Yoshichika Ōnuki<sup>4</sup>, Hiroki Takahashi<sup>5</sup> and Nobuo Mōri<sup>6</sup>

<sup>1</sup> Department of Physics, Kyushu University, Ropponmatsu, Fukuoka 810-8560, Japan

<sup>2</sup> Research Centre for Materials Science at Extreme Conditions, Osaka University, Toyonaka, Osaka 560-8531, Japan

<sup>3</sup> Department of Physics, Tokyo Metropolitan University, Hachioji, Tokyo 192-0397, Japan

<sup>4</sup> Department of Physics, Osaka University, Toyonaka, Osaka 560-0043, Japan

<sup>5</sup> Department of Physics, CHS, Nihon University, Setagaya-ku, Tokyo 156-8550, Japan

<sup>6</sup> Department of Physics, Saitama University, Saitama 338-8570, Japan

Received 12 January 2004

Published 7 May 2004

Online at [stacks.iop.org/JPhysCM/16/3385](http://stacks.iop.org/JPhysCM/16/3385)

DOI: 10.1088/0953-8984/16/20/010

## Abstract

The electrical resistivity  $\rho(T)$  of  $Y_{1-x}U_xPd_3$  ( $x = 0, 0.05$  and  $0.2$ ) and the lattice constants for  $x = 0$  have been measured at high pressure. It is found that the cubic  $Cu_3Au$  structure is stable up to 12 GPa at room temperature. The Kondo temperature  $T_K$  was extracted from the  $\rho(T)$  curve and it was found that it increases with pressure. A logarithmic temperature dependence characteristic of the Kondo effect was found for  $x = 0.2$  in the temperature range above about  $0.5T_K$ . Fermi liquid behaviour in  $\rho(T)$  for  $x = 0.05$ , i.e.,  $\rho(T) \propto T^2$ , is observed and its stability at high pressure is discussed. The pressure dependence of the Kondo temperature  $T_K$  is discussed using the Grüneisen parameters at  $T_K$ ,  $\Gamma_K$ . It appears that the values of  $\Gamma_K$  are the same for these two compounds ( $x = 0.05$  and  $0.2$ ):  $\Gamma_K = 12$ . The  $T$ -linear behaviour in  $\rho(T)$  for  $x = 0.2$ , which is characteristic behaviour for non-Fermi liquids, is collapsed by an application of pressure and typical Fermi liquid quadratic temperature dependence recovers at high pressure. From the result for  $x = 0.2$ , the power  $n$  of the temperature in  $\rho(T) \propto T^n$  is determined as 1.0 at ambient pressure and 1.9 at 5.8 GPa. It is pointed out that the hybridization effect due to the application of pressure gives rise to a crossover from a non-Fermi liquid state to Fermi liquid state. But the crossover temperature  $T_{cr}$  shows a pressure dependence different from that predicted by the two-channel Kondo model.

## 1. Introduction

It has been reported that some intermetallic compounds including U or Ce show a lot of interesting electronic properties such as heavy fermions (HF), the Kondo effect and

superconductivity [1]. Among them, the compounds showing behaviour substantially different from the normal Landau Fermi liquid (FL) type have been extensively studied [2–4]. The electronic state displaying these behaviours has been called the ‘non-Fermi liquid’ (NFL) state. As for the electrical resistivity,  $\rho(T)$  for these compounds shows a weak power law at low temperatures, such as  $T^n$  ( $n = 1–1.5$ ) [5, 6], which is in sharp contrast to that for normal FL behaviour:  $T^2$  at low temperature. Anomalous behaviours have been observed for other physical quantities such as magnetic susceptibility and specific heat [3–5]. Several theoretical models from different points of view for interpreting these anomalous properties have been presented [4]. But the origin of the NFL state has not been completely understood yet.

The instability of the NFL state under the influence of perturbation or changing the control parameters has been studied extensively by many investigators [5–7]. In this area, high pressure study of NFL gives us a lot of important information because high pressure is considered as a ‘uniform perturbation’ and it gives rise to an electronic and structural phase transition or crossover in the materials having highly correlated marginal electronic states, which supplies a lot of crucial information for clarifying the electronic and magnetic structures of these materials [8]. Furthermore, since the disorder in the doped sample has been pointed out to play an important role in these systems [9, 10], high pressure study of undoped materials showing NFL behaviours is highly desired.

Until now, we have reported mainly, for several Ce compounds, on the pressure-induced crossover from the concentrated Kondo (CK) state or the HF state to the intermediate valence (IV) state in which the valence of the rare earth elements is not integer [11]. Since HF compounds generally have low Kondo temperature  $T_K$  but IV compounds have high  $T_K$ , the crossover is usually accompanied by a large increase of the Kondo temperature and a large decrease of the Grüneisen parameter for  $T_K$  at high pressure [12]. On the basis of high pressure work on the NFL, it has been reported that the NFL state becomes unstable at high pressure, showing a crossover to the normal FL [7, 13–16]. The results have been discussed on the basis of several different viewpoints. This also emphasizes the importance of pressure as a perturbation in tuning the electronic state of NFL compounds. However, in most work on pressure-induced crossover in NFL compounds (mostly for Ce compounds), almost all experimental research has been focused mainly on the ground state properties around 1 K or below, i.e., on the low temperature properties. But for Ce based compounds, we have pointed out the importance of the high temperature properties in connection with the Kondo effect [17].

$Y_{1-x}U_xPd_3$  exhibits a variety of interesting magnetic behaviours such as spin glasses, the Kondo effect and magnetic ordering, depending on  $x$  [3, 5, 18, 19]. Among these properties, the most interesting aspect of this pseudobinary compound is the NFL behaviours observed near  $x = 0.2$ : the approximately  $T$ -linear dependence ( $n = 1.0–1.1$ ) in the electrical resistivity and a  $T \log T$  dependence in the specific heat have been observed. In the high temperature range above about 80 K, a logarithmic temperature dependence in  $\rho(T)$  was also observed, but there is no antiferromagnetic ordering at least down to 0.2 K [20]. This compound is a prototypical material showing NFL behaviour. With decreasing  $x$ ,  $T_K$  increases, the NFL state quickly becomes unstable and then finally FL is stabilized at a low concentration of U ( $x \leq 0.1$ ). As was mentioned in the foregoing section,  $T_K$  for CK and HF systems changes drastically on applying pressure. We expect also a lot of variety in the electronic states of  $Y_{1-x}U_xPd_3$  compounds on tuning  $T_K$  by applying pressure. However, the crossovers from NFL to FL reported until now were mainly for doped samples at ambient pressure or limited to a relatively low pressure range below 2 GPa, which may not be enough to induce the crossover in the sample with  $x = 0.2$ . It is interesting to observe an electronic crossover of this prototypical NFL compound at high pressure above 2 GPa and to compare the electronic state with those of other materials showing NFL and/or FL behaviour.

In the present work we measured the temperature dependent electrical resistivity  $\rho(T)$  for  $Y_{1-x}U_xPd_3$  compounds having  $x = 0.05$  and  $0.2$  at high pressure in order to examine the electronic crossover from the NFL to the FL state (and vice versa) induced by high pressure and furthermore the stability of the Kondo state under pressure. The lattice constants for  $x = 0$  ( $YPd_3$ ) are observed to obtain the bulk modulus and to check the pressure-induced crystal structure change. The present results are explained in connection with the  $x$ - $T$  phase diagram and the Grüneisen parameters for the Kondo temperature  $T_K$ . The electronic state for  $x = 0.2$  at low temperature will be discussed, taking into account critical fluctuation near the phase boundary, and then compared with several theoretical models.

## 2. Experimental procedures

### 2.1. Sample preparation

The polycrystalline samples of  $Y_{1-x}U_xPd_3$  with  $x = 0, 0.05$  and  $0.2$  were prepared by arc melting the constituent elements under an argon atmosphere [18]. All the samples were remelted several times to ensure homogeneity and annealed in evacuated quartz tubes for 100 h at  $900^\circ\text{C}$ . X-ray diffraction analysis shows that all the samples are single phase with the cubic  $Cu_3Au$  type crystal structure. The lattice parameter  $a$  ( $\text{\AA}$ ) changes linearly as a function of U concentration  $x$  as  $a = 4.0701 + 0.0193x$  ( $\text{\AA}$ ).

### 2.2. X-ray diffraction study under high pressure

Crystal structure and lattice constants under high pressure were investigated by means of x-ray diffraction. Hydrostatic pressure was generated by using WC Bridgman anvils having a face of 3 mm diameter [21]. A 4:1 methanol/ethanol mixture was used as a pressure transmitting medium. The powdered sample and NaCl were placed in a 0.3 mm hole at the centre of a beryllium disc gasket having 0.5 mm thickness. In order to obtain diffraction patterns with sharp lines and low background, we used a Guinier type focusing camera with a bent quartz monochromator. The diffraction lines were recorded on highly sensitive curved film. The pressure was determined by using Decker's equation of states for NaCl [22]. The  $P$ - $V$  relation was observed only for  $YPd_3$  ( $x = 0$ ) at room temperature.

### 2.3. Electrical resistance measurements under high pressure

Electrical resistance was measured in the temperature range between 4.2 and 300 K by using a standard dc four-probe method. Hydrostatic pressure below 2 GPa was generated by using a WC piston and a Cu-Be cylinder device. A 1:1 mixture of Fluorinert, FC70 and FC77, was used as a pressure transmitting medium. Above 2 GPa, we used a cubic anvil type high pressure apparatus. The pressure was changed only at room temperature in order to minimize the internal strain in the sample and kept constant within  $\pm 1\%$  throughout each measurement. The details of the high pressure systems were reported previously [23, 24].

## 3. Results

### 3.1. Pressure dependence of the volume and electrical resistance at room temperature

Figure 1 shows the lattice constants of  $YPd_3$  as a function of pressure below 12 GPa at room temperature. The cubic  $Cu_3Au$  crystal structure is stable up to 12 GPa since no new diffraction lines were observed at high pressure. It was found that the compression curve could be

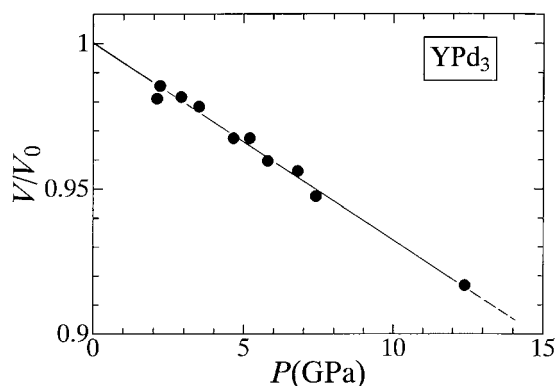


Figure 1. The pressure dependences of the lattice constants of  $\text{YPd}_3$  at room temperature.

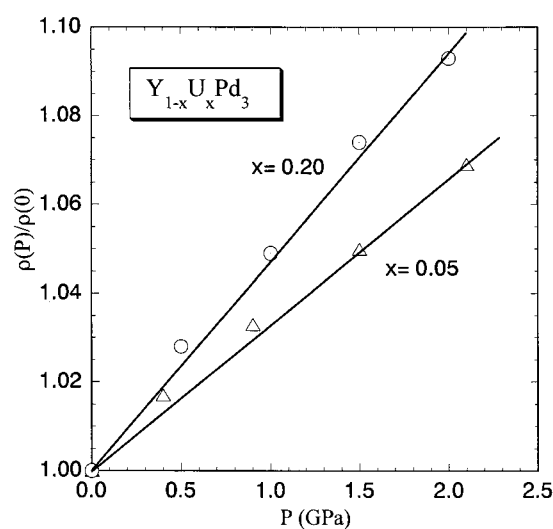
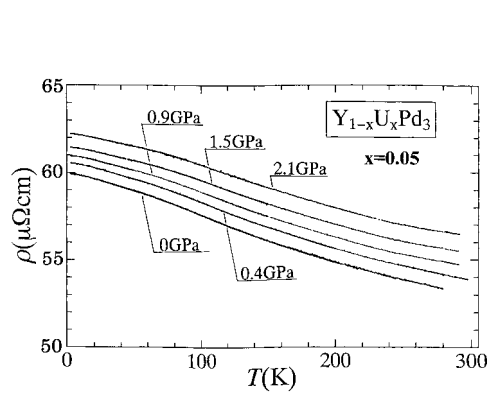


Figure 2. The relative change of the electrical resistivity,  $\rho(P)/\rho(0)$ , for  $x = 0.05$  and  $0.2$  at room temperature.

approximated by a straight line, as shown in the figure. The bulk modulus  $B$  ( $= -V\partial P/\partial V$ ) is estimated to be 148 GPa, which is smaller than that of  $\text{URu}_2\text{Si}_2$  ( $B = 215$  GPa) [25] but larger than that of  $\text{UGe}_2$  ( $B = 69$  GPa) [26]. Considering the fact that the lattice constant for  $x = 0.2$  is almost the same as that for  $x = 0$  [5], the bulk moduli for  $x = 0, 0.05$  and  $0.2$  may be nearly the same. This result will be used in the following section when we calculate the Grüneisen parameters.

The normalized electrical resistivity  $\rho(P)/\rho(0)$  for  $x = 0.05$  and  $0.2$  at room temperature is shown in figure 2 as a function of pressure up to 2 GPa, where  $\rho(0)$  is the resistivity at ambient pressure.  $\rho$  for the two samples increases with increasing pressure, approximately in a linear fashion. The pressure coefficient of  $\rho$  is estimated to be  $(1/\rho)(\partial\rho/\partial P) = 30 \times 10^{-3} \text{ GPa}^{-1}$  for  $x = 0.05$ . The pressure coefficient of  $\rho$  for  $x = 0.2$  is  $46 \times 10^{-3} \text{ GPa}^{-1}$ , which is 1.5 times larger than that for  $x = 0.05$ , suggesting that the conduction electrons are scattered in a complex way on the border of the instability of the electronic state near  $x = 0.2$ , which may give rise to an increase in the pressure coefficient of  $\rho$ . The electrical resistivity for  $x = 0.2$



**Figure 3.** The electrical resistivity for  $x = 0.05$  as a function of temperature at various pressures.

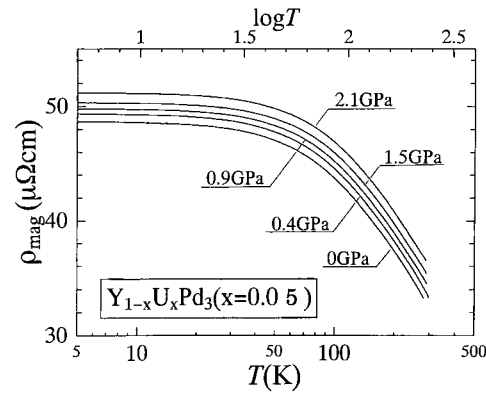


**Figure 4.** The electrical resistivity for  $x = 0.05$  with a logarithmic scale for temperature at various pressures.

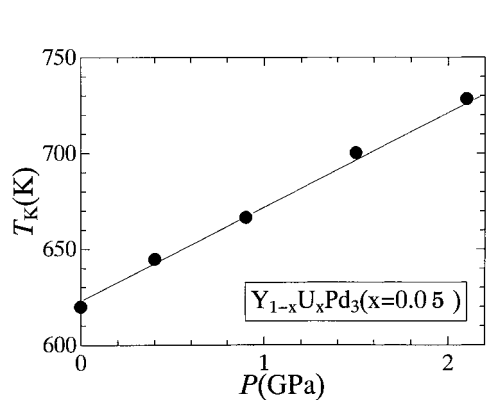


**Figure 5.** The Kondo temperature  $T_K$  for  $x = 0.05$  as a function of pressure.

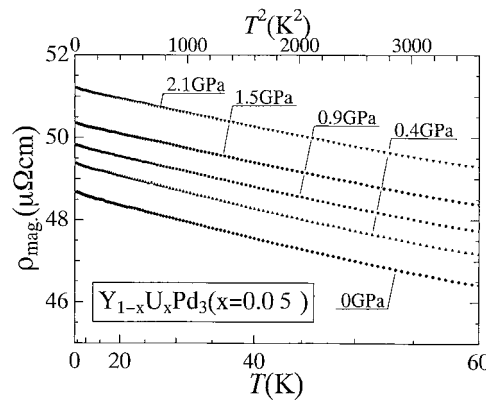


**Figure 6.**  $\rho(T)$  as a function of  $T^2$  for  $x = 0.05$  at high pressure.

is found to increase with pressure up to 6 GPa at room temperature, having almost the same pressure coefficient as mentioned above.

### 3.2. Temperature dependent electrical resistivity for $x = 0.05$ under high pressure

Figure 3 shows the  $\rho(T)$  curve at various pressures up to 2.1 GPa.  $\rho(T)$  shows a smooth decrease with increasing temperature even at high pressure; all  $\rho(T)$  curves seem to be almost parallel without any crossing but the values of  $\rho$  increase with pressure as was mentioned in relation to figure 2. The magnetic part of the resistivity  $\rho_{\text{mag}}$  was estimated by the equation  $\rho_{\text{mag}}(T) = \rho(T, x = 0.05) - \rho(T, x = 0 (\text{YPd}_3))$ , assuming that the  $\rho(T)$  of  $\text{YPd}_3$  (see figure 8 in the following section) is mainly dominated by phonon scattering. Figure 4 shows the results;  $\rho_{\text{mag}}(T)$  is shown with a logarithmic scale for  $T$  at various pressures.

In the present work, we define the value of the Kondo temperature  $T_K$  as the temperature where the value of  $\rho_{\text{mag}}(T)/\rho_{\text{mag}}(T = 4.2 \text{ K})$  is 0.5 [27].  $T_K$  for  $x = 0.05$  was obtained by an extrapolation of the present  $\rho_{\text{mag}}(T)$  curve to high temperature. Figure 5 shows  $T_K$  as a function of pressure.  $T_K$  increases almost linearly with pressure up to 2 GPa having a rate of

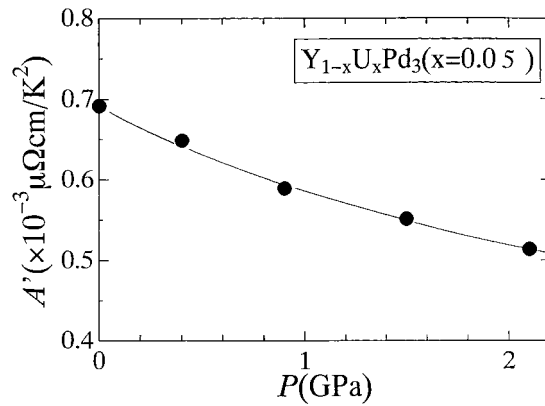


Figure 7. The coefficients of the  $T^2$  term in  $\rho(T)$  for  $x = 0.05$ ,  $A'$ , as a function of pressure.

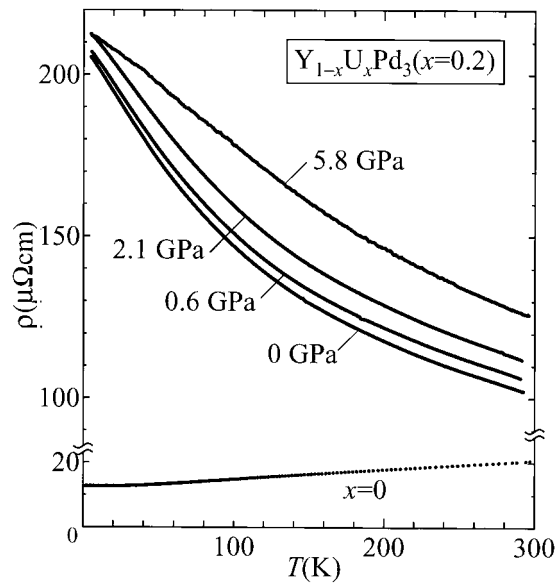
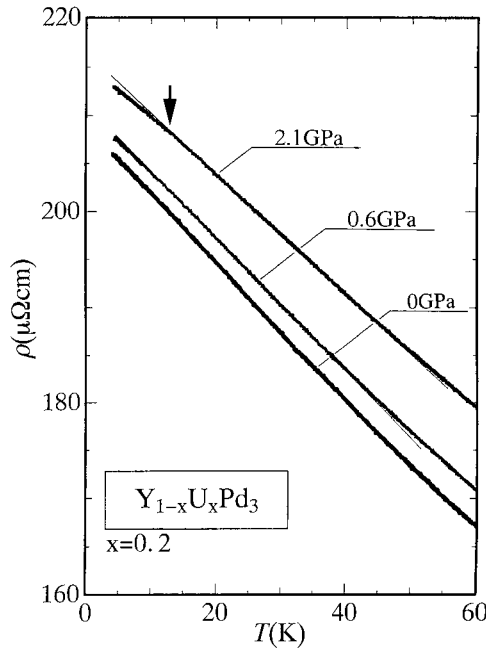


Figure 8.  $\rho(T)$  as a function of  $T$  for  $x = 0.2$  at high pressure including  $\rho(T)$  for  $x = 0$  as a reference.

$\partial T_K / \partial P = 50 \text{ K GPa}^{-1}$ . Usually  $\rho(T)$  for Kondo compounds shows normal Fermi liquid properties such as a  $T^2$  dependence at low temperature. In order to examine this temperature dependence, we plotted the values of  $\rho_{\text{mag}}(T)$  as a function of  $T^2$ , in figure 6. A  $T^2$  dependence in the  $\rho_{\text{mag}}(T)$  curve,  $\rho_{\text{mag}}(T) = \rho_0 - A'T^2$  ( $\rho_0$ : residual resistivity), is found over the wide range of temperature below 50 K, which indicates that the ground state for  $x = 0.05$  is well described as a Fermi liquid. The values of  $A'$  are plotted in figure 7 as a function of pressure. It is found that  $A'$  decreases with pressure:  $A'$  is decreased by about 30% on applying 2 GPa. Considering that  $A'$  is proportional to  $T_K^{-2}$  [28], this implies that  $T_K$  increases with pressure, which is consistent with the result in figure 5. We will discuss this point in detail later.



**Figure 9.**  $\rho(T)$  for  $x = 0.2$  below 60 K at various pressures. A small deviation from the linear temperature dependence is observed below 12 K at 2.1 GPa, which is shown by an arrow.

### 3.3. Temperature dependent electrical resistivity for $x = 0.2$ at high pressure

$\rho(T)$  for  $x = 0.2$  is shown in figure 8 at various pressures together with that for  $x = 0$  ( $YPd_3$ ). It is evident that the  $\rho(T)$  curve at 5.8 GPa is very different from those below 2 GPa, particularly below 100 K. Figure 9 shows the electrical resistivity below 60 K as a function of  $T$  at 0, 0.6 and 2.1 GPa. It is found that the linear temperature dependence in  $\rho$ , which is evidence of NFL behaviour, is well observed below 50 K; i.e.,  $\rho(T)$  below 50 K is approximated by the equation  $\rho(T) = \rho_0(1 - T/T_1)$ , where  $\rho_0$  is the residual resistivity and  $T_1$  is the characteristic temperature which may be related to the Kondo or spin fluctuation temperature. But at 2.1 GPa, a small deviation from the linear temperature dependence is found below about 12 K, which may be a precursor of the collapse of the NFL state. We will discuss later the origin of this deviation. Figure 10 shows the coefficients  $A$  of the  $T$ -linear term,  $A = \rho_0/T_1$ , and  $T_1$  as a function of pressure. The magnitude of  $A$  at ambient pressure ( $0.72 \mu\Omega \text{ cm K}^{-1}$ ) is nearly the same as those reported previously [4]. The value of  $A$  is found to decrease with increasing pressure, having a rate  $(1/A)(\partial A/\partial P) = -5.7 \times 10^{-2} \text{ GPa}^{-1}$ . From the linear extrapolation of  $A(P)$ ,  $A$  is 0 around 18 GPa, where the NFL state is expected to disappear.

Figure 11 shows the magnetic part of the electrical resistivity  $\rho_{\text{mag}}(T)$  at various pressures with a logarithmic scale for  $T$ , which was estimated by means of the same method as mentioned in section 3.2. The Kondo temperature  $T_K$  was also defined in the same way as that for  $x = 0.05$ . The results are shown in figure 12.  $T_K$  increases almost linearly with increasing pressure below 2 GPa, but the point at 5.8 GPa deviates upwards slightly from that extrapolated from low pressure below 2 GPa. It should be noted that the effect of pressure on  $T_K$  is opposite to the effect of the U concentration  $x$  [5, 18]:  $T_K$  decreases with  $x$  but increases with pressure.

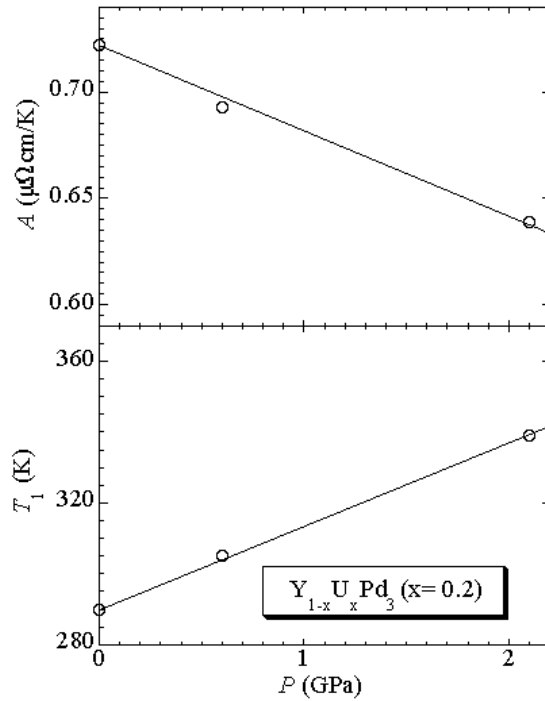


**Figure 10.** The coefficients of the linear term  $A$  and the characteristic temperature  $T_1$  as a function of pressure for  $x = 0.2$ .

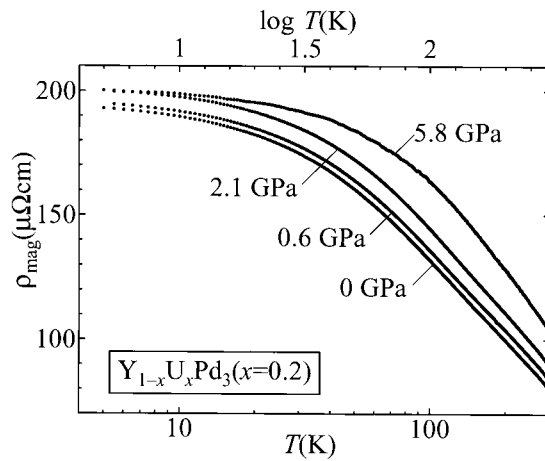


**Figure 11.** The magnetic part of the electrical resistivity  $\rho_{\text{mag}}(T)$  for  $x = 0.2$  on a logarithmic scale at high pressure.

#### 4. Discussion

In this section we discuss the experimental results obtained in the present work in connection with the Kondo effect and the crossover from a NFL state to a FL one. We divide the discussion into four parts.

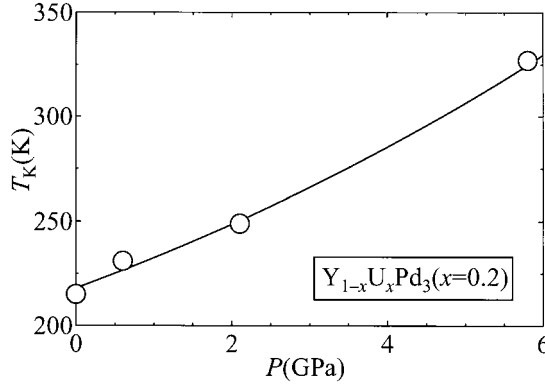


**Figure 12.** The Kondo temperature  $T_K$  for  $x = 0.2$  as a function of pressure.

#### 4.1. Stability of the Kondo state under high pressure—high temperature electronic properties above 100 K

We discuss the high temperature behaviour of  $\rho(T)$ , in which Kondo scattering dominates  $\rho(T)$ . In the foregoing section, we obtained the Kondo temperature  $T_K$  as a function of pressure, where we found an approximately linear dependence against pressure.  $T_K$  may be described by the following equation in the single-impurity regime:

$$T_K \propto \exp\left[-\frac{1}{|JN(0)|}\right], \quad (1)$$

where  $J$  is the s-f exchange interaction and  $N(0)$  is the density of states at the Fermi level.  $J$  is written as

$$J \sim \frac{\langle V_{sf}^2 \rangle}{\epsilon_{5f}}, \quad (2)$$

where  $V_{sf}$  is the strength of hybridization and  $\epsilon_{5f}$  is the energy difference between the 5f level and the Fermi level.  $\epsilon_{5f}$  may be expressed as  $\epsilon_{5f} \sim \epsilon_0 + \epsilon_1 x - \omega P$ , where  $\epsilon_0$ ,  $\epsilon_1$  and  $\omega$  are constants [5, 29]. This indicates that the effect of  $x$  on  $J$  or  $T_K$  is opposite to that of pressure, which is the same as the case for CeR alloys (R: rare earth element) [29].

Since  $V_{sf}$  increases and  $\epsilon_{5f}$  decreases with increasing pressure,  $J$  shows an increase on applying pressure. This indicates that  $T_K$  is enhanced by applying pressure. The pressure dependence of  $T_K$  is derived from equations (1) and (2) as  $T_K \sim (T_K)_0 e^{\gamma P}$ , where  $(T_K)_0$  is  $T_K$  at  $P = 0$  and  $\gamma$  is a positive constant. In this derivation, we assumed that  $\langle V_{sf}^2 \rangle$  and  $N(0)$  are constant and pressure is not too high. The solid line in figure 12 was plotted by assuming  $\gamma = 7.3 \times 10^{-2} \text{ GPa}^{-1}$  and  $T_K(0) = 215 \text{ K}$ ; the experimental results are well reproduced by this equation. On the same assumptions, when pressure is constant, we can derive the following relation for the concentration ( $x$ ) dependence of  $T_K$ :  $T_K = T_K(0) \exp(-\theta x)$ , where  $\theta$  is a positive constant. This means that  $T_K(x)$  decreases with increasing U concentration.

On the other hand, the value of  $\gamma$  is obtained as  $8.0 \times 10^{-2} \text{ GPa}^{-1}$  for  $x = 0.05$  by using the data for  $T_K$  shown in figure 5. These two values are approximately the same. This means that as far as the effect of pressure on the Kondo state is concerned, there is no significant difference between  $x = 0.05$  and 0.2. In other words, the high temperature behaviour of  $\rho(T)$  can be treated in the framework of the Kondo single-impurity model.

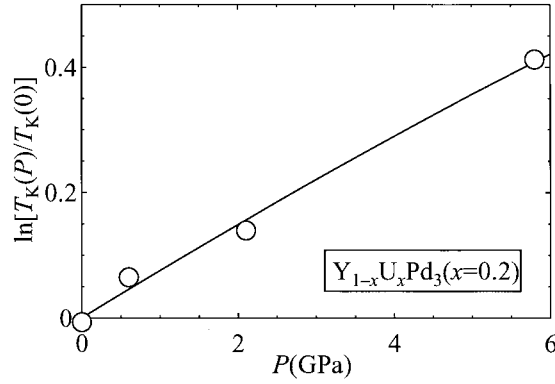


**Figure 13.**  $\ln[T_K(P)/T_K(0)]$  as a function of pressure for  $x = 0.2$ .

#### 4.2. Estimation of Grüneisen parameters for $Y_{1-x}U_xPd_3$

The Grüneisen parameter is often used to evaluate the electronic state of highly correlated electron systems [8, 11, 12, 17, 25]. So we attempt to estimate this parameter for  $T_K$ . The Grüneisen parameter of  $T_K$  is defined as

$$\Gamma_K \equiv -\frac{\partial \ln T_K}{\partial \ln V} = B \frac{\partial \ln T_K}{\partial P}, \quad (3)$$

where  $B$  is the isothermal bulk modulus. The pressure dependences of  $T_K$  were shown in figures 5 and 12 for  $x = 0.05$  and  $0.2$ , respectively. Equation (3) is rewritten as  $\Gamma_K = B \partial \ln(T_K(P)/T_K(0))/\partial P$ , where  $T_K(0)$  is  $T_K$  at ambient pressure. Figure 13 shows the pressure dependence of the value of  $\ln[T_K(P)/T_K(0)]$  for  $x = 0.2$ . The slope of the plot corresponds to  $\Gamma_K/B$  [12]. The value of  $\Gamma_K/B$  is estimated to be  $0.08 \text{ GPa}^{-1}$ .  $\Gamma_K$  for  $x = 0.2$  is 12 at ambient pressure, assuming the value of  $B$  to be the same as that of  $YPd_3$  ( $=148 \text{ GPa}$ ), which is smaller than those of  $UAl_2$  ( $\Gamma \sim 20$ ) [8] and  $URu_2Si_2$  ( $\Gamma \sim 30$ ) [25]. It is interesting to note that the magnitude of  $\Gamma_K$  for  $x = 0.2$  is comparable with that for the intermediate valence compounds  $CePd_3$  ( $\Gamma \sim 6$ ) [30] and  $CeNi$  ( $\Gamma \sim 9$ ) [31].  $\Gamma_K$  for  $x = 0.05$  is calculated in the same way, using the data in figure 5, to be 12, which is the same as that for  $x = 0.2$ . This result indicates that there is no significant difference in pressure effect on the Kondo state above 100 K between the  $x = 0.05$  and  $0.2$  cases, as was pointed out in the foregoing section.

Here we apply the compressible Kondo model [32] to equation (1). The volume change of  $|JN(0)|$  is assumed as

$$|JN(0)| = |JN(0)|_0 \exp\left(-q \frac{V - V_0}{V_0}\right), \quad (4)$$

where  $q$  is a constant between 6 and 8 and  $|JN(0)|_0$  is  $|JN(0)|$  at ambient pressure. By using equations (1) and (4) we obtain

$$|JN(0)|_0 = \frac{q}{\Gamma_K}. \quad (5)$$

When we derived equation (5), we used the following approximation:  $\exp(q(V - V_0)/V_0) = 1 + q(V - V_0)/V_0$ , which is valid at low pressure because the volume change is small. Assuming  $q = 6$  [32], we obtain 0.5 for both  $x = 0.2$  and  $0.05$ . This is larger than those for  $URu_2Si_2$  (0.2) and  $UAl_2$  (0.3), but the same as that for  $\alpha$ -Ce ( $\sim 0.5$ ) [33]. The results indicate that the 5f electrons for  $x = 0.2$  and  $0.05$  are more itinerant than those in  $URu_2Si_2$  and  $UAl_2$ .

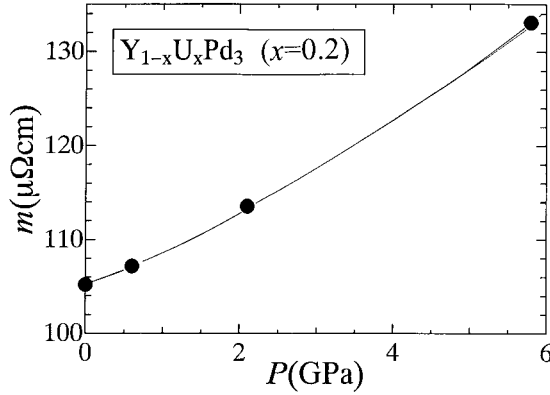


**Figure 14.** The coefficients of the  $\log T$  term  $m$  for  $x = 0.2$  as a function of pressure.

It is well known that the Kondo effect is manifested in the existence of a  $\log T$  term in the electrical resistivity. The electrical resistivity of dilute Kondo alloys may be described as

$$\rho(T) = \rho_B - C|JN(0)|^3 \log T, \quad (6)$$

where  $C$  is the constant and  $\rho_B$  is the temperature independent resistivity calculated from Born first-order perturbation of  $J$ . From the above equation (6), the slope  $m$  in the  $\rho$  versus  $\log T$  curve is derived to be

$$m = C|JN(0)|^3. \quad (7)$$

The values of  $m$  for  $x = 0.2$  are plotted in figure 14 as a function of pressure. In this calculation of  $m$ , we used the data in the range  $0.5T_K < T < 1.1T_K$  ( $T_K = 215$  K at ambient pressure for  $x = 0.2$ ). For this reason, we did not calculate the values of  $m$  for  $x = 0.05$  because  $T_K$  for  $x = 0.05$  is 620 K at ambient pressure and then  $0.5T_K$  is 310 K, which is outside the temperature range in the present experiment. So in this section we limited our discussion to the  $x = 0.2$  case. It is found that the value of  $m$  increases substantially with pressure for  $x = 0.2$ , as has been observed in many Ce based HF systems [12].

On the basis of the compressible Kondo model, we can explain the results in figure 14 as follows.  $|JN(0)|^3$  is described from equation (4) as

$$|JN(0)|^3 \approx |JN(0)|_0^3 \left( 1 + 3q \frac{V_0 - V}{V_0} \right). \quad (8)$$

From equations (7) and (8), we get the magnitude of  $m$  as proportional to  $1 + 3q(V_0 - V)/V_0 \approx 1 + 3q\kappa P$ , where  $\kappa$  is the compressibility. This implies that  $m$  increases with pressure, which explains qualitatively the results in figure 14.

#### 4.3. Pressure-induced crossover from the NFL to the FL—low temperature electronic properties

Here we discuss first the relation between the values of  $T_K$  and the coefficients of the  $T^2$  term for  $x = 0.05$ . In the Kondo compounds, the electrical resistivity at low temperature ( $T \ll T_K$ ) is approximated by the following temperature dependence:

$$\rho(T) = \rho_0 \left( 1 - \left( \frac{T}{T_K} \right)^2 \right), \quad (9)$$

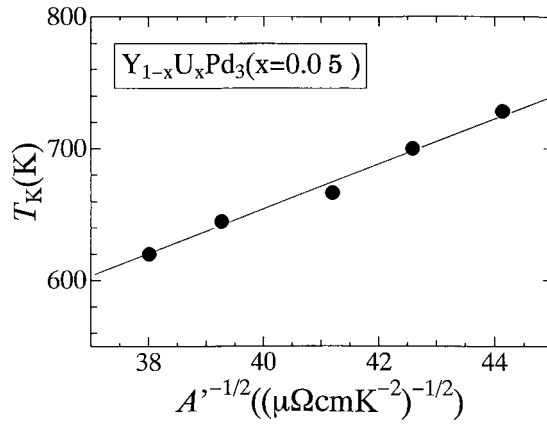


**Figure 15.**  $T_K$  as a function of  $1/\sqrt{A'}$  for  $x = 0.05$ .

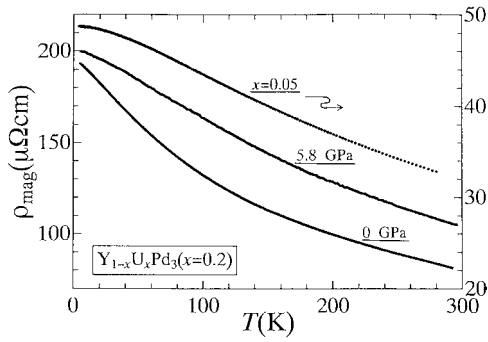
where  $\rho_0$  is the residual resistivity. In this approximation, the value of  $A'$  is roughly proportional to  $1/T_K^2$ . Figure 15 shows the relation between  $T_K$  and  $1/\sqrt{A'}$  at different pressures for  $x = 0.05$ . It is found that there is a good linear relationship between  $T_K$  and  $1/\sqrt{A'}$ . Using equation (9), we obtain the value of  $\Gamma_K$  as 13, which is in good agreement with the value obtained in section 4.2: 12. This suggests that the behaviour for  $x = 0.05$  is well described by the single-impurity Kondo model over a wide range of temperature.

Next we consider the ground state for  $x = 0.2$  at high pressure. The NFL behaviour below 2.1 GPa is evidenced by the existence of  $T$ -linear behaviour in  $\rho(T)$ , which was also observed below about 50 K at ambient pressure in the present work, as shown in figure 9. The coefficient  $A$  of the  $T$ -linear term decreases with increasing pressure, which may be explained by the increase of  $T_1$  at high pressure.  $T_1$  is related to some kind of fluctuation such as a spin or spatial one. Critical fluctuations associated with antiferromagnetic ordering were observed for  $x = 0.2$  at low temperature down to 0.2 K using neutron scattering [20]. In this sense, the decrease of  $A$  (or the increase in  $T_1$ ) suggests that the critical fluctuations near the phase boundary ( $x \sim 0.2$ ) between the NFL state and spin glass state [5] are suppressed by application of pressure. If antiferromagnetic ordering took place,  $T_1$  would become 0 and  $A$  would diverge near a critical value of a control parameter.

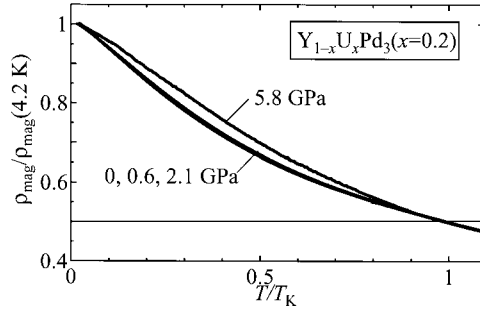
To allow comparison of the electronic state at 5.8 GPa and that at ambient pressure, the  $\rho_{\text{mag}}(T)$  curves are shown in figure 16 along with that for  $x = 0.05$ , which shows the typical FL behaviour. It is easily seen that the overall behaviour of  $\rho_{\text{mag}}(T)$  at 5.8 GPa is similar to that for  $x = 0.05$  at ambient pressure. This implies that the electronic state for  $x = 0.2$  at 5.8 GPa can be considered as a normal FL one.

Figure 17 shows the normalized resistivity  $\rho_{\text{mag}}(T)/\rho_{\text{mag}}(4.2 \text{ K})$  as a function of the reduced temperature  $T/T_K$  at various pressures. The data below 2.1 GPa are found to fall on a universal curve. This indicates that the electronic state or NFL state is almost independent of pressure up to 2.1 GPa. But the curve at 5.8 GPa substantially deviates from the universal curve below 2.1 GPa. The large change in the temperature dependence suggests a crossover in the electronic state from the NFL to another state on applying pressure.

In order to see the result more clearly and examine the power law in  $T$ , we plot the values of  $1 - \rho_{\text{mag}}(T)/\rho_{\text{mag}}(0)$  below 30 K in figure 18 both at ambient pressure and at 5.8 GPa as a function of  $T$  on a logarithmic scale. It is found that  $\rho_{\text{mag}}(T)$  at low temperature below 30 K changes from a  $T$ -linear dependence ( $n = 1.0$ ) at ambient pressure to a  $T^n$  ( $n = 1.9$ )



**Figure 16.** The temperature dependence of  $\rho_{\text{mag}}(T)$  for  $x = 0.2$  at 0 and 5.8 GPa and that for  $x = 0.05$  for comparison.



**Figure 17.** The normalized electrical resistivity,  $\rho_{\text{mag}}(T)/\rho_{\text{mag}}(4.2\text{ K})$ , as a function of the reduced temperature,  $T/T_K$ , for  $x = 0.2$ .

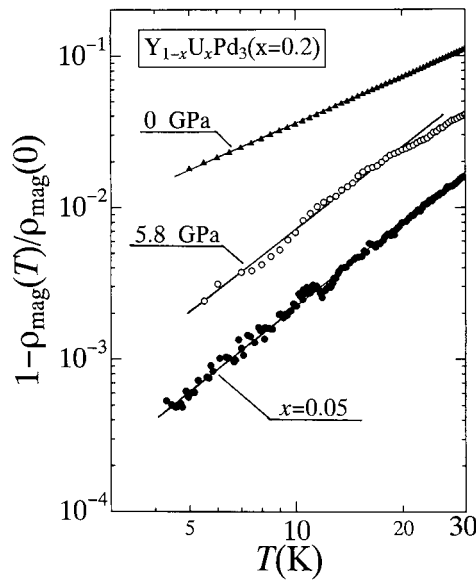


**Figure 18.** The magnetic part of the electrical resistivity for  $x = 0.2$ ,  $\rho_{\text{mag}}(T)$ , as a function of  $\log T$ . The data for  $x = 0.05$  are also shown for comparison.

dependence below about 17 K and the line for  $x = 0.05$ , which shows FL behaviour, is almost parallel to that at 5.8 GPa.

The change in the power from 1 to 1.9 suggests a collapse of the NFL state followed by the recovery of the FL state at high pressure. This result indicates that the crossover from NFL to FL states takes place at a pressure between 2.1 and 5.8 GPa, which is smaller than 18 GPa, where the value of  $A$  may vanish as was mentioned before. This is the first report of such a crossover induced by pressure for the prototype NFL compound  $x = 0.2$ .

Several theoretical models based on different viewpoints, for example the two-channel Kondo effect [34, 35], proximity to a quantum critical point [3, 36] and distribution of Kondo temperatures [37], have been proposed to explain the transport and thermodynamic properties of NFL compounds. However, there have been no theories succeeding in explaining all aspects of NFL behaviours [4]. Furthermore, it is not clear at present which model should be applied to explain the high pressure behaviour of NFL compounds. It is well known that the strength

of hybridization is increased by application of pressure and the electronic properties of the Kondo compounds have been interpreted in terms of a change in the hybridization caused by doping or pressure.

The effect of hybridization on the stability of FL and/or NFL compounds has been investigated by Koga and Shiba [38, 39] on the basis of the two-channel Kondo model. They calculated the phase diagram of the stability region of the FL and NFL as a function of Coulomb  $U$  and Hund couplings  $J_H$ .

According to their calculation, the enhancement of the strength of hybridization is found to stabilize the FL state compared with the NFL state. In other words, the application of pressure, which implies an increase of hybridization, gives rise to a crossover from NFL to FL behaviour. The present result seems to be explained qualitatively by taking their result into account as far as the crossover from the NFL to the FL state is concerned. Furthermore, the theory predicts that the temperature of crossover from NFL to FL behaviour,  $T_{cr}$ , decreases as the electronic state of the system approaches the NFL/FL boundary.  $T_{cr}$  may be described approximately as  $T_{cr} \propto |J_H - J_{H,b}|^\alpha$ , where  $J_{H,b}$  is the value of  $J_H$  at the boundary and  $\alpha$  is a constant, in the range 8–9 [40]. If we assume  $T_{cr} = T_1$ , the present result indicates that  $T_{cr}$  increases with increasing pressure as shown in figure 10, i.e.,  $T_{cr}$  increases as the system approaches the FL/NFL boundary, which is in sharp contrast to the theoretical prediction. In other words, the present result suggests that there is no such boundary in the pressure change of the electronic state for  $x = 0.2$  and the two-channel Kondo model may not be applicable in explaining the pressure change of characteristic temperatures or the pressure-induced crossover for  $x = 0.2$ .

The electrical resistivity  $\rho(T)$  for NFL compounds has been calculated by Moriya and Takimoto on the basis of the self-consistent renormalization (SCR) theory of spin fluctuations [41]. Around the critical boundary,  $\rho(T)$  shows a  $T^{3/2}$  dependence followed by a  $T$ -linear dependence as  $T$  increases. Off the critical boundary region,  $\rho(T)$  is proportional to  $T^2$ , indicating the recovery of FL behaviour. As was shown in figure 18,  $\rho(T)$  for  $x = 0.2$  at 5.8 GPa is similar to that for  $x = 0.05$ , the Fermi liquid compound, which is also proved by the existence of a  $T^2$  dependence at low temperature. The facts suggest that the spin fluctuation for  $x = 0.2$  is expected to be suppressed by the application of pressure, which indicates an increase of  $T_1$ , and then the NFL behaviour is collapsed to give rise to the recovery of the FL behaviour.

Recently, a phase diagram of heavy fermions including the quantum critical point has been presented by Continentino [42]; the Fermi liquid behaviour is expected to be stable off the critical region and the coherence temperature  $T_{coh}$  increases as the value of  $|JN(0)|$  (or pressure) increases. If we assume  $T_{coh}$  as  $T_1$  or  $T_K$ , the low temperature properties of  $Y_{1-x}U_xPd_3$  ( $x = 0.2$ ) may be qualitatively explained according to this diagram. In other words, since the sample for  $x = 0.2$  is basically just on the quantum critical point, we expect the non-Fermi liquid behaviour and the pressure to have the effect of moving this sample off the critical point, which also gives rise to an increase in  $T_1$  or  $T_K$ .

Roughly speaking, the common feature of these theories is that the NFL behaviours may collapse at high pressure showing a recovery of FL behaviour, but there is a difference between the semiquantitative explanations of the characteristic temperatures such as  $T_1$  or  $T_K$ . Judging from the present results and the above-mentioned discussion, it is plausible to consider that the sample with  $x = 0.2$  exists near or just on the quantum critical point [3, 36, 42] with a large magnetic fluctuation showing NFL behaviour, but with increasing pressure the quantum fluctuation is suppressed resulting in a crossover from the NFL to the FL state. In order to discuss which model is suitable for the pressure dependence of the NFL behaviour in the present work, more quantitative analysis of the experimental results is needed, not only for the resistance but also for the susceptibility or specific heat at high pressure. It seems difficult to explain all aspects of NFL behaviours by applying one theoretical model.

#### 4.4. The relation between the U concentration $x$ and the effect of pressure

In the compounds  $Y_{1-x}U_xPd_3$ , the lattice constants increase slightly with  $x$ , i.e., the lattice expands with  $x$ , which is opposite to the pressure effect. Here we derive the quantitative relation between the pressure  $P$  (GPa) and  $x$  by using the Kondo temperature  $T_K$  and lattice constant  $a$  as implicit variables. The fractional increase  $\Delta a$  (Å) in the lattice constant is obtained from the result in section 2.1 as a function of the U concentration  $x$ :  $\Delta a = 19.3 \times 10^{-3} \Delta x$ . On the other hand, the relation between the lattice constant and the pressure is obtained from the bulk modulus. From the bulk modulus in section 3.1, we obtain  $\Delta a(P) = -9.2 \times 10^{-3} \Delta P$ , where  $\Delta P$  is in GPa. Using these two relations, we get the following equation:

$$\Delta P = -2.1 \Delta x. \quad (10)$$

Since the difference in  $x$  between  $x = 0.05$  and  $0.2$  is  $-0.15$ , the value of  $\Delta P$  is estimated to be 0.3 GPa from the above equation (10). This result implies that the electronic state for  $x = 0.2$  becomes similar to that for  $x = 0.05$  on applying 0.3 GPa. But in section 4.3, we observed that the electronic state for  $x = 0.2$  becomes the same as that for  $x = 0.05$  above 4–5 GPa, which is extremely large compared to the estimated value—by an order of magnitude. This indicates that scaling using the lattice constants or the volume is impossible for this compound and the pressure-induced crossover from NFL to FL behaviour for  $x = 0.2$  cannot be explained by just considering the lattice compression.

The Kondo temperature  $T_K$  of this material decreases with increasing  $x$  [5, 18]. Next we consider this using  $T_K$  as an implicit parameter. In section 4.1, we showed that  $T_K$  can be described as  $T_K(P) = (T_K)_0 \exp(\gamma P)$ . The fractional change in  $T_K$  is derived as  $\Delta T_K/T_K = \gamma \Delta P$ . On the other hand,  $\ln T_K$  at ambient pressure is well known to be a linear function of  $x$  because of the relation  $T_K(x) = T_K(x = 0) \exp(-\theta x)$  [5]. We get  $\Delta T_K/T_K = -\theta \Delta x$ . Thus we get the relation  $\Delta P = -\theta/\gamma \Delta x$ . By using the pressure dependence of  $T_K$  and  $\theta = 7.1$ , we obtain

$$\Delta P = -88 \Delta x. \quad (11)$$

If we put  $\Delta x = -0.15$ , we get  $\Delta P = 13$  GPa. This means that about 13 GPa is needed for  $x = 0.2$  to get the same electronic state as for  $x = 0.05$ . It is interesting to note that a pressure of several GPa is needed to destroy the NFL state for  $x = 0.2$ , which is comparable with the pressure mentioned above. This indicates that the change in the ‘effective pressure’,  $\Delta P$ , is not due to just a change in the lattice constant but also a change in the electronic state followed by a small change in the lattice constant. Taking these results into account, the electronic state for  $Y_{1-x}U_xPd_3$  compounds, particularly for  $x = 0.2$ , can be considered to be a marginal state on the border of magnetic instability.

## 5. Conclusion

In the present study, we have measured the electrical resistivity of  $Y_{1-x}U_xPd_3$  ( $x = 0, 0.05$  and  $0.2$ ) and lattice constant of  $YPd_3$  at high pressure. The main conclusions are summarized as follows:

- (1) The  $Cu_3Au$  structure of  $YPd_3$  is stable up to 12 GPa at room temperature.
- (2) As far as the pressure effect on the Kondo state above 100 K is concerned, there is no great difference between  $x = 0.05$  and  $0.2$  because the Grüneisen parameter for  $T_K$  for  $x = 0.2$  is the same as that for  $x = 0.05$ .
- (3) The non-Fermi liquid behaviour at ambient pressure for  $x = 0.2$  shows a crossover at high pressure above 4–5 GPa, followed by a recovery of Fermi liquid behaviour.

- (4) The quantitative relation between pressure and U concentration has been discussed and the change in the internal (or effective) pressure is mainly dominated by the contribution from a change in the electronic state induced by a small compression in the lattice constant.

## References

- [1] Grewe N and Steglich F 1991 *Handbook on the Physics and Chemistry of Rare Earths* vol 14, ed K A Gschneidner and L Eyring Jr (Amsterdam: Elsevier) p 343
- [2] Seaman C L, Maple M B, Lee B W, Ghamaty S, Torikachvili M S, Kang J S, Liu L Z, Allen J W and Cox D L 1991 *Phys. Rev. Lett.* **67** 2882
- [3] Andraka B and Tsvetlik A M 1991 *Phys. Rev. Lett.* **67** 2886
- [4] Stewart G R 2001 *Rev. Mod. Phys.* **73** 797
- [5] Maple M B, Dickey R P, Herrmann J, de Andrade M C, Freeman E J, Gajewski D A and Chau R 1996 *J. Phys.: Condens. Matter* **8** 9773 and see the references therein
- [6] Knebel G, Eggert C, Schmid T, Krimmel A, Dressel M and Loidl A 1997 *Physica B* **230–232** 593
- [7] von Löhneysen H 1996 *J. Phys.: Condens. Matter* **8** 9689 and see the references therein
- [8] Thompson J D and Lawrence J M 1994 *Handbook on the Physics and Chemistry of Rare Earths* vol 19, ed K A Gschneidner Jr *et al* (Amsterdam: Elsevier) p 383
- [9] Steglich F, Buschinger B, Gegenwart P, Lohmann M, Helfrich R, Langhammer C, Hellmann P, Donnevert L, Thomas S, Link A, Geibel C, Lang M, Sparn G and Assmus W 1996 *J. Phys.: Condens. Matter* **8** 9909
- [10] Castro Neto A H, Castilla G and Jones B A 1998 *Phys. Rev. Lett.* **81** 3531
- [11] Kagayama T, Oomi G, Takahashi H, Mōri N, Ōnuki Y and Komatsubara T 1991 *Phys. Rev. B* **44** 7690
- [12] Kagayama T and Oomi G 1996 *J. Phys. Soc. Japan* **65** 42
- [13] Bogenberger B and Löhneysen H v 1995 *Phys. Rev. Lett.* **74** 1016
- [14] Chau R, Han S H, Maple M B, Löhneysen H v and Aronson M C 1997 *Physica B* **230–232** 600
- [15] Umeo K, Kadomatsu H and Takabatake T 1996 *Phys. Rev. B* **54** 1194
- [16] Gabani S, Bauer E, Berger S, Flachbart K, Padeno Y, Paul C, Pavlik V and Shitsevalova N 2003 *Phys. Rev. B* **67** 172406
- [17] Kagayama T, Oomi G, Ito E, Ōnuki Y and Komatsubara T 1994 *J. Phys. Soc. Japan* **63** 3927
- [18] Aoki Y, Terayama K, Sato H, Maeda K and Ōnuki Y 1995 *Physica B* **206/207** 451
- [19] Zochowski S W, de Podesta M, Lester C and McEwen K A 1995 *Physica B* **206/207** 489
- [20] Dai P, Mook H A, Seaman C L, Maple M B and Koster J P 1995 *Phys. Rev. Lett.* **75** 1202
- [21] Kagayama T and Oomi G 1995 *J. Magn. Magn. Mater.* **140–144** 1227
- [22] Decker D L 1971 *J. Appl. Phys.* **42** 3239
- [23] Mōri N and Takahashi H 1990 *Atsuryoku Gijutsu (Pressure Engineering) J. High Pressure Inst. Japan* **28** 124 (in Japanese)
- [24] Oomi G and Kagayama T 1997 *Physica B* **239** 191
- [25] Kagayama T, Oomi G, Iki K, Mōri N, Ōnuki Y and Komatsubara T 1994 *J. Alloys Compounds* **213/214** 387
- [26] Oomi G, Ohashi M, Honda F, Haga Y and Onuki Y 2003 *J. Phys.: Condens. Matter* **15** S2039
- [27] Hamann D R 1967 *Phys. Rev.* **158** 570
- [28] Yoshimori A and Kasai H 1983 *J. Magn. Magn. Mater.* **30–34** 475
- [29] Alascio B, López A and Olmedo C F E 1973 *Phys. Rev. B* **7** 1274
- [30] Sawamura T, Kagayama T and Oomi G 1997 *Physica B* **239** 106
- [31] Oomi G and Mōri N 1994 *J. Alloys Compounds* **207/208** 275
- [32] Lavagna M, Lacroix C and Cyrot M 1983 *J. Phys. F: Met. Phys.* **13** 1007
- [33] Allen J W and Martin R M 1982 *Phys. Rev. Lett.* **49** 1105
- [34] Cox D L 1987 *Phys. Rev. Lett.* **59** 1240
- [35] Cox D L and Zawadowski A 1998 *Adv. Phys.* **47** 599 and see the references therein
- [36] Continentino M A 1994 *Phys. Rep.* **239** 179
- [37] Miranda E, Dobrosavljevic V and Kotliar G 1996 *J. Phys.: Condens. Matter* **8** 9871
- [38] Miranda E, Dobrosavljevic V and Kotliar G 1997 *Phys. Rev. Lett.* **78** 290
- [39] Koga M and Shiba H 1995 *J. Phys. Soc. Japan* **64** 4345
- [40] Koga M and Shiba H 1997 *J. Phys. Soc. Japan* **66** 1485
- [41] Koga M 1995 *Thesis* Tokyo Institute of Technology
- [42] Moriya T and Takimoto T 1995 *J. Phys. Soc. Japan* **64** 960
- [43] Continentino M A 2000 *Eur. Phys. J. B* **13** 31



ELSEVIER

Available online at [www.sciencedirect.com](http://www.sciencedirect.com)

SCIENCE @ DIRECT®

Physica C 388–389 (2003) 235–236

PHYSICA C

[www.elsevier.com/locate/physc](http://www.elsevier.com/locate/physc)

# Pressure effect on a ferromagnetic transition temperature of $\text{RuSr}_2\text{GdCu}_2\text{O}_8$

Jun Shibata <sup>a,\*</sup>, Hirotugu Goto <sup>a</sup>, Hiroki Takahashi <sup>a</sup>,  
Yuh Yamada <sup>b</sup>, Akiyuki Matsushita <sup>c</sup>

<sup>a</sup> College of Humanities and Sciences, Nihon University, 3-25-40 Sakurajousui, Setagaya 156-8550, Japan

<sup>b</sup> Shimane University, 1060 Matsue-shi, Nishikawazu-cyo 690-0823, Japan

<sup>c</sup> NIMS, 1-2-1 Sengen, Tsukuba-shi 305-0047, Japan

## Abstract

A number of attention has been paid for  $\text{RuSr}_2\text{GdCu}_2\text{O}_8$  because of the coexistence of ferromagnetic state and superconducting state below about 30 K. In order to investigate the character of the superconducting state which coexists with ferromagnetism, the pressure experiments on a ferromagnetic transition temperature have been performed. The enhancement of ferromagnetic transition temperature was observed with increasing pressure. High-pressure X-ray experiments on this material are in progress.

© 2003 Elsevier Science B.V. All rights reserved.

*Keywords:* Ferromagnetism; Superconductivity; Pressure effect; Ru1212

## 1. Introduction

$\text{RuSr}_2\text{GdCu}_2\text{O}_8$  (Ru1212) discovered in recent years is an interesting material in which ferromagnetic state and superconducting state coexist. The lattice structure of Ru1212 is similar to that of  $\text{YBa}_2\text{Cu}_3\text{O}_{7-\delta}$  (YBCO). Ru1212 is derived from the YBCO structure by replacing Y with Gd, Ba with Sr, and the  $\text{CuO}$  chains with a  $\text{RuO}_2$  plane, respectively. This system was first reported by Bauernfeind et al. [1] as superconducting but not magnetic material. However, Ru1212 have a Curie temperature ( $T_{\text{Curie}}$ )  $\sim 135$  K and bulk superconducting transition temperature ( $T_{\text{C}}$ )  $\sim 0$ –46 K, depending on the heat treatment. Although there is a judgment that ferromagnetic impurities  $\text{SrRuO}_3$  with  $T_{\text{Curie}} \sim 160$  K is contained [2], field-induced ferromagnetism was observed by neutron diffraction measurements [3]. It is reported that Ru moments with parallel to  $c$ -axis incline gradually to  $ab$ -plane with applying field. Yamada et al.

[4] reported pressure effect on the  $T_{\text{C}}$  up to 8 GPa by electrical resistivity measurements. They observed the onset temperature increase and the offset temperature decreases with applying pressure. However, since the average of onset and offset temperature does not change so much, they indicated that the pressure effect on  $T_{\text{C}}$  is small and transition width broadened with pressure. Yamada et al. synthesized another superconductor  $\text{FeSr}_2\text{GdCu}_2\text{O}_8$  (Fe1212) with the same crystal structure as Ru1212 in which ferromagnetism does not exist. They observed both onset and offset  $T_{\text{C}}$  of Fe1212 increase with applying pressure, in contrast to Ru1212. In this work the pressure effect of a ferromagnetic transition temperature has been measured by AC susceptibility method, in order to study the ferromagnetic state and the relation between ferromagnetic and superconducting state.

## 2. Experimental

Ru1212 was synthesized by solid-state reaction of stoichiometric powders of  $\text{RuO}_2$ ,  $\text{SrCO}_3$ , and  $\text{CuO}$ .

\* Corresponding author.

E-mail address: [happyjun@sol.dti.ne.jp](mailto:happyjun@sol.dti.ne.jp) (J. Shibata).

The mixture was first decomposed in air at 950 °C and heated for 24 h. It was pressed into pellets and heated at 960 °C for 24 h in air. Next sintering step took place in flowing nitrogen at 960 °C for 24 h, and heated at 1060 °C for 44 h in flowing oxygen. Last sintering step took place in flowing oxygen at 300 °C under 100 atm for 36 h. This Ru1212 shows superconducting transition temperature  $T_C = 31$  K and ferromagnetic transition temperature  $T_{\text{Curie}} = 135$  K. Pressure generating equipment is a cubic-anvil apparatus that was used to generate hydrostatic pressures up to 8 GPa at temperatures down to 15 K in NIMS. The mixture of Fluorinert FC70 and FC77(1:1) was used for the pressure transmitting medium.

### 3. Results and discussion

Fig. 1 shows the output signal of AC susceptibility measurements as a function of temperature at each pressures. The sudden change at around 30 K and the cusp at around 140 K correspond to  $T_C$  and  $T_{\text{Curie}}$ , respectively. The pressure dependence of  $T_C$  and  $T_{\text{Curie}}$  are shown in Figs. 2 and 3. From Fig. 2  $T_{\text{Curie}}$  increases with pressure at a rate of 6 K/GPa. However, this pressure effect is larger than the previous results measured at the magnetic field of 2 T [4]. It seems that the ferromagnetic state is strongly affected by the external field. On the other hand, the cusp-shape anomaly accompanied by ferromagnetic transition becomes sluggish at higher pressure. This behavior is considered that the ferromagnetic moment in Ru is suppressed by pressure. Concerning superconductivity,  $T_C$  does not change so much with applying pressure as shown in Fig. 3, which is consistent with the electrical resistivity measurements [4]. Thus this pressure dependence is considered to depend on whether the system has ferromagnetic state or

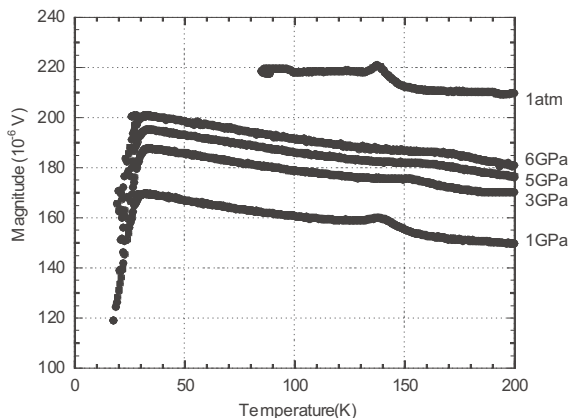


Fig. 1. Temperature dependence of the susceptibility of Ru1212 under various applied pressures.

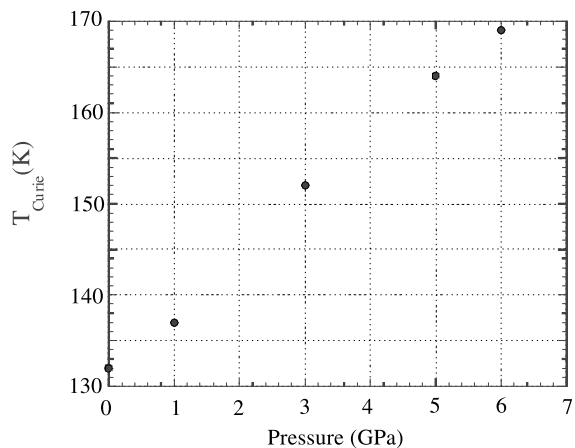


Fig. 2. Pressure dependence of the ferromagnetic transition temperature of Ru1212.

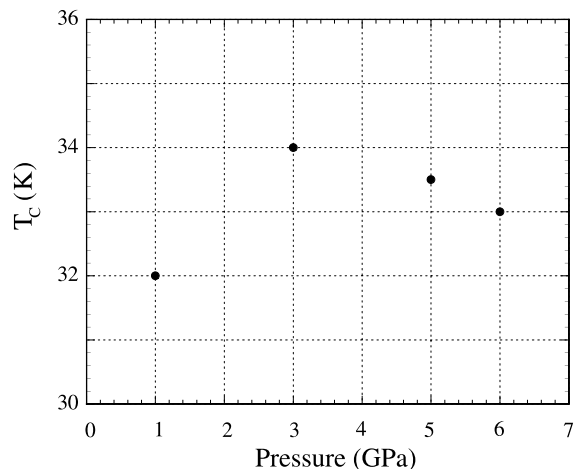


Fig. 3. Pressure dependence of the superconducting transition temperature of Ru1212.

not. High-pressure experiments with changing magnetic field are in progress. High-pressure X-ray measurements for Ru1212 and Fe1212 have been carried out. Precise refinements are now in progress in order to clarify the relation between crystal structure and magnetic properties.

### References

- [1] L. Bauernfeind, W. Widder, H.F. Braun, *Physica C* 254 (1995) 151.
- [2] I. Felner, U. Asaf, S. Reich, Y. Tsabba, *Physica C* 311 (1999) 163.
- [3] H. Takagiwa, J. Akimitsu, H. Kawano-Furukawa, H. Yoshizawa, *J. Phys. Soc. Jpn.* 70 (2001) 333.
- [4] Y. Yamada et al., in: *Proceedings of AIRAPT in Beijing*, 2001.

## Electronic phase diagram of a hole-doped two-leg ladder system, $\text{Sr}_{14-x}\text{Ca}_x\text{Cu}_{24}\text{O}_{41}$

N. MOTOYAMA<sup>1</sup>, H. EISAKI<sup>1(\*)</sup>, S. UCHIDA<sup>1</sup>, N. TAKESHITA<sup>2(\*\*)</sup>,  
N. MÔRI<sup>2(\*\*\*)</sup>, T. NAKANISHI<sup>3</sup> and H. TAKAHASHI<sup>3</sup>

<sup>1</sup> *Department of Superconductivity, The University of Tokyo  
2-11-16 Yayoi, Bunkyo-ku, Tokyo 113-8656, Japan*

<sup>2</sup> *Institute for Solid State Physics, University of Tokyo  
Kashiwanoha, Kashiwa-shi, Chiba 277-8581, Japan*

<sup>3</sup> *College of Humanities and Sciences, Nihon University  
3-25-40 Sakurajosui, Setagaya-ku, Tokyo 156-8550, Japan*

(received 13 September 2001; accepted in final form 6 March 2002)

PACS. 72.15.Nj – Collective modes (e.g., in one-dimensional conductors).

PACS. 74.25.Fy – Transport properties (electric and thermal conductivity, thermoelectric effects, etc.).

PACS. 74.72.Jt – Other cuprates.

**Abstract.** – We have investigated the evolution of the electronic state of hole-doped two-leg ladder compounds,  $\text{Sr}_{14-x}\text{Ca}_x\text{Cu}_{24}\text{O}_{41}$  with Ca content  $x$  ( $x = 0-12$ ) and hydrostatic pressure  $P$  ( $P \leq 8$  GPa) by measuring anisotropic resistivity on single crystals. An insulator-to-metal transition occurs by applying  $P \sim 6.5$  GPa for  $\text{Sr}_{14}\text{Cu}_{24}\text{O}_{41}$  which is activation-type insulating at low  $P$ . The compounds with  $x \leq 8$  show an insulating behavior at all  $P$ , though the doped hole density is fairly high (0.07–0.17 holes/Cu). On the other hand, the compounds with  $x \geq 10$  become a superconductor by applying pressure  $P = 3-5$  GPa. From these results, we constructed an  $x$ - $P$  phase diagram.

Ladder materials show many novel and interesting properties, such as spin gap, hole pairing, and superconductivity, which are characteristics in common with high- $T_c$  cuprates. The most intensively studied material is  $\text{Sr}_{14}\text{Cu}_{24}\text{O}_{41}$ , since this is the only known system capable at the moment of carrier doping into a two-leg ladder system. A spin gap with  $\sim 500$  K [1] is observed. Carrier density ( $n$ ) can be controlled by substituting Sr by Ca [2]. The most intriguing fact is an occurrence of superconductivity in heavily Ca-substituted material under pressure [3], which is theoretically predicted for a ladder system [4].

However, superconductivity in this system has been explored for only heavily Ca-substituted compounds [3, 5]. Although  $\text{Sr}_{14}\text{Cu}_{24}\text{O}_{41}$  compound has fairly high hole density  $n \sim 0.07$  per ladder Cu [2], which is a sufficient amount in order to realize high- $T_c$  superconductivity for two-dimensional (2D) cuprates, it is an insulator at ambient pressure [6]. The reason for the

---

(\*) Present address: Geballe Laboratory for Advanced Materials, Stanford University, McCullough Building, Room 346, Stanford University - Stanford, CA94305, USA.

(\*\*) Present address: Joint Research Center for Atom Technology (JRCAT) - 1-1-4 Higashi, Tsukuba-shi, Ibaraki 304-0046, Japan.

(\*\*\*) Present address: Saitama University - 255 Shimookubo, Saitama-shi, Saitama 338-8570, Japan.

insulating nature of  $\text{Sr}_{14}\text{Cu}_{24}\text{O}_{41}$  is not well understood. Several measurements, such as resistivity ( $\rho$ ) [7], NQR [8], and microwave conductivity [9], suggest that a charge-ordered state might be realized in this compound. Theories also predicted that a charge-ordered state is a possible phase competing with superconducting phase in the ladder system [10]. This charge-ordered state at  $\text{Sr}_{14}\text{Cu}_{24}\text{O}_{41}$  might make this system insulating in spite of its considerable high hole density.

We can make the compound conductive by substituting Ca for Sr, and even realize a metallic behavior ( $d\rho/dT > 0$ ) at moderate temperatures  $T$  above  $\sim 100$  K for  $x \geq 10$  [6]. However, even in this case the compound is an insulator with the resistivity increasing divergently as  $T \rightarrow 0$ , which was also ascribed to the charge ordering of the hole pairs formed on ladders [11,12].

To get better understanding of the competition between charge order and superconductivity and make the roles of pressure and Ca substitution clear, we measured resistivity as a function of  $T$  for  $\text{Sr}_{14-x}\text{Ca}_x\text{Cu}_{24}\text{O}_{41}$  with various  $x$ 's ( $x = 0-12$ ) under hydrostatic pressure  $P$  ( $P \leq 8$  GPa). Due to the restriction of measurements under very high  $P$  ( $P \geq 3$  GPa), the resistivity is only an available and reliable probe to explore the electronic state under such high  $P$ . It is found that the compound with  $x \leq 8$  continues to be an insulator with its resistivity increasing divergently as  $T \rightarrow 0$  up to the highest  $P$ , except for  $x = 0$  which undergoes an insulator-to-metal transition at  $P \sim 6.5$  GPa. On the other hand, for  $x \geq 10$ , we observed a superconducting transition at  $P \geq 3-5$  GPa. From these results, we can construct an  $x$ - $P$  phase diagram of this system.

We prepared single crystals of  $\text{Sr}_{14-x}\text{Ca}_x\text{Cu}_{24}\text{O}_{41}$  ( $x = 0, 3, 6, 8, 10, 11,$  and  $12$ ) grown by the traveling-solvent-floating-zone (TSFZ) method [6]. The growth was done using an infrared furnace under oxygen gas at 1 MPa. The single crystals have typically about 4 mm diameter and 50 mm length. These single crystals were characterized using a Laue diffractometer and found to be composed of a single domain. The resistivity measurements were performed by the 4-probe method in the  $T$ -range between 2 K and 300 K. Dots of silver paste were heated as electrodes on the samples at 300 °C in oxygen. To generate hydrostatic pressure up to 8 GPa, a cubic-anvil-type apparatus was used [13].

In fig. 1, we show the  $P$ -dependence of the resistivity for  $\text{Sr}_{14}\text{Cu}_{24}\text{O}_{41}$  parallel to the  $c$ -axis (along the ladder legs,  $\rho_c$ ), and  $a$ -axis (along the ladder rungs,  $\rho_a$ ) [14].  $\rho_c$  and  $\rho_a$  show an activation-type (activation energy  $\sim 0.21$  eV) insulating behavior at ambient pressure. Upon applying  $P$ , the resistivity in both directions decreases drastically (note the logarithmic scales for resistivities in fig. 1). With increasing  $P$  a step-like increase of the resistivity becomes apparent, indicative of some underlying transition to the insulating state. The resistivity step shifts toward low temperatures with  $P$ . Above 6 GPa, both  $\rho_c$  and  $\rho_a$  show metallic  $T$ -dependences over the whole  $T$ -range, although a bump remains in  $\rho_a$  due possibly to an incomplete transition to the metallic state by inhomogeneity in  $P$ . For  $P = 8$  GPa the value of  $\rho_c$  is  $\sim 2$  m $\Omega$  cm at room temperature and decreases to  $\sim 300$   $\mu\Omega$  cm at  $\sim 10$  K. These values are comparable to those of the in-plane resistivity for two-dimensional (2D)  $\text{La}_{2-x}\text{Sr}_x\text{CuO}_4$  with hole density  $x \sim 0.07$  and  $T_c \sim 22$  K. However, no superconductivity is observed in this metallic state down to 2 K.

In fig. 2(a),  $\rho_c(T)$  for  $x = 3, 6, 8,$  and  $\text{Sr}_{13}\text{Y}_1\text{Cu}_{24}\text{O}_{41}$  compound are shown at various  $P$ 's. The  $\text{Sr}_{13}\text{Y}_1\text{Cu}_{24}\text{O}_{41}$  has slightly lower hole density in the ladders ( $n \sim 0.05$ ) than  $\text{Sr}_{14}\text{Cu}_{24}\text{O}_{41}$ . The magnitude of  $\rho_c$  continuously decreases with increasing  $P$  for all compounds investigated. Although there appears a  $T$ -range in which  $d\rho/dT > 0$  for  $x = 6$ , all three compounds are insulators with the resistivity increasing divergently as  $T \rightarrow 0$  at any  $P$ 's, up to 8 GPa. It never becomes metallic even at very high  $P$ . The high- $P$  metallic phase has so far been observed only for  $x = 0$  ( $\text{Sr}_{14}\text{Cu}_{24}\text{O}_{41}$ ).

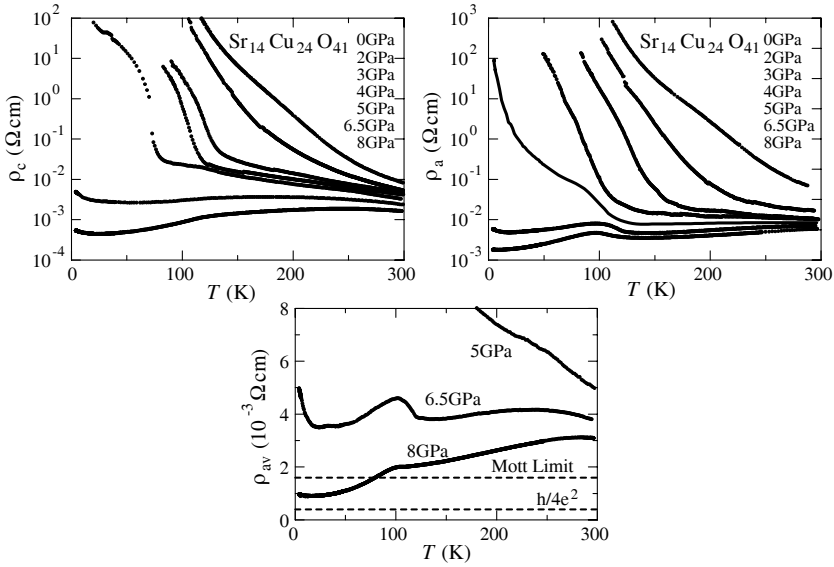


Fig. 1 – The temperature-dependences of  $\rho_c$  and  $\rho_a$  for  $\text{Sr}_{14}\text{Cu}_{24}\text{O}_{41}$  at various  $P$ 's between 0 and 8 GPa (from top to bottom curves in each panel). The geometrically averaged resistivity  $\rho_{av} = \sqrt{\rho_c \rho_a}$  at three  $P$ 's near the metal-insulator transition is plotted in the bottom panel.

The  $x = 10$  compound shows a different behavior from those for  $x \leq 8$  compounds (fig. 2(b)). Even at  $P \sim 0$ ,  $\rho_c$  shows a metallic  $T$ -dependence ( $d\rho/dT > 0$ ) at moderate temperatures. With the increase of  $P$ , the metallic  $T$ -range widens, though the resistivity eventually goes up at low  $T$ . Finally, an onset of superconductivity is observed at 5 GPa (see the right panel of fig. 2(b)). The critical pressure  $P_c$  of the superconducting (SC) onset decreases with the increase of  $x$ . In the present experiment  $P_c \sim 4$  GPa and 3.5 GPa for  $x = 11$  and 12 [15], respectively (the value of  $P_c$  is indicated by the cross mark in fig. 3 together with the results of the previous work for  $x = 11.5$  [5] and 13.6 [3]). After an abrupt onset of superconductivity  $T_c$  gradually decreases with increasing  $P$ , and the onset is no longer seen above 2 K for  $P = 8$  GPa. From this, we infer that the SC region might have an upper bound for  $P$ . An indication that SC tends to degrade at higher  $P$  was seen in the previous experiment on  $x = 11.5$  [5] and 13.6 [3]. The nature of the “over-pressure” state is not clear. After the onset of SC at  $P_c$ ,  $T_c$  gradually decreases with increasing  $P$ . The  $x = 11$  and 12 compounds show essentially the same behavior as that for  $x = 11.5$ . However, the disappearance of SC at “over”-pressures is not seen below 8 GPa. These data suggest that the superconducting phase has an upper bound in  $P$  and beyond this bound the compound would become a “non-SC” metal [5]. In order to clarify the nature of the high- $P$  non-SC phase, the experiment above 8 GPa is necessary. The  $x = 10$  compound appears to show a re-entrance to the insulating state at 8 GPa. Probably,  $x = 10$  is marginal because the insulating phase of the lower  $x$  would be mixed up with the  $P$ -induced superconducting phase due to the fluctuation of  $x$  in the sample. Based on these results and the extrapolated behaviors to  $T = 0$  K, we illustrate the  $x$ - $P$  phase diagram in the ground state as shown in fig. 3.

Coming back to the insulator-to-metal transition in  $\text{Sr}_{14}\text{Cu}_{24}\text{O}_{41}$ , Carter *et al.* [7] reported that the resistivity for  $x = 0$  shows a crossover by cooling at  $T \sim 150$  K at ambient pres-

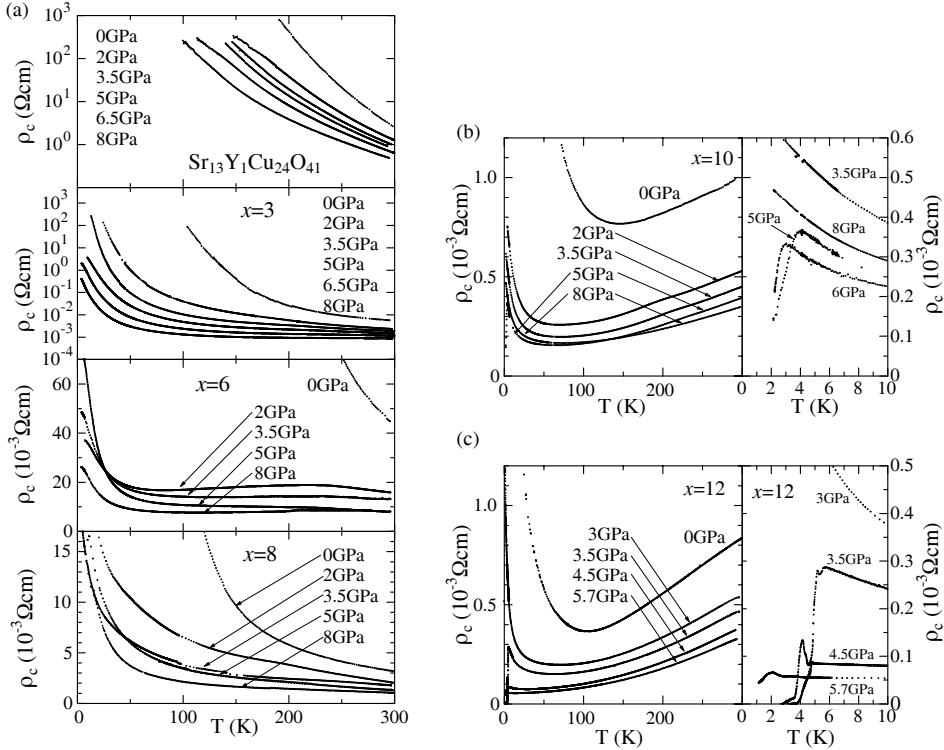


Fig. 2 – (a) The results for  $\text{Sr}_{14-x}\text{Ca}_x\text{Cu}_{24}\text{O}_{41}$  ( $x = 3, 6,$  and  $8$ ) and  $\text{Sr}_{13}\text{Y}_1\text{Cu}_{24}\text{O}_{41}$  at various  $P$ 's. (b)  $\rho_c(T)$  for  $\text{Sr}_4\text{Ca}_{10}\text{Cu}_{24}\text{O}_{41}$  at various  $P$ 's. The data near the onset of the superconductivity are shown in the right panel. (c) The same set of  $\rho_c(T)$  data for  $\text{Sr}_2\text{Ca}_{12}\text{Cu}_{24}\text{O}_{41}$ .

sure. We observed in our resistivity measurements under  $P$  that this crossover transforms into a sharp transition probably due to an increase in the interladder coupling strength with increasing  $P$ . Such a sharp resistivity jump is reminiscent of a charge-density-wave (CDW) transition in quasi-one- and two-dimensional systems [16]. As mentioned earlier, several measurements [7–9] suggest that a charge ordering may occur in this system. Hence, the insulating state of the  $x = 0$  compound at moderate  $P$  is understood as a charge localization associated with the charge ordering. At higher  $P$ , the charge-ordered state is destroyed and gives way to a metallic state. In this metallic state, the anisotropic ratio  $\rho_a/\rho_c$  is 3–5, nearly independent of  $T$ , and the magnitude of anisotropy is comparable to the result of the band calculation [17]. This fact indicates that this metallic state is at least 2D, or even 3D. In fact the insulator-metal transition takes place at the geometrically averaged resistivity  $\rho_{\text{av}} = \sqrt{\rho_c \rho_a} \sim 1.6 \text{ m}\Omega\text{cm}$  which is near the Mott-Ioffe-Regel critical resistivity for 3D localization (inset of fig. 1).

An alternative scenario to explain this  $P$ -induced insulator-to-metal transition in the  $x = 0$  compound is that more holes may be transferred from chains into ladders by  $P$  like the case of Ca-substitution [2]. At the moment we have no way to estimate how many holes increase under high  $P$ . However, considering that the magnitude of the resistivity in the metallic state at 8 GPa (fig. 1) is comparable to that of  $\text{La}_{2-x}\text{Sr}_x\text{CuO}_4$  with  $x \sim 0.07$ , the estimated hole density  $n = 0.07$  at  $P \sim 0$  may not increase appreciably at high  $P$ .

In fig. 3 we see that the insulating phase occupies most part of the  $x$ - $P$  phase diagram

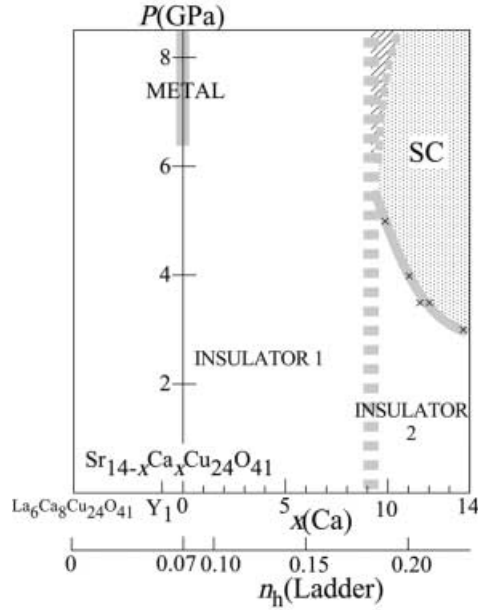


Fig. 3 – The  $x$ - $P$  phase diagram for  $\text{Sr}_{14-x}\text{Ca}_x\text{Cu}_{24}\text{O}_{41}$ . The “minus”  $x$ -axis is for  $\text{Sr}_{14-x}\text{Y}_x\text{Cu}_{24}\text{O}_{41}$  and  $\text{La}_6\text{Ca}_8\text{Cu}_{24}\text{O}_{41}$ . The ladder hole density ( $n_h$ (ladder)) estimated by the optical spectrum is also indicated in the transverse axis ( $n_h$  is not necessarily linear with  $x$ ). The crossover in the nature of the insulating state is indicated by the thick-dashed vertical line. The SC phase is restricted at high  $P$  and for  $x \geq 10$  and the experimentally determined critical pressure  $P_c$  is plotted as cross marks.

( $T = 0$  K). For compounds with  $x \geq 10$ , there is a  $T$ -region where  $d\rho_c/dT > 0$  and  $d\rho_a/dT < 0$  even at low pressures [5, 6]. At  $P = 0$ , the minimum ( $T_m$ ) in  $\rho_c(T)$  gradually shifts to higher temperatures with decreasing  $x$  from 12 ( $n_h \sim 0.21$ ,  $T_m \sim 60$  K) to 10 ( $n_h \sim 0.19$ ,  $T_m \sim 140$  K). However, upon reducing  $x$  from 10,  $T_m$  accelerates its increase, and for  $x = 8$  ( $n_h \sim 0.17$ ) the resistivity minimum, *i.e.* the high- $T$  metallic behavior, is not seen (below 400 K) even at  $P = 8$  GPa. In addition, the optical conductivity spectrum of  $x = 11$  for light polarized parallel to the rungs ( $\sigma_a(\omega)$ ) [12] gave evidence for the development of a pseudogap with lowering  $T$  which would be associated with a formation of hole pairs. The hole pairs tend to be localized at low  $T$  by quantum interference effects in the presence of disorder [18] or by forming a charge-ordered array which is pinned by defects or impurities on the ladders. The pseudogap width rapidly increases, from  $\sim 700$   $\text{cm}^{-1}$  for  $x = 11$  to  $\sim 1100$   $\text{cm}^{-1}$  for  $x = 8$  [12], and for  $x = 6$   $\sigma_a(\omega)$  no longer shows a well-defined pseudogap [19].

From these results we speculate that the nature of the insulating state would rapidly change upon reducing  $x$  from 10. At high hole densities (Insulator 2) the insulating state is likely a charge-ordered state of hole pairs which would be weakly pinned. At low hole densities (Insulator 1) the doped holes could no longer form pairs, and single holes form a charge-ordered state in  $x = 0$ . Randomness introduced by Ca-substitution and/or oxygen excess or oxygen deficiency may also play a role in the robustness of a localized state in the low- $x$  compounds. Probably, the different nature of the two insulating states might be connected with the occurrence or non-occurrence of superconductivity.

The fact that the superconducting state is observed only in high- $P$  and large- $x$  regions sug-

gests that superconductivity in this system requires the following two effects simultaneously: i) promotion of hole-pair formation by increasing the hole density in the ladders via heavy Ca-substitution, and ii) increase of interladder coupling (dimensionality) by applying high  $P$ . The anisotropic resistivity measurement for  $x = 11.5$  [5] demonstrated that the superconducting transition occurs when  $\rho_{av}$  per ladder plane comes near  $h/4e^2$ , the universal 2D resistivity suggestive of an increase in electronic dimensionality from one to two. We conclude that the primary effect of  $P$  is to increase the dimensionality of the electronic state by way of increasing interladder coupling and hence dissociating hole pairs. A collapse of the spin gap at high  $P$  [20] is a direct evidence for the pair dissociation. We speculate that the pairing correlation remains in the ladder planes at high  $P$ , which would trigger the formation of Cooper pairs in the 2D ladder planes. More systematic NMR measurements under  $P$  are necessary in order to confirm this scenario and to fully understand the phase diagram presented in this work.

\* \* \*

We are grateful to J. AKIMITSU and T. NAGATA for the collaboration in the early stage of this study. This work is supported by a Grant-in-Aid for Scientific Research and a COE Grant from the Ministry of Education, Culture, Sports, Science and Technology.

## REFERENCES

- [1] TSUJI S., KUMAGAI K., KATO M. and KOIKE Y., *J. Phys. Soc. Jpn.*, **65** (1996) 3474.
- [2] OSAFUNE T., MOTOYAMA N., EISAKI H. and UCHIDA S., *Phys. Rev. Lett.*, **78** (1997) 1980.
- [3] UEHARA M. *et al.*, *J. Phys. Soc. Jpn.*, **65** (1996) 2764.
- [4] DAGOTTO E., RIERA J. and SCALAPINO D., *Phys. Rev. B*, **45** (1992) 5744; RICE T. M., GOPALAN S. and SIGRIST M., *Europhys. Lett.*, **23** (1993) 445.
- [5] NAGATA T. *et al.*, *Phys. Rev. Lett.*, **81** (1998) 1090.
- [6] MOTOYAMA N. OSAFUNE T., KAKESHITA T., EISAKI H. and UCHIDA S., *Phys. Rev. B*, **55** (1997) 3386.
- [7] CARTER S. A. *et al.*, *Phys. Rev. Lett.*, **77** (1996) 1378.
- [8] TAKIGAWA M., MOTOYAMA N., EISAKI H. and UCHIDA S., *Phys. Rev. B*, **57** (1998) 1124.
- [9] KITANO H. *et al.*, *Europhys. Lett.*, **56** (2001) 434.
- [10] TSUNETSUGU H., TROYER M. and RICE T. M., *Phys. Rev. B*, **49** (1994) 16078; TSUNETSUGU H., TROYER M. and RICE T. M., *Phys. Rev. B*, **51** (1995) 16456; HAYWARD C. A. and POILBLANC D., *Phys. Rev. B*, **53** (1996) 11721.
- [11] RUZICKA B., DEGIORGI L., AMMERHAHL U., DHALENNE G. and REVCOLEVSKI A., *Eur. Phys. J. B*, **6** (1998) 301.
- [12] OSAFUNE T., MOTOYAMA N., EISAKI H. and UCHIDA S., *Phys. Rev. Lett.*, **82** (1999) 1313.
- [13] MÔRI N. and TAKAHASHI H., *Jpn. J. Appl. Phys. Ser.*, **8** (1993) 182.
- [14] A preliminary result was published by EISAKI H. *et al.*, *Physica C*, **341-348** (2000) 363.
- [15] A part of the data for  $x = 12$  was reported by NAKANISHI T. *et al.*, *Physica B*, **281-282** (2000) 957.
- [16] For example, *Electronic Properties of Inorganic Quasi-One-Dimensional Materials*, edited by MONCEAU P. (Reidel, Dordrecht) 1985; *Structural Phase Transitions in Layered Transition Metal Compounds*, edited by MOTIZUKI K. (Reidel, Dordrecht) 1986.
- [17] ARAI M. and TSUNETSUGU H., *Phys. Rev. B*, **56** (1997) 4305.
- [18] KIM E. H., *Phys. Rev. Lett.*, **86** (2001) 1315.
- [19] KOJIMA K., OSAFUNE T., MOTOYAMA N. and UCHIDA, S., unpublished.
- [20] MAYAFFRE H. *et al.*, *Science*, **279** (1998) 345.



ELSEVIER

Physica B 322 (2002) 408–412

**PHYSICA B**

www.elsevier.com/locate/physb

# Metal to insulator transition of filled skutterudite $\text{PrRu}_4\text{P}_{12}$ at low temperatures and high pressures

Ichimin Shirovani<sup>a,\*</sup>, Junichi Hayashi<sup>a</sup>, Takafumi Adachi<sup>a</sup>, Chihiro Sekine<sup>a</sup>, Takateru Kawakami<sup>b</sup>, Takeshi Nakanishi<sup>c</sup>, Hiroki Takahashi<sup>c</sup>, Jie Tang<sup>d</sup>, Akiyuki Matsushita<sup>d</sup>, Takehiko Matsumoto<sup>d</sup>

<sup>a</sup> Faculty of Engineering, Muroran Institute of Technology, 27-1, Mizumoto, Muroran-shi, 050-8585, Japan

<sup>b</sup> Faculty of Engineering Science, Osaka University, Toyonaka-shi 560-8531, Japan

<sup>c</sup> College of Humanities & Science, Nihon University, Tokyo 156-8550, Japan

<sup>d</sup> National Institute for Materials Science, Tsukuba-shi 305-0047, Japan

Received 31 August 2001; received in revised form 19 March 2002; accepted 21 May 2002

## Abstract

X-ray diffraction of a single crystal of  $\text{PrRu}_4\text{P}_{12}$  has been studied at ambient pressure.  $\text{PrRu}_4\text{P}_{12}$  has a filled skutterudite-type structure; space group:  $\text{Im}\bar{3}$ , lattice constant:  $a = 8.055(4) \text{ \AA}$ ,  $Z = 2$ ,  $D_{\text{calc}} = 5.826 \text{ g/cm}^3$ . Positional parameters and interatomic distances in the phosphide were determined. By use of synchrotron radiation, powder X-ray diffraction patterns of  $\text{PrRu}_4\text{P}_{12}$  were measured up to 50 GPa at room temperature. The lattice constant monotonically decreases with increasing pressure. The cell volume vs. pressure curve for  $\text{PrRu}_4\text{P}_{12}$  is fitted with the Birch equation of state. The bulk modulus of the phosphide is  $207 \pm 12 \text{ GPa}$ . The resistivity of  $\text{PrRu}_4\text{P}_{12}$  was measured as a function of temperature at high pressures. The metal to insulator transition is found at around 62 K under ambient pressure. The transition temperature ( $T_{\text{MI}}$ ) rapidly increases with pressure at the rate of about 0.9 K/GPa up to 4.5 GPa. Above 6 GPa,  $T_{\text{MI}}$  abruptly decreases with increasing pressure. The semiconductor-like behavior below  $T_{\text{MI}}$  for  $\text{PrRu}_4\text{P}_{12}$  is markedly suppressed at around 8 GPa. The metal to insulator transitions at low temperatures and high pressures are discussed. © 2002 Elsevier Science B.V. All rights reserved.

**Keywords:** Metal–insulator transition; Resistivity; Skutterudite compound; High pressure; X-ray diffraction

## 1. Introduction

Ternary metal pnictides with a general formula  $\text{LnT}_4\text{X}_{12}$  (Ln = lanthanide; T = transition metal; X = pnictogen) crystallize with a filled skutteru-

dite-type structure [1,2]. This structure is cubic, space group  $\text{Im}\bar{3}$ ,  $Z = 2$ . Ln atoms locate at (0 0 0) and  $(\frac{1}{2} \frac{1}{2} \frac{1}{2})$  of a cubic structure like BCC. The transition metal atoms (T) are in the center of a distorted octahedral environment of six pnictogen atoms. The skutterudite-type structure is characterized by formation of well-defined  $\text{X}_4^-$  groups. The skutterudite compounds show interesting electrical and magnetic properties at low temperatures [3,4].

\*Corresponding author. Tel.: +81-143-46-5544; fax: +81-143-46-5501.

E-mail address: sirotani@eee.elec.muroran-it.ac.jp (I. Shirovani).

We have found an interesting metal to insulator (MI) transition for  $\text{PrRu}_4\text{P}_{12}$  at around 60 K under ambient pressure [5]. Anomalous behavior in the magnetic susceptibility is not observed at around 60 K. This suggests that the MI transition in  $\text{PrRu}_4\text{P}_{12}$  is not caused by magnetic ordering [5]. PrL2-edge XANES measurements indicate that the valence state in the Pr atoms is trivalent down to 20 K [6]. Below the transition temperature ( $T_{\text{MI}}$ ) an energy gap of  $\text{PrRu}_4\text{P}_{12}$  is estimated to be about  $100 \text{ cm}^{-1}$  from the optical reflection spectrum [7]. The Raman spectra of the phosphide are measured between 6 and 300 K; the  $380 \text{ cm}^{-1}$  mode assigned to the vibration involving P atoms shows softening and broadening below the  $T_{\text{MI}}$  [8]. A slight jump in the thermal expansion coefficient is found at the  $T_{\text{MI}}$  [9]. The small anomaly in the specific heat appears at the  $T_{\text{MI}}$  [10]. Recently, using the electron diffraction technique, superlattice spots in the single crystal of  $\text{PrRu}_4\text{P}_{12}$  are observed below the  $T_{\text{MI}}$  [11].

We have studied X-ray diffraction of a single crystal at ambient pressure and powder X-ray diffraction of  $\text{PrRu}_4\text{P}_{12}$  up to 50 GPa at room temperature. The resistivity of  $\text{PrRu}_4\text{P}_{12}$  has been measured at low temperatures and high pressures. In this report, the metal to insulator transition of  $\text{PrRu}_4\text{P}_{12}$  at high pressure is discussed.

## 2. Experimental details

X-ray diffraction of a single crystal of  $\text{PrRu}_4\text{P}_{12}$  was studied at room temperature (295 K). Intensity data were collected on a Rigaku automatic four-circle diffractometer using graphite-monochromated  $\text{MoK}\alpha$  radiation. The structure was refined with a full-matrix least-squares program; space group:  $\text{Im-3}$ , lattice constant:  $a = 8.055(4) \text{ \AA}$ ,  $Z = 2$ ,  $D_{\text{calc}} = 5.826 \text{ g/cm}^3$ ,  $F_{000} = 830.00$ ,  $\mu(\text{MoK}\alpha) = 119.96$ . The conventional residual ( $R$ ) and the weighted residual ( $R_w$ ) are 0.032 and 0.034, respectively. Single crystals of  $\text{PrRu}_4\text{P}_{12}$  were grown by a Sn flux method. The mixtures with atomic ratio  $\text{Pr}:\text{Ru}:\text{P}:\text{Sn} = 1:4:20:50$  were heated at  $1000^\circ\text{C}$  for a week and then cooled down slowly to  $600^\circ\text{C}$  at  $2^\circ\text{C/h}$  [11].

By use of synchrotron radiation, powder X-ray diffraction patterns of  $\text{PrRu}_4\text{P}_{12}$  were measured with a diamond-anvil cell and an imaging plate up to 50 GPa at room temperature [12]. The incident beam was monochromatized with Si (1 1 1) double crystals to a wavelength of  $0.6888 \text{ \AA}$ . The pressure in the diamond-cell was determined from a pressure shift in the sharp R-line fluorescence spectrum of ruby. A 4:1 methanol–ethanol solution was used as the pressure-transmitting fluid.

A high-pressure apparatus with a cubic-anvil device was used for the resistivity measurement of  $\text{PrRu}_4\text{P}_{12}$  under hydrostatic conditions up to 8 GPa at low temperatures down to 4.2 K [13]. Polycrystals of  $\text{PrRu}_4\text{P}_{12}$  were used for measurements of the resistivity and the powder X-ray diffraction. These samples were prepared at high temperatures and high pressures [5].

## 3. Results and discussion

Fig. 1 shows the crystal structure of  $\text{PrRu}_4\text{P}_{12}$  determined from X-ray data of the single crystal. The resulting positional and thermal parameters are given in Table 1. The interatomic distances and angles are listed in Table 2. This structure is similar to that of  $\text{LaFe}_4\text{P}_{12}$  that has already been determined from single crystal counter data by

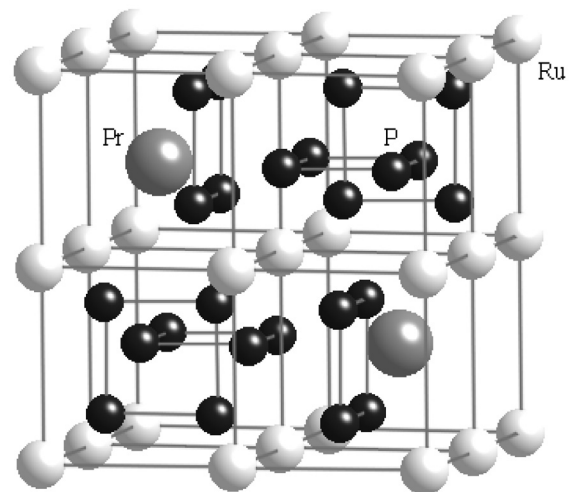


Fig. 1. Crystal structure of  $\text{PrRu}_4\text{P}_{12}$ . The Ru atom is taken as the origin (000).

Table 1  
Positional and thermal parameters in PrRu<sub>4</sub>P<sub>12</sub> at ambient pressure

	Pr	Ru	P
Im $\bar{3}$	2(a)	8(c)	24(g)
<i>x</i>	0	0.2500	0
<i>y</i>	0	0.2500	0.3579
<i>z</i>	0	0.2500	0.1437
U <sub>11</sub>	0.0074 (3)	0.0019 (3)	0.0051 (4)
U <sub>22</sub>	U <sub>11</sub>	U <sub>11</sub>	0.0033 (4)
U <sub>33</sub>	U <sub>11</sub>	U <sub>11</sub>	0.0035 (4)
Beq	0.582 (4)	0.151 (4)	0.31 (2)

Table 2  
Interatomic distances and angles in PrRu<sub>4</sub>P<sub>12</sub> at ambient pressure

Interatomic distances (Å)		Interatomic angle (deg)	
Pr–P	3.107 (1) (12 ×)	Pr–P–Ru	78.04 (3)
Pr–Ru	3.488 (1) (8 ×)	Pr–P–P'	158.13 (2)
Ru–P	2.355 (1) (6 ×)	Pr–P–P''	68.13 (2)
P–P'	2.314 (2) (1 ×)	Ru–P–P'	111.67 (2)
P–P''	2.289 (2) (1 ×)	Ru–P–P''	111.33 (2)
		Ru–P–Ru	117.56 (5)
		P'–P–P''	90

Patterson and Fourier methods [1]. The skutterudite-type structure is characterized by formation of rectangular P<sub>4</sub><sup>4-</sup> clusters. The P–P distances in PrRu<sub>4</sub>P<sub>12</sub> are 2.289 Å along the shorter edge and 2.314 Å along the longer edge. These are rather shorter than the P–P distances (2.289 and 2.356 Å) in LaFe<sub>4</sub>P<sub>12</sub> although the cell volume of PrRu<sub>4</sub>P<sub>12</sub> is considerably larger than that of the iron compound. The Ru–P distance is shorter than the sum of atomic radius (1.34 Å) of Ru atom and the covalent radius (1.06 Å) of P atom. The Pr–P distance almost agrees with the sum of the atomic radius (1.82 Å) of the Pr atom and the atomic radius (1.28 Å) of the P atom. These distances in PrRu<sub>4</sub>P<sub>12</sub> suggest metallic bond character. The X-ray diffraction of PrRu<sub>4</sub>P<sub>12</sub> has been studied at low temperatures. The positional parameter of the phosphorus atom is insensitive to temperature. The ratio of lattice constant ( $a_0 - a_T/a_0$ ;  $a_0$ —room temperature,  $a_T$ —low temperatures) of PrRu<sub>4</sub>P<sub>12</sub> decreases with decreasing temperature

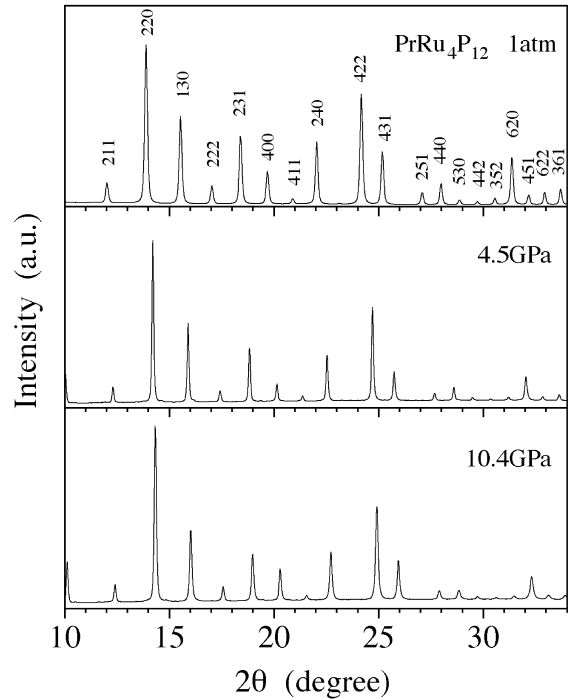


Fig. 2. Powder X-ray diffraction patterns of PrRu<sub>4</sub>P<sub>12</sub> at high pressures.

at the rate of  $-8.7 \times 10^{-4}/\text{K}$ . This value is slightly smaller than the result of the linear thermal expansion measured by the three terminal capacitance method [9].

Fig. 2 shows powder X-ray diffraction patterns of PrRu<sub>4</sub>P<sub>12</sub> with synchrotron radiation at high pressures and room temperature. The diffraction lines shift to the high angle region with increasing pressure. The width of the diffraction lines becomes broad at higher pressures. Fig. 3 shows the lattice constant vs. pressure curve for PrRu<sub>4</sub>P<sub>12</sub> up to 50 GPa at room temperature. The structural anomaly in PrRu<sub>4</sub>P<sub>12</sub> is not observed up to 50 GPa at room temperature. The ratio of the lattice constant ( $a_0 - a_P/a_0$ ,  $a_0$ —ambient pressure,  $a_P$ —high pressures) decreases at the rate of  $-2.1 \times 10^{-2}/\text{GPa}$  up to 4.5 GPa. Thus, the pressure dependence of the lattice constant is much larger than its temperature dependence. The pressure vs. volume curve for PrRu<sub>4</sub>P<sub>12</sub> can be fitted by a Birch equation of state [14]. The bulk

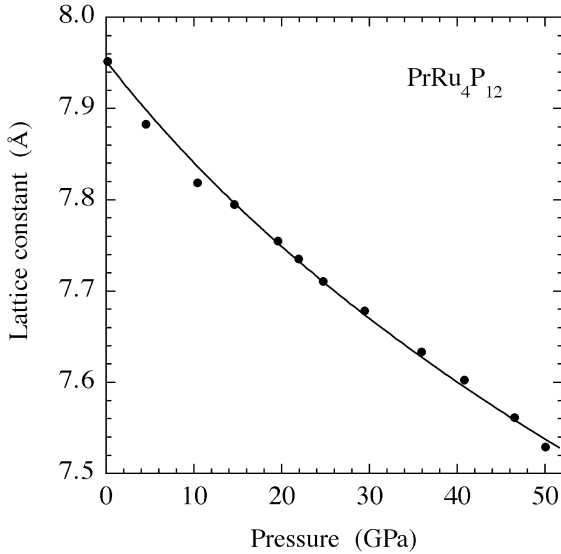


Fig. 3. Lattice constant vs. pressure curve for  $\text{PrRu}_4\text{P}_{12}$ .

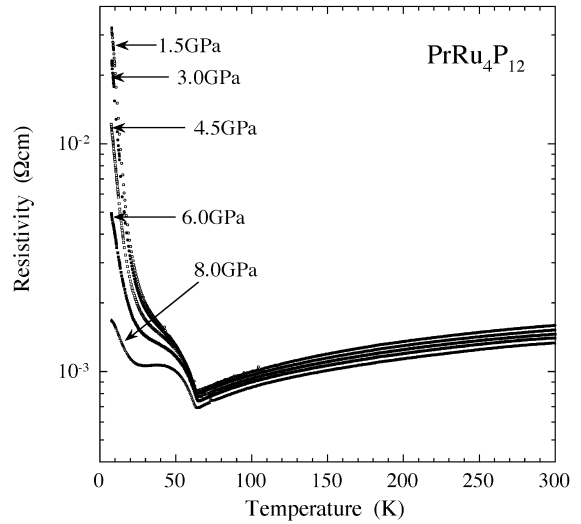


Fig. 4. Resistivity vs. temperature curves for  $\text{PrRu}_4\text{P}_{12}$  at high pressures.

modulus obtained by a least-squares fit is  $207 \pm 12$  GPa for  $\text{PrRu}_4\text{P}_{12}$ . This value is about 2.8 times that of  $\text{PrP}$  with a NaCl-type structure [12].  $\text{PrRu}_4\text{P}_{12}$  is a very hard material.

Fig. 4 shows the electrical resistivity vs. temperature curves for  $\text{PrRu}_4\text{P}_{12}$  at high pressures. The resistivity decreases with increasing pressure up to 8 GPa under hydrostatic conditions. When the temperature dependence of the resistivity of the phosphide is measured at constant pressures, the MI transitions are observed at low temperatures and high pressures. The semiconductor-like behavior below the  $T_{\text{MI}}$  in  $\text{PrRu}_4\text{P}_{12}$  is markedly suppressed at around 8 GPa. Fig. 5 shows the effect of pressure on  $T_{\text{MI}}$  for  $\text{PrRu}_4\text{P}_{12}$ .  $T_{\text{MI}}$  rapidly increases with pressure at the rate of about 0.9 K/GPa up to 4.5 GPa. Above 6 GPa,  $T_{\text{MI}}$  abruptly decreases with increasing pressure.

$\text{PrRu}_4\text{P}_{12}$  shows the MI transition at around 62 K under ambient pressure. This anomalous behavior does not arise from magnetic ordering and valence fluctuations based on the f electrons in Pr [5,6]. A  $\lambda$ -like second order-type anomaly in the specific heat appears at  $T_{\text{MI}}$ ; this does not depend on the magnetic field at least up to 12 T [10]. Superlattice spots in the single crystal of  $\text{PrRu}_4\text{P}_{12}$  are observed below the  $T_{\text{MI}}$ ; this may arise from

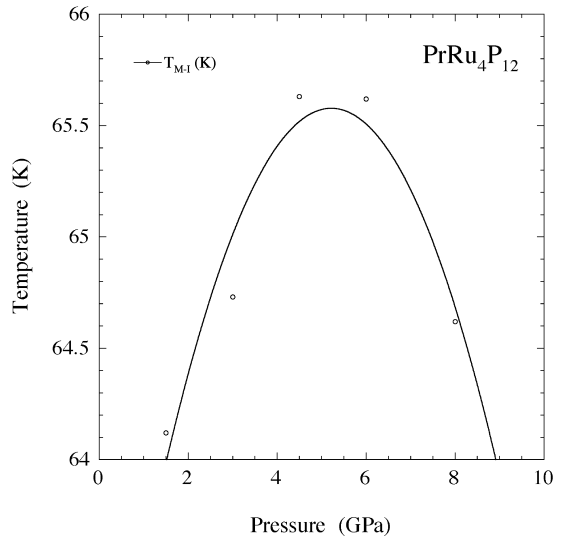


Fig. 5.  $T_{\text{MI}}$  plotted as a function of pressure for  $\text{PrRu}_4\text{P}_{12}$ .

the opening of a band gap due to a nesting of the Fermi surface [11]. The appearance of the superlattice structure provides two possible origins of the MI transition, a charge density wave (CDW) transition or antiferro-quadrupolar (AFQ) ordering. Matsuhira et al. suggest that the MI transition in  $\text{PrRu}_4\text{P}_{12}$  is due to the CDW transition rather

than the AFQ transition from the detailed study of the electronic specific heat [15].

We have studied the magnetic susceptibility and electrical resistivity of the alloys  $\text{La}_{1-x}\text{Pr}_x\text{Ru}_4\text{P}_{12}$  diluted by La atom [16]. As the lattice constant in the alloys increases with increasing La concentration, the average Pr–Pr distances increase.  $T_{\text{MI}}$  of the alloys shifts to lower temperatures with increasing La concentration.

The lattice constant of  $\text{PrRu}_4\text{P}_{12}$  decreases from 8.057 Å at ambient pressure to 7.887 Å at 4.5 GPa. Thus, the distance between the nearest Pr atoms decreases from 6.98 Å at ambient pressure to 6.82 Å at 4.5 GPa. The increase of inter-site interactions between Pr atoms drives up  $T_{\text{MI}}$ . This tendency is consistent with the result of the alloys  $\text{La}_{1-x}\text{Pr}_x\text{Ru}_4\text{P}_{12}$ . However,  $T_{\text{MI}}$  surprisingly decreases with increasing pressure above 4.5 GPa although the Pr–Pr distances shorten successively with pressure. The resistivity of  $\text{PrRu}_4\text{P}_{12}$  below  $T_{\text{MI}}$  is remarkably suppressed at around 8 GPa. The f-electrons in  $\text{PrRu}_4\text{P}_{12}$  may easily be itinerant in the crystal at higher pressures. Thus, these results suggest that the MI transition in  $\text{PrRu}_4\text{P}_{12}$  may disappear at very high pressures. As  $\text{PrRu}_4\text{As}_{12}$  shows superconductivity at around 2.4 K [17],  $\text{PrRu}_4\text{P}_{12}$  may behave as a superconductor at very high pressures.

### Acknowledgements

This work was partly supported by a Grant-in-Aid for Scientific Research from the Ministry of Education, Science and Culture of Japan: No. 13874040(IS) and No. 14204032(IS).

### References

- [1] W. Jeitschko, D. Braun, *Acta Crystallogr. B* 33 (1977) 3401.
- [2] D.J. Braun, W. Jeitschko, *J. Less-Common Met.* 72 (1980) 147.
- [3] G.P. Meisner, *Physica B* 108 (1980) 763.
- [4] M.S. Torikachvili, J.W. Chen, Y. Dalichaouch, R.P. Guertin, M.W. McElfresh, C. Rossel, M.B. Maple, G.P. Meisner, *Phys. Rev. B* 36 (1987) 8660.
- [5] C. Sekine, T. Uchiumi, I. Shirovani, T. Yagi, *Phys. Rev. Lett.* 79 (1997) 3218.
- [6] C.H. Lee, H. Oyanagi, C. Sekine, I. Shirovani, M. Ishii, *Phys. Rev. B* 60 (1999) 13253.
- [7] T. Nanba, M. Hayashi, I. Shirovani, C. Sekine, *Physica B* 259–261 (1999) 853.
- [8] C. Sekine, H. Saito, A. Sakai, I. Shirovani, *Solid State Commun.* 109 (1999) 449.
- [9] K. Matsuhira, T. Takikawa, T. Sakakibara, C. Sekine, I. Shirovani, *Physica B* 281&282 (2000) 298.
- [10] C. Sekine, T. Inaba, I. Shirovani, M. Yokoyama, H. Amitsuka, T. Sakakibara, *Physica B* 281&282 (2000) 303.
- [11] C.H. Lee, H. Matsuhata, A. Yamamoto, T. Ohta, H. Takazawa, K. Ueno, C. Sekine, I. Shirovani, T. Hirayama, *J. Phys. Condens. Matter* 13 (2001) L45.
- [12] J. Hayashi, I. Shirovani, K. Takeda, T. Uchiumi, S. Kimura, T. Adachi, T. Kikegawa, Science and technology of high pressure, in: M.H. Manghani, W.J. Nellis, M.F. Nicol (Eds.), *Proceedings of AIRAPT-17*, Universities Press, Hyderabad, India, 2000, p. 722.
- [13] H. Takahashi, A.T. Yamamoto, N. Mori, S. Adachi, H. Yamauchi, S. Tanaka, *Physica C* 218 (1993) 1.
- [14] F. Birch, *Phys. Rev.* 71 (1947) 809.
- [15] K. Matsuhira, Y. Hinatsu, C. Sekine, I. Shirovani, *Physica B* 312&313 (2002) 829.
- [16] C. Sekine, T. Inaba, K. Kihou, I. Shirovani, *Physica B* 281&282 (2000) 300.
- [17] I. Shirovani, T. Uchiumi, K. Ohno, C. Sekine, Y. Nakazawa, K. Kanoda, S. Todo, T. Yagi, *Phys. Rev. B* 56 (1997) 7866.

# 圧力装置の現状

## Recent Progress in High-Pressure Apparatus

高橋 博樹

Hiroki TAKAHASHI

Recently there has been a lot development in high-pressure work in physics. The quality of hydrostatic pressure is an important factor. In this article recent advances in the high-pressure apparatuses for precise experiments are reviewed. A piston-cylinder cell, opposed-type anvil cells, and a cubic-type anvil cell are described.

[*high pressure apparatus, piston-cylinder cell, DAC, Bridgman anvil cell, cubic anvil cell*]

### 1. はじめに

高圧力技術は、物性実験技術のなかでも近年大きく発展してきた分野の一つである。大型施設を利用することなく手軽に利用可能で、ノウハウも十分に公開され、装置によっては製品として購入することも可能であることから、近年飛躍的に普及し様々な分野で利用されている。また応用範囲が広がり、高圧力技術を用いたデータが物性研究の重要局面で利用されるにつれ、データのクオリティに関しても厳しい注文が付けられるようになった。実際、データのクオリティに関しては、1気圧での測定と同程度のものが要求されることも多い。現在最も普及している高圧装置であるピストンシリンダー装置は、圧力媒体として液体を用い、物性測定法を工夫することによって、かなり良質のデータを得ることが可能である。このように本稿では、多様化している装置の現状をふまえ、今回の特集記事のイントロダクションとして様々な高圧装置とそれらを利用した物性測定法を紹介し、できる範囲でその実験結果と意義についても紹介する。詳細は他稿に譲るが、どのような条件で、どの程度の圧力範囲まで精密測定が可能かということについてもふれる。

### 2. 様々な高圧装置

#### 2.1 ピストンシリンダー装置

ピストンシリンダー装置は Fig. 1 に示すようにピストンとシリンダーによって構成され、シリンダー内に試料と圧力媒体を封入し、ピストンに荷重をかけることによって内部に静水圧を発生する装置である。基本的な構造は確立されており、用途に応じ様々な形状が設計されている。構成材料としてはタンゲステンカーバイドや非磁性 CuBe 合金などの高強度

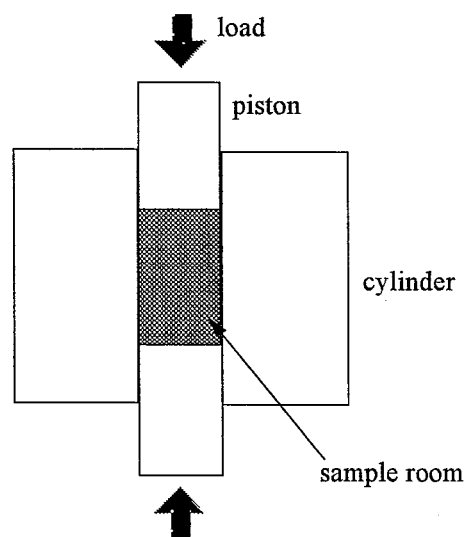


Fig. 1. Piston-cylinder type high pressure cell.

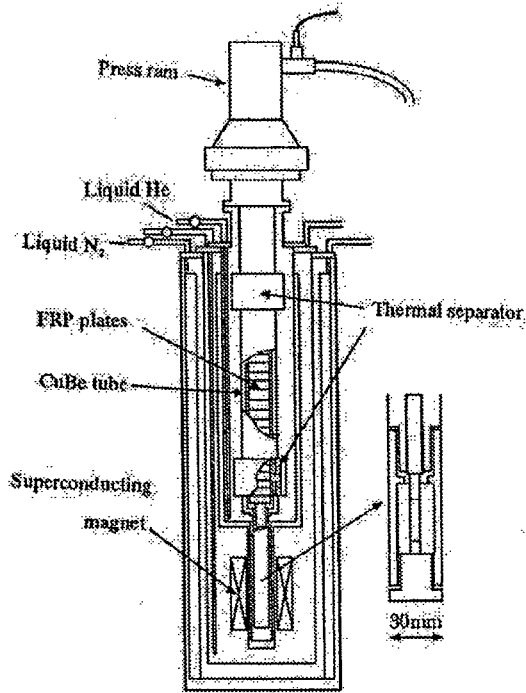


Fig. 2. High pressure system at low temperature. The load is kept constant during changing temperature [1].

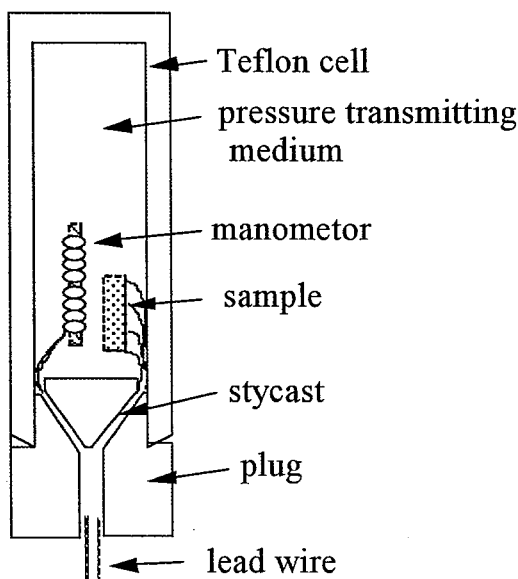


Fig. 3. Sample cell for electrical resistivity measurement by a DC four terminal method.

材が用いられることが多く、通常 2~3 GPa までの圧力が発生可能である。圧力媒体は測定に応じ、不活

性液体のフロリナートや鉱物油、有機溶媒などが用いられている。

ピストンシリンダー型圧力発生装置の利用方法には大きく分けて二通りある。一つは直接加圧しながら定荷重の下で物性測定を行う方法であり、もう一つは圧力をクランプして使用する方法である。

Fig. 2 に東京大学物性研究所に設置されている定荷重型低温高圧発生装置の概略図を示す。2~300 K の温度範囲と 20 T までの磁場範囲で物性測定ができるように設計されており、温度変化中においても油圧プレスで荷重を制御し FRP 積層板を通じて荷重をピストンに加えることができるようになっているため、物性測定を行っている間、低温でも試料部の圧力を一定に保つことができる。Fig. 3 に実際の直流四端子法による電気抵抗測定用のアセンブリを示す。Fig. 3 に示すように試料部にはテフロン製のカプセルを用いて液体の圧力媒体の漏れを防ぎ、内部からのリード線の取り出しには金属製プラグにスタイキャストを埋め込んで漏れを防いでいる。同様の圧力封入技術を用いることによって電気抵抗測定の他に、コイルを使用した交流帯磁率測定(相互インダクタンス法)、ストレインゲージを用いた熱膨張測定、交流ブリッジを用いた誘電率測定、NQR 測定、熱電能測定などがこれまでに行われてきている。また外部磁場を印加することによりホール係数測定や磁気抵抗測定も行われている。しかしながら、この方法は、装置全体が大がかりとなり、手軽に始めようという装置ではない。

一方、Fig. 4 に示すクランプ型ピストンシリンダー装置は、室温でプレスを用いて試料部に圧力を印加し、ナットでその圧力を保持する機能を備えている。このように圧力を保持した状態で持ち運び可能であり、種々の測定系に組み込むことが可能であるので、現在広く普及している。物性測定は基本的に定荷重型と同様の測定が可能であるが、物性測定に応じて様々なタイプが考案されている。また温度範囲は希釈冷凍機を用いることにより数十ケルビンの低温まで測定が可能であり、磁場もパルス磁場を用いることによってより高い磁場下での測定が可能である。以下、応用例を述べる。

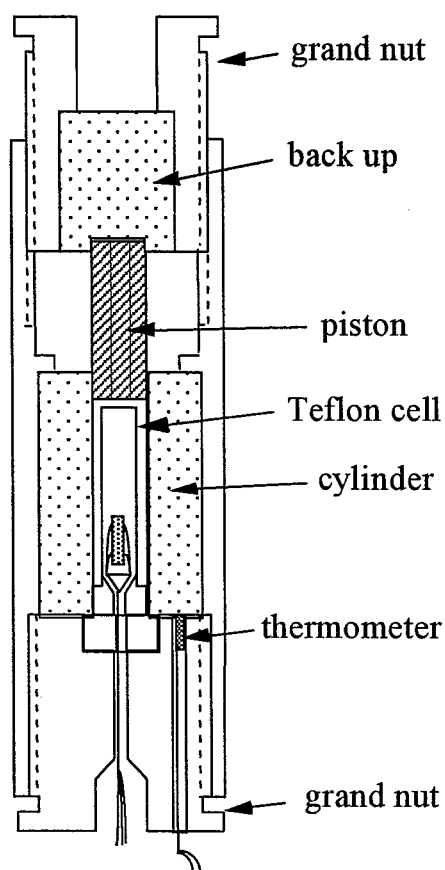


Fig. 4. Clamp-type piston cylinder cell.

- ① 精密磁化測定[2]。市販の SQUID マグネトメーターに高压セルを挿入して測定する方法，磁気天秤を用いた方法，引き抜き法による方法などが行われている。これらは全て従来用いられてきた測定系に高压装置を組み込んだもので，非磁性の压力装置を用い，試料の磁化を压力装置ごと測定する方法である。
- ② 比熱測定。高压下では断熱法と交流法が行われている。断熱法は，熱容量の小さいセルを用いて試料の比熱を装置ごと測定する方法であり，交流法は試料室内で熱測定を行う方法である。
- ③ 中性子線回折実験。原子炉では中性子線を比較的良好に透過するアルミナ製のシリンダーを用いたいわゆる Machan タイプ[3]と呼ばれる高压装置が用いられることが多い。シリンダーを外から機械的に締め付けることにより压力は 3 GPa 近くまで発生可能である。また，より高い压力での測定のためには，サファイア製の対向アンビル装置[4]が開発されて

いる。压力は，6 GPa まで発生可能である。

以上が，ピストンシリンダー装置の現状であるが，最近，CuBe 合金よりも強度の高い非磁性超硬材料である NiCrAl[5]や MP35N[6]を材料としたピストンシリンダー装置による実験が行われている。これらのセルではクランプ型で 3 GPa を越える压力を発生させることが可能であり，今後普及すると思われる。

## 2.2 対向アンビル装置

対向アンビル装置は Fig. 5 に示すように先端の面積を小さく加工した一对のアンビルを用意し，压力封入のためのガスケットをアンビル間に挟んでプレスで荷重をかけることによって压力を発生する装置である。試料はガスケットの中に压力媒体とともに封入される。

### 2.2.1 ブリッチマンアンビル装置

ブリッチマンにより開発された方法であり，超硬材料の特性を最大限引き出すためにマッシュサポートの原理を用いている。これは，アンビルの先端部を細く底面を広くし，先端部にかかる応力を分散させて高い压力を発生する方法である。タングステンカーバイドのアンビルを用いて，10 GPa 以上の压力を発生させることが可能ではあるが，軸性の压力であり高压力を発生するために静水圧性を犠牲にせざるを得ない欠点がある。そのため，精密測定用

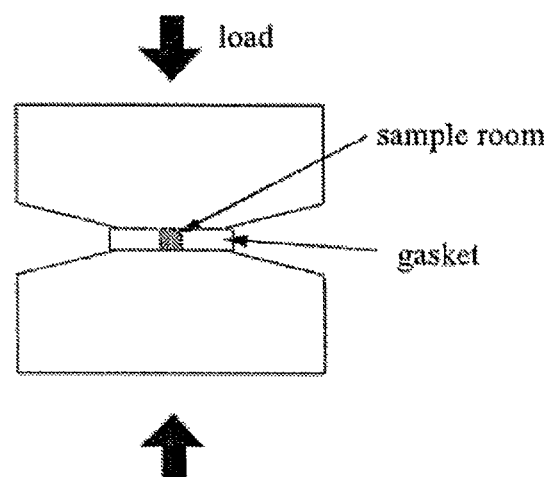


Fig. 5. Bridgman type cell.

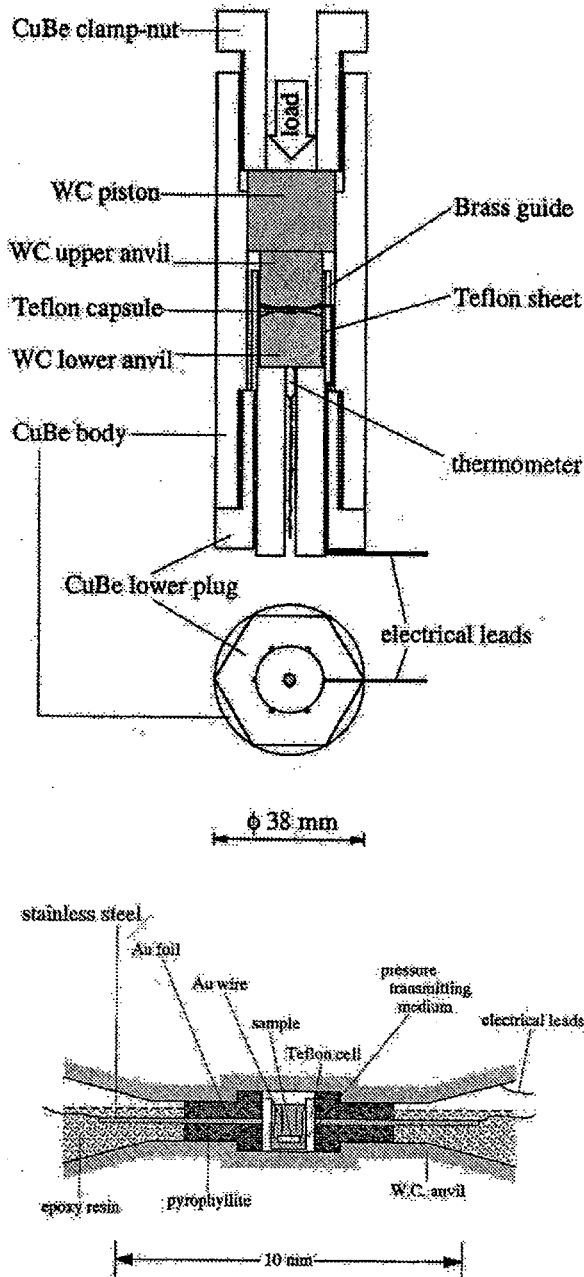


Fig. 6. Modified Bridgman anvil cell [7].

に静水圧発生に改良を加えたブリッチマンアンビル装置[7]が考案されている。概略を Fig. 6 に示す。アンビル先端に「くぼみ」をもうけそこにテフロンカプセルをおいて加圧するように設計されている。テフロンカプセル内には液体の圧力媒体とともに試料が封入されている。カプセル内部からはリード線を取り出すことができ、直流四端子法による電気抵抗

や交流帯磁率の測定が可能である。定荷重加圧方式で開発が進められ低温は 1.6 K 程度、圧力は最高 8 GPa まで発生可能である。また、クランプタイプとすることによって希釈冷凍機との組み合わせで数十ケルビンの低温まで測定が可能である。Fig. 7 にこの装置を用いた測定例としてスピラダー物質  $(\text{Sr}_{1-x}\text{Ca}_x)_{14}\text{Cu}_{24}\text{O}_{41}$  の磁気抵抗を示す[7]。1 気圧での測定値と比べても遜色なく、この装置で可能な磁場温度圧力条件下での精密測定はほとんど他に例がない。液体を圧力媒体とし、クランプタイプで 3 GPa 以上発生できる装置としては次に示すダイヤモンドアンビルセルがあるが、試料室がきわめて微小なために精密測定が手軽にできないという欠点がある。

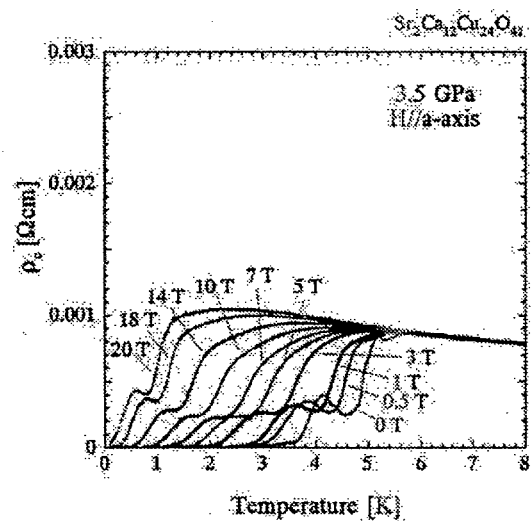


Fig. 7. Magneto-resistance of  $(\text{Sr}_{1-x}\text{Ca}_x)_{14}\text{Cu}_{24}\text{O}_{41}$  under high pressure using modified Bridgman anvil cell [7].

## 2. 2. 2 ダイヤモンドアンビルセル(DAC)

DAC は Fig. 8 に示すようにダイヤモンド製のアンビルと金属ガスケットからなる部分をアンビルの平行度を保ちながら上下からスムーズに荷重をかけることのできる装置である。荷重をかける方式としては、ピストン・スクリュー方式、ヘリウムガス駆動方式、レバー式、ブラケット方式などが報告されており物性測定により様々な改良が施されている。DAC に関しての詳細な説明は省略するが、最近圧力媒体としてヘリウム等のガスを圧力媒体としてガスケットに充填する方法が確立され、これを用いるこ

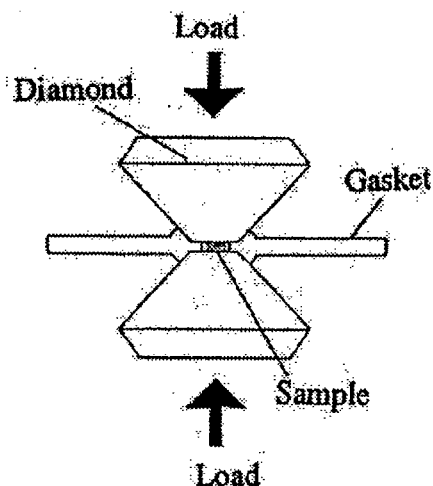


Fig. 8. Diamond anvil cell (DAC).

とによって静水圧性の非常に高い状態でX線回折実験等が行われるようになった。発生圧力は100 GPaを越える圧力領域である。

また、DACを用いた高压磁気測定法として、SQUIDマグネトメーターの検出コイルをDACのアンビルの軸方向に微小振動させる磁化測定システム[8]や、DACを市販のSQUIDマグネトメーターと組み合わせて使用する測定が行われている。

### 3. マルチアンビルプレス装置

マルチアンビルプレス装置は一軸性の大きなブリッチマンアンビルに比べ試料容積をはるかに大きくとることができ静水圧性も高くできるように工夫された装置である。ホール[9]が開発した4方向から均等に加圧できるテトラヘドラルアンビル装置に始まり6方向から均等に加圧できるキュービックアンビル装置が開発された[10]。Fig. 9に概略を示す。キュービックアンビル装置の発生圧力はアンビルの材質とアンビル先端のサイズできまり、タングステンカーバイドの先端3 mm角のアンビルを用いたときの最高発生圧力は13 GPaである。従来、高温高压下での物質合成や、放射光を用いたX線回折実験用に精力的に開発されてきた装置である。しかしながらアンビルを電極とした直流四端子法による電気抵抗測

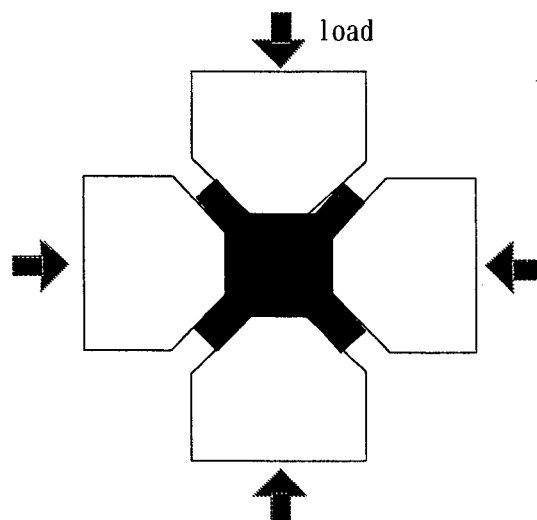


Fig. 9. Multi-anvil type high pressure apparatus.

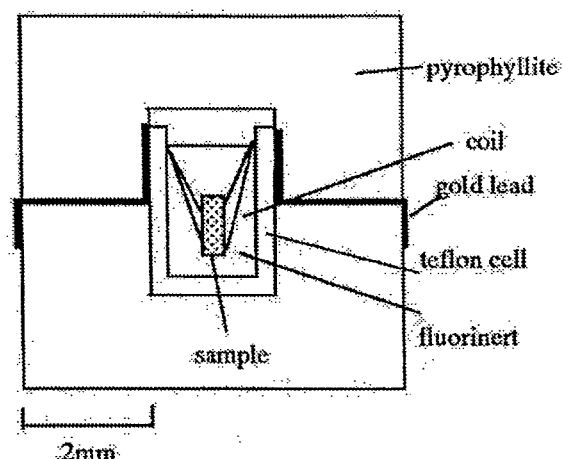


Fig. 10. A sample assembly for cubic anvil press.

定や交流帯磁率測定が可能であることから低温用の装置として物性研で開発が行われた。Fig. 10に電気抵抗測定用に開発された立方体のガスケット部を示す。試料は液体の圧力媒体とともにテフロンセルに封入されるので室温では静水圧中で加圧が可能である。試料サイズはピストンシリンダー型よりもかなり小さくなるが、DACと比べるとはるかに大きくなるため、精密測定が可能である。また、圧力発生方法は直接加圧しながら定荷重の下で物性測定を行う方式であり、圧力も精密に制御することが可能で

ある。Fig. 11 に測定例として代表的な酸化物超伝導体  $\text{Hg}_2\text{Ba}_2\text{Ca}_2\text{Cu}_3\text{O}_{16}$  の交流帯磁率を示す[11]。この物質は現時点で最も高い超伝導転移温度を高圧下で示す物質である。また、最近の展開としてキュービックプレスを用いた非磁性材料で作製し、超伝導磁石とを組み合わせることによって高圧力低温強磁場下の物性測定が進められている。

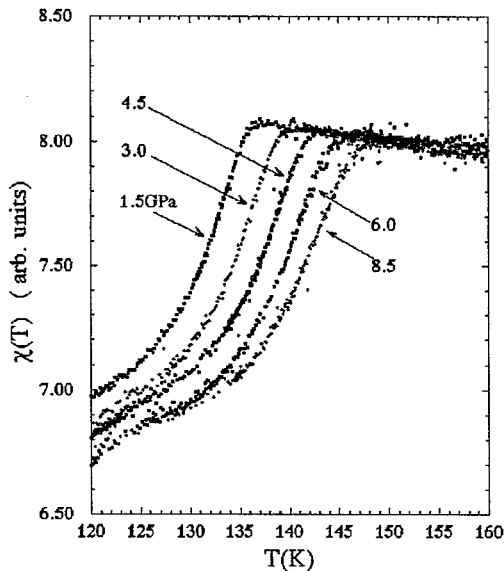


Fig. 11. AC susceptibility of  $\text{Hg}_2\text{Ba}_2\text{Ca}_2\text{Cu}_3\text{O}_{16}$  using cubic anvil press [12].

#### 4. ガス圧力発生装置

最も静水圧性のよい圧力発生装置はガス直接加圧方式である。日本国内では高圧ガスの取り扱いについて法規で大きく規制されていることもあり、物性測定にはさほど利用されていない。海外では製品として購入可能であり、最高発生圧力は低いものの物性測定に利用されている。通常、ヘリウムガスが用いられ、増圧機で直接加圧を行う。市販のものはCuBe合金製のシリンダータイプの高圧セルにキャピラリーでガスを送る構造になっており、最高発生圧力は約1.5 GPa程度である。セルよりリード線を取り出すことにより、低温強磁場下クランプ式ピストンシリンダー装置と同様の物性測定が可能である。圧力制御に関しては、液体ヘリウムが固化しない範囲で低温で圧力を変化させることも可能である。

また、精密な中性子線回折実験をするために直接ヘリウムガスで試料を加圧する方式が海外のパルス中性子源で行われている[12]。これは中性子線に対し透過率の高いアルミ製の高圧セルに増圧機で加圧されたヘリウムガスを送り込む構造になっており、1気圧と同程度の精度で回折パターンを得ることが可能である。ただし、アルミのセル強度の問題から0.6 GPaが最高圧である。

直接加圧方式とは異なるが先に述べたようにDACにヘリウムガスを封入したX線回折実験が封入技術の進展と共に普及している。またDACを用いた電気抵抗測定や帯磁率測定にもヘリウムガス媒体が利用されているが、技術的に難しくまださほど普及していない。

#### 5. 圧力較正

プレスを使って加圧する装置では、プレスの発生荷重と高圧装置の発生圧力の関係を事前に調べ、その関係を用いて発生圧力を決める。通常、よく調べられている物質の相転移点や、電気抵抗や超伝導転移点の圧力効果を利用して圧力較正を行う。ピストンシリンダー装置の場合は $\text{NH}_4\text{F}$ 、 $\text{Hg}$ 、 $\text{Bi}$ がそれぞれ0.36 GPa、0.76 GPa、2.55 GPaで相転移を示すことからこれを室温の圧力定点として、またその中間の圧力に対してはマンガン抵抗ゲージが圧力に対し直線的に変化することを利用する。低温ではSnの超伝導転移温度の圧力変化 $T_c(\text{K}) = 3.733 - 0.495P(\text{GPa})$ [13]やPb、Inなどの超伝導転移温度の圧力変化を用いて圧力を決定する。直接加圧方式の場合は室温と低温の圧力変化は小さいが、クランプ型では低温で1割以上の圧力が抜ける場合があるので低温でも発生圧力を確認しておく必要がある。ブリッチマンアンビルやキュービックアンビル装置においても同様の方法を用いて圧力を決定している。Tl、Ba、Bi、Snの室温における相転移圧力がそれぞれ3.68 GPa、5.53 GPa、7.68 GPa、9.4 GPaであることを圧力定点として利用する。

ダイヤモンドアンビルセルの場合には試料室にルビーの小粒をいれ、ダイヤモンドを通してレーザー

で励起し、蛍光スペクトルを測定することにより圧力を決定する。

## 6. おわりに

最近の物性科学で高圧力技術が重要な役割を果たした実験についていくつか紹介する。高温超伝導の分野では  $\text{Hg}_2\text{Ba}_2\text{Ca}_2\text{Cu}_3\text{O}_{16}$  で最高の超伝導転移温度 164 K を高圧で記録している。また、理論的に超伝導となることが予想されていたスピニラダー系酸化物について、約 3 GPa で超伝導となることが初めて高圧力下で示され、磁場下での振る舞いも高圧力下で精密に調べられた。高圧力下でのみ観測される現象については高圧力技術が必須であり、それにとともに測定技術も発展してきた。ヘビーフェルミオン分野でも物性が圧力に対して大きく変化することから様々な成果が得られている。最近のトピックスとしては強磁性体として知られていた  $\text{UGe}_2$  が高圧力下で強磁性が抑制され約 1–1.6 GPa で超伝導となる事が報告されたことがあげられる[14]。一方、ダイヤモンドアンビルセルを用いた圧力誘起超伝導探索によりヨウ素、イオウ、酸素などの分子性結晶や鉄元素でも超伝導が報告されている[15]。

現在広く普及している高圧力技術は、発生圧力は 2–3 GPa と、さほど高くはないが精密なデータへの要求が大きい。今後はダイヤモンドアンビルセル等を用いたさらに高い圧力領域での精密測定の確立が望まれ、普及することが期待される。

## 参考文献

- [1] 毛利信男: 実験物理学講座 2「基礎技術 2」(丸善 1999) 本河光博, 三浦登編 p.187.
- [2] 上床美也: 高圧力の科学と技術, **11**, 181 (2001).
- [3] 小野寺昭史ら: 固体物理, **27**, 27 (1992).
- [4] 長壁豊隆: 高圧力の科学と技術, **11**, 203 (2001).
- [5] M. Eremets: in *High Pressure Experimental Methods* (Oxford University Press, Oxford, 1996).
- [6] I.R. Walker: Rev. Sci. Instrum., **70**, 3402 (1999).
- [7] T. Nakanishi, N.Takeshita, N.Mori: Rev. Sci. Instrum., **73**, 1828 (2002).
- [8] M. Ishizuka, K. Amaya, S. Endo: Rev. Sci. Instrum., **65**, 3307 (1995).
- [9] H.T. Hall: Rev. Sci. Instrum., **29**, 267 (1958).
- [10] N. Môri, Y. Okayama, H. Takahashi, Y. Haga, T.Suzuki: Jpn. J. Appl. Phys., Series **8**, 182 (1993).
- [11] H. Takahashi, A. Tokiwa-Yamamoto, N. Môri, S. Adachi, H. Yamauchi, S. Tanaka: Physica, **C218**, 1 (1993).
- [12] J.D. Jorgensen Shiyou Pei, P. Lightfoot, D.G. Hinks, B.W. Veal, B. Dabrowski, A.P. Paulikas, R. Kleb, I.D. Brown: Physica, **C171**, 93 (1990).
- [13] C.A. Swenson: in *Metallurgy at High pressure and High Temperature* (Gordon & Breach, New York, 1964).
- [14] S.S. Saxena, P. Agarwal, K. Ahilan, F.M. Grosche, R.K. Haselwimmer, M.J. Steiner, E. Pugh, I.R. Walker, S.R. Julian, P. Monthoux, G.G. Lonzarich, A. Huxley, I. Sheikin, D. Brathwaite, J. Flouquet: Nature, **406**, 587 (2000).
- [15] K. Shimizu, T. Kimura, S. Furomoto, K. Takeda, K. Kontani, Y. Onuki, K. Amaya: Nature, **412**, 16 (2001).

[2002年7月29日受理]



ELSEVIER

Journal of Magnetism and Magnetic Materials 226–230 (2001) 246–248



www.elsevier.com/locate/jmmm

# High-pressure effect on transport properties of spin-ladder compounds $\text{Na}_{1-x}\text{Ca}_x\text{V}_2\text{O}_5$ and $\text{Ca}_{0.7}\text{Li}_{0.3}\text{V}_2\text{O}_5$

H. Takahashi<sup>a,\*</sup>, T. Nakanishi<sup>a</sup>, T. Arima<sup>b</sup>, M. Noguchi<sup>b</sup>, M. Oyanagi<sup>b</sup>,  
N. Takeshita<sup>c</sup>, N. Môri<sup>c</sup>

<sup>a</sup>Department of Physics, College of Humanities and Sciences, Nihon University, 2-25-40 Sakurajousui, Setagaya-ku, Tokyo 156-8550, Japan

<sup>b</sup>Institute of Materials Science, University of Tsukuba, 1-1-1 Tennoudai, Tsukuba, Ibaraki 305-0006, Japan

<sup>c</sup>Institute for Solid State of Physics, The University of Tokyo, 5-1-5 Kashiwanoha, Kashiwa, Chiba 277-8581, Japan

## Abstract

Electrical resistivity of layered vanadium oxides  $\text{Na}_{1-x}\text{Ca}_x\text{V}_2\text{O}_5$  and  $\text{Ca}_{0.7}\text{Li}_{0.3}\text{V}_2\text{O}_5$  has been measured under high pressures of up to 10 GPa. These compounds have V–O networks forming a two-leg spin-ladder layer in some composition range. In the spin-ladder compound  $\text{Na}_{1-x}\text{Ca}_x\text{V}_2\text{O}_5$ , electrical resistivity measurements show semiconducting behavior. However, the electrical resistivity has been significantly reduced under high pressure, although it remains semiconducting up to 8 GPa. On the other hand, the electrical resistivity of  $\text{Ca}_{0.7}\text{Li}_{0.3}\text{V}_2\text{O}_5$  which also has a two-leg spin-ladder layer is lower than  $\text{Na}_{1-x}\text{Ca}_x\text{V}_2\text{O}_5$  by several orders of magnitude. The electrical resistivity of  $\text{Ca}_{0.7}\text{Li}_{0.3}\text{V}_2\text{O}_5$  was greatly reduced even at low-temperature range by applying pressure. © 2001 Elsevier Science B.V. All rights reserved.

**Keywords:** Spin ladder; Metal–insulator transition; Pressure

## 1. Introduction

Great attention has been paid to the so-called spin-ladder materials. While several cuprate high- $T_C$  superconductors have been found out, discovery of new superconducting materials is strongly desired to elucidate the high- $T_C$  mechanism and find out new superconductors having higher  $T_C$ . In such an investigation spin-ladder materials were thought to be good candidates as new superconducting systems. Spin-gap behavior which is one of the characteristic properties of cuprate superconductors was theoretically predicted [1,2] and later observed in even-leg spin-ladder materials such as  $\text{SrCu}_2\text{O}_3$  [3,4].  $\text{Sr}_{14-x}\text{Ca}_x\text{Cu}_{24}\text{O}_{41}$  has also been studied as a spin-ladder material; its electrical resistivity is greatly reduced by substituting Ca for Sr showing semiconducting behavior over the entire composition

ranges. However, insulator–metal transition occurs under high pressure. In addition to the insulator–metal transition, superconductivity was discovered at pressure larger than 4 GPa [5] with  $T_C$  increasing up to 12 K at 6 GPa. The effect of high pressure seems to play an important role for the delocalization of carriers in the ladder layer. Although the characterization of this superconductivity is difficult due to the necessity of a high-pressure technique, a recent advanced high-pressure technique revealed the magnetic properties of this superconducting material [6].

Recently, doping effects on vanadate spin-ladder materials have been intensively investigated in relation to low-dimensional magnetic and electronic properties [7,8]: spin-gap behavior has been reported in  $\text{CaV}_2\text{O}_5$  [9], and substitution of Na for Ca has been achieved, leading to a greatly reduced electrical resistivity in the  $\text{Na}_{1-x}\text{Ca}_x\text{V}_2\text{O}_5$  system [10,11]. However, they show semiconducting behavior over the entire substitution range. Hence, high-pressure techniques are expected to be a powerful tool to study metallization in this system. Here we report the pressure effects on the electrical

\* Corresponding author. Fax: + 81-3-5317-9432.

E-mail address: hiroki@chs.nihon-u.ac.jp (H. Takahashi).

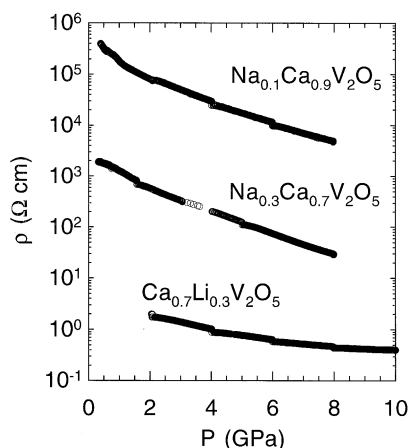


Fig. 1. Pressure dependence of the electrical resistivity for  $\text{Na}_{0.1}\text{Ca}_{0.9}\text{V}_2\text{O}_5$ ,  $\text{Na}_{0.3}\text{Ca}_{0.7}\text{V}_2\text{O}_5$ , and  $\text{Ca}_{0.7}\text{Li}_{0.3}\text{V}_2\text{O}_5$ .

resistivity of this system and lately synthesized  $\text{Ca}_{0.7}\text{Li}_{0.3}\text{V}_2\text{O}_5$ . The electrical resistivity of  $\text{Ca}_{0.7}\text{Li}_{0.3}\text{V}_2\text{O}_5$  is much smaller than that for the  $\text{Ca}_{1-x}\text{Na}_x\text{V}_2\text{O}_5$  system.

Polycrystalline samples of  $\text{Na}_{1-x}\text{Ca}_x\text{V}_2\text{O}_5$  and  $\text{Ca}_{0.7}\text{Li}_{0.3}\text{V}_2\text{O}_5$  have been synthesized under high-pressure conditions. The lattice constants along the  $a$  and  $b$ -axis remain almost constant with changing  $x$ , while the one along the  $c$ -axis decreases with decreasing  $x$ . Details of sample preparations are described elsewhere [10,11]. Electrical resistivity measurements were carried out under high pressures at low temperature by means of a DC four-probe technique. A cubic-anvil apparatus was used to generate hydrostatic pressures up to 10 GPa at temperatures down to 4 K. During these measurements the

pressure was controlled to be kept constant on both cooling and heating processes.

Fig. 1 shows the pressure dependence of the electrical resistivity at room temperature for  $\text{Na}_{0.1}\text{Ca}_{0.9}\text{V}_2\text{O}_5$ ,  $\text{Na}_{0.3}\text{Ca}_{0.7}\text{V}_2\text{O}_5$ , and  $\text{Ca}_{0.7}\text{Li}_{0.3}\text{V}_2\text{O}_5$ . The electrical resistivity is greatly reduced under high pressure for each material, as shown in Fig. 1. While the electrical resistivities of  $\text{Na}_{0.1}\text{Ca}_{0.9}\text{V}_2\text{O}_5$  and  $\text{Na}_{0.3}\text{Ca}_{0.7}\text{V}_2\text{O}_5$  decrease to  $\frac{1}{100}$  the value at 8 GPa compared with the one at 1 atm, the electrical resistivity of  $\text{Ca}_{0.7}\text{Li}_{0.3}\text{V}_2\text{O}_5$  decreases to  $\frac{1}{2}$  the value at 10 GPa. Figs. 2(a) and (b) show the temperature dependence of the electrical resistivity at several constant pressures for  $\text{Na}_{0.1}\text{Ca}_{0.9}\text{V}_2\text{O}_5$  and  $\text{Ca}_{0.7}\text{Li}_{0.3}\text{V}_2\text{O}_5$ , respectively. From Fig. 2(a) the electrical resistivity of  $\text{Na}_{0.1}\text{Ca}_{0.9}\text{V}_2\text{O}_5$  decreases with pressure and the shape of the  $\rho(T)$  curve does not change significantly up to the maximum pressure. On the other hand, it is observed from Fig. 2(b) that the electrical resistivity of  $\text{Ca}_{0.7}\text{Li}_{0.3}\text{V}_2\text{O}_5$  decreases with pressure especially in the low-temperature range. However, the electrical resistivity still displays semiconducting behavior even at the maximum pressure of 10 GPa.

In spin-ladder materials it is thought that the conduction of carriers occurs through the ladder layer. All these experiments make it clear that the pressure plays an important role in delocalizing carriers in the ladder layer, which is similar to the pressure effect observed in the  $\text{Sr}_{14-x}\text{Ca}_x\text{Cu}_{24}\text{O}_{41}$  system. From Fig. 1 the lowest resistivity for  $\text{Ca}_{0.7}\text{Li}_{0.3}\text{V}_2\text{O}_5$  is  $4 \times 10^{-1} \Omega \text{ cm}$  at 300 K and 10 GPa. In the superconducting  $\text{Sr}_{2.5}\text{Ca}_{11.5}\text{Cu}_{24}\text{O}_{41}$  spin-ladder system, the electrical resistivity is about  $4 \times 10^{-4} \Omega \text{ cm}$  at 300 K and 3 GPa [12]. The electrical resistivity in usual high- $T_C$  superconductors is less than  $1 \times 10^{-3} \Omega \text{ cm}$  at 300 K. Thus, further carrier doping and/or applying higher pressure are thought to be necessary to give rise to the insulator–metal transition in this

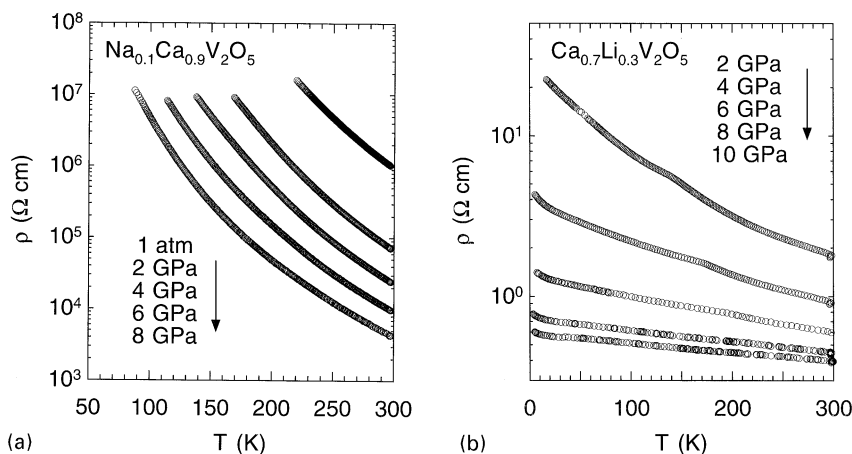


Fig. 2. Temperature dependence of the electrical resistivity for (a)  $\text{Na}_{0.1}\text{Ca}_{0.9}\text{V}_2\text{O}_5$  and (b)  $\text{Ca}_{0.7}\text{Li}_{0.3}\text{V}_2\text{O}_5$  measured at constant pressures, respectively.

system. Superconductivity is also expected in such a metallic phase.

This work was partly supported by Grant-in-Aid Nos. 10440114 and 11554015 from the Ministry of Education, Science and Culture of Japan.

## References

- [1] E. Dagotto, J. Riera, D. Scalapino, *Phys. Rev. B* 45 (1992) 5744.
- [2] T.M. Rice, S. Gopalan, M. Sigrist, *Europhys. Lett.* 23 (1993) 445.
- [3] M. Azuma, Z. Hiroi, M. Takano, K. Ishida, Y. Kitaoka, *Phys. Rev. Lett.* 73 (1994) 3463.
- [4] K. Ishida, Y. Kitaoka, K. Asayama, M. Azuma, Z. Hiroi, M. Takano, *J. Phys. Soc. Japan* 63 (1994) 3222.
- [5] M. Uehara, T. Nagata, J. Akimitsu, H. Takahashi, N. Môri, K. Kinoshita, *J. Phys. Soc. Japan* 65 (1996) 3764.
- [6] T. Nakanishi, N. Motoyama, H. Mitamura, N. Takeshita, H. Takahashi, H. Eisaki, S. Uchida, T. Goto, H. Ishimoto and N. Môri, in this volume.
- [7] H. Iwase, M. Isobe, Y. Ueda, H. Yasuoka, *J. Phys. Soc. Japan* 65 (1996) 2397.
- [8] M. Onoda, N. Nishiguchi, *J. Solid State Chem.* 127 (1996) 359.
- [9] M. Isobe, Y. Ueda, *J. Magn. Magn. Mat.* 177–181 (1998) 671.
- [10] P.N. Rogers, R.N. Shelton, *Solid State Commun.* 114 (2000) 607.
- [11] T. Arima and M. Noguchi, private communication.
- [12] T. Nagata, M. Uehara, J. Goto, J. Akimitsu, N. Motoyama, H. Eisaki, S. Uchida, H. Takahashi, T. Nakanishi, N. Môri, *Phys. Rev. Lett.* 81 (1998) 1090.

**Pressure-induced semiconductor-metal-semiconductor transitions in FeS**

Hisao Kobayashi\*

*Department of Physics, Tohoku University, Sendai 980-8578, Japan*

Nao Takeshita and Nobuo Mōri

*Institute for Solid State Physics, The University of Tokyo, Chiba 277-8581, Japan*

Hiroki Takahashi

*College of Humanities and Sciences, Nihon University, Tokyo 156-8550, Japan*

Takashi Kamimura

*Department of Physics, Tohoku University, Sendai 980-8578, Japan*

(Received 11 July 2000; published 1 March 2001)

The semiconductor-metal-semiconductor transitions in stoichiometric FeS compounds were observed under nearly hydrostatic pressure condition up to 8 GPa and a temperature down to 4 K. In the low-pressure semiconductor state, the energy gap caused by the electron correlation decreases with a volume reduction. On the other hand, FeS in a high-pressure semiconductor state is a band insulator and the energy gap increases with pressure when the gap is formed between the occupied nonbonding and unoccupied antibonding bands. In the metallic phase at intermediate pressure range FeS can be regarded as a strongly correlated metal because of the large quadratic temperature dependence of resistivity at low temperature.

DOI: 10.1103/PhysRevB.63.115203

PACS number(s): 71.30.+h, 62.50.+p

**I. INTRODUCTION**

It is well known that the electron correlation plays an important role in 3*d* transition-metal compounds since conventional one-electron band-structure calculations do not explain some of the experimental results in many of these compounds. Accordingly, there is a tendency for 3*d* electrons to be localized in these compounds and then systems become antiferromagnetic insulators. The electronic properties of these compounds have been renewed as interesting subjects since the discovery of high- $T_c$  superconductors because the parent compounds are antiferromagnetic insulators. One of the interesting properties in these compounds is an insulator-metal transition. Recently Zaanen, Sawatzky, and Allen (ZSA) have developed a general framework for these compounds using the three-band Hubbard model.<sup>1</sup> The ligand-to-metal charge-transfer energy  $\Delta$  and the ligand-to-metal hybridization interaction  $t_{pd}$ , as well as the *d-d* Coulomb interaction  $U$  are explicitly included as parameters in their model Hamiltonian.

The possible ground states of transition-metal compounds can be classified into four regimes based on the relative magnitudes of  $\Delta$ ,  $U$ , and the bandwidth  $W$  according to the ZSA scheme. In the Mott-Hubbard regime for  $U < \Delta$ , there are an insulating state with a gap due to  $U$  for  $U > W$  and a *d*-type metallic state for  $U < W$  where both holes and electrons are in the *d* bands. On the other hand, for  $U > \Delta$ , compounds become the charge-transfer insulators if  $\Delta > W$  and *p*-type metals if  $\Delta < W$  where holes are in the anion valence band. Although the character of elements in these compounds is dominant in these high-energy-scale charge fluctuations, this ZSA scheme has been successful to describe the ground-state properties of these compounds. Since pressure can change a bond length as well as a bond angle, these parameters such as

$\Delta$ ,  $U$  and  $W$  can be varied much larger by pressure than by temperature and magnetic field. Thus there is great interest to study pressure-induced phase transitions in these compounds.

In 3*d* transition-metal chalcogenides the ligand-to-metal hybridization interaction generally becomes stronger than that in oxides because of the large covalency between the transition-metal *d* orbitals and the anion *p* orbitals. At the ambient conditions, stoichiometric FeS has the troilite crystal structure that is closely related to a NiAs type and is an antiferromagnetic semiconductor with  $T_N = 589$  K. The phase transition from the troilite to NiAs type structures occurs at about 420 K.<sup>2,3</sup> FeS is believed to belong to the intermediate regime, where  $\Delta \leq U$  and  $U$  is not so large.<sup>4,5</sup> As indicated by high-pressure x-ray diffraction measurements,<sup>6-9</sup> it undergoes two successive first-order phase transitions with increasing pressure at room temperature. The first transition occurs at 3.5 GPa and the structure transforms to a MnP type. The second transition takes place at 6.5 GPa with about 7% volume reduction. The structure above 6.5 GPa was determined to have a monoclinic unit cell with space group  $P2_1/a$ .<sup>10</sup>

The previous high-pressure resistance measurement<sup>11</sup> indicated that FeS shows a slight increase in resistance with temperature above 8 GPa. On the other hand, recently non-metallic behaviors in resistance were observed at 6 and 10 GPa down to about 80 K.<sup>12</sup> The measurement of <sup>57</sup>Fe Mössbauer spectra was carried out under pressure up to about 15 GPa.<sup>13</sup> It was found that the significant change in volume dependence of the center shift occurs around 6.5 GPa. This result indicates a distinct change of the 3*d* electron configuration on Fe ion at the second phase transition. Recently, the Mössbauer study showed the nonmagnetic quadrupole spectrum down to 5 K at 12 GPa and the x-ray emission experi-

ments under pressure observed the pressure-induced reduction of the satellite amplitude in these spectra around 6.3 GPa.<sup>12,14</sup> These results strongly suggest that this second phase transition is the high-spin to low-spin transition in the  $\text{Fe}^{2+}$  ion.

It was indicated that FeS belongs to the boundary between the charge-transfer and Mott-Hubbard insulators in the ZSA scheme.<sup>1,4</sup> Its pressure-induced phase transitions have been very controversial since the two successive structural phase transitions were observed. The electrical resistivity of stoichiometric FeS compound was measured under hydrostatic pressure up to 8 GPa in the temperature range from 4 K to room temperature. We report evidence of pressure-induced semiconductor-metal-semiconductor transitions in FeS and discuss the electronic properties in each phase from the temperature dependence of resistivity.

## II. EXPERIMENT

Polycrystalline samples were prepared using the following procedure. Appropriate amounts of starting materials Fe (99.998% purity) and S (99.9999% purity) were sealed in an evacuated silica tube and then were heated to 900 °C for several days; the product was ground in an Ar atmosphere and kept at 900 °C for further several days. Sulfur vapor reacted to the iron block completely during these processes. The almost stoichiometric FeS compound was produced by slow cool from 800 °C. The obtained sample was analyzed by the x-ray diffraction using  $\text{Cu } K\alpha$  radiation and was confirmed to be in single phase with the troilite structure. The estimated lattice parameters,  $a$  and  $c$ , are  $(5.965 \pm 0.001)$  and  $(11.757 \pm 0.002)$  Å, respectively. Iron sulfide,  $\text{Fe}_{1-x}\text{S}$ , has a substantial deficiency at the iron sites in the range  $0 \leq x \leq 0.15$ . The obtained sample has a purely stoichiometric composition with experimental accuracy as determined using the empirical relation for the concentration of Fe in  $\text{Fe}_{1-x}\text{S}$  vs the (102) interplanar spacing with the NiAs-type structure,<sup>15</sup> which corresponds to the (114) interplanar spacing with the troilite structure.

A cubic-anvil type apparatus was used to measure the electrical resistance under pressure up to 8 GPa at temperature down to 4 K.<sup>16</sup> The force applied to the apparatus was controlled to keep constant during measurements; these measurements were always performed at constant pressure. Pressure was retained nearly hydrostatic in a Teflon cell filled with Fluorinert as a pressure-transmitting medium. Pressure was calibrated by a measurement of resistance of Bi metal under applied force at room temperature. The electrical resistance under high pressure was measured by a standard dc four-probe technique. Gold wires of 20  $\mu\text{m}$  in diameter were used as electrical leads with silver paint contact on the surface of sample. The typical size of sample under pressure is about  $0.7 \times 0.3 \times 0.3 \text{ mm}^3$ . The temperature dependence of resistance was measured with increasing temperature at various pressures and the pressure was always increased at room temperature. All resistance data were obtained in the Ohmic relation between applied current and observed voltage. The absolute accuracy of resistivity under pressure is limited because of the uncertainties in determinations of length be-

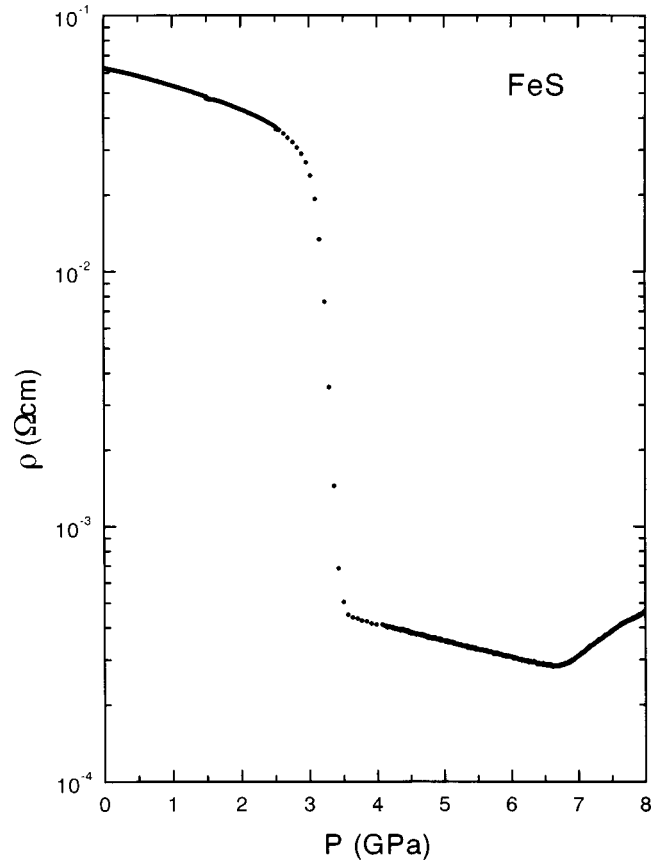


FIG. 1. Pressure dependence of resistivity  $\rho$  in stoichiometric FeS compound at room temperature.

tween the electrical leads and area perpendicular to the current. Then the obtained resistance data under pressure were normalized to the absolute resistivity determined at the ambient conditions although the estimated resistivity in the cubic-anvil type apparatus at the ambient conditions is roughly consistent with the absolute one.

## III. EXPERIMENTAL RESULTS

Figure 1 shows the room temperature electrical resistivity,  $\rho$ , of FeS as a function of pressure. Initially the  $\rho$  value decreases exponentially with increasing pressure up to 2.5 GPa and abruptly decreases around 3.5 GPa. Furthermore,  $\rho$  decreases up to 6.6 GPa and then increases with increasing pressure. These two anomalies in pressure dependence of  $\rho$  indicate the occurrence of two successive phase transitions and these transition pressures are consistent with those of the structural phase transitions.<sup>6,10</sup> Although the phase transition at 6.6 GPa is a first order one with about 7% volume reduction, the pressure dependence of  $\rho$  varies with no discontinuity around 6.6 GPa and there is no observable hysteresis with pressure. The about two orders decrease of magnitude in  $\rho$  around 3.5 GPa suggests that a activation energy in  $\rho$  should go to zero. From now on, we call the phases below 3.5 GPa, between 3.5 and 6.6 GPa, and above 6.6 GPa as phases I, II, and III, respectively.

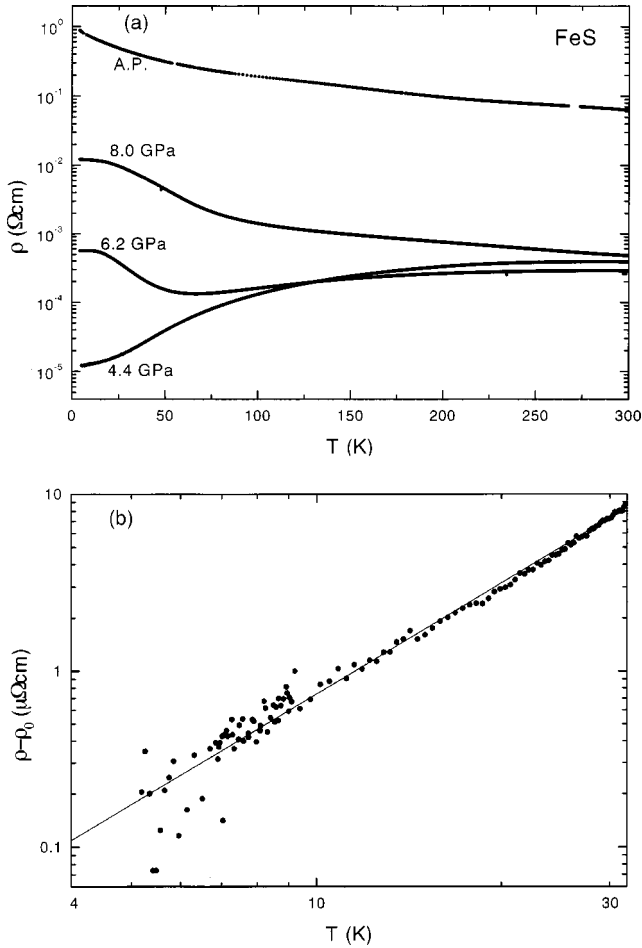


FIG. 2. Typical temperature dependencies of resistivity  $\rho$  in stoichiometric FeS compound at various pressure (a) and a plot of  $(\rho - \rho_0)$  vs  $T$  at 4.4 GPa as logarithmic scales, (b) where  $\rho_0$  is the residual resistivity. The solid line represents the result of fitting.

Figure 2(a) shows the typical temperature dependencies of  $\rho$  at various pressure. As seen in this figure, the resistivity exhibits nonmetallic behavior below 3 GPa, where a temperature coefficient of  $\rho$  is negative in the whole observed temperature range. Although there are some tendencies for  $\rho$  to saturate at low temperature, the resistivity exhibits activated behavior above 150 K, which is referred to as the intrinsic property. Since the electronic contribution in low-temperature specific heat of FeS is almost zero at ambient pressure,<sup>17</sup> the ground state has an insulating character. Thus the value of activation energy  $E_a$  is estimated from the resistivity curves in the intrinsic temperature region by the equation

$$\rho = \rho_\infty \exp(E_a/2k_B T), \quad (1)$$

where  $\rho_\infty$  is the high-temperature resistivity and  $k_B$  is the Boltzmann's constant.

The  $E_a$  values estimated by this way are shown in Fig. 3 as a function of pressure. The  $E_a$  value at ambient pressure ( $38.9 \pm 0.1$ ) meV, is in good agreement with the value 40 meV determined previously by measurements of resistivity

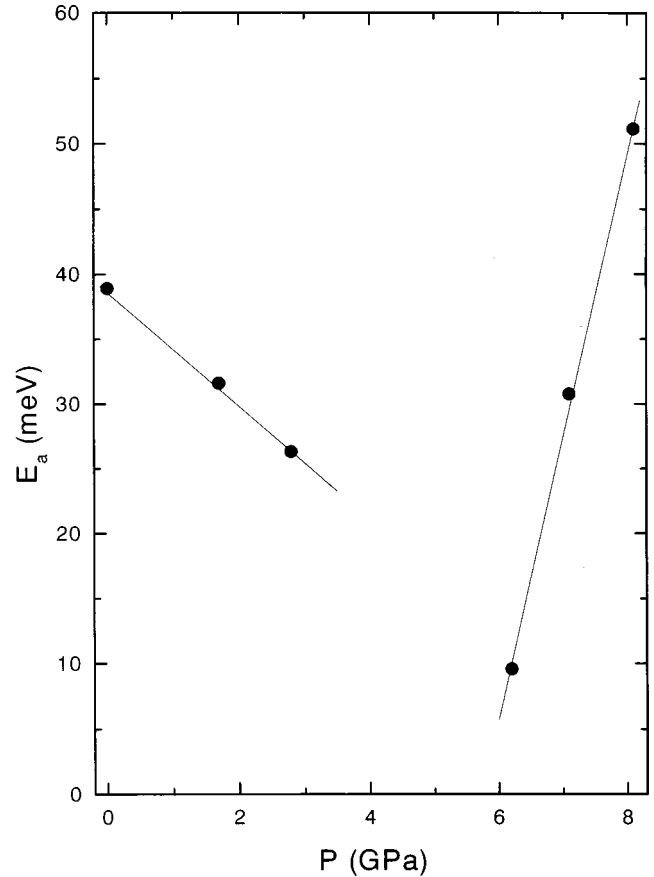


FIG. 3. Pressure dependence of the activation energy  $E_a$  in the semiconductor states of FeS. The solid lines represent the results of fitting.

on a single crystal  $\text{Fe}_{0.996}\text{S}$ .<sup>3</sup> Since the  $E_a$  value decreases with pressure, we obtained a linear fit of the form

$$E_a = (39.0 \pm 0.3) - (4.5 \pm 0.2)P(\text{GPa}) \text{ meV} \quad (2)$$

within the accuracy of the data. The critical pressure is evaluated to be  $(8.7 \pm 0.1)$  GPa by extrapolating  $E_a$  to zero, a value that is much higher than the critical pressure, 3.5 GPa, at room temperature.

As seen in Fig. 2(a), the temperature dependence of  $\rho$  at 4.4 GPa clearly shows a metallic behavior down to 4 K. Accordingly the anomaly in pressure dependence of  $\rho$  around 3.5 GPa at room temperature corresponds to a pressure-induced semiconductor-metal transition in FeS. The residual resistivity  $\rho_0$  is  $11.90 \mu\Omega \text{ cm}$  and the residual resistivity ratio is 32 at 4.4 GPa. These values are comparable with those of pressure induced metallic state of  $\text{V}_2\text{O}_3$ .<sup>18</sup> The  $\rho_0$  value is much smaller than those of metallic states in carrier-doped systems.<sup>19</sup> The temperature dependence of  $\rho$  is markedly different from a usual metal. Figure 2(b) shows a plot of  $(\rho - \rho_0)$  vs  $T$  at 4.4 GPa as logarithmic scales. Experimental results indicate a relation  $(\rho - \rho_0) \propto T^\nu$ , and the  $\nu$  value is estimated to be  $(2.09 \pm 0.05)$  at 4.4 GPa. This nearly quadratic temperature dependence of  $\rho$  implies that the electron-electron collision is an important effect in low-temperature resistivity in phase II. It was found that  $\rho$  is

almost independent of temperature above 270 K. The similar tendency for resistivity to saturate was observed above 300 K in the metallic state of  $V_2O_3$ .<sup>18</sup>

Further increasing pressure above 6.6 GPa, the temperature dependence of  $\rho$  shows nonmetallic behavior again as seen in Fig. 2(a). This result is consistent with that of the recent resistance measurement at 10 GPa down to about 80 K.<sup>12</sup> In our previous paper,<sup>13</sup> we proposed the nonmagnetically metallic state of FeS in this phase. However, our proposed electronic state is inconsistent with the present result of  $\rho$ . The anomaly in pressure dependence of  $\rho$  around 6.6 GPa at room temperature, thus, indicate a re-entrant metal-semiconductor transition. As observed in phase I, there are similar tendencies for  $\rho$  to saturate at low temperature. However,  $\rho$  exhibits activated behavior above 200 K. Thus the  $E_a$  value is estimated from the resistivity curves in the intrinsic temperature region using Eq. (1). As shown in Fig. 2(a), significant anomaly is found at 55 K in the temperature dependence of  $\rho$  at 6.2 GPa. At higher temperature  $\rho$  behaves like metallic and at lower temperature  $\rho$  nonmetallic. Accordingly the  $E_a$  value at 6.2 GPa is estimated in the temperature between 30 and 50 K. The obtained  $E_a$  values are also shown in Fig. 3 as a function of pressure. In contrast with the pressure dependence of  $E_a$  in phase I, it is found that  $E_a$  increases with pressure in phase III. Within the accuracy of the data, we also obtained linear fit of the form

$$E_a = (-125 \pm 6) + (21.8 \pm 0.5)P \text{ (GPa)} \text{ meV.} \quad (3)$$

If  $\rho_\infty$  in Eq. (1) is assumed to be independent of pressure and  $E_a = \alpha(P - P_c)$ , the resistivity would increase exponentially with pressure. It is noted that  $\alpha$  as determined from the slope of  $\rho$  at room temperature for  $P \geq 6.8$  GPa is 20.4 meV/GPa in good agreement with  $dE_a/dP$  determined from Eq. (3).

#### IV. DISCUSSION

As shown in Fig. 3, it seems that  $E_a$  depends linearly on pressure in phase I. However, the critical pressure 8.7 GPa, determined from Eq. (2), is much higher than 3.5 GPa where pressure dependence of  $\rho$  shows anomaly at room temperature. According to the ZSA scheme, the pressure dependence of gap in electronic structure is related to the pressure dependence of  $U$  or  $\Delta$ ,  $W$ , and the hybridization of the electron configurations. These values do not depend directly on pressure but on a bond length as well as bond angle. From the pressure dependence of volume<sup>6,7</sup> and Eq. (2), we approximately obtained a linear dependence of  $E_a$  on the volume with the form

$$E_a = (38.8 \pm 0.1) - (335 \pm 4)\Delta V/V_0 \text{ meV,} \quad (4)$$

where  $\Delta V/V_0 = [V(0) - V(P)]/V(0)$ . The critical value of  $\Delta V/V_0$  is estimated to be  $(0.11 \pm 0.01)$ , which corresponds to be the volume of phase II with MnP-type structure. Thus it is suggested that the volume reduction induced by pressure in phase II is sufficient to close the gap caused by the electronic correlation in phase I.

It is confirmed that the semiconductor-metal transition takes place at around 3.5 GPa in FeS. At least, the structure

of FeS transforms from the troilite to the MnP-type with this transition at room temperature. Thus, this transition is possibly caused by the electronic correlation and/or electron-phonon coupling. First we will discuss a distortion in the  $FeS_6$  octahedra with this structural transition. The  $FeS_6$  octahedra in the troilite structure with hexagonal symmetry have more complex distortion than the trigonal one from  $O_h$  symmetry. A quantitative measure of distortion in octahedra is given by a quadratic elongation,  $\lambda$ , and an octahedral angle,  $\sigma_\theta^2$ , which are linearly correlated.<sup>20</sup> The mean values of  $\lambda$  and  $\sigma_\theta^2$  are defined as

$$\bar{\lambda} = \sum_{i=1}^6 \left( \frac{l_i}{l_0} \right)^2 / 6 \quad (5)$$

and

$$\bar{\sigma}_\theta^2 = \sum_{i=1}^{12} (\theta_i - 90^\circ)^2 / 11, \quad (6)$$

respectively, where  $l_0$  is the center-to-vertex distance for an octahedron with  $O_h$  symmetry whose volume is equal that of the distorted octahedron with bond lengths  $l_i$ , and  $\theta_i$  are bond angles. At the ambient conditions,  $\bar{\lambda} = 1.019$  and  $\bar{\sigma}_\theta^2 = 59.92$  of the  $FeS_6$  octahedra with the troilite structure.<sup>6</sup> Although the MnP-type structure has an orthorhombic symmetry, the value of  $\delta (= c/\sqrt{3}b - 1)$ , which is a measure of orthorhombic distortion from the hexagonal symmetry, is evaluated to be just 0.7% in phase II. In 3d-monopnictides with the MnP-type structure,<sup>21</sup> these  $\delta$  values are about 7%, which are 10 times larger than that in phase II. Thus the  $b$ - $c$  plane has the pseudo-hexagonal cell matrix in phase II. At 6.3 GPa and room temperature,  $\bar{\lambda} = 1.018$  and  $\bar{\sigma}_\theta^2 = 63.04$ , which are comparable to those in phase I. Consequently, the distortion of the Fe atom's coordination polyhedra does not essentially change at this structural phase transition.

Next we will discuss the electronic states of Fe ion in phases I and II. It was found by Mössbauer spectroscopy under pressure<sup>12,13</sup> that the Fe state in FeS has divalent with high-spin configuration up to 6.3 GPa. Recently this result is confirmed by x-ray emission spectroscopy under pressure where well-defined satellite below 13 eV from the main peak was observed in the emission spectra up to 6.3 GPa.<sup>14</sup> Since the center shift of Fe in FeS decreases linearly with decreasing volume up to 6.3 GPa, there is no discontinuous charge transfer between Fe and S ions at the semiconductor-metal transition. Therefore the electronic correlation plays an important role in this pressure-induced collapse of energy gap in spite of the structural transformation. It is noticed that there is antiferromagnetic order in FeS up to 6.6 GPa at room temperature.<sup>12,13,22</sup>

The temperature dependence of  $\rho$  in phase II is well characterized with the relation,  $\rho = \rho_0 + AT^2$ , at least up to 30 K. The coefficient  $A$  was obtained to be  $(7.52 \pm 0.02) \times 10^{-3}$  and  $(5.4 \pm 0.3) \times 10^{-3} \mu\Omega \text{ cm/K}^2$  at 4.4 and 5.5 GPa, respectively, by the least-squares fitting in the temperature range between 4 and 25 K. These values are about 500 times larger than the typical values of transition metals<sup>23</sup> and comparable

with those of the highly correlated electron systems.<sup>18,19</sup> This large  $A$  value suggests that the electronic state in phase II is a highly correlated metal. The pressure-induced decrease in  $A$  is attributed to the decrease of the electron correlation because  $W$  increases with pressure and  $U$  decreases because of increasing a screening effect.

At higher temperature in phase II,  $\rho$  linearly increases from 80 K and is almost independent of temperature above 270 K. It seems that the tendencies for  $\rho$  to saturate in the metallic  $V_2O_3$  above 300 K are caused by the strongly electron-electron scattering effect because the large  $A$  value was observed. In normal metals, the characteristic temperature of flattening in resistivity is an order of the Fermi energy. However, the large enhancement of effective mass due to the correlation in metal decreases this characteristic temperature. If we regard the flattening in  $\rho$  of FeS as the effect of large mass enhancement, the characteristic temperature is evaluated to be an order of room temperature. This evaluated characteristic temperature is probably too low because the  $A$  values in FeS are five times smaller than those in the metallic  $V_2O_3$ . Thus, whether the observed anomaly in  $\rho$  of metallic FeS at high temperature is coupled with the highly correlated metal state is still an open question for experiment.

It was found by the present electronic measurements that the phase III shows nonmetallic behavior down to 4 K. The estimated  $E_a$  value increases with pressure at the rate of 21.8 meV/GPa in phase III, while  $E_a$  decreases with pressure in phase I. This increment of  $E_a$  with pressure cannot be expected for the insulators where the electronic correlation causes to open up a gap in electronic structure. Accordingly, phase III is most likely to be a band insulator rather than the Mott-Hubbard or charge-transfer insulator.

This nonmetallic behavior is consistent with the results of previous and recent Mössbauer and x-ray emission measurements where the Fe state in this phase is suggested to have the low-spin Fe(II) state.<sup>12,14</sup> Even though the lower local symmetry and the probability of covalent bonding complicate the situation in FeS, the large volume reduction at this phase transition suggests that not only the bandwidth but also the hybridization of the electron configurations is increased.

These increments with the compression would induce the high-spin to low-spin transition in the  $Fe^{2+}$  ion as observed in the system  $FeS_2$ - $MnS_2$ .<sup>24,25</sup>

Although the local symmetries at Fe sites in this phase are more distorted from  $O_h$  symmetry than those in phases I and II, the orbitals of Fe  $3d$  with an  $e_g$  doublet character would have a large overlap with the S  $3p$  orbitals. This  $\sigma$ -type overlap forms the antibonding state with highest energy and the bonding state with lowest energy around the Fermi level where the former is predominantly of Fe  $3d$  character and the later predominantly of S  $3p$  character. Therefore, the low-spin Fe(II) state in FeS consists of the occupied nonbonding band with a mainly  $t_{2g}$  triplet character where degeneracy is lifted by the distortion and the unoccupied antibonding band. Since the increment of  $E_a$  with pressure was observed in this phase, the gap between the nonbonding and antibonding bands increases more rapidly with the pressure-induced overlap than the bandwidth.

## V. CONCLUSION

We have measured the electrical resistivity of stoichiometric FeS compound under pressure. It was found that the semiconductor-metal and metal-semiconductor transitions occur at 3.5 and 6.6 GPa, respectively. In phase I,  $E_a$  decreases linearly with  $\Delta V/V_0$  and the estimated critical  $\Delta V/V_0$  value corresponds to be the volume of phase II with the MnP-type structure. The volume reduction induced by pressure in phase II is sufficient to close the gap caused by the electronic correlation in phase I. On the other hand,  $E_a$  increases with pressure and then phase III is most likely to be a band insulator. As result of the large volume reduction in phase III, the Fe state changes from the high-spin to low-spin Fe(II) state and the electronic structure consists of the occupied nonbonding and unoccupied antibonding bands around the Fermi level. In phase II, the resistivity rises quadratically with temperature at low temperature. It was found that the  $A$  values are much larger than the typical values of transition metals. This large  $A$  value suggests that the electronic state in phase II is a highly correlated metal.

\*Email: kobayash@nuclear.phys.tohoku.ac.jp

- <sup>1</sup>J. Zaanen, G. A. Sawatzky, and J. W. Allen, Phys. Rev. Lett. **55**, 418 (1985).
- <sup>2</sup>J. L. Horwood, M. G. Townsend, and A. H. Webster, J. Solid State Chem. **17**, 35 (1976).
- <sup>3</sup>J. R. Gosselin, M. G. Townsend, and R. J. Tremblay, Solid State Commun. **19**, 799 (1976).
- <sup>4</sup>J. Zaanen, G. A. Sawatzky, and J. W. Allen, J. Magn. Magn. Mater. **54-57**, 607 (1986).
- <sup>5</sup>K. Shimada, T. Mizokawa, K. Mamiya, T. Saitoh, A. Fujimori, K. Ono, A. Kakizaki, T. Ishii, M. Shirai, and T. Kamimura, Phys. Rev. B **57**, 8845 (1998).
- <sup>6</sup>H. E. King, Jr. and C. T. Prewitt, Acta Crystallogr., Sect. B: Struct. Crystallogr. Cryst. Chem. **38**, 1877 (1982).
- <sup>7</sup>T. Kamimura, M. Sato, H. Takahashi, N. Mōri, H. Yoshida, and T. Kaneko, J. Magn. Magn. Mater. **104-107**, 255 (1992).
- <sup>8</sup>Y. Fei, C. T. Prewitt, H. K. Mao, and C. M. Bertka, Science **268**,

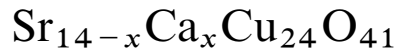
1892 (1995).

- <sup>9</sup>K. Kusaba, Y. Syono, T. Kikegawa, and O. Shimomura, J. Phys. Chem. Solids **58**, 241 (1997).
- <sup>10</sup>R. J. Nelmes, M. I. McMahon, S. A. Belmonte, and J. B. Parise, Phys. Rev. B **59**, 9048 (1999).
- <sup>11</sup>S. Minomura and H. G. Drickamer, J. Appl. Phys. **34**, 3043 (1963).
- <sup>12</sup>S. Takele and G. R. Hearne, Phys. Rev. B **60**, 4401 (1999).
- <sup>13</sup>H. Kobayashi, M. Sato, T. Kamimura, M. Sakai, H. Onodera, N. Kuroda, and Y. Yamaguchi, J. Phys.: Condens. Matter **9**, 515 (1997).
- <sup>14</sup>J. P. Rueff, C. C. Kao, V. V. Struzhkin, J. Badro, J. Shu, R. J. Hemley, and H. K. Mao, Phys. Rev. Lett. **82**, 3284 (1999).
- <sup>15</sup>P. T. Toulmin and P. B. Barton, Geochim. Cosmochim. Acta **28**, 641 (1964).
- <sup>16</sup>N. Mōri, Y. Okayama, H. Takashi, Y. Haga, and T. Suzuki, Jpn. J. Appl. Phys. Series **8**, 182 (1993).

- <sup>17</sup>H. Kobayashi, T. Nozue, T. Matsumura, T. Suzuki, and T. Kamimura, *J. Phys.: Condens. Matter* **11**, 8673 (1999).
- <sup>18</sup>D. B. McWhan and T. M. Rice, *Phys. Rev. Lett.* **22**, 887 (1969).
- <sup>19</sup>Y. Tokura, Y. Taniguchi, Y. Okada, Y. Fujishima, T. Arima, K. Kumagai, and Y. Iye, *Phys. Rev. Lett.* **70**, 2126 (1993).
- <sup>20</sup>K. Robinson, G. V. Gibbs, and P. H. Ribbe, *Science* **172**, 567 (1971).
- <sup>21</sup>K. Adach and S. Ogawa, *Landolt-Börnstein* (Springer-Verlag, Berlin, 1990), Vol. III/27a.
- <sup>22</sup>W. G. Marshall, R. J. Nelmes, J. S. Loveday, S. Klotz, J. M. Besson, G. Hamel, and J. B. Parise, *Phys. Rev. B* **61**, 11 201 (2000).
- <sup>23</sup>K. Miyake, T. Matsuura, and C. M. Varma, *Solid State Commun.* **71**, 1149 (1989), and references therein.
- <sup>24</sup>R. C. Cohen, I. I. Mazin, and D. G. Isaak, *Science* **172**, 567 (1971).
- <sup>25</sup>C. B. Barger, M. Avinor, and H. G. Drickamer, *Inorg. Chem.* **10**, 1338 (1971).



# Anisotropy of the upper critical field of the spin-ladder



T. Nakanishi<sup>a,b,\*</sup>, N. Motoyama<sup>c</sup>, H. Mitamura<sup>a</sup>, N. Takeshita<sup>a</sup>, H. Takahashi<sup>b</sup>,  
H. Eisaki<sup>c</sup>, S. Uchida<sup>c</sup>, T. Goto<sup>a</sup>, H. Ishimoto<sup>a</sup>, N. Môri<sup>a</sup>

<sup>a</sup>*Institute for Solid State Physics, University of Tokyo, Kashiwa-shi, Chiba 277-8581, Japan*

<sup>b</sup>*Department of Physics, College of Humanities and Sciences, Nihon University, 3-25-40 Sakurajosui, Setagaya-ku, Tokyo 156-8550, Japan*

<sup>c</sup>*Department of Superconductivity, University of Tokyo, Tokyo 113-8656, Japan*

## Abstract

We report on the resistive upper critical field,  $H_{c2}(T)$  for the hole-doped two-leg ladder  $\text{Sr}_{14-x}\text{Ca}_x\text{Cu}_{24}\text{O}_{41}$  ( $x = 12$ ) single crystal, which becomes superconducting with  $T_c \sim 5$  K in a pressure above  $\sim 3.0$  GPa. From the results of magneto-transport measurements on a single sample at a pressure of 3.5 GPa,  $H_{c2}(T)$  has been determined up to 20 T along the  $a$ -axis ( $\perp$  ladder) and up to 7 T both along the  $b$ -axis ( $\perp$  ladder-plane) and along the  $c$ -axis ( $\parallel$  ladder). A clear difference in  $H_{c2}(T)$  is observed among these three directions, indicating that this system has an anisotropic superconducting ground state. Also, it is found that  $H_{c2}^b(T)$  shows non-linearity near  $T_c$  at zero field and no saturation down to  $T/T_c \sim 0.03$ , exhibiting an upward curvature. Furthermore,  $H_{c2}^c$  is found to exceed the Pauli limit by a factor of more than 2. This fact suggests a possibility of triplet superconductivity. © 2001 Elsevier Science B.V. All rights reserved.

**Keywords:** Spin ladders; Superconductors; Low-dimensional system; High pressure

Since the discovery of superconductivity in the hole-doped two-leg ladder compound  $\text{Sr}_{14-x}\text{Ca}_x\text{Cu}_{24}\text{O}_{41}$  [1,2], the study of ladder materials has been one of the most attractive and active ones in the field of low-dimensional systems [3]. This spin-ladder system becomes superconducting with  $T_c \sim 5$  K in a pressure above  $\sim 3.0$  GPa, and, at present, is the only known superconducting ladder material, although its superconducting properties have been reported only in a previous paper [4], describing preliminary results for the upper critical field of the  $\text{Sr}_2\text{Ca}_{12}\text{Cu}_{24}\text{O}_{41}$  single crystal. Those results suggest that superconducting correlations along the interladder direction are stronger than along the ladder direction, although the normal state conductivity is

higher along the  $c$ -axis ( $\parallel$  ladder) than along the  $a$ -axis ( $\parallel$  interladder) [2]. However, in those experiments three different batches of the single crystal were used for each AC susceptibility measurement in the field along different axis. Therefore, a possibility still remains that the results depend on the measured batches because the superconductivity begins to appear at a certain critical pressure, the value of which may depend on the batch. In other words, it is difficult to reproduce the same high-pressure condition, which induces the superconductivity, in each measurement. In order to eliminate the above possibility, here we perform magneto-transport measurements on a single sample to clarify the anisotropy of the upper critical field of  $\text{Sr}_2\text{Ca}_{12}\text{Cu}_{24}\text{O}_{41}$ .

Single crystals of  $\text{Sr}_2\text{Ca}_{12}\text{Cu}_{24}\text{O}_{41}$  were grown by the travelling-solvent floating zone method using an infrared furnace under oxygen gas. Using a newly developed self-clamped high-pressure cell [5,6] which employs Bridgman anvils with a Teflon capsule filled with a pressure transmitting medium (a 1:1 mixture of Fluorinert FC 70 and FC 77), we can pressurize a delicate sample such as oxide or organic crystals under hydrostatic conditions up

\* Correspondence address: Department of Physics, College of Humanities and Sciences, Nihon University, 3-25-40, Sakurajosui, Setagaya-ku, Tokyo 156-8550, Japan. Tel.: + 81-3-3329-1151, ext. 5514; fax: + 81-3-5317-9432.

E-mail address: tn@chs.nihon-u.ac.jp (T. Nakanishi).

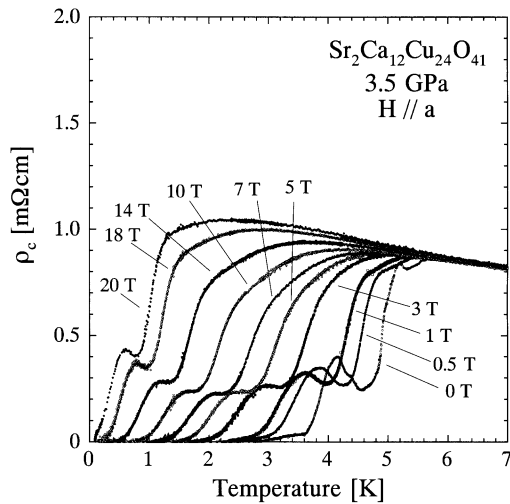


Fig. 1. Temperature dependence of resistivity along the  $c$ -axis,  $\rho_c$ , of  $\text{Sr}_2\text{Ca}_{12}\text{Cu}_{24}\text{O}_{41}$  at 3.5 GPa in various magnetic fields applied along the  $a$ -axis.

to  $\sim 6$  GPa and measure the absolute values of electrical resistivity by four-probe technique. Because of its compact body, we can attach the high-pressure cell to a dilution refrigerator which can be set in a superconducting magnet of cylindrical 20 T or horizontally rotatable split-type 7 T. By using these apparatuses, the temperature dependence of resistivity along the  $c$ -axis was measured on a single sample in fields up to 20 T along the  $a$ -axis ( $\perp$  ladder) and up to 7 T along the  $b$ -axis ( $\perp$  ladder-plane) and the  $c$ -axis ( $\parallel$  ladder) at temperatures down to  $\sim 140$  mK.

As a typical result, the temperature dependence of the resistivity along the  $c$ -axis,  $\rho_c$ , of  $\text{Sr}_2\text{Ca}_{12}\text{Cu}_{24}\text{O}_{41}$  at a pressure of 3.5 GPa in various magnetic fields applied along the  $a$ -axis up to 20 T is shown in Fig. 1. As seen in the figure, the transition shifts to lower temperatures as the magnetic field is increased although a resistive hump, the origin of which is unknown at present, is observed in the transition. Fig. 2 shows the resistive upper critical field,  $H_{c2}$  for  $H\parallel a$ , defined by several ways as illustrated in the inset. This figure indicates that essential feature of the behavior of  $H_{c2}$  is independent of the way determining  $T_c$ . From the result,  $H_{c2}$ , defined as a midpoint of the transition, is summarized in Fig. 3, together with the results for  $H\parallel b$  and  $H\parallel c$ , where the measuring current is always parallel to the  $c$ -axis. As seen in Fig. 3, the temperature dependence of  $H_{c2}$  is different for these three directions such as  $H_{c2}^a > H_{c2}^b > H_{c2}^c$  within this measured temperature and magnetic field range, which are in line with the normal state conductivity anisotropy [2,7] and in contrast to the previous result [4]. One of the possible reasons of this discrepancy may be due to the sample dependence in the previous measurements. Fig. 3 clearly

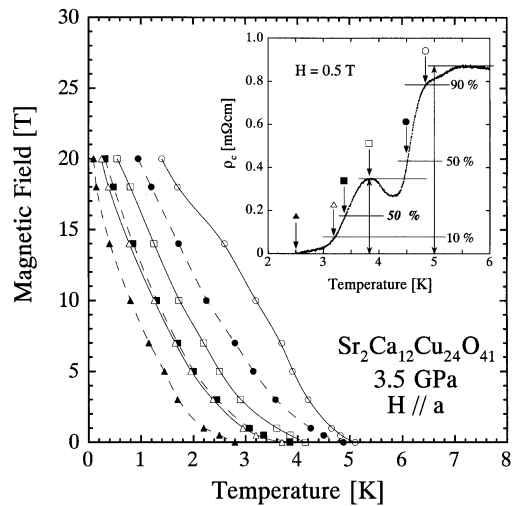


Fig. 2. Temperature dependence of the resistive upper critical field,  $H_{c2}(T)$ , of  $\text{Sr}_2\text{Ca}_{12}\text{Cu}_{24}\text{O}_{41}$  at 3.5 GPa for  $H\parallel a$ -axis, where several ways determining  $T_c$  are used as illustrated in the inset.

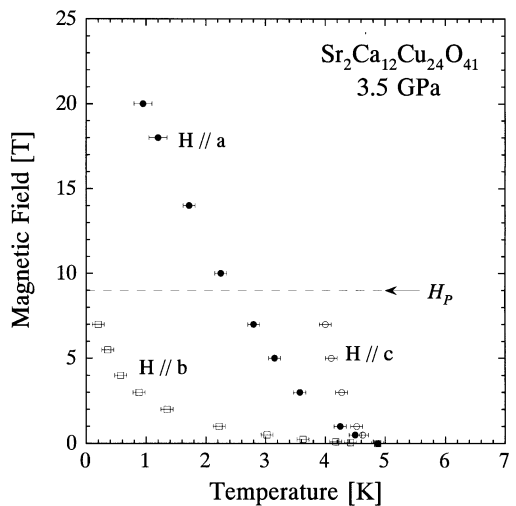


Fig. 3. Temperature dependence of the resistive upper critical field,  $H_{c2}(T)$ , of  $\text{Sr}_2\text{Ca}_{12}\text{Cu}_{24}\text{O}_{41}$  at 3.5 GPa for  $H\parallel a$ -axis (closed circles),  $H\parallel b$ -axis (open squares) and  $H\parallel c$ -axis (open circles). A broken line indicates the Pauli limit,  $H_p$ .

indicates that the superconducting phase in the present ladder system is an anisotropic one in the three directions. If we use the Werthamer–Helfand–Hohenberg formula [8] as  $H_{c2}(0) = -0.7T_c(0)(dH_{c2}/dT_c)_{T_c(0)}$  by using the slope near  $T_c(0)$ , we obtain the following estimated values:  $H_{c2}^a(0) \sim 8$  T,  $H_{c2}^b(0) \sim 0.7$  T,  $H_{c2}^c(0) \sim 27$  T which corresponds to the Ginzburg–Landau coherence length as  $\xi_a \sim 120$  Å,  $\xi_b \sim 10$  Å,  $\xi_c \sim 400$  Å. As easily

seen in Fig. 3, these estimated values of  $H_{c2}(0)$  are well below the obtained experimental values, indicating that the behavior of  $H_{c2}$  in this ladder material is not described by the conventional picture. In particular, it is found that  $H_{c2}^b$  shows non-linearity near  $T_c(0)$  and no saturation down to  $T/T_c \sim 0.03$ , exhibiting an upward curvature. These behaviors are quite different from those of conventional BCS superconductors in which  $H_{c2}$  exhibits negative curvature with saturation at low temperatures. Such anomalous temperature dependences of  $H_{c2}$  are similar to that of some high- $T_c$  superconductors (HTSC) in the case of applying magnetic fields perpendicular to the  $\text{CuO}_2$  planes, which have been recently observed in  $\text{Tl}_2\text{Ba}_2\text{CuO}_6$  [9],  $\text{Bi}_2\text{Sr}_2\text{CuO}_y$  [10] and  $\text{La}_{2-x}\text{Sr}_x\text{CuO}_4$  [11]. Thus, this anomalous behavior of  $H_{c2}$  is found to be a similarity between the ladders and HTSC in the superconducting properties in the magnetic field while some similarities in the normal state properties have been pointed out so far [3]. The other important fact seen in Fig. 3 is that  $H_{c2}^a$  exceeds the value of the Pauli limit (in this case  $\sim 9.0\text{ T}$  as indicated by a broken line in Fig. 3) by a factor of more than 2, which is given by  $H_p(T=0) = 1.84 T_c(0)$  for isotropic s-wave pairing without spin-orbit scattering [12,13] (or being reduced by a factor of 0.86 for anisotropic singlet pairing [14]). Such a large evolution of  $H_{c2}$  at low temperatures has been observed in the quasi-one-dimensional molecular superconductor  $(\text{TMTSF})_2\text{PF}_6$  [15] in which the spin-triplet pairing may be realized [16].

Therefore, the behavior of  $H_{c2}^a$  exceeding the Pauli limit suggests a possibility of triplet superconductivity in  $\text{Sr}_{14-x}\text{Ca}_x\text{Cu}_{24}\text{O}_{41}$ .

This work was supported by a Grant in Aid for Scientific Research from the Japanese Ministry of Education, Science and Culture.

## References

- [1] M. Uehara et al., J. Phys. Soc. Jpn. 65 (1996) 2764.
- [2] T. Nagata et al., Phys. Rev. Lett. 81 (1998) 1090.
- [3] E. Dagotto, Rep. Prog. Phys. 62 (1999) 1525.
- [4] T. Nakanishi et al., Physica B 281 & 282 (2000) 957.
- [5] T. Nakanishi, Ph.D. Thesis, University of Tokyo, 2000 (Chapter 2) (in Japanese).
- [6] T. Nakanishi et al., to be published.
- [7] N. Motoyama et al., Phys. Rev. 55 (1997) R3386.
- [8] N.R. Werthamer, E. Helfand, P.C. Hohenberg, Phys. Rev. 147 (1966) 295.
- [9] A.P. Mackenzie et al., Phys. Rev. Lett. 71 (1993) 1238.
- [10] M.S. Osofsky et al., Phys. Rev. Lett. 71 (1993) 2315.
- [11] Y. Ando et al., Phys. Rev. 60 (1999) 12475.
- [12] A.M. Clogston, Phys. Rev. Lett. 9 (1962) 266.
- [13] B.S. Chandrasekar, Appl. Phys. Lett. 1 (1962) 7.
- [14] Y. Hasegawa, H. Fukuyama, J. Phys. Soc. Jpn. 56 (1987) 877.
- [15] I.J. Lee et al., Phys. Rev. Lett. 78 (1997) 3555.
- [16] I.J. Lee et al., cond-mat/0001332.

## 特集—低温高圧技術の進展と物性研究—

# DAC を用いた低温物性測定

Low Temperature Measurements Using a Diamond Anvil Cell

高橋 博樹

Hiroki TAKAHASHI

Recent developments of DAC (diamond anvil cell) experiments at low temperatures are briefly reviewed. Magnetic susceptibility measurements have been improved and the SQUID system is applied to the DAC measurements. Electrical resistivity measurements in the DAC are also reviewed. A DAC is a powerful tool in the investigation of superconductors and magnetic materials.

[DAC, low temperature, magnetic susceptibility, electrical resistivity, superconductivity, high-TC superconductor]

### 1. はじめに

近年の低温高圧研究では扱いが手軽でコンパクトなクランプ型のピストンシリンダー高圧発生装置やダイヤモンドアンビルセル (DAC) 高圧発生装置などが広く使用され、学会講演等でも多くのグループによって高圧下での物性測定データが発表されている。広く普及しているピストンシリンダー型装置では試料容積を大きくとる事が可能であるが、最近の材料開発により改良されているものの、最高発生圧力は数 GPa に限られている。一方、DAC では試料容積を大きくとることは難しいが 100 GPa を越える圧力領域での研究が可能であるため多くの研究者を引きつけている。筆者は磁性や超伝導を含む強相関電子系物質の研究を専門としており、高い圧力よりも高圧下でのデータの精密さを要求される場合が多い。ピストンシリンダー型装置では試料容積を大きくとれるので静水圧下での精密測定技術はかなり確立している。DAC の場合はヘリウムガスを圧力媒体に用いることが可能であるのでむしろ静水圧性に関しては優れた面が多い。しかしながら、微量試料に対するセッティングの難しさや、微量シグナルに対する測定上の難しさなど問題点も多い。このような状況の中で実際にどのように DAC が低温高圧測定へ応用されているのかということと、現在までにどのような成果が得られているのかということについて、主に磁性、超伝導の分野について筆者のグループの成果も含めて報告する。

### 2. ダイヤモンドアンビルセル高圧発生装置

DAC は広い研究領域における高圧研究手段として用いられて久しく、専門書も出版され[1]、本誌特集記事のほか非常に多くの解説やレビュー記事[2]が書かれているのでここでは DAC そのものについては簡単な紹介にとどめる。

よく知られているように DAC は Fig. 1 に示すように、ダイヤモンドアンビルと金属ガスケットからなる部分を上下からアンビルの平行度を保ち、試料をモニターしながらスムーズに荷重をかけることのできる装置である。

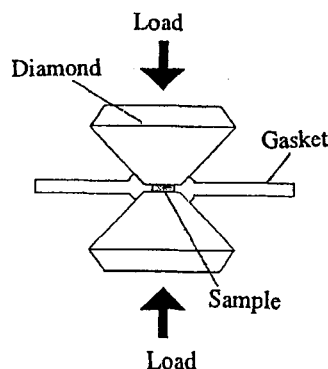


Fig. 1. Essential parts of diamond anvil cell.

〒156-8550 東京都世田谷区桜上水 3-25-40 日本大学文理学部物理・応用物理学科  
Department of Physics & Applied Physics, College of Humanities & Sciences, Nihon University, 3-25-40, Setagaya-ku, Tokyo 156-8550

荷重をかける方式としてはピストン・スクリー方式、ヘリウムガス駆動方式、レバー式、プラケット方式等が報告されている。Fig. 2 に現在われわれが使用しているピストン・スクリー方式とヘリウムガス駆動方式のDACを示す。

ピストン・スクリー方式はあらかじめ加圧装置で加圧を行い、クランプした状態で種々の測定を行う。低温実験の場合は、クランプ方式のため温度変化中に圧力が変化する可能性があることと、一つの圧力測定ごとにクライオスタットを分解しDACを取り出し圧

力を変えてまた組み上げるという煩雑な作業が伴うという弱点がある。しかしながら、この方式は装置の小型化が可能であり、構造が簡単で試料のセッティング等が簡便であることから、広く低温で使用されている。また、温度変化中の圧力変化に対しては、樹脂を加圧軸に挿入することにより温度変化による熱収縮を相殺する工夫がされている[3]。

一方、ヘリウムガス駆動方式では加圧装置を内蔵しているため、外部よりヘリウムガス圧を変化させることによって低温でも圧力を変化させることが可能である。またガス圧を微妙に変化させることによって、よりスムーズに加圧する事も可能である。また、DACを圧力を変える毎に低温装置から出し入れする必要はなく、温度変化中も圧力を一定に保てる。X線回折実験など光学系のアラインメント調整が必要な実験では、圧力変化のためのセルの取り外しによるアラインメント再調整の必要がないという利点がある。しかしながら、加圧装置を内蔵しているため装置が大きくなり低温用の試料空間に入らなかったり、十分に冷却できないという問題が生じることがある。このため加圧装置を低温部から離れたところに持ってくる工夫もなされている[4]。

### 3. 低温高压測定

#### 3.1 圧力測定

ルビー蛍光法はルビーの  $R_1$  線が圧力に対しシフトすることを利用した正確かつ簡便な DAC の圧力決定方法である。低温で注意しなければならないのは  $R_1$  線のシフトが温度変化のみで見られことである[5]。低温では圧力に対する  $R_1$  線のシフトする割合が温度によらないとみて、一定温度でのシフト量から圧力を決定している[6]。ただし、川村らによると低温におけるルビースケールは NaCl スケールとの比較によると室温での値からわずかにずれることを報告している[7]。筆者らのグループでは液体窒素温度以下の低温の圧力決定は液体窒素を用いて行っている。CuBe の熱収縮が窒素温度以下ではさほど大きくないことからそれ以下の温度では圧力は温度変化に対してほとんど変化しないと考えている。

一方、超伝導転移温度の圧力依存性から圧力を決定することも可能である。Pb や Sn など超伝導転移温度が高圧下でよく調べられている物質の帯磁率や電気抵抗を試料と同時に測定する事により圧力を決定している[8]。

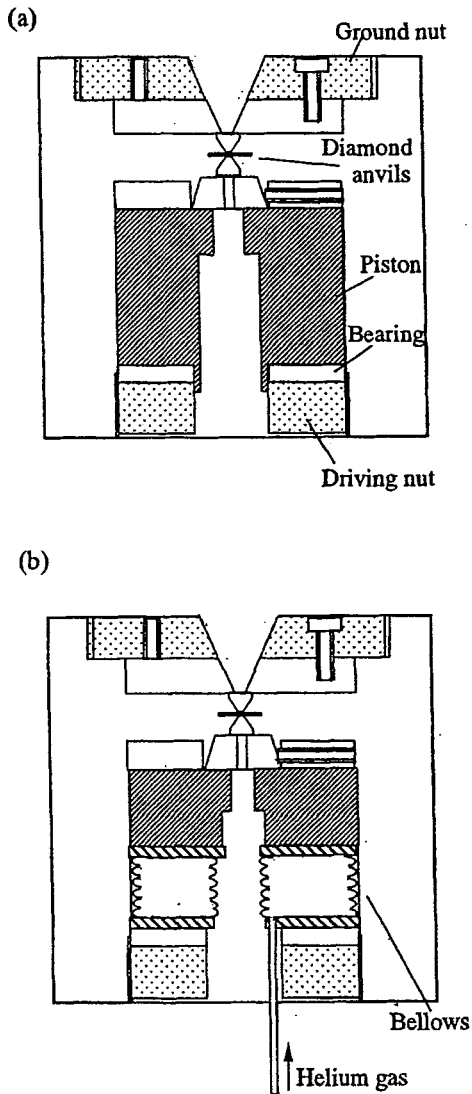


Fig. 2. Schematic view of typical diamond anvil cells, (a) piston-screw type and (b) pneumatic loading type.

### 3.2 磁氣的測定

低温高圧下での磁氣的測定は本特集号上床氏の解説に詳しく述べられている。低温高圧下では変位法、試料振動法、相互誘導法（交流帯磁率測定法）、ファラデー法などの磁氣測定法が行われているが、ここではそのなかでも DAC と組み合わせた磁氣測定について紹介する。

#### 3.2.1 交流帯磁率測定

我々のグループも含め DAC で広く行われている高圧下での磁氣測定法の一つは交流帯磁率測定である。Fig. 3 にシステム構成図を示す。試料の周りに巻いた一次コイルで交流磁場を発生し二次コイルに発生する誘導起電力を測定することで、コイルの相互インダクタンスを求め試料の帯磁率を求める。通常、ロックインアンプを用いて信号の増幅を行う。この手法はピストンシリンダー装置やキュービックアンビル装置でもよく用いられている。Fig. 4 に交流帯磁率測定に用いる DAC とコイルの構成図を示す。ここでは二次コイルと直列に巻いた補償コイルでバックグラウンド信号を打ち消している。また、二次コイルが検出する信号

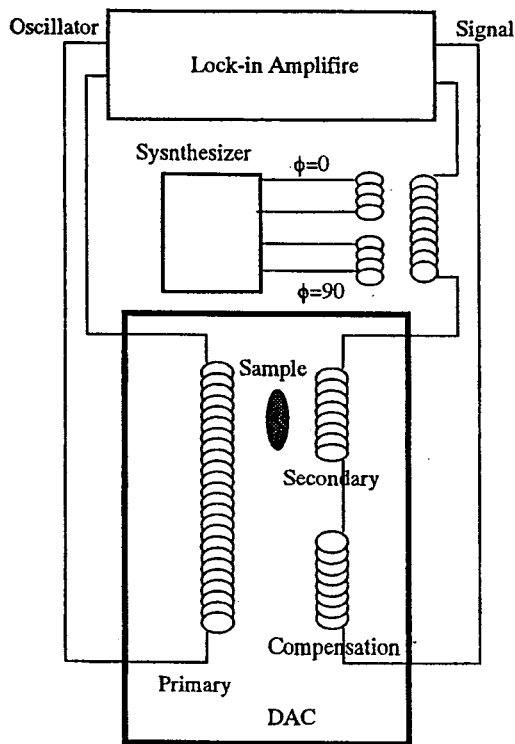


Fig. 3. AC susceptibility measurement system.

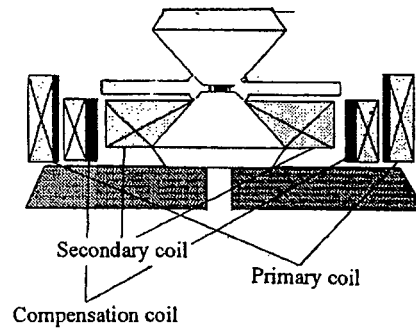


Fig. 4. AC susceptibility measurement assembly for DAC.

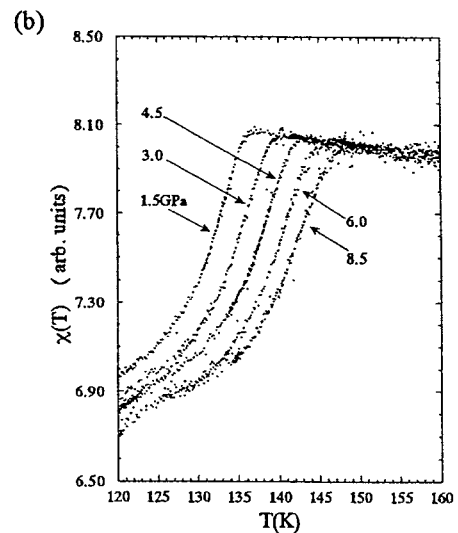
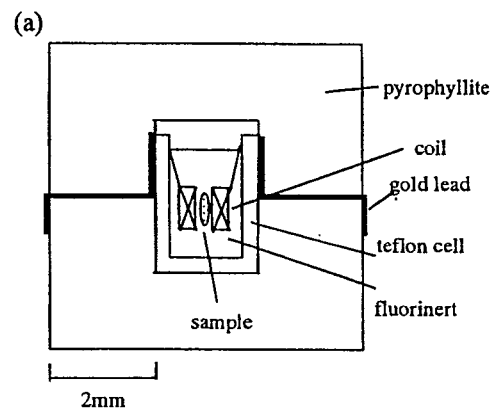


Fig. 5. (a) Assembly of AC susceptibility measurement using a cubic anvil press. (b) Pressure dependence of AC susceptibility for  $\text{HgCa}_2\text{Ba}_2\text{Cu}_3\text{O}_8$ . The superconducting transitions are observed.

は試料の双極子モーメントによる磁束の変化であり、信号強度は距離の3乗に反比例して減少する。それ故コイルをなるべく試料に近づけたほうが測定に有利となるので、Fig. 4 に示すように最も試料に近い位置に二次コイルを配置している。

ここで他の高圧装置との比較を行う。キュービックアンビルセルやピストンシリンダー型装置では圧力セルの容積が DAC よりも大きいことから、試料に二次コイルを直接巻くことも可能である。Fig. 5 にキュービックアンビルセルを用いた酸化物超伝導体  $\text{HgCa}_2\text{Ba}_2\text{Cu}_3\text{O}_8$  の交流帯磁率測定の結果を示す[9]。この物質は現在最も高い  $T_c$  を持つ物質で、高圧下で 150 K をこえる世界最高の  $T_c$  を記録した物質である。またこの超伝導転移温度の最高記録は破られていない。

キュービックアンビル装置の場合、試料の重さは 1 mg 程度であるのに対し DAC で測定する場合には試料の重さは 1  $\mu\text{g}$  の程度である。それ故 DAC の場合検出信号はきわめて小さくなる。Fig. 6 に筆者らのグル

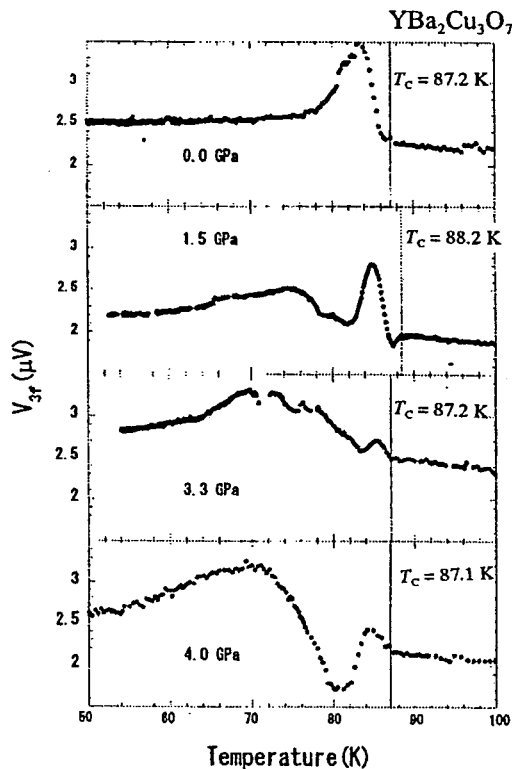


Fig. 6. Pressure dependence of AC susceptibility for  $\text{YBa}_2\text{Cu}_3\text{O}_{7-d}$  using DAC.

ープが DAC を用いて測定した  $\text{YBa}_2\text{Cu}_3\text{O}_{7-d}$  の高圧下の交流帯磁率測定の結果を示す。信号が非常に微弱であることから、ここでは三次高調波を用いて信号を検出している。三次高調波を用いることにより試料のない場合のブランク信号をほぼゼロにすることができるので高い感度で試料からの信号を検出することができる。またガスケットはバックグラウンド信号を抑えるために非磁性の材料が好ましい。我々のグループでは CuBe 合金板を使用している。その他、非磁性の Ta-W 合金、NiCrAl 合金やレニウム板などが磁性実験に用いられている。川村らはガスケットを超伝導物質で覆うことによって磁束を効率よく試料部に導入するとともにガスケットの磁気遮蔽も行っている[10]。

### 3.2.2 SQUID

Webb らはダイヤモンドのまわりに超伝導線でコイルを巻き試料の磁気モーメントの変化を SQUID マグネトメーターで検出するという高感度測定を行っている[11]。また、石塚らは SQUID マグネトメーターの検出コイルをダイヤモンドの周りに巻き、コイルをアクチュエーターで小さく振動させることにより、試料磁化の磁束勾配を高感度に検出し、高圧下での磁気測定を行っている[12]。これらの SQUID を用いた測定では原理的にきわめて微弱な磁束の変化を検出できるので感度が高く、前節でのべた交流帯磁率測定法に比べて得られる磁気的情報は多い。ただし、非常に高い感度が得られる一方、装置の構造が複雑であり、ノイズやバックグラウンドを抑えるための磁気遮蔽を注意深く行わなければならない。

また近年、非常に簡便に高精度な磁気測定のできる SQUID マグネトメーターが市販されるようになってきており、多くの研究機関に普及している。筆者の研究室でも最近 SQUID マグネトメーター (MPMS, Quantum Design 社製) を導入した。ここ数年、いくつかのグループで市販の SQUID マグネトメーターにピストンシリンダー型高圧発生装置を組み込んだ高圧下での磁気特性測定が行われている[13]。この装置では試料の位置を変位させたときの磁束の変化をコイルで検出するので、変位の際の高圧装置自身による磁束の変化を極力減らす為に高圧容器は変位方向に長い形状に設計されている。また、試料スペースが内径 9 mm に限られていることから外径は 8.5 mm に設計されている。非磁性の CuBe 合金を使用したピストンシリンダー型装置であるので発生圧力は 2 GPa 以下である。

一方、最近竹田らは外径 8.5 mm の DAC を製作し市販の SQUID マグネトメーターに組み込んで約 10

GPa 程度の圧力まで磁気測定を行っている[14]。試料が微量であるので帯磁率の微妙な変化を求めるのは困難であるが、強磁性転移や超伝導転移は検出可能である。Fig. 7 に市販の SQUID マグネトメーターを用いた圧力実験の概略図を示す。

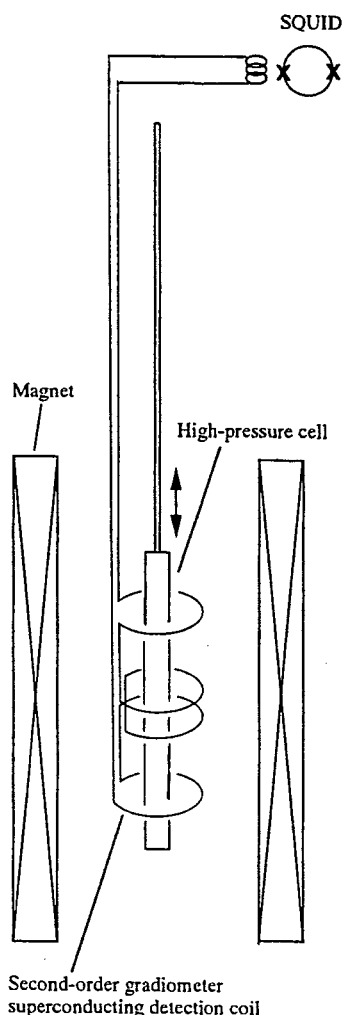


Fig. 7. Schematic drawing of MPMS SQUID magnetometer.

### 3.2.3 その他の磁気測定法

その他の高圧下の磁気測定法には変位法（引き抜き法）、試料振動法、ファラデー法（磁気天秤）等があり、クランプ型のピストンシリンダー装置を用いて測定が行われている。いずれの場合も試料とともに高圧装置全体の磁性を測定しているため、後で高圧容器の磁性を差し引くなどの磁気補償が必要である。DAC では試料からの磁気信号がきわめて小さいため、パツ

クグラウンドやノイズの扱いが難しく、これらの方法が試みられることは少ない。

### 3.3 電気的測定と高温超伝導研究

金属-絶縁体転移を示す強相関電子系物質等の研究では磁氣的測定よりも電気的測定の方が多くの情報を得られる場合がある。高圧下の電気抵抗測定は必要に応じて様々な高圧装置を使用して行われている。ガスあるいは液体媒体を直接増圧機で圧縮する装置が最も単純であるが発生圧力は 2 GPa 以下であり、またピストンシリンダー型では 3 GPa 程度の圧力まで発生可能である。また、多面体アンビル装置や対向アンビル装置では液体媒体を用いて 10 GPa 以上の圧力下での測定が可能である。

一方、DAC を用いた電気抵抗測定はいろいろなグループによって試みられている。DAC は対向アンビル装置であり、金属ガスケットを用いずに金属箔を電極として試料に重ねラッピングフィルムを圧力媒体として加圧する方法も可能である [15]。しかしながら、静水圧性をあげ高圧力をめざすためには金属ガスケットを用いる必要がある。金属ガスケットを用いた場合、電極とガスケットを絶縁するために金属ガスケットを  $\text{Al}_2\text{O}_3$  [16] やポリマー [17] などにてコーティングする方法がとられる。ガスケットの中には圧力媒体として液体媒体の他  $\text{MgO}$ ,  $\text{NaCl}$  や  $\text{CaSO}_4$  などの柔らかい粉末固体を用いる場合 [16, 18] や、試料自身を圧力媒体とする場合 [19] もある。液体媒体としてはフロリナート、Daphne オイルなどが用いられるが、最も静水圧性にすぐれているのはヘリウムガスをガスケット中に充填し圧力媒体とする場合である [20]。Fig. 8 に清水らによる液体媒体を用いた場合の試料のセッティングの様式図を示す [3]。金属試料の場合は金線や白金線を試料に溶接することで電極を形成する事ができるが、酸化物超伝導体や有機伝導体の場合は銀ペーストなどの導電性接着剤を用いてリード線を接着し電極を形成する。以上述べてきた DAC での電気抵抗測定は試料のセッティングが非常に難しくまた加圧中にリード線の断線、接触等のトラブルが起きやすいため誰でも定常的に結果を出すのは難しい。しかしながら、小型で最も高い圧力が発生可能であり、また希釈冷凍機と組み合わせたり、強磁場装置と組み合わせた測定を行うことも可能であることから今後の進展が期待される。

高温超伝導体の分野では、1986 年に  $(\text{La,Ba})_2\text{CuO}_4$  の超伝導が発見されて以来 [21]、そのメカニズムを探るために精力的に高圧実験が行われ、大きな圧力効果が報告されてきた。キュービックアンビルプレスを用

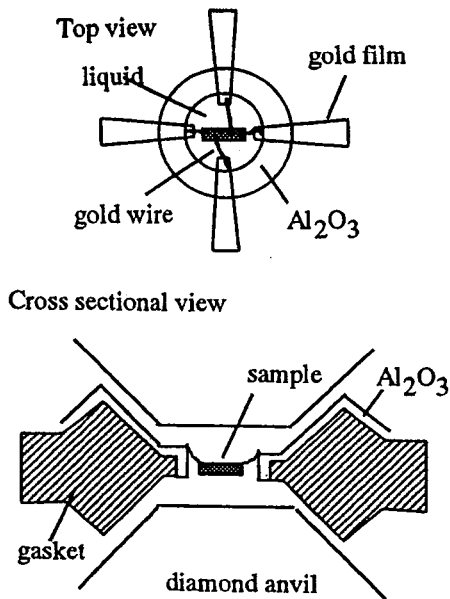


Fig. 8. Schematic drawing of the sample assembly for electrical resistivity measurement using DAC.

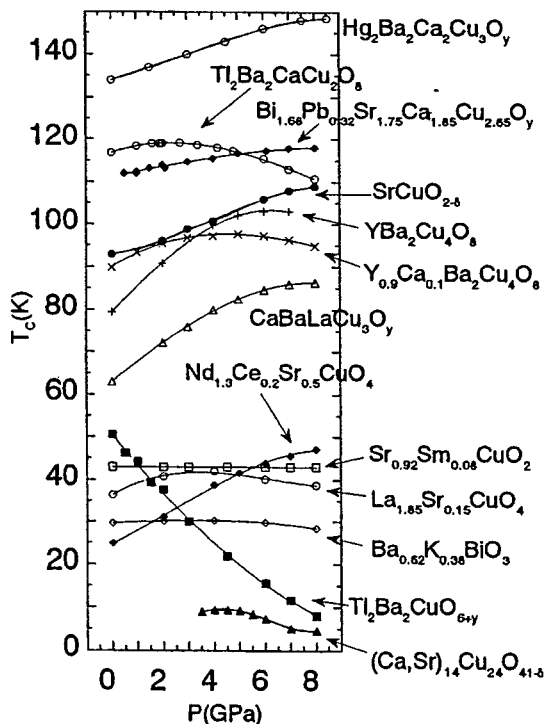


Fig. 9.  $T_c$  as a function of pressure for several high- $T_c$  superconductors.

使って筆者らが測定した結果を Fig. 9 に示す[22]。主な成果は以下の通りである。(1)  $\text{Nd}_{1.3}\text{Ce}_{0.2}\text{Sr}_{0.5}\text{CuO}_4$  などのように非常に大きな  $T_c$  の enhancement がある物質群の存在。これらの物質では、圧力によって物質中の電荷分布が変化し、伝導面である Cu-O 面にホールキャリアが大きく増加する事によって  $T_c$  が大きく増加すると考えられる。現在最高の  $T_c$  を持つ  $\text{HgBa}_2\text{Ca}_2\text{Cu}_3\text{O}_8$  の  $T_c$  が高圧下で 150 K にも達しているが、DAC を用いたの電気抵抗測定では 30 GPa で 164 K を記録している[23]。(2)  $\text{TlBa}_2\text{Cu}_2\text{O}_{6+y}$  などのように圧力で  $T_c$  が大きく抑制される物質の存在。酸化物超伝導体において 1 気圧下で元素置換によってキャリアをドーピングする場合、キャリアの増加につれて  $T_c$  は増加し、最適値をすぎると  $T_c$  は減少に転ずる。 $T_c$  の圧力による抑制はこのキャリア増加に伴う  $T_c$  の減少に関係していると考えられる。(3)  $T_c$  の圧力効果がほとんど見られない物質の存在。結晶構造的に圧力下で電荷分布が変化しにくく、Cu-O 面内の電子構造が圧力下でほとんど変化していないためと考えられる。(4)  $\text{Cu}_2\text{O}_3$  面というスピラダー面を持つ  $\text{Sr}_{14-x}\text{Ca}_x\text{Cu}_{24}\text{O}_{41}$  が高圧下で金属—絶縁体転移を示した後、超伝導になることを高圧下で初めて示した。高温超伝導体と同様に層状銅酸化物であるが、高温超伝導体とは本質的に異なる  $\text{Cu}_2\text{O}_3$  面を持つ物質であり、理論的に超伝導が予測されていたにもかかわらず、1 気圧下では成功せず、高圧下で初めて超伝導を示すことができた物質である。以上、高温超伝導体では Cu-O 伝導面が圧力下で影響を受けやすく超伝導現象に大きく影響を与えることや、圧力によって置換効果だけでは実現できない電子状態の変化が可能であることなど、新しい物理現象を調べる上で圧力が非常に有効な手段であることを示している。

最近、超伝導研究の分野では  $\text{MgB}_2$  など新物質の発見があり[24]、まだまだ新しい物質が開発される可能性が示された。圧力は物質の電荷分布や磁気的・電気的相互作用を物質の組成を変えないで制御することができるのであって、その制御領域を広げるためにはより高い圧力をめざす必要がある、DAC に対する期待は大きい。また単純な物質である酸素やイオウなどの元素が 100 GPa 付近の圧力で超伝導を示すことも DAC を用いた実験で報告されている[25]。ヘビーフェルミオンの分野でも  $\text{CeCu}_2\text{Ge}_2$  が高圧下で初めて超伝導を示すことが DAC によって示されている[26]。

#### 3.4 その他の測定

その他、本稿では詳しくとりあげなかったが、DAC

を用いた低温高压実験にはX線回折実験, X線吸収, 光学測定, メスバウワースペクトル測定や NMR などがあり, 近年の周辺装置の精密化にともなって格段の進展がある。

近年, 地球科学の分野を中心に DAC を利用した高压合成実験が活発に行われている。筆者のグループでも DAC で酸素を圧力媒体として加圧し, YAG レーザーで加熱することにより酸化物合成実験を行っている。あらかじめ DAC の周りに帯磁率測定用のコイルを巻いておくことで, 合成した試料を DAC 内に封じたまま低温高压で評価するシステムを構築している。将来, 再び低温高压関係の記事を書く機会に恵まれることがあれば高压合成と低温高压測定を組み合わせた実験に関する成果も報告したいと思う。

#### 4. おわりに

本稿では DAC を用いた磁性と超伝導に関する低温高压実験についての現状を紹介した。物質の電子状態や磁性に関しては, 精密な実験データを要求される場合が多いが, DAC の改良や測定技術の進展によってデータの質も向上してきており, これからはますます信頼度の高い実験データが出てくることを期待している。また, 本稿では紹介しなかったが, X線や光学測定は DAC の比較的得意とする分野であるので, 今後, これらの実験とうまく連携をとりながら研究を進めていくことがさらに重要になってくると思われる。

#### 謝 辞

本論を執筆するに際し, 国内外の研究事情をご教示いただいた広島大学大学院先端物質科学研究科中村文彦博士, 産業技術総合研究所竹下直博士, 大阪大学基礎工学部清水克哉博士, および振動コイルを使った SQUID について親切にご教示いただいた大阪大学極限科学センター石塚守博士に深く謝意を表します。

#### 参考文献

- [1] 箕村茂編:「超高压」共立出版実験物理学講座 18 (1988), M.I. Eremets: in *High Pressure Experimental methods* (Oxford University Press, Oxford 1996).
- [2] 特集記事: 高压力の科学と技術 No.1, 8, (1998), No.4, 9, (1999), A. Jayaraman: *Rev. Mod. Phys.*, **55**, 65 (1983).
- [3] 清水克哉, 天谷喜一: 高压力の科学と技術, **9**, 293 (1999).
- [4] R.K.W. Haselwimmer, A.W. Tyler, E. Pugh: *Rev. High Pressure Sci. Technol.*, **7**, 481 (1998).
- [5] D.M. Adams, R. Appleby, S.K. Sharma: *J.Phys. E: Sci. Instrum.*, **9**, 1140 (1976).
- [6] R.A. Noack, W.B. Holtzapfel: *High Pressure Science and Technology*, ed. By Timmerhaus and M.S.Barber (Plenum, New York, 1979), p.748 (1979).
- [7] 中野和高, 中畑功, 松井直樹, 原俊文, 小林本忠, 赤浜裕一, 川村春樹, 大石泰生: 高压力の科学と技術 **8** 特別号, 67 (1998).
- [8] B. Bireckoven, J. Wittig: *J.Phys. E:Sci. Instrum.*, **21**, 841 (1988).
- [9] H. Takahashi, A. Tokiwa-Yamamoto, N. Mōri, S. Adachi, H. Yamauchi, S. Tanaka: *Physica C***218**, 1 (1993).
- [10] H. Kawamura, T. Tachikawa: *Cryogenics*, **20**, 564 (1980).
- [11] A.W. Webb, D.U. Gubser, L.C. Towle: *Rev. Sci. Instrum.*, **47**, 59 (1976).
- [12] M. Ishizuka, S. Endo: *Rev. High Pressure Sci. Technol.*, **7**, 484 (1998).
- [13] J. Diederichs, A.K. Gangopadhyay, J.S. Schilling: *Phys. Rev.* **B54**, R9662 (1996), Y. Uwatoko, T. Hotta, E. Matsuoka, H. Mori, T. Ohki, J.L. Sarro, J.D. Thompson, N. Mori, G. Oomi: *Rev. Sci. Instrum.*, **47**, 1508 (1998).
- [14] 美藤正樹, 谷本泰三, 河江達也, 竹田和義, 中辻慎一: 高压力の科学と技術 **10** 特別号, 120 (2000).
- [15] N. Sakai, K. Takemura, K. Tsuji: *J.Phys. Soc. Jpn.*, **51**, 1811 (1982).
- [16] R.L. Reichlin: *Rev. Sci. Instrum.*, **54**, 1674 (1983).
- [17] S.W. Tozer, H. E. King, Jr.: *Rev. Sci. Instrum.*, **56**, 260 (1985).
- [18] David-Erskine, Peter Y. Yu: *Rev. Sci. Instrum.*, **58**, 406 (1987).
- [19] E.N. van Eenige, R. Griessen, R.J. Wijngaarden, J. Karpinski, E. Kaldis, R. Rusiecki, E. Jilek: *Physica C***168**, 482 (1990).
- [20] J. Thomasson, C. Ayache, I.L. Spain, M. Villedieu: *J. Appl. Phys.* **68**, 5933 (1990).
- [21] J.G. Bednorz, K.A. Muller: *Z. Phys.* **B64**, 189 (1986).
- [22] H. Takahashi, N. Mori: in *Studies of High temperature Superconductors 16*, p.1 (1996), M. Uehara, T. Nagata, J. Akimitsu, H. Takahashi, N. Mori, K. Kinoshita: *J. Phys. Soc. Jpn.*, **65**, 3764 (1996).
- [23] L. Gao, Y.Y. Xue, F. Chen, Q. Xiong, R.L. Meng, D. Ramierz, C.W. Chu, J.H. Eggert, H.K. Mao: *Phys. Rev.*

B50, 4260 (1994).

- [24] J. Nagamatsu, N. Nakazawa, T. Muranaka, Y. Zenitani, J. Akimitsu: *Nature* **410**, 63 (2001).  
[25] K. Amaya, K. Shimizu, N. Takeshita, S. Kometani,

M.I. Eremets, A. Onodera, T.C. Kobayashi, T. Mizutani, M. Ishizuka, S. Endo, M. Takai, N. Hamaya, I. Shirovani: *Rev. High Pressure Sci. Technol.*, **7**, 688 (1998).  
[2001年6月12日受理]



ELSEVIER

Journal of Magnetism and Magnetic Materials 226–230 (2001) 246–248



www.elsevier.com/locate/jmmm

# High-pressure effect on transport properties of spin-ladder compounds $\text{Na}_{1-x}\text{Ca}_x\text{V}_2\text{O}_5$ and $\text{Ca}_{0.7}\text{Li}_{0.3}\text{V}_2\text{O}_5$

H. Takahashi<sup>a,\*</sup>, T. Nakanishi<sup>a</sup>, T. Arima<sup>b</sup>, M. Noguchi<sup>b</sup>, M. Oyanagi<sup>b</sup>,  
N. Takeshita<sup>c</sup>, N. Môri<sup>c</sup>

<sup>a</sup>Department of Physics, College of Humanities and Sciences, Nihon University, 2-25-40 Sakurajousui, Setagaya-ku, Tokyo 156-8550, Japan

<sup>b</sup>Institute of Materials Science, University of Tsukuba, 1-1-1 Tennoudai, Tsukuba, Ibaraki 305-0006, Japan

<sup>c</sup>Institute for Solid State of Physics, The University of Tokyo, 5-1-5 Kashiwanoha, Kashiwa, Chiba 277-8581, Japan

## Abstract

Electrical resistivity of layered vanadium oxides  $\text{Na}_{1-x}\text{Ca}_x\text{V}_2\text{O}_5$  and  $\text{Ca}_{0.7}\text{Li}_{0.3}\text{V}_2\text{O}_5$  has been measured under high pressures of up to 10 GPa. These compounds have V–O networks forming a two-leg spin-ladder layer in some composition range. In the spin-ladder compound  $\text{Na}_{1-x}\text{Ca}_x\text{V}_2\text{O}_5$ , electrical resistivity measurements show semiconducting behavior. However, the electrical resistivity has been significantly reduced under high pressure, although it remains semiconducting up to 8 GPa. On the other hand, the electrical resistivity of  $\text{Ca}_{0.7}\text{Li}_{0.3}\text{V}_2\text{O}_5$  which also has a two-leg spin-ladder layer is lower than  $\text{Na}_{1-x}\text{Ca}_x\text{V}_2\text{O}_5$  by several orders of magnitude. The electrical resistivity of  $\text{Ca}_{0.7}\text{Li}_{0.3}\text{V}_2\text{O}_5$  was greatly reduced even at low-temperature range by applying pressure. © 2001 Elsevier Science B.V. All rights reserved.

**Keywords:** Spin ladder; Metal–insulator transition; Pressure

## 1. Introduction

Great attention has been paid to the so-called spin-ladder materials. While several cuprate high- $T_C$  superconductors have been found out, discovery of new superconducting materials is strongly desired to elucidate the high- $T_C$  mechanism and find out new superconductors having higher  $T_C$ . In such an investigation spin-ladder materials were thought to be good candidates as new superconducting systems. Spin-gap behavior which is one of the characteristic properties of cuprate superconductors was theoretically predicted [1,2] and later observed in even-leg spin-ladder materials such as  $\text{SrCu}_2\text{O}_3$  [3,4].  $\text{Sr}_{14-x}\text{Ca}_x\text{Cu}_{24}\text{O}_{41}$  has also been studied as a spin-ladder material; its electrical resistivity is greatly reduced by substituting Ca for Sr showing semiconducting behavior over the entire composition

ranges. However, insulator–metal transition occurs under high pressure. In addition to the insulator–metal transition, superconductivity was discovered at pressure larger than 4 GPa [5] with  $T_C$  increasing up to 12 K at 6 GPa. The effect of high pressure seems to play an important role for the delocalization of carriers in the ladder layer. Although the characterization of this superconductivity is difficult due to the necessity of a high-pressure technique, a recent advanced high-pressure technique revealed the magnetic properties of this superconducting material [6].

Recently, doping effects on vanadate spin-ladder materials have been intensively investigated in relation to low-dimensional magnetic and electronic properties [7,8]: spin-gap behavior has been reported in  $\text{CaV}_2\text{O}_5$  [9], and substitution of Na for Ca has been achieved, leading to a greatly reduced electrical resistivity in the  $\text{Na}_{1-x}\text{Ca}_x\text{V}_2\text{O}_5$  system [10,11]. However, they show semiconducting behavior over the entire substitution range. Hence, high-pressure techniques are expected to be a powerful tool to study metallization in this system. Here we report the pressure effects on the electrical

\* Corresponding author. Fax: + 81-3-5317-9432.

E-mail address: hiroki@chs.nihon-u.ac.jp (H. Takahashi).

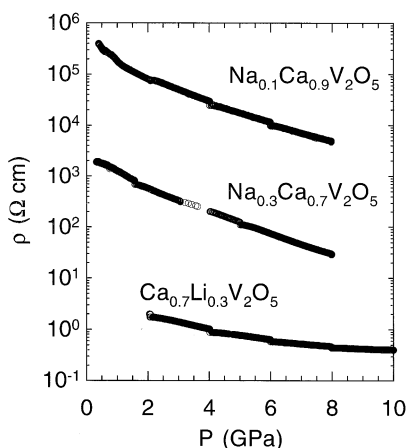


Fig. 1. Pressure dependence of the electrical resistivity for  $\text{Na}_{0.1}\text{Ca}_{0.9}\text{V}_2\text{O}_5$ ,  $\text{Na}_{0.3}\text{Ca}_{0.7}\text{V}_2\text{O}_5$ , and  $\text{Ca}_{0.7}\text{Li}_{0.3}\text{V}_2\text{O}_5$ .

resistivity of this system and lately synthesized  $\text{Ca}_{0.7}\text{Li}_{0.3}\text{V}_2\text{O}_5$ . The electrical resistivity of  $\text{Ca}_{0.7}\text{Li}_{0.3}\text{V}_2\text{O}_5$  is much smaller than that for the  $\text{Ca}_{1-x}\text{Na}_x\text{V}_2\text{O}_5$  system.

Polycrystalline samples of  $\text{Na}_{1-x}\text{Ca}_x\text{V}_2\text{O}_5$  and  $\text{Ca}_{0.7}\text{Li}_{0.3}\text{V}_2\text{O}_5$  have been synthesized under high-pressure conditions. The lattice constants along the  $a$  and  $b$ -axis remain almost constant with changing  $x$ , while the one along the  $c$ -axis decreases with decreasing  $x$ . Details of sample preparations are described elsewhere [10,11]. Electrical resistivity measurements were carried out under high pressures at low temperature by means of a DC four-probe technique. A cubic-anvil apparatus was used to generate hydrostatic pressures up to 10 GPa at temperatures down to 4 K. During these measurements the

pressure was controlled to be kept constant on both cooling and heating processes.

Fig. 1 shows the pressure dependence of the electrical resistivity at room temperature for  $\text{Na}_{0.1}\text{Ca}_{0.9}\text{V}_2\text{O}_5$ ,  $\text{Na}_{0.3}\text{Ca}_{0.7}\text{V}_2\text{O}_5$ , and  $\text{Ca}_{0.7}\text{Li}_{0.3}\text{V}_2\text{O}_5$ . The electrical resistivity is greatly reduced under high pressure for each material, as shown in Fig. 1. While the electrical resistivities of  $\text{Na}_{0.1}\text{Ca}_{0.9}\text{V}_2\text{O}_5$  and  $\text{Na}_{0.3}\text{Ca}_{0.7}\text{V}_2\text{O}_5$  decrease to  $\frac{1}{100}$  the value at 8 GPa compared with the one at 1 atm, the electrical resistivity of  $\text{Ca}_{0.7}\text{Li}_{0.3}\text{V}_2\text{O}_5$  decreases to  $\frac{1}{2}$  the value at 10 GPa. Figs. 2(a) and (b) show the temperature dependence of the electrical resistivity at several constant pressures for  $\text{Na}_{0.1}\text{Ca}_{0.9}\text{V}_2\text{O}_5$  and  $\text{Ca}_{0.7}\text{Li}_{0.3}\text{V}_2\text{O}_5$ , respectively. From Fig. 2(a) the electrical resistivity of  $\text{Na}_{0.1}\text{Ca}_{0.9}\text{V}_2\text{O}_5$  decreases with pressure and the shape of the  $\rho(T)$  curve does not change significantly up to the maximum pressure. On the other hand, it is observed from Fig. 2(b) that the electrical resistivity of  $\text{Ca}_{0.7}\text{Li}_{0.3}\text{V}_2\text{O}_5$  decreases with pressure especially in the low-temperature range. However, the electrical resistivity still displays semiconducting behavior even at the maximum pressure of 10 GPa.

In spin-ladder materials it is thought that the conduction of carriers occurs through the ladder layer. All these experiments make it clear that the pressure plays an important role in delocalizing carriers in the ladder layer, which is similar to the pressure effect observed in the  $\text{Sr}_{14-x}\text{Ca}_x\text{Cu}_{24}\text{O}_{41}$  system. From Fig. 1 the lowest resistivity for  $\text{Ca}_{0.7}\text{Li}_{0.3}\text{V}_2\text{O}_5$  is  $4 \times 10^{-1} \Omega \text{ cm}$  at 300 K and 10 GPa. In the superconducting  $\text{Sr}_{2.5}\text{Ca}_{11.5}\text{Cu}_{24}\text{O}_{41}$  spin-ladder system, the electrical resistivity is about  $4 \times 10^{-4} \Omega \text{ cm}$  at 300 K and 3 GPa [12]. The electrical resistivity in usual high- $T_C$  superconductors is less than  $1 \times 10^{-3} \Omega \text{ cm}$  at 300 K. Thus, further carrier doping and/or applying higher pressure are thought to be necessary to give rise to the insulator-metal transition in this

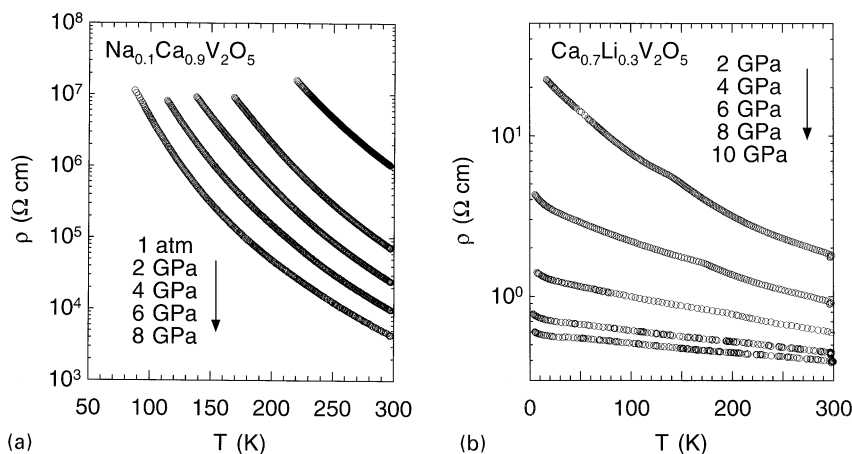


Fig. 2. Temperature dependence of the electrical resistivity for (a)  $\text{Na}_{0.1}\text{Ca}_{0.9}\text{V}_2\text{O}_5$  and (b)  $\text{Ca}_{0.7}\text{Li}_{0.3}\text{V}_2\text{O}_5$  measured at constant pressures, respectively.

system. Superconductivity is also expected in such a metallic phase.

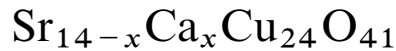
This work was partly supported by Grant-in-Aid Nos. 10440114 and 11554015 from the Ministry of Education, Science and Culture of Japan.

## References

- [1] E. Dagotto, J. Riera, D. Scalapino, *Phys. Rev. B* 45 (1992) 5744.
- [2] T.M. Rice, S. Gopalan, M. Sigrist, *Europhys. Lett.* 23 (1993) 445.
- [3] M. Azuma, Z. Hiroi, M. Takano, K. Ishida, Y. Kitaoka, *Phys. Rev. Lett.* 73 (1994) 3463.
- [4] K. Ishida, Y. Kitaoka, K. Asayama, M. Azuma, Z. Hiroi, M. Takano, *J. Phys. Soc. Japan* 63 (1994) 3222.
- [5] M. Uehara, T. Nagata, J. Akimitsu, H. Takahashi, N. Môri, K. Kinoshita, *J. Phys. Soc. Japan* 65 (1996) 3764.
- [6] T. Nakanishi, N. Motoyama, H. Mitamura, N. Takeshita, H. Takahashi, H. Eisaki, S. Uchida, T. Goto, H. Ishimoto and N. Môri, in this volume.
- [7] H. Iwase, M. Isobe, Y. Ueda, H. Yasuoka, *J. Phys. Soc. Japan* 65 (1996) 2397.
- [8] M. Onoda, N. Nishiguchi, *J. Solid State Chem.* 127 (1996) 359.
- [9] M. Isobe, Y. Ueda, *J. Magn. Magn. Mat.* 177–181 (1998) 671.
- [10] P.N. Rogers, R.N. Shelton, *Solid State Commun.* 114 (2000) 607.
- [11] T. Arima and M. Noguchi, private communication.
- [12] T. Nagata, M. Uehara, J. Goto, J. Akimitsu, N. Motoyama, H. Eisaki, S. Uchida, H. Takahashi, T. Nakanishi, N. Môri, *Phys. Rev. Lett.* 81 (1998) 1090.



# Anisotropy of the upper critical field of the spin-ladder



T. Nakanishi<sup>a,b,\*</sup>, N. Motoyama<sup>c</sup>, H. Mitamura<sup>a</sup>, N. Takeshita<sup>a</sup>, H. Takahashi<sup>b</sup>,  
H. Eisaki<sup>c</sup>, S. Uchida<sup>c</sup>, T. Goto<sup>a</sup>, H. Ishimoto<sup>a</sup>, N. Môri<sup>a</sup>

<sup>a</sup>*Institute for Solid State Physics, University of Tokyo, Kashiwa-shi, Chiba 277-8581, Japan*

<sup>b</sup>*Department of Physics, College of Humanities and Sciences, Nihon University, 3-25-40 Sakurajosui, Setagaya-ku, Tokyo 156-8550, Japan*

<sup>c</sup>*Department of Superconductivity, University of Tokyo, Tokyo 113-8656, Japan*

## Abstract

We report on the resistive upper critical field,  $H_{c2}(T)$  for the hole-doped two-leg ladder  $\text{Sr}_{14-x}\text{Ca}_x\text{Cu}_{24}\text{O}_{41}$  ( $x = 12$ ) single crystal, which becomes superconducting with  $T_c \sim 5$  K in a pressure above  $\sim 3.0$  GPa. From the results of magneto-transport measurements on a single sample at a pressure of 3.5 GPa,  $H_{c2}(T)$  has been determined up to 20 T along the  $a$ -axis ( $\perp$  ladder) and up to 7 T both along the  $b$ -axis ( $\perp$  ladder-plane) and along the  $c$ -axis ( $\parallel$  ladder). A clear difference in  $H_{c2}(T)$  is observed among these three directions, indicating that this system has an anisotropic superconducting ground state. Also, it is found that  $H_{c2}^b(T)$  shows non-linearity near  $T_c$  at zero field and no saturation down to  $T/T_c \sim 0.03$ , exhibiting an upward curvature. Furthermore,  $H_{c2}^c$  is found to exceed the Pauli limit by a factor of more than 2. This fact suggests a possibility of triplet superconductivity. © 2001 Elsevier Science B.V. All rights reserved.

**Keywords:** Spin ladders; Superconductors; Low-dimensional system; High pressure

Since the discovery of superconductivity in the hole-doped two-leg ladder compound  $\text{Sr}_{14-x}\text{Ca}_x\text{Cu}_{24}\text{O}_{41}$  [1,2], the study of ladder materials has been one of the most attractive and active ones in the field of low-dimensional systems [3]. This spin-ladder system becomes superconducting with  $T_c \sim 5$  K in a pressure above  $\sim 3.0$  GPa, and, at present, is the only known superconducting ladder material, although its superconducting properties have been reported only in a previous paper [4], describing preliminary results for the upper critical field of the  $\text{Sr}_2\text{Ca}_{12}\text{Cu}_{24}\text{O}_{41}$  single crystal. Those results suggest that superconducting correlations along the interladder direction are stronger than along the ladder direction, although the normal state conductivity is

higher along the  $c$ -axis ( $\parallel$  ladder) than along the  $a$ -axis ( $\parallel$  interladder) [2]. However, in those experiments three different batches of the single crystal were used for each AC susceptibility measurement in the field along different axis. Therefore, a possibility still remains that the results depend on the measured batches because the superconductivity begins to appear at a certain critical pressure, the value of which may depend on the batch. In other words, it is difficult to reproduce the same high-pressure condition, which induces the superconductivity, in each measurement. In order to eliminate the above possibility, here we perform magneto-transport measurements on a single sample to clarify the anisotropy of the upper critical field of  $\text{Sr}_2\text{Ca}_{12}\text{Cu}_{24}\text{O}_{41}$ .

Single crystals of  $\text{Sr}_2\text{Ca}_{12}\text{Cu}_{24}\text{O}_{41}$  were grown by the travelling-solvent floating zone method using an infrared furnace under oxygen gas. Using a newly developed self-clamped high-pressure cell [5,6] which employs Bridgman anvils with a Teflon capsule filled with a pressure transmitting medium (a 1:1 mixture of Fluorinert FC 70 and FC 77), we can pressurize a delicate sample such as oxide or organic crystals under hydrostatic conditions up

\* Correspondence address: Department of Physics, College of Humanities and Sciences, Nihon University, 3-25-40, Sakurajosui, Setagaya-ku, Tokyo 156-8550, Japan. Tel.: + 81-3-3329-1151, ext. 5514; fax: + 81-3-5317-9432.

E-mail address: tn@chs.nihon-u.ac.jp (T. Nakanishi).

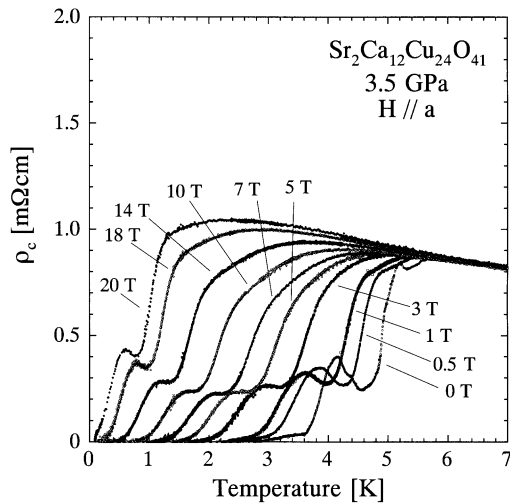


Fig. 1. Temperature dependence of resistivity along the  $c$ -axis,  $\rho_c$ , of  $\text{Sr}_2\text{Ca}_{12}\text{Cu}_{24}\text{O}_{41}$  at 3.5 GPa in various magnetic fields applied along the  $a$ -axis.

to  $\sim 6$  GPa and measure the absolute values of electrical resistivity by four-probe technique. Because of its compact body, we can attach the high-pressure cell to a dilution refrigerator which can be set in a superconducting magnet of cylindrical 20 T or horizontally rotatable split-type 7 T. By using these apparatuses, the temperature dependence of resistivity along the  $c$ -axis was measured on a single sample in fields up to 20 T along the  $a$ -axis ( $\perp$  ladder) and up to 7 T along the  $b$ -axis ( $\perp$  ladder-plane) and the  $c$ -axis ( $\parallel$  ladder) at temperatures down to  $\sim 140$  mK.

As a typical result, the temperature dependence of the resistivity along the  $c$ -axis,  $\rho_c$ , of  $\text{Sr}_2\text{Ca}_{12}\text{Cu}_{24}\text{O}_{41}$  at a pressure of 3.5 GPa in various magnetic fields applied along the  $a$ -axis up to 20 T is shown in Fig. 1. As seen in the figure, the transition shifts to lower temperatures as the magnetic field is increased although a resistive hump, the origin of which is unknown at present, is observed in the transition. Fig. 2 shows the resistive upper critical field,  $H_{c2}$  for  $H\parallel a$ , defined by several ways as illustrated in the inset. This figure indicates that essential feature of the behavior of  $H_{c2}$  is independent of the way determining  $T_c$ . From the result,  $H_{c2}$ , defined as a midpoint of the transition, is summarized in Fig. 3, together with the results for  $H\parallel b$  and  $H\parallel c$ , where the measuring current is always parallel to the  $c$ -axis. As seen in Fig. 3, the temperature dependence of  $H_{c2}$  is different for these three directions such as  $H_{c2}^a > H_{c2}^b > H_{c2}^c$  within this measured temperature and magnetic field range, which are in line with the normal state conductivity anisotropy [2,7] and in contrast to the previous result [4]. One of the possible reasons of this discrepancy may be due to the sample dependence in the previous measurements. Fig. 3 clearly

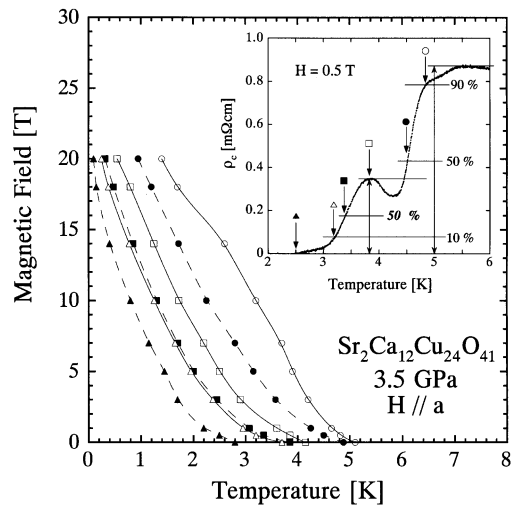


Fig. 2. Temperature dependence of the resistive upper critical field,  $H_{c2}(T)$ , of  $\text{Sr}_2\text{Ca}_{12}\text{Cu}_{24}\text{O}_{41}$  at 3.5 GPa for  $H\parallel a$ -axis, where several ways determining  $T_c$  are used as illustrated in the inset.

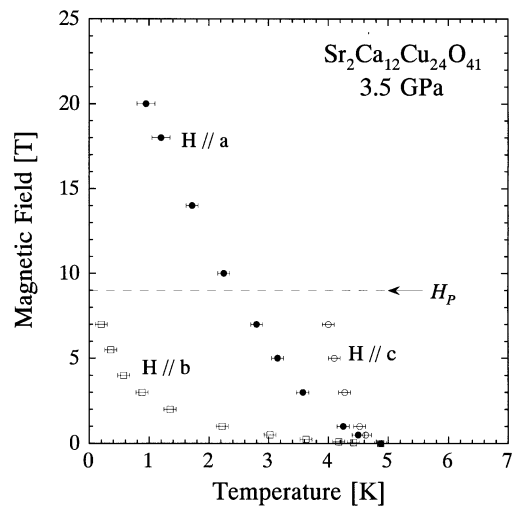


Fig. 3. Temperature dependence of the resistive upper critical field,  $H_{c2}(T)$ , of  $\text{Sr}_2\text{Ca}_{12}\text{Cu}_{24}\text{O}_{41}$  at 3.5 GPa for  $H\parallel a$ -axis (closed circles),  $H\parallel b$ -axis (open squares) and  $H\parallel c$ -axis (open circles). A broken line indicates the Pauli limit,  $H_p$ .

indicates that the superconducting phase in the present ladder system is an anisotropic one in the three directions. If we use the Werthamer–Helfand–Hohenberg formula [8] as  $H_{c2}(0) = -0.7T_c(0)(dH_{c2}/dT_c)_{T_c(0)}$  by using the slope near  $T_c(0)$ , we obtain the following estimated values:  $H_{c2}^a(0) \sim 8$  T,  $H_{c2}^b(0) \sim 0.7$  T,  $H_{c2}^c(0) \sim 27$  T which corresponds to the Ginzburg–Landau coherence length as  $\xi_a \sim 120$  Å,  $\xi_b \sim 10$  Å,  $\xi_c \sim 400$  Å. As easily

seen in Fig. 3, these estimated values of  $H_{c2}(0)$  are well below the obtained experimental values, indicating that the behavior of  $H_{c2}$  in this ladder material is not described by the conventional picture. In particular, it is found that  $H_{c2}^b$  shows non-linearity near  $T_c(0)$  and no saturation down to  $T/T_c \sim 0.03$ , exhibiting an upward curvature. These behaviors are quite different from those of conventional BCS superconductors in which  $H_{c2}$  exhibits negative curvature with saturation at low temperatures. Such anomalous temperature dependences of  $H_{c2}$  are similar to that of some high- $T_c$  superconductors (HTSC) in the case of applying magnetic fields perpendicular to the  $\text{CuO}_2$  planes, which have been recently observed in  $\text{Tl}_2\text{Ba}_2\text{CuO}_6$  [9],  $\text{Bi}_2\text{Sr}_2\text{CuO}_y$  [10] and  $\text{La}_{2-x}\text{Sr}_x\text{CuO}_4$  [11]. Thus, this anomalous behavior of  $H_{c2}$  is found to be a similarity between the ladders and HTSC in the superconducting properties in the magnetic field while some similarities in the normal state properties have been pointed out so far [3]. The other important fact seen in Fig. 3 is that  $H_{c2}^a$  exceeds the value of the Pauli limit (in this case  $\sim 9.0\text{ T}$  as indicated by a broken line in Fig. 3) by a factor of more than 2, which is given by  $H_p(T=0) = 1.84 T_c(0)$  for isotropic s-wave pairing without spin-orbit scattering [12,13] (or being reduced by a factor of 0.86 for anisotropic singlet pairing [14]). Such a large evolution of  $H_{c2}$  at low temperatures has been observed in the quasi-one-dimensional molecular superconductor  $(\text{TMTSF})_2\text{PF}_6$  [15] in which the spin-triplet pairing may be realized [16].

Therefore, the behavior of  $H_{c2}^a$  exceeding the Pauli limit suggests a possibility of triplet superconductivity in  $\text{Sr}_{14-x}\text{Ca}_x\text{Cu}_{24}\text{O}_{41}$ .

This work was supported by a Grant in Aid for Scientific Research from the Japanese Ministry of Education, Science and Culture.

## References

- [1] M. Uehara et al., J. Phys. Soc. Jpn. 65 (1996) 2764.
- [2] T. Nagata et al., Phys. Rev. Lett. 81 (1998) 1090.
- [3] E. Dagotto, Rep. Prog. Phys. 62 (1999) 1525.
- [4] T. Nakanishi et al., Physica B 281 & 282 (2000) 957.
- [5] T. Nakanishi, Ph.D. Thesis, University of Tokyo, 2000 (Chapter 2) (in Japanese).
- [6] T. Nakanishi et al., to be published.
- [7] N. Motoyama et al., Phys. Rev. 55 (1997) R3386.
- [8] N.R. Werthamer, E. Helfand, P.C. Hohenberg, Phys. Rev. 147 (1966) 295.
- [9] A.P. Mackenzie et al., Phys. Rev. Lett. 71 (1993) 1238.
- [10] M.S. Osofsky et al., Phys. Rev. Lett. 71 (1993) 2315.
- [11] Y. Ando et al., Phys. Rev. 60 (1999) 12475.
- [12] A.M. Clogston, Phys. Rev. Lett. 9 (1962) 266.
- [13] B.S. Chandrasekar, Appl. Phys. Lett. 1 (1962) 7.
- [14] Y. Hasegawa, H. Fukuyama, J. Phys. Soc. Jpn. 56 (1987) 877.
- [15] I.J. Lee et al., Phys. Rev. Lett. 78 (1997) 3555.
- [16] I.J. Lee et al., cond-mat/0001332.